Transactions of the ASME®

Transactions of the ASME, Journal of Fluids Engineering (ISSN 0098-2202) is published quarterly (Mar., June, Sept., Dec.) for $130.00 per year by The American Society of Mechanical Engineers, 345 East 47th Street, New York, NY 10017. Second class postage paid at New York, NY and additional mailing offices. POSTMASTER: Send address changes to Transactions of the ASME, Journal of Fluids Engineering, c/o THE AMERICAN SOCIETY OF MECHANICAL ENGINEERS, 22 Law Drive, Box 2300, Fairfield, NJ 07007-2300.
CHANGES OF ADDRESS must be received at Society headquarters seven weeks before they are to be effective. Please send old label and new address.
PRICES: To members, $40.00, annually: to nonmembers, $130.00. Add $24.00 for postage to countries outside the United States and Canada.
STATEMENT from By-Laws. The Society shall not be responsible for statements or opinions advanced in papers or . . . printed in its publications (B7.1, Par. 3).

INDEXED by Applied Mechanics Reviews and Engineering Information, Inc.
Canadian Goods & Services Tax Registration #126148048

Journal of Fluids Engineering

Published Quarterly by The American Society of Mechanical Engineers

VOLUME 115 • NUMBER 2 • JUNE 1993

Journal of Fluids Engineering

Technical Forum

Questions in Fluid Mechanics— Reverse Transition Phenomena in Helically Coiled Pipes

by Joseph A. C. Humphrey[1] and Donald R. Webster[1]

Since J. Thomson's pioneering studies in 1876 and 1877, on the origin of windings in rivers in alluvial plains, flows through curved conduits have been the subject of considerable fundamental and practical research. Classical contributions to the field were sequentially made by J. Eustice, W. R. Dean, C. M. White, and G. I. Taylor in the first third of this century. In particular, Taylor sought to establish the connection between the character of the motion of a fluid passing through a helically coiled pipe and the increase in friction factor arising within it relative to a corresponding straight pipe flow. The increase in friction had been attributed by some to the onset of turbulence but, in his 1928 investigation of steady streamlined flow, Dean showed theoretically that at low Reynolds number it was due to the cross-stream pressure-driven secondary motion.

In his inimitable way, Taylor proved by means of dye visualization that, as in a straight pipe, below a critical value of the Reynolds number the motion of a fluid passing through a helically coiled pipe is laminar. In fact, Taylor actually observed two values *delimiting a range* for this critical Reynolds number. The larger value corresponded to the lowest speed at which the flow in the coil appeared completely turbulent, and the smaller to the highest speed at which it displayed the first signs of irregular oscillations. Both values were observed to *exceed significantly* the approximate value of 2300 characterizing transition to turbulence in a straight pipe flow.

Taylor's findings were to provide incontrovertible support for White's earlier conjectures, based on friction factor measurements, that: (i) below a critical value of the Reynolds number, now known to correspond to the *lower* limit of the range observed by Taylor, the increase in friction for the streamlined flow through a helical coil relative to an equivalent straight pipe is due to the cross-stream secondary motion and not to turbulence, (ii) at a critical value of the Reynolds number, now known to correspond to the *upper* limit of the range observed by Taylor, the slope of the normalized friction factor curve for the flow through a coil changes abruptly when plotted against the Dean number; and, (iii) the amount by which the larger critical Reynolds number for a coil exceeds the critical value of 2300 for an equivalent straight pipe depends on the ratio between the diameter of the coiled pipe and its radius of curvature, d/R.

[1]Department of Mechanical Engineering, University of California at Berkeley, Berkeley, CA 94720.

Taylor's verification in 1929 of White's conjectures was based on a simple but rather remarkable observation: that for certain coupled geometrical and dynamical conditions, respectively characterized by d/R and the Reynolds number, a helically coiled pipe has the potential for relaminarizing a turbulent flow passing through it. Curiously, 64 years subsequent to this discovery, *the precise manner by which the relaminarization occurs remains unknown!* We base this claim on our inability to uncover in the archive literature a conclusive analysis of this problem, or of the two closely related configurations consisting of flow through a straight horizontal pipe with buoyancy or rotation driving the cross-stream motion. Thus, we pose for consideration by the fluid mechanics community a fundamental question with rather general implications: "How does a turbulent flow become laminar in passing through a helically coiled pipe?"

The reader should note that the more commonly asked question, "How does a laminar flow become turbulent in passing through a helically coiled pipe?," is *not well-posed* since, from Taylor's observations and those of others after him, the smaller critical Reynolds number for a coiled pipe is larger than the commonly accepted value for a straight pipe and, *without contrivance*, the flow entering a coiled pipe from a straight pipe will already be turbulent for a turbulent condition in the coil!

A serious consideration of the first question above begs the following additional question: "How does the relaminarized flow leaving a helically coiled pipe undergo transition to turbulence in a straight pipe?" While the answer to this question is also not precisely known, the limited data available are thought provoking. From the measurements of Sreenivasan and Strykowski (*Experiments in Fluids*, Vol. 1, pp. 31–36, 1983) it appears that for a coil with $d/R = 1/8.6$, as long as the Reynolds number remains less than 5200, approximately, the flow in the straight pipe downstream of the coil remains laminar for pipe length to diameter ratios as large as 937! Above this value of Reynolds, transition takes place spontaneously and is characterized by the appearance of slugs (discrete regions of turbulence occupying the entire pipe cross-section). What is so curious about this finding is that by the 937 diameter location the secondary motion originating in the coil is bound to be extremely small in the straight pipe and cannot be responsible for the upward shift in the critical Reynolds number for the straight pipe.

Transition and reverse transition (relaminarization) phe-

nomena are notoriously complex to explain. Ultimately, however, it is the competition between the mechanisms that respectively produce and dissipate turbulent kinetic energy, modulated by advective and redistributive transport processes, that determines the state of motion for a strongly sheared fluid. For example, from simple arguments supported by the limited data available, the first author has shown that *negative* production of turbulent kinetic energy is a significant contributor to the balance of this quantity, especially near the inner radius wall, for the high Reynolds number flow in a U-bend of square cross-section with $d/R = 1/3.35$.

Therefore, the possibility exists that, provided the rate of viscous dissipation exceeds the net rate of production of turbulent kinetic energy, the turbulent flow in a helically coiled pipe should relaminarize completely. The length of coil required for this to occur will depend on the concurrent advective and redistributive transport processes of turbulent kinetic energy. However, detailed descriptions of the mean velocity and Reynolds stress components (especially near the coil wall) necessary to quantify the magnitude and extent of turbulent kinetic energy production, positive or negative, are unavailable. Likewise, the redistributive transport processes among the Reynolds stresses remain unquantified and their relative importance unknown. Presumably, the experimental difficulties lie with the geometrical complexity of the coil which, even with a non-intrusive laser-Doppler technique, defies accurate experimentation. The theoretical difficulties lie with our current inability to predict the behavior of transitional and turbulent flows from first principles.

These difficulties notwithstanding, the flow configuration consisting of a helically coiled pipe with straight upstream and downstream tangents represents an excellent fluid mechanics paradigm for investigating many intriguing questions on transition and, especially, reverse transition phenomena.

U.S. Competitiveness: A Fluid Engineer's Viewpoint

by John F. Foss[1]

Column 3—A Contribution to U.S. Competitiveness—An Academic Initiative

This is a contribution to the series of JFE editorials addressing U.S. competitiveness in the international economic and technological arenas. Dussord[2] has set the context for the series and Werle[3] has provided insights and recommendations as one representative of the industrial community. The subsequent editorial will present the perspective of a government (viz., NASA) researcher/administrator. The present communication is written from the perspective of an academician; its purpose is to share an idea which can impact not only U.S. competitiveness but also the academic research community. It is perceived to be a new[4] idea which, if adopted, should strengthen the university and business participants.

U.S. universities presently contribute to U.S. competitiveness in their traditional roles of providing education in the engineering sciences and design and in the creation of new knowledge. These activities are well established and the requirements for their success is well understood. Werle[3] has adequately and properly addressed these contributions of the academic community.

The new idea presented here involves the introduction of a new component to the "academic research support paradigm." This paradigm, that most faculty members have accepted as a norm, holds that the granting agency pays for the creation of new knowledge and that the principal products are a student's thesis and journal publications. The current source of funds for most university research is the federal government; for the fluid mechanics community, the most significant agencies include the DOD, DOE, NASA, and the NSF. It is widely recognized (see, e.g., Bromley[5]) that these resources will not meet the future research support requests of the academic community. Hence, the portent is that many competent researchers will have to supplement the traditional (i.e., DOD, etc.) sources in order to fully utilize their intellectual creativity and to sustain their research program at a critical mass level.

The industrial sector is a candidate source of support and the new idea relates to the acquisition of this support in a novel manner. A concomitant feature of the new idea is its contribution to national competitiveness as clarified below.

The new idea can be set in contrast to a non-novel university-industry interaction. If the industrial partner serves the same role as a government agency, then the existing mechanisms to acquire and utilize the support can continue in the familiar pattern. This source of support will have minimal impact on university research programs. Specifically, the same limitations on discretionary expenditures, as described by Bromley for the federal agencies, characterize the present and anticipated situations of most members of the industrial community. A concomitant of the limited financial resources is that the existing corporate research staffs are desirous of executing that research work—which is to be carried out—in-house. In addition, for-profit organizations have little motivation to pay for work whose main result is an open publication.

The new idea is for a faculty member to work in close cooperation with industrial colleagues whose corporate responsibilities can be described as close-to-product. There are several defining attributes which characterize the responsibilities and situations of these colleagues: (i) the knowledge base to address the full range of their tasks is typically quite broad, (ii) their in-house resources (instrumentation and data acquisition/processing equipment, developed CFD codes, etc.) may not be competitive with those diagnostic and computational resources available to most faculty, and (iii) corporate entities whose responsibilities are close-to-product will (likely) have the maximum discretionary expenditure limits in the corporation.

The focused knowledge and insights of a Ph.D. researcher

[1]Department of Mechanical Engineering, Michigan State University, East Lansing, MI.

[2]Dussourd, J. L., 1992, "U.S. Technological Competitiveness: A Fluid Engineer's Viewpoint, Column 1—Gridlock Among Fluids Engineers," ASME JOURNAL OF FLUIDS ENGINEERING, Vol. 114, pp. 485-486, Dec.

[3]Werle, M. J., 1993, "U.S. Competitiveness: A Fluid Engineer's Viewpoint, Column 2—A Business/Industry Perspective on Closing the Technology/Simulation Gap," ASME JOURNAL OF FLUIDS ENGINEERING, Vol. 115, pp. 2-3, Mar.

[4]The claim of "new" derives from the writer's familiarity with many academic colleagues and the knowledge that relatively few of them practice the suggestions contained herein. Exceptions can be cited, but the claim of "new" is supported by their rarity.

[5]Bromley: D. A., 1992, "Renewing the Promise, Research-Intensive Universities and the Nation," Pres. Council of Adv. on Sci. and Tech.," suggests that the current limited funding is but the first installment of a long term contraction. NSF funding is directed toward "Emerging Technologies" . . . which fluid mechanics per se is not . . . and DOD, NASA, DOE will operate with limited budgets into the foreseeable future.

nomena are notoriously complex to explain. Ultimately, however, it is the competition between the mechanisms that respectively produce and dissipate turbulent kinetic energy, modulated by advective and redistributive transport processes, that determines the state of motion for a strongly sheared fluid. For example, from simple arguments supported by the limited data available, the first author has shown that *negative* production of turbulent kinetic energy is a significant contributor to the balance of this quantity, especially near the inner radius wall, for the high Reynolds number flow in a U-bend of square cross-section with $d/R = 1/3.35$.

Therefore, the possibility exists that, provided the rate of viscous dissipation exceeds the net rate of production of turbulent kinetic energy, the turbulent flow in a helically coiled pipe should relaminarize completely. The length of coil required for this to occur will depend on the concurrent advective and redistributive transport processes of turbulent kinetic energy. However, detailed descriptions of the mean velocity and Reynolds stress components (especially near the coil wall) necessary to quantify the magnitude and extent of turbulent kinetic energy production, positive or negative, are unavailable. Likewise, the redistributive transport processes among the Reynolds stresses remain unquantified and their relative importance unknown. Presumably, the experimental difficulties lie with the geometrical complexity of the coil which, even with a non-intrusive laser-Doppler technique, defies accurate experimentation. The theoretical difficulties lie with our current inability to predict the behavior of transitional and turbulent flows from first principles.

These difficulties notwithstanding, the flow configuration consisting of a helically coiled pipe with straight upstream and downstream tangents represents an excellent fluid mechanics paradigm for investigating many intriguing questions on transition and, especially, reverse transition phenomena.

U.S. Competitiveness: A Fluid Engineer's Viewpoint

by John F. Foss[1]

Column 3—A Contribution to U.S. Competitiveness—An Academic Initiative

This is a contribution to the series of JFE editorials addressing U.S. competitiveness in the international economic and technological arenas. Dussord[2] has set the context for the series and Werle[3] has provided insights and recommendations as one representative of the industrial community. The subsequent editorial will present the perspective of a government (viz., NASA) researcher/administrator. The present communication is written from the perspective of an academician; its purpose is to share an idea which can impact not only U.S. competitiveness but also the academic research community. It is perceived to be a new[4] idea which, if adopted, should strengthen the university and business participants.

U.S. universities presently contribute to U.S. competitiveness in their traditional roles of providing education in the engineering sciences and design and in the creation of new knowledge. These activities are well established and the requirements for their success is well understood. Werle[3] has adequately and properly addressed these contributions of the academic community.

The new idea presented here involves the introduction of a new component to the "academic research support paradigm." This paradigm, that most faculty members have accepted as a norm, holds that the granting agency pays for the creation of new knowledge and that the principal products are a student's thesis and journal publications. The current source of funds for most university research is the federal government; for the fluid mechanics community, the most significant agencies include the DOD, DOE, NASA, and the NSF. It is widely recognized (see, e.g., Bromley[5]) that these resources will not meet the future research support requests of the academic community. Hence, the portent is that many competent researchers will have to supplement the traditional (i.e., DOD, etc.) sources in order to fully utilize their intellectual creativity and to sustain their research program at a critical mass level.

The industrial sector is a candidate source of support and the new idea relates to the acquisition of this support in a novel manner. A concomitant feature of the new idea is its contribution to national competitiveness as clarified below.

The new idea can be set in contrast to a non-novel university-industry interaction. If the industrial partner serves the same role as a government agency, then the existing mechanisms to acquire and utilize the support can continue in the familiar pattern. This source of support will have minimal impact on university research programs. Specifically, the same limitations on discretionary expenditures, as described by Bromley for the federal agencies, characterize the present and anticipated situations of most members of the industrial community. A concomitant of the limited financial resources is that the existing corporate research staffs are desirous of executing that research work—which is to be carried out—in-house. In addition, for-profit organizations have little motivation to pay for work whose main result is an open publication.

The new idea is for a faculty member to work in close cooperation with industrial colleagues whose corporate responsibilities can be described as close-to-product. There are several defining attributes which characterize the responsibilities and situations of these colleagues: (i) the knowledge base to address the full range of their tasks is typically quite broad, (ii) their in-house resources (instrumentation and data acquisition/processing equipment, developed CFD codes, etc.) may not be competitive with those diagnostic and computational resources available to most faculty, and (iii) corporate entities whose responsibilities are close-to-product will (likely) have the maximum discretionary expenditure limits in the corporation.

The focused knowledge and insights of a Ph.D. researcher

[1]Department of Mechanical Engineering, Michigan State University, East Lansing, MI.

[2]Dussourd, J. L., 1992, "U.S. Technological Competitiveness: A Fluid Engineer's Viewpoint, Column 1—Gridlock Among Fluids Engineers," ASME JOURNAL OF FLUIDS ENGINEERING, Vol. 114, pp. 485-486, Dec.

[3]Werle, M. J., 1993, "U.S. Competitiveness: A Fluid Engineer's Viewpoint, Column 2—A Business/Industry Perspective on Closing the Technology/Simulation Gap," ASME JOURNAL OF FLUIDS ENGINEERING, Vol. 115, pp. 2-3, Mar.

[4]The claim of "new" derives from the writer's familiarity with many academic colleagues and the knowledge that relatively few of them practice the suggestions contained herein. Exceptions can be cited, but the claim of "new" is supported by their rarity.

[5]Bromley: D. A., 1992, "Renewing the Promise, Research-Intensive Universities and the Nation," Pres. Council of Adv. on Sci. and Tech.," suggests that the current limited funding is but the first installment of a long term contraction. NSF funding is directed toward "Emerging Technologies" . . . which fluid mechanics per se is not . . . and DOD, NASA, DOE will operate with limited budgets into the foreseeable future.

stand in contrast to the breadth of knowledge required of such an industrial colleague. Hence, the academician can be expected to make distinctive contributions (see also (ii)) when the product development task involves his/her area of expertise. Item (iii) suggests that these contributions can be readily acknowledged by appropriate payments. It is considered to be self-evident that a contribution to the close-to-product group's task is synonymous with a contribution to their competitiveness. The corresponding contribution to the researcher's program is less direct; it is identified below.

For its reference value, consider the unlikely situation that a generous benefactor provides, to a university researcher, substantial funds with the only restriction that they be spent for student support, supplies, equipment maintenance, etc. in support of the researcher's program. Such funds would, of course, be welcome. If the researcher wished to provide an in-kind return of the favor, his/her expertise could be brought to bear on issues of concern to the benefactor. It is the central thesis of the new idea that the logical equivalent of this unlikely (but favorable) situation is for the funds received from the close-to-product group to exceed the out-of-pocket expenses to execute the agreed to work statement and for the faculty member to be free to trade the application of his/her expertise for the general support of his/her research program. This conceptual plan is viable precisely because the out-of-pocket expenses may be one-half or less of a fixed price contract whose cost is competitive with alternative suppliers of similar services.

It is pertinent to note that the proposal for a new relationship between faculty members and our close-to-product industrial colleagues does not simply derive from a theoretical conception of how the world might operate; it is based upon the writer's multi-year and mutually beneficial interaction with the Ford Motor Co. In addition, the proposal is made with the conviction that the writer's successful experience is not, in principle, extraordinary. It is held as a reasonable postulate that many faculty colleagues could benefit from such relationships if they made the effect to seek them. It can also be confidently predicted that: (i) such a relationship will not spontaneously occur, and (ii) that it will not occur without the active efforts of the faculty member. A concomitant factor in the writer's successful experience, and a factor that would appear to play an important role in any similar experience for other faculty members, is the foresight of a manager to anticipate the benefits of such an interaction and his/her skill to utilize the contributions of an academician. The following suggestions to establish such a relationship are derived from the writer's experience.

The "courtship" period may involve some low-return efforts ("loss leader" in retail parlance) but a long term mutually beneficial relationship is certainly worth such an investment. The "first date" could be an exploratory visit by the faculty member to a candidate close-to-product group or the attendance of one or more of their group members at a university sponsored short course. These initial contacts and tasks may involve relatively prosaic matters; however, sustained interactions and contributions can lead to a situation in which the faculty member's in-depth knowledge is employed for the much more interesting and rewarding work of identifying new products or processes. Such efforts would constitute the "Development" side of R and D. Clearly, the most significant contributions to the company's competitiveness will come from such development efforts.

It is pertinent to identify the significant correlation between the present proposal and the well articulated suggestions by M. J. Werle in the preceding JFE editorial.[3] He notes the futility of a "technology push from the research end" which contrasts with the effectiveness of the "business pull from the products and services end." The individuals who best understand the "business pull" are clearly our colleagues in the close-to-product groups. The present suggestion, the "new" concept, that faculty serve the needs of industry in exchange for indirect financial support of their research, was not addressed by Werle.

Finally, and to the point of U.S. competitiveness, the writer is comfortable with the prediction that if this proposal were widely implemented, the extant intellectual resources resident in our universities would make a significant impact on the products and processes of our industrial sector. For those who are familiar with the relationship between German universities and their industrial community, the present proposal will also be buttressed by the recognition that such relationships are common practices in an obviously successful modern industrial state.

Research Directions in Concentrated Suspensions[1]

by Alan L. Graham,[2] Lisa A. Mondy,[3] James R. Abbott,[4] and Howard Brenner[5]

The microstructure of a concentrated suspension influences the macroscopic rheological properties of that suspension. In turn, the flow of the suspension influences the microstructure in a tightly coupled reciprocal process. In both suspension rheometry and the processing of filled systems, the common assumption is that the suspended particles are distributed randomly and homogeneously. For example, conventional viscometers, which impose macroscopic flow fields, are traditionally used to measure the viscosities of suspensions. This viscosity, in many cases, may not be that of the homogeneous suspension originally introduced into the viscometer, but rather may represent a property governed by the flow-induced, inhomogeneous structure created by the inhomogeneous flow. Such structures may be intrinsically different for various classes of flow fields associated with different viscometers.

Migration and ordering of suspended particles have been hypothesized to create viscosity measurements that vary with the total strain to which a given suspension has been subjected (e.g., Leighton and Acrivos, 1987). Microstructural changes

[1]This work was sponsored by the U.S. Department of Energy, at Los Alamos National Laboratory, under Contract W-7405-ENG-36 with the University of California and at Sandia National Laboratories, under Contract DE-AC04-76DP00789. All the authors gratefully acknowledge support for this work from Division of Engineering and Geosciences, Office of Basic Energy Sciences, the U.S. Department of Energy. Work at Los Alamos and Sandia National Laboratories was also partially supported by the Office of Naval Research.

[2]Los Alamos National Laboratory, Los Alamos, New Mexico 87545.
[3]Sandia National Laboratories, Albuquerque, New Mexico 87185.
[4]Los Alamos National Laboratory, Los Alamos, New Mexico 87545.
[5]Department of Chemical Engineering, Massachusetts Institute of Technology, Cambridge, MA 02139.

stand in contrast to the breadth of knowledge required of such an industrial colleague. Hence, the academician can be expected to make distinctive contributions (see also (ii)) when the product development task involves his/her area of expertise. Item (iii) suggests that these contributions can be readily acknowledged by appropriate payments. It is considered to be self-evident that a contribution to the close-to-product group's task is synonymous with a contribution to their competitiveness. The corresponding contribution to the researcher's program is less direct; it is identified below.

For its reference value, consider the unlikely situation that a generous benefactor provides, to a university researcher, substantial funds with the only restriction that they be spent for student support, supplies, equipment maintenance, etc. in support of the researcher's program. Such funds would, of course, be welcome. If the researcher wished to provide an in-kind return of the favor, his/her expertise could be brought to bear on issues of concern to the benefactor. It is the central thesis of the new idea that the logical equivalent of this unlikely (but favorable) situation is for the funds received from the close-to-product group to exceed the out-of-pocket expenses to execute the agreed to work statement and for the faculty member to be free to trade the application of his/her expertise for the general support of his/her research program. This conceptual plan is viable precisely because the out-of-pocket expenses may be one-half or less of a fixed price contract whose cost is competitive with alternative suppliers of similar services.

It is pertinent to note that the proposal for a new relationship between faculty members and our close-to-product industrial colleagues does not simply derive from a theoretical conception of how the world might operate; it is based upon the writer's multi-year and mutually beneficial interaction with the Ford Motor Co. In addition, the proposal is made with the conviction that the writer's successful experience is not, in principle, extraordinary. It is held as a reasonable postulate that many faculty colleagues could benefit from such relationships if they made the effect to seek them. It can also be confidently predicted that: (i) such a relationship will not spontaneously occur, and (ii) that it will not occur without the active efforts of the faculty member. A concomitant factor in the writer's successful experience, and a factor that would appear to play an important role in any similar experience for other faculty members, is the foresight of a manager to anticipate the benefits of such an interaction and his/her skill to utilize the contributions of an academician. The following suggestions to establish such a relationship are derived from the writer's experience.

The "courtship" period may involve some low-return efforts ("loss leader" in retail parlance) but a long term mutually beneficial relationship is certainly worth such an investment. The "first date" could be an exploratory visit by the faculty member to a candidate close-to-product group or the attendance of one or more of their group members at a university sponsored short course. These initial contacts and tasks may involve relatively prosaic matters; however, sustained interactions and contributions can lead to a situation in which the faculty member's in-depth knowledge is employed for the much more interesting and rewarding work of identifying new products or processes. Such efforts would constitute the "Development" side of R and D. Clearly, the most significant contributions to the company's competitiveness will come from such development efforts.

It is pertinent to identify the significant correlation between the present proposal and the well articulated suggestions by M. J. Werle in the preceding JFE editorial.[3] He notes the futility of a "technology push from the research end" which contrasts with the effectiveness of the "business pull from the products and services end." The individuals who best understand the "business pull" are clearly our colleagues in the close-to-product groups. The present suggestion, the "new" concept, that faculty serve the needs of industry in exchange for indirect financial support of their research, was not addressed by Werle.

Finally, and to the point of U.S. competitiveness, the writer is comfortable with the prediction that if this proposal were widely implemented, the extant intellectual resources resident in our universities would make a significant impact on the products and processes of our industrial sector. For those who are familiar with the relationship between German universities and their industrial community, the present proposal will also be buttressed by the recognition that such relationships are common practices in an obviously successful modern industrial state.

Research Directions in Concentrated Suspensions[1]

by Alan L. Graham,[2] Lisa A. Mondy,[3] James R. Abbott,[4] and Howard Brenner[5]

The microstructure of a concentrated suspension influences the macroscopic rheological properties of that suspension. In turn, the flow of the suspension influences the microstructure in a tightly coupled reciprocal process. In both suspension rheometry and the processing of filled systems, the common assumption is that the suspended particles are distributed randomly and homogeneously. For example, conventional viscometers, which impose macroscopic flow fields, are traditionally used to measure the viscosities of suspensions. This viscosity, in many cases, may not be that of the homogeneous suspension originally introduced into the viscometer, but rather may represent a property governed by the flow-induced, inhomogeneous structure created by the inhomogeneous flow. Such structures may be intrinsically different for various classes of flow fields associated with different viscometers.

Migration and ordering of suspended particles have been hypothesized to create viscosity measurements that vary with the total strain to which a given suspension has been subjected (e.g., Leighton and Acrivos, 1987). Microstructural changes

[1]This work was sponsored by the U.S. Department of Energy, at Los Alamos National Laboratory, under Contract W-7405-ENG-36 with the University of California and at Sandia National Laboratories, under Contract DE-AC04-76DP00789. All the authors gratefully acknowledge support for this work from Division of Engineering and Geosciences, Office of Basic Energy Sciences, the U.S. Department of Energy. Work at Los Alamos and Sandia National Laboratories was also partially supported by the Office of Naval Research.

[2]Los Alamos National Laboratory, Los Alamos, New Mexico 87545.
[3]Sandia National Laboratories, Albuquerque, New Mexico 87185.
[4]Los Alamos National Laboratory, Los Alamos, New Mexico 87545.
[5]Department of Chemical Engineering, Massachusetts Institute of Technology, Cambridge, MA 02139.

accompanying the shear flow of colloidal suspensions have been inferred via light- and small-angle-neutron-scattering techniques (e.g., Ackerson and Pusey, 1988; Laun et al., 1992) and more recently observed using visualization techniques using a laser sheet (Chow et al., 1993).

Noninvasive nuclear magnetic resonance imaging (NMRI) techniques have recently shown great potential for the study of two-phase flow microstructures including the measurement of both concentration and velocity distributions (Majors et al., 1989; Maneval et al., 1992). Recent experiments using NMRI show shear-induced microstructural changes in suspensions of neutrally buoyant, noncolloidal spheres (600 μm < diameter < 3.2 mm) subjected to flow between rotating concentric cylinders separated by a wide gap (Abbott et al., 1991). Wide gaps create an inhomogeneous shear flow, absent in narrow-gap Couette flow devices. The effects of particle size distribution are currently being investigated (Chow et al., 1993; Husband et al., in preparation), as too are the effects of particle shape and suspending liquid rheology (currently under study at Lovelace Medical Foundation, Albuquerque).

However, the mechanism creating microstructural changes and the effect of such changes upon the macroscopic properties of dispersed systems are still not clearly understood. For example, continuum models that treat the neutrally buoyant suspensions as hypothetical single-phase fluids have little linkage to existing knowledge of the individual particle motions occurring in concentrated suspensions. Efforts to extend single-particle theory to higher particle concentrations display, for the most part, only qualitative agreement with experimental data; moreover, such theories do not predict shear-induced particle migration. More recently, researchers have undertaken to solve this problem by extending to suspension flows theories developed for granular flows (e.g. McTigue and Jenkins, 1992; Nott and Brady, 1993). Blending of these two approaches, together with a firm correlation to microrheological observations, should be a primary research objective in the future.

Theoretical developments will rely heavily on experimental data, much of which is currently unavailable. Existing data on viscometric flows should be expanded to include more complex, multidimensional flows, possessing varying amounts of shear and elongation. This future database should include information on individual particle motions, as well as velocity and concentration profiles, in order to be of maximum use to theoreticians.

Although much of our current phenomenological understanding is focused on low Reynolds number flows occurring in real suspensions, natural and industrial flows span the entire range of Reynolds numbers. Turbulence and potential flows of concentrated suspensions have received little attention and should be addressed. Similarly instabilities and heat transfer in concentrated suspensions need more experimental and theoretical development. Finally, although the fundamentals of foam and emulsion flows have been examined (e.g., Reinelt and Kraynik, 1990), further investigation is warranted to understand the behavior of concentrated dispersions where compressibility effects are important or where both phases are deformable.

References

Abbott, J. R., Tetlow, N., Graham, A. L., Altobelli, S. A., Fukushima, E., Mondy, L. A., and Stephens, T. S., 1991, "Experimental Observations of Particle Migration in Concentrated Suspensions: Couette Flow," *J. Rheol.*, Vol. 3, pp. 773–797.

Ackerson, B. J., and Pusey, P. N., 1988, "Shear-Induced Order in Suspensions of Hard-Spheres," *Phys. Rev. Lett.*, Vol. 61, pp. 1033–1036.

Chow, A. W., Ylitalo, C. M., and Leighton, D. T., 1993, "Particle Migrations and Size Segregation of Concentrated Bimodal and Polydisperse Suspensions in Tube Flow," manuscript in preparation.

Husband, D. M., Ganani, E., Mondy, L. A., and Graham, A. L., 1993, "Particle Migration in Concentrated Suspensions of Bimodel Spheres: Pipe, Couette, and Open Surface Flows," submitted to *Rheo. Acta*.

Laun, H. M., Bung, R., Hadicke, E., and Hingmann, R., 1992, "Rheology and Shear-Induced Particle Structures of Concentrated Electrostatically Stabilized Polymer Dispersions," *Theoretical and Applied Rheology*, Vol. 2, P. Moldenaers and R. Keunings, eds.), pp. 616–618, Elsevier, New York.

Leighton, D. T., and Acrivos, A., 1987, "The Shear-Induced Migration of Particles in Concentrated Suspensions," *J. Fluid Mech.*, Vol. 18, pp. 415–439.

Majors, P. D., Givler, R. C., and Fukushima, E., 1989, "Velocity and Concentration Measurements in Multiphase Flows by NMR," *J. Magn. Res.*, pp. 235–243.

Maneval, J. E., Powell, R. L., McCarthy, M. J., and McCarthy, K. L., 1992, "Magnetic Resonance Imaging of Multi-phase Systems," *Particulate Two-Phase Flow*, M. C. Roco, ed., Chapter 4, Butterworth Heinemann, Stoneham, MA.

McTigue, D. S., and Jenkins, J. T., 1992, "Channel Flow of a Concentrated Suspension," *Advances in Micromechanics of Granular Materials*, Elsevier Science Publisher, New York.

Nott, P. R., and Brady, J. F., 1993, "Pressure-Driven Flow of Suspensions: Simulation and Theory," submitted to *J. Fluid Mech.*.

Reinelt, D. A., and Kraynik, A. M., 1990, "On the Shearing Flow of Foams and Concentrated Emulsions," *J. Fluid Mech.*, Vol. 215, pp. 431–455.

Numerical Uncertainty in Fluid Flow Calculations: Needs for Future Research

by Ismail Celik[1]

Computational fluid dynamics (CFD) has established itself as a viable technique for performing research and solving engineering problems, and when used correctly, can give accurate results for many fairly complex problems. This success has led to an ever increasing number of journal publications, many code developers, and surprisingly many users in the industry. Commercial CFD packages are often marketed by claiming that a particular code can solve almost every fluid flow problem, while many users, both in industry and academia, stand aloof from quantitative error measures, instead being dazzled by colorful computer generated output. This is mostly due to insufficient education in the scientific computing discipline which often leads (intentional or not) to misuse and wrong conclusions. Every year, hundreds of papers are published in conference proceedings, and journals, on the advancement and application of CFD techniques. Whenever something is spawned in such large quantities it is very easy to lose sense of quality control. To assert quality, papers often end with a conclusion such as "good agreement is found between experiments and predictions" to which the readers have become so immune that it no longer has meaning. Unfortunately, very little information is provided about the numerical uncertainty and the experimental data are often treated as if they are 100 percent accurate.

To improve the quality of the large number of papers being published there is urgent need for implementing a policy re-

[1]Department of Mechanical and Aerospace Engineering, West Virginia University, Morgantown, WV 26505-6101.

accompanying the shear flow of colloidal suspensions have been inferred via light- and small-angle-neutron-scattering techniques (e.g., Ackerson and Pusey, 1988; Laun et al., 1992) and more recently observed using visualization techniques using a laser sheet (Chow et al., 1993).

Noninvasive nuclear magnetic resonance imaging (NMRI) techniques have recently shown great potential for the study of two-phase flow microstructures including the measurement of both concentration and velocity distributions (Majors et al., 1989; Maneval et al., 1992). Recent experiments using NMRI show shear-induced microstructural changes in suspensions of neutrally buoyant, noncolloidal spheres (600 μm < diameter < 3.2 mm) subjected to flow between rotating concentric cylinders separated by a wide gap (Abbott et al., 1991). Wide gaps create an inhomogeneous shear flow, absent in narrow-gap Couette flow devices. The effects of particle size distribution are currently being investigated (Chow et al., 1993; Husband et al., in preparation), as too are the effects of particle shape and suspending liquid rheology (currently under study at Lovelace Medical Foundation, Albuquerque).

However, the mechanism creating microstructural changes and the effect of such changes upon the macroscopic properties of dispersed systems are still not clearly understood. For example, continuum models that treat the neutrally buoyant suspensions as hypothetical single-phase fluids have little linkage to existing knowledge of the individual particle motions occurring in concentrated suspensions. Efforts to extend single-particle theory to higher particle concentrations display, for the most part, only qualitative agreement with experimental data; moreover, such theories do not predict shear-induced particle migration. More recently, researchers have undertaken to solve this problem by extending to suspension flows theories developed for granular flows (e.g. McTigue and Jenkins, 1992; Nott and Brady, 1993). Blending of these two approaches, together with a firm correlation to microrheological observations, should be a primary research objective in the future.

Theoretical developments will rely heavily on experimental data, much of which is currently unavailable. Existing data on viscometric flows should be expanded to include more complex, multidimensional flows, possessing varying amounts of shear and elongation. This future database should include information on individual particle motions, as well as velocity and concentration profiles, in order to be of maximum use to theoreticians.

Although much of our current phenomenological understanding is focused on low Reynolds number flows occurring in real suspensions, natural and industrial flows span the entire range of Reynolds numbers. Turbulence and potential flows of concentrated suspensions have received little attention and should be addressed. Similarly instabilities and heat transfer in concentrated suspensions need more experimental and theoretical development. Finally, although the fundamentals of foam and emulsion flows have been examined (e.g., Reinelt and Kraynik, 1990), further investigation is warranted to understand the behavior of concentrated dispersions where compressibility effects are important or where both phases are deformable.

References

Abbott, J. R., Tetlow, N., Graham, A. L., Altobelli, S. A., Fukushima, E., Mondy, L. A., and Stephens, T. S., 1991, "Experimental Observations of Particle Migration in Concentrated Suspensions: Couette Flow," *J. Rheol.*, Vol. 3, pp. 773–797.

Ackerson, B. J., and Pusey, P. N., 1988, "Shear-Induced Order in Suspensions of Hard-Spheres," *Phys. Rev. Lett.*, Vol. 61, pp. 1033–1036.

Chow, A. W., Ylitalo, C. M., and Leighton, D. T., 1993, "Particle Migrations and Size Segregation of Concentrated Bimodal and Polydisperse Suspensions in Tube Flow," manuscript in preparation.

Husband, D. M., Ganani, E., Mondy, L. A., and Graham, A. L., 1993, "Particle Migration in Concentrated Suspensions of Bimodel Spheres: Pipe, Couette, and Open Surface Flows," submitted to *Rheo. Acta*.

Laun, H. M., Bung, R., Hadicke, E., and Hingmann, R., 1992, "Rheology and Shear-Induced Particle Structures of Concentrated Electrostatically Stabilized Polymer Dispersions," *Theoretical and Applied Rheology*, Vol. 2, P. Moldenaers and R. Keunings, eds.), pp. 616–618, Elsevier, New York.

Leighton, D. T., and Acrivos, A., 1987, "The Shear-Induced Migration of Particles in Concentrated Suspensions," *J. Fluid Mech.*, Vol. 18, pp. 415–439.

Majors, P. D., Givler, R. C., and Fukushima, E., 1989, "Velocity and Concentration Measurements in Multiphase Flows by NMR," *J. Magn. Res.*, pp. 235–243.

Maneval, J. E., Powell, R. L., McCarthy, M. J., and McCarthy, K. L., 1992, "Magnetic Resonance Imaging of Multi-phase Systems," *Particulate Two-Phase Flow*, M. C. Roco, ed., Chapter 4, Butterworth Heinemann, Stoneham, MA.

McTigue, D. S., and Jenkins, J. T., 1992, "Channel Flow of a Concentrated Suspension," *Advances in Micromechanics of Granular Materials*, Elsevier Science Publisher, New York.

Nott, P. R., and Brady, J. F., 1993, "Pressure-Driven Flow of Suspensions: Simulation and Theory," submitted to *J. Fluid Mech.*.

Reinelt, D. A., and Kraynik, A. M., 1990, "On the Shearing Flow of Foams and Concentrated Emulsions," *J. Fluid Mech.*, Vol. 215, pp. 431–455.

Numerical Uncertainty in Fluid Flow Calculations: Needs for Future Research

by Ismail Celik[1]

Computational fluid dynamics (CFD) has established itself as a viable technique for performing research and solving engineering problems, and when used correctly, can give accurate results for many fairly complex problems. This success has led to an ever increasing number of journal publications, many code developers, and surprisingly many users in the industry. Commercial CFD packages are often marketed by claiming that a particular code can solve almost every fluid flow problem, while many users, both in industry and academia, stand aloof from quantitative error measures, instead being dazzled by colorful computer generated output. This is mostly due to insufficient education in the scientific computing discipline which often leads (intentional or not) to misuse and wrong conclusions. Every year, hundreds of papers are published in conference proceedings, and journals, on the advancement and application of CFD techniques. Whenever something is spawned in such large quantities it is very easy to lose sense of quality control. To assert quality, papers often end with a conclusion such as "good agreement is found between experiments and predictions" to which the readers have become so immune that it no longer has meaning. Unfortunately, very little information is provided about the numerical uncertainty and the experimental data are often treated as if they are 100 percent accurate.

To improve the quality of the large number of papers being published there is urgent need for implementing a policy re-

[1]Department of Mechanical and Aerospace Engineering, West Virginia University, Morgantown, WV 26505-6101.

garding numerical uncertainty analysis (or quantitative error estimation). However, currently we lack a sound knowledge base for formulating such a policy especially concerning the fundamentals and theoretical aspects of numerical uncertainty. Unfortunately, at present, the level of effort either by individual investigators or professional organizations as well as by relevant federal agencies (e.g., NSF) is very limited for advancing the knowledge base on this important topic. The limited number of activities and publications in this area are reviewed by Celik (1992) and Celik et al. (1993).

The major topics of interest are: (i) separation of numerical errors from modeling errors (ii) identification, estimation, and reduction of numerical errors, (iii) assessment of computer codes and computational schemes with respect to numerical uncertainty-bench marking.

(i) Methods need to be devised to separate numerical errors from those inherent to mathematical models. The ideal numerical method with a sufficiently refined grid should give the "exact" solution to a well posed mathematical model (i.e., governing equations with a set of boundary conditions). If a mathematical model does not represent a physical phenomenon well even a perfect numerical solution may not agree with experimental data. An assessment of an approximate mathematical model can not be made unless the numerical errors are negligibly small. But the reduction of numerical errors requires in the limit a zero mesh size. Research is needed in the area of direct numerical simulations (DNS) using well-established mathematical models so that the approximate mathematical models, in particular the turbulence models, can be evaluated.

(ii) There is urgent need for development of methods for identifying the sources and quantification of numerical errors. On this topic the papers by Ferziger (1993) and Roache (1993) form a good basis for future research topics. Grid refinement studies and Richardson extrapolation should be extended to mixed order methods, non-uniform, non-Cartesian and unstructured grids, as well as to cases which involve shocks, discontinues, and singularities.

(iii) For proper assessment of computer codes and numerical schemes bench mark problems should be established in joint collaboration of experimentalist and computational analysts. Coupled numerical-experimental studies are needed to determine the type of experiments and quantities to be measured.

References

Celik, I., 1992, "Numerical Uncertainty in Fluid Flow Calculations: An Assessment of Current Status and Needs for Future Research," *Basic Research Needs in Fluid Mechanics*, eds., O. C. Jones and D. P. Telionis, ASME Publication FED-Vol. 134, pp. 27–30.

Celik, I., Chen, C. J., Roach, P. J., and Scheuerer, G., 1993, *Proceedings of the Symposium on Quantification of Uncertainty in Computational Fluid Dynamics*, ASME Fluids Engineering Conference, Washington, D.C., June 20–24, 1993.

Ferziger, J. H., 1993, "Estimation and Reduction of Numerical Error," *Proc. Symp. on Quantification of Uncertainty in Computational Fluid Dynamics*, eds., I. Celik, C. J. Chen, P. J. Roache, and G. Scheuerer, ASME Fluids Engineering Conference, Washington, D.C., June 20–24, 1993.

Roache, P. J., 1993, "A Method for Uniform Reporting of Grid Refinement Studies," *Proc. Symp. on Quantification of Uncertainty in Computational Fluid Dynamics*, eds., I. Celik, C. J. Chen, P. J. Roache, and G. Scheuerer, ASME Fluids Engineering Conference, Washington, D.C., June 20–24, 1993.

One-Equation Near-Wall Turbulence Modeling With the Aid of Direct Simulation Data

W. Rodi
University of Karlsruhe,
Karlsruhe, Germany

N. N. Mansour
NASA Ames Research Center,
Moffett Field, CA 94035

V. Michelassi
University of Florence,
Florence, Italy

The length scales appearing in the relations for the eddy viscosity and dissipation rate in one-equation models were evaluated from direct numerical (DNS) simulation data for developed channel and boundary-layer flow at two Reynolds numbers each. To prepare the ground for the evaluation, the distribution of the most relevant mean-flow and turbulence quantities is presented and discussed, also with respect to Reynolds-number influence and to differences between channel and boundary-layer flow. An alternative model is examined in which $(\overline{v'^2})^{1/2}$ *is used as velocity scale instead of* $k^{1/2}$*. With this velocity scale, the length scales now appearing in the model follow closely a linear relationship near the wall. The resulting length-scale relations together with a DNS based relation between* $\overline{v'^2}/k$ *and* $y^* = k^{1/2}y/\nu$ *form a new one-equation model for use in near-wall regions. The new model was tested as near wall component of a two-layer model by application to developed-channel, boundary-layer and backward-facing-step flows.*

1 Introduction

One-equation eddy-viscosity models have recently regained popularity as components of two-layer turbulence models (see e.g., Rodi, 1991). In these, one-equation models are used only near walls in the viscosity-affected region, say up to wall distances where the ratio of eddy viscosity to molecular viscosity takes values of 20 to 40, which corresponds to wall distances of up to $y^+ \approx 80$ in boundary-layer flow. Outside this near-wall region, other, more general models are employed such as the two-equation k-ϵ model or Reynolds-stress-equation models.

In existing one-equation models, the local state of the turbulence is characterized by the velocity scale $k^{1/2}$ and the length scale l. The turbulent kinetic energy k is calculated from a transport equation, while the l-distribution is prescribed empirically. In attached near-wall flows, the only Reynolds stress of importance in the momentum equations is the shear stress $-\overline{u'v'}$, which is determined from the eddy-viscosity relation

$$-\overline{u'v'} = \nu_t U_{,y} \tag{1}$$

In one-equation models, the eddy viscosity is calculated from

$$\nu_t = C_\mu k^{1/2} l_\mu \tag{2}$$

and the distribution of k from the following transport equation for k:

$$Uk_{,x} + Vk_{,y} = \left[\left(\nu + \frac{\nu_t}{\sigma_k}\right)k_{,y}\right] - \overline{u'v'}\,U_{,y} - \epsilon \tag{3}$$

The dissipation rate ϵ appearing in this equation is determined from

$$\epsilon = k^{3/2}/l_\epsilon \tag{4}$$

When the coefficient C_μ in (2) is chosen as the square of the structure parameter $\overline{u'v'}/k$ under local equilibrium conditions, the length scales l_μ and l_ϵ are the same in the log-law region, but they may differ very close to the wall. They are usually prescribed empirically by formulae of the following type

$$l_\mu = C_l y(1 - \exp(-y^*/A_\mu^*)) \tag{5}$$

$$l_\epsilon = C_l y(1 - \exp(-y^*/A_\epsilon^*)) \tag{6}$$

where

$$y^* = k^{1/2}y/\nu \tag{7}$$

and A_μ^* and A_ϵ^* are empirical constants. Hence, the length scales basically increase linearly with distance from the wall at the same rate, but their magnitude is reduced near the wall by exponential damping functions, which are similar to the van Driest damping function in the mixing-length model and are different for l_μ and l_ϵ. This is basically the model due to Wolfshtein (1969)), while Norris and Reynolds (1975)) used a different damping function for the dissipation scale l_ϵ near the wall:

$$l_\epsilon = \frac{C_l y}{1 + C_\epsilon/y^*} \tag{8}$$

Of course, the length scales grow linearly only near the wall; altogether a ramp function is assumed with a uniform l-dis-

Contributed by the Fluids Engineering Division for publication in the JOURNAL OF FLUIDS ENGINEERING. Manuscript received by the Fluids Engineering Division February 20, 1991; revised manuscript received January 19, 1993. Associate Technical Editor: D. M. Bushnell.

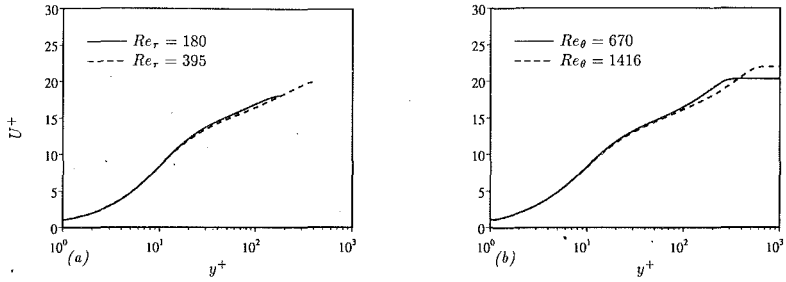

Fig. 1 Velocity profiles in wall coordinates. (*a*) channel; (*b*) boundary layer

tribution in the outer part of the flow. However, in this paper we are concerned only with one-equation modeling in the near wall region. The argument in the damping functions is taken as $y^* = k^{1/2}y/\nu$ and not $y^+ = U_\tau y/\nu$ because the functions should also work for separated flows where U_τ can go to zero.

The length-scale prescriptions (5) and (6) are based on compatibility with the universal logarithmic velocity distribution and lean heavily on experience with the mixing-length distribution near the wall, i.e., on the van Driest damping law. So far, the validity of the prescriptions could not be checked directly with the aid of data but only indirectly through their use in flow calculations. Direct numerical simulation (DNS) data are now available to test the length-scale relations directly and to form the basis for developing improved prescriptions if necessary. To this end, l_μ- and l_ϵ-distributions are calculated in this paper from DNS data for developed channel (Kim et al. 1987 and Kim, 1990) and boundary-layer (Spalart, 1988) flows at two Reynolds numbers each, and these data are compared with the existing empirical relations. The influence of the Reynolds number is thereby also examined. Following Durbin (1991)), alternative modeling with the normal fluctuations $(\overline{v'})^{1/2}$ as velocity scale instead of $k^{1/2}$ is also investigated, and a new one-equation model for near-wall use only is proposed. This new model is combined with the standard k-ϵ model in the outer flow to form a two-layer model, and calculations obtained with this are presented for developed-channel and boundary-layer flows and for separated flow over a step. The results are compared with two-layer model calculations employing the Norris-Reynolds one-equation model near the wall and with the DNS and experimental data.

2 Basic Quantities Needed for Model Evaluation

The ground for the model evaluation needs to be prepared first by providing distributions of basic quantities in channel flow and boundary layers as computed from the DNS data. Here, the influence of the Reynolds number and of the flow situation (channel flow versus boundary layer) is examined with the quantities plotted in wall coordinates. As components of two-layer models, one-equation models are mostly used for globally high-Reynolds-number situations and hence the model relations should correspond closely to such situations. Hence, it is important to examine how closely the DNS data obtained for the highest Reynolds numbers correspond to experimental data achieved at high Reynolds numbers.

All quantities to be presented in the following are made dimensionless with the friction velocity U_τ and with ν, and they are plotted against $y^+ = U_\tau y/\nu$. First, the velocity distribution is given in the usual semi-log plot in Fig. 1. For channel flow (Fig. 1(a)), there appears to be a reasonably well established log law for both Reynolds numbers, but for the lower Reynolds number ($\mathrm{Re}_\tau = 180$) the constant C in the log law is above the standard value 5, while for $\mathrm{Re}_\tau = 395$ the velocity distribution follows the standard log law over a significant part of the channel half-width. At fairly low Reynolds numbers, the increase in the log-law constant C with decreasing Reynolds number is a well-known phenomenon. For the boundary layer at the lower Reynolds number ($\mathrm{Re}_\theta = 667$), the velocity distribution follows the log law in a small region only, while at the higher Reynolds number ($\mathrm{Re}_\theta = 1416$) this region is fairly extensive (up to nearly $y^+ \approx 100$). For both channel and boundary-layer flows, the von Kármán constant derived from the data is $\kappa = 0.41$. Hence, in the higher-Reynolds-number cases, the velocity distribution corresponds to the observed distribution at much higher Reynolds numbers over a significant portion of the flow.

Figure 2 shows for channel flow the distribution of the RMS values of the fluctuating velocity components u, v, and w compared with measurements of various experiments at high Reynolds numbers, as compiled by Myong and Kasagi (1988). The measurements show considerable scatter, and extreme data points should not be considered trustworthy. The DNS data exhibit a surprising dependence on the Reynolds number even close to the wall, particularly so for the component w. However, there is a clear trend with increasing Reynolds number toward the mean of the experimental data, and the DNS data for $\mathrm{Re}_\tau = 395$ are already a fairly good representation of the high-Reynolds-number experimental data. Hence it may be concluded that the higher-Re channel flow data correspond closely to high-Re channel flow for which the quantities considered are independent of Reynolds number. In Fig. 3, the corresponding DNS data for the boundary layer are presented at two Reynolds numbers. Here a similar Re-dependence is found, and it is interesting to note that, except very close to the wall, the fluctuating velocities in the boundary layer are somewhat higher than in the channel flow. This may be due partly to the differences in the flow situation with the shear stress $-\overline{u'v'}$ falling more quickly with distance from the wall in the channel flow than in the boundary layer, but to some extent it is also due to the fact that the boundary-layer flow at $\mathrm{Re}_\theta = 1416$ represents a higher Reynolds-number case than the channel flow at $\mathrm{Re}_\tau = 395$. This can be inferred from the higher y^+- and ν_t/ν-values in the boundary layer (see Figs. 1 and 7). The ratios $\overline{u'^2}/k$, $\overline{v'^2}/k$ and $\overline{w'^2}/k$ are shown for both flows in Fig. 4. Up to $y^+ \approx 100$, there is generally little influence of the Reynolds number on these ratios, and there is also fairly good agreement between channel and boundary-layer flow. An exception is $\overline{w'^2}/k$, which has a larger dip near the wall in the channel-flow case. For the higher-Reynolds-number cases, constant values are a reasonable approximation to the data for $y^+ \geq 80$, with $\overline{u'^2}/k \approx 1$, $\overline{v'^2}/k \approx 0.41$ and $\overline{w'^2}/k \approx 0.59$. The distribution of the structure parameter $-\overline{u'v'}/k$ is given in Fig. 5. For the channel flow, the range where this parameter assumes approximately the standard value of 0.3 is much narrower than for the boundary layer. However, in the higher Re case the value of 0.3 is reached in the boundary layer only at fairly large y^+-distances.

The ratio of production to dissipation of turbulent kinetic

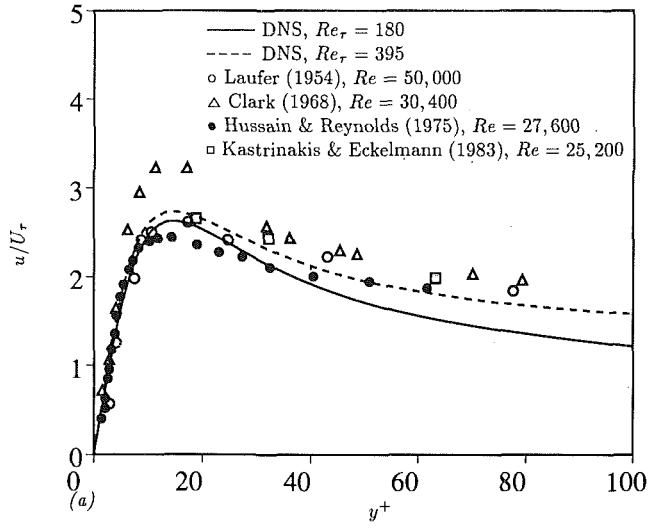

Fig. 2(a)

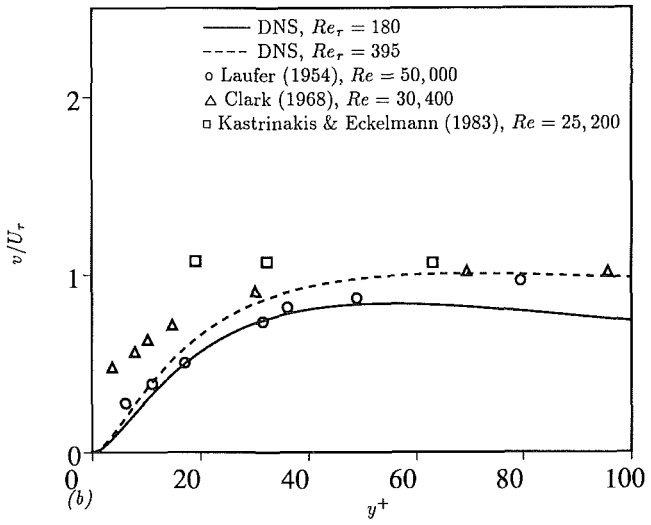

Fig. 2(b)

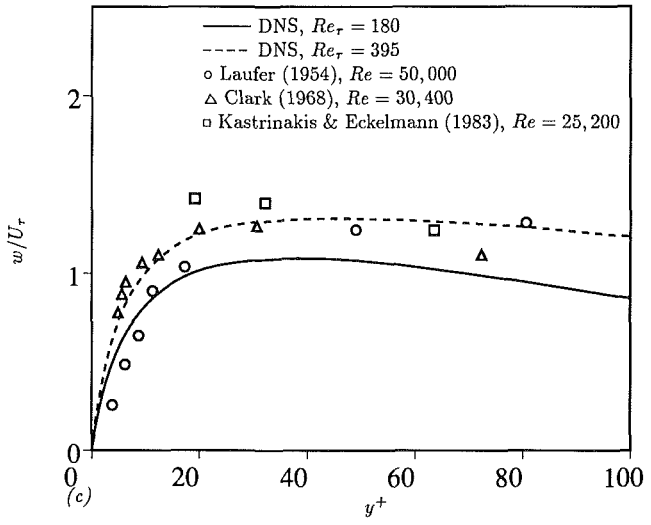

Fig. 2(c)

Fig. 2 RMS fluctuations in developed channel flow, comparison with high-Reynolds-number data compiled by Myong and Kasagi (1988)

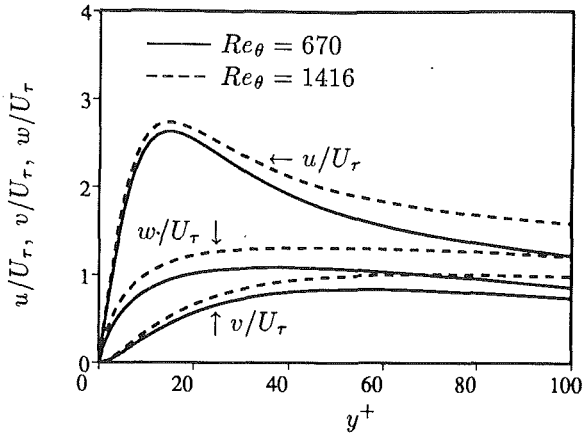

Fig. 3 RMS fluctuations in boundary layers

energy, P/ϵ, which plays an important role in modeling, is given in Fig. 6. In channel flow, a substantial region with local equilibrium ($P/\epsilon \approx 1$) is present only in the higher-Reynolds number case. For the boundary-layer situation, such a region is limited to $y^+ \approx 80 - 100$, while further away from the wall, production dominates dissipation and P/ϵ reaches a maximum of about 1.4. Finally, in Fig. 7, the ratio of turbulent to molecular viscosity, ν_t^+, is presented. The level of this quantity reached is a good indicator of the influence of viscous effects on the flow, that is whether the Reynolds number is high enough for these effects to be unimportant. Clearly the low-Re channel flow does not satisfy this criterion with ν_t^+ reaching values of only about 15. The higher-Re boundary layer reaches the highest levels of ν_t^+, as was to be expected. In the log-law region with $U_{,y}^+ = 1/\kappa y^+$, there follows from (1):

$$\nu_t^+ = -\overline{u'v'}^+ \kappa y^+ \tag{9}$$

Near the wall, ν_t^+ from the DNS data has the gradient κ, but is does not follow exactly $\nu_t^+ = \kappa y^+$ but falls below this relation because this is based on $-\overline{u'v'}^+ = 1$ while the actual shear stress is below the wall shear stress. Very near the wall, the damping of the eddy viscosity is visible, which needs to be accounted for in any turbulance model.

3 One-Equation Models Based on $k^{1/2}$ as Velocity Scale

Length scale l_μ. The nondimensional length-scale l_μ^+ defined by

$$l_\mu^+ = \frac{l_\mu U_\tau}{\nu} = \frac{\nu_t^+}{C_\mu k^{+1/2}} \tag{10}$$

was determined from the DNS data and is presented in Fig. 8. Its distribution is compared with the relationship

$$C_\mu^{3/4} l_\mu^+ = (-\overline{u'v'}^+)^{1/2} \kappa y^+ \tag{11}$$

which follows when ν_t^+ in (10) is determined from (9) based on the log law and when k^+ is assumed proportional to the shear stress $-u'v'^+$ via

$$k^+ = \frac{-\overline{u'v'}^+}{C_\mu^{1/2}} \tag{12}$$

In relation (12), $-\overline{u'v'}/k$ is the structure parameter, for which a standard value of .3 has been taken so that $C_\mu = 0.09$. In Fig. 8, actually $C_\mu^{3/4} l_\mu^+$ is plotted which corresponds to the Prandtl mixing length usually assumed to be κy^+ in the log-law region. As relation (11) assumes the log law to hold and the structure parameter $-\overline{u'v'}/k$ to have a value of 0.3, the

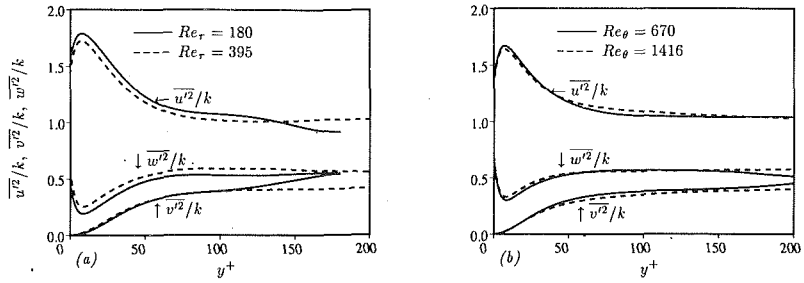

Fig. 4 Distribution of $\overline{u'^2}/k$, $\overline{v'^2}/k$, $\overline{w'^2}/k$. (*a*) channel; (*b*) boundary layer

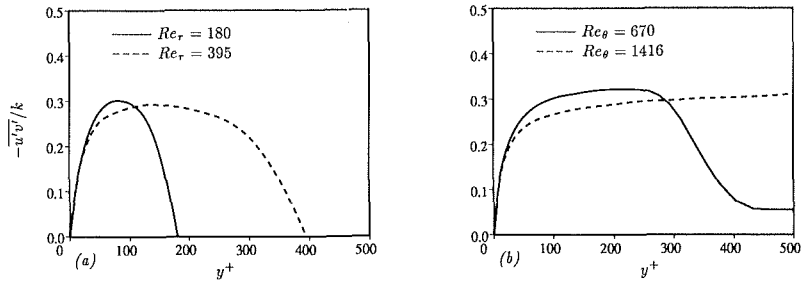

Fig. 5 Distribution of structure parameter $-\overline{u'v'}/k$. (*a*) channel; (*b*) boundary layer

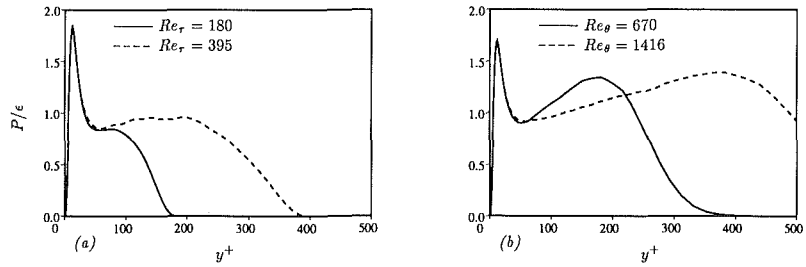

Fig. 6 Distribution of ratio of production to dissipation rate of turbulent kinetic energy P/ϵ. (*a*) channel; (*b*) boundary layer

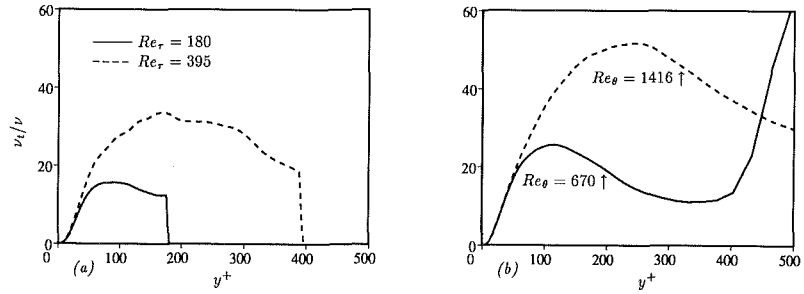

Fig. 7 Distribution of dimensionless eddy viscosity ν_t/ν. (*a*) channel; (*b*) boundary layer

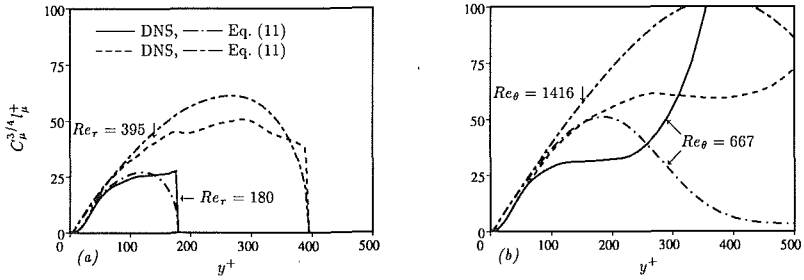

Fig. 8 Distribution of length scale $C_\mu^{3/4} l_\mu^+$. (*a*) channel; (*b*) boundary layer (see Fig. 8(*a*) for legend)

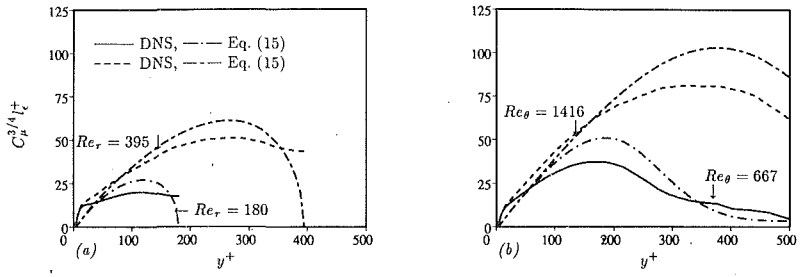

Fig. 9 Distribution of length scale $C_\mu^{3/4} l_\epsilon^+$. (*a*) channel; (*b*) boundary layer (see Fig. 9(*a*) for legend)

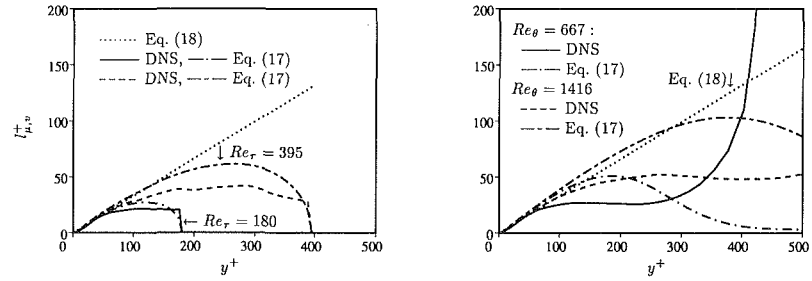

Fig. 10 Distribution of length scale $l_{\mu,v}^+$. (*a*) channel; (*b*) boundary layer

DNS data agree fairly well with this distribution in regions where these assumptions are approximately valid. Further away from the wall, the assumptions are not even approximately valid, so that there are considerable differences, particularly so for the boundary layer. The differences in the curves for the various Reynolds numbers can be much reduced when l_μ/δ is plotted versus y/δ, where δ is the shear-layer thickness (channel half-width or boundary-layer thickness). $C_\mu^{3/4} l_\mu/\delta = C_\mu^{3/4} l_\mu^+/\mathrm{Re}_\tau$ then is approximately 0.13 in the outer region of channel flow ($y/\delta > 0.4$) and 0.095 for boundary layers in the region $.4 < y/\delta < .8$. Equation (11) can be seen to approximate the l_μ-distribution reasonably well in the near-wall region, but not too close to the wall. There, l_μ falls below the distribution (11) because of the near-wall damping of turbulent momentum transfer. A damping function à la van Driest is therefore required in this region and Rodi and Mansour (1990) compared the damping function in (5) with the DNS data and proposed an improved function on the basis of these data.

Dissipation length l_ϵ. The nondimensional length scale l_ϵ^+ used for determining the dissipation rate which is defined by

$$l_\epsilon^+ = \frac{k^{+3/2}}{\epsilon^+} \tag{13}$$

is plotted in Fig. 9. When k^+ in this relation is eliminated with the aid of (12) and ϵ^+ is determined from

$$\epsilon^+ = P^+ = -\overline{u'v'}^+ U_{,y^+}^+ = \frac{-\overline{u'v'}^+}{\kappa y^+} \tag{14}$$

assuming local equilibrium and the log law to hold, there results the following relation for l_ϵ^+:

$$C_\mu^{3/4} l_\epsilon^+ = (-\overline{u'v'}^+)^{1/2} \kappa y^+ \tag{15}$$

This is identical to relation (11) for the length scale l_μ^+ showing that, under the assumptions involved in these relations, both length scales are the same. Not too close to the wall, the behavior of l_ϵ determined from the DNS data is similar to that of l_μ, but this similarity does not extend to the channel center or the boundary-layer edge. Also, close to the wall significant differences are obvious which depend strongly on the Reynolds number. (This dependence does *not* disappear when l_ϵ/δ is plotted versus y/δ). A sizable region exists where l_ϵ^+ is larger than described by Eq. (15) or even larger than the linear relation κy^+. The maximum deviation occurs at $y^+ \approx 15$, where the distribution of the dissipation rate ϵ has a plateau (see Fig. 15(*d*)). Here, existing one-equation models which reduce l_ϵ below the linear distribution through the damping functions in (6) or (8) predict a peak in ϵ as shown in Fig. 15(*d*). Judging from the DNS data, the damping functions used for l_ϵ in existing models therefore change the l_ϵ-distribution in the wrong direction.

4 New One-Equation Model Based on $(\overline{v'^2})^{1/2}$ as Velocity Scale

Durbin (1991) suggested that, in near-wall shear layers, the normal fluctuations $(\overline{v'^2})^{1/2}$ may be a better velocity scale for characterizing the turbulent motion than $k^{1/2}$ and that no damping functions may be needed when this velocity scale is used. Hence, it is intriguing to examine whether this choice of velocity scale leads to corresponding length scales which are easier to prescribe empirically. Of course, the question then also needs to be answered as to how $\overline{v'^2}$ can be related to other known quantities in the context of a one-equation model.

Length-scale $l_{\mu,v}$. When $k^{1/2}$ is replaced by $(\overline{v'^2})^{1/2}$ in the eddy-viscosity relation (2), there follows:

$$\nu_t = (\overline{v'^2})^{1/2} l_{\mu,v} \tag{16}$$

It should be noted that any constant that may occur has been absorbed in $l_{\mu,v}$. In Fig. 10, the distribution of the dimensionless length scale $l_{\mu,v}^+$ as determined from the DNS data is compared with the distribution from the following approximate formula:

$$l_{\mu,v}^+ = \frac{\nu_t^+}{(\overline{\nu'^2}^+)^{1/2}} = \frac{-\overline{u'v'}^+ \kappa y^+}{(\overline{v'^2}^+)^{1/2}} \tag{17}$$

This formula is again obtained by replacing the eddy viscosity by relation (9) based on the log law. Further, it can be seen from Fig. 3 that $\overline{v'^2}^+$ is approximately 1 not too close to the wall, and this value was inserted in relation (17) for the straight line shown in Fig. 10. The figure indicates that, for larger y^+-values, the DNS data deviate more from the approximation

curve than in the case of l_μ (see Fig. 8). However, close to the wall ($y^+ < 60$) the $l^+_{\mu,v}$ data follow much closer the approximate linear relation. Hence, there is considerably less damping than in the case of l_μ. This is due to the fact that $\overline{v'^2}/k$ decreases near the wall (see Fig. 4) and that right at the wall $l_{\mu,v} \propto y$ while $l_\mu \propto y^2$. There appears to be some damping, but to first approximation the data can be described by

$$l_{\mu,v} = C_{l,\mu} y \tag{18}$$

where the factor $C_{l,\mu}$ is somewhat smaller than κ. As can be seen from Fig. 11, the linear distribution with $C_{l,\mu} = 0.33$ approximates the data fairly well up to $y^+ \approx 60$. It may be also of interest that $l_{\mu,v}/\delta = l^+_{\mu,v}/\mathrm{Re}_\tau$ is approximately 0.12 in the outer part of channel flow and 0.08 in boundary-layer regions with $.4 < y/\delta < .8$.

Dissipation length $l_{\epsilon,v}$. When $(\overline{v'^2})^{1/2}$ is used as velocity scale, the dissipation relation corresponding to (4) reads:

$$\epsilon = \frac{(\overline{v'^2})^{1/2} k}{l_{\epsilon,v}} \tag{19}$$

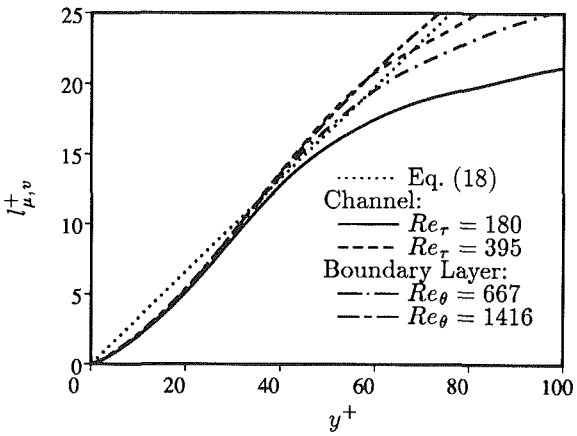

Fig. 11 Distribution of length scale $l^+_{\mu,v}$ near the wall

which is practically a relation between a velocity scale, a length scale and the time scale k/ϵ. The dimensionless length scale $l^+_{\epsilon,v}$ can be approximated as

$$l^+_{\epsilon,v} = \frac{k^+}{\epsilon^+} (\overline{v'^2}^+)^{1/2} = \frac{1}{C_\mu^{1/2}} \kappa y^+ (\overline{v'^2}^+)^{1/2} \tag{20}$$

which again results from the elimination of k^+ with the aid of (12) and ϵ^+ with the aid of (14), involving local-equilibrium and log-law assumptions. In Fig. 12, $C_\mu^{1/2} l^+_{\epsilon,v}$ determined from the DNS data is plotted together with the line κy^+ resulting from (20) by assuming again that $\overline{v'^2}^+$ has a value of 1. Figure 12 shows that this linear relation approximates the channel flow data near the wall very well, while the data indicate a somewhat larger slope for the boundary layer. This is due to the fact that, in the boundary layer, $\overline{v'^2}^+$ is somewhat larger than 1 in the region considered (see Fig. 3). Further, the lower-Reynolds-number cases follow the linear distribution only up to rather small y^+-values. In the bulk of the flow at larger y^+ distances, constant values of $l^+_{\epsilon,v}$ are approached. When $l^+_{\epsilon,v}$ is made dimensionless with δ, $C_\mu^{1/2} l_{\epsilon,v}/\delta \approx 0.14$ for both channel and boundary-layer flows. Near the wall, a linear distribution appears reasonable, but in the immediate vicinity of the wall this must be modified to yield the correct behavior of ϵ as y approaches zero. A modification analogous to the one in (8) was chosen, and the final $l_{\epsilon,v}$ distribution recommended reads

$$l_{\epsilon,v} = 1.3y \Big/ \left(1 + 2.12 \frac{\nu}{\sqrt{\overline{v'^2}}\, y}\right) \tag{21}$$

Since $\overline{v'^2} \propto y^4$ and $k \propto y^2$ this distribution leads to the correct behavior $\epsilon \propto y^0$ as y goes to zero. In Fig. 13, the $l_{\epsilon,v}$-distribution (21) is compared with the various DNS data for the near wall region. It can be seen to be a reasonable compromise to the data and describes well the deviation from the linear distribution at very small y^+ values.

Determination of $\overline{v'^2}$. When $(\overline{v'^2})^{1/2}$ is used as velocity scale in the turbulence model, the distribution of $\overline{v'^2}$ needs to

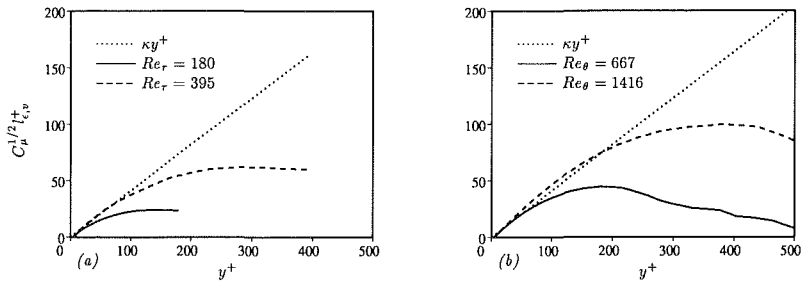

Fig. 12 Distribution of dissipation length $C_\mu^{1/2} l^+_{\epsilon,v}$. (*a*) channel; (*b*) boundary layer

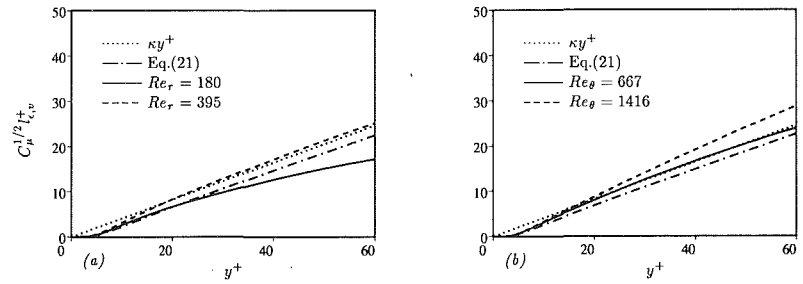

Fig. 13 Distribution of dissipation length $C_\mu^{1/2} l^+_{\epsilon,v}$ near the wall. (*a*) channel; (*b*) boundary layer

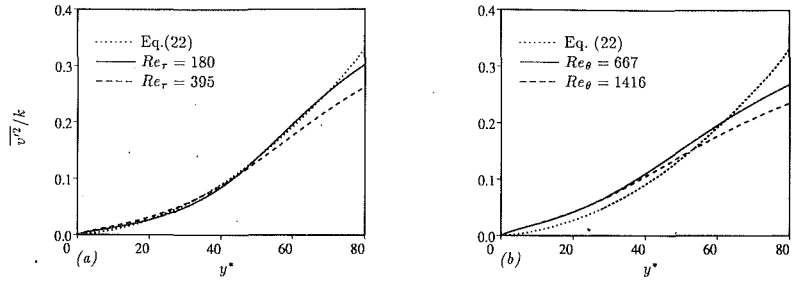

Fig. 14 Variation of $\overline{v'^2}/k$ versus y^*, (*a*) channel; (*b*) boundary layer

be determined. Figure 4 indicates that $\overline{v'^2}/k$ has a reasonably universal distribution with y^+ near the wall. Hence, $\overline{v'^2}$ is determined from k through an empirical relation between $\overline{v'^2}/k$ and a suitable wall distance, based on the DNS data. The wall distance $y^* = k^{1/2}y/\nu$ is taken to make the model applicable also to separated flows. The following relation based on the channel data is used

$$\frac{\overline{v'^2}}{k} = 4.65\times 10^{-5}y^{*2} + 4.00\times 10^{-4}y^* \qquad (22)$$

which is compared in Fig. 14 with the DNS data. It can be seen that up to $y^* = 60$ the empirical relation describes the DNS data fairly well.

5 Application of the New One-Equation Model

The new one-equation model was tested as a component of a two-layer model, referred to as TLV, in which it is applied only in the viscosity-affected near- wall region while the flow outside this region is calculated with the standard $k - \epsilon$ two-equation model of Launder and Spalding (1974). In the latter, the eddy viscosity is determined from $\nu_t = c_\mu k^2/\epsilon$. k appearing in this relation is also calculated from the k-equation (3) but the dissipation rate ϵ is calculated from a model transport equation. Standard values of the empirical constants are employed except for σ_k appearing in the diffusion term of the k-Eq. (3) which was given a value of 1.3 instead of the standard value of 1.0 in both one- and two-equation model components. The calculation examples include developed channel flow at $\mathrm{Re}_\tau = 180$ and 395 and boundary-layer flow at $\mathrm{Re}_\Theta = 670$ and 1410 for which DNS data are available as discussed above. Profiles are presented here only for the higher Reynolds number cases; results for the low Reynolds number cases can be found in a supporting laboratory report (Rodi et al., 1992). Test calculations were also carried out for the flow over a backward-facing step involving separation, which was studied experimentally by Driver and Seegmiller (1985). The calculations with the new TLV two-layer model are compared with results obtained with an existing two-layer model due to Cordes et al. (1993) referred to as TLK because the near-wall one-equation model component uses $k^{1/2}$ as velocity scale. It is the one-equation model due to Norris and Reynolds (1975) consisting of Eqs. (2) to (5) and (8) with $C_\mu = 0.09$, $A_\mu^* = 50.5$, $C_l = 2.495$ and $C_\epsilon = 5.3$. In the TLK model, the standard value of $\sigma_k = 1.0$ is used and the two model components are matched at locations where $\nu_t/\nu = 36$ which corresponds to $y^+ = 80 - 90$. Since the empirical relation (22) for $\overline{v'^2}/k$ used is accurate only in the range up to $y^+ \approx 50$, it was necessary to match the two components in the TLV model closer to the wall and a position was adopted where $\nu_t/\nu = 16$.

5.1 Developed Channel Flow. For the channel flow, the numerical calculations were performed with a simplified form of an implicit finite-difference method developed by Michelassi (1988). Ninty-one grid points were placed across the channel half-width and were clustered in the near-wall region. For the higher Re_τ case, the profiles of velocity U, eddy viscosity ν_t, turbulent kinetic energy k and dissipation rate ϵ are shown in Fig. 15 where they are compared with the DNS data. All quantities are made dimensionless with U_τ and ν and are plotted in a semi-logarithmic way in order to emphasize the behavior in the near-wall region. The velocity-profile predictions with both TLV and TLK models are indistinguishable up to $y^+ \approx 100$ and they agree well with DNS data. In the channel center, only the TLV predictions agree closely with the DNS data while the TLK model predicts the velocity to be too low. It should be mentioned that in these calculations U_τ was fixed while the flow rate was allowed to adjust itself. The underprediction of velocity in the channel center is caused by serious overprediction of the eddy viscosity, as can be seen in Fig. 15(*b*). In developed channel flow, the total (viscous plus turbulent) shear stress has a linear distribution. In the central part of the channel, the viscous stress is negligible so that the turbulent shear stress varies linearly and its distribution is independent of the turbulence model used. Hence according to (1), an overprediction of ν_t must cause the velocity gradient to be too small and in turn an underpredition of the velocity itself in the channel center. The differences in the ν_t- and consequently U-predictions in the channel center are entirely due to the different values of the constant σ_k used in the $k - \epsilon$ model component. It is now well known that in order to produce the observed dip in ν_t toward the channel center, σ_k must be raised from its original value of 1.0 to the value of the constant σ_ϵ (= 1.3). Near the wall, where the one-equation model is switched on, the TLV and TLK models give virtually the same ν_t-distribution which is in good agreement with the DNS data. The same remarks apply to the shear-stress distribution (not shown here, see Rodi et al., 1992). The profiles of turbulent kinetic energy k^+ are compared in Fig. 15(*c*). The TLV profile is in fairly good agreement with the DNS data while the TLK model underpredicts the peak value considerably. This is due to an overprediction of the dissipation rate ϵ in this region ($y^+ \approx 15$) as can be seen from Fig. 15(*d*). While both models predict the turbulent kinetic energy to behave as $k^+ = c_k y^{+2}$ very near the wall, the growth rate expressed by c_k is predicted too small by the TLK model. DNS gives $c_k = 0.1$ whereas the TLK model yields only 0.03. The TLV model somewhat overpredicts the growth rate ($c_k = 0.13$) but is still in relatively good agreement with the DNS data.

The largest differences between the TLK and TLV predictions are for the dissipation rate near the wall, as can be seen from Fig. 15(*d*). In common with most other low-Re models, the TLK model predicts the maximum of ϵ away from the wall at about $y^+ \approx 12$ and a drop to a fairly low wall value, which is directly related to the value of $c_k(\epsilon^+ = 2c_k)$. On the other hand, the TLV model predicts nearly the correct shape of the ϵ-profile and the maximum to be at the channel wall. That the ϵ-distribution predicted by the TLK model would be at variance with the DNS data could be inferred already from Fig. 9 showing that the dissipation length l_ϵ evaluated from the DNS data is considerably larger near the wall than assumed in the Norris-

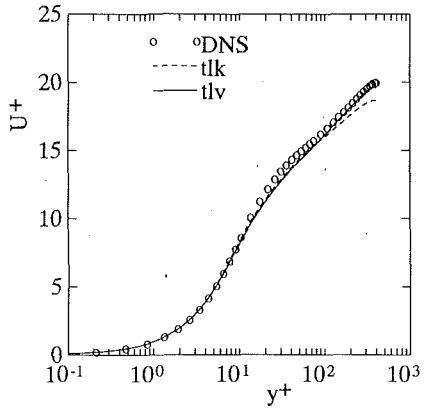

Fig. 15(*a*)

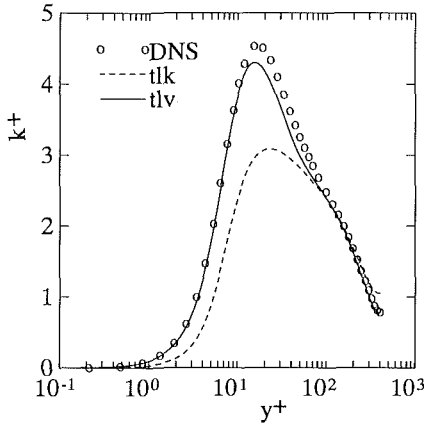

Fig. 15(*b*)

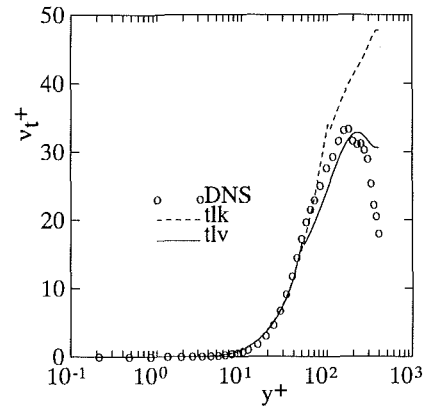

Fig. 15(*c*)

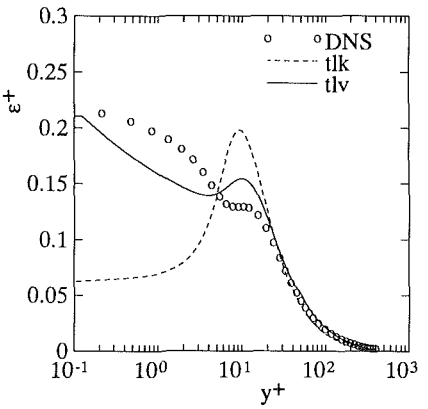

Fig. 15(*d*)

Fig. 15 Profiles in developed channel flow at $Re_\tau = 395$. (*a*) Velocity U^+; (*b*) eddy viscosity ν_t^+; (*c*) turbulent kinetic energy k^+ (*d*) dissipation rate ϵ^+.

Table 1 Integral parameters for the boundary-layer flow

model	$c_f \times 10^3$	H
DNS $Re_\theta = 670$	4.86	1.50
TLK $Re_\theta = 670$	5.25	1.45
TLV $Re_\theta = 670$	4.77	1.54
DNS $Re_\theta = 1410$	4.14	1.43
TLK $Re_\theta = 1410$	4.20	1.40
TLV $Re_\theta = 1410$	3.88	1.45

Reynolds one-equation model. Calculating the ϵ-distribution from (19) together with the dissipation-length distribution (21) brings about the much improved ϵ-prediction with the TLV model.

Basically the same remarks can be made on the $Re_\tau = 180$ case, for which the results are given in Rodi et al. (1992). At this lower Reynolds number, the TLK model shows an even stronger underprediction of the velocity in the channel center, and the accuracy generally deteriorates because the viscosity-affected layer occupies nearly the entire computation domain. However, in spite of the fact that in the TLV model the matching of the two model components occurs closer to the wall and hence a smaller part is simulated with a viscosity-dependent near-wall model, the predictions with the TLV model are still in better agreement with the DNS data than those with the TLK model.

5.2 Boundary-Layer Flow. The boundary-layer flow was computed with a 2-D version of the 3-D implicit finite-volume procedure of Majumdar et al. (1992), using a rectangular grid. The calculation domain covers a streamwise distance x such that $Re_\Theta = 300$ at the inflow boundary and $Re_\theta = 1410$ at the outflow boundary. The domain extends in normal direction to $y^+ \approx 1190$ which is approximately half of the streamwise distance. The whole calculation domain was divided into 10 subdomains each having 1/10 of the total length in the x-direction. In each subdomain a 162 × 122 grid was used with 50 grid points in the near-wall region up to $y^+ = 50$. The resulting exit profiles provided the inlet profiles for the next subdomain. For the first subdomain, the inlet profiles were specified in accordance with the DNS data of Spalart (1988) at $Re_\theta = 300$.

The skin friction coefficient and the shape factor H are compared with the DNS data in Table 1 at the two x-locations where $Re_\theta = 670$ and 1410. At the lower Reynolds number, the TLV-model results are in better agreement with the DNS data than the TLK-model results; this trend is reversed at the higher Reynolds number where the TLV model underpredicts the friction coefficient. This can be traced to the fact that the velocity in the outer part of the boundary layer and in the free stream is overpredicted (the friction velocity U_τ was fixed in the calculations) as can be seen from Fig. 16(*a*). This behavior is caused by an underprediction of the shear stress by the TLV model near the edge of the boundary layer, which is shown in Fig. 16(*b*). On the other hand, the TLK model predicts the correct velocity and shear-stress distributions at the boundary-layer edge. This difference in model behavior is again due to the different values of σ_k used. In combination with the other constants in the $k - \epsilon$ model, $\sigma_k = 1.0$ appears to be more suitable for boundary layers than $\sigma_k = 1.3$ which gives better results for channel flow. In the inner part of the boundary layer, both models yield virtually the same velocity profile which is in very good agreement with the DNS data (Fig. 16(*a*)). The shear-stress distribution is also in close agreement, with the TLV model yielding slightly superior predictions very near the wall (Fig. 16(*b*). Figure 16(*c*) compares predicted k^+-profiles with DNS data. As for the channel flow, the TLV model predicts the near-wall and peak behavior of k^+ very well, while the TLK model predicts too slow a rise of k and a considerably too low peak. In the region $y^+ \approx 100$, both models underpredict somewhat the k-level, and similar to the

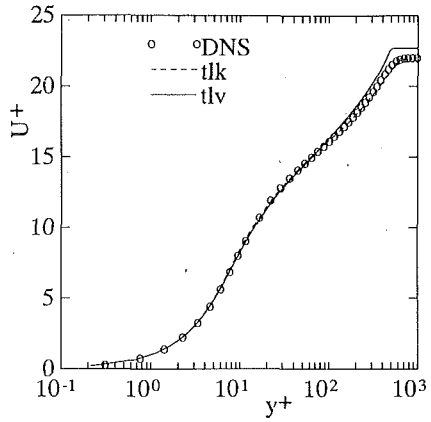

Fig. 16(*a*)

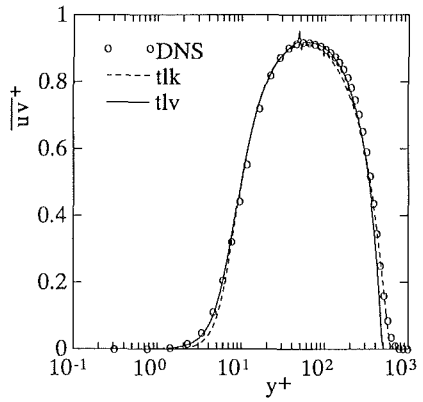

Fig. 16(*b*)

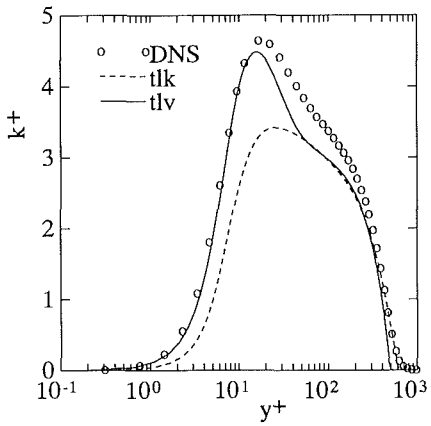

Fig. 16(*c*)

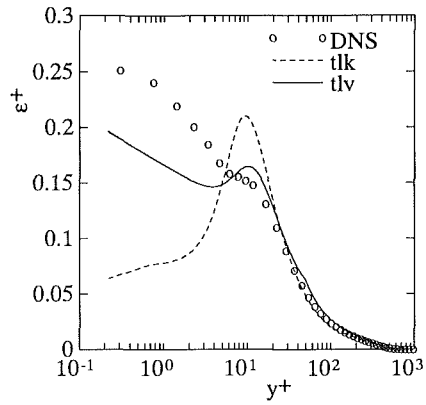

Fig. 16(*d*)

Fig. 16 Profiles in boundary layer at Re_θ = 1416. (*a*) Velocity U^+; (*b*) shear stress $\overline{uv}^+$; (*c*) turbulent kinetic energy k; (*d*) dissipation rate ϵ^+.

$\overline{uv}$-behavior, the TLV model underpredicts k at the edge of the boundary layer while the TLK model has the correct behavior there. Concerning the ϵ-distribution shown in Fig. 16(*d*), the two models show the same behavior as discussed for the channel flow. The ϵ-profile computed by the TLV model is again in much better agreement with the DNS data than that obtained with the TLK model. Still, the wall value of ϵ is underpredicted by the TLV model, but beyond $y^+ \approx 8$ there is good agreement with the DNS data. On the other hand, the TLK model shows agreement with DNS data only beyond $y^+ \approx 25$.

The profiles at the lower Reynolds number of $Re_\Theta = 670$ show similar trends and are available in Rodi et al. (1992).

5.3 Backward-Facing Step Flow. The test case with the step height being 1/8 of the inlet channel height was chosen because Driver and Seegmiller (1985) had conducted very detailed LDV experiments on this flow. The upper channel was is parallel to the lower wall and the Reynolds number based on the inlet channel height and the inlet reference velocity is approximately 3×10^5. The computations were carried out with the same implicit finite-volume solver used also for the boundary-layer calculation. A second-order accurate spatial discretization was used in the solver. The calculation domain extended from four step heights upstream to 32 step heights downstream of the step. A Cartesian grid was used with 151 points in the streamwise direction and 101 points in the cross-stream direction. Further grid refinement produced no changes in the computed results. The grid was clustered near the wall and the first gird point away from the wall was at $y^+ \approx 2$. With the TLK model, 45 points were located in the inner region where the one-equation model was applied, while typically 25 points were located in this region when the TLV model was employed. The two models give virtually indistinguishable results for all quantities. Figure 17(*a*) shows the distribution of the friction coefficient c_f along the bottom wall. The reattachment point is predicted at $x/H = 5.7$ while the observed value is 6.2. When the standard $k - \epsilon$ model with wall functions is used, reattachment is predicted at $x/H \approx 4.8$ and the maximum negative value of c_f in the reverse-flow region is underpredicted (see Rodi, 1991). Figure 17(*a*) shows that the two-layer models overpredict the negative c_f somewhat but simulate fairly well the redevelopment of c_f downstream of reattachment. Figures 17(*b*) and 17(*c*) show the velocity and shear-stress profiles respectively at various downstream locations. Only one line is given since the TLV and TLK models produced indistinguishable results. In general, the velocity field can be seen to be well predicted, but in the separation region the negative velocities are too high close to the wall, causing the excessive negative c_f discussed already, and reattachment occurs somewhat too early. The shear stress is somewhat overpredicted in the curved free-shear layer bordering the separation region which is probably due to the fact that the $k - \epsilon$ model effective in this region does not account properly for streamline curvature effects on turbulence.

The details in near-wall modeling seem to be insignificant in this case because the flow development is determined mainly by the modeling of the free shear layer which is the same with the TLV and TLK models. However, the TLV formulation was found to have a numerical advantage over the TLK model because it allowed for faster convergence of the solution. Typically 1000 iterations were needed for the TLK model to reach a converged solution with an integral over all residua of $\approx 10^{-7}$, whereas 600 iterations were needed to reach the same residua level when the TLV model was used. This may be traced to the fact that the TLV model does not use the highly nonlinear exponential damping function which is part of the TLK model.

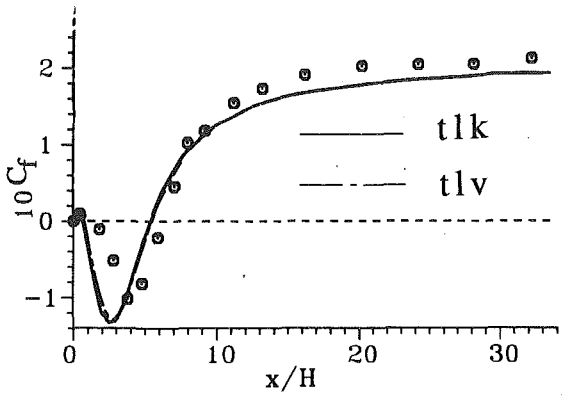

Fig. 17(*a*)

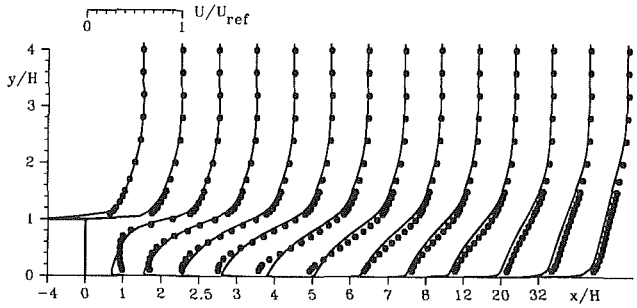

Fig. 17(*b*)

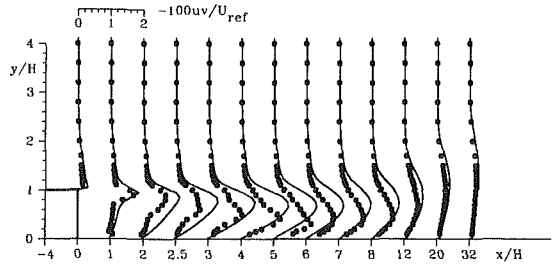

Fig. 17(*c*)

Fig. 17 Flow over backward facing step; lines are predictions, o • measurements of Driver and Seegmiller (1985). (*a*) Friction coefficient along bottom wall; (*b*) Velocity profiles; (*c*) shear stress profiles.

6 Conclusions

The DNS data have shown that, for the Reynolds numbers investigated, there is still considerable influence of the Reynolds number on the quantities plotted in wall coordinates. However, for the higher Reynolds numbers simulated, the quantities are already close to those observed in experiments at much higher Reynolds numbers. On the other hand, for both channel and boundary layer the lower-Reynolds-number cases are subject to considerable viscous effects.

The length scale l_μ in the eddy-viscosity relation of existing one-equation models follows a near-linear behavior near the wall, but very close to the wall it falls below this distribution and requires the introduction of a damping function similar to that for the mixing-length distribution. The distribution of the dissipation length scale l_ϵ evaluated from the DNS data shows a pronounced hump at $y^+ \approx 15$ and lies considerably above the linear distribution near the wall. This behavior is not described by the l_ϵ prescriptions used in existing models. When the normal fluctuations $(\overline{v'^2})^{1/2}$ are introduced as velocity scale instead of $k^{1/2}$, the corresponding length scales are better behaved, i.e., the dissipation length $l_{\epsilon,v}$ does not have a hump and the length $l_{\mu,v}$ is subject to much less damping. Near the wall, both length scales can be approximated quite well by linear relations; only $l_{\epsilon,v}$ needs to be damped very closed to the wall.

It was found that $\overline{v'^2}/k$ is a fairly universal function of $y^* = k^{1/2}y/\nu$ near the wall, and an empirical relation was proposed for use in one-equation models which avoids solving an additional equation for $\overline{v'^2}$. Together with the length-scale relations introduced, this forms a new one-equation model which, as the near-wall component of a two-layer model, was tested by application to channel flow, boundary-layer flow and backward-facing step flow. In the first two test cases, the new model produced considerably improved k- and ϵ- profiles near the wall compared with profiles obtained with a two-layer model employing an existing one-equation submodel. In the backward-facing step case the differences in the results were insignificant, but the new model required considerably fewer iterations in the numerical solution. The new model should now be tested for a wider range of flows.

Acknowledgment

The authors are grateful to Dr. Kim for providing the unpublished direct simulation data for the channel flow at $Re_\tau = 395$. The first author (WR) would like to acknowledge the generous support of the Center for Turbulence Research.

References

Clark, J. A., 1968, "A Study of Incompressible Turbulent Boundary Layers in Channel Flow," ASME *Journal of Basic Engineering*, Vol. 90, pp. 455–468.

Cordes, J., Rodi, W., and Cho, N. H., 1993, "Calculation of Separated Flows With a Two-Layer Turbulence Model," *Physics of Separated Flows—Numerical, Experimental and Physical Aspects*, ed. K. Gersten, *Notes on Numerical Fluid Mechanics*, Vol. 40, Vieweg.

Driver, D. M., and Seegmiller, H. L., 1985, "Features of a Reattaching Turbulent Shear Layer in Divergent Channel Flow," *AIAA Journal*, Vol. 23, pp. 163–171.

Durbin, P. A., 1991, "Near-Wall Turbulence Closure Modeling Without Damping Functions," *Theoretical and Computational Fluid Dynamics*, Vol. 3, p. 1.

Hussain, A. K. M. F., and Reynolds, W. C., 1975, "Measurement of Fully Developed Turbulent Channel Flow," ASME JOURNAL OF FLUIDS ENGINEERING, Vol. 97, pp. 568–580.

Kastrinakis, E. G., and Eckelmann, H., 1983, "Measurement of Streamwise Vorticity Fluctuations in a Turbulent Channel Flow," *Journal of Fluid Mechanics*, Vol. 137, pp. 165–186.

Kim, J., Moin, P., and Moser, R., 1987, "Turbulence Statistics in Fully Developed Channel Flow at Low Reynolds Number," *Journal of Fluid Mechanics*, Vol. 177, pp. 133–166.

Kim, J, 1990, private communication.

Laufer, J., 1954, "The Structure of Turbulence in Fully Developed Pipe Flow," NACA Report 1174.

Launder, B. E., and Spalding, D. B., 1974, "The Numerical Computation of Turbulent Flows," *Computer Methods in Applied Mechanics and Engineering*, Vol. 3, pp. 269–289.

Majumdar, S., Rodi, W., Zhu, J., 1992, "Three-Dimensional Finite-Volume Method for Incompressible Flows With Complex Boundaries," ASME JOURNAL OF FLUIDS ENGINEERING, Vol. 114, pp. 496–503.

Michelassi, V., 1988, "Testing of Turbulence Models by an Artificial Compressibility Solution Method," Report SFB 210/T/93, University of Karlsruhe, Germany.

Myong, H. K., and Kasagi, N., 1988, "An Anisotropic $k - \epsilon$ Model Taking into Account the Near-Wall Limiting Behavior of Turbulence," *Proceedings 20th Turbulence Symposium*, Tokyo.

Norris, L. H., and Reynolds, W. C., 1975, "Turbulent Channel Flow With a Moving Wavy Boundary," Report No. FM-10, Stanford University, Department of Mechanical Engineering.

Rodi, W., 1991, "Experience With Two-Layer Models Combining the $k - \epsilon$ Model with a One-Equation Model Near the Wall, Paper AIAA 91-0216.

Rodi, W., and Mansour, N. N., 1990, "One-Equation Near-Wall Turbulence Modeling With the Aid of Direct Simulation Data," *Proceedings of Summer Program 1990*, Center for Turbulence Research, Stanford.

Rodi, W., Mansour, N. N., and Michelassi, V., 1992, "One-Equation Near-Wall Turbulence Modeling with the Aid of Direct Simulation Data," Report SFB 210/T/93, University of Karlsruhe, Germany.

Spalart, P. R., 1988, "Direct Simulation of a Turbulent Boundary Layer Up to $R_\theta = 1410$," *Journal of Fluid Mechanics*, Vol. 187, pp. 61–98.

Wolfshtein, M., 1969, "The Velocity and Temperature Distribution in One-Dimensional Flow with Turbulence Augmentation and Pressure Gradient," *International Journal of Heat and Mass Transfer*, Vol. 12, pp. 301–118.

H. Kato

Y. Fujii

H. Yamaguchi

M. Miyanaga

Department of Naval Architecture and
Ocean Engineering,
University of Tokyo,
Bunkyo, Tokyo, 113, Japan

Frictional Drag Reduction by Injecting High-Viscosity Fluid Into Turbulent Boundary Layer

This paper presents a new method to reduce turbulent frictional drag by injecting high-viscosity fluid into the boundary layer. When the turbulent region of the boundary layer is filled with high-viscosity fluid, and the viscosity of the viscous sublayer is kept low, the Reynolds stress in the turbulent region is reduced and therefore requires a greater velocity gradient to transfer the momentum. The greater velocity gradient in the turbulent region results in a reduction of the velocity gradient at the viscous sublayer, which causes a drop in shear stress at the wall. Such a boundary-layer structure could be created by injecting two different fluids from double slits on a wall. Sugar syrup and water were used as the high-viscosity fluid and the low-viscosity fluid, respectively. The shear stress was directly measured by shear stress pick-ups mounted flush on the wall. The shearing stress was reduced by more than 50 percent at the optimum injection condition. A water/water injection experiment was also performed to show the effect of injection itself.

Introduction

One of the highest priorities of fluid dynamists and designers is the reduction of viscous drag acting on a body. Viscous drag can usually be divided into two components—form drag and frictional drag. Form drag is mainly caused by flow separation, and its prevention techniques have been studied for decades (for example, Lachmann, 1961).

Delaying the transition to turbulent flow has been the focus in many attempts to reduce frictional drag. Research work to control the turbulent boundary layer by active or passive means, such as compliant walls, riblets, Large Eddy Break Up Device/ Outer Layer Device (LEBU/OLD), etc. (for example, Hough, 1980; Liepmann and Narasimha, 1987; Gyr, 1989) has been the recent trend. A good review on this field was given by Bandyopadhyay (1986). For liquids, several other methods, such as polymer solutions (Toms effect) and micro-bubble ejection have been proposed and examined. Virk (1975) thoroughly reviewed the effects of polymer solutions. He showed that when the polymer effect began to reduce the frictional drag, the turbulent velocity distribution changed and the Reynolds stress was reduced at the inner region of the boundary layer. He also suggested that the polymer molecules interfered with the turbulent bursting process in the buffer layer. Tiederman et al. (1985) found that the polymer had a direct effect on the flow structures in the buffer layer, $10 < y^+ < 100$.

Micro-bubble ejection seems to be another very effective method in reducing frictional drag. Bogdevich et al. (1977) showed the local frictional resistance reduced to one order of magnitude less than that of the original turbulent boundary layer. Madavan et al. (1984, 1985a, 1985b) made an extensive study of the micro-bubble effect. According to their hypothesis, the mechanism of frictional resistance reduction was due to the reduction of turbulent mixing length especially in buffer region, that was caused by the increase in effective viscosity of water with many micro bubbles. The decrease in the turbulence intensity in the buffer region causes an increase of the mean velocity gradient there. It causes, in turn, the decrease of the velocity gradient in the viscous sublayer.

These previous studies lead to a method to reduce the frictional resistance by creating stratified layers with different viscosity fluids—probably the high viscosity fluid in the buffer layer and/or the turbulent region. In this paper, the authors present characteristics of such a boundary layer that was formed by ejecting a high viscosity fluid from an upstream slit and water from a downstream slit on a flat plate in a water tunnel.

Mechanism of Drag Reduction

The shearing stress in a turbulent boundary layer is expressed as,

$$\tau = \mu \frac{\partial \overline{u}}{\partial y} - \rho \overline{u' v'}, \tag{1}$$

where $\overline{\ }$ and $'$ are time averaged and nonsteady components, respectively.

The momentum transfer is mainly a result of the Reynolds stress, $-\rho \overline{u' v'}$ and the velocity gradient $\partial \overline{u}/\partial y$ is very small in the turbulent region of the boundary layer. However, the velocity gradient should be large in viscous sublayer to transfer the same amount of momentum. The increase in the viscosity of the fluid in turbulent region causes the decrease of the

Contributed by the Fluids Engineering Division and presented at the 1st Joint ASME-JSME Fluids Engineering Conference, Portland, Oregon, June 23–27, 1991, of The American Society of Mechanical Engineers. Manuscript received by the Fluids Engineering Division May 26, 1991; revised manuscript July 18, 1992. Associate Technical Editor: T. T. Huang.

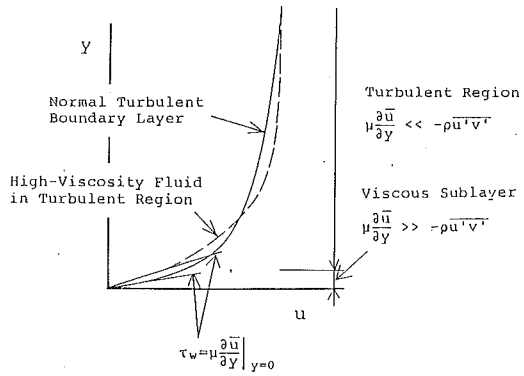

Fig. 1 Concept of frictional drag reduction

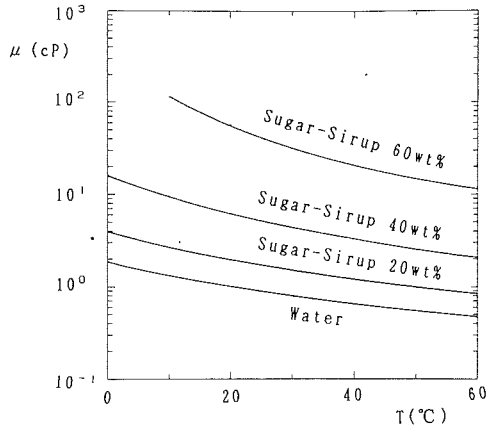

Fig. 2 Viscosity of sugar syrup

Reynolds stress, resulting in the increase of the term $\mu\,\partial\bar{u}/\partial y$. Then, the velocity gradient $\partial\bar{u}/\partial y$ might increase even if the viscosity μ has increased, because the momentum is mainly transferred by the Reynolds stress in the turbulent region. In such a case one can expect the decrease of the velocity gradient near the wall as shown in Fig. 1. Therefore, if we can produce a kind of "sandwich structure" fluid stratified layer of low-high-low viscosity, the frictional resistance will decrease in the turbulent boundary layer.

Experimental Apparatus and Experimental Method

The experiment was conducted in a recirculating water tunnel at the University of Tokyo. The recirculating water tunnel is usually used as a cavitation tunnel. There were several candidate liquids for the high viscosity fluid, such as glycerin, ethylene glycol etc. Sugar syrup was finally chosen as the high viscosity fluid, because it did not pollute the environment. The viscosity of sugar syrup can vary depending on its concentration and temperature (Fig. 2).

The tunnel had a rectangular test section with dimensions of 120 mm × 50 mm in section. The outline of two side windows is shown by the dotted line in Fig. 3. The windows are smaller than the test section. The test body was made of stainless steel and had a convex shape with a flat top (Fig. 3), which allowed the boundary-layer velocity distribution to be measured by a laser Doppler velocimeter. The test body had two slits for injecting the fluids in the boundary layer.

The double slits were 10 mm apart, with an angle of 20 degrees to the flat wall, and a width of 0.6 mm (Fig. 4). The outlet of the slits was carefully rounded to prevent the ejected fluids from separating from the flat wall.

The test section allowed for five shearing stress pick-ups to be embedded on the flat wall (Fig. 3). For the experiment, four active pick-ups and one dummy pick-up (at the most downstream position) were installed. The pick-ups were numbered 1-4 from upstream to downstream. Each shearing stress pick-up had a floating disk of 5 mm in diameter, which was supported by two parallel cantilever beams. The shearing stress acting on the floating disk deforms the two beams. The deformation of the beam is detected by strain gauges attached to them (Fig. 5). Capacity of the pick-up is 500 Pa which corresponds to the 1 g force to the disk. The disk moves about 0.1 mm for each gram of force. The frequency response limit is 30 Hz. A static force calibration of the pick-ups was performed as follows: Each pick-up was hung vertically, and a thread with a small hook was glued on the floating disk. Then small weights (up to 1 g) were hung on hook. However, during the course of the experiment this type of calibration was shown to be insufficient. The insufficiency of this method of calibration will be discussed later.

Signals of the pick-ups were recorded in two 6 channel digital data recorders. Number of data for one run was 8192 with the sampling time of 2 ms. The data were processed by a personal computer (NEC PC 9801E).

It was necessary to eject water and sugar syrup at low constant flow rate. There was no suitable pump available for the present purpose. Therefore, compressed-air pressure tanks were used to eject the fluids. The ejection setup is shown in Fig. 6. Flow rate was measured by a rotameter. The rotameter was calibrated with the sugar syrup just before each run by a measuring glass and a stop watch. The viscosity of the sugar syrup was measured with a capillary tube-type viscometer. The liquid's temperature was also measured at this time.

The total amount of injected sugar was accounted for, and the bulk water was refilled when its sugar concentration reached 2 percent by weight. The size of the test body and the maximum speed available were not large enough for turbulent flow. Therefore, a turbulence stimulator was used. After several stimulators were tested at various positions, a circular rod of 5 mm diameter was placed at the entrance of the test section, 115 mm upstream of the leading edge of the test body. The effect of the turbulence stimulator will be discussed later.

The measurements were taken on the narrow wall of the test section. The typical boundary-layer thickness was about 6 mm, which was approximately one-eighth of the test section's width. Similar experiments were made in a developed two-dimensional duct flow. (for example, Tiederman et al., 1985). Those experiments required a long starting region which was impossible for the present experiment because of the limitations of the

Nomenclature

C_f = frictional resistance coefficient
L = test body length
Q = injection flow rate
Re = Reynolds number based on main flow velocity and test body length
T = temperature
U = main flow velocity
u = velocity to x direction
v = injection velocity, velocity to y direction
x = coordinate parallel to wall
y = coordinate vertical to x
δ = boundary layer thickness
μ = viscosity
ρ = density
τ = shearing stress

Subscript

0 = without injection
1 = downstream injection
2 = upstream injection
s = sugar syrup
w = water
∞ = reference value

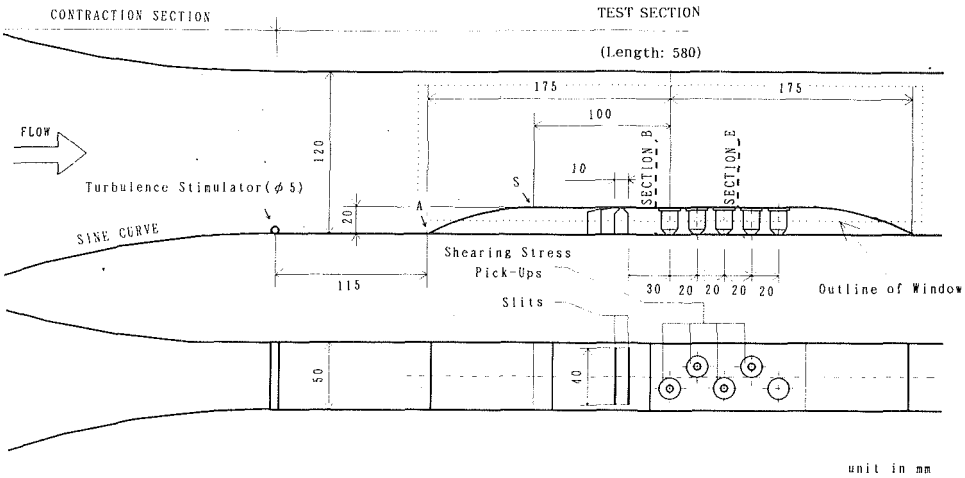

Fig. 3 Flat plate with double slits

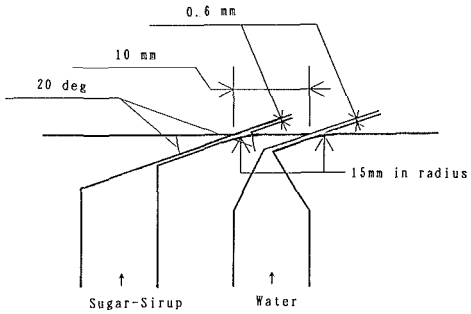

Fig. 4 Details of injection slits

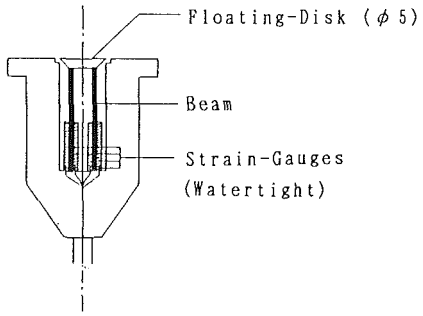

Fig. 5 Details of shearing stress pick-up

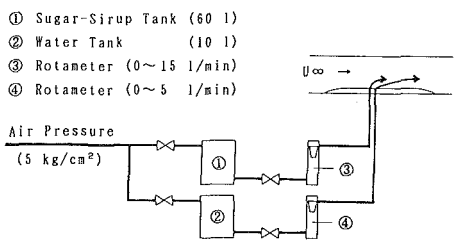

Fig. 6 Injection setup

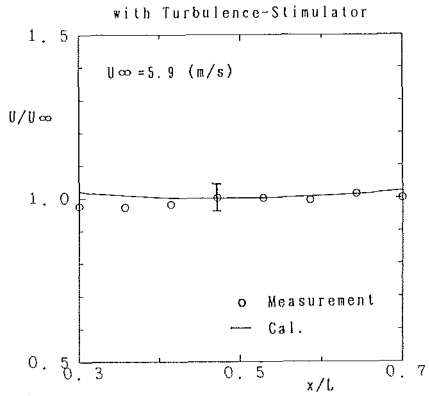

Fig. 7 Main flow velocity distribution (Uncertainty of data: ±4 percent)

facility. Therefore, the present experiment was conducted in a two-dimensional boundary-layer flow with the disturbance originating at the corners and gradually disturbing the two-dimensional boundary layer. Figure 11 shows the disturbance in the two-dimensional boundary layer.

Experimental Results and Discussions

Velocity Distribution Over the Test Body. As mentioned before, the test body had a convex shape. The velocity distribution, especially on the flat part, was examined analytically as well as empirically.

The velocity distribution was calculated by combining an ideal fluid flow calculation where singularities, source and sink and vorticities, were distributed on the wall surface, with the boundary layer calculation, using the momentum integration method (Yamaguchi et al., 1988). The calculation also included the effect of the upper wall of the test section.

The velocity distribution was measured by a Laser Doppler Velocimeter (LDV). The measurement was made at the nominal main flow velocity, U_∞ = 5.9 m/s and 10.2 m/s. Figure 7 shows the main flow velocity distribution at U_∞ = 5.9 m/s along the test body. U is defined as the velocity at the edge of the boundary layer. The abscissa is nondimensionalized by the test body length of 350 mm. The main flow velocity is high at the shoulder of the test body, and increases gradually downstream because of the development of the boundary layer. However, the increase is so small that we can assume the main flow velocity is constant at the middle ($x/L \simeq 0.5$).

Typical velocity distributions in boundary layers are shown in Fig. 8, where sections B and E are 10 mm upstream and 50 mm downstream, respectively, of the center of the test section (see Fig. 3). They correspond to x/L = 0.471 and 0.643. The boundary-layer thickness, displacement, and momentum thicknesses were δ = 6.3 mm, δ_1 = 0.88 mm and δ_2 = 0.63 mm, respectively, at section B with U_∞ = 5.9 m/s. The velocity distributions agree with the empirical formula of turbulent flow as seen in Fig. 8. The velocity distribution without the turbulence stimulator was also measured at section B. It shows that the flow is not fully turbulent, and demonstrates the effect of turbulence stimulator. The result with the turbulence stim-

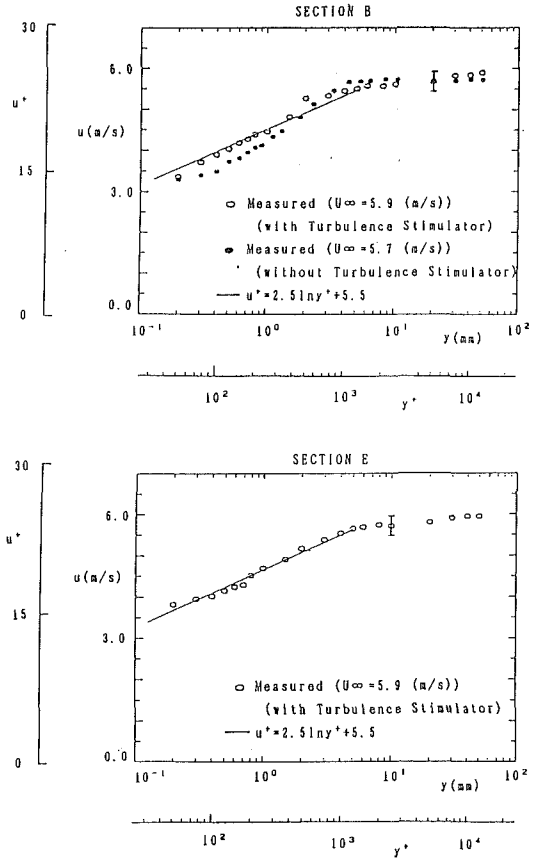

Fig. 8 Velocity distribution in boundary layer without injection (Uncertainty of data: ±4 percent)

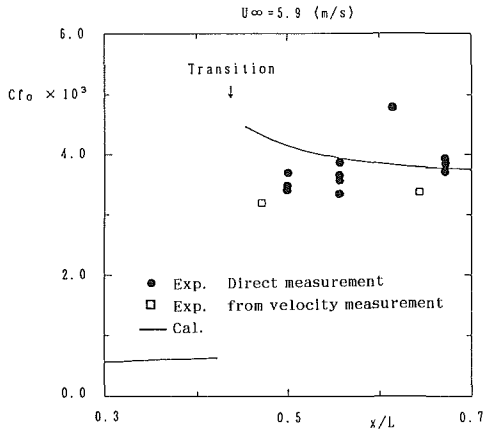

Fig. 9 Shearing stress measurement without injection (Uncertainty of data: $\pm 0.6 \times 10^{-3}$)

ulator will be mainly discussed in the following chapter. The measured velocity distribution at $U_\infty = 10.2$ m/s (not shown here) closely approximates the empirical log law even without the stimulator.

Wall Shearing Stress. The wall shearing stress is one of the most difficult properties to measure, even indirectly. In the present experiment, the wall shearing stress was measured directly using pick-ups shown in Fig. 5.

The wall shearing stress measurement was very similar between $U_\infty = 5.9$ m/s and 10.2 m/s. Data at $U_\infty = 5.9$ m/s are shown in Fig. 9. The estimated shearing stress from the velocity distribution (cf. Fig. 8) is shown by open square marks. The boundary-layer calculation was made using the momentum

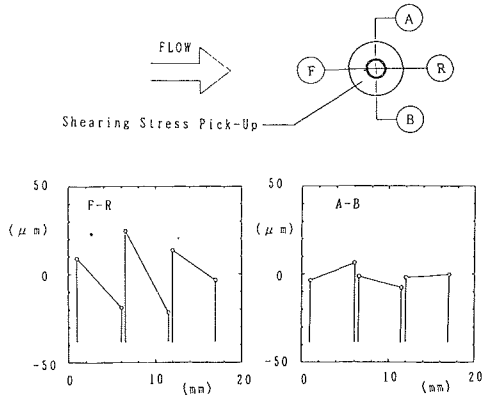

Fig. 10 Surface irregularity of shearing stress pick-up No. 3

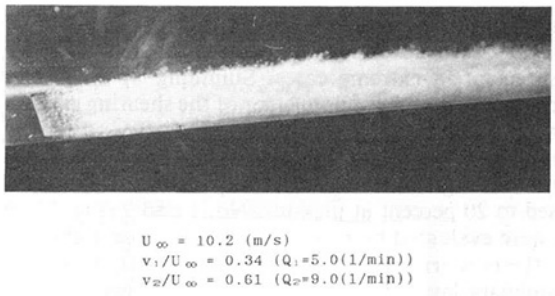

Fig. 11 Appearance of sugar syrup injection

integration method. The starting point of the boundary layer was assumed to be the leading edge of the test body (point A in Fig. 3). Smith's criterion was used for the estimation of transition (Cebeci and Bradshaw, 1977). The calculation took no account of the effect of the upstream boundary layer or of the turbulence stimulator. Therefore, the actual transition might occur far upstream of the calculated point shown in Fig. 9.

The measured shearing stress agrees fairly well with the calculation, and its reproducibility was also satisfactory. However, the measurement by pick-up No. 3 ($x/L = 0.614$) was unexpectedly high. The shape of pick-up No. 3 was examined by a microscope, and it was determined that the leading edge of the floating disk was about 40 μ m higher than the surface of the mount block, as shown in Fig. 10. The other pick-ups were also examined and it was determined that their irregularity was within ± 5 μm. The irregularity of 40 μm corresponds to about $y^+ \simeq 9$ at $U_\infty = 5.9$ m/s and the dynamic pressure acting on the side wall of the floating disk amounts 0.014 g, which corresponds to $\Delta C_f = 0.4 \times 10^{-3}$. The above estimation explains, to some extent, why only pick-up No. 3 gives such a high value, as seen in Fig. 9, though the reading is still too high. This fact also shows that a static calibration using weights is not sufficient for the present type of shearing stress pick-up. Moreover, it is desirable to calibrate pick-ups in flow conditions.

It was decided to make reference measurements without injection before and after the series of injection experiments. The effects of injection were also evaluated by comparing them with those reference measurements. During one series of experiments, the repeatability of data was good and twice the standard deviation of the data was less than 6 percent, which was mainly caused by the fluctuation of main flow velocity and the vibration of the floating disk. The estimated errors of injection velocity and fluid viscosity were less than 2.5 and 10 percent, respectively. The error of viscosity was large because of the inaccuracy of the temperature estimation (up to 2 degrees

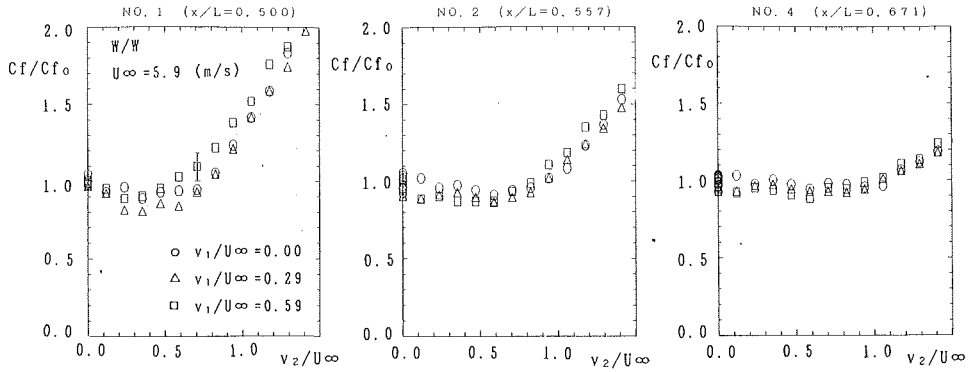

Fig. 12 Results of shearing stress measurements (water/water, $U_\infty = 5.9$ (m/s))

during the viscosity measurement). The error of viscosity measurement caused an error of 5 percent in the shearing stress measurement in extreme cases. Summing up these random errors, the maximum random error of the shearing stress measurement was estimated within 9 percent (95 percent confidence). There was a bias error in the stress measurement because of the mal-alignment of the pick-up surfaces. The error increased to 20 percent at pick-ups No. 1 and 2 (Fig. 9). When data were evaluated by relative values to those without injection, the bias error could reduce to 5 percent. It was caused by boundary layer change with and without injection. Therefore, the uncertainty of C_f/C_{fo} value was estimated within 14 percent (95 percent confidence).

Effect of Injection Into Boundary Layer. Besides the water/sugar syrup injection experiment, an experiment with water/water injection (injecting water from both slits) was performed to examine the effect of injection itself.

As seen in Fig. 11, the injected sugar syrup became white because of the large difference in the index of refraction between water and sugar syrup. Because of that, the flow and the mixing process could be observed easily. However, the LDV could not be used since it was being used in a forward scatter mode at the time.

The experimental conditions were;

Main flow velocity: $U_\infty = 5.9 \pm 0.1$ m/s, 10.2 ± 0.1 m/s
Reynolds number:
$\mathrm{Re} = U_\infty L/\nu = (1.78 \sim 1.95 \pm 0.03) \times 10^6$,
$(3.07 \sim 3.36 \pm 0.04) \times 10^6$
Viscosity of sugar syrup: $\mu_s = 11.9 \sim 47.2 \pm 0.2$cP
Injection rate Water: $0 \sim 15 \pm 0.1$ l/min
Sugar syrup: $0 \sim 10 \pm 0.08$ l/min.

The viscosity range of sugar syrup corresponds to $\mu_s/\mu_w =$ 14–49. The mean injection velocity was also defined by dividing the injection rate by the sectional area of the ejection slit.

Water/Water Injection. The result of the water/water injection experiment is shown in Fig. 12, where v_1 and v_2 are mean injection velocities of the downstream slit and the upstream slit, respectively. The result of pick-up No. 3 was not illustrated because of unreliability. The ordinate is the ratio of the frictional coefficient to the reference value of no injection, which was measured before and after the test series.

When we assume a stratified flow, the fluid injected from the downstream slit would flow at the wall and the fluid from the upstream slit would flow over it.

The injection reduced the wall shearing stress to some extent when the injection velocity was low. In the present case, the shearing stress reduced gradually until v_2/U_∞ reached about 0.5. There seemed to be an optimum value for v_1, also. When the velocities of v_1 and v_2 increased beyond the optimum values, the shearing stress began to increase rapidly. In these conditions, the injected flow became a wall-jet, which caused an increase in the shearing stress. This injection effect decayed rapidly downstream. It indicated that the mixing effect is large in the boundary layer. The measurement at $U_\infty = 10.2$ m/s showed the similar tendency as seen in Fig. 13.

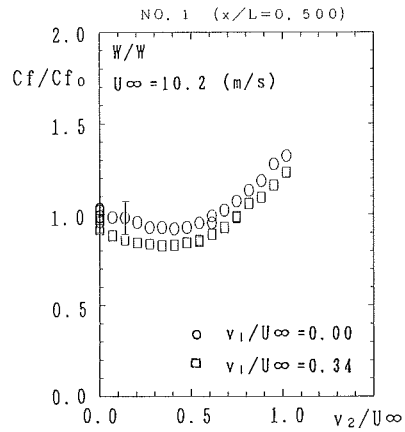

Fig. 13 Results of shearing stress measurements (water/water, $U_\infty = 10.2$ (m/s)) (Uncertainty of data in Figs. 12 and 13: ±9 percent)

Water/Sugar Syrup Injection. The effect of high-viscosity fluid injection into the buffer and turbulent regions was examined by injecting sugar syrup from the upstream slit. The typical result is shown in Figs. 14 and 15.

The reduction in shearing stress is greater than the water/water injection especially at lower main flow velocity. If the high-viscosity fluid alone is injected into the bottom of the boundary layer, there is an increase in shearing stress at the wall. It is the case of $v_1/U_\infty = 0$ in Figs. 14 and 15. If water is injected with the proper flow rate from the downstream slit, the reduction effect is remarkable. The shearing stress was almost half at the pick-up No. 1 in the condition of $U_\infty = 5.9$ m/s, $\mu_s/\mu_w = 22$, $v_1/U_\infty = 0.29$ and $v_2/U_\infty = 0.65$. Since the reduction includes the effect of the injection itself, the effect of high-viscosity fluid might be 10–20 percent less, judging from the water/water injection result.

The overall tendency of injection is similar to that of water/water injection. Increasing the sugar syrup flow rate v_2, the shearing stress begins to drop, reaching minimum, then it begins to increase steeply. At a higher main velocity, $U_\infty =$ 10.2 m/s, the effect is small even at pick-up No. 1. Because of the limitation of injection power, maximum injection rate of sugar syrup v_2 was limited to $v_2/U_\infty = 0.6$. The optimum injection rate seems larger than that limitation.

The drag-reduction almost disappears at pick up No. 4, which corresponds to about 15 times the boundary-layer thick-

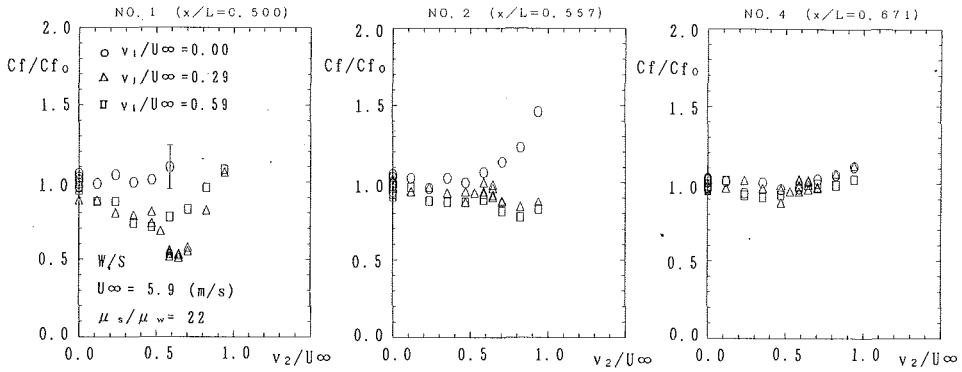

Fig. 14 Results of shearing stress measurements (water/sugar, $U_\infty = 5.9$ (m/s))

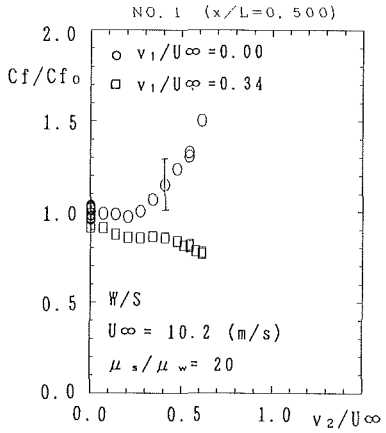

Fig. 15 Results of shearing stress measurements (water/sugar, $U_\infty = 10.2$ (m/s)) (Uncertainty of data in Figs. 14 and 15: ±14 percent)

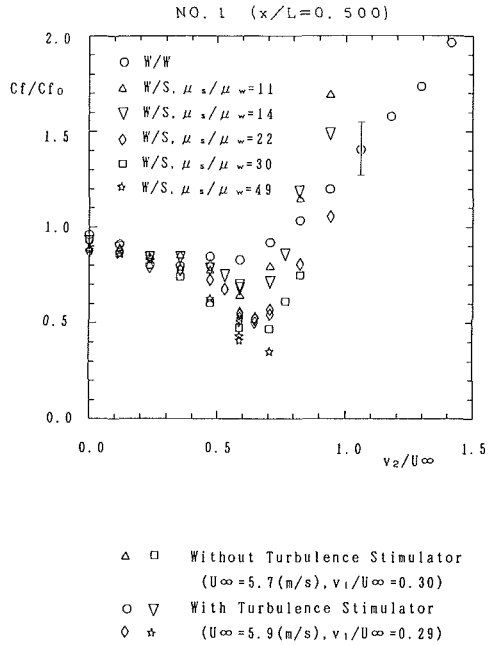

Fig. 16 Effect of μ_s/μ_w on C_f/C_{fo} (Uncertainty of data: ±14 percent)

ness. The downstream persistence of drag-reduction is worse compared to other methods, such as polymer or microbubbles. The reason for the poorer drag reduction with our method is not clear; the meager drag reduction may have something to do with the turbulent mixing effect of the boundary layer. A preliminary boundary-layer calculation, including turbulent diffusion of high-viscosity fluids, showed a similar tendency to decay, (Fujii (1991)). Another possible reason is that the 3-D disturbance originated at the corners of the test body, affecting pick-up number 4 the most.

Tiederman et al. (1985) measured drag reduction of 2-D duct flow by injecting a polymer through a single slit in the wall. The amount of polymer needed was one to two orders of magnitude less than the present result. It seems impractical to apply the present method to an actual case at the present stage of study, because of the large amount of sugar syrup.

Tiederman et al. also injected glycerin solution to determine the effect of viscosity. Their condition corresponds to the present case of $v_l = 0$. They observed almost no effect of viscosity increase, perhaps because of the very small injection amount of fluids whose viscosity was insignificant.

In the preliminary experiment, the downstream part of the slit outlet had a sharp edge of 160 deg, and there was practically no reduction of shearing stress. After reforming the slit outlet into a round shape, the data of Figs. 14 and 15 were obtained. It suggests that if the injection is made suitable for the stratified flow, a more effective reduction might be realized.

Before the present experiment, a series of similar experiment were made without a turbulence stimulator (Kato et al., 1990). As mentioned before, the boundary layer was not fully turbulent at $U_\infty = 5.7$ m/s. The reduction effect, both with and without turbulence stimulator, is summarized in Fig. 16. The effect increased with the injection of higher viscosity fluid in the range of the present experiment. The reduction rate reached 65 percent by the fluid of $\mu_s/\mu_w = 49$. The effect seems greater without stimulator, though the difference is small.

Figure 17 demonstrates clearly the importance of low-viscosity fluid injection into the bottom of the boundary layer. When the low-viscosity fluid is not injected ($v_l/U_\infty = 0$), the injection of the high viscosity fluid creates a reverse effect, that is, an increase in shearing stress. Increasing the flow rate of the low-viscosity fluid, causes a reduction in the shearing stress.

The present experimental result supports Madavan's result that the skin-friction reduction by microbubble injection was mainly due to effective viscosity increase by microbubbles. (Madavan et al., 1985b).

Conclusions

The wall shearing stress was directly measured at a turbulent boundary layer on a flat wall by injecting high viscous sugar syrup and water from upstream and downstream slits, respectively.

The wall shearing stress was reduced 50 to 65 percent at the optimum combination of sugar syrup and water injection rates. A water/water injection experiment was also made for com-

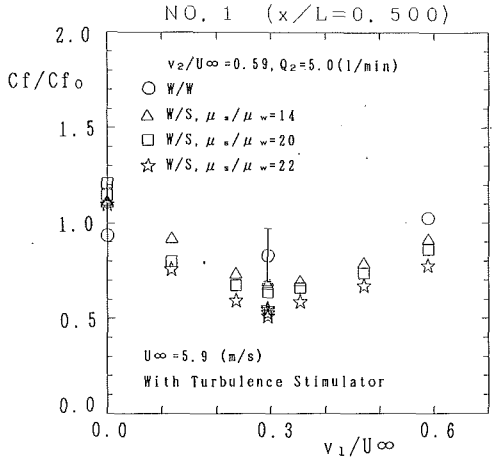

Fig. 17 Effect of v_1/U_∞ on C_f/C_{fo} (Uncertainty of data: ±14 percent)

parison, where a reduction of up to 20 percent was observed. However, the mechanism of the reduction seems different in the both cases.

Within the range of the experiment, the water/sugar syrup injection was more effective at lower main flow velocity. Injecting high viscosity fluid was also effective in reducing the wall shearing stress.

The reduction effect decayed rapidly downstream from the injection slit, possibly due to the mixing effect in the injected boundary layer.

The reduction mechanism of the wall shearing stress is thought to be as follows: The high viscosity fluid reduces the intensity of Reynolds stress in the turbulent region resulting in an increase of the velocity gradient there. The increase causes the reduction of the velocity gradient in the viscous sublayer, which results in the reduction of wall shearing stress. The present study is, however, in the preliminary stage, and it is necessary to measure more detailed properties such as turbulence, Reynolds stress etc., for a better understanding of the mechanism.

Acknowledgments

The authors thank the members of the Fluids Engineering Laboratory, Department of Naval Architecture and Ocean Engineering, University of Tokyo, especially Mr. D. Masumoto for his sincere efforts at the beginning of this research.

References

Bandyopadhyay, P. R., 1986, "Review—Mean Flow in Turbulent Boundary Layers Distributed to Alter Skin Friction," ASME JOURNAL OF FLUIDS ENGINEERING, Vol. 108, pp. 127–140.

Bogdevich, V. G., Evseev, A. R., Malyuga, A. G., and Migirenko, G. S., 1977, "Gas-saturation Effect on Near Wall Turbulence Characteristics," *2nd International Conference on Drag Reduction*, BHRA Fluid Eng. Paper D2, pp. D2-25 ~ D2-37.

Cebeci, T., and Bradshaw, P., 1977, *Momentum Transfer in Boundary Layers*, Hemisphere Co.

Fujii, Y., 1991, "Frictional Drag Reduction by Injecting High-Viscosity Fluid," Master thesis, Dept. of Naval Architecture and Ocean Engineering, University of Tokyo (in Japanese).

Gyr, A. (ed.), 1989, "Structure of Turbulence and Drag Reduction," *IUTAM Symposium*, Zurich, Switzerland, Springer-Verlag.

Hough, G. R. (ed.), 1980, "Viscous Flow Drag Reduction," *Progress in Astro. and Aero.*, Vol. 72, AIAA.

Kato, H., Fujii, Y., Yamaguchi, H., and Miyanaga, M., 1990, "Frictional Drag Reduction by Injecting High-Viscosity Fluid," *J. Soc. Naval Arch. Japan* (in Japanese).

Lachmann, G. V. (ed.), 1961, *Boundary Layer and Flow Control*, Vol. 1, 2, Pergamon Press.

Liepmann, H. W., and Narasimha, R. (eds.), 1987, "Turbulence Management and Relaminarisation," *IUTAM Symposium Bangalore*, India, Springer-Verlag.

Madavan, N. K., Deutsch, S., and Merkle, C. L., 1984, "Reduction of Turbulent Skin Friction by Microbubbles," *Phys. Fluids*, Vol. 27, No. 2, pp. 356–363.

Madavan, N. K., Deutsch, S., and Merkle, C. L., 1985a, "Measurements of Local Skin Friction in a Microbubble-modified Turbulent Boundary Layer," *Journal of Fluid Mechanics*, Vol. 156, pp. 237–256.

Madavan, N. K., Merkle, C. L., and Deutsch, S., 1985b, "Numerical Investigations into the Mechanisms of Microbubble Drag Reduction," ASME JOURNAL OF FLUIDS ENGINEERING, Vol. 107, pp. 370–377.

Tiederman, W. G., Luchik, T. S., and Bogard, D. G., 1985, "Wall-layer Structure and Drag Reduction," *Journal of Fluid Mechanics*, Vol. 156, pp. 419–437.

Virk, P. S., 1975, "Drag Reduction Fundamentals," *AIChE Journal*, Vol. 20, No. 4, pp. 625–656.

Yamaguchi, H., Kato, H., Sugatani, A., Kamijo, A., Honda, T., and Maeda, M., 1988, "Development of Marine Propellers with Better Cavitation Performance," 3rd Report, *J. Soc. Naval Arch. of Japan*, Vol. 164, pp. 28–42.

G. W. Anderson

J. J. Rohr

S. D. Stanley

Naval Ocean Systems Center,
San Diego, CA 92152

The Combined Drag Effects of Riblets and Polymers in Pipe Flow

The additional skin friction effect produced by a 3M riblet surface, used in conjunction with low concentration polymer solutions, is investigated in fully developed, turbulent pipe flow. Generally at the low concentrations of Polyox 301 and guar gum studied, the absolute drag reduction of the 3M riblets appears to be independent of the polymer presence, with a maximum between 5 and 7 percent occurring around $h^+ = 12$. Comparisons with previous polymer studies with 3M riblets, sand roughened and commercially rough surfaces are made.

1 Introduction

Riblets refer to streamwise micro-grooved surfaces which were originally developed at NASA Langley Research Center in the late 70s for reducing turbulent skin friction. One of the better drag-reducing geometries found, and employed here, are symmetric, sharply peaked, v-groove riblets. These riblets provide 5 to 7 percent drag reduction when the riblet height in wall units, h^+, is between 11 and 15 (Walsh and Lindemann, 1984; Walsh, 1990). The grooves are defined by peak height, h, peak-to-peak spacing, s, and are illustrated in Fig. 1.

Drag reduction by dilute polymer solutions, discovered in the late 40s, has been found to reduce frictional resistance in turbulent flow by as much as 70 to 80 percent (Hoyt, 1972). It is well known (Wells and Spangler, 1967; Wu and Tulin, 1972) that for the type of dilute polymer solutions studied here, the polymer additives must be in the wall region for reduced wall shear stress to occur.

A unified theory based on first principles, accounting for the drag reduction associated with either polymers or riblets, has yet to be developed. It is ultimately hoped that, through investigating the combined effects of riblets and polymers, new insights will arise which will lead to a better understanding of how each phenomenon reduces turbulent skin friction.

2 Background

2.A Riblets in Pipes. For more than a century after Darcy's (1857) classical experiments were performed with pipes of different roughness, it had been universally accepted that a smooth surface would always offer the least flow resistance. Flouting conventional wisdom the surface of fast moving sharks have for at least a million years (Reif, 1985) continued to display fine longitudinal grooves on their scales, which appear to follow the flow lines about their body (Reif and Dinkelacker, 1982). This observation has led to one of several approaches which has resulted in the development of riblets. Other approaches resulted from attempts to modify near-wall turbulent structures (Liu et al., 1966) and exploit the skin-friction reductions obtained in corner flows (Eckert and Irvine, 1956; Kennedy et al., 1973). An excellent overview of past and present riblet research can be found by Walsh (1990). Although the drag reduction achieved by riblets is modest in comparison to polymers, these devices are particularly significant to aviation and may soon be utilized on commerical transport aircraft (McLean et al., 1987; Walsh et al., 1988; Walsh, 1989; Szodruch, 1991).

The riblet experiments reported in the literature to date deal almost exclusively with developing external flows (Coustols and Savill, 1989; Lowson et al., 1989). For these flows, drag reduction has been achieved in air (Walsh, 1978; 1979; 1982; 1983; Bechert et al., 1985; Sawyer and Winter, 1987) and water (Reidy and Anderson, 1988; Beauchamp and Philips, 1988); and at transonic (McLean et al., 1987) and supersonic (Gaudet, 1989) speeds. Initially it was not known (Bushnell, 1985) whether riblets used in internal flows, because of the mass flow constraint, would behave differently than in external flows. Figure 2 contains riblet measurements taken from both developing external flows (symbols) and more recent, fully developed, internal, pipe flows (curves). The percent drag reduction achieved by riblets as a function of h^+ clearly exhibits a similar characteristic signature for both flow conditions. All

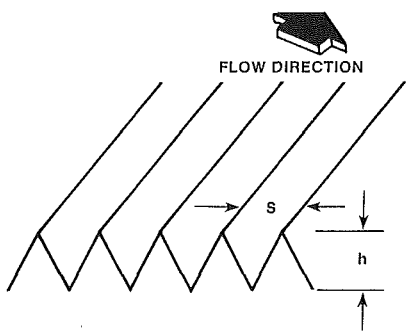

Fig. 1 Riblet groove geometry ($h = s$)

Contributed by the Fluids Engineering Division for publication in the JOURNAL OF FLUIDS ENGINEERING. Manuscript received by the Fluids Engineering Division March 30, 1992. Associate Technical Editor: D. M. Bushnell.

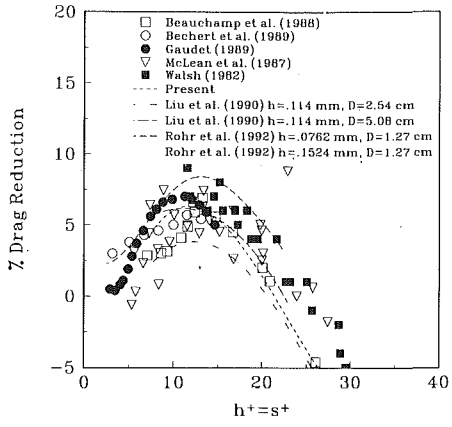

Fig. 2 Comparison of riblet percent *DR* versus h^+ results for internal (curves) and external (symbols) flows in water

the experiments from which the data in Fig. 2 were taken used sharply peaked, v-groove ($h = s$) riblets, and except for the experiments of Walsh (1982), were manufactured by the 3M Company.

2.B Riblets in Polymer Solutions. In general (Bushnell, 1985), there has been little research studying the combined effect of different drag reduction techniques. Previous results concerning the net drag reduction of riblets and polymers, moveover, have been conflicting. Reidy and Anderson (1988) have reported that when a drag-reducing polymer solution of 2 wppm polyacrylamide was used in conjunction with 3M riblets in pipe flow, the total drag reduction was approximately equal to the sum of the drag reductions of the two techniques used separately. A possible synergistic effect was noted at high Reynolds numbers. However, between identical riblet experiments there was considerable scatter in their data. Reidy and Anderson (1988) noted that due to their short test section, the flow over the riblets may not have been fully developed.

Rohr et al., (1989) have found, in some preliminary studies at low Reynolds numbers, no difference in drag reduction between smooth-vinyl and 3M riblet covered pipes when 2.5, 10 and 40 wppm polymer solutions of Polyox 301 flowed through them. They acknowledged, however, the importance of extending their work to higher Reynolds numbers.

Christodoulou et al. (1991) have also studied the combined effects of 3M riblets and polymers (Polyox 301 and polyacrylamide) on drag reduction in pipe flows. The degree of impact by the 3M riblets was found to be both a function of polymer type and concentration. At low concentrations (2, 5 and to some degree 10 wppm) of either polymer, and for values of $h^+ < 10$, the 3M riblets appeared to provide roughly the same increase in percent drag reduction, percent *DR*, as found in solvent. Otherwise for both polymers the range of h^+ values within which percent *DR*, occurred, as well as the h^+ value associated with maximum percent *DR*, diminished with increasing concentration.

Beauchamp and Philips (1988) studied 3M riblet and polymer drag reduction on an axisymmetric body falling through a polymer solution of Polyox 301. In their 1986 study the drag reducing effects of the riblets and polymer were found to be synergistic at low values of Reynolds number and approximately additive at high. However, when the experiment was repeated in 1987 the data showed essentially no difference in drag reduction when, for the same concentration and polymer, a 3M riblet surface was substituted for a smooth surface. Beauchamp and Philips conjectured that the original (1986) polymer solution was degraded and thus had a lower molecular weight distribution than the 1987 polymer solution. Consequently, polymer onset would not be the same for the two experiments and this could explain the difference in performance of the riblets in these polymer solutions.

Choi et al. (1989) has found that the combined use of a polymer coating with riblets (Hoechst U-groove) on a one-third scale yacht model results in an overall improvement in the percent drag reduction characteristics over either of the two methods used alone. Some synergism was noted at the higher flow speeds. A deficiency of Choi et al.'s (1989) experiments was that the net drag measured included form and wave drag components. The drag reduction by riblets alone was only between 1 and 2 percent.

The present experiments attempt to mitigate some of the deficiencies in previous riblet-polymer studies, as future work will undoubtedly improve this endeavor. Shear sensitive and shear resistant polymers are employed in high Reynolds number, fully developed, pipe flows with and without riblets. All comparisons between smooth and 3M riblet surfaces involve essentially simultaneous measurements taken from the same transducer. Given the inconsistent accounts of previous riblet-polymer studies, the primary goal here is to establish the basic trends characterizing how riblets perform in dilute polymer solutions (Section 4) and to propose a simple model (Section 5) consistent with observations. Corresponding measurements taken from polymer flows in sand-roughened (Virk, 1971b) and commercially-rough (Green et al., 1985) pipes are also included for comparison.

3 Experimental Setup/Procedure

3.A Experimental Setup. The experiments were performed in a simple, single pass, system of which a sketch appears in Fig. 3. Polymer solutions were gently mixed in a 600-gallon stainless-steel holding tank from which fluid was gently drawn into a 600-gallon stainless-steel tank which could be pressurized. Air pressure, up to 250 psia, provided maximum Reynolds numbers of nearly 500,000 in the 2.54 cm pipe employed. The solvent for these experiments was fresh, untreated water taken from a lake. The polymer solutions studied were shear stable guar gum at 100 wppm and shear degradable Polyox 301 at 2, 4, and 8 wppm. Higher polymer concentrations were not used because compared to riblets, they produce much greater drag reduction and it was not initially known to

Nomenclature

D = diameter of pipe
percent DR = $((f_{\text{smooth}} - f_{\text{riblet}})/(f_{\text{smooth}}))_{\text{Re}}$ * 100 percent
k_s = sand grain roughness height
k_s^+ = sand grain height in wall units = $(k_s u^*)/(\nu)$
ΔL = distance along pipe length for differential pressure measurement
ΔP = pressure drop along pipe
Q = volume flow rate
Re_D = UD/ν_s
U = mean velocity
f = Darcy-Weisbach friction factor = $(2\Delta PD)/\rho U^2 L)$
h = riblet height
h^+ = riblet height in wall units = $(hu^*)/(\nu_s)$
s = riblet groove spacing
s^+ = riblet groove spacing in wall units = $(su^*)/(\nu_s)$
u^* = friction or shear stress velocity = $(\tau_{\text{wall}}/\rho)^{1/2}$
ν = kinematic viscosity
ν_s = kinematic viscosity of solvent (lake water)
ρ = density of water
τ_{wall} = wall shear stress

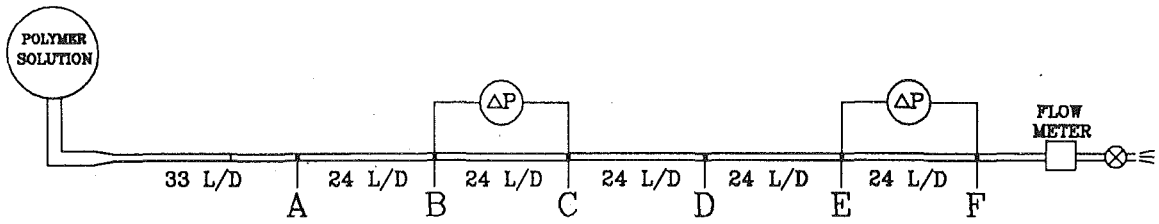

Fig. 3 Schematic of pipe-flow facility

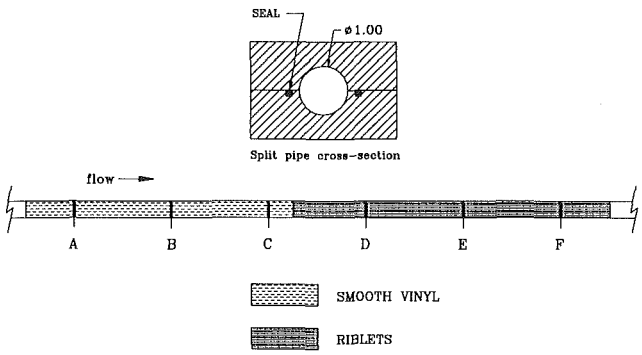

Fig. 4 Smooth/riblet series configuration

what degree there would be competition between these drag reducing processes.

For the present riblet-polymer study a split pipe was fabricated by milling a half-round groove of 1.27-cm radius in two bars of aluminum which were 2.54 cm by 7.62 cm and 3.66 m long. This allowed for easy installation of both the control (smooth vinyl) and 3M riblet material and provided ready access to the pressure holes for deburring. The smooth-vinyl sheets used as a reference surface were 0.12 mm thick. The height and peak-to-peak spacing of the 3M riblets employed were 0.1524 mm. The pipe halves were fastened by pairs of 6.35 mm bolts spaced every 10.16 cm on either side of pipe centerline. The spilt pipe was kept watertight by O-ring packing glands placed in grooves on either side of the flow passage. Preceeding the split pipe was a smooth pipe, 2.54 cm in diameter and 0.559 m long.

Six pressure taps were located at distances of 0.305 (A), 0.610 (B), 1.52 (C), 2.13 (D), 2.74 (E), and 3.35 (F) m from the upstream end of the split pipe. The pressure drop between various combinations of the 6 available pressure taps was measured by four Validyne Model DP-15 variable reluctance pressure transducers having full-scale output of 0.2, 2, 8, and 32 psia. Due to the limited dynamic range of the pressure transducers, care must be taken to prevent them from being overpressurized. A system of electronically actuated solenoid valves was used to enable the data acquisition computer to select which pressure taps to monitor, as well as the appropriate pressure transducer to use. The flow rate was measured by Micro Motion Mass Flowmeters (Models C200 and D40).

3.B Procedure. Initially the entire split pipe was covered with either smooth vinyl or 3M riblet material. Pressure-drop measurements along the split pipe determined the entrance length required for fully developed flow over each surface throughout the Reynolds numbers of interest. It was found that the smooth vinyl and 3M riblets could be positioned in series and still provide adequate lengths of fully developed turbulent flow over both surfaces. The first 1.68 m of the pipe was covered with smooth vinyl and the remaining 1.98 m with the 0.1524 mm (0.006 in) 3M riblets (see Fig. 4). The riblet test section was placed downstream of the smooth control so, as in previous riblet-polymer experiments, if polymer degradation occurred it would not positively bias the assessment of riblet drag reduction. Pressure-drop measurements across the control surface were collected between 91.4 (B) and 152.4 (C) cm from the beginning of the split pipe. Across the riblet test surface, pressure drops were measured between 106.7 (E) and 167.6 (F) cm from the beginning of the riblet surface. This initial development length ($L/D \sim 42$) is significantly longer than those used in previous riblet (Liu et al., 1990) and riblet/polymer (Christodoulou et al., 1991) experiments in pipes ($L/D < 10$, personal communication O. Riccius). In external flows (only solvent data available) the extent of the initial development length over a riblet surface has also been found to be small, less than 5 boundary layers (Walsh, 1988; Squire and Savill, 1989; Christodoulou et al., 1991). All comparisons between smooth and 3M riblet surfaces, whether in solvent or polymer solutions, resulted from pressure drop measurements recorded alternately across each surface, by the same transducer, and at identical flow settings. This procedure was found advantageous because it eliminated errors associated with the drift and calibration of the transducers, as well as any variations resulting from slightly different mixtures of polymer solutions.

Determining the appropriate value of the pipe diameter is of serious concern (Bandyopadhyay, 1986) since the pipe diameter is raised to the 5th power in the calculation of friction factor. As in previous pipe flow studies with riblets (Nitschke, 1984; Reidy and Anderson, 1988; Rohr et al., 1989; Liu et al., 1990) and sand-roughness (Nikuradse, 1933), the equivalent diameter used in calculations of the resistance coefficient and Reynolds number is defined to be equal to a perfectly round smooth pipe of the same cross-sectional area. The equivalent diameter was calculated by determining the volume of water necessary to fill the pipe.

4 Results

4.A Solvent and Polymer Pipe Flows Over Smooth and 3M Riblet Surfaces (f versus Re). Since the seminal pipe flow experiments of Reynolds (1883), the unifying principles underlying smooth pipe flow (without polymer) have been most clearly expressed when the data are plotted nondimensionally in terms of friction factor and Reynolds number. The Darcy-Weisbach friction factor, f, and the Reynolds number, Re_D, are defined respectively as:

$$f = (2\Delta P D)/(\rho U^2 L) \tag{1}$$

and

$$\mathrm{Re}_D = UD/\nu_s. \tag{2}$$

Figure 5(a) presents a compilation of f versus Re pipe data, for different surfaces, for cases where no polymer was present. The sand-roughened and commercially-rough pipe data were obtained from Nikuradse (1933) and Green et al. (1985), respectively. Nikuradse acquired his data in pipes covered with similarly shaped sand grains of different size. Green et al. (1985) had employed, in the present facility, a 2.606-cm diameter, hard-drawn copper tube as their "smooth" pipe and a galvanized-steel water pipe with an average inside diameter of 2.69 cm for their "rough" case. Reynolds number versus friction factor data from their "smooth" pipe were found to

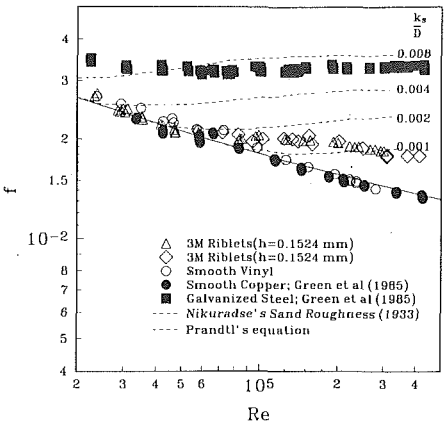

Fig. 5(*a*) Friction factor versus Reynolds number for pipe flows of water over different surfaces

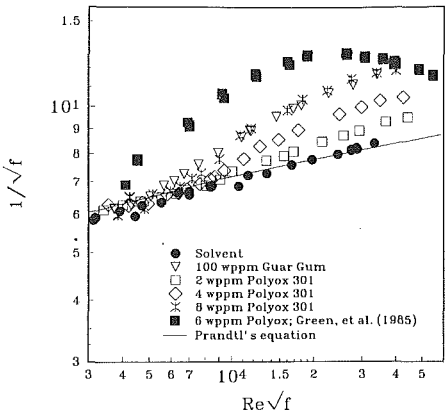

Fig. 6(*a*) Prandtl coordinates for pipe flows of solvent (water) and polymer solutions over a smooth surface

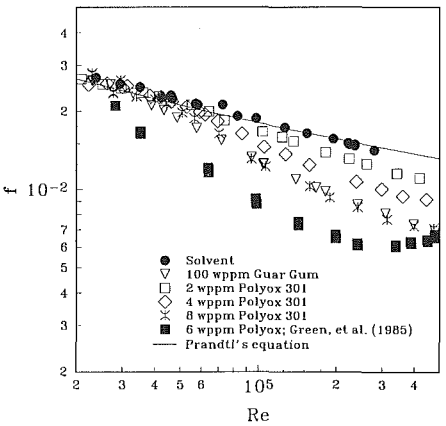

Fig. 5(*b*) Friction factor versus Reynolds numbers for pipe flows of solvent (water) and polymer solutions over a smooth surface

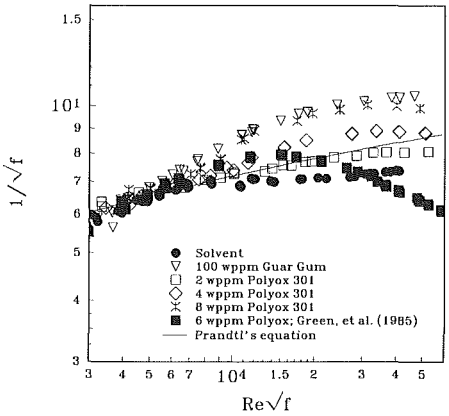

Fig. 6(*b*) Prandtl coordinates for pipe flows of solvent (water) and polymer solutions over 3M riblets (h = 0.1524 mm) and Green et al.'s (1985) galvanized steel pipe

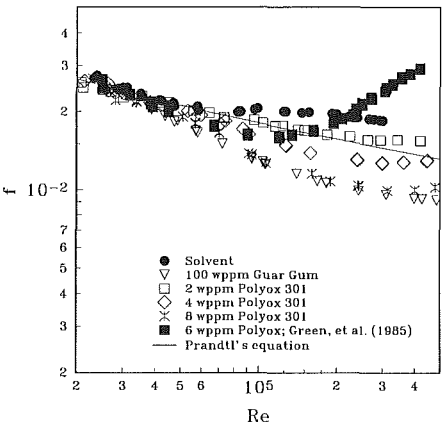

Fig. 5(*c*) Friction factor versus Reynolds number for pipe flows of solvent (water) and polymer solutions over 3M riblet (h = 0.1524 mm) and Green et al.'s (1985) galvanized steel pipe

conform to the accepted values for hydraulically smooth pipes, while measurements in their "rough" pipe had indicated, via the Moody diagram, a relative roughness of about 0.0055. The equivalent sand-roughness for their "rough" pipe was therefore 0.147 mm (consistent with what is typically quoted for galvanized pipe) although, of course, the surface is far from being uniformly rough.

Considering first the smooth pipe data in Fig. 5(*a*), the difference in friction factor values at low Reynolds numbers between the split (open circles-present data) and seamless (solid line-Prandtl (Schlicting, 1979)) pipe data, warrant some comment. Deviations from the Prandtl line have been also found in other spilt pipe test sections (Rohr et al., 1989). It is presumed that these discrepancies are associated with the seams and milling process associated with each split pipe's fabrication. Nevertheless, the character of the drag reduction achieved when a smooth surface is replaced by a riblet one, has been observed to be independent of whether these surfaces are within split or seemless pipes, or for that matter, on flat plate or axisymmetric bodies (Rohr et al., 1992). Hereafter the distinction between split pipes and conventionally seamless pipes will be disregarded unless it is felt to be of some significance.

Also seen in Fig. 5(*a*), the friction factors for the 0.1534 mm 3M riblet surface (triangles and diamonds) are less than those for the smooth-vinyl surface for Reynolds numbers between about 20,000 and 60,000. These differences, which will be seen more clearly in later figures (Fig. 7(*a*,*b*)), reflect the expected riblet drag reduction with a maximum of about 7 percent. After a Reynolds number of about 60,000 the 3M riblets begin to act as a drag-increasing rough surface, with an equivalent sand particle height of about $h/4$. Sawyer and Winter (1987) have found similar results for v-groove riblets ($h/s = 1.28, 2.08$) in this same flow regime. At higher Reynolds numbers, where the drag increasing properties of 3M riblets have not previously been investigated, friction factors are found to become increasingly smaller. This behavior is contrary to that of the sand roughened and galvanized steel pipes where the friction factor is observed to remain constant.

It is interesting to note that there is some evidence (Tani, 1988) of drag reduction resulting from sand grain roughness, which is thought to originate in the nearly quiescent flow at

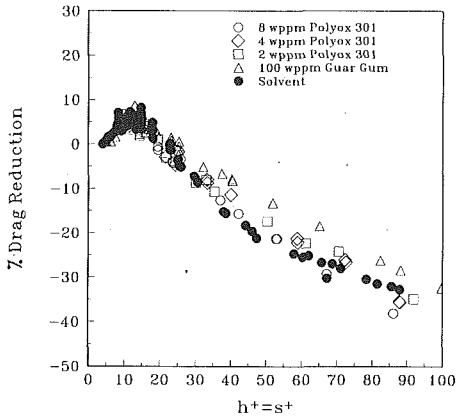

Fig. 7(*a*) Riblet percent *DR* versus h^+ results for pipe flows of solvent and polymer solutions over 3M riblets (h = 0.1524 mm)

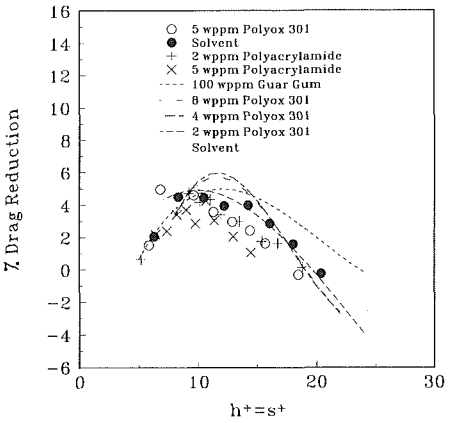

Fig. 7(*b*) Riblet percent *DR* versus h^+ comparison of present results (curves) with Christodoulou et al., 1991, results (symbols) for pipe flows of solvent (water) and polymer solutions

the base of the roughness elements. Tani (1989) has suggested that Nikuradse's pressure drop measurements taken along a sand roughened pipe (from which the dotted lines in Fig. 5(*a*) are derived) indicate no region of drag reduction because of a compensating increase in drag by the wake component of the velocity profile. On a flat plate, where this is not the case, Abe et al. (1989) have reported a regime of net drag reduction (about half as much as what they found for riblets) for k^+ values less than 6.

Figure 5(*b*) displays, again in f versus Re coordinates, the drag reducing effect of polymer solutions when the surface over which they flow is smooth. Several features characterizing the performance of the polymers are worth noting. For all the present measurements of polymer flows over smooth surfaces, once a decrease in the friction factor by the polymer begins, it always becomes greater with increasing Reynolds number and concentration. It is to be noted, however, that a similar monotonic decrease of friction faction with increasing Reynolds number is not observed for the Polyox 301 data of Green et al. (1985) which instead displays a rolloff in friction-reducing performance, around a Reynolds number of 300,000. Rolloff of Polyox 301 in smooth pipes has been previously correlated by Green et al. (1985) with the beginning of significant molecular shear degradation.

The lack of this feature in the present data is noteworthy and suggests that the higher molecular weight fraction of the Polyox 301 used in the present study has been degraded. Lower drag reduction for the same polymer concentrations would then be expected (Hoyt, 1986). This is in fact observed, the present Polyox 301 behavior in Fig. 5(*b*) at 8 wppm provides significantly less drag reduction than the 6 wppm solution of Green et al. (1985). The principal impact of using less effective polymers occurs when comparisons are made with other investigators (Section 4B) using the same type polymer. Within this context it is important to realize that the Polyox 301 drag reducing effects reported herein are probably indicative of what would normally occur at significantly lower concentrations, had the polymer not been degraded.

Figure 5(*c*) shows the drag reducing performance of the same polymer solutions illustrated in Fig. 5(*b*), but for galvanized steel and 3M riblet pipes, again in the same f versus Re_D format. These data were collected downstream from, and almost simultaneously with, their smooth pipe counterparts. The Prandtl line appears both in Figs. 5(*b*) and (*c*), thereby offering a convenient reference for gross comparisons between the two figures. Contrasting the relative positions of the polymer data for the smooth-vinyl (Fig. 5(*b*)) and 3M riblet (Fig. 5(*c*)) surfaces to the Prandtl line, it appears that for Reynolds numbers between roughly 20,000 and 60,000 the 3M riblets provide additional drag reduction in all the polymer solutions studied. This particular feature will be better illustrated later in Figs. 7(*a*) and (*b*). At higher Reynolds numbers, friction factors in polymer flows over 3M riblet surfaces are always less than their smooth pipe counterparts. This is true regardless of whether the polymer is shear degradable (Polyox 301) or shear resistant (guar gum). Green et al. (1985) have hypothesized that this behavior is a consequence of the reduced effectiveness experienced by all polymers in reducing the form drag associated with individual roughness elements, which at high Reynolds numbers protrude outside the viscous sublayer.

Rolloff in the 3M riblet pipe is now observed for all the Polyox 301 solutions, and appears imminent for the 100 wppm guar gum solution if higher Reynolds numbers had been achieved. Green et al. (1985) have observed rolloff for 200 wppm solutions of guar gum in the galvanized steel pipe. Whereas the 8 wppm Polyox 301 and 200 wppm guar gum solutions performed nearly identically in the smooth pipe (Fig. 5(*b*)) at the highest Reynolds numbers tested, for the same flow regime in the 3M riblet covered pipe, the shear degradable Polyox 301 now performs noticeably poorer.

For the case of the commercially smooth and rough pipes, over the entire flow regime investigated, polymer friction reduction was *always* poorer for the rough surface. Finally, as can be seen in Fig. 5(*c*) for Polyox 301 (and inferred from Green et al. (1985) for guar gum), at mid-to-high Reynolds numbers, the detrimental effect on polymer drag reduction by the commercially rough pipe is much greater than for the 3M riblet case. The same pressure drops and volume flow rates, from which the present data in Figs. 5(*a—c*) were determined are used throughout the remaining figures to calculate the appropriate values corresponding to the new coordinates.

4.B Onset of Drag Reduction for Polymer Flows Over Smooth and 3M Riblet Surfaces ($1/f^{1/2}$ Versus $\mathrm{Re}\{f^{1/2}\}$). It is customary (Virk, 1971a,b) in smooth pipe, polymer flows to plot the data in semilogarithmic Prandtl coordinates. Virk (1971a) had found that in this format the difference in slope between polymer solution and solvent is related to the molar concentration and to the number of backbone chain links in the macromolecule. The x-axis is now proportional to the friction velocity, u^*, and at a fixed friction velocity the y-axis is proportional to the average flow rate. Thus the greater the drag reduction, the larger the positive y-separation from the Prandtl line. The friction velocity is believed to be the operative parameter related to the stretching and subsequent high elongational viscosity of polymer molecules (Hoyt, 1986). It has been observed (Hoyt, 1986) that the elongation of the polymer molecules occurs only above a critical u^*.

Figures 6(*a*) and (*b*) are plotted in semilogarithmic Prandtl coordinates for smooth and rough (galvanized-steel and 3M riblet) surfaces, respectively. As seen in Fig. 6(*a*) the polymer solutions tested generally display the characteristic behavior associated with polymer drag reduction in smooth pipes (Virk et al., 1967). There is, however, a noticeable discrepancy between the threshold values for the drag reduction onset for guar gum and Polyox 301 for the present data. Normally at the concentrations tested here, Polyox 301 would have a conspicuously lower threshold friction velocity than guar gum (see Green et al., 1985). It is known (Hoyt, 1972) that polymers with higher molecular weights have lower threshold values. The higher threshold values observed for the present Polyox 301 solutions are consistent with the other evidence indicating that the polymer was degraded. As expected (Virk, 1971*b*; Hoyt, 1972) the different Polyox 301 concentrations had little effect on drag reduction onset.

Cursory comparisons of the location where drag reduction onset occurs for smooth-vinyl (Fig. 6(*a*)) and 3M riblet (Fig. 6(*b*)) surfaces, in the polymer solutions tested, suggest slightly smaller values of $\mathrm{Re}(f)^{1/2}$ when the 3M riblets were present. For example, the drag reduction onset for the 100 wppm guar gum flowing over the smooth-vinyl surface appears to occur at a $\mathrm{Re}(f)^{1/2}$ value of about 4500, whereas with the 3M riblets, $\mathrm{Re}(f)^{1/2}$ is about 4000 ($h^+ = 8$). However, as evident from Fig. 2, riblet drag reduction phenomenon are acting more or less independently, but because their drag reducing domains overlap, it appears that the polymer solutions flowing over a riblet surface have a lower wall shear stress threshold. It should be noted that both Virk (1971b) and Green et al. (1985) have found essentially no difference between the threshold friction velocity associated with the onset of polymer drag reduction in either sand roughened or commercially rough pipes. Outside the region of drag reduction enhancement, polymer pipe flow over a 3M riblet surface has features similar to what Virk (1971) has found for sand-grain rough surfaces. In this range, for both sand grain and 3M riblet surfaces, individual values of $1/f^{1/2}$ and their average slopes are smaller compared to a smooth pipe surface, and with increasing $\mathrm{Re}\,(f)^{1/2}$ (particularly for the higher Polyox 301 concentrations) exhibit a concave downward curvature.

4.C 3M Riblet Percent Drag Reduction With and Without Polymers (Percent *DR* Versus h^+). In order to better distinguish the additional drag effects of riblets in pipe flows of polymer solutions, experimental results have previously been plotted in terms of percent riblet drag reduction, percent *DR*, as a function of h^+. The percent riblet drag reduction in fully developed pipe flow for both solvent and polymer solutions is defined as:

$$\text{percent } DR = \text{percent}((f_{\text{smooth}} - f_{\text{riblet}})/f_{\text{smooth}})_{\text{Re}} * 100. \quad (3)$$

The value of h^+ is determined using the friction velocity occurring within the riblet covered pipe when percent *DR* is calculated. An equality of percent *DR* in water and dilute polymer solution, for the same size 3M riblets and value of h^+, corresponds to equal absolute changes in wall shear stress as a result of the riblet presence.

The uncertainty in the two quantities shown in Fig. 7(*a*), percent *DR* and h^+, are shown by error bars for a few typical points. By definition the quantity h^+ depends on h, the riblet height, ν, the kinematic viscosity, and u^*. The uncertainty in the value of h is unknown but since the same riblets were used for all the data in Fig. 7(*a*) the uncertainty in h would not contribute to scatter in the data but would rather shift all the data along the x axis, left or right. For this reason no contribution for uncertainty in h is included in the uncertainty analysis. The value for ν is determined by measuring the fluid temperature and then using the tabulated value of ν for the solvent (fresh water) at that temperature. The uncertainty in ν is estimated to be 0.5 percent and is due to the uncertainty in the temperature measurement. The value for u^* depends on the quantities ΔP, L, D, and ρ. The value for ρ is determined from tabulated values for the solvent based on the measured temperature. The density of water is a weak function of temperature so the uncertainty of the measured temperature creates a relatively small uncertainty in the density, less that 0.1 percent. The distance between the pressure taps is known within $+/-$ 1 mm and therefore for the typical distance of 60.96 cm the uncertainty in L is 0.16 percent. The diameter is known within $+/-$ 0.05 mm and therefore for a 2.54-cm diameter pipe the uncertainty in the diameter is 0.2 percent. The major contribution to the uncertainty in u^* is the ΔP measurement. The uncertainty in the pressure transducers is estimated to be $+/-$ 2 percent of the full scale of the transducer. The lowest range transducer (0.2 psia full scale) tends to be more sensitive to calibration errors and zero drift and therefore the uncertainty in measured pressure in this range is estimated to be $+/-$ 4 percent of full scale. These uncertainties include calibration errors, zero drifts, nonlinearities and temperature effects. Note that u^* is a function of the square root of ΔP, L, D and ρ and therefore the uncertainty in u^* contributed by each variable is reduced by the radical.

Because of the experimental setup, the volume flow rate for the smooth and riblet sections of the pipe are identical, as are the fluid viscosity and density. Thus, for the calculation of percent *DR*, which is a function of the ratio of the friction factors, these terms drop out. Also, the same transducer is used for the measurement of pressure in both the smooth and riblet sections and since the ratio of the pressures is used in the calculation of percent *DR* many of the uncertainties in the pressure transducer measurement drop out. In fact the major uncertainty in the percent *DR* calculation is the quality of the pressure tap ports, and the uncertainties in D and L. The uncertainties for D and L were given above as 0.2 percent and 0.16 percent, respectively. The friction factor is a function of the diameter raised to the fifth power so the uncertainty due to the diameter is increased to 1.0 percent (5 times 0.2 percent). The uncertainty due to the pressure tap quality is estimated to be less than 3.5 percent, based on the author's experience with the repeatibility of the pressure measurements with multiple applications of riblets and smooth vinyl to the inside of pipes.

Figure 7(*a*) shows riblet percent *DR* versus h^+ behavior for solvent and polymer solutions. The similarity between solvent and polymer data suggests that the 3M riblet drag reducing effect is approximately additive at the low polymer concentrations studied herein. Closer scrutiny reveals that for h^+ values greater than about 20 the different data sets begin to diverge. In particular, between h^+ values of 20 and 24, Fig. 7(*a, b*) shows some evidence of drag reduction synergism occurring for the guar gum solution.

The tendency of riblet drag reduction to decrease and become negative with increasing stream velocity has been attributed to the accompanying thinning of the boundary layer (Wilkenson et al., 1988) and penetration of the riblet peaks through the viscous sublayer (Kelman et al., 1989). It is conceivable that the decrease of the turbulent momentum transport in the presence of polymer throughout the buffer layer (Virk et al., 1967; Patterson et al., 1977) may tend to ameliorate the riblet-turbulence interactions which determine the zero-cross-over point for riblet drag reduction. This process could provide a candidate mechanism for the more than additive drag reduction observed. Reidy and Anderson (1988) and Choi et al. (1989) have all reported similar findings in this same flow regime. They have associated this riblet-polymer synergism to the riblets diminishing polymer degradation. However, guar gum which is resistant to shear degradation, nonetheless exhibits (exclusively as seen in Fig. 7(*a*)) this synergistic behavior.

With increasing shear (higher values of h^+) the divergence

between the different data sets shown in Fig. 7(*a*) grows, presumably reflecting (at least in part) different tolerances to polymer degradation. As anticipated, at the higher values of h^+ where riblets decrease polymer drag reduction (percent *DR* is negative), they are less detrimental in the shear-stable guar gum solution.

In Fig. 7(*b*) the data from Fig. 7(*a*) are replotted as lines to allow for easier comparison with the relevant data of Christodoulou et al. (1991). Christodoulou et al.'s (1991) measurements of Polyox 301 and polyacrylamide were collected in a seamless 2.54-cm diameter pipe, where sheets of 0.11-mm 3M riblet films were rolled up and then pressed onto the inner pipe wall. Previously Liu et al. (1990), employing the same pipe and 3M riblets found, for water without polymers, maximum drag reductions between 5 to 7 percent. The more recent percent *DR* peak observed by Christodoulou et al. (1991) for water, as seen in Fig. 7(*b*) is only around 4 percent. Christodoulou et al. (1991) have attributed this variation to possible contamination and degradation of the 3M riblet surface.

The Christodoulou et al. (1991) data plotted in Fig. 7(*b*) clearly show that the performance of their 3M riblets in dilute polymer solutions is similar to that of the present study. At higher concentrations (not shown), Christodoulou et al. (1991) have found that riblet drag reduction diminishes with increasing polymer concentration and increasing h^+. It might be anticipated that in a polymer solution, as the flow field around the riblet surface becomes increasingly modified, as evidenced by greater drag reduction, the ability of the riblets to reduce turbulent skin friction would become increasingly impaired.

Concerning the lack of riblet drag reduction reported by Rohr et al. (1989) in similar experiments, this may be attributed to the low h^+ values achieved in their study. Maximum h^+ values were only about 5 which, in reference to Figs. 2 and 7(*a*), are probably not large enough to see much, if any, riblet drag reduction.

5 Discussion

Although there is much disparity between the riblet-polymer data to date, there appears to exist a certain flow regime where drag reduction is approximately additive. Beauchamp and Philips (1988) have hypothesized that since both phenomena act in the near wall region of the turbulent boundary layer, a roughly additive effect might be expected if they involved different length scales. However Beauchamp and Philips (1988) do not distinguish what length scales are associated with each phenomenon. This distinction may not be possible as both riblets (Liu et al., 1990) and polymers (Lumley, 1973; Hibberd et al., 1982; Reidiger, 1989) are known to be associated with the fine structure of the flow. Moreover, the onset of polymer drag reduction has been construed (Hoyt, 1972) to reflect the beginning of the production of turbulent scales small enough to be affected by the additive molecules. Yet throughout the present measurements, although polymer onset occurs at values of h^+ close to where peak values of 3M riblet drag reduction in water are found (Fig. 6(*b*)), no detrimental competition between scales for drag reduction is observed.

We believe it more promising to interpret the additional drag reduction of riblets in polymer solutions in terms of two separate albeit overlapping) regions of flow where each phenomenon is more effective. A similar approach has been taken toward interpreting the "approximately additive" drag reducing effects found when riblets and LEBU's were used together (Walsh and Lindemann, 1984). Here the LEBU is believed to operate on the large-scale outer structure and indirectly on the wall structure (Corke et al., 1982), while the riblets' region of operation is only close to the wall (Walsh, 1990). For drag-increasing, *k*-type, rough walls Bandyopadhyay (1986) has also reported a corresponding trend, i.e., the absolute drag performance of the LEBU device to first order remained unchanged whether the wall was rough or smooth.

In the scenario presently proposed for riblets and polymers, the principal operative regions are y^+ between about 10 to 100 for the polymers and below around 13 for the riblets (where y is measured from the riblet peaks). These numbers are estimates meant only to roughly define the buffer layer of the polymer in the presence of riblets, and the region of riblet influence in solutions of polymer. They are based on the common consensus of previous polymer and riblet studies where each phenomenon was studied separately. For example the mode of action of the polymers on smooth (Tiederman et al., 1985) and sand-roughened (Virk, 1971b) surfaces has been determined to be within the buffer region, while remaining largely ineffectual within the viscous sublayer (Tiederman et al., 1985), or in the quiescent region of flow in the grooves between riblet peaks (Reed and Bushnell, 1990). In the buffer layer polymer molecules may be extended, thereby increasing extensional viscosity and perhaps inhibiting the breakup of low-speed streaks (Tulin, 1966; Choi et al., 1989); or through cross-stream molecular entanglement resist the formation of steamwise vortices (Lumley, 1967; Hoyt, 1972).

The effect of riblets on the other hand has been thought to be most pronounced near the surface, either within the grooves (Wilkinson and Lazos, 1987; Wilkinson et al., 1988) or the peaks where spanwise motion is inhibited (Bacher and Smith, 1986; Bechert et al., 1989; Choi, 1989; Johansson et al., 1991). Flow visualization studies of riblets (Bacher and Smith, 1986; Walsh, 1990) indicate little noticeable change in the outer flow structure above about $y^+ = 13$.

It is known that polymers, even at low concentrations, have effects on flow structures near the wall (Oldaker and Tiederman, 1977; Luchik and Tiederman, 1984). Within the present "cartoon" characterization of riblet-polymer interaction, additive drag reducing effects would be expected only when the effect of the polymer on the flow near the riblet surface is minimal. Possible riblet-polymer synergism could exist at h^+ values around 25 where the zero-drag-reduction point would normally occur in water. Here it is hypothesized that a limited polymer influence on the flow structures about the riblet peaks could possibly extend the range of riblet drag reduction before the peaks begin to act as drag increasing roughness. However, with greater polymer drag reduction (which is a function of the nature of the polymer, its concentration, wall shear stress, where onset occurs, etc.) the influence of the polymer "diffuses" closer to the riblet surface and increasingly interferes with the riblet drag reducing process(es), eventually circumventing it entirely. Under maximum polymer drag reduction conditions Virk (1971b) has found no drag increasing effect by any of the sand roughened surfaces studied for k^+ values less than 12 (in solvent, sand roughness effects began at $k^+ = 5$). It seems reasonable to assume that riblets would not in principle act differently, i.e., their drag reducing effect under maximum polymer drag reduction conditions and comparable values of h^+, would likewise be "washed-out."

Clearly further experiments are required before the interactions of riblets and polymers are understood and a more sophisticated model(s) can be developed. Given the paucity of consistent data, even repetition of previous experimental conditions would be welcome.

6 Conclusions

A series of pipe flow experiments at low polymer concentrations have demonstrated that the drag reducing effects of 3M riblets are approximately additive. The additional drag reduction provided by riblets in dilute polymer solutions peaks between 5 and 7 percent and occurs around $h^+ = 12$, which is similar to their performance in solvent. The guar gum data suggest that the value of h^+ where the riblets begin to act as

roughness (normally occuring around $h^+ = 20$) can be delayed by the polymer presence. This behavior could possible account for previous reports of riblet-polymer synergism. A simple model has been proposed whereby the combinative drag reducing effects of riblets and polymers is viewed as a consequence of each phenomenon being more effective in different (albeit adjacent) regions of the flow. It is hypothesized that as the polymer's effect diffuses closer to the wall, riblets will become increasingly less effective within the polymer-altered flow field.

Additionally, the pipe flow data for solvent at high Reynolds numbers suggest that the riblets do not exhibit typical "fully rough" behavior.

References

Abe, K., Matsumoto, H., and Tani, I., 1989, "Drag Reduction by Sand Roughness," Presented at the *Proceeding of the Second IUTAM Symposium on Structure of Turbulence and Drag Reduction*, Zurich, Switzerland, July 25–28.

Bacher E. V., and Smith C. R., 1986, "Turbulent Boundary-layer Modification by Surface Riblets," *AIAA Journal*, Vol. 24, No. 8, pp. 1382–1384.

Bandyopadhyay, P. R., 1986, Review-"Mean Flow in Turbulent Boundary Layers Disturbed to Alter Skin Friction," ASME JOURNAL OF FLUIDS ENGINEERING, Vol. 108, pp. 127–140.

Beauchamp, C. H., Philips, R. B., 1988, "Riblet and Polymer Drag Reduction on an Axisymmetric Body," Presented at the *Symposium on Hydrodynamic Performance Enhancement for Marine Applications*, Newport, RI, Oct. 31–Nov. 1, pp. 127–134.

Bechert, D. W., Hoppe, G., and Reif, W. E., 1985, "On the Drag Reduction of the Shark Skin," AIAA Paper No. 85-0546.

Bechert, D. W., and Bartenwerfer, M., 1989, "The Viscous Flow on Surfaces with Longitudinal Ribs," *Journal of Fluid Mechanics*, Vol. 206, pp. 105–129.

Bushnell, D. M., 1985, "Turbulent Drag Reduction for External Flows. Aircraft Drag Prediction and Reduction," AGARD R-723, pp. 5-1 to 5-26.

Choi, K. S., 1989, "Near-wall Structure of a Turbulent Boundary Layer with Riblets," *Journal of Fluids Mechanics*, Vol. 208, pp. 417–458.

Choi, K. S., Gadd, G. E., Pearcey, H. H., Savill, A. M., Svensson, S., 1989, "Drag Reduction with a Combined Use of Riblets and Polymer Coating," *Drag Reduction in Fluid Flows, Techniques for Friction Control*, eds., Sellin and Moses, Ellis Horwood-Publishers, West Sussex, England, pp. 271–277.

Christodoulou, C., Liu, K. N., and Joseph, D. D., 1991, "Combined Effects of Riblets and Polymers on Drag Reduction in Pipes," *Physics of Fluids A*, Vol. 3, No. 5, pp. 995–997.

Corke, T. C., Nagib, H. M., and Guezence, Y., 1982, "A New View on the Origin, Role, and Manipulation of Large Turbulent Boundary Layers," NASA Contractor Report 165861.

Coustols, E., and Savill, A. M., 1989, "Resume of Important Results Presented at the Third Turbulent Drag Reduction Working Party," *Applied Scientific Research*, Vol. 46, pp. 183–196.

Darcy, H., 1857, Memoires a l'Acadamie d.Sciences, Bd 15, Nr 6, 141.

Eckert, E. R. G., and Irvine, T. F., Jr., 1956, "Flow in Corners of Passages with Noncircular Cross Section," *Trans. ASME*, Vol. 78, pp. 709–718.

Gaudet, L., 1989, "Properties of Riblets at Supersonic Speed," *Applied Scientific Research*, Vol. 46, pp. 245–254.

Green, J., Anderson, G., and Edmonds, D., 1985, "Performance Rolloff of Friction-reducing Polymers at High Shear in Pipes," NOSC Technical Report 1066, Naval Ocean System Center, San Diego, CA.

Hibberd, M. F., Kwade, M., and Scharf, R., 1982, "Influence of Drag Reducing Additives on the Structure of Turbulence in a Mixing Layer," *Rheology Acta*, Vol. 21, pp. 582–586.

Hoyt, J. W., 1972, "The Effect of Additives on Fluids Friction," ASME *Journal of Basic Engineering*, Vol. 94, pp. 258–285.

Hoyt, J. W., 1986, "Drag Reduction," *Encyclopedia of Polymer Science and Engineering*, Vol. 5, 2nd Ed., J. Wiley, pp. 129–152.

Johansson, A. V., Alfredsson, P. H., and Kim, J., 1991, "Evolution and Dynamics of Shear-layer Structures in Near-wall Turbulence," *Journal of Fluid Mechanics,* Vol. 224, pp. 579–599.

Kelman, J. K., Shearer, I., and Hall, J., 1989, "Riblet Surface Pressure Losses in Single and Two Phase Flow, *Drag Reduction in Fluid Flows, Techniques for Friction Control*, eds., Sellin and Moses, Ellis Horwood Publishers, West Sussex, England, pp. 327–334.

Kennedy, J. F., Hsu, S. T., and Liu, J. T., 1973, "Turbulent Flows Past Boundaries with Small Streamwise Fins," *Journal of the Hydraulics Division, Proceedings of the ASCE*, Vol. 99, No. HY4, pp. 605–617.

Liu, C. K., Kline, S. J., Johnston, J. P., 1966, "An Experimental Study of Turbulent Boundary Layers on Rough Walls," Report MD-15, Thermosciences Division, Department of Mechanical Engineering, Stanford University.

Liu, K. N., Christodoulou, C., Riccius, O., and Joseph, D. D., 1990, "Drag Reduction in Pipes Lined with Riblets," *AIAA Journal*, Vol. 28, No. 10, pp. 1697–1698.

Lowson, M. V., Bates, J. H. T., and Jewson, A. R., 1989, "Drag Reduction by Riblets in a Two-dimensional Duct," *Drag Reduction in Fluid Flows, Techniques for Friction Control*, eds. Sellin and Moses, Ellis Horwood Publishers, West Sussex, England, pp. 77–81.

Luchik, T. S., Tiederman W. G., 1984, "Bursting Rates in Channel Flows and Drag Reducing Channel Flows," *Symposium on Turbulence*, University of Missouri.

Lumley, J. L., 1967, "The Toms Phenomenon, Anomalous Effects in Turbulent Flow of Dilute Solutions of High Molecular Weight Linear Polymers," *Applied Mechanics Review*, Vol. 20, No. 12, pp. 1139–1149.

Lumley J. L., 1973, "Drag Reduction in Turbulent Flow by Polymer Additives," *Journal of Polymer Science, Macro-Molecular Reviews*, Vol. 7, pp. 283–290.

McLean, J. D., George-Falvey D. N., and Sullivan, P. P., 1987, "Flight Test of Turbulent Skin Friction Reduction by Riblets," *Proceedings of the Royal Aeronautical Society International Conference on Turbulent Drag Reduction By Passive Means*, RAeS, London, Vol. 2, pp. 408–424.

Nikuradse, J., 1933, Translation of "Laws of Flow in Rough Pipes," National Advisory Commission of Aeronautics, Technical Memorandum 1292.

Nitschke, P., 1984, Translation of "Experimental Investigation of the Turbulent Flow in Smooth and Longitudinally Grooved Tubes," NASA, Technical Memorandum 77480.

Oldtaker, D. K., and Tiederman, W. G., 1977, "Spatial Structure of the Viscous Sublayer in Drag Reducing Channel Flow," Physics of Fluids, Vol. 20, No. 10, PtII, pp. S133–S144.

Patterson, G. K., Chosnek, J., and Zakin, Z. L., 1977, "Turbulence Structure in Drag Reducing Polymer Solutions," *Physics of Fluids*, Vol. 20, No. 10, PtII, pp. S89–S99.

Reed, J. C., and Bushnell, D. B., 1990, "Groove Augmented Polymer Drag Reduction," *12th Symposium on Turbulence*, Univ. of Mo.

Reed, J. C., and Weinstein, L. W., 1988, "A Study of Injected Air/Longitudinal Grooved Surface Interaction," Presented at the *Proceedings of the Symposium on Hydrodynamic Performance Enhancement for Marine Applications*, Newport RI, Oct. 31–Nov. 1, pp. 193–198.

Reidiger, S., 1989, "Influence of Drag Reducing Additives on a Plane Mixing Layer," *Drag Reduction in Fluid Flows, Techniques for Friction Control*, eds., Sellin and Moses, Ellis Horwood Publishers, West Sussex, pp. 303–310.

Reidy, L. W., and Anderson, G. W., 1988, "Drag Reduction for External and Internal Boundary Layers Using Riblets and Polymers," AIAA Paper No. 88-0138.

Reif, W. E., Dinkelacker, A., 1982, "Hydrodynamics of the Squamation in Fast Swimming Sharks," Neues Jahrbuch fur Geologie und Palaontologie, Abhandungen Band, Vol. 164, pp. 184–187.

Reif, W. E., 1985, "Squamation and Ecology of Sharks," Courier Forschungsinstitut Senckenberg, Frandfurt/M., Nr 78, p.255.

Reynolds, O., 1883, "An Experimental Investigation of the Circumstances which Determine whether the Motion of Water Will be Direct or Sinuous, and of the Law of Resistance in Parallel Channels," *Philosophical Transactions of the Royal Society*, London, Vol. 174, pp. 935–982.

Rohr, J., Anderson, G. W., Reidy, L. W., 1989, "An Experimental Investigation of the Drag Reducing Effects of Riblets in Pipes," *Drag Reduction in Fluid Flows, Techniques for Friction Control*, eds., Sellin and Moses, Ellis Horwood Publishers, West Sussex, pp. 263–270.

Rohr, J., Anderson, G. W., Reidy, L. W., 1992, "A Comparison of the Drag-reducing Benefits of Riblets in Internal and External Flows," Accepted to *Experiments in Fluids*.

Sawyer, W. G., and Winter, K. G., 1987, "An Investigation of the Effect on Turbulent Skin Friction of Surfaces with Streamwise Grooves," *Proceedings of the Royal Aeronautical Society International Conference on Turbulent Drag Reduction By Passive Means*, RAeS, London, Vol. 2, pp. 330–362.

Schlichting, H., 1979, Boundary Layer Theory, McGraw-Hill, New York.

Squire, L. C., and Savill, A. M., 1989, "Drag Measurements on Planar Riblet Surfaces at High Subsonics Speeds," *Applied Scientific Research*, Vol. 46, pp. 229–243.

Szodruch, J., 1991, "Viscous Drag Reduction on Transport Aircraft," AIAA Paper No. 91-0685.

Tani, I., 1988, "Drag Reduction by Riblet Viewed as Roughness Problem," *Proceedings of the Japan Academy*, Vol. 64, Series B, pp. 21–24.

Tani, I., 1989, "Re-evaluation of Nikuradse's Experimental Data for Rough Pipes," *Proceedings of the Japan Academy*, 65, Series B, pp. 133–135.

Tiederman, W. G., Luchik, T. S., and Bogard, D. G., 1985, "Wall-layer Structure and Drag Reduction," *Journal of Fluid Mechanics 156*, pp. 419–437.

Tulin, M. P., 1966, "Hydrodynamic Aspects of Macromolecular Solutions," *Proceedings of the 6th Symposium on Naval Hydrodynamics*, Washington, ONR ACR-136, pp. 3–18.

Virk, P. S., Merrill, E. W., Mickley, H. S., Smith, K. A., Mollo-Christensen, E. I., 1967, "The Toms Phenomenon, Turbulent Pipe Fow of Dilute Polymer Solutions," *Journal of Fluid Mechanics*, Vol. 30, Part 2, pp. 305–328.

Virk, P. S., 1971a, "An Elastic Sublayer Model for Drag Reduction by Dilute Solutions of Linear Macromolecules," *Journal of Fluid Mechanics*, Vol. 45, Part 3, pp. 417–440.

Virk, P. S., 1971b, "Drag Reduction in Rough Pipes," *Journal of Fluid Mechanics*, Vol. 45, Part 2, pp. 225–246.

Walsh, M. J., 1978, "Drag and Heat Transfer on Surfaces with Small Longitudinal Fins," AIAA Paper No. 78-1161.

Walsh, M. J., 1979, "Drag Characteristics of V-groove and Traverse Curvature Ribets," Viscous Flow Drag Reduction, ed. Hough, G. H., Vol. 72, *Progress in Astronautics and Aeronautics*, pp. 168–184.

Walsh, M. J., 1982, "Turbulent Boundary Layer Drag Reduction Using Riblets," AIAA Paper No. 82-0169.

Walsh, M. J., 1983, "Riblets as a Viscous Drag Reduction Technique," *AIAA Journal*, Vol. 21, No. 4, pp. 485-486.

Walsh, M. J., Lindemann, A. M., 1984, "Optimization and Application of Riblets for Turbulent Drag Reduction," AIAA Paper No. 84-0347.

Walsh, M. J., Sellers III, W. L., and McGinely, C. B., 1988, 'Riblet Drag Reduction at Flight Conditions," AIAA Paper No. 88-2554.

Walsh, M. J., 1990, "Effect of Detailed Surface Geometry on Riblet Drag Reduction Performance," *Journal of Aircraft*, Vol. 27, No. 6, pp. 572-573.

Walsh, M. J., 1990, "Riblets. Viscous Flow Drag Reduction in Boundary Layers," eds., Bushnell, D. M., and Hefner, J. N., Vol. 123, *Progress in Astronautics and Aeronautics*, pp. 203-254.

Wells, C. S., and Spangler, J. G., 1967, "Injection of a Drag-reducing Fluids into Turbulent Pipe Flow of a Newtonian Fluids," *Physics of Fluids*, Vol. 10, No. 9, pp. 1890-1894.

Wilkinson, S. P., and Lazos, J. B., 1987, "Direct Drag and Hot-wire Measurements on Thin-element Riblet Arrays," Presented at the *IUTAM Symposium on Turbulence Management and Relaminarization*, Bangalore, India, Jan. 19-23.

Wilkinson, S. P., Anders, J. B., Lazos, B. S., and Bushnell, D. M., 1988, "Turbulent Drag Reduction Research at NASA Langley, Progress and Plans," *International Journal of Heat and Fluids Flow*, Vol. 9, No. 3, pp. 266-277.

Wu, T., and Tulin, M., 1972, "Drag Reduction by Ejecting Additive Solutions into a Pure Water Boundary Layer," ASME *Journal of Basic Engineering*, Vol. 74, pp. 749-756.

Z. Y. Wang
Associate Professor,
Department of Power Machinery Engineering,
Xi'an Jiaotong University,
Xi'an Shaanxi,
P. R. China

J. Jovanovic
Doctor,
Lehrstuhl fur Stromungsmechanik,
Universitat Erlangen—Nurnberg,
D-8500 Erlangen, Germany

Drag Characteristics of Extra-Thin-Fin-Riblets in an Air Flow Conduit

An experimental study of riblets with extra thin fins (5 μm thick) is presented. A drag reduction of 2–3 percent per quarter conduit wall is indicated when h^+ is around 3–15 in a square section of air flow conduit lined with the extra-thin-fin-riblets (ETFR) on one side wall. The pressure distributions along the conduit indicate the influence of the riblet front step on the drag reduction performance in the conduit flow. The measurement methods and the detailed structure of the ETFR are also discussed.

Introduction

Since the first experiments were conducted in order to reduce turbulent skin friction through a direct interaction with the flow structure near the wall by means of fine flow-aligned internal manipulators, i.e., a "riblet" surface, numerous experiments have been performed on a flat plate tested in a wind tunnel and in pipes for water flow and air flow.

During the past decade, some of the important experiments were completed at NASA (Walsh et al., 1978, 1980, 1983, 1984), who discovered that a 7–8 percent drag reduction could be achieved when the nondimensional height of the riblet, h^+, was about 15 and s^+ was below 30, where h^+ and s^+ were defined in terms of law-of-the-wall coordinates. The results have been generally confirmed (Bechert and Hoppe, 1985; Beauchamp and Philips, 1988; Reidy and Anderson, 1988).

Besides the investigations on the drag reducing effects for flat plates, the performance of riblets in a pipe flow is of great interest as well. The pipe flow experiments can provide an opportunity for investigating whether the drag reducing effects in developing (flat plate) and in fully developed (pipe) flows are similar. In fully developed pipe air flow, only a 3 percent drag reduction was found when $h^+ = 11$–15 (Nitschke, 1983). In her study, rounded peaks were machined on the pipe's interior surface, and the drag reduction was determined by using pressure drop measurements over a length of 120 pipe diameters. In a pipe water flow (Liu et al., 1989) a 5–7 percent drag reduction was reported, and the maximum drag reduction occurred at $h^+ = 11$–16 wall units.

Most studies have focused on one of the most important factors of the riblets, i.e., geometry. Walsh et al. (1978, 1980, 1982 and 1984) investigated a ribbed surface with a wide variety of rib geometries including rectangular, V-grooved, razor blade, semi-circular grooved, and alternating transverse curvature. The representative dimensions of a riblet are its height h and spacing s. Walsh found in his experiments that triangular grooves were among the most effective in drag reduction. Up to now the generally accepted riblet geometries are sharply peaked symmetric V-grooves and U-grooves, and they are currently manufactured by the 3M company.

Investigations of riblets with other geometries were also reported (Liu et al., 1966 and Kennedy et al., 1973). In Liu's case, the flow-aligned rectangular fins had heights of $h^+ = 11$–45 and spacings of $s^+ = 190$–373. He found a 3–4 percent net drag reduction for these particular fin heights and spacings. In Kennedy's case, h^+ and s^+ were equal to 70–150, 50–1100 respectively, and an increased drag was found. Wilkinson and Lazos reported (1987, 1988) their investigations of Thin-Element-Riblets tested in a low speed wind tunnel at the NASA Langley Research Center, and the maximum drag reduction of 8 percent was achieved for the model of $s = 0.025$ in., $h = 0.02$ in. when $s^+ = 12$ and $h^+ = 50$. The present study of riblets with rectangular fins is similar to the previous Thin-Element-Riblets, but utilizes thinner riblets, 5 μm thick riblet peaks and minimum dimensions of $h = 0.1$ mm, $s = 0.2$ mm.

Several physical explanations have been given for a possible mechanism for turbulent drag reduction with riblets. Choi et al. (1986, 1989) and Falco (1989) argued that the sharp peak riblets impeded the lateral movement of longitudinal nearwall vortices and retarded the flow in the riblet grooves, thus thickening the viscous sublayer and increasing the stability of wall streaks. Bechert et al. (1985, 1986) further pointed out that the height by which the riblets protruded into the boundary layer flow is of crucial importance.

Extra-Thin-Fin-Riblets and Experimental Apparatus

Extra-Thin-Fin-Riblets. A riblet consisting of extra thin fins (ETFR in short) was employed in our experiments, consisting of metal strip foils with different thicknesses; fine foils 5 μm thick are used as fins and thick strip foils are used as spacers. Figure 1(*a*) shows a microphotograph of the riblet cross section taken under a stereomicroscope. Figure 1(*b*) is a vertical view. The foil surface is of high quality and its smooth finish is the same as the inner surface of the aluminum conduit used in the test. The foils are stacked in such a way that the thin foils protrude over the flat surface formed by the thick strip foils. The peak height, h, of the fins depends on the size of the protrusion, and the peak-to-peak spacing, s, is adjusted by the thick foils.

Contributed of the Fluids Engineering Division for publication in the JOURNAL OF FLUIDS ENGINEERING. Manuscript received by the Fluids Engineering Division January 3, 1992; revised manuscript received July 16, 1992. Associate Technical Editor: D. M. Bushnell.

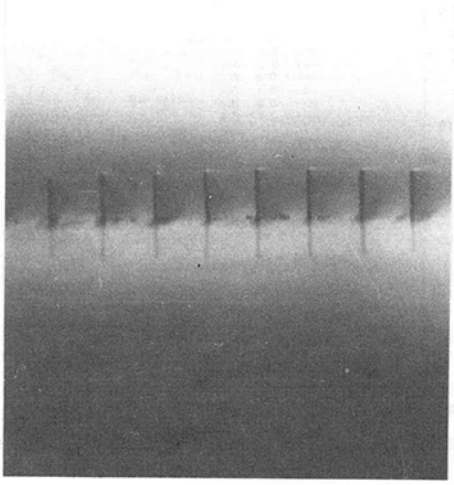

Fig. 1 1(*a*) photomicrograph of the ETFR cross-section for $s = h = 0.1$ mm

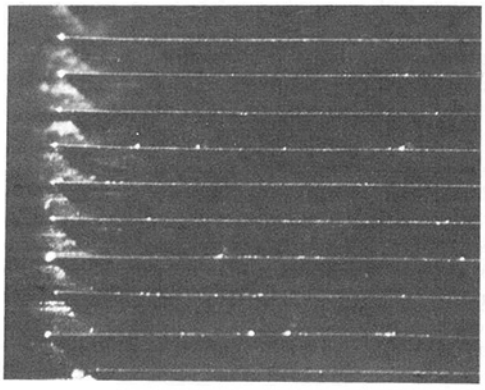

Fig. 1(*b*) photomicrograph of a vertical view of the ETFR for $s = h = 0.2$ mm

The dimensions of the formed rib surfaces are 500 mm long and 21 mm wide. This size is the same as a quarter part duct cut away from the test section of the conduit (see next section of the chapter). The riblet dimensions in the present tests are $h = 0.1$ mm, 0.2 mm, 0.4 mm and $s = 0.2$ mm, 0.4 mm, 0.8 mm.

Test Facilities. The tests were conducted in a 6-meter-long air conduit with a 21 mm by 21 mm square test section. The conduit is connected to a compressed air pipe system. The experimental apparatus with its dimensions is schematically represented in Fig. 2.

The reference pressure drop ΔP_c is measured between 1.0 m and 3.0 m from the leading edge of the conduit entrance, so as to allow a comparison of the pressure drop between the

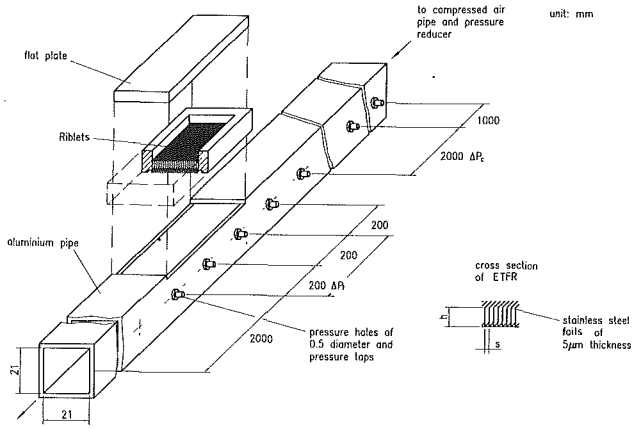

Fig. 2 Schematic drawing of test facility with dimensions

smooth and ribbed surfaces under the same flow condition by keeping ΔP_c constant. A quarter part of the conduit wall 500 mm long was cut off, and when a well finished flat plate of the same length is fixed in its place, the altered conduit performs the same as the original one. In the tests of the ETFR, the rib troughs are on the level of the conduit interior surface. The reason why only one side wall was ribbed lies in the following considerations. This design keeps the test section geometry constant during assembly and disassembly of the riblets, and it ensures the use of the same pressure holes in all cases as the hole structure plays an important role in the fluid pressure measurement. It is impossible to have holes bored identically on different ribbed surfaces. Finally, the design enables us to take measurements on the ribbed surface from the far wall.

Six fine holes with a diameter of 0.5 mm at equal hole pair intervals are drilled in one wall perpendicular to the test surface. The distance between each of the two holes is 200 mm. The pressure holes are treated carefully to remove debris, as poor holes usually lead to incorrect measurements. A constant pressure drop per meter for ΔP_c/m and ΔP_t/m indicates fully developed channel turbulent flow. During the tests, the smooth surface and the ribbed surface are interchanged in the cut part, while the test section geometry, the hole position and the hole structure are kept constant. The pressures are measured by differential pressure gauges.

The fluid velocity in the conduit is regulated by a pressure valve connected to the compressed air pipe. The system yields a maximum air velocity of 40 m/s. A digital thermometer is placed at an outlet of the conduit to measure the fluid temperature.

We have,

Nomenclature

ρ = density of fluid (kg/m^3)
ν = kinematic viscosity of fluid (m^2/s)
μ = dynamic viscosity (kg/m•s)
λ = friction coefficient
λ_{rib} = friction coefficient of ribbed surface
λ_{smooth} = friction coefficient of smooth surface
$\lambda_{non\text{-}c}$ = friction coefficient for noncircular conduit
A = height of conduit with rectangular cross section (m)
B = width of conduit with rectangular cross section (m)
D_h = hydraulic diameter of conduit (m)
h = height of peak of riblets (m)
h^+ = height of peak of the riblets in law-of-the-wall variables
P_{rib} = pressure on ribbed surface
P_{smooth} = pressure on smooth surface
s = spacing of riblets
s^+ = spacing of riblets in law-of-the-wall variables
$K_{non\text{-}c}$ = shape correction factor
L, l = length (m)
ΔP_c = reference pressure (N/m^2)
ΔP_{smooth} = pressure drop of smooth surface (N/m^2)
ΔP_{rib} = pressure drop of ribbed surface (N/m^2)
ΔP_t = pressure drop in the test section (N/m^2)
ΔP_l = differential pressure over length l (N/m^2)
Re_{Dh} = Reynolds number for square conduit
U = mean velocity (m/s)

$$\mathrm{Re}_{D_h} = \frac{UD_h}{\nu} \tag{1}$$

$$D_h = \frac{2AB}{A+B} \tag{2}$$

where D_h is the hydraulic diameter, and A and B are the height and width of the rectangular cross section respectively. D_h is 21 mm in the present experiment, and A and B are 21 mm. The friction coefficient, λ, is given by:

$$\lambda_{\text{non-c}} = \frac{\Delta P_l}{(\rho U^2/2)(l/D_h)} = K_{\text{non-c}}\lambda \tag{3}$$

$$\lambda = \frac{0.3164}{\mathrm{Re}_{D_h}^{0.25}} \quad 4000 \le \mathrm{Re}_{D_h} \le 100000 \tag{4}$$

where $K_{\text{non-c}}$ is a shape correction factor and is equal to 1.0 for square cross sections. The distance l for measuring the pressure drop is 400 mm in the present study.

The height and spacing of the riblet in wall units are calculated by the following commonly adopted equations,

$$h^+ = \frac{h}{\nu}\sqrt{\frac{D_h \Delta P}{4\rho l}} \tag{5}$$

$$s^+ = \frac{s}{\nu}\sqrt{\frac{D_h \Delta P}{\rho l}} \tag{6}$$

The percentage drag reduction per quarter conduit basis is calculated from

$$\%\ \text{Drag Reduction} = \frac{\lambda_{\text{smooth}} - \lambda_{\text{rib}}}{\lambda_{\text{smooth}}} \tag{7}$$

For a certain reference pressure drop ΔP_c, the fluid velocity U is constant, so that the drag reduction per quarter conduit basis can be rewritten as

$$\%\ \text{Drag Reduction} = \frac{\Delta P_{\text{smooth}} - \Delta P_{\text{rib}}}{\Delta P_{\text{smooth}}} \tag{8}$$

The uncertainty of the ΔP_c, ΔP_{smooth}, or ΔP_{rib} measurements is ± 1 percent, and the uncertainty of the % Drag Reduction is estimated to be ± 2 percent.

Measurement Procedure and Results

Measurement Method and Procedure. There exist two methods to determine the drag reduction of the riblets for a pipe flow. In the first method, the mass flow is measured, and the resistance coefficient can be written as a function of mass flow m, hydraulic diameter D_h, and pressure drop ΔP_l in the test section. In order to evaluate effectiveness of the riblets a relative resistance coefficient is more convenient, defined herein as

$$\lambda_{\text{relative}} = \frac{\lambda_{\text{rib}}}{\lambda_{\text{smooth}}} \tag{9}$$

$$\lambda_{\text{relative}} \propto \frac{D_h^5}{m^2}\Delta P_l \tag{10}$$

A one percent error in pipe diameter measurement results in a five percent difference in λ, and a one percent measurement uncertainty in mass flow rate results in a two percent change in λ. Instead of using a flow meter, the reference pressure drop is utilized to calculate λ, and the following formula is derived from (1), (3), (4):

$$\lambda_{\text{relative}} \propto \frac{D_h^5}{\Delta P_C^{8/7}}\Delta P_l \tag{11}$$

Comparing Eq. (11) with (10), less error results in the calculation of λ by means of ΔP_c measurement than by measurement of m and a greater accuracy can be obtained in pressure measurement than in air mass flow measurement.

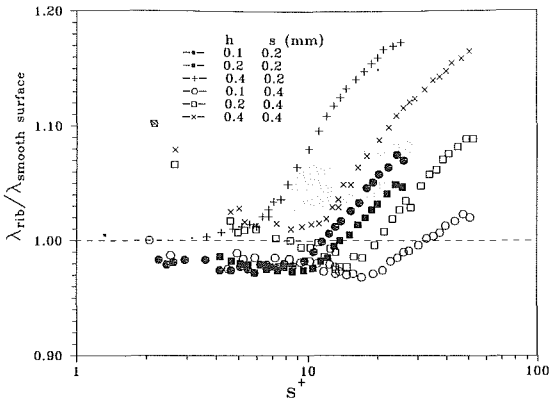

Fig. 3(*a*) Relative friction coefficient λ versus s^+, the uncertainty of the relative friction coefficient λ is estimated to be $\pm$ 2 percent

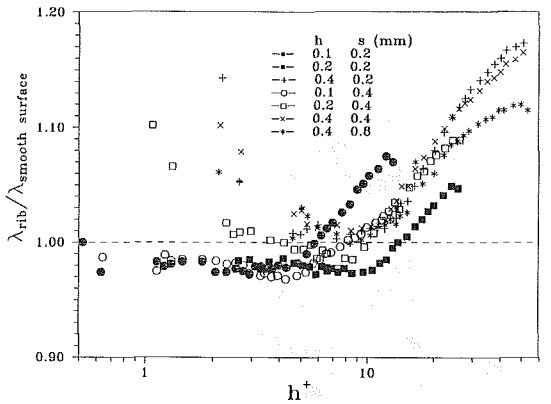

Fig. 3(*b*) Relative friction coefficient λ versus h^+, the uncertainty of the relative friction coefficient λ is estimated to be $\pm$ 2 percent

It is worth mentioning that the method is of significance only for the study of the relative resistance coefficient, because the empirical formulas (3) and (4) are used in the derivation of the coefficient, which varies with different pipe conditions. The error caused by using the empirical formulas has an influence on the absolute value of the resistance coefficient, but the error is offset in the case of the relative value.

An effective diameter is used in the calculation of the resistance coefficient, λ, by some investigators. It is defined as the diameter of a smooth pipe which would have the same cross-sectional area as a ribbed surface pipe and is determined by calculation or experiment. In the present experiment, the hydraulic diameter D_h is used, and all equations for noncircular pipes are based on D_h. Because the peaks of the riblets in our case are made of very thin foils 5 μm of thick, they have little influence on the cross-sectional area. For instance, the ETFR with $h = 0.2$ mm and $s = 0.2$ mm only takes up 0.23 percent of the cross-sectional area for a smooth pipe. For the V-groove with the same dimensions h and s, the value is 0.48 percent. No diameter correction is therefore necessary. As a matter of fact, if this factor is taken into consideration, a slightly higher percentage of drag reduction would be indicated.

Many measures are taken to ensure constant measurement conditions, D_h and pressure hole conditions are not changed during the experiments and the only variation is the surface structure on a quarter part wall. ΔP_c and ΔP_l are measured simultaneously, and ΔP_{rib} is measured immediately after the ΔP_{smooth} measurement using the same metering device.

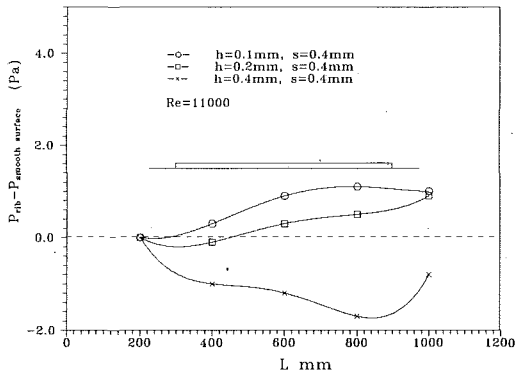

Fig. 4 Pressure distribution over the riblets for the various dimensions of the ETFR, the uncertainty of the pressure differences ΔP_{smooth} and ΔP_{rib} measurements is ± 2 percent

Measurement Results. Percentage drag reduction for the variation in s^+ and h^+ can be found in Fig. 3(*a*) and Fig. 3(*b*), respectively.

The data consistently indicate a net drag reduction within $2 < s^+ < 30$ and $3 < h^+ < 15$, a maximum drag reduction of two to three percent per quarter conduit occurs at $s^+ = 10$ and $s^+ = 15$ for $s = 0.2$ mm, $h = 0.2$ mm and $s = 0.4$ mm, $h = 0.1$ mm, respectively. In order to make comparisons with other investigations, assuming that the mean wall shear stress on the three walls not covered by the riblets is not significantly changed by the presence of the riblets on the fourth wall, a value for the change in the mean wall shear stress on the riblet covered wall could be determined. Based upon the reduction in the mean wall shear stress on the riblet covered wall, the value of the drag reduction is four times that obtained from a quarter conduit covered by riblets, i.e., an 8 ~ 12 percent drag reduction could be expected although this involves some approximations. The result is consistent with Lazos and Wilkinson's external flow experiment of Thin-Element-Riblets. In their case, a drag reduction of eight percent was reported.

In another correlative internal flow experiment carried out by Nitschke in 1983, drag reduction was obtained when $8 < s^+ < 23$ with a maximum value of three percent in the neighborhood of $s^+ = 11$–15 ($h^+ = 0.91\ s^+$), in her case the same flow condition, turbulent air pipe flow, and the same method, the pressure drop measurement, were used, but with a quite different riblet geometry, grooves with rounded peaks machined on the interior surface of the pipe.

The experiments show that there is no drag reduction when $h > 0.4$ mm in all cases. A pressure distribution in the riblet test section was measured in an attempt to investigate the riblet performance from its front edge to the rear edge. In Fig. 4(*a*) relative pressure is plotted along the test section with the relative pressure defined as $P_{rib} - P_{smooth}$ so as to distinguish the lower pressure drop differences from the absolute pressure drop for the two surfaces in the conduit. As discussed in the introduction the riblets would thicken the viscous sublayer due to the zero velocity in the riblets, and unlike external (flat plate) flows where there is no opposite wall, in a conduit flow the velocity over the riblets will increase to maintain a constant mass flow rate. This has an effect of equivalent cross-sectional area reduction, and in turn, a pressure drop increase. As can be seen in Fig. 4 the value of $P_{rib} - P_{smooth}$ for $h = 0.4$ mm decreases at the leading edge of the riblets and increases at the trailing edge, similar to contracted pipe behavior.

There is a possible physical explanation for the no-drag-reduction effect. It is apparent that the front step of the riblets disturbs the passing flow and increases resistance like an obstacle, and the higher the riblet, the greater the influence. in the region of the first 200 mm, in which the front step is included, the drag reduction was dominant only for a very low step, i.e., $h = 0.1$ mm. Compared with the second 200 mm region the value of pressure gradient is smaller, see Fig. 4. The value diminishes as h increases to 0.2 mm, and in this case the drag reduction could still be found for the entire riblet length, see the curve for $h = 0.2$ mm in Fig. 4. No drag reduction was found when $h = 0.4$ mm, and a greater pressure gradient occurred in the first 200 mm.

For technical reasons the test section is only 0.5 meter long, whereas in Liu et al's (1990) internal flow experiments a 1.5 m-long-pipe with a 25.4 mm-in-diameter was lined with riblets with an alternate test section 2.4 m-long-pipe with a 50.8 mm-in-diameter. In Walsh's (1980) investigations the test section was 91.4 cm long.

The test section in our case might not be long enough to get rid of the disturbance influence caused by the front step of the riblets.

Summary and Conclusions

- Compared with the previous designs of rectangular-fin-riblets, the ETFR has thinner peaks (0.5 μm) and smaller dimensions of h and s. The design and construction of the riblets provided the investigators with a convenient means to study riblets with various h and s values.
- The ETFR indicates a 2–3 percent drag reduction when h^+ is about 3–15 wall units for a quarter part of the conduit wall. The measurements were taken in a square air flow conduit.
- The experimental results show that the front step and trailing edge of the fins will cause a pressure change. The pressure decreases at the leading edge and increases at the trailing edge. The front step may cause disturbances to the passing flow and increase the pressure loss. No drag reduction is found when $h > 0.4$ mm, the test section might not be long enough to relax front step disturbance for this case.

Acknowledgments

The authors wish to thank Prof. Dr. F. Durst for his many helpful advice and discussion. Finally, the authors gratefully acknowledge the funding provided by the Huo-Yingdong Foundation for the publication fee.

References

Bartenwerfen, M., and Bechert, D. W., 1991, *Die Viskose Stromung uber Behaarten Ober flachen*, Z. Flugwiss. Weltraumforsch. 15, pp. 19–26.

Beauchamp, C. H. and Philips, R. G., 1988, "Riblet and Polymer Drag Reduction on an Axisymmetric Body," Paper presented at the *Symposium on Hydrodynamic Performance Enhancement for Marine Applications*, Newport, Oct 31–Nov 1.

Bechert, D. W., Hoppe, G., and Reif, W.-E., 1985, "On the Drag Reduction of the Shark Skin," AIAA Pap. No. 85-0546.

Choi, K.-S., 1986, "A New Look at the Near-Wall Turbulence Structure," *Advances in Turbulence*, J. Mathieu and G. Comte-Bellot, eds., Springer.

Choi, K.-S., 1989, "Near-Wall Structure of a Turbulent Boundary Layer with Riblets," *Journal of Fluid Mechanics*, Vol. 208, pp. 417–458.

Falco, R. E., 1989, "The Effects of Riblets on the Stability of Artificially Produced Streaks," Paper presented at the meeting Turbulent Drag Reduction Working Party.

Idelchik, I. E., *Handbook of Hydraulic Resistance*, Second Edition, State Scientific Research Institute for Industrial and Sanitary Gas Purification.

Kennedy, J. F., Hsu, Sheng-Tien, and Lin, Jung-Tai, 1973, "Turbulent Flow Past Boundaries with Small Streamwise Fins," *Journal of the Hydraulics Division*, Proceedings of the American Society of Civil Engineers, Vol. 99, No. HY4, Apr.

Kwing-So Choi, 1989, "Near-wall Structure of a Turbulent Boundary Layer with Riblets," *Journal of Fluid Mechanics*, Vol. 208, pp. 417–458.

Lazos, B. S., and Wilkinson, S. P., 1988, "Turbulent Viscous Drag Reduction with Thin-Element Riblet," *AIAA Journal*, Vol. 26, Apr., pp. 496–498.

Liu, C. K., Kline, S. J., and Johnston, J. P., 1966, "An Experimental Study of Turbulent Boundary Layer on Rough Walls," Report MD-15, Thermosciences Division, Dept. of Mechanical Engineering, Stanford University.

Liu, K. N., Christodoulou, C., Riccius, O., and Joseph, D. D., 1989, "Drag Reduction in Pipes Lined with Riblets," *AIAA Journal*, Vol. 28, No. 10, Oct.

Nitschke, P., 1983, "Experimental Investigation of the Turbulent Flow in Smooth and Longitudinal Grooved Pipes, Max-Plank Institute fur Stromungsforschung, Gottingen, FRG.

Reidy, L. W., and Anderson, G. W., 1988, "Drag Reduction for External and Internal Boundary Layers Using Riblets and Polymers," AIAA Pap. No. 88-0138.

Walsh, M. J., and Weinstein, L. M., 1978, "Drag and Heat Transfer on Surface with Small Longitudinal Fins," AIAA Paper No. 78-1161, AIAA 11th Fluid and Plasma Dynamics Conference, Seattle, WA, July 11-12.

Walsh, M. J., 1980, "Drag Characteristics of V-Groove and Transverse Curvature Riblets, *Viscous Drag Reduction Progress in Astronautics and Aeronautics*, Vol. 72, Gary R. Hough, ed.

Walsh, M. J., 1983, "Riblets as a Viscous Drag Reduction Technique," *AIAA Journal*, Vol. 21 Apr., p. 485.

Walsh, M. J., and Lindemann, A. M., 1984, "Optimization and Application of Riblets for Turbulent Drag Reduction," AIAA Paper 84-0347, Jan.

Walsh, M. J., 1982, "Turbulent Boundary Layer Drag Reduction Using Riblets," Presented at the AIAA 12th Aerospace Sciences Meeting.

Wilkinson, S. P., and Lazos, B. S., 1987, "Direct Drag and Hot-Wire Measurements on Thin-Element Riblet Arrays," Paper presented at the IUTAM Symposium on Turbulence Management and Relaminarization, Bangalore, India, Jan. 19-23.

Use of Subdomains for Inverse Problems in Branching Flow Passages

Ajay K. Agrawal
Assistant Professor.
Assoc. Mem. ASME

S. Krishnan
Graduate Student.

Tah-teh Yang
Professor.
Fellow ASME

Department of Mechanical Engineering,
Clemson University,
Clemson, SC 29634-0921

For inverse problems in complex flow passages, a calculation procedure based on a multizone Navier-Stokes method was developed. A heuristic approach was employed to derive wall shape corrections from the wall pressure error. Only two subdomains sharing a row of control volumes were used. The grid work in the common region was identical for both subdomains. The flow solver, inverse calculation procedure, multizone Navier-Stokes method and subdomain inverse calculation procedure were validated independently against experimental data or numerical predictions. Then, the subdomain inverse calculation method was used to determine the wall shape of the main duct of a branching flow passage. A slightly adverse pressure gradient was prescribed downstream of the sidebranch. Inverse calculations resulted in a curved wall diffuser for which the wall pressure distribution matched the design (prescribed) wall pressure distribution. The present method was illustrated for laminar, incompressible flows in branching passages. However, the method presented is flexible and can be extended for turbulent flows in multiply connected domains.

Introduction

Inverse flow problems determine a geometry which achieves a prescribed distribution for some flow property at physical boundaries. One of the main objectives of inverse flow calculations is to attain desired flow conditions by means of beneficial or favorable boundary conditions. For inverse problems in flow passages, oftentimes a pressure distribution, based on experience with similar systems, is prescribed at the boundaries.

Yang and co-workers (Nelson et al., 1975 and Nelson and Yang, 1977) presented an inverse calculation procedure for incompressible, irrotational flows in axisymmetric circular and annular passages. The governing equations were transformed into a coordinate system where the velocity potential function and stream function were the independent variables. The transformed equations were solved to obtain a wall shape that could meet a particular requirement of wall pressure distribution. Later, Yang (1985) modified their earlier analysis to include rotational, inviscid flows. In short curved wall diffusers, agreement between experimentally observed and analytically predicted wall pressure distributions was unsatisfactory, suggesting that the viscous effects could be significant.

To account for viscous effects, inviscid calculations in the inviscid core are often done in conjunction with the boundary layer analysis. Strawn and Kline (1983) developed an inverse calculation procedure for curved wall diffusers that would increase the pressure recovery. Their analysis was based on a momentum integral equation, a boundary layer entrainment equation, and a potential core of uniform velocity. Optimum diffusers were considered to have continuous incipient separation along their wall boundary layers. The separation was characterized by the wall distribution of the shape factor (ratio of boundary layer displacement thickness to the boundary layer thickness) or the stall margin. Once the shape factor or the stall margin distribution was prescribed at the wall, the diffuser geometry could be obtained.

A similar procedure presented by Laidler and Myring (1984) also allowed for viscous/inviscid interactions. Laidler and Myring (1984) used inverse procedures for both the core flow and the boundary layer. A duct shape was obtained for a prescribed distribution of wall friction velocity. Ahmed and Myring (1986) extended the analysis by Laidler and Myring (1984) to include the effects of compressibility.

An inverse procedure in association with a direct flow solver applies to a wider range of problems. With this approach, an inverse flow problem is solved by repeatedly using a direct flow solver to refine a guess geometry until the prescribed flow conditions are reached. The use of a direct flow solver to carry out the inverse calculations avoids the viscous/inviscid interaction. Hence, the inverse procedure can be applied to a wider variety of problems as it can be used to account for rotational flow effects and viscous effects.

Ntone and Yang (1986) used a Navier-Stokes solver simplified by the thin-layer approximation to design axisymmetric passages. The wall geometry was modified from two guess wall geometries and their wall pressure distributions. The wall modification employed the secant method often used in numerical

Contributed by the Fluids Engineering Division for publication in the JOURNAL OF FLUIDS ENGINEERING. Manuscript received by the Fluids Engineering Division January 30, 1992; revised manuscript received June 6, 1993. Associate Technical Editor: R. K. Agarwal.

solutions of nonlinear equations. This modification was continued until the wall pressure distribution was close to the prescribed wall pressure distribution.

Flow configurations consisting of combined passages, such as manifold, dump diffuser, and diffusers with bleed or suction slots, have been used for many applications. However, a limited amount of information is available to guide the unified design of duct combinations. Hokenson and Su (1977) used inviscid flow analysis for the unified inlet/diffuser design. However, strong viscous effects in duct combinations warrant a design method based on Navier–Stokes equations, which is the primary objective of the present work.

In recent years, Navier–Stokes methods to compute flow fields in complex configurations have advanced. For example, curvilinear coordinate systems conforming to arbitrary boundaries of the flow domain are commonly used today. However, geometries involving duct combinations are not suitable for grid generation using the body-fitted coordinates. On the other hand, such configurations can be dealt with more easily by using the multizone Navier–Stokes methods. The general approach of the multizone method is to break a complex domain into several simple subdomains, sometimes called blocks or zones. Grids are generated independently in each zone. The governing equations are solved in each subdomain, and the boundary conditions between zones are communicated during the solution process.

Karki and Patankar (1986) used the subdomain approach to obtain a flow field in an annular dump diffuser. Leschziner and Dimitriadis (1989) also applied this approach to compute a flow field in junctions of internal combustion engine manifolds. More recently, Tolpadi and Braaten (1991) used multiple blocks to study the flow field in a branched turboprop inlet duct.

In this study, an inverse design procedure based on the multizone Navier–Stokes method was developed. The method was tested and validated against known results and then was applied to design a bifurcating flow passage.

Flow Solver

A general purpose fluid dynamics code was used for flow calculations. This code is applicable to steady/unsteady, laminar or turbulent flow of compressible/incompressible fluids in a Cartesian, cylindrical or curvilinear coordinate system. The present work was applied to laminar, incompressible flows in axisymmetric passages. Computations were done using a body-fitted coordinate system.

Governing Equations. Conservation equations of mass and momentum are expressed in Cartesian tensor notation as

$$\frac{\partial}{\partial x_j}(\rho V_j) = 0 \tag{1}$$

$$\frac{\partial}{\partial x_j}(\rho V_j V_i) = -\frac{\partial p}{\partial x_i} + \frac{\partial}{\partial x_j}\left[\mu \frac{\partial V_i}{\partial x_j}\right] \tag{2}$$

Solution Procedure. The governing equations for dependent variables, e.g., axial and radial velocities, reduce to a general form as

$$\overline{\nabla}(\rho \overline{V} \bullet \phi + \overline{J}_\phi) = S_\phi \tag{3}$$

where ϕ represents the dependent variable, $\overline{V}$ is the velocity vector, $\overline{J}_\phi$ is the diffusive flux vector, and S_ϕ is the volumetric source of ϕ. Integration of the generalized Eq. (3) over a control volume results in the finite difference equations of the general form

$$a_P \phi_P = a_N \phi_N + a_S \phi_S + a_H \phi_H + a_L \phi_L + S_\phi \tag{4}$$

where a_N, a_S, a_H, and a_L are linking coefficients which connect each neighbor with the nodal value ϕ_P. These coefficients were obtained, using the power-law scheme, in terms of the mass-flow rates across the cell faces and the diffusive coefficients. The set of coupled nonlinear equations was solved implicitly in an iterative manner. Coupling between velocity and pressure fields was provided by a variant of SIMPLE algorithm (Patankar, 1980), SIMPLEST.

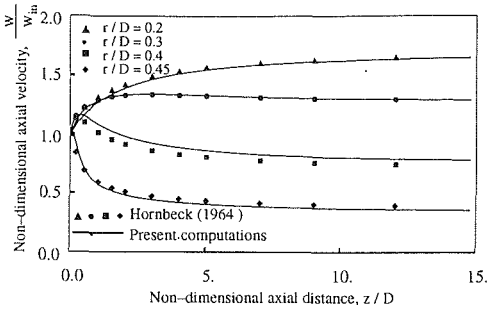

Fig. 1 Axial velocity in the entrance region of a pipe. D = 0.01 m, w_{in} = 0.043 m/s, and Re = 426

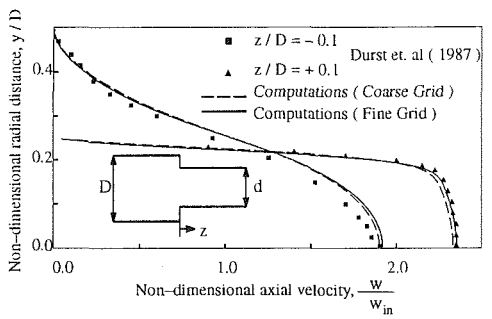

Fig. 2 Axial velocity in the plane sudden contraction. D = 0.01 m, w_{in} = 0.043 m/s, Re = 426, and d/D = 0.5

Validation. The flow solver was validated using two test cases: (1) developing flow in a pipe and (2) fully developed flow in a plane sudden contraction. For the first test case, the pipe diameter (D) was 0.01 m, the mean axial velocity at the inlet (w_{in}) was 0.043 m/s, and the inlet Reynolds number ($w_{in}D/\nu$) was 426. A total of 1800 grids (15 radial and 120 axial) with clustering near the wall, centerline, and inlet were used. Figure 1 shows computed axial velocity distributions at several radial locations in the entrance region of the pipe. These results compared well with similar results from Hornbeck (1964), also shown in Fig. 1.

For the second test case, the computed results were compared with experimental data obtained by Durst et al. (1987) who used laser Doppler anemometry to measure axial velocity profiles. In this case, the passage gap at the inlet (D) was 0.01 m, the average inlet velocity (w_{in}) was 0.043 m/s, the inlet Reynolds number was 426, and the passage gap after contraction (d) was 0.5 D. Flow at the passage inlet was fully developed. Computations were done in a rectangular domain with regions blocked to represent a plane sudden contraction. A coarse and a refined grid were used for flow field computations. The coarse grid consisted of 6000 grids (50 radial and 120 axial) of which 1,975 grids were blocked to the flow. Meanwhile, the fine grid consisted of 8400 grids (70 radial and 120 axial) of which 2070 grids were blocked to the flow. Figure 2 shows the computed and measured axial velocity profiles just prior to and after the contraction. Figure 2 exhibits good agreement between the experimental data and numerical predictions. Furthermore, computed results from the coarse and fine grids match, indicating that the computations are independent of the grid size.

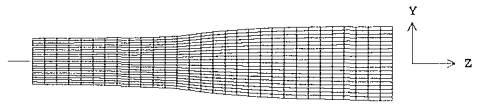

Fig. 3 Grid arrangement in a straight pipe followed by a curved wall diffuser

Design (Inverse) Procedure

The design procedure is a sequence of direct calculations during which the wall geometry is updated iteratively. The important operations, in order of their execution, are listed in the following:

(1) Guess a trial geometry, generate the body-fitted grid, and calculate geometric coefficients.
(2) Iteratively solve the finite difference equations to calculate the flow field.
(3) Determine the wall correction from the difference between the design wall pressure and the computed wall pressure.
(4) Obtain the new geometry, regenerate the body-fitted grid, and recalculate the geometric coefficients.
(5) Repeat steps 2 to 4 until the wall correction is within a prescribed tolerance.

A key element in this procedure is the scheme by which the wall shape corrections are derived from the wall pressure error. Unlike Zannetti (1980) or Thompkins and Tong (1982) who relate the wall correction and wall pressure error in terms of wall compatibility equations, the present work uses a heuristic approach. The local wall correction ΔY is obtained in terms of the local error in the wall pressure gradient. Thus,

$$\Delta Y = \alpha\ abs[\Delta P_c - \Delta P_d]^n \tag{5}$$

with

α = proportionality constant
ΔP_c = computed wall pressure gradient
ΔP_d = design wall pressure gradient
$n = 1.0$ if $[\Delta P_c - \Delta P_d] < 1.0$
$= 0.5$ if $[\Delta P_c - \Delta P_d] > 1.0$

Here, instead of the wall pressure, the wall pressure gradient is used to determine the wall correction. The local wall pressure gradient reflects the local wall slope. On the other hand, the local wall pressure represents a cumulative effect of the wall shape. The proportionality constant is a function of fluid density, and it also serves as a relaxation factor. The new geometry is obtained as follows:

$$Y_{\text{new}} = Y_{\text{old}} - \Delta Y \quad \text{if } \Delta P_c > \Delta P_d \tag{6a}$$

and

$$Y_{\text{new}} = Y_{\text{old}} + \Delta Y \quad \text{if } \Delta P_c < \Delta P_d \tag{6b}$$

Equations 6(a)-6(b) follow from the fact that a passage with a higher area ratio (exit area/inlet area) produces a higher pressure gradient/recovery than a passage with a lower area ratio. Thus, when the computed pressure gradient is greater than the design pressure gradient, it follows that the computed area ratio must be more than the design area ratio. Hence, the wall radius is decreased by a value ΔY given by Eq. (5). A similar explanation can be given for the case when the wall pressure gradient is less than the design pressure gradient.

The present approach is a simplified version of the MGM algorithm used by Malone et al. (1989) for airfoil design. The MGM algorithm relates the wall correction and wall slope to errors in both pressure and pressure gradient. Such an approach avoids discontinuous surfaces. However, in the present work, smoothness of the wall geometry was maintained by imposing a few constraints. For example, the maximum wall correction during a geometry change was limited to a fraction (≈ 0.5) of the grid size. Moreover, it was found computationally efficient to start with a small proportionality constant, $\alpha = 5.5 \times 10^{-4}$, which gradually increased by up to two orders of magnitude during iterations.

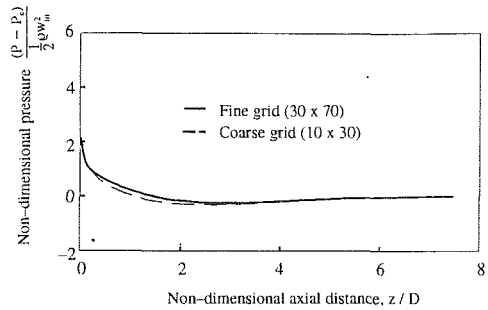

Fig. 4 Effect of grid size on wall pressure distribution

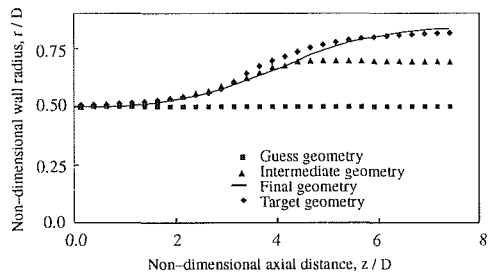

Fig. 5 Sequence of wall geometries during inverse solution of a straight pipe followed by a curved wall diffuser. D = 0.06 m, w_{in} = 10.0 m/s, Re = 150, ρ = 1.0 kg/m^3, and L/D = 7.53.

The new wall geometry was often computed without obtaining a fully converged solution for the old geometry. Typically, this partial convergence was considered reached when field residuals decreased by two orders of magnitude. After updating the wall geometry, the new grid was generated by linearly distributing the wall movement ΔY to all the grid points in the radial direction. The flow field calculated prior to the geometry change was used as the guess field for calculations in the updated geometry.

Validation. The design procedure was tested for a straight pipe followed by a curved wall diffuser. To establish the design wall pressure distribution, the direct flow solver was used to compute the flow field in a specific flow passage. The inlet diameter (D) was 0.06 m, the axial velocity at the inlet (w_{in}), 10.0 m/s, was uniform, the inlet Reynolds number ($w_{in}D/\nu$) was 150 and the density was 1.0 kg/m^3. The length of the diffuser (L) was 7.53 D, and the exit diameter was 1.67 D. A reference pressure of zero was specified at the diffuser exit. A coarse grid (10 radial and 30 axial) and a fine grid (30 radial and 70 axial) were used for flow field computations. The coarse grid used for computations is shown in Fig. 3. The computed wall pressure distributions were independent of the grid size (Fig. 4).

The computed wall pressure distribution was then used as the target value for inverse calculations. A circular pipe was used as the guess geometry. Furthermore, the wall geometry was constrained so as not to exceed the exit radius or to be less than the radius at the inlet. Calculations were done with the coarse grid only. Figures 5 and 6, respectively, show sequences of wall geometries and the corresponding wall pressure distributions during inverse calculations, along with the target values. During successive geometry changes, the wall geometry approached and finally reached the target value, even though the initial guess was rather crude. The wall geometry was modified after approximately 25 flow iterations, and the target geometry was reached after 24 such geometry changes.

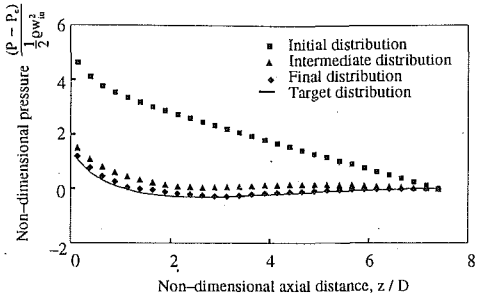

Fig. 6 Sequence of wall pressure distributions during inverse solution of a straight pipe followed by a curved wall diffuser. D = 0.06 m, w_{in} = 10.0 m/s, Re = 150, ρ = 1.0 kg/m^3, and L/D = 7.53.

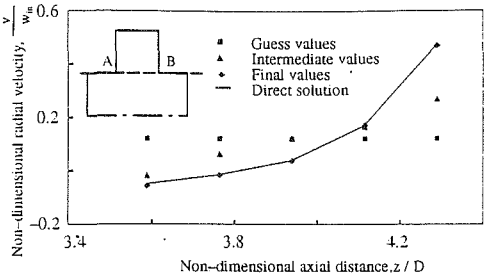

Fig. 8 Comparison of radial velocity profiles along AB in the T-junction obtained by a direct method to that obtained by the subdomain method. D = 0.05 m, w_{in} = 10.0 m/s, Re = 125, ρ = 1.0 kg/m^3, L/D = 7.0

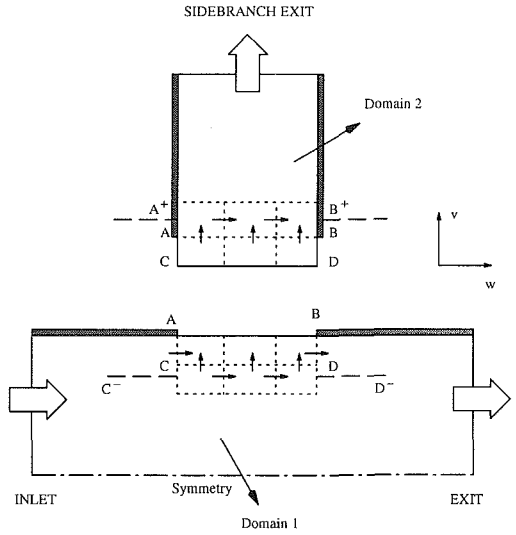

Fig. 7 Schematic of the two domains to implement the subdomain approach in a T-junction

Subdomain Method

The direct flow solver was modified to use the subdomain (multizone) approach. In this work, only two subdomains are used. Figure 7 shows two domains to implement the subdomain method in a T-junction. Domain 1 and domain 2 overlap in the region ABCD. The grid work in the common region was identical for both the subdomains. The computational procedure can be described with respect to Fig. 7 as follows:

(1) Compute the flow field in domain 1. Input mass and momentum flow rates at the inlet, no slip at the wall and a reference pressure at the exit. Use the guess radial velocity along AB and the guess axial velocity along A^+B^+.

(2) Save the radial velocity along CD, and the axial velocity at AC and BD and along C^-D^-.

(3) Compute the flow field in domain 2. Input no slip conditions at the walls and a reference pressure at the exit. At CD, input the radial velocity saved during step 2. Similarly, input the saved axial velocity at AC, BD, and along A^+B^+.

(4) Save the radial velocity along AB and the axial velocity along A^+B^+.

(5) Repeat steps 1 to 4 until velocities in the common region $ABCD$ converge.

The flow field computations were done independently in each subdomain. Therefore, at the end of the computations in a subdomain, the geometric data and flow field data were stored in disk files before computations were started for another subdomain.

The present subdomain approach with one row of overlapping control volumes compromises well between computational efficiency and ease of implementation. Karki and Patankar (1986) used several rows of overlapping control volumes, thereby increasing the computational effort. Leschziner and Dimitridis (1989) avoided physically overlapping the domains, whereby the streamwise conservation equation was solved separately along the interface between two subdomains before boundary conditions were transferred.

Validation. The subdomain method was validated for a T-junction geometry (Figure 7) to ensure that the boundary conditions transferred accurately between the domains. The validation was carried out by comparing computed results from the direct method to those by the subdomain method. For these calculations, the inlet diameter was 0.05 m, the inlet axial velocity, 10.0 m/s, was uniform, the inlet Reynolds number was 125, and the density was 1.0 kg/m^3. The length of the main passage (L) was 7 D, and the sidebranch starting at an axial location (z) of 3.5 D was 0.86 D wide. A reference pressure of zero was specified at the exit of the main passage. The pressure at the sidebranch exit was fixed at -40.0 Pa. For direct calculations, a rectangular physical domain with 800 grids (20 radial and 40 axial) was used. Of these grids 350 were impermeable to the flow. These calculations indicate that 42 percent of the inlet mass exited through the sidebranch.

In subdomain calculations, the guess radial velocity (v), 0.122 w_{in}, was uniform along AB. This guess velocity resulted in the desired mass flow through the sidebranch. A zero reference pressure was specified at both the main passage and the sidebranch exits. The flow geometry was mapped by only 455 grids, 400 grids (10 radial and 40 axial) in domain 1 and 55 grids (11 radial and 5 axial) in domain 2.

Figure 8 compares radial velocity profiles along AB obtained by the direct method to that by the subdomain method. Figure 8 also shows the guess and intermediate velocity distributions for the subdomain method. These results show that the guess radial velocity profile was updated during subdomain calculations and that it ultimately matched the profile obtained by direct calculations. Similar comparisons at several other locations indicated that the subdomain method accurately transferred boundary conditions between domains.

Results and Discussions

The flow chart in Fig. 9 shows the computational steps for inverse calculations using the subdomain method. As shown in this figure, the computational procedure is started by guessing the flow field in the common region of domain 1. Guess boundary conditions and the known boundary conditions, such as the velocity and mass flow rate at the inlet, no slip at walls, and a reference pressure at the exit, are then used to compute the flow field in domain 1. After several flow iterations, either the wall geometry is updated or the flow field in the common region is saved for flow calculations in domain 2. If the wall geometry is updated, a new grid is generated and the flow field is computed in the new domain 1. Otherwise, the previously

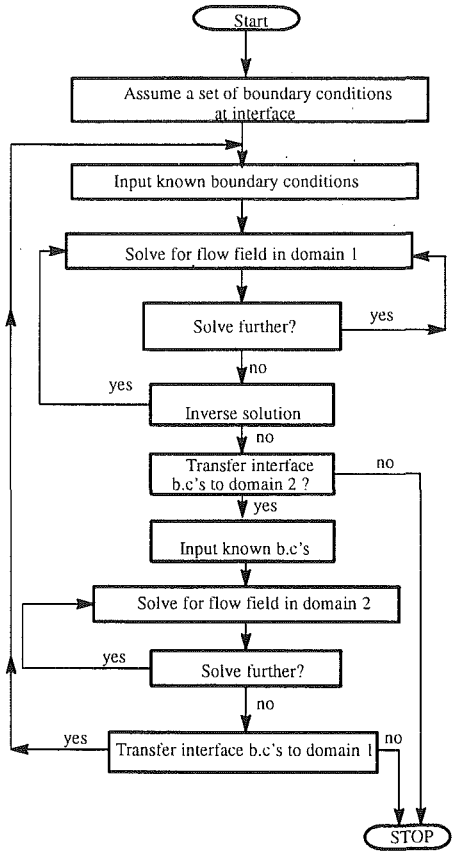

Fig. 9 Flow chart for inverse solution using subdomains

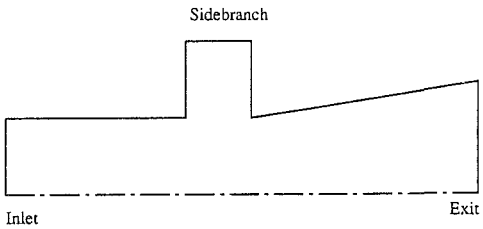

Fig. 10 Guess geometry for inverse solution of the T-junction

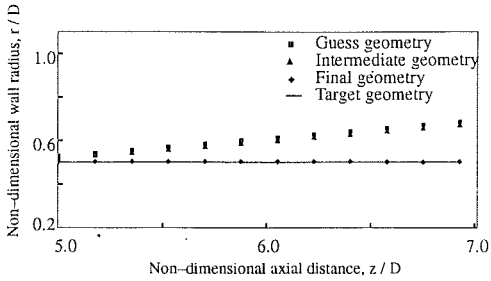

Fig. 11 Sequence of wall geometries during inverse solution of the T-junction.
D = 0.05 m, w_{in} = 10.0 m/s, Re = 125, ρ = 1.0 kg/m^3, and L/D = 7.0.

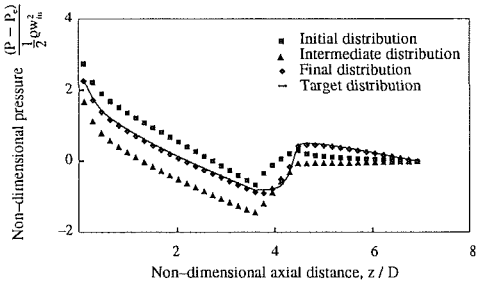

Fig. 12 Sequence of wall pressure distributions during inverse solution of the T-junction.
D = 0.05 m, w_{in} = 10.0 m/s, Re = 125, ρ = 1.0 kg/m^3, and L/D = 7.0.

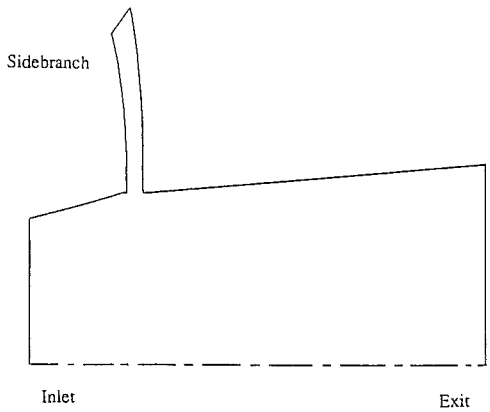

Fig. 13 Guess geometry for inverse solution of the branching flow passage

saved flow field in the common region and the known boundary conditions at the walls and the exit may be used to compute the flow field in domain 2. Subsequently, the updated boundary conditions in the common region may be used to compute the flow field in domain 1. This process is repeated until the inverse solution and the subdomain method produce the design wall pressure distribution and until the flow field in the common region is within a prescribed tolerance. In the present work, the subdomain method updated boundary conditions at the interface whenever consecutive wall corrections were in opposing directions.

The flow field obtained by direct calculations in the T-junction geometry (Fig. 7) provided target values to validate the design procedure using subdomains. The guess geometry, shown in Fig. 10, indicates that the design must produce a straight wall downstream of the sidebranch. Next, Figs. 11 and 12, respectively, show sequences of the wall geometries and the corresponding wall pressure distribution during geometry changes. These figures show that the design process approached and finally reached the target values. The wall geometry was updated 15 times, the boundary conditions were transferred 7 times, and the total flow iterations were 390 for domain 1 and 115 for domain 2.

Finally, Fig. 13 depicts a branching flow passage designed by the method developed in this study. For this flow configuration, the inlet diameter was 0.06 m, the inlet axial velocity, 0.262 m/s, was uniform, the inlet Reynolds number was 2120, and the density was 1.25 kg/m^3. The length of the main passage (L) was 1.5 D and the sidebranch starting at an axial location (z) of 0.3 D was 0.054 D wide. Eighteen percent of the total inlet mass was expected to exit through the sidebranch. An adverse pressure distribution downstream of the sidebranch was prescribed (Fig. 14). The design was started by guessing a straight wall downstream of the sidebranch (Fig. 13 or 15). The flow geometry was mapped by 2916 grids, 2800 grids (40 radial and 120 axial) in the main passage and 116 grids (29 radial and 4 axial) in the sidebranch.

Figures 14 and 15, respectively, show sequences of the wall pressure distributions and wall geometries downstream of the sidebranch. The wall geometry changed during inverse calculations, and the corresponding pressure distribution approached the target values. The resultant geometry is a curved wall diffuser which provides a higher pressure recovery com-

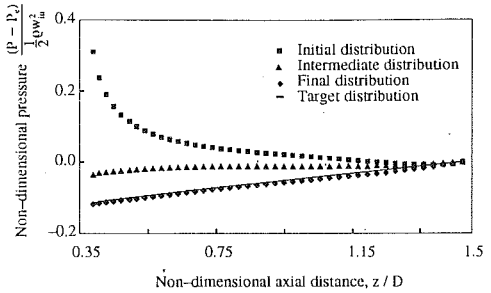

Fig. 14 Sequence of wall pressure distributions during inverse solution of the branching flow passage.
D = 0.05 m, w_{in} = 10.0 m/s, Re = 125, ρ = 1.0 kg/m^3, and L/D = 7.0

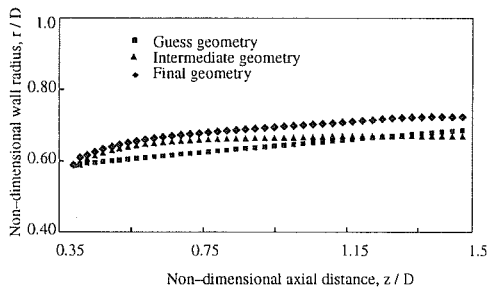

Fig. 15 Sequence of wall geometries during inverse solution of the branching flow passage.
D = 0.05 m, w_{in} = 10.0 m/s, Re = 125, ρ = 1.0 kg/m^3, and L/D = 7.0

pared to a straight wall diffuser. The wall geometry was updated 51 times, the boundary conditions were transferred 6 times, and the total flow iterations were 600 for domain 1 and 100 for domain 2.

Concluding Remarks

Prior work on inverse calculations is limited to simple flow configurations. Only a limited amount of information is available to guide the unified design of duct combinations. The present work is an attempt to conduct inverse calculations in complex flow passages. This endeavor was accomplished by adding an inverse procedure and a subdomain procedure to a viscous flow solver. The method was demonstrated for inverse calculations in a branching flow passage.

The procedure developed here broadens the scope of inverse design to complex flow passages. However, some operational issues are yet to be resolved. For example, how often should the interface boundary conditions be updated and how should a simultaneous multidomain inverse design be conducted? The design (prescribed) pressure distribution might be physically unrealistic in a given flow configuration. Thus, the design might not lead to the target values. Furthermore, a range of geometries or multiple geometries might satisfy design pressure distribution. Therefore, the designer must establish a local or a global criterion to ensure minimum deviation from the design pressure distribution.

Acknowledgments

This work was supported partially from the DoE/METC Contract No. DE-AC21-89MC26041. Authors would like to thank Esther Martin for help in preparation of this manuscript.

References

Ahmed, N. M. A., and Myring, D. F., 1986, "An Inverse Method for the Design of Axisymmetric Optimal Diffusers," *International Journal for Numerical Methods in Engineering*, Vol. 22, pp. 377–394.

Durst, F., Schierholz, W. F., and Wunderlich, A. M., 1987, "Experimental and Numerical Investigations of Plane Duct Flows with Sudden Contraction," ASME JOURNAL OF FLUIDS ENGINEERING, Vol. 109, pp. 376–383.

Hokenson, G. J., and Su, F. Y., 1977, "Unified Inlet/Diffuser Design by an Inverse Method," *AIAA Journal*, Vol. 15, pp. 39–45.

Hornbeck, R. W., 1964, "Laminar Flow in the Entrance Region of a Pipe," *Applied Science Research*, Section A, Vol. 13, pp. 224–232.

Karki, K. C., and Patankar, S. V., 1986, "Use of Subdomains for Flow Computations in Complex Geometries," *Numerical Methods in Heat Transfer*, J. L. S. Chen and K. Vafai, eds., ASME HTD, Vol. 62, pp. 7–12.

Laidler, P., and Myring, D. F., 1984, "The Inverse Problem for Incompressible Internal Flows," *Aeronautical Journal*, Paper No. 1149, pp. 38–45.

Leschziner, M. A., and Dimitridis, K. P., 1989, "Computation of Three-Dimensional Turbulent Flow in Non-Orthogonal Junctions by a Branch-Coupling Method," *Computers and Fluids*, Vol. 17, No. 2, pp. 371–396.

Malone, J. B., Narramore, J. C., and Sankar, L. N., 1989, "An Efficient Airfoil Design Method Using the Navier–Stokes Equations," *Computational Methods for Aerodynamic Design (Inverse) and Optimization*, AGARD Conference Proceeding No. 463, pp. 5-1 to 5-18.

Nelson, C. D., Yang, T., and Hudson, W. G., 1975, "The Design and Performance of Axially Symmetrical Contoured Wall Diffusers Employing Suction Boundary Layer Control," ASME *Journal of Engineering for Power*, pp. 125–130.

Nelson, C. D., and Yang, T., 1977, "Design of Branched and Unbranched Axially Symmetrical Ducts with Specified Pressure Distribution," *AIAA Journal*, Vol. 15, pp. 1272–1277.

Ntone, F., and Yang, T., 1986, "Inverse Design of Axisymmetric Flow Passages Using Compressible Viscous Flow Theory," *Communications in Applied Numerical Methods*, Vol. 2, pp. 83–89.

Patankar, S. V., 1980, *Numerical Heat Transfer and Fluid Flow*, McGraw-Hill, New York.

Strawn, R. C., and Kline, S. J., 1983, "A Stall Margin Design Method for Planar and Axisymmetric Diffusers," ASME JOURNAL OF FLUIDS ENGINEERING, Vol. 105, pp. 28–33.

Thompkins, W. T., and Tong, S. S., 1982, "Inverse or Design Calculations for Nonpotential Flow in Turbomachinery Blade Passages," ASME *Journal of Engineering for Power*, Vol. 104, pp. 281–285.

Tolpadi, A. K., and Braaten, M. E., 1991, "Numerical Study of Branched Turboprob Inlet Ducts Using a Multiple Block Grid Procedure," ASME Paper 91-GT-339.

Yang, T., 1985, "An Investigation of High Performance, Short, Thrust Augmenting Ejector," ASME JOURNAL OF FLUIDS ENGINEERING, Vol. 107, pp. 23–30.

Zannetti, L., 1980, "Time-Dependent Method to Solve the Inverse Problem for Internal Flows," *AIAA Journal*, Vol. 18, pp. 754–758.

Streamwise Computation of Three-Dimensional Flows Using Two Stream Functions

M. S. Greywall
Department of Mechanical Engineering,
Wichita State University,
Wichita, Kansas 67208

An approach to compute three-dimensional flows using two stream functions is presented. The independent variables used are χ, a spatial coordinate, and ξ and η, values of stream functions along two sets of suitably chosen intersecting stream surfaces. The dependent variables used are the streamwise velocity, and two functions that describe the stream surfaces. Since the value of a stream function is constant along the solid boundaries, this choice of variables makes it easy to satisfy the boundary conditions. To illustrate the approach, computations of incompressible potential flow through a circular-to-rectangular transition duct are also presented.

I Introduction

Since the introduction of the stream function by Lagrange (1781) for two-dimensional plane flows and by Stokes (1842) for axisymmetric flows, the use of a stream function to study two-dimensional flows has been extensive. Besides the well-known examples given in introductory fluid mechanics books, in the recent past, the stream function, along with the vorticity, has been used extensively to compute two-dimensional incompressible viscous flows. Kwon and Pletcher (1986) have used the stream function and the axial velocity as the dependent variables to compute two-dimensional incompressible separated channel flow. Streamlines of the incompressible potential flow corresponding to a given geometry have also been used to construct boundary-fitted grid systems for the computation of viscous flows (Meyder, 1975; Ghia et al., 1981; and Farrel and Adamczyk, 1982). A survey of the use of streamlines to generate a grid is included in the review article on grid generation by Thompson et al. (1982).

The corresponding development for three-dimensional flows, that is the use of two stream functions to study three-dimensional flows, so far has been limited. Several authors in the past have introduced two stream functions to describe three-dimensional flows. Among the pioneering works are the works of Clebsch (1857), Prasil (1926), Maeder and Wood (1954), and Yih (1957). Clebsch (1857) introduced stream functions for three-dimensional flows by the use of a theorem by Jacobi (quoted in Clebsch) on the general solution of an n-dimensional continuity equation, and Yih (1957) by integrating the equations of a stream line. In both these works the stream surface equations were expressed as,

$$\xi = \Xi(x,y,z); \quad \eta = H(x,y,z) \tag{1.1a,b}$$

where ξ and η are the values of stream functions along the stream surfaces Ξ and H, respectively, and the velocity vector is given by,

$$\mathbf{v} = \text{grad}\Xi \times \text{grad}H \tag{1.2}$$

The present work takes as its starting point the existence of two stream functions that will describe three-dimensional steady flows. From that point on we develop techniques for computing three dimensional flows using two stream functions. The stream surfaces in the present work are defined parametrically by equations such as

$$x = \chi, \quad y = Y(\chi,\xi,\eta), \quad \text{and} \quad z = Z(\chi,\xi,\eta), \tag{1.3a,b,c}$$

For a given value of x (1.1a,b) and (1.3b,c) are inverse relations of each other. In the present work, an important compliment to the use of two stream functions to describe three-dimensional flows is the choice of the independent and the dependent variables. As discussed in detail in the next section, the independent variables used to describe the flow are χ, ξ, and η; and the dependent variables, U, the streamwise velocity, and two functions that describe the stream surfaces. With these variables Greywall (1980, 1983, 1985, 1988) studied two and three-dimensional flows with various degrees of approximations. In the present paper, we present a general theory for studying three-dimensional viscous flows using the aforementioned variables. The present work is restricted to steady flows.

II Independent and Dependent Variables

In this section we introduce the independent and the dependent variables. The independent variables are χ, ξ, and η. Variable χ is a spatial coordinate along the main flow direction. Variables ξ and η are the values of stream functions along two suitably chosen sets of intersecting stream surfaces. A stream surface along which the stream function ξ is constant is referred to as a ξ = constant surface or as a χ-η surface. Similar nomenclature is used for stream surfaces along which η is constant. As discussed in the earlier studies (as, for example,

Contributed by the Fluids Engineering Division for publication in the JOURNAL OF FLUIDS ENGINEERING. Manuscript received by the Fluids Engineering Division December 30, 1991; revised manuscript received November 16, 1992. Associate Technical Editor: S. A. Ragab.

in Maeder and Wood, 1954 and Yih, 1957), in general, for three-dimensional flows there is no unique way to define two sets of interacting stream surfaces. For a given flow there are numerous choices for the Ξ and H stream surfaces that will cover the given flow. However, to take advantage of the (χ, ξ, η) choice of the independent variables the general shapes of the Ξ and H stream surfaces are to be selected to facilitate the imposition of the required boundary conditions. In the present paper, we present three different combinations of two basic types of Ξ and H stream surfaces that should cover many flows of practical interest. The two basic types of stream surfaces considered are: plane stream surfaces and cylindrical stream surfaces. The plane stream surfaces are not necessarily flat. The boundaries of plane stream surfaces intersect the flow boundaries. The cylindrical stream surfaces are not necessarily straight circular cylinders. The cylindrical stream surfaces are nested within each other. From these two basic types of stream surfaces we form three different combinations, each consisting of two sets of intersecting stream surfaces, to model three different types of flows. These three different types of flows are named: (i) plane flows, (ii) axial flows, and (iii) circulating flows. "Plane" flows are modeled with one set of ξ = constant plane stream surfaces and one set of η = constant plane stream surfaces as shown in Fig. 1(*a*). This type of modeling is proposed for studying flows that are bounded by flat boundaries. "Axial" flows are modeled with one set of ξ = constant cylindrical stream surfaces and one set of η = constant plane stream surfaces such that one edge of all the η = constant stream surfaces meet in the axis of the flow as shown in Fig. 1(*b*). This type of modeling is proposed for studying flows that are bounded by curved boundaries. "Circulating" flows are modeled with one set of ξ = constant cylindrical stream surfaces and one set of η = constant plane stream surfaces as shown in Fig. 1(*c*). The intersection of the ξ = constant stream surfaces and η = constant stream surfaces are closed curves. This type of modeling is proposed for the study of circulating flows.

The stream surfaces are defined parametrically by the following equations:

Plane flows: $x=\chi$, $y=Y(\chi,\xi,\eta)$, and $z=Z(\chi,\xi,\eta)$, (2.1*a*)

Axial flows: $x=\chi$, $r=R(\chi,\xi,\eta)$, and $\theta=\Theta(\chi,\xi,\eta)$, (2.1*b*)

Circulating flows: $x=X(\chi,\xi,\eta)$, $r=R(\chi,\xi,\eta)$, and $\theta=\chi$ (2.1*c*)

In (2.1) x, y, and z are the rectangular Cartesian coordinates, and x, r, and θ are polar cylindrical coordinates. Let $U(\chi, \xi, \eta)$ represent the streamwise velocity. The dependent variables used to describe the plane, axial, and circulating flows are, respectively,

$$(U,Y,Z), \quad (U,R,\Theta), \quad \text{and} \quad (U,X,R) \tag{2.2}$$

Let $\mathbf{g}_\chi$ and $\mathbf{g}_\xi$ represent the coordinate vectors of the χ-ξ stream surfaces, and $\mathbf{g}_\chi$ and $\mathbf{g}_\eta$ the coordinate vectors of the χ-η stream surfaces (these vectors are calculated in the next section). Since the coordinate vector g_χ is common to both the χ-ξ and the χ-η stream surfaces, it is tangent to the stream line defined by the intersection of the χ-ξ and the χ-η stream surfaces. Since U is the streamwise velocity, we note, for later use, that U is along g_χ.

III Transport Equations and the Related Metrics

Equations for the transport of mass, momentum, and energy in a general curvilinear coordinate system have been derived previously and are given in books and review articles, among others, by Aris (1989), Flugge (1972), and Serrin (1959). In this section we adapt these equations to a streamwise curvilinear coordinate system (χ, ξ, η). It is called streamwise, since, by virtue of the χ coordinate lines, it is aligned with the streamlines. The transport equations are presented in terms of the metric of a streamwise curvilinear coordinate system.

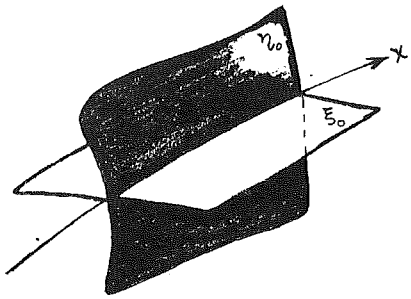

Fig. 1(*a*) General shape of a ξ = const stream surface intersecting a η = const stream surface for "plane" flows

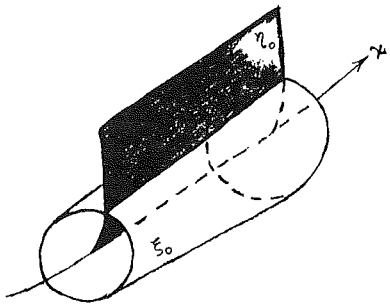

Fig. 1(*b*) General shape of a ξ = const stream surface intersecting a η = const stream surface for "axial" flows

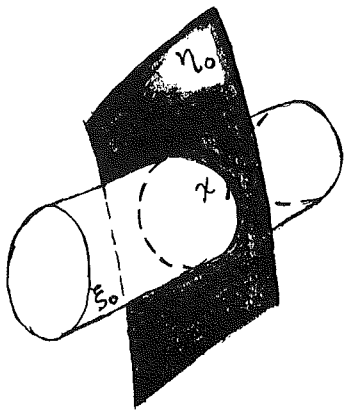

Fig. 1(*c*) General shape of a ξ = const stream surface intersecting a η = const stream surface for "circulating" flows

Latin letters i, j, k, and m are used for free and dummy indices. Whenever the same Latin letter i, j, k, or m appears in a product, once as a subscript and once as a superscript, it is understood that this means a sum over all terms. A subscript preceeded by a comma denotes an ordinary partial derivative. Covariant base vectors $\mathbf{g}_i$ of the (χ, ξ, η) coordinate system are calculated from the transformation formula,

$$\mathbf{g}_i=\frac{\partial \hat{x}^j}{\partial x^i}\,\hat{\mathbf{g}}_j \tag{3.1}$$

where x^i represent the coordinate lines of the (χ, ξ, η) system and $\hat{x}^j$ are the coordinate lines of the (x, y, z) system for the plane flows, and the coordinate lines of the (x, r, θ) system for the axial and the circulating flows. In (3.1) $\hat{\mathbf{g}}_j$ are the base vectors of the $\hat{x}^j$ system and are for the (x, y, z) and the (x, r, θ) system, respectively,

$$\hat{\mathbf{g}}_x=(1,0,0);\quad \hat{\mathbf{g}}_y=(0,1,0);\quad \hat{\mathbf{g}}_z=(0,0,1) \tag{3.2a}$$

$$\hat{\mathbf{g}}_x=(1,0,0);\quad \hat{\mathbf{g}}_r=(0,\cos\Theta,\sin\Theta);\quad \hat{\mathbf{g}}_\theta=(0,-R\sin\Theta,R\cos\Theta) \tag{3.2b}$$

Carrying out the transformation (3.1), we obtain for the covariant base vectors of the plane flow (χ, ξ, η) coordinate system

$$\mathbf{g}_\chi=(1,Y_{,\chi},Z_{,\chi});\quad \mathbf{g}_\xi=(0,Y_{,\xi},Z_{,\xi});\quad \mathbf{g}_\eta=(0,Y_{,\eta},Z_{,\eta}) \tag{3.3}$$

All these three covariant base vectors are expressed by the single equation,

$$\mathbf{g}_i=(\delta_{i\chi},Y_{,i},Z_{,i}) \tag{3.4}$$

where $\delta_{i\chi}$ is the Kronecker delta. The covariant components of the metric tensor, g_{ij}, defined by $g_{ij}=\mathbf{g}_i\cdot\mathbf{g}_j$ are given by:

$$g_{ij}=\delta_{i\chi}\delta_{j\chi}+Y_{,i}Y_{,j}+Z_{,i}Z_{,j} \tag{3.5}$$

The determinant, g, of the matrix of the metric coefficients is

$$g=(\mathbf{g}_\chi\cdot\mathbf{g}_\xi\times\mathbf{g}_\eta)^2=(Y_{,\xi}Z_{,\eta}-Y_{,\eta}Z_{,\xi})^2. \tag{3.6}$$

Since $\sqrt{g}$ appears often later in the transport equations, we denote $\sqrt{g}$ by D. Corresponding results for the axial and circulating flows are:

Axial Flows:

$$\mathbf{g}_i=(\delta_{i\chi},R_{,i}\cos\Theta-\Theta_{,i}R\sin\Theta,\ R_{,i}\sin\Theta+\Theta_{,i}R\cos\Theta) \tag{3.7a}$$

$$g_{ij}=\delta_{i\chi}\delta_{j\chi}+R_{,i}R_{,j}+R^2\Theta_{,i}\Theta_{,j} \tag{3.7b}$$

$$D=R(R_{,\xi}\Theta_{,\eta}-R_{,\eta}\Theta_{,\xi}) \tag{3.7c}$$

Circulating Flows:

$$\mathbf{g}_i=(X_{,i},\ R_{,i}\cos\Theta-\delta_{i\chi}R\sin\Theta,R_{,i}\sin\Theta+\delta_{i\chi}R\cos\Theta) \tag{3.8a}$$

$$g_{ij}=X_{,i}X_{,j}+R_{,i}R_{,j}+\delta_{i\chi}\delta_{j\chi}R^2 \tag{3.8b}$$

$$D=R(X_{,\xi}R_{,\eta}-X_{,\eta}R_{,\xi}) \tag{3.8c}$$

As discussed in Section II, the velocity vector at any point is directed along g_χ. Thus, the contravariant velocity components u^ξ and u^η are zero everywhere. To calculate u^χ we use the relation

$$U^2=u^iu^jg_{ij}=u^\chi u^\chi g_{\chi\chi}. \tag{3.9}$$

Thus, u^i, the contravariant velocity components are:

$$u^\chi=U/\sqrt{g_{\chi\chi}};\quad u^\xi=0;\quad u^\eta=0. \tag{3.10a,b,c}$$

The covariant velocity components, u_i, are calculated from

$$u_i=g_{ij}u^j=g_{i\chi}u^\chi, \tag{3.11}$$

and are:

$$u_\chi=\frac{g_{\chi\chi}}{\sqrt{g_{\chi\chi}}}U;\quad u_\xi=\frac{g_{\chi\xi}}{\sqrt{g_{\chi\chi}}}U;\quad u_\eta=\frac{g_{\chi\eta}}{\sqrt{g_{\chi\chi}}}U. \tag{3.12}$$

The contravariant velocity components, $\hat{u}^j$, in the $\hat{x}^j$ coordinate system are given by,

$$\hat{u}^j=\frac{\partial\hat{x}^j}{\partial x^i}u^i=\frac{\partial\hat{x}^j}{\partial\chi}u^\chi \tag{3.13}$$

and the physical velocity components, $\hat{u}(j)$, in the $\hat{x}^j$ coordinate system by,

$$\hat{u}(j)=\sqrt{\hat{g}_{jj}}\,\hat{u}^j\quad\text{(no sum over } j) \tag{3.14}$$

where $\hat{g}_{jj}$, the covariant components of the metric tensor of the $\hat{x}^j$ coordinate system, are for the (x, y, z) system $\hat{g}_{xx}=1$; $\hat{g}_{yy}=1$; $\hat{g}_{zz}=1$, and for the (x, r, θ) system $\hat{g}_{xx}=1$; $\hat{g}_{rr}=1$; $\hat{g}_{\theta\theta}=r^2=R^2$. We, thus, obtain the physical velocity components for the,

Plane flows: $\hat{u}(x)=\dfrac{U}{\sqrt{g_{\chi\chi}}}$; $\hat{u}(y)=\dfrac{UY_{,\chi}}{\sqrt{g_{\chi\chi}}}$; and $\hat{u}(z)=\dfrac{UZ_{,\chi}}{\sqrt{g_{\chi\chi}}}$ (3.15a)

Axial flows: $\hat{u}(x)=\dfrac{U}{\sqrt{g_{\chi\chi}}}$; $\hat{u}(r)=\dfrac{UR_{,\chi}}{\sqrt{g_{\chi\chi}}}$; and $\hat{u}(\theta)=\dfrac{RU\Theta_{,\chi}}{\sqrt{g_{\chi\chi}}}$ (3.15b)

Circulating flows: $\hat{u}(x)=\dfrac{UX_{,\chi}}{\sqrt{g_{\chi\chi}}}$; $\hat{u}(r)=\dfrac{UR_{,\chi}}{\sqrt{g_{\chi\chi}}}$; and $\hat{u}(\theta)=\dfrac{RU}{\sqrt{g_{\chi\chi}}}$ (3.15c)

Vorticity components are calculated from $\omega^k=\epsilon^{ijk}u_j|_i$, ($\epsilon^{ijk}$, the permutation tensor, is equal to $+1/D$, $-1/D$, or 0 depending on whether i, j, k is a cyclic, an anticyclic, or an acyclic sequence) and are

$$\omega^\chi=(u_{\eta,\xi}-u_{\xi,\eta})/D,\quad \omega^\xi=(u_{\chi,\eta}-u_{\eta,\chi})/D,\quad \omega^\eta=(u_{\xi,\chi}-u_{\chi,\xi})/D \tag{3.16a,b,c}$$

Continuity Equation:

$$\frac{\partial\rho}{\partial t}+\operatorname{div}(\rho\mathbf{v})=0, \tag{3.17}$$

where ρ is density. In streamwise computation of flow fields, u_χ is the only non-zero contravariant velocity component and the preceding equation becomes,

$$\frac{\partial\rho}{\partial t}+\frac{1}{D}\frac{\partial}{\partial\chi}(D\rho u^\chi)=0. \tag{3.18}$$

For steady flow $\rho_{,t}=0$, and we obtain on integrating the remaining part of (3.18)

$$D\rho u^\chi=\text{ a constant along }\chi. \tag{3.19}$$

We set the constant of integration equal to one. This choice of the integration constant along with the given inflow velocity distribution, as illustrated in the example computations given in Section IV, determines the location of the $\xi=$ const and $\eta=$ const stream surfaces at the inlet. The steady-state continuity equation thus becomes,

$$u^\chi=\frac{1}{\rho D}, \tag{3.20}$$

and with the help of (3.10a)

$$U=\frac{\sqrt{g_{\chi\chi}}}{\rho D}. \tag{3.21}$$

Momentum Equation:

$$\rho\frac{D\mathbf{v}}{Dt}=\rho\frac{\partial\mathbf{v}}{\partial t}+\rho u^i\mathbf{v}_{,i}=\mathbf{F}, \tag{3.22}$$

where $\mathbf{F}$ is the force (surface and body) per unit volume. Once again, since u^χ is the only nonzero contravariant velocity component, the covariant momentum equation for steady flow reduces to,

$$\rho u^\chi u_i|_\chi=F_i \tag{3.23}$$

By expressing the covariant derivative $u_i|_\chi$ in terms of g_{ij}, we obtain

$$\rho Dg_{\chi i,\chi}-g_{\chi i}(\rho D)_{,\chi}-\frac{1}{2}\rho Dg_{\chi\chi,i}=\rho^2D^3F_i \tag{3.24}$$

Another variation of momentum Eq. (3.23) is obtained by expressing for $u_i|_\chi$ in terms of ω^i and U,

$$\rho UU_{,\chi}=F_\chi,\quad \rho UU_{,\xi}=F_\xi-\omega^\eta,\quad \rho UU_{,\eta}=F_\eta+\omega^\xi. \tag{3.25a,b,c}$$

Energy Equation:

$$\frac{\partial(\rho e)}{\partial t}+\operatorname{div}(\rho e\mathbf{v})=-\operatorname{div}\mathbf{q}+\operatorname{div}(\mathbf{T}.\mathbf{v})+\rho\mathbf{v}.\mathbf{b}, \tag{3.26}$$

where e is the energy (sum of internal, kinetic, and potential)

per unit mass, **q** the heat flux, **T** the stress tensor, and **b** the body force per unit mass. Once again using the fact that u^x is the only nonzero velocity component, we obtain from (3.26) for steady flow,

$$\frac{1}{D}\frac{\partial}{\partial\chi}(D\rho e u^x) = -\frac{1}{D}\frac{\partial}{\partial x^j}(Dq^j) + \frac{1}{D}\frac{\partial}{\partial x^j}(DT^{ij}u_j) + \rho u^x b_x. \tag{3.27}$$

Calculation of F_i:

We separate the pressure, the viscous, and the body force contributions to F_i and write

$$F_i = -p_{,i} + f_i + \rho b_i \tag{3.28}$$

where b_i is the body force. The viscous contribution, f_k, is given by,

$$f_k = g_{ki}f^i = g_{ki}\tau^{ij}|_j = g_{ki}\left(\frac{1}{D}\frac{\partial}{\partial x^j}(D\tau^{ij}) + \tau^{jm}\Gamma^i_{jm}\right) \tag{3.29}$$

where

$$\tau^{ij} = -\frac{2}{3}\mu u^m|_m g^{ij} + \mu(g^{jm}u^i|_m + g^{im}u^j|_m). \tag{3.30}$$

The stress tensor T^{ij} is given by

$$T^{ij} = -pg^{ij} + \tau^{ij} \tag{3.31}$$

The contravariant components of the metric tensor, g^{ij}, and a "parabolic" approximation to the stress tensor are given in Greywall (1991).

IV Potential Flow

In this section we present the isentropic approximation to the transport equations of the preceding section. For an isentropic flow without body forces,

$$F_i = -p_{,i} = \rho(U^2/2)_{,i} = \rho(g_{\chi\chi}/2\rho^2D^2)_{,i} \tag{4.1}$$

where we have used (3.21) to express U in terms of the metric. From here on i stands only for ξ and η. Upon substituting F_i from (4.1) into (3.24), we obtain after some rearrangement,

$$g_{\chi i,\chi}D - g_{\chi i}D_{,\chi} - g_{\chi\chi,i}D + g_{\chi\chi}D_{,i} = \frac{D}{\rho}(g_{\chi i}\rho_{,\chi} - g_{\chi\chi}\rho_{,i}) \tag{4.2a}$$

With a little algebra (4.2*a*) can be rewritten as,

$$(g_{\chi i}/\rho D)_{,\chi} - (g_{\chi\chi}/\rho D)_{,i} = 0. \tag{4.2b}$$

Equation (4.2*b*) can also be obtained by setting the vorticity ω^i (3.16*b* and 3.16*c*) equal to zero and using (3.20) along with (3.11) to express u_i. The terms on the right-hand-side of (4.2*a*) represent the effects of compressibility, and vanish for an incompressible flow. Upon substitution of appropriate expressions for $g_{\chi i}$, $g_{\chi\chi}$, and D from Section III for a given type of flow, (4.2*a*) will yield two equations (one with i set equal to ξ and another with i set equal to η) for the two stream surfaces of that particular flow. To illustrate the procedure we present sample calculations for an incompressible axial flow. For incompressible potential flow (4.2*a*) yields the following two stream surface equations,

$\chi - \xi$ (η = const) stream surface:

$$g_{\chi\xi,\chi}D - g_{\chi\xi}D_{,\chi} - g_{\chi\chi,\xi}D + g_{\chi\chi}D_{,\xi} = 0 \tag{4.3a}$$

$\chi - \eta$ (ξ = const) stream surface:

$$g_{\chi\eta,\chi}D - g_{\chi\eta}D_{,\chi} - g_{\chi\chi,\eta}D + g_{\chi\chi}D_{,\eta} = 0 \tag{4.3b}$$

where,

$$g_{\chi\chi} = 1 + R^2_{,\chi} + R^2\Theta^2_{,\chi}, \quad g_{\chi\xi} = R_{,\chi}R_{,\xi} + R^2\Theta_{,\chi}\Theta_{,\xi}, \tag{4.4a,4.4b}$$

$$g_{\chi\eta} = R_{,\chi}R_{,\eta} + R^2\Theta_{,\chi}\Theta_{,\eta}, \quad \text{and} \quad D = R(R_{,\xi}\Theta_{,\eta} - R_{,\eta}\Theta_{,\xi}) \tag{4.4c,4.4d}$$

Equations (4.3) are two coupled partial differential equations for $R(\chi, \xi, \eta)$ and $\Theta(\chi, \xi, \eta)$. These equations were solved for flow through the circular-to-rectangular transition duct shown in Fig. 2. This duct is termed "AR410" in the family of transition ducts designed at NASA Lewis Research Center. The duct cross-section in the y-z plane is given by the super-ellipse equation,

$$\left(\frac{z}{a(x)}\right)^{n(x)} + \left(\frac{y}{b(x)}\right)^{n(x)} = 1 \tag{4.5}$$

where x is the spatial distance along the duct centerline, and y and z are the cross-stream cartesian coordinates. At the beginning of the transition $a = b = r = 10.214$ centimeters and $n = 2$. At the end of the transition $a = 3b = 1.546r$ and $n = 10$. The length of the transition section is equal to $3.125r$. The variations of a, b, and n with x are given in Davis (1991).

Flow rate through the duct is set equal to 10. Due to symmetry the computations are carried out in the first quadrant. The stream surface $\eta = 0$ is the surface $\theta = 0$ (x-y plane in Fig. 2), and $\eta = 2.5$ is the surface $\theta = \pi/2$ (x-z surface in Fig. 2). The stream surface $\xi = 0$ is the centerline, and the stream surface $\xi = 10$ is the duct wall. We label the grid along χ, ξ, and η by i, j, and k, respectively. The computations are carried out using uniform grid spacings $\Delta\chi$, $\Delta\xi$, and $\Delta\eta$. Equations (4.3) are finite differenced using center differencing at all the interior grid points and using three point formulas at the boundary grid points. The resulting non-linear finite difference equations are linearized by using Newton linearization and written in the form,

$$aR_{i,j,k} + b\Theta_{i,j,k} = c. \tag{4.6}$$

Equation (4.5) also, after being transformed into polar cylindrical coordinates and Newton linearized, is written in the form (4.6). The algorithm to solve the finite difference equations is divided into two parts; (1) solutions of R and Θ at the boundary surfaces and (2) solutions of R and Θ in the interior region. At the boundaries that form the stream surfaces ($k = 1$, $k = k\max$, and $j = j\max$) the appropriate stream surface equation (Eq.(4.6) for ξ or η) is solved in conjunction with the equation that describes the geometry of that surface. At the inlet $R_{1,j,k}$ and $\Theta_{1,j,k}$ are determined from the given inflow velocity distribution. Stream surface $j = 1$ is the centerline, $R_{1,2,k}$ and $\Theta_{1,2,k}$ are determined from the given inflow velocity distribution so that the flow rate through the stream surface $j = 2$ is equal to $\Delta\xi$. For uniform inlet velocity distribution, assumed in the present computations, the stream surface $j = 2$ is a circle with area equal to $\Delta\xi$. Proceeding in the same way, the remaining $R_{1,j,k}$ and $\Theta_{1,j,k}$ are determined. At the exit boundary $i = i\max$, R and Θ are calculated by setting their second derivatives with respect to χ equal to zero. At all the interior grid points the two stream surface equations (Eq.(4.6) for ξ, and η) are solved simultaneously for $R_{i,j,k}$ and $\Theta_{i,j,k}$. The surface and the interior solutions are carried out in tandem, iteratively.

After (4.3) are solved for R and Θ, the streamwise velocity (speed), U, is calculated from the continuity Eq. (3.21), and then the pressure distribution from the Bernoulli's equation,

$$c_p = \frac{p - p_0}{\frac{1}{2}\rho U_0^2} = 1 - \frac{U^2}{U_0^2} = 1 - \frac{g_{\chi\chi}}{\rho^2D^2U_0^2}. \tag{4.7}$$

where p_0 and U_0 are the values of pressure and velocity at the duct inlet, D and $g_{\chi\chi}$ were calculated from $R_{i,j,k}$ and $\Theta_{i,j,k}$ using central differencing on the interior grid points and three point differencing on the boundary grid points. The duct transition section extends from $x/r = 1.0$ to $x/r = 4.125$. Calculations were started at $x/r = 0.4375$ ($x/r = 0$ is the zero of the AR410 geometric data given in Davis (1991)) and continued to $x/r = 4.75$. Computations were carried out with $i\max = 70$, $j\max$

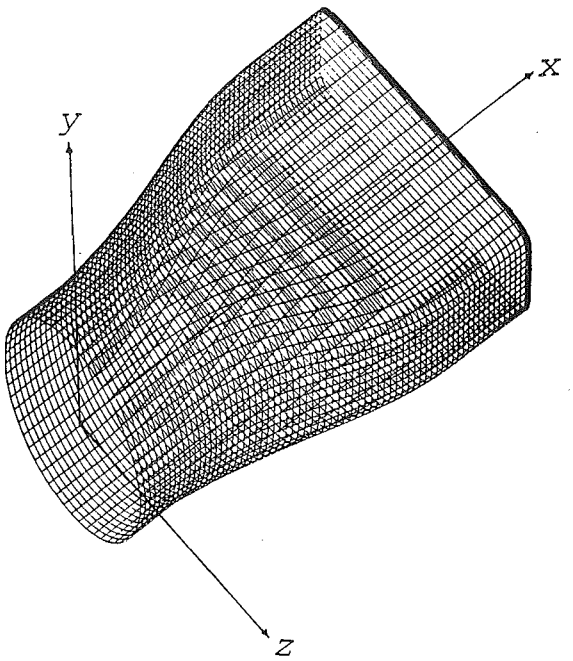

Fig. 2 Circular-to-rectangular transition duct

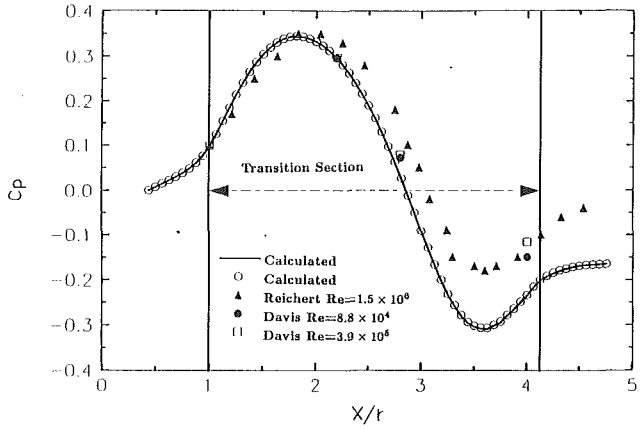

Fig. 3 Comparison of the computed c_p along the center of the top wall of the "AR410" duct (Fig. 2) with the experimental data of Davis (1991) and Reichert et al. (1991). The solid line represents the computed c_p distribution along the "AR410" duct, and the circles along this line represent the mirror image of the computed c_p along the mirror image of AR410.

= 15, and $k\max$ = 15. Further computational details are given in Greywall and Youssef (1992).

The axial lines in Fig. 2 are the computed streamlines of the surface flow (the cross-stream lines were added to improve visualization of the duct shape). Computed shapes of various stream surfaces are given in Greywall and Youssef (1992). In Fig. 3 the solid line shows the computed c_p along the center of the top wall (Fig. 2). The results are compared with the available experimental data of Davis (1991) and Reichert et al. (1991) for the AR410 transition duct. The pressure distribution along the center of the top wall is the experimental data common to both sets of experiments. In these two experiments p_0 and U_0, used in the calculations of c_p, were measured at different locations upstream of the transition. To make the comparison meaningful both sets of experimental c_p data were shifted to get a starting match with the computed value of c_p at the start of the transition (x/r = 1 in Fig. 3). Besides the obvious fact that we are comparing potential flow calculations with turbulent flow experimental data, the comparison is made more difficult by the fact that in both the experiments flow entered the transition section with a non-negligible boundary layer thickness (measurements of $\delta/r \simeq .08$ to 0.3 reported at locations upstream of the transition). As the flow proceeds along the duct the effects of viscous dissipation accumulate and as expected, and as seen from Fig. 3, the potential flow c_p deviates more and more from the viscous flow c_p. As an internal check on the algorithm, a mirror image of the duct was attached at the end of the circular-to-rectangular transition duct, so that the duct went back from rectangular to circular. The circles along the solid line in Fig. 3 show the mirror image of the computed c_p along the rectangular-to-circular section of the extended duct. The two pressure distributions are indistinguishable.

To conclude this section we present one special case of circulating flows. For two-dimensional circulating flows in χ-R

$$X_{,\chi} = X_{,\xi} = R_{,\eta} = 0, \quad \text{and} \quad X_{,\eta} = 1 \tag{4.8a}$$

and we have from (3.8b) and (3.8c)

$$g_{\chi\chi} = R^2 + R^2_{,\chi}, \quad g_{\chi\xi} = R_{,\chi}R_{,\xi}, \quad \text{and} \quad D = -RR_{,\xi} \tag{4.8b}$$

With the help of (4.8), (4.2) becomes,

$$R^2_{,\xi}R_{,\chi\chi} - 2R_{,\chi}R_{,\xi}R_{,\chi\xi} + (R^2 + R^2_{,\chi})R_{,\xi\xi} - RR^2_{,\xi} = 0 \tag{4.9}$$

We note that the free line vortex given by

$$R = \text{const } e^{\xi} \tag{4.10}$$

is a solution of Eq. (4.9).

V Concluding Remarks

A theory to compute three-dimensional flows using two stream functions is presented. Two commonly used steps for computing flow fields: (1) boundary fitted grid generation and (2) solution of Navier–Stokes equations on the generated grid, are combined into a single step. For three-dimensional flows there is yet no general theory to define two sets of intersecting stream surfaces to cover a given flow. In the present work, we have presented three different combinations, each consisting of two sets of intersecting stream surfaces, which cover many flows of practical interest. However, a general theory regarding the selection of two sets of intersecting stream surfaces to cover a given flow for the most efficient computation is needed. In the computation of flows with recirculating regions, zonal approach is optional when the velocity is used as the dependent variable. In the present approach the only way to compute such flows is to use circulating flow stream surfaces for the recirculating flow regions and plane or axial flow stream surfaces for the main flow and then try to match the solutions. Also, further work is needed to compute flows with a swirling inflow velocity distribution.

Acknowledgments

We thank Dr. Julie Mathis for her reading of the manuscript, and Mr. Ali Youssef for his help in developing the numerical code for the computation of flow through transition ducts. The work was partially supported by NASA-Lewis Internal Fluid Dynamics Division through 1989 and 1990 NASA/ASEE Summer Faculty program.

References

Aris, R., 1989, *Vectors, Tensors, and the Basic Equations of Fluid Mechanics*, Dover Publications, New York, N.Y.

Clebsch, A., 1857, "Ueber eine allgemeine Transformation der hydrodynamischen Gleichungen," *Crelle*, Vol. 54, pp. 293–312.

Davis, D. O., 1991, "Experimental Investigation of Turbulent Flow Through a Circular-to-Rectangular Transition Duct," NASA Technical Memorandum 105210.

Farrel, C., and Adamczyk, J., 1982, "Full Potential Solution of Transonic Quasi-Three-Dimensional Flow Through a Cascade," ASME *Journal of Engineering for Power*, Vol. 104, pp. 143–153.

Flugge, W., 1972, *Tensor Analysis and Continuum Mechanics*, Springer-Verlag, Berlin Heidelberg, New York.

Ghia, U., Ghia, K. N., Rubin, S. G., and Khosla, P. K., 1981, "Study of Incompressible Flow Separation Using Primitive Variables," *Computers and Fluids*, Vol. 9, pp. 123–142.

Greywall, M. S., 1980, "Streamwise Computation of Duct Flows," *Computer Methods in Applied Mechanics and Engineering*, Vol. 21, pp. 231–247.

Greywall, M. S., 1983, "Streamwise Computation of Three-Dimensional Parabolic Flows," *Computer Methods in Applied Mechanics and Engineering*, Vol. 36, pp. 71–93.

Greywall, M. S., 1985, "Streamwise Computation of Two-Dimensional Incompressible Potential Flows," *Journal of Computational Physics*, Vol. 59, pp. 224–231.

Greywall, M. S., 1988, "Streamwise Computation of Three-Dimensional Potential Flows," *Journal of Computational Physics*, Vol. 78, pp. 178–193.

Greywall, M. S., 1991, "Computation of Three-Dimensional Flows Using Two Stream Functions," National Institute for Aviation Research, The Wichita State University, NIAR Report 91-27.

Greywall, M. S., and Youssef, A., 1992, "Streamwise Computation of Potential Flow Through Circular to Rectangular Transition Duct," National Institute for Aviation Research, The Wichita State University, NIAR Report 92-17.

Kwon, O. K., and Pletcher, R. H., 1986, "A Viscous-Inviscid Interaction Procedure—Part 1: Method for Computing Two-Dimensional Incompressible Separated Flows," ASME JOURNAL OF FLUIDS ENGINEERING, Vol. 108, pp. 64–70.

Lagrange, J. L., 1781, "Memoire sur la theorie du mouvement des fluids," *Nouveaux Memoires de L'Academie Royale des Sciences et Belles-Lettres*, Oeuvres, iv) pp. 151–198.

Maeder, P. F., and Wood, A. D., 1954, "Stream Functions and Transonic Similarity in Three-Dimensional Flow," Division of Engineering, Brown University, Technical Report WT-14, Oct.

Meyder, R., 1975, "Solving the Conservation Equations in Fuel Rod Bundles Exposed to Parallel Flows by Means of Curvilinear-Orthogonal Coordinates," *Journal of Computational Physics*, Vol. 17, pp. 53–67.

Prasil, F., 1926, *Technische Hydrodynamik*, Juluis Springer, Berlin.

Reichert, B. A., Hingst, W. R., and Okiishi, T. H., 1991, "An Experimental Comparison of Nonswirling and Swirling Flow in a Circular-to-Rectangular Transition Duct," NASA Technical Memorandum 104359, Also AIAA paper AIAA-91-0342.

Serrin, J., 1959, *Handbuch der Physik*, Band VIII/1 Springer-Verlag, Berlin, Gottingen, Heidelberg.

Stokes, G. G., 1842, "On the Steady Motion of Incompressible Fluids," *Transactions of the Cambridge Philosophical Society*, Vol. vii, (Paper i, 1) Also available in, Stokes, G. G., *Mathematical and Physical Papers*, Vol I, Cambridge University Press, 1880.

Thompson, J. F., Warsi, Z. U. A., and Mastin, C. W., 1982, "Boundary-Fitted Coordinate Systems for Numerical Solution of Partial Differential Equations—A Review," *Journal of Computational Physics*, Vol. 47, pp. 1–108.

C-S, Yih, C-S., 1957, "Stream Functions in Three-Dimensional Flows," *La Houille Blanche*, Vol. 3, pp. 445–450.

Prediction of Pressure Drop for Incompressible Flow Through Screens

E. Brundrett
Department of Mechanical Engineering,
University of Waterloo,
Waterloo, Ontario, Canada, N2L 3G1

A new pressure loss correlation predicts flow through screens for the wire Reynolds number range of 10^{-4} to 10^{4} using the conventional orthogonal porosity and a function of wire Reynolds number. The correlation is extended by the conventional cosine law to include flow that is not perpendicular to the screen. The importance of careful specification of wire diameter for accurate predictions of porosity is examined. The effective porosity is influenced by the shape of the woven wires, by any local damage, and by screen tension.

Introduction

The purpose of this paper is to propose a general correlation equation for pressure drop through woven wire and cloth screens for incompressible flow, for the wire Reynolds number range of $0.0001 \leq \mathrm{Re}_d \leq 10{,}000$, based on the average approach velocity, the wire diameter and the kinematic viscosity of the fluid ($\mathrm{Re}_d = U.d/v$). Existing work reported over a period of more than 40 years by; Schubauer et al. (1948), Pinker and Herbert (1967), Tan-achitat et al. (1982), Groth and Johansson (1988), and Munson (1988) are used to create the new correlation. The discussion is extended to quantify errors produced by screen porosity variation due to manufacturing tolerances, local screen damage and variable tension created during installation.

Existing Pressure Loss Correlations

Pinker and Herbert (1967) examined in detail the then existing correlations for pressure drop through screens. Based upon compressible flow conditions, they noted that the effective open area of a screen must be somewhat greater than that obtained by the simple orthogonal procedure of subtracting the wire blockage from the area of each mesh spacing. Nevertheless, the orthogonal open area is traditionally used in pressure drop correlations, where each pair of warp and weft wire has the area $(1/m)^2$, and the orthogonal or projected open area is $(1/m-d)^2$ (Fig. 1). The screen porosity is a more convenient and dimensionless parameter defined as the ratio of open to total mesh area which can be generalized for nonsquare weaves with mesh warp and weft spacings respectively of m_1, m_2 and warp and weft wire diameters respectively of d_1, d_2 as,

$$\alpha = \frac{\left(\frac{1}{m}-d\right)^2}{\frac{1}{m^2}} = (1-md)^2 = (1-m_1d_1)(1-m_2d_2) \qquad (1)$$

Contributed by the Fluids Engineering Division for publication in the JOURNAL OF FLUIDS ENGINEERING. Manuscript received by the Fluids Engineering Division April 23, 1992. Associate Technical Editor: D. M. Bushnell.

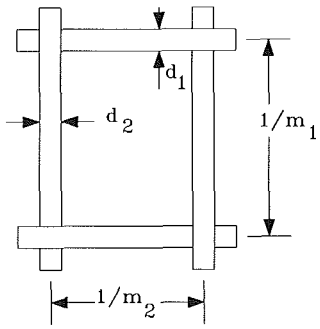

Fig. 1 Screen dimensions for an unequal number of warp and weft wires or threads

Pinker and Herbert (1967) examined many previous attempts to separate the incompressible flow pressure drop coefficient (K_0) defined for flow perpendicular to the screen in terms of the screen pressure drop ΔP and upstream velocity U as,

$$\Delta P = K_0 \times 0.5\rho U^2 \qquad (2)$$

They concluded that K_0 could be separated into two independent components, a screen porosity function $G(\alpha)$ and a function based on the wire Reynolds number $f(\mathrm{Re}_d)$. They examined four functions; $(G_1(\alpha) = (1-\alpha)/\alpha^2)$ (Weighardt, 1953), $(G_2(\alpha) = (1-\alpha^2)/\alpha^2)$ (Annand, 1953), $(G_3(\alpha) = (1-\alpha)^2/\alpha^2))$ (Pinker and Herbert, 1967), and $(G_4(\alpha) = (1-\alpha_v)/\alpha_v^2)$ (Grootenhuis, 1954), where α_v is a 'volumetric porosity' which permits skin friction losses to be computed for the total surface area of the warp and weft wires. They decided that $G_2(\alpha)$ provided the best correlation of their data, as did Groth and Johansson (1988), Munson (1988), and this writer. However, some authors have reported their results using the $G_1(\alpha)$ porosity function, but this writer could not obtain as good predictions using this function, particularly for the work of Schubauer et al. (1948), of Groth and Johansson (1988), and of Munson (1988).

Schubauer et al. (1948) extended their investigation for upstream flow angles other than perpendicular as defined by the approach angle $\theta(\theta = 0$ for perpendicular flow). They found

that the empirical correlation of pressure loss coefficient K_θ versus approach angle was satisfactorily provided by plotting $K_\theta/\cos^2(\theta)$ versus $\mathrm{Re}_d\cos(\theta)$, for the range $0 \le \theta \le 45$ deg, where $K_\theta = K_0$ if $\theta = 0$. Hence, the general expression for K_θ is,

$$K_\theta = \cos^2\theta \times G_2(\alpha) \times f(Re_d \times \cos\theta) \tag{3}$$

Recently Munson (1988) has proposed a correlation of K_0 for fully developed laminar pipe flow from experimental data in the range of $0.0001 \le \mathrm{Re}_d \le 3$, as;

$$f(\mathrm{Re}_d) = \frac{4.75}{\mathrm{Re}_d} \tag{4}$$

However, as shown below, this correlation significantly under predicts his $\mathrm{Re}_d > 1$ data.

For $\mathrm{Re}_d > 800$ Pinker and Herbert (1967) found that $f(\mathrm{Re}_d) \approx 0.54$; while Groth and Johansson (1988) found that $f(\mathrm{Re}_d) \approx 0.45$. The value of Groth and Johansson is in better agreement with all other data sources. Unfortunately, Pinker and Herbert located their flow measurement orifice plate only 16 pipe diameters upstream of the screen test station, and duct Mach numbers of $0.1 \le M_d \le 0.48$ were examined. Also, an unsubstantiated graphical procedure was used to extrapolate their pressure loss data to $M_d \to 0$.

Data Transcription

Some tabulated pressure drop data were provided by Tanachitat et al. (1982) and by Groth and Johansson (1988). In addition, graphical data were provided by Schubauer et al. (1948), Pinker and Herbert (1967), Groth and Johansson (1988), and Munson (1988). All pressure drop versus Re_d graphs were photographically enlarged by a photocopier to permit manual scaling of the data points using a draughtsman's scale. Considerable care and time were taken to reduce to a minimum any transcription errors due to scale reading and due to any local grid distortions created by the history of reproduction of each graph from the original to the enlarged current working copy. The estimated random error created by this writer in the process of transcribing the data points was determined by repeated independent readings obtained for randomly selected points at different times over a three week period. The range of errors was dependent upon the scale of the original graph and the location of the data points within each plot and was never greater than ± 1 percent. Similar errors may have occurred during the construction of early manually prepared graphs. Hence, a doubling of all the transcription errors to ± 2 percent is realistic.

General Form of the $f(\mathrm{Re}_d)$ Correlation

The data of Schubauer et al. (1948) and Groth and Johansson (1988) were successfully correlated by the screen porosity function $G_2(\alpha)$ and a three component function of wire Reynolds number and the approach flow angle (Eq. (3)). For flow normal to any screen $f(\mathrm{Re}_d)$ evolved through trial and error to the form,

$$f(\mathrm{Re}_d) = \frac{C_1}{\mathrm{Re}_d}\,(\mathrm{I}) + \frac{C_2}{\log(\mathrm{Re}_d + 1.25)}\,(\mathrm{II}) + C_3\log(\mathrm{Re}_d)(\mathrm{III}) \tag{5}$$

where, $C_1 \approx 7.0$, $C_2 \approx 0.9$, $C_3 \approx 0.05$ provided good agreement with the data. Term I is dominant for $\mathrm{Re}_d < 1$ and is similar in form to that for drag of cylinders and friction loss in pipes. Term II is a blending function which is significant for $0.1 \le \mathrm{Re}_d \le 100$. This term was made well behaved throughout the full range by the artifice of adding the constant of 1.25 to the wire Reynolds number. Term II is similar to the blending function adopted by Haaland (1983) for his explicit solution for pipe friction factor in turbulent pipe flow. Term III creates the required high Reynolds number nearly constant value for $f(\mathrm{Re}_d)$ that is observed in all of the data sets with $\mathrm{Re}_d > 200$. The final values for the constants of Eq. (5) were developed after considering the pipe flow screen data of Munson (1988).

Upstream Parabolic Velocity Profile

Munson (1988) examined pressure loss through four woven wire screens with equal warp and weft properties for the range $0.0001 \le \mathrm{Re}_d \le 3.1$, for upstream fully developed laminar pipe flow. His findings can be converted to uniform velocity profile conditions by assuming that the pressure drop across each screen was not dependent upon radial position, and hence, was constant at each and every point of the screen. Second, it can be seen that Term I will dominate for the majority of Munson's data as shown by his recommended correlation (Eq. (4)). A local value for C_1 ($C_{1\mathrm{loc}}$) can be obtained from the average value $C_{1\mathrm{ave}} = 4.75$ recommended by Munson by considering the profile dependent flux of Momentum (σ_M) and of Kinetic Energy (σ_{KE}) (White, 1986). Thus,

$$\Delta P = \int\int \frac{C_{1\mathrm{loc}}}{\mathrm{Re}_{d\,\mathrm{loc}}}\,0.5\rho U_{\mathrm{loc}}^2\,(U_{\mathrm{loc}} \cdot dA)$$

$$= \frac{C_{1\mathrm{ave}}}{\mathrm{Re}_{d\,\mathrm{ave}}}\,\sigma_{KE}\,0.5\rho U_{\mathrm{ave}}^2\,(U_{\mathrm{ave}} \cdot A) \tag{6}$$

Substituting for $\mathrm{Re}_{d\,\mathrm{loc}} = (U_{\mathrm{loc}}d)/v$, and for $\mathrm{Re}_{d\,\mathrm{ave}} = (U_{\mathrm{ave}}d)/v$ and simplifying yields,

$$C_{1\mathrm{loc}}\frac{1}{A}\int\int\left(\frac{U_{\mathrm{loc}}}{U_{\mathrm{ave}}}\right)^2 dA = C_{1\mathrm{loc}}\sigma_M = C_{1\mathrm{ave}}\sigma_{KE} \tag{7}$$

For laminar pipe flow $\sigma_M = 1.333$, and $\sigma_{KE} = 2.0$ (White, 1986), hence,

$$C_{1\mathrm{loc}} = \frac{\sigma_{KE}}{\sigma_M}\,C_{1\mathrm{ave}} = \frac{2.0}{1.333} \times 4.74 = 7.125 \tag{8}$$

For uniform flow $\sigma_M = \sigma_{KE} = 1.0$ everywhere, and hence, $C_{1\mathrm{ave}} = C_{1\mathrm{loc}} = 7.125$. Thus with C_1 defined, the constants C_2 and C_3 (Eq. (5)) were further refined. Also, the experimental data of Munson (1988) were adjusted to uniform velocity conditions by the ratio $\sigma_{KE}/\sigma_M = 1.5$ and then were used to extend the uniform flow data range to $\mathrm{Re}_d \to 0.0001$.

General Incompressible Flow Correlation

Term I can be specified for either laminar pipe flow or for uniform upstream conditions by introducing σ_{KE} and σ_M. Then Eq. (5) was refined through correlation of the uniform flow data of Schubauer et al. (1948), Groth and Johansson (1988), and the converted data of Munson (1988), to yield;

$$K_\theta = \cos^2\theta \times \frac{1-\alpha^2}{\alpha^2} \times \left[\frac{\sigma_M}{\sigma_{KE}} \times \frac{7.125}{\mathrm{Re}_d\cos\theta} + \frac{0.88}{\log(\mathrm{Re}_d\cos\theta + 1.25)} + 0.055\log(\mathrm{Re}_d\cos\theta)\right] \tag{9}$$

For incompressible turbulent flow in the power law velocity profile range of 1/7th to 1/9th, the correction of Term I for profile is $0.964 \le \sigma_M/\sigma_{KE} \le 0.977$. Hence, the correction is probably not justified in view of the other error sources, such as the accurate determination of the pressure drop, velocity, fluid density, and screen porosity.

Figure 2 shows the pipe data of Munson (1988) and the pipe form of the general correlation ($\sigma_M = 1.333$ and $\sigma_{KE} = 2.000$). The correlation predicts each data point to within the range of ± 8 percent over the range $0.0001 \le \mathrm{Re}_d \le 3.1$, with an average error of $+1.1$ percent and a standard deviation of the errors of 5.8 percent. Munson employed four screens with $0.368 \le \alpha \le .653$ and stated that "uncertainties in the final data were determined to be ± 7 percent in A_1 ($C_{1\mathrm{ave}}$) and ± 5 percent

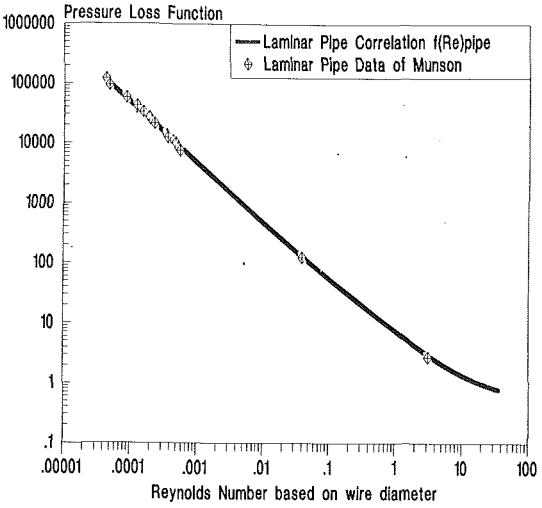

Fig. 2 Correlation of the pipe data of Munson (1988) by $f(\mathrm{Re}_d)$

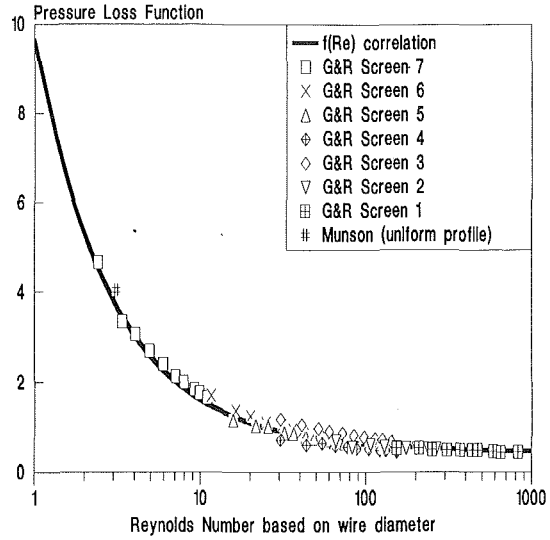

Fig. 3 Correlation of the uniform profile data of Groth and Johansson (1988) by $f(\mathrm{Re}_d)$

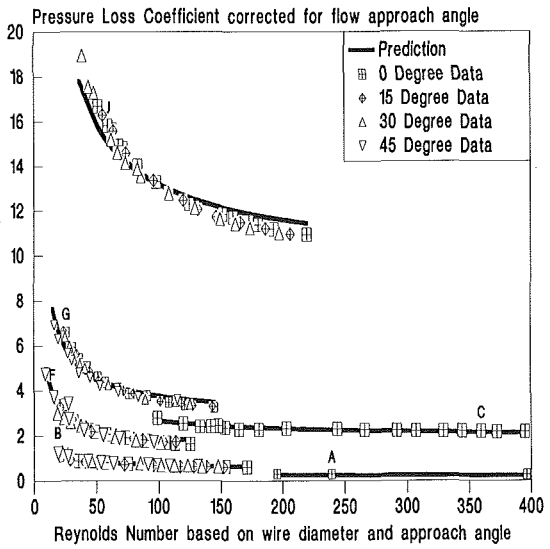

Fig. 4 Correlation of some of the uniform profile screen data of Schubauer et al. (1948) for various values of θ by K_θ

in Re at 20:1 odds." Hence, the correlation of the data by Eq. (9) is within the combined experimental and transcription errors.

Figure 3 presents the seven screen tests of Groth and Johansson (1988) and the one uniform profile converted data point of Munson (1988) that lies within the range $1 \le \mathrm{Re}_d \le 1000$. No experimental error bounds are provided by Groth and Johansson. However, their reduced experimental data of $f(\mathrm{Re}_d)$ are correlated with an average error of -0.2 percent and an average standard deviation of 3.2 percent. However the predictions screen by screen are poorer, ranging from -20.0 percent to $+23.0$ percent. The consistently high or low trends of certain screens can be explained by minor adjustments of screen porosity achieved by very small adjustments of warp and weft wire diameters described below.

The experimental pressure drop coefficients (K_0) of Tan-achitat et al. (1982) were predicted with an average error of -1.1 percent. The standard deviation of errors of 7.9 percent and the limits of -9.5 percent to $+10.9$ percent were again within the expected ranges.

Finally, predictions of $K_\theta/\cos^2\theta$ for six of the ten screens tested by Schubauer et al. (1948) (Fig. 4) show very good apparent agreement but in fact screen A has a significant average prediction error of -15.4 percent, and screen K has an average prediction error of $+18.4$ percent. However, on average the prediction error for the ten screens is only $+2.5$ percent and the standard deviation of the errors is 3.8 percent. The large and consistent errors of screens A, D, and K are examined next.

Quantification of Screen Porosity and $G_2(\alpha)$

On average the correlation of pressure drop through screens for incompressible flow is within -1.1 to $+2.5$ percent, ($+2.5$ percent (Schubauer et al., 1948); -1.1 percent (Tan-achitat et al., 1982); -0.2 percent (Groth and Johansson, 1988); and $+1.1$ percent (Munson, 1988)); and averaged over all four sets of data the error is $+0.58$ percent. Yet, large discrepancies exist for the average errors of individual screens. Usually, the mesh spacing can be defined to a much higher level of accuracy than the wire diameter since it is averaged over a measurement distance of say 20 to 50 mm. However, wires must be individually measured, often as samples extracted from wire salvage that have significant kinking created by the weaving process. Such wires have been measured for diameter by this writer using a micrometer to a precision of no better than ± 0.0125 mm (± 0.00049 in). Thus, errors in the specification of screen porosity (Eq. (1)) and of $G_2(\alpha)$ appear to be primarily due to wire diameter measurement errors. However, minor variations in wire spacing will influence the performance of the screen locally, and hence may create an unacceptable degradation of downstream flow quality (Pinker and Herbert, 1967), but the average pressure drop through the screen will be influenced very little for wire Reynolds numbers $50 \le \mathrm{Re}_d \le 10{,}000$.

Examining the change in $G_2(\alpha)$ with change in screen porosity, and particularly for changes in wire diameter, the derivative yields;

$$dG_2(\alpha) = -2\alpha^{-3}d\alpha \tag{10}$$

The percentage change of $G_2(\alpha)$ for $\Delta\alpha$ is the most useful expression for the effect of wire and mesh errors; and as a first approximation attributing all screen dimensional errors to the wire diameter error Δd yields,

$$\%\text{error } G_2(\alpha) = \frac{\Delta G_2(\alpha)}{G_2(\alpha)} \times 100 = \frac{-200\alpha^{-3}\Delta\alpha}{\frac{1-\alpha^2}{\alpha^2}}$$

$$= +400\,\frac{m\Delta d}{\alpha^{0.5} - \alpha^{2.5}} \tag{11}$$

As expected, the percentage error increases with increasing m,

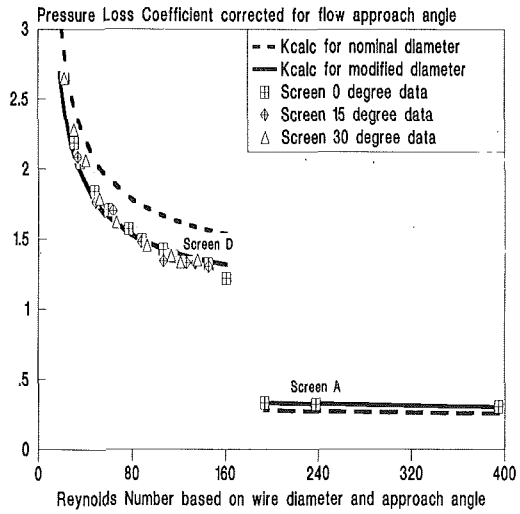

Fig. 5 Improved correlation of K_θ of Screens A and D of Schubauer et al. (1948) by porosity adjustment

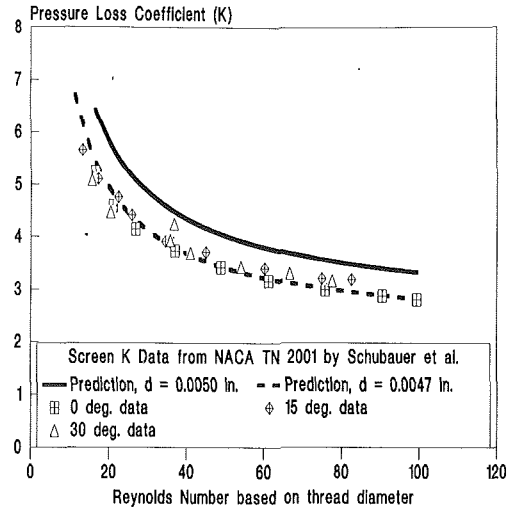

Fig. 6 Improved K_θ correlation of Screen K of Schubauer (1948) by adjustment of wire diameter

the wires per mm (per in.), due to the accumulative error of any measurement inaccuracy Δd. Also, the porosity has a slight effect upon the percentage error. Fine mesh screens ($m > 1.25$/mm) present a serious potential error and should not be specified for precision application such as wind tunnels without first achieving a significant reduction of the measurement error Δd.

All screens, with the exception of Screens, A, D, and K of Schubauer et al. (1948), are correlated within expected error bounds of ± 10 percent. Furthermore, Screens G and H are from the same roll of woven wire cloth; yet, Screen G prediction has an average error of $+1.0$ percent, while Screen G has an average error of -8 percent. The investigators noted that these screens were "not of precision manufacture." For screen A, a decrease of screen porosity of -3.0 percent reduces the average prediction error of Screen A from -15.4 to 0.0 percent (Fig. 5). This screen is very porous ($m = 0.157$/mm (4/in.), $d = 0984$ mm (0.025 in.) and it is possible that the effective porosity is reduced by the weave process and possible post rolling of the screen. Screen D is also very well correlated by reducing the wire diameter from 0.178 to 0.165 mm (0.007 to 0.0065 in.) (Fig. 5) for a reduction in average prediction error from $+16.3$ to -0.20 percent. Finally, Screen K, the 2.91 thread/mm (74/in.) "abnormal" bolting cloth has an average prediction error that is reduced from 18.4 to 0.0 percent by reducing the thread diameter from 0.127 mm to 0.119 mm (from 0.005 to 0.0047 in.) (Fig. 6).

These observations show the importance of accurately determining the warp and weft wire or thread diameters of a screen to an accuracy sufficient to permit an acceptable level of prediction of the pressure drop coefficient. Typically, a coefficient accuracy of $\pm$ 10 percent requires some sampling and careful measurement of wire diameter, while an accuracy of ± 5 percent or better will probably require the use of optical measurement procedures and adequate sampling of the warp and weft wires or threads.

The effect of dirt buildup on screens can be quantified by Eq. (11). Closely spaced wire meshes exhibit the greatest sensitivity to dirt for any specified porosity. For applications with limited opportunity for thorough wire cleaning, it may well be desirable to increase mesh spacing and wire diameter to decrease the dirt induced $+\Delta G_2(\alpha)$ that will occur between the periods of maintenance.

An unsuccessful screen repair by East (1972) is certainly related to these findings. He used a piece of "identical" screen with each wire of the patch carefully end welded to the screen. Even so, the downstream velocity profiles clearly showed the patch location and in his case exhibited a significant flow retardation. He concluded that variations in screen tension at the patch and a possible difference in wire diameter between patch and screen were significant factors.

Finally, for a sensitive application such as a wind tunnel, a screen should be constructed from sequential pieces from a single roll of stock that has been carefully examined for freedom from local damage, variations in wire shape, and that has an acceptably small variation in warp and weft wire diameters.

Acknowledgments

Research for this paper was supported in part by a wind tunnel operating grant awarded to the writer by the Natural Sciences and Engineering Research Council of Canada.

References

Annand, W. J. D., 1953, "The Resistance To Air Flow of Wire Gauzes," *Journal Royal Aeronautical Society*, Vol. 57.

East, L. F., 1972, "Spatial Variations of the Boundary Layer in a Large Low-Speed Wind Tunnel," *Aeronautical Journal*, Jan., pp. 43–44.

Grootenhuis, P., 1954, "A Correlation of the Resistance to Air Flow of Wire Gauzes," *Proceedings Institute of Mechanical Engineers*, Vol. 168, p. 837.

Groth, J., and Johansson, A. V., 1988, "Turbulence Reduction by Screens," *Journal of Fluid Mechanics*, Vol. 197, pp. 139–155.

Haaland, S. E., 1983, "Simple and Explicit Formulas for the Friction Factor in Turbulent Pipe Flow," ASME JOURNAL OF FLUIDS ENGINEERING, Vol. 105, pp. 89–90.

Munson, B. R., 1988, "Very Low Reynolds Number Flow Through Screens," ASME JOURNAL OF FLUIDS ENGINEERING, Vol. 110, pp. 462–463.

Pinker, R. A., and Herbert, M. V., 1967, "Pressure Loss Associated With Compressible Flow Through Square-Mesh Wire Gauzes," *Journal of Mechanical Engineering Science*, Vol. 9, No. 1, pp. 11–23.

Schubauer, G. B., Spangenberg, W. G., and Klebanoff, P. S., 1948, "Aerodynamic Characteristics of Damping Screens," NACA TN 2001.

Tan-achitat, J., Nagib, H. M., and Loehrke, R. I., 1982, "Interaction of Free-Stream Turbulence with Screens and Grids: A Balance Between Turbulence Scales," *Journal of Fluid Mechanics*, Vol. 114, pp. 501–528.

Weighardt, K. E. G., 1953, "On the Resistance of Screens," *Aeronautical Quarterly*, Vol. 4.

White, F. M., 1986, *Fluid Mechanics*, Second Edition, McGraw-Hill.

Partial Cavities: Global Behavior and Mean Pressure Distribution

Q. Le[1]

J. P. Franc

J. M. Michel

Laboratoire des Ecoulements Géophysiques et Industriels, Institut de Mécanique de Grenoble, 38041 Grenoble cédex, France

The results of an experimental work concerning the behavior of flows with partial cavities are presented. The tests were carried out using a plano-convex foil placed in the free surface channel of the I.M.G. Hydrodynamic Tunnel. The experimental conditions concerning ambient pressure, water velocity, and body size were such that various and realistic kinds of flows could be realized. The main flow regimes are described and correlated to the values of foil incidence and cavitation parameter. Attention is paid to the shedding of large vapor pockets into the cavity wake and its possible periodic character. Aside from classical consideration to the cavity length and shedding frequency in the periodic regime, results concerning the wall pressure distribution in the rear part of the cavity are given. They lead to distinguish thin, stable, and closed cavities from the thick ones in which the reentrant jet plays a dominant role for the shedding of vortical structures and the flow unsteadiness.

1 Introduction

From a number of years the cavitating flow regime has become more and more accepted in hydraulic manufacturing, for example for first stage inducers of pumps used either in common industrial situation or in more advanced technology. Such an evolution in the industrial viewpoint involves that cavitation is taken in account from the first stage of the machine design. In particular, it requires that cavitating flows can be modeled in order to make possible the performance prediction for machines at off-design points together with the estimate of cavitation erosion risk. That requirement is still far from being fulfilled at the present time. For example, it is known (Furuya, 1980; Yamaguchi and Kato, 1983; Ito, 1986; Lemonnier and Rowe, 1988) that modeling of partial, steady cavities is not simple: due to the inverse character of the flow representation in the vicinity of the cavity and its wake, several numerical solutions can be built inside the framework of potential theory, each one depending on the particular boundary conditions which are adopted in that region. An additional difficulty arises from the open or closed character of the cavity wake which results in variations of the drag coefficient. Thus, in the simple case of two-dimensional flow around a partially cavitating hydrofoil, it happens that the prediction of global parameters such as cavity length and forces coefficients, given the wall geometry and the cavitation number, is not always possible. As regards the risk of erosion, only little is known on the flow agressivity and its link with the mean flow regime.

We present here the results of an experimental study (Le Q.,1989) intended to increase the available information on the basic two-dimensional partially cavitating flows which can be encountered on most blades of hydraulic rotating machinery. The present paper is concerned with the global behavior and the mean aspects of the flow, especially in the cavity closure region, while the results of pressure peak measurements are the subject of a second paper in the same issue of the Journal. It is believed that such results can be used as a guide for the choice of a flow model and the estimate of damage potential.

Partial cavities are described with some details in the textbook by Knapp et al. (1970) which emphasizes the cyclic regime with shedding of large vapor structures at the rear of the cavity. The same viewpoint is adopted by Lush and Peters (1982) for cavities attached at the throat of a converging-diverging duct. For those authors, the shedding is due to the development of an instability at the cavity interface, whereas for Furness and Hutton (1975) the leading mechanism is reentrant jet. A detailed study of large vapor structures shedding, using laser anemometry and conditional sampling, was presented by Kubota et al. (1987). The same technique was used by Avellan and Dupont (1988) in order to describe the velocity field in the vicinity of rather short and stable partial cavities at high Reynolds number. Nguyen The (1986) established that measurements of wall mean pressure in the case of cavitating flows were feasible with ordinary devices; he gave a detailed description of the cyclic regime and found an almost constant value for the Strouhal number based on the cavity length.

In the present work, we classify the different cavitating regimes which appear at the upper side of a plane-convex hydrofoil according to the values of both cavitation number and angle of attack. Special attention is paid to the following topics: cavity length, shedding frequency, and mean pressure profile at the rear of the cavity. The Reynolds number is between 1 and 2.4 million so that the configuration is expected to be significant for most industrial situations.

2 Experimental Setup

The Hydrodynamic Tunnel is described by Briançon-Marjollet and Michel (1990). The foil was placed in the second test section (depth 40 cm, width 12 cm) at a submersion depth of 20 cm under the free surface. Its upper side is plane and its

[1]Now at the National Polytechnic Institute, Hanoi, Vietnam.

Contributed by the Fluids Engineering Division for publication in the JOURNAL OF FLUIDS ENGINEERING. Manuscript received by the Fluids Engineering Division December 15, 1991. Associate Technical Editor: M. L. Billet.

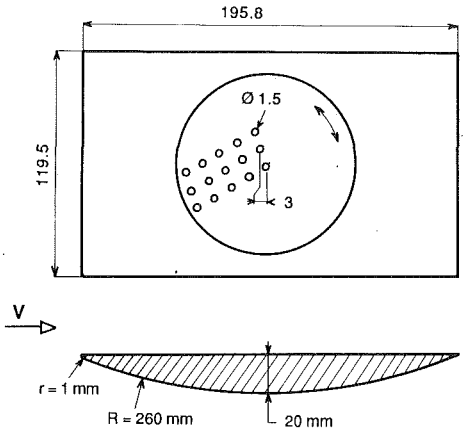

Fig. 1

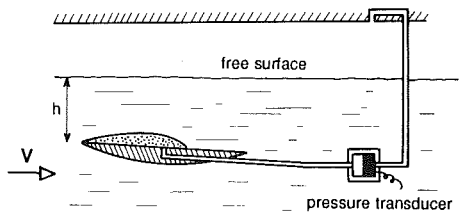

Fig. 2

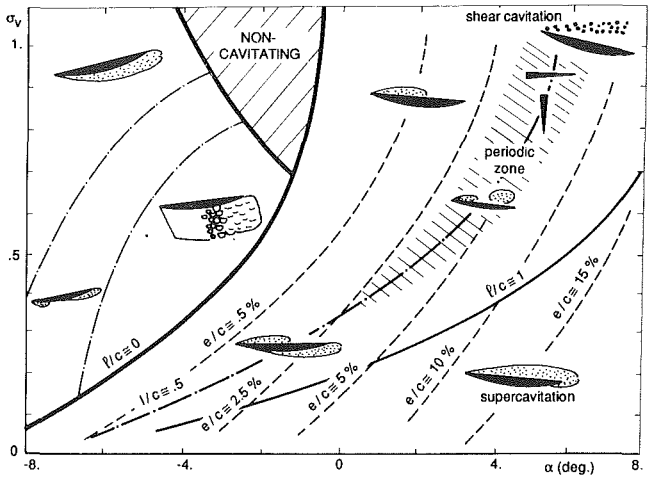

Fig. 3 Main cavitation patterns at Re = 2 × 10^6

lower side circular (radius 26 cm) with a maximum thickness of 2 cm. The leading edge is rounded with a radius of 1 mm so that the chord is about 196 mm. A circular plate on which pressure holes or pressure transducers are implanted can be rotated at the foil upper side (Fig. 1). It allows us to make measurements in the region of the cavity closure at abscissae between 54 and 138 mm as counted from the leading edge.

Most of the tests were made with water velocities of 5 and 10 m/s to which correspond Reynolds numbers of about 10^6 and 2.10^6, respectively. The value of the cavitation number σ_v could be then established in the range 0.05–1.3. Partial cavities on the foil upper side were obtained by varying the angle of attack between −6 and +8 deg. As seen on Fig. 3, developed cavities were also present near the trailing edge at the foil lower side. They could be accompanied by transient explosive bubbles: the rough foil shape results in pressure coefficients of about −1 which are sufficient to activate air nuclei with critical pressure lower than −20,000 Pa. In the present paper however the main interest is focused to upper side cavities. Measuring the local mean pressure along the cavity closure region is not an obvious task. After some attempts it appeared that the classical method using pressure holes (1.5 mm in diameter) can be adopted if holes are followed by short pipes and a chamber where static pressure is measured by a pressure transducer (see Fig. 2), even though some bubbles are present into the tubes. The errors resulting from differences in the water column height can be reduced to a negligible value if all the measuring line is placed at the same altitude. That was systematically checked by injecting a small amount of air in the measuring line: the transducer output signal did not show any appreciable variation when water or air were present in the pipe.

Then the measurements can be repeated without any appreciable variation. Fifteen holes were drilled on the rotating plate at abscissae differing by 3 mm in order to obtain the pressure profiles.

3 Global Behavior of Partial Cavities

3.1 Cavitation Patterns. Figure 3 shows the main cavitation patterns with reference to the values of the incidence α and the cavitation number σ_v, the Reynolds number Re being close to 2.10^6 (for other values of Re, the results are not significantly modified). The domain of interest is between the curves $l = 0$ and $l = c$ (l is the cavity length at the foil upper side as measured under natural light, c is the chord). Those curves are relative to incipient cavitation and supercavitation, respectively. The curves of equal relative cavity thickness e/c are also shown. The shedding of large vapor structures corresponds to e/l greater than 0.05 approximately. On the contrary, periodical shedding is limited to the shaded area. Thus it is visible that shedding is not necessarily cyclic. On Fig. 3, the direction of increasing frequency for variable incidence or variable pressure is indicated by two narrow triangles: as expected, the frequency decreases when l is increased.

When varying both parameters α and σ_v we can keep l constant and observe the subsequent variations of the thickness e: such variations can be seen on Fig. 4 for l = 72 mm or l/c = 0.37.

3.2 Cavity Length. The relation between the cavity length and the cavitation number, either for partial or super cavities, is presented in Fig. 5.

For cavities with shedding of vapor structures, the maximum length is concerned. In the region of large cavity lengths, above 70 to 100 mm, the slope of curves is large, particularly for the small σ_v: then large variations of the flow geometry are com-

Nomenclature

c = foil chord
e = cavity thickness
f = shedding frequency
h = foil submersion depth
l = cavity length
p_0 = pressure at the channel free surface
p_v = vapor pressure
U = channel water velocity
α = foil incidence
μ = water viscosity
ρ = water density
Re = $\rho cU/\mu$: Reynolds number
σ_v = $2[p_0 + \rho gh - p_v]/\rho U^2$: cavitation parameter
C_p = $2[p - (p_0 + \rho gh)]/\rho U^2$: pressure coefficient

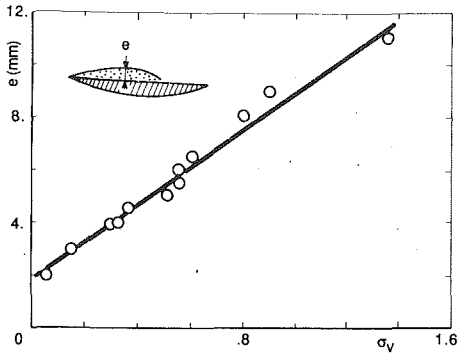

Fig. 4 Cavity thickness versus cavitation number ($l \cong 72$ mm)

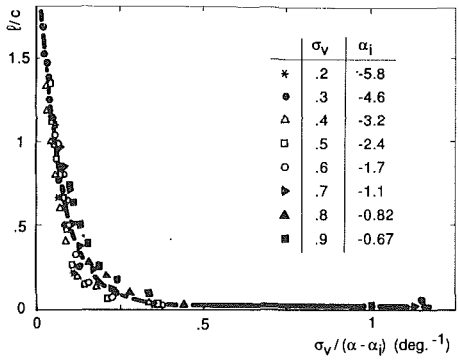

Fig. 6 Cavity length versus nondimensional parameter $\sigma_v/(\alpha - \alpha_i)$

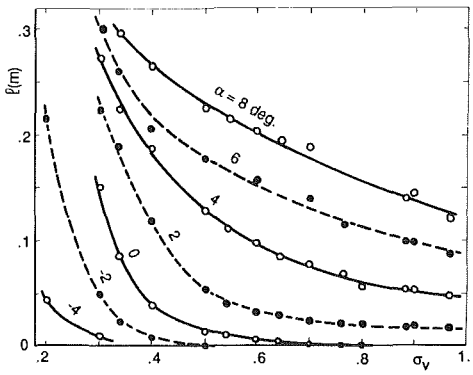

Fig. 5 Cavity length versus cavitation number

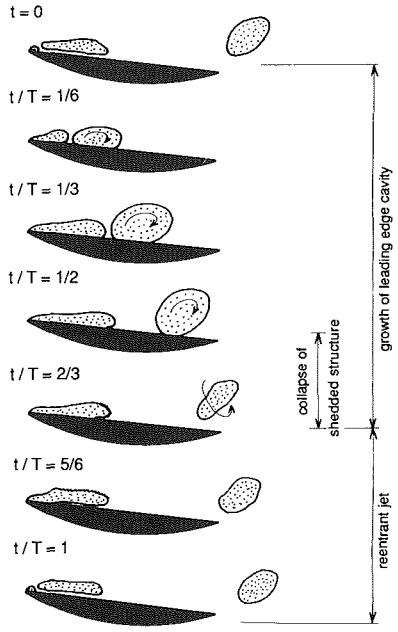

Fig. 7 Periodic shedding mechanism

patible with small changes in the pressure gradient. That fact is favorable to appearance of flow unsteadiness.

All the experimental points collapse well enough around a unique curve (see Fig. 6) if l/c is represented versus the nondimensional parameter: $\sigma_v/[\alpha - \alpha_i(\sigma_v)]$, where $\alpha_i(\sigma_v)$ corresponds to the curve $l = 0$ in FIg. 3. Recall the parameter σ_v/α is introduced by the linearized theory which considers that for a slender body the cavitation number is proportional to the angle of attack at a constant cavity length. Here the incidence is corrected by its value at cavitation inception.

Experimental results concerning the relation between the cavity length and the relative cavity under pressure are currently used to support model results. It must be noted here that the parameter $H\sigma_v$ does not always represent the correct value of the cavity under pressure. Thus results of Figs. 5 and 6 have to be used with consideration to the parameter $\Delta\sigma$ which will be introduced in Fig. 13.

3.3 Periodic Shedding. By means of high speed films the kinematics of shedding over a period can be observed (Fig. 7). In the most regular cases, the attached cavity grows during about two thirds of the period while the vapor pocket released at the initial instant near the leading edge is conveyed downstream. It explodes firstly as described by Kubota et al. (1987), and then collapses at time $t = 2T/3$. At this instant the reentrant jet starts to flow upwards. An important point is that the new vapor structure is shed into the wake at the instant when the reentrant jet reaches the vicinity of the leading edge.

Indeed, as the cavity inside cannot be seen, the existence of reentrant jet is not obvious. In a first step it was inferred from perturbations of the cavity surface travelling against the main flow at a speed almost equal to U with $U = 10$ m/s, i.e., at a relative velocity not far from 20 m/s: such a value cannot be easily understood unless motion of subjacent material particles is called for. In a second step, water colored with fluorescein was injected into the cavity through a pressure hole at the abscissa $x = 84$ mm, the maximum cavity length being 90 mm and the incidence 4, 5 deg.

Then it became clear that cyclic reentrant jet was present since colored water could be seen near the leading edge at some instants of the period and only around the vapor pocket shed into the wake at other instants.

The Strouhal number $S = fl/U$, where f is the shedding frequency measured under stoboscopic light, is found to be almost constant, its value turning around 0.28, as shown on Fig. 8. That fact tends to confirm the role of the reentrant jet in the shedding of vapor structures. Let βU the reentrant jet velocity and $l/\beta U$ the time required to cover the cavity length. This time is approximately equal to T/3 (see Fig. 7) so that we can estimate the S-value by $S = \beta/3$ which gives 0.3 for $\beta = 0.9$. In general the β-value decreases with the cavity thickness and for the thinner cavities the reentrant jet does no longer reach the leading edge: both effects contribute to keep nearly constant the Strouhal number.

Potential flows of inviscid fluids with free surfaces exhibit reentrant jet as a typical feature (e.g., Efros, 1946, Gilbarg and Serrin, 1950). More, as discussed by Benjamin and Ellis (1966), the reentrant jet, when reaching an opposite free surface, results in the formation of a doubly connected liquid domain which makes possible the appearance of new circulation. Thus, reentrant jet contributes to the shedding of circulation into the cavity wake together with other mechanisms

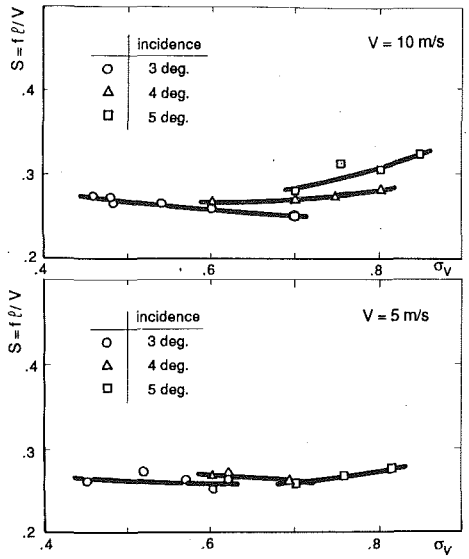

Fig. 8 Strouhal number versus cavitation number

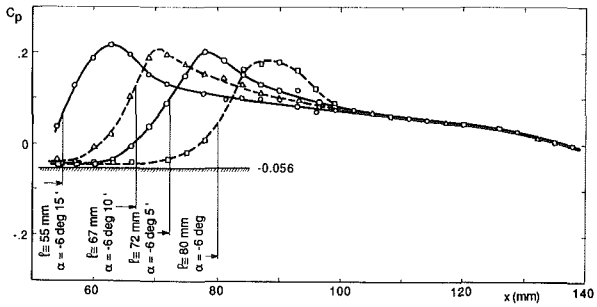

Fig. 9 Pressure coefficient distribution for σ_v = 0.056 and V = 10 m/s

related to the actual viscous behavior of the liquid (Franc and Michel, 1985; Avellan and Dupont, 1988). That contribution can be easily estimated: as shown in Fig. 7, when a vapor pocket is shed downstream, it rolls as a vortical structure and ultimately is transformed in a rough horseshoe vortex before collapsing. The circulation around each vapor pocket is estimated as $\gamma(\sqrt{1+\sigma_v} + \beta)\, l\, U$ where γl is the part of the cavity length covered by the reentrant jet. Thus the production rate of circulation is approximately $\gamma(\sqrt{1+\sigma_v} + \beta)SU^2$. The coefficient of U^2 is about 0.6 for the thick partial cavities having a well formed reentrant jet; it becomes smaller when the cavity is thinner.

The case of large vapor pockets shed without any periodicity was observed but not studied in a detailed way. There is no phase regulator in that case but reentrant jet probably is still responsible of pocket shedding. If this conjecture is correct, the characteristic time of shedding can still be estimated by an expression such as $\gamma l/\beta U$.

3.4 Mean Pressure in the Cavity Closure Region. Figures 9, 10, and 11 show the pressure distributions which are obtained for three values of the cavitation number, respectively, .056, .55, and .81. In each case the different cavity lengths correspond to varying angles of attack. An overpressure is seen near the cavity end for the smallest value of σ_v. It disappears progressively when σ_v increases. Roughly speaking, the overpressure corresponds to the thin, stable cavities while cavities with large vapor pockets shedding don't present the pressure maximum. Both kinds of cavities can be called closed and open, respectively. The disappearance of the overpressure can be attributed either to the motion of the cavity closure or to pure unsteady effects.

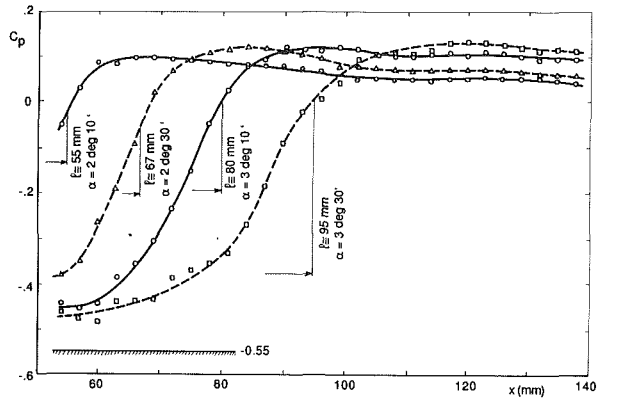

Fig. 10 Pressure coefficient distribution for σ_v = 0.55 and V = 10 m/s

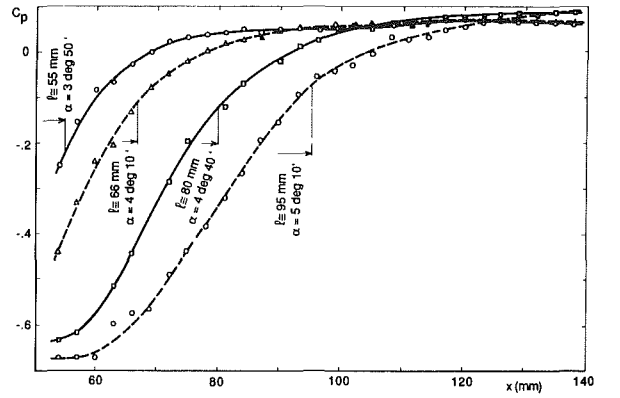

Fig. 11 Pressure coefficient distribution for σ_v = 0.81 and V = 10 m/s

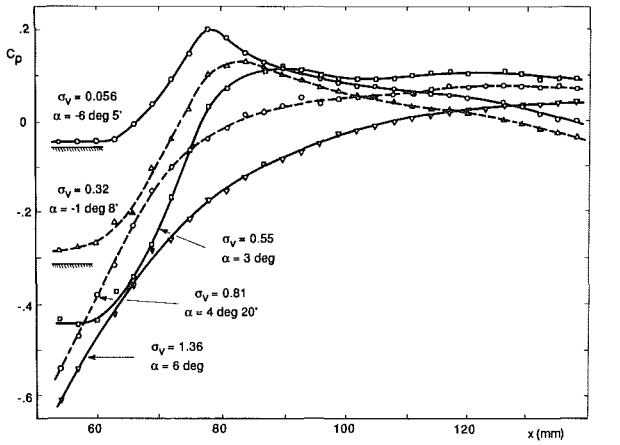

Fig. 12 Influence of partial cavitation pattern on pressure coefficient distribution at constant cavity length ($l \cong$ 72 mm)

The evolution of the pressure distribution when σ_v changes, the cavity length keeping the same value 72 mm, is shown on Fig. 12. For σ_v = 1.36, it is more cavitation in the separated shear layer than a true cavity, but the pressure distribution seems to be in continuity with other cases: the cavity oscillation, with emission of vaporous vortical structures, finally leads to the structure of open recirculation zone.

In Figs. 9 to 12, we can observe firstly that the pressure coefficient is not always constant in the region corresponding to the cavity. Secondly, when it is constant, its value *Cpc* is not necessarily equal to the expected value $-\sigma_v$, the difference becoming larger for the open cavities. That is due to the presence of water in front of the pressure hole at some instants of

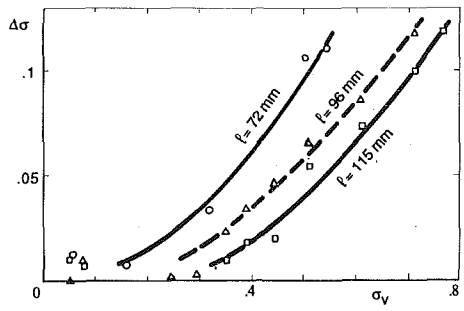

Fig. 13 Variation of difference $\Delta\sigma$ versus σ_v

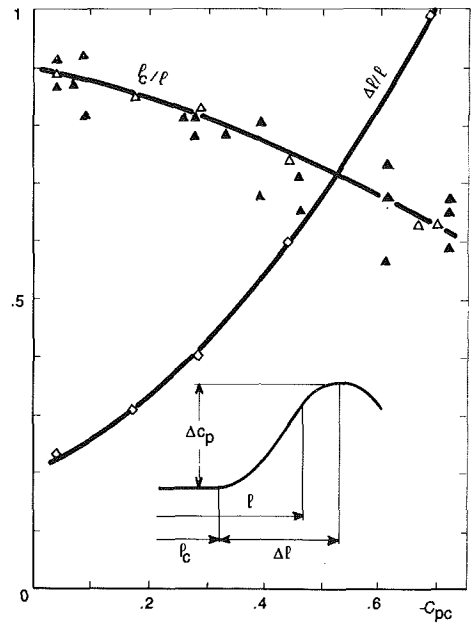

Fig. 14 Variation of ratios $|c/l$ and $\Delta l/l|$ versus $-C_{pc}$

the cycle. Then, in order to describe more precisely the cavity and its wake, it becomes useful to consider the following quantities:

- lc, the length corresponding to a constant value of the pressure coefficient
- Δl, the difference between the abscissa of the maximum pressure coefficient and lc
- $\Delta\sigma$, the difference $Cpc + \sigma_v$
- ΔCp, the difference between the maximum value of Cp in the near wake of the cavity and Cpc

Figure 13 shows the variations of $\Delta\sigma$ versus the cavitation number σ_v for several values of the cavity length. The difference $\Delta\sigma$ can reach the value 0.2.

In Fig. 14 are presented the ratios lc/l and $\Delta l/l$ versus $|Cpc|$. The first ratio decreases and the second one increases as $|Cpc|$ becomes larger, i.e., the cavity becomes more and more open. At the same time, the difference ΔCp also increases as shown in Fig. 15, although the pressure maximum is removed far from the cavity closure.

4 Concluding Remarks

The closed or open character of the cavity end, which is particularly visible on pressure distributions, seems to be connected to the behavior of the reentrant jet and thus to the cavity thickness. In case of thick cavities, the jet can go against the main flow over a significant part of the cavity length and

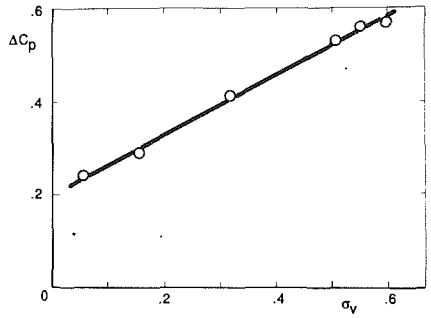

Fig. 15 Variation of difference ΔC_p versus σ_v (l = 72 mm – V = 10 m/s)

contribute to the detachment of a large vapor pocket. Contrarily, this counterflow is not possible in case of thin cavities firstly because the jet momentum is very small and secondly because the space available for its motion is narrow: friction between adjacent layers prevents a large development of the jet. This one is confined to a small region near the cavity closure and flow unsteadiness does not spread far from there.

The reentrant jet is associated to the production of vorticity: in case of periodic cavities, the shedding rate of circulation by that mechanism can be estimated.

From the viewpoint of modeling, the closed or open cavities correspond to different boundary conditions (Lemonnier and Rowe, 1988; Favre, 1988; Yamaguchi and Kato, 1989). It is known that closed models give rise to a maximum of the pressure coefficient near the cavity end. For example, such a model was used by the first author (Le, 1989) in order to adjust some model free parameters with reference to the experimental values of Δl and ΔCp. More generally, the present results tend to restrict the field of application of closed models to steady flow around stable, thin cavities whereas a model taking the flow unsteadiness in account will be more appropriate for open cavities.

Uncertainties

The errors on the parameters V, α, σ_v, p_0, Re, which define the experimental conditions, can be considered small. For example, $\Delta\alpha$ = .1 deg, ΔV = .03 m/s, $\Delta V/V$ = .3 percent for V = 10 m/s. Taking the error on the pressure in account, we find $\Delta\sigma_v/\sigma_v$ of the order one percent.

The precision on frequency is good also (error less than 1 percent) when the periodic regime is well established. For other parameters (cavity lengths l and lc, cavity thickness e, pressure coefficient C_p), the errors depend on the cavitating regimes: smaller for closed, stable cavities, larger for open cavities. The range of uncertainties is then between 2 and 10 percent.

References

Avellan, F., and Dupont, P., 1988, "Etude du sillage d'une poche de cavitation partielle se développant sur un profil hydraulique bi-dimensionnel," La Houille Blanche, No. 7/8, pp. 507–515.

Briançon-Marjollet, L., and Michel, J. M., 1990, "The Hydrodynamic Tunnel of I.M.G.: Former and Recent Equipments," ASME JOURNAL OF FLUIDS ENGINEERING, Vol. 113, No. 3, pp. 338–342.

Benjamin, T. B., and Ellis, A. T., 1966, "The Collapse of Cavitation Bubbles and the Pressures Produced Against Solid Boundaries," *Phil. Trans. Royal Soc.* (London), Series A 260, pp. 221–240.

Efros, D., 1946, "Hydrodynamical Theory of Two-Dimensional Flow with Cavitation," C. R. Ac. Sc. URSS, Vol. LI, No. 4, pp. 267–270.

Favre, N., 1988, "Résolution du problème inverse par petites perturbations d'un écoulement potentiel incompressible," *Thése, EPFL1010, Lausanne*, June 1988.

Franc, J. P., and Michel, J. M., 1985, "Attached Cavitation and the Boundary Layer: Experimental Investigation and Numerical Treatment," *Journal of Fluid Mechanics*, Vol. 154, pp. 63–90.

Furness, R. A., and Hutton, S. P., 1975, "Experimental and Theoretical

Studies of Two-Dimensional Fixed-Type Cavities," ASME JOURNAL OF FLUIDS ENGINEERING, Vol. 97, No. 4, pp. 515–522.

Furuya, O., 1980, "Non-Linear Theory for Partially Cavitating Cascade Flows," *IAHR 10th Symp.*, Tokyo, *Proceedings*, pp. 221–241.

Gilbarg, D., and Serrin, J., 1950, "Free Boundaries and Jets in the Theory of Cavitation," *Journal of Mathematics and Physics*, Vol. 29, pp. 1–12.

Golden, D. W., 1975, "A Numerical Method for Two-Dimensional Cavitating Flow," MIT Dept. of Ocean Eng., Rep. No. 81512-1.

Ito, J., 1986, "Calculation of Partially Cavitating Thick Hydrofoil and Examination of a Flow Model at Cavity Termination," *International Symposium on Cavitation*, Sendai, *Proceedings*, pp. 209–214.

Knapp, R. T., Daily, J. N., and Hammitt, F. G., 1970, Cavitation, McGraw-Hill, New York.

Kubota, S., Kato, H., Yamaguchi, H., and Maeda, M., 1987, "Unsteady Structure Measurement of Cloud Cavitation on a Foil Section Using Conditional Sampling Technique," *International Symposium on Cavitation Research Facilities and Techniques*, Boston, Dec. 1987, Proc., pp. 161–168.

Le, Q., 1989, "Etude Physique du Comportement des Poches de Cavitation Partielle," Thesis, INPG, Grenoble, Sept.

Lemonnier, H., and Rowe, A., 1988, "Another Approach in Modelling Cavitating Flows," *Journal of Fluid Mechanics*, Vol. 195, Oct., pp. 557–580.

Lush, P. A., and Peters, P. I., 1982, "Visualisation of the Cavitating Flow in a Venturi-Type Duct using High Speed Cine Photography," *International Association for Hydraulic Research Symposium*, Amsterdam, Sept., *Proceedings*, Vol. 1, No. 5.

Nguyen, The M., 1986, "Fermetures de Poches de Cavitation Partielle: Cinematique—Pressions à la Paroi," These, Grenoble, Oct.

Yamaguchi, H., and Kato, H., 1983, "On Application of Non Linear Cavity Flow Theory to Thick Foil Section," IME, 2nd Conference on Cavitation, Edinburgh, Sept., *Proceedings*, pp. 167–174.

Partial Cavities: Pressure Pulse Distribution Around Cavity Closure[1]

Q. Le[2]

J. P. Franc

J. M. Michel

Institut de Mécanique de Grenoble,
38041 Grenoble, Cedex, France

Pressure pulse height spectra (PPHS) are measured in the case of partial cavitation attached to the leading edge of a hydrofoil. It is shown that the distributions of pressure pulses around cavity closure may significantly differ according to the type of cavity. In the case of a thin, well-closed and stable cavity, the pressure pulse distributions exhibit a strong maximum centered on the visible cavity termination. As the cavity becomes thicker and increasingly open and unsteady, the pressure pulse distribution widens. In the limit case of a cavity periodically shedding bubble clusters, no definite maximum in the pressure pulse distribution is observed. In addition, scaling of pressure pulse height spectra is approached from measurements at two different velocities. It is shown that the pressure pulse height spectra can be correctly transposed from a velocity to another one from two basic scaling rules concerning pulse heights and production rates of bubbles.

1 Introduction

A cavitating flow produces generally a large number of vapor structures as bubbles or small-scale hollow vortices that are convected downstream. When they reach high pressure zones, they collapse and can cause erosion to the solid walls. If close enough to the wall, the collapsing structures induce pressure pulses on its surface. Then the erosion capability of the whole cavitating flow can be characterized by a pressure pulse height spectrum (PPHS). PPHS is defined at any location on the wall and generally differs from a location to another one.

PPHS can be considered as a measure of the aggressiveness of a cavitating flow; it is purely hydrodynamic characteristic if the interaction between the fluid and the material (or the transducer sensitive part) can be neglected. This interaction is measured by the ratio of the acoustic impedances $(\rho c)_{\text{liquid}}/(\rho c)_{\text{solid}}$. In the case of water and stainless steel, it is smaller than 4 percent: the backward motion of the wall under the action of a pressure impact does not damp significantly the liquid overpressure and so does not alter PPHS. This difficulty on principle will appear of minor importance with respect to other measuring difficulties which will be discussed later on.

Once the erosion capability of a cavitating flow has been determined, the problem is to estimate the damage (in terms of pitting rate, mass loss . . .) caused on the material by the given PPHS. The simplest approach consists in characterizing the material by a threshold (see for instance Hammitt, 1979 or Lecoffre et al., 1985): the collapse of a vapor structure produces a permanent pit only if the height of the associated pressure pulse exceeds the material threshold. More sophisticated models taking into account mechanical and metallurgical properties of the material can be used (Karimi and Léo, 1987; Franc et al., 1991).

The experimental determination of PPHS raises a few basic difficulties. First, the pressure transducer must have a very high natural frequency to reproduce as reliably as possible the sudden rise in pressure of duration of a few μs or less. If not, the signal height is underestimated. Second, the sensitive surface must be very small and in theory smaller than the size of the impacted area, to avoid once more an underestimation of the pulse height. If not, the measured pressure is actually the equivalent mean pressure which would give the same output if it were uniformly applied to the whole sensitive surface. A simple way to get a first estimate of the actual pulse height is to consider a pulse height amplification factor equal to the ratio of the sensitive surface area to the mean area of erosion pits. Such an estimation is presented in Section 4. Finally, the transducer must obviously be sufficiently resistant not to be damaged.

Though all these requirements cannot always be fulfilled, several investigators carried out measurements of PPHS and interesting results have been obtained. De and Hammitt (1982) measured PPHS in a cavitating venturi in order to correlate the acoustic power derived from PPHS with the cavitation damage rate. Fry (1989) developed an analogue pulse height analyzer to investigate PPHS on two cavitation sources: a wedge and a circular cylinder. Fry shows that it is possible to find a height threshold where the noise ratio for the two sources matches their erosion ratio. Iwai et al. (1991) used PPHS measurements to explain the progression of the erosion in a vibratory device.

[1]This paper is the revised version of a paper contributed at the 3rd Int. Symp. on Cavitation Noise and Erosion in Fluid Systems, ASME Winter Annual meeting, San Francisco, Ca, Dec. 10-15, 1989.

[2]Now at the National Polytechnic Institute, Hanoï, Vietnam.

Contributed by the Fluids Engineering Division for publication in the JOURNAL OF FLUIDS ENGINEERING. Manuscript received by the Fluids Engineering Division December 15, 1991. Associate Technical Editor: M. L. Billet.

The present study is devoted to the measurement of PPHS in the case of a partial cavity attached to the leading edge of a foil for which we know that there is generally a maximum of erosion in the cavity closure region. The flow configuration is described in another paper (Le et al., 1992) in the same issue of the Journal which presents in detail the different cavity patterns and the corresponding mean pressure distributions. In the present paper, we analyze how PPHS changes along the hydrofoil in relation to the global behavior of the cavity. In addition, the problem of scaling PPHS is approached from measurements at two different velocities.

2 Experimental Conditions

The experimental setup has been described by Le et al. (1992). The tests were carried out in the hydrodynamic tunnel of the "Institute of Mechanics of Grenoble" (France) on the foil section presented in Fig. 1. The flat upperside was chosen for an easy mounting of the pressure transducers. Nine identical pressure transducers were mounted. They are held on a circular plate which can be rotated to change the location of the measuring points. In particular, all transducers can be set at the same abscissa in order to compare their response and proceed to an in-situ relative calibration (see Section 3).

The transducers are made of piezoelectric ceramic disks whose main characteristics are:

—thickness: 1 mm
—diameter: 0.9 mm
—natural frequency: 1.7 MHz
—sensitivity: 20 V/MPa.

The sensitivity and natural frequency given above are relative to the primary ceramic without its protecting coating. A complementary calibration is needed to determine the actual sensitivity of the final transducer[3].

The signal processing consists in transforming the pressure pulses into square pulses whose height is equal to the maximum height of the pressure pulse and whose duration can be adjusted from 1 to 20 μs. It is chosen so that further oscillations of the signal which are not due to a collapse but to unwanted internal oscillations do not trigger a false pulse. Then an adjustable threshold is imposed before counting. The counting time was generally chosen equal to 100 seconds.

3 Dynamic Calibration

A dynamic calibration suitable to the analysis of cavitation pressure pulses needs to be carried out on a calibrated pressure solicitation of low rise time and high amplitude comparable with the ones due to the collapse of a bubble, say a few hundred of MPa for a time of the order of the microsecond. At the present time, we are developing a special calibration device which should allow to get near these orders of magnitude, but it is not yet available. The only dynamic calibration which was carried out for the present study was relative to low frequencies (< 1 kHz) and low amplitudes (see Nguyen The et al., 1987). It gave a sensitivity from 0.5 to 1.5 V/MPa, slightly variable from one transducer to another one. The value of 1 V/MPa can be used as an order of magnitude to convert Volts into MPa. We must be fully aware that such a procedure leads to a very crude estimate of pressure pulse amplitudes. Though actual amplitudes are of great importance for a further prediction of cavitation erosion, it is not the central part of this paper which is devoted to a relative comparison of histograms.

[3]At the present time, we use piezoelectric films to build pressure transducers.

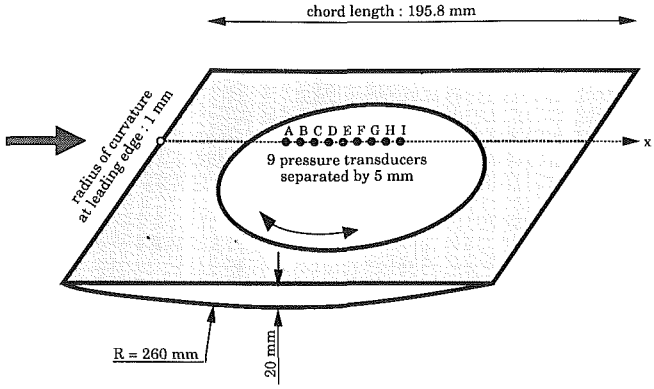

Fig. 1 Sketch of the foil

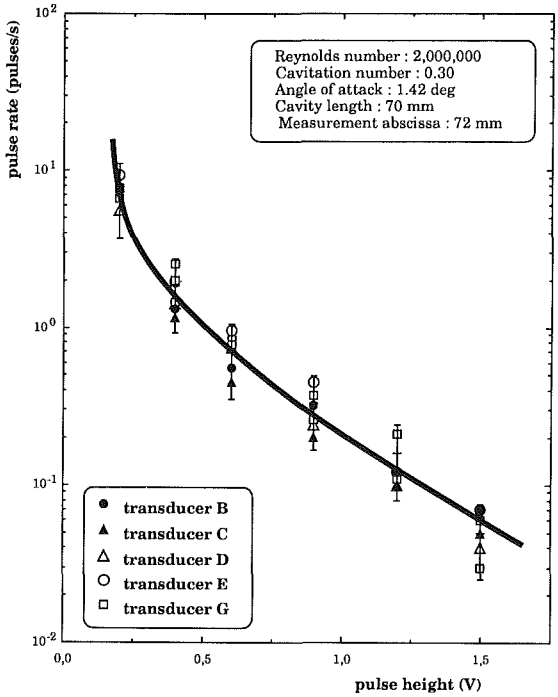

Fig. 2 In-situ relative calibration of 5 pressure transducers

In view of the difficulties to make an accurate absolute dynamic calibration at high frequency and high amplitude, we decided to make an in-situ relative dynamic calibration. This is realized by turning the circular plate (see Fig. 1) so that the nine pressure transducers are at the same abscissa. For this configuration and for given test conditions (angle of attack, velocity and cavitation number), a PPHS is measured by each transducer. *The comparison of the different PPHS allowed us to compare the responses of the different transducers. This operation was performed under various test conditions. A typical example is given in Fig. 2.* It corresponds to five pressure

Nomenclature

c = density of vapor structures (structures/cm^3)
f = shedding frequency (Hz)
H = pulse height
l = cavity length
N = pulse rate (pulses/s)
$\dot{n}$ = pulse rate per unit surface area (pulses/mm^2/s)
α = angle of attack (deg)
σ_v = cavitation parameter
V = flow velocity

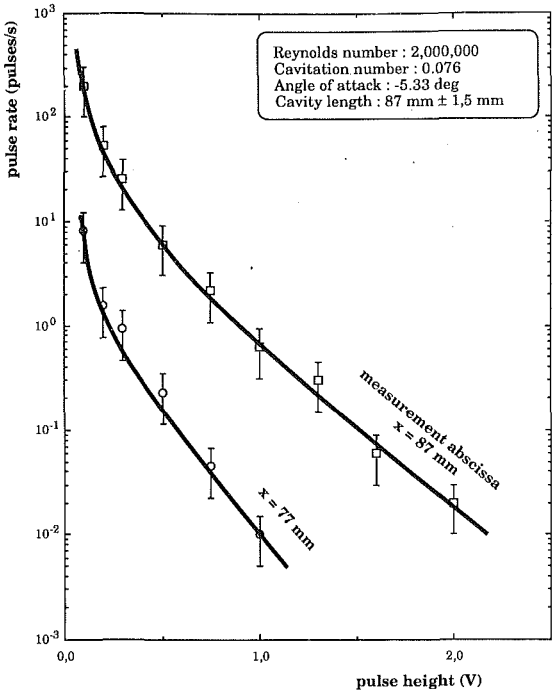

Fig. 3 Pressure pulse height spectra at different abscissa (cavitation number: 0.076)

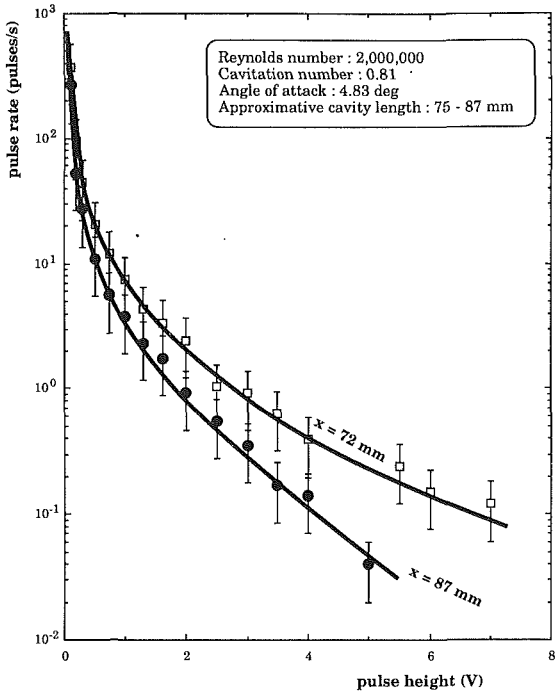

Fig. 5 Pressure pulse height spectra at different abscissa (cavitation number: 0.81)

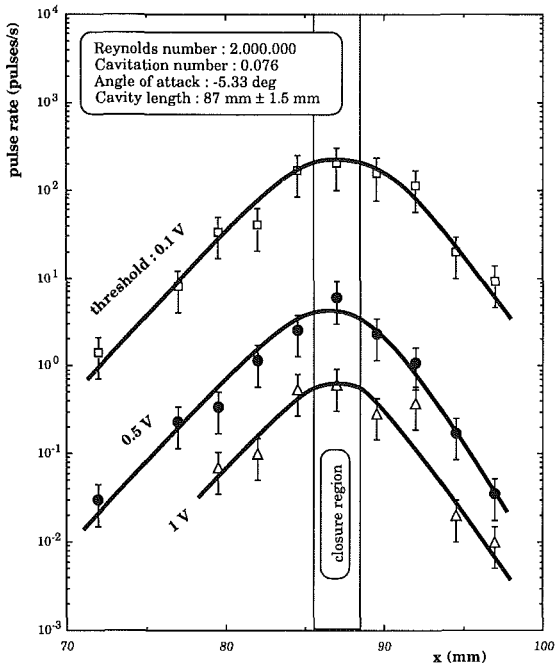

Fig. 4 Pressure pulse distribution around cavity closure for different height thresholds

transducers over the nine which are mounted. We observe that the five accumulative spectra can be superimposed with a good enough precision so that we can suppose that all pressure transducers have the same response. The differences which are observed from a transducer to another one may be due to differences in sensitivity but also to a possible default in bidimensionality even if the cavity globally looks very bidimensional. It results from all the in-situ relative calibrations which were performed that PPHS are known within a maximum uncertainty of the order of ±50 percent. As spectra generally extend over 4 decades (or even more), this uncertainty in logarithmic coordinates represents only 12 percent (or less) of the total measuring scale.

4 Pressure Pulse Distribution

Pulse rates given in the present paper correspond to the total number of pulses recorded on the 0.64 mm^2 sensitive surface area of the transducers; PPHS refer here to accumulative data i.e., the ordinate corresponds to the frequency of pulses whose height is greater than a variable threshold given in abscissca.

We present here measurements of PPHS for different operating conditions corresponding to different types of partial cavities. Figures 3 and 4 are relative to a low value of the cavitation number (σ_v = 0.076) for which the leading edge cavity is thin, well-closed and very stable; the cavity termination fluctuates only on about 3 mm. Figure 5 presents PPHS in the case of a cavity which periodically sheds large clouds of vapor structures (σ_v = 0.81).

When comparing PPHS of Figs. 3 and 5, it clearly appears that cloud cavitation is much more aggressive than a stable cavity, even at its termination which is the point of maximum aggressiveness. First, pressure pulse heights are much higher; for σ_v = 0.81, the maximum measured pulse height is 7 V whereas it is only 2 V for σ_v = 0.076. Secondly, pulse rates are also higher; at given amplitudes of 1 V and 2 V, we counted, respectively:

—for σ_v = 0.076: 0.62 and 0.02 pulses/s.
—for σ_v = 0.81: 7.51 and 2.43 pulses/s.

There is a ratio of 12 and 120, respectively, in pulse rates between the case of cloud cavitation and the case of a stable cavity. Our measurements confirm the well-known fact that, from an erosion view point, cloud cavitation is much more severe than a stable cavity. Moreover, they show that PPHS can be considered as a quantitative measure of the erosion capability of a cavitating flow.

To go further into the quantification of aggressiveness, it is necessary to convert the values of pulse height in pressure units. If we suppose that pressure pulses result from an impact on a surface of mean characteristic size of the order of 100 μm

(see for instance Belahadji et al., 1991), the amplification factor due to the difference between the transducer sensitive area and the impacted area is 81. If, in addition we consider a sensitivity coefficient of the order of 1V/MPa as it results from preliminary calibration, pulse heights of 2V and 7V would correspond to pressure amplitudes of 160 MPa and 560 MPa. These values have to be compared to the elastic and rupture limits of the 316 L stainless steel presently used which are respectively 500 MPa and 650 MPa. These very rough estimates are in agreement with the fact that no erosion is observed on the foil at the velocity of 10 m/s considered here. However, the maximum overpressure in the case of cloud cavitation appears close to the material limits; then it can be conjectured that a moderate increase in aggressiveness (due to an increase in velocity or in some cases to unsteadiness) could cause pitting of the foil. Actually, pitting has been observed in the case of an oscillating stainless-steel hydrofoil whereas the flow velocity never exceeded 8 m/s (Franc and Michel, 1988). Then the present estimates of pressure pulse amplitudes seem reasonable with respect to our own experience. Nevertheless, they have to be considered with care as the method of conversion of pulse height into pressure amplitude (including calibration) needs further developments. It is one of our objectives.

In the case of a very steady cavity termination (i.e., at low cavitation number), pulse rate is maximum at cavity closure. Whereas the maximum in the mean pressure distribution occurs somewhat downstream of the observed point of cavity closure (see Le et al., 1992, Fig. 9), the maximum in pulse rate distribution is exactly centered on this point. The width of the pressure pulse distribution is greater than the apparent width of the region in which the cavity termination fluctuates. In particular, pulses have been recorded upstream the cavity termination point, in a zone which is always covered by the cavity. Downstream, pulses are due to the collapse of vapor structures which are not visible to the naked eye.

The influence of the cavitation number on the pressure pulse distribution is shown in Fig. 6. The cavity length is kept constant which needs to increase the angle of attack when the cavitation number is increased. *By cavity length we mean the maximum length of the cavity estimated visually under stroboscopic lighting.* It appears firstly that the distribution is widening as the cavitation number increases. This is due to a more and more unstable cavity closure which tends to widen the distribution of bubbles and then of pressure pulses. For the highest value of the cavitation number ($\sigma_v = 0.59$), no definite maximum in the pressure pulse distribution can be noticed in the measuring zone. In that case, the cavity is very unsteady and sheds periodically cavitating vortical structures. The cavity length oscillates between a maximum length of about 87 mm and a minimum length of about 30 mm. Unsteadiness appears to be the main factor of extension of the region of bubble collapse.

Second, it appears on Fig. 6 that the pulse rate increases with σ_v which depicts an increase in the concentration of bubbles. This is coherent with visualizations which show that the whole cavity becomes more and more bubbly as the cavitation number is increased.

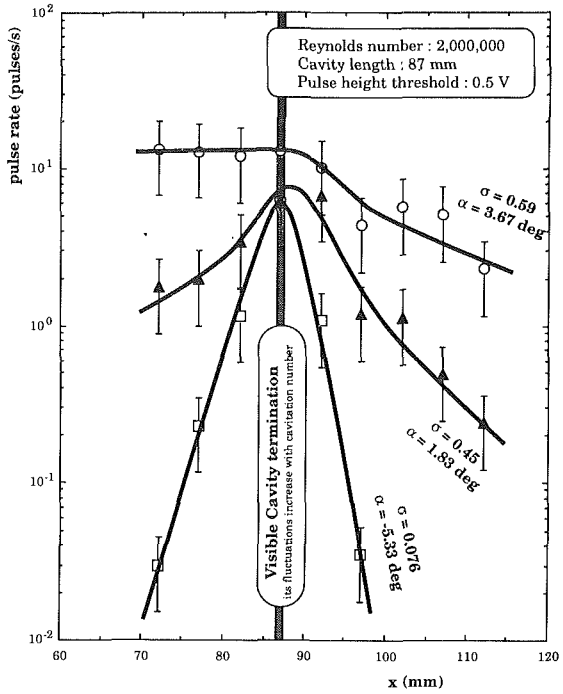

Fig. 6 Influence of partial cavity pattern on pressure pulse distribution at constant cavity length

5 Similarity Law for PPHS

The aim of the present section is to study how PPHS are scaled with a change of velocity. It requires one to know jointly how pulse heights are changed and how the production rate of bubbles varies. To approach this problem, PPHS were measured at two different velocities (5 m/s and 10 m/s). From such measurements, we cannot directly answer the double question of scaling pulse height and production rate. But we can easily check if spectra are correctly scaled when two distinct hypothesis on pulse heights and production rates are made.

If the velocity is doubled, we have checked (Le et al., 1992) that the shedding frequency of large vapor structures is approximately doubled according to the classical similarity law. Concerning the much smaller structures as bubbles or microscale cavitating vortices which are responsible of the measured pressure pulses, we shall assume, following Lecoffre et al. (1985), that the Strouhal similarity law still applies to their production rate. In other words, we suppose that for both velocities, each large structure breaks up into the same number of small bubbles. Then our first assumption consists in considering that the production rate of bubbles is proportional to the velocity.

Concerning pulse heights, it is generally assumed that the impact pressure results from a shock wave mechanism. Then the impact pressure is given by a water-hammer type formula $\rho c V_j$ where ρc is the acoustic impedance of the fluid and V_j the velocity of the fluid/vapor interface. In a first approach, considering a nondimensional form of the Rayleigh-Plesset equation in which surface tension and air content are neglected, it can be assumed that the interface velocity V_j in the final stage of collapse is proportional to the characteristic flow velocity V in so far as the cavitation parameter is kept constant. Hence, the pulse heights are themselves proportional to the velocity. This is our second hypothesis.

In consideration of these two assumptions, we can easily deduce how PPHS are affected by a change of velocity. If the velocity is multiplied by a factor k, pulse heights as well as pulse rates are multiplied by the same factor k; so, if $\dot{N}_V(H)$ is the rate of pulses whose height is greater than H at velocity V, we have:

$$\dot{N}_{kV}(kH) = k\dot{N}_v(H)$$

Figures 7 and 8 present for two different values of the cavitation number the measured PPHS at 5 m/s and 10 m/s as well as the estimated PPHS at 10 m/s obtained from the measured ones at 5 m/s by means of the above scaling formula. Although the transposition is not perfect, transposed PPHS appear to be a correct estimate of the actual PPHS in both cases.

Finally, we try to estimate the density of vapor structures in a cloud from the present results for the case of a periodic

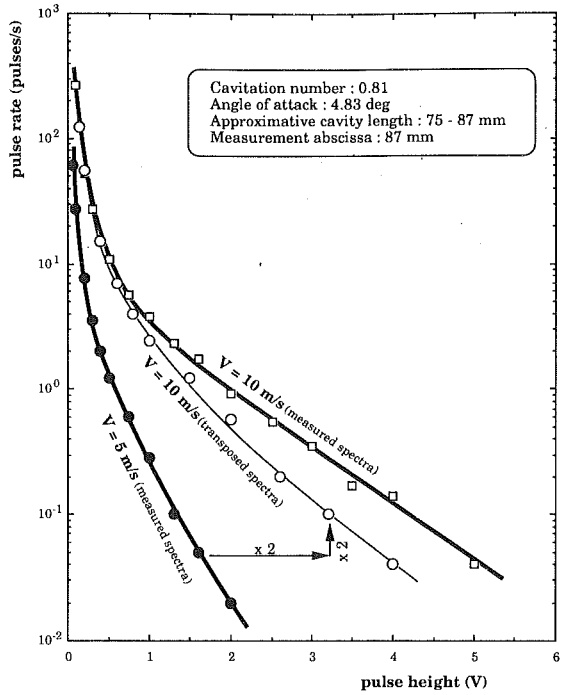

Fig. 7 Similarity law for cumulative pressure pulse height spectra (cavitation number: 0.81)

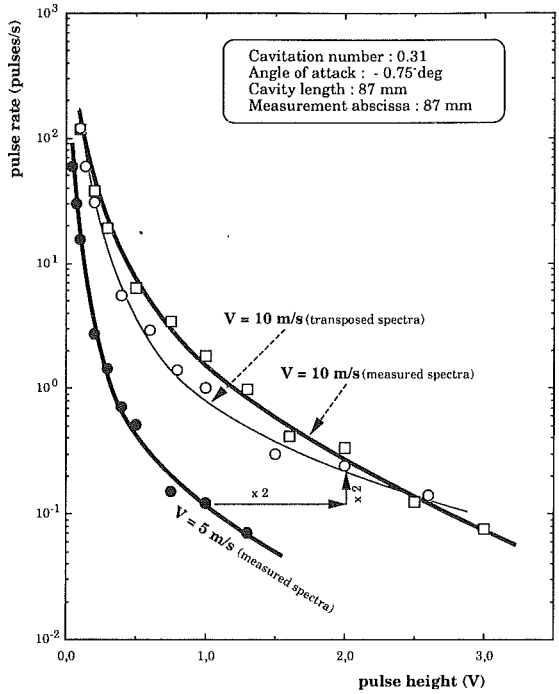

Fig. 8 Similarity law for cumulative pressure pulse height spectra (cavitation number: 0.31)

behavior characterized by the shedding frequency f. According to our global analysis of the periodic shedding mechanism (Le et al., 1992), the volume of cavity which is shed during a unit time and for a unit span is $l.e.f(\mathrm{m}^3/\mathrm{m}/\mathrm{s})$, where l and e are, respectively, the length and the thickness of the cavity. The total number of pressure pulses measured on the surface covered by the cavity[4] is $\dot{n}.l$ (pulses/m/s), where $\dot{n}$ is the pulse rate per unit surface area. The ratio of the number of pulses to the cavity volume leads to the following density:

$$c = \frac{\dot{n}}{ef}$$

In the case $\sigma_v = 0.59$, $V = 10$ m/s, we have:

$\dot{n}_{(H>0.1\mathrm{V})} \cong 380$ pulses/mm^2/s[5]
$\dot{n}_{(H>1\mathrm{V})} \cong 5.2$ pulses/mm^2/s[5]
$e \cong 10$ mm
$f \cong 39.4$ Hz

then:

$c_{(H>0.1\mathrm{V})} \cong 960$ structures/cm^3
$c_{(H>1\mathrm{V})} \cong 13$ structures/cm^3

These values can be compared to direct measurements of bubble density. Yamaguchi, et al. (1990) measured the bubble density (excluding cavitating vortices) by a laser holographic system. The bubble concentration depends strongly upon the size and the type of cavitation considered. For unstable sheet cavitation shedding clouds ($\sigma = 1.50$) which is typically the type of cavitation considered here, they counted 121 bubbles with a diameter greater than 70 μm in the measuring volume of 3.1 cm^3. The bubble density is then of the order of 39 bubbles/cm^3. Although no definite conclusion can be drawn at present from the comparison of direct measurements of bubble density with estimations obtained from wall measurements of pulse rates, a few basic question can be raised.

In particular, what is the ratio of bubbles in a cloud which actually give a pulse on the wall when they collapse? In other words, in comparison with the cavity thickness for instance, what is the characteristic thickness of the layer which contains the bubbles collapsing on the wall as opposed to the ones collapsing in the bulk? It probably depends upon the cut-off pulse height; the smaller it is, the more bubbles away from the wall are concerned.

6 Conclusion

This paper presents measurements of pressure pulse height spectra for different patterns of partial cavitation. The following summarizes the important conclusions.

1. PPHS appears to be an appropriate way to characterize the hydrodynamic aggressiveness of a cavitating flow. In particular, measured PPHS show that, from an erosion viewpoint, cloud cavitation is much more severe than a thin, well-closed and stable sheet cavity: maximum pulse heights are higher as well as pulse rates.
2. In the case of a well-closed sheet cavity, a strong maximum exists in the pressure pulse distribution, whatever the pulse height threshold may be. It is centered on the cavity closure determined visually. As the cavitation number is increased at constant cavity length, the partial cavity is progressively opening and becoming more and more unsteady, and correlatively the pressure pulse distribution is widening. In the case of high values of the cavitation number for which the cavity periodically sheds bubble clusters, no definite maximum in the pressure pulse distribution is observed.
3. Measurements of PPHS at two different velocities allowed us to approach the problem of scaling PPHS. It is shown that PPHS are correctly scaled if we suppose that:
—the production rate of the bubbles which are responsible of pressure pulses is controlled by the Strouhal similarity law;
—the pulse heights are proportional to the flow velocity as it can be expected if the impact pressure results from a shock wave process.

[4]Still during a unit time and for a unit span.
[5]This value is estimated from a mean value on the nine measuring locations.

References

Belahadji, B., Franc, J. P., and Michel, J. M., 1991, "A Statistical Analysis of Cavitation Erosion Pits," ASME JOURNAL OF FLUIDS ENGINEERING, Vol. 113, pp. 700–706.

De, M. K., Hammitt, F. G., 1982, "New Method for Monitoring and Correlating Cavitation Noise to Erosion Capability," ASME JOURNAL OF FLUIDS ENGINEERING, Vol. 104, pp. 434–442.

Franc, J. P., and Michel, J. M., 1988, "Unsteady Attached Cavitation on an Oscillating Hydrofoil," *Journal of Fluid Mechanics*, Vol. 193, pp. 171–189.

Franc, J. P., Michel, J. M., and Karimi, A., 1991, "An Analytical Method for the Prediction of Cavitation Erosion," *Cavitation 91*, Portland, FED Vol. 116, pp. 127–133.

Fry, S. A., 1989, "The Damage Capacity of Cavitating Flow From Pulse Height Analysis," ASME JOURNAL OF FLUIDS ENGINEERING, Vol. 111, pp. 502–509.

Hammitt, F. G., 1979, "Cavitation Erosion: The State of the Art and Predicting Capability," *Applied Mechanics Review*, Vol. 32, No. 6, pp. 665–675.

Iwai, Y., Okada, T., Nashiyan, and Fukuda, Y., 1991, "Formation and Progression of Vibratory Cavitation Erosion," *Cavitation 91*, Portland, FED, Vol. 116, pp. 119–125.

Karimi, A., Leo, W. R., 1987, "Phenomenological Model for Cavitation Erosion Rate Computation," *Materials Science and Engineering*, Vol. 95, pp. 1–14.

Le, Q., 1989, "Etude Physique du Comportement des Poches de Cavitation Partielle," Thesis, INPG, Grenoble, Sept.

Lecoffre, Y., Marcoz, J. Franc, J. P., and Michel, J. M., 1985, "Tentative Procedure for Scaling Cavitation Damage," *Symposium on Cavitation in Hydraulic Structures and Turbomachinery*, Albuquerque, FED Vol. 25, pp. 1–12.

Le, Q., Franc, J. P., and Michel, J. M., 1992, "Partial Cavities: Global Behavior and Mean Pressure Distribution," JOURNAL OF FLUIDS ENGINEERING, Vol. 115, pp. 243–248.

Li, S., Zhang, Y., and Hammitt, F. G., 1986, "Characteristics of Cavitation Bubble Collapse Pulses, Associated Pressure Fluctuations and Flow Noise," *Journal of Hydraulic Research*, Vol. 24, No. 2, pp. 109–122.

Nguyen The M., Franc, J. P., and Michel, J. M., 1987, "On Correlating Pitting Rate and Pressure Peak Measurements in Cavitating Flows," *International Symposium on Cavitation Research Facilities and Techniques*, Boston, FED Vol. 57, pp. 207–216.

Yamaguchi, H., Kato, H., Kamijo, A., and Maeda, M., 1990, "Development of Laser Holography System for the Measurement of Cavitation Bubble Clusters," *ASME Cavitation and Multiphase Flow Forum.*

The Flow Structure and Statistics of a Passive Mixing Tab

W. J. Gretta
Fluid Systems Engineering, Inc.,
Morristown, NJ 07960

C. R. Smith
Department of Mechanical Engineering
and Mechanics,
Lehigh University,
Bethlehem, PA 18015

Water channel flow visualization and anemometry studies were conducted to examine the flow structure and velocity statistics in the wake of a passive mixing tab designed for enhancement of cross-stream mixing by generation of flow structures characteristic of turbulent boundary layers. Flow visualization reveals that the mixing tab generates a wake comprising a combination of counterrotating, streamwise vortices enveloped by distinct hairpin vortex structures. The counterrotating streamwise vortices are observed to stimulate a strong ejection of fluid along the symmetry plane, which results in very rapid cross-stream mixing. The hairpin vortices are found to undergo successive amalgamation and coalescence downstream of the device, which aids in the streamwise mixing and outward penetration of ejected fluid. After an initially intense mixing process, the mixing tab wake rapidly develops mean velocity, turbulence intensity, and boundary layer integral properties characteristic of a significantly thickened turbulent boundary layer.

1 Introduction

Recent developments in the study of turbulence have indicated that there are coherent, identifiable structures which give rise to the behavior of turbulent boundary layers. One particular structure of turbulence is the hairpin vortex, which takes on many forms, but is basically formed by three-dimensional deformation and roll-up of boundary layer vorticity. Theodorsen (1952) was one of the first researchers to cite the probable presence of hairpin flow structures as a key element in the development and perpetuation of turbulence, arguing for their presence based on his evaluation of the necessary dynamics of turbulence dictated by the vorticity transport equation. Head and Bandyopadhyay (1982), employing detailed evaluations of smoke visualizations of a turbulent boundary layer over a range of Reynolds numbers, came to the conclusion that a turbulent boundary layer is dominated by a "forest" of hairpins whose scales vary directly with the magnitude of the Reynolds number. Perry and Chong (1982) expanded the hairpin concept to suggest that a turbulent boundary layer consists of a hierarchy of hairpin vortices; they demonstrate that such a model can give rise to statistics comparable to those measured experimentally for a turbulent boundary layer. Acarlar and Smith (1987a,b), using detailed flow visualization and velocity measurements of artificially generated hairpin flow structures, demonstrate the remarkable similarity of visualization and velocity patterns for hairpin vortices to comparable turbulent boundary layer patterns. In a follow-on study, Smith and Lu (1989), using pattern recognition techniques applied to quantitative flow visualization, demonstrate the multiple presence of hairpin vortices over a range of scales as significant flow structures within a turbulent boundary layer. More recently, a detailed evaluation of a direct numerical simulation of a turbulent boundary layer by Robinson (1991) has indicated the presence of multiple hairpin-like vortices, most generally asymmetric in shape, which exhibit a distribution of scales and characteristics not unlike the symmetric hairpin models proposed previously. Robinson also indicates that such structures are intimately involved in the significant transport of fluid both to and away from the surface.

A number of investigators have also suggested streamwise vortices embedded within turbulent boundary layers as significant flow structures of boundary layer turbulence (e.g., Smith and Schwartz, 1983; Ersoy and Walker, 1985; Robinson, 1991). As a consequence, single streamwise vortices and corotating and counterrotating pairs have all been examined experimentally to determine the interaction of such vortices with the fluid very near surfaces, and thus their relationship to turbulence production (e.g., Pauley and Eaton, 1982; Smith et al., 1991a,b). It is established that the presence of streamwise vorticity above a surface causes the ejection of wall-region fluid from the surface (Peridier et al., 1991; Smith et al., 1991a,b), as well as inducing movement of free-stream fluid toward the wall. This activity results in the replacement of low-momentum near-wall fluid with higher-momentum free-stream fluid, which increases both local mixing and enhances heat transfer from (or to) the surface.

The cumulative results of these and other studies indicate the potential importance of hairpin and streamwise vortices in the turbulence process, suggesting that the forced synthesis of such vortex flow structures by passive means may be an effective method for initiating mixing enhancement. It is well known that passive vortex generators can be very effective for separation control by "energizing" boundary layers (Stevens and Collins, 1955; Lin and Howard, 1989). The general premise behind vortex generators is that the generation of vortices will have a positive effect on surface mixing, however, the dynamics of such vortex-induced mixing processes and the rationale for successful vortex generator designs is often poorly understood. In fact, in some cases, vortex generator designs have even been

Contributed by the Fluids Engineering Division for publication in the JOURNAL OF FLUIDS ENGINEERING. Manuscript received by the Fluids Engineering Division March 30, 1992. Associate Technical Editor: D. M. Bushnell.

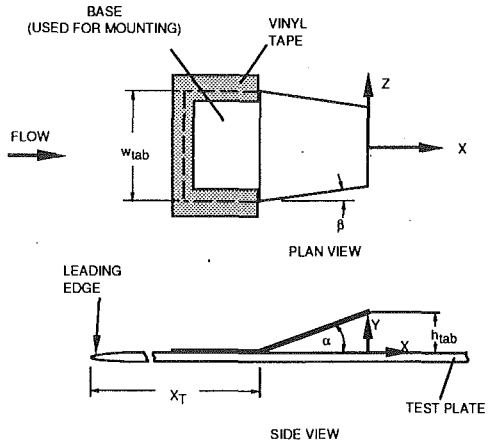

Fig. 1 Schematic of a mixing tab, experimental mounting arrangement, and dimensional parameters

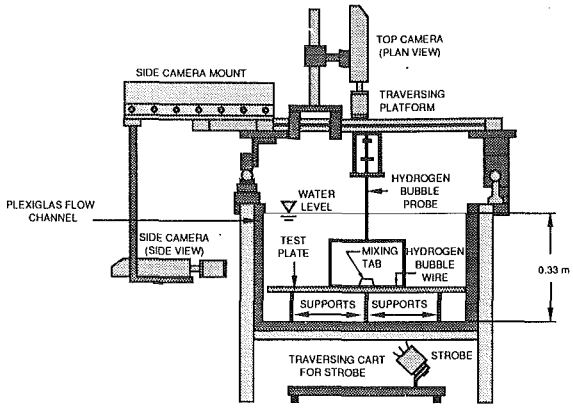

Fig. 2 End-view of water channel equipped with video cameras for hydrogen bubble visualization experiments

shown to be arbitrary in their function—often performing better when their direction was reversed (Lin et al., 1991).

The present study was undertaken to evaluate the flow characteristics of a symmetric, tapered mixing tab[1] illustrated in Fig. 1, which has been shown to be an effective passive surface-mounted mixing tab for enhancement of cross-stream mixing in industrial applications[2] (see Smith et al., 1989, and Fasano, 1991). The intent of the mixing tab is to initiate a turbulent-type flow pattern of hairpin and streamwise vortices at scales in excess of those of a turbulent boundary layer, and thus "force" elevated cross-stream mixing of mass and momentum. The design rationale is that the synthesized vortex structures will elevate the fluctuation-associated transport (i.e., turbulence) levels above those of a natural turbulent boundary layer, or alternatively will create turbulent-like mixing in an otherwise laminar flow regime. Note that in most practical cases the scale of the mixing tab is in excess of the boundary layer thickness, since the intent is to generate mixing in excess of the boundary layer, but such tabs have been shown to operate effectively at scales less than the boundary layer thickness as well [more on the order of a boundary layer trip] (Gretta, 1990).

In the present study, emphasis is placed on understanding the flow structure of the mixing tab wake, and the evolution of the wake structure with downstream distance. This is accomplished using both flow visualization and hot-film anemometry measurements to:

(i) examine the physical behavior of the flow created by the mixing tab;

(ii) evaluate the mechanisms by which the tab-generated flow structures evolve; and

(iii) determine the metamorphosis of measured velocity statistics relative to conventional turbulent boundary layer statistics.

2 Experimental Equipment and Techniques

Experiments were conducted in a free-surface plexiglas water channel at Lehigh University. An end-view of the channel configured for the present study is shown in Fig. 2. The test section of the channel is 5 m long, 0.9 m wide, and the water depth was kept at approximately 0.33 m. The characteristics of the facility have been reported previously (e.g., Acarlar and Smith, 1987a), and has a test-section spanwise uniformity was ±2 percent, with corresponding free-stream turbulence intensity of 0.2 percent.

A plexiglas test plate, 2.44 m long, 1.27 cm thick, with a 5:1 half-ellipse leading edge, was employed as the test surface for the majority of the visualization and anemometry experiments (see Fig. 2). Three lengthwise supports are used to stiffen the plate and elevate it above the channel floor boundary layer.

Hydrogen bubble visualization (Schraub et al., 1965) was used extensively to characterize the flow patterns generated by the mixing devices, employing a 25 μm diameter platinum wire as the cathode and a 6 mm diameter carbon rod as the anode in an electrolytic circuit. By pulsing the current density to the wire using a specially designed power supply, time lines of hydrogen bubbles could generated, as required.

The visualization results were recorded using a high-speed video system providing 120 frames per second with an effective shutter speed of 10 ms (strobe flash duration), which is synchronized with strobe illumination and the hydrogen bubble generator. Viewed results are tape recorded, and can be played back in real time, slow-motion forward or reverse, as well as still-frame sequences. Photographs are obtained from the video screen using a conventional 35 mm camera. A detailed description of the video system is given by Gretta (1990).

As shown in Fig. 2, a traversing overhead platform provides mounting for visualization and velocity probes, as well as plan and side-view video cameras. The video system allows both plan and side views to be viewed simultaneously on the video monitor. Combined end and plan views could be taken as well. To obtain end-views, a mirror angled at 45 deg to the flow was located on the test plate approximately 70 cm downstream of the hydrogen bubble wire, which negated any pressure gradient effects on the flow in the vicinity of the bubble wire. The end-view behavior of the flow was observed and recorded using the side-view camera focused on the angled mirror.

Local velocity characteristics were obtained using a DISA 55D01 constant temperature anemometer utilizing a DISA 55R15 hot-film probe and DISA 55H22 probe support. The probe support was mounted in a DISA 55E40 traversing mechanism, which was attached to the traversing channel platform. The output of the anemometer was fed through an analog-to-digital converter to a personal computer. An in-house data acquisition program was used to acquire and process the data.

Calibration of the hot-film probe was done prior to acquisition of each set of data. The probe was towed at selected velocities through a quiescent channel using the traversing platform motor drive. Ten velocity measurements (2048 points at 0.015 second intervals) spanning a range from 0 to 0.24 m/sec were used to fit a fourth-order voltage-velocity curve. The maximum experimental uncertainties were established using standard techniques (Kline and McClintock, 1953) as ±3 percent for mean velocity, ±4 percent for turbulence intensity, ±5 percent for displacement and momentum thicknesses, and ±0.1 mm for linear dimensions (95 percent confidence level).

[1]Note that we term this device a mixing tab rather than a "vortex" generator," since it provides flow structure more complex than the normal streamwise vortex generators.

[2]Marketed under the tradename "Vortab," patent nos. 4929088 and 4981368.

The mixing tabs employed were fabricated from 2.3 mm thick polycarbonate material which is easily cut or formed, and is transparent such that visualizations could be performed in the immediate vicinity of the device itself. A small portion near the base of the tabs was extended to allow mounting to the test surface using vinyl tape (see Fig. 1). The flow around this attachment portion of the tab was viewed with hydrogen bubble visualization and found to have little or no effect on the approach flow field to the tab.

3 Results and Discussion

The results are presented as follows. First, an overall model of the flow structure, as evaluated from detailed flow visualization studies, is presented and the processes of flow structure development and evolution are outlined. Second, detailed hydrogen bubble visualization results are used to illustrate the formation and evolution of flow structures from a single tab. Third, hot-film anemometry results are presented, illustrating the mean velocity, turbulence intensity, and selected boundary layer parameters generated by the tabs; these statistical characteristics are compared and contrasted with similar statistical behavior for a typical turbulent boundary layer.

Throughout this paper, both vertical and streamwise distances are referenced in terms of nondimensional tab height, h_{tab} (see Fig. 1). The streamwise location of the tab is specified by X_T, which is the distance from the leading edge of the test plate to the base of the tab; distances downstream from the trailing edge, or tip, of the tab are specified by X; vertical distances from the wall are designated by Y. For the present study, the geometry of the tab was fixed as:

$$\alpha = 27 \text{ deg}$$

$$\beta = 10 \text{ deg}$$

$$h_{tab} = 2.92 \text{ cm}$$

$$w_{tab} = 6.35 \text{ cm}$$

In an extended study (Gretta, 1990), the above tab angles were determined to be near the optimal for promoting vertical transport of fluid away from the plate with minimal energy losses. Since the intent of these mixing tabs is to accelerate mixing well in excess of the boundary layer region, the tab height was chosen to correspond to roughly twice the local boundary layer thickness. Companion studies (Gretta, 1990) indicate that the process promoted by the tab is essentially the same whether less than or in excess of the boundary layer height. The height employed is representative, but not necessarily optimal (which depends on the particular application for the tab).

3.1 Flow Structure Model. Using both dye and hydrogen bubble visualization, the mixing tabs were observed to generate an array of relatively coherent structures, as illustrated schematically in Fig. 3. This series of views are simplified schematics of the characteristic flow structures which are observed to form with either a laminar or turbulent upstream boundary layer, although the flow structures are more coherent and more distinct for the laminar boundary layer case.

As shown, the mixing tab initially generates two distinctive types of flow structure. The first of these is a pair of large counter-rotating vortices, similar to the tip vortices from an airfoil. As the flow passes over the tab, the pressure differential between the upper and lower tab surfaces causes fluid to migrate from the high-pressure upper surface toward the low-pressure lower surface, wrapping around the edges of the tabs and initiating a spiraling motion. This spiraling motion develops to each side of the tab, creating counter-rotating vortices which induce a common upflow motion on the plane of symmetry of the tab. This common upflow transports near-wall fluid away from the wall due to a process of viscous-inviscid

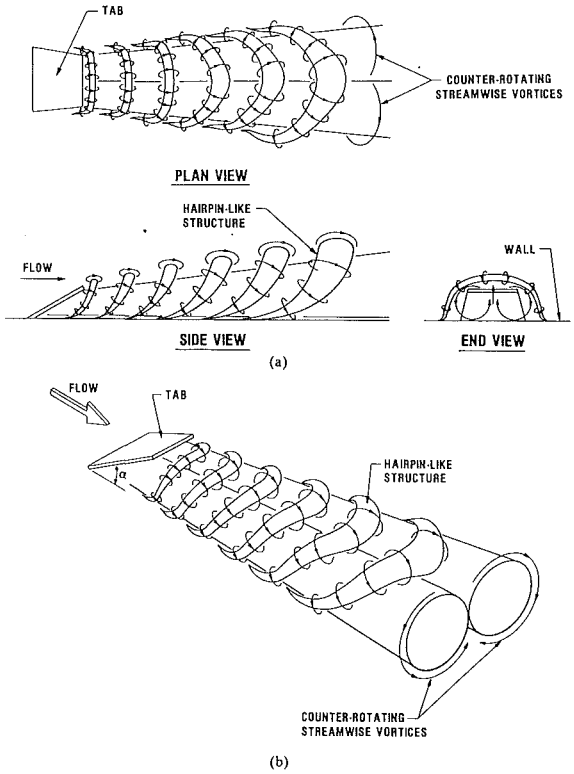

Fig. 3 Development of interacting structures in wake of mixing tab. (*a*) plan, end, and side views (*b*) perspective view.

interaction (Peridier et al., 1991). This is an important aspect of the flow, since this movement is what facilitates the transmission of low-momentum fluid from the wall region into the outer flow, similar to the "eruptive" momentum transport which occurs in a turbulent boundary layer, as discussed by Smith et al. (1991b).

The second observed flow structure is a periodic sequence of hairpin-like vortices, shed from the upper edge of the tab, as illustrated schematically in Fig. 3. The vortex tubes comprising these hairpin structures are a collection of vortex lines which are solenoidal, and must either extend to infinity, end in a closed loop, or as in this case, extend into the wall shear layers. Because the vortex tubes are contiguous, they will stretch and deform, yet still maintain rotation. As these hairpin vortices advect downstream they entrain more and more fluid from the free-stream, which results in an increase in the overall extent of the cumulative wake of the tab. The hairpin-like vortices also interact with the counter-rotating vortices to further enhance fluid transport. The common upward flow region of the counter-rotating vortices pumps fluid toward the hairpin-like vortices, which subsequently entrain the low-momentum fluid and carry it farther away from the surface region. As will be shown in the following section, the hairpin-like vortices evolve with streamwise distance, both by scavenging low-momentum fluid and by coalescence and amalgamation with other hairpin vortices. This amalgamation is observed to be an important element of the overall growth and mixing process.

Note that the shape of the mixing tab, tapering to a flat upper edge, is quite important to the fluid transport process. Systematic examination (Gretta, 1990) of tab geometries ranging from a broader-tip-than-base to a sharp tip (saw-tooth shape), showed that the geometry reported on here produces the optimal ejection of fluid from the surface into the outer region. In particular, the saw-tooth shape performs the most poorly in terms of fluid transport, because of reduced generation of hairpin flow structures, which are spawned in the

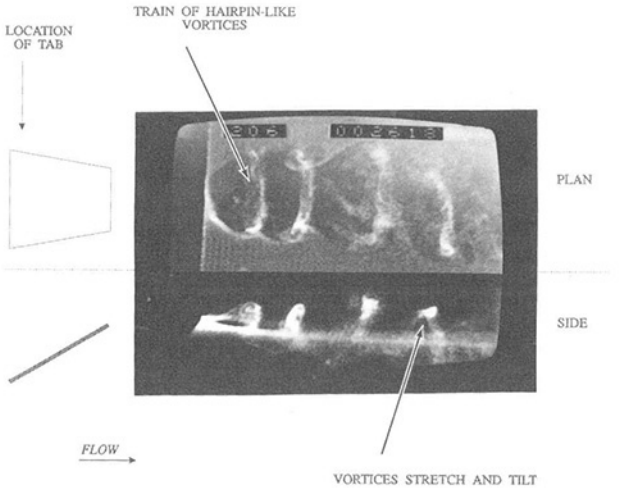

Fig. 4 A combined plan and side-view of hairpin-like vortex generation with bubble wire at $X = 2h_{tab}$, $Y = 1.3h_{tab}$, $U_\infty = 6.8$ cm/s

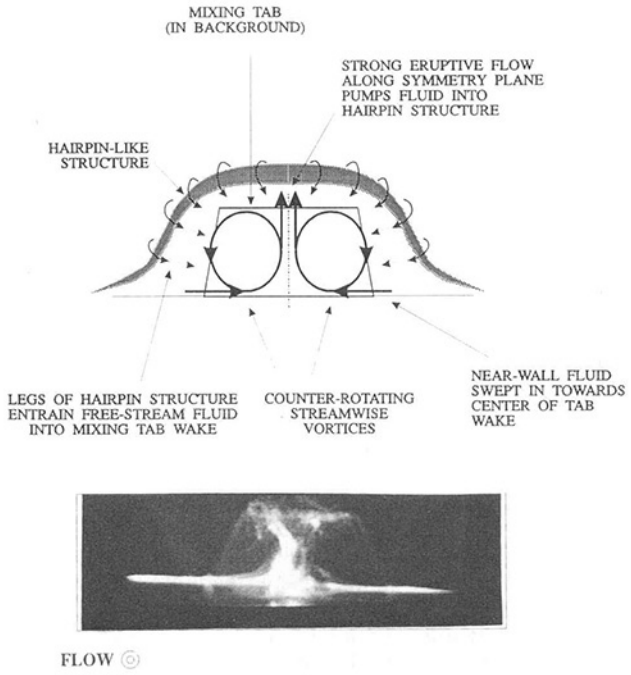

Fig. 5 End-view schematic of fluid movement in wake of mixing tab with accompanying H_2 bubble wire photograph illustrating fluid movement away from surface. Bubble wire at $X = 2h_{tab}$, $Y = 0.3h_{tab}$, and $U_\infty = 6.8$ cm/s

cross-stream shear layer generated at the tab upper edge. Note that the presence of these hairpin-type flow structures has proven important in the function of other effective vortex generating-type devices, such as the Wheeler vortex generator reported by Lin et al. (1991) [see their Fig. 5].

3.2 Visualization Results To establish the flow structure model outlined above, plan, end, and side-views using both horizontal and vertical hydrogen bubble wires were used to closely examine the flow behavior for a mixing tab mounted on the centerline of the test plate at $X_T = 70.5$ cm. A laminar approach flow to the tab was used, with a free-stream velocity of $U_\infty = 6.8$ cm/s, which gave a Reynolds number at the tab location of $Re_\delta = 1100$; all sequences shown are for a single tab. The pictures shown are the best visualized representations of the behavior, which were observed to be generic over a range of Reynolds numbers.

Figure 4 shows a combined plan and side-view hydrogen bubble flow visualization of the flow structure downstream of a tab. A horizontal bubble wire was positioned so that the hairpin-like vortices could be clearly observed as they were shed from the tab; as shown, these initial flow structures are quite coherent. Note that the legs of the hairpin-like structure are only partially visualized in the plan-view portion of the picture, but were observed to be important to the entrainment of free-stream fluid into the wake of tab.

Figure 5 illustrates the pumping action of the streamwise vortices in the wake of the tab, shown both schematically and in an end-view photograph of a hydrogen bubble visualization with a horizontal wire. The bubble wire was positioned at $X = 2h_{tab}$, a distance downstream of the tab where the common upflow motion is quite strong, and at $Y = 0.3h_{tab}$ above the surface. The "bright" region in the end view illustrates the outward penetration of low-velocity, bubble-marked fluid from the surface. As fluid moves away from the surface, it will either be entrained into the rotation of the hairpin-like vortices or will continue to spiral in the longitudinal vortices. The ejection of fluid on the symmetry plane is balanced by a strong lateral motion of fluid adjacent to the plate, the fluid moving bisymmetrically inward toward a low pressure region[3] on the symmetry plane of the tab wake.

In the tab wake, the legs of the hairpin-like vortices aid in inducing flow into the counterrotating vortices. The counter-rotating and hairpin-like vortices appear to form separately, but continuously interact as they move downstream. The counterrotating vortices help transport low-momentum fluid from the wall into the outer region of the boundary layer. This low-momentum fluid, in turn, is entrained into the hairpin-like vortices.

Figure 6 shows three side-view scenes, taken on the symmetry plane using a vertical hydrogen bubble wire, which illustrate stages in the streamwise development of the tab wake. Note that the approximate position of the wire relative to the tab is indicated in the caption. Figure 6(*a*) illustrates the heads of the hairpin-like structures as they just begin to form and coalesce. The rapid coalescence of these hairpin flow structures facilitates both the growth in scale and the vertical penetration of the tab wake into the outer flow. Perry and Chong (1982) suggest that wall turbulence is comprised of hierarchies of interacting "young" and "old" hairpins, and that hairpins "pair" or coalesce with other adjacent hairpins as they translate in the streamwise direction, which facilitates streamwise growth of the boundary layer. In the present study, as the tab wake moves downstream, this coalescence of vortex structures was clearly visible, and is evidenced by the growth of scales and vertical extent of the tab wake (Figs. 6(*a*) and (*b*)), similar to the Perry and Chong model. By $X/h_{tab} \approx 10$ [Fig. 6(*c*)], the flow has lost most of the observable "coherence" seen in Fig. 6(*a*) and begins to appear turbulent[4].

3.3 Velocity Measurements. Velocity behavior downstream of the mixing tabs was established using a spanwise array of five tabs (see Fig. 7) to assure that the central flow would be effectively free of end effects. The tabs were spaced the equivalent of the tab base width apart, a spacing which was shown to be the optimal spacing for wake penetration into the outer flow (Gretta, 1990).[5] The studies reported here were conducted using a laminar approach flow at $U_\infty = 12$ cm/s, yielding a Reynolds number at the base of the tab of $Re_\delta = 1700$ ($\delta \approx 1.5$ cm). Profiles of mean velocity and turbulence

[3] A result of the lateral pressure gradient imposed by the counter-rotating vortices.

[4] A video tape illustrating the evolution of the flow structure in the wake of the tab is available on request from the authors.

[5] Where the effects of tab geometry, spacing, and turbulent approach flow on tab wake penetration and growth are reported.

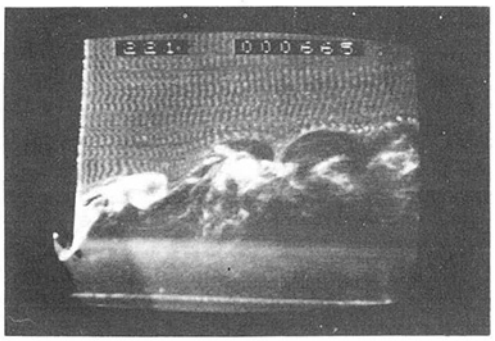

(a)

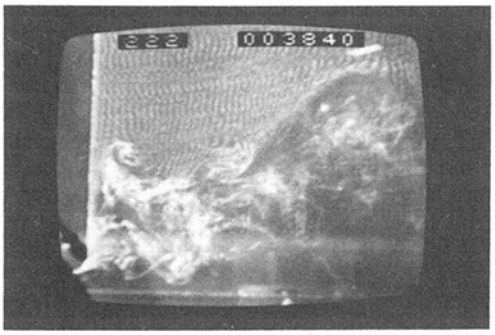

(b)

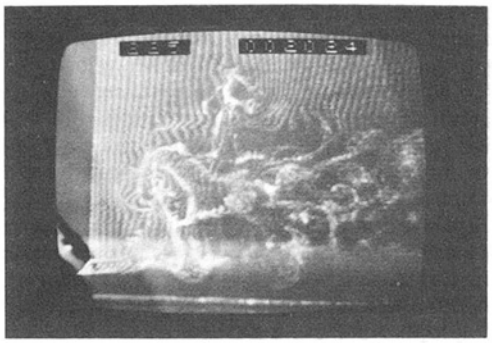

(c)

Fig. 6 Side-view visualization sequence showing growth of tab wake. U_∞ = 6.8 cm/s. (*a*) $X = 2h_{tab}$; hairpin-like vortices shed from tip of tab. (*b*) $X = 4h_{tab}$; hairpin-like vortices amalgamate in streamwise direction. (*c*) $X = 10h_{tab}$; evolution to chaotic turbulent boundary layer behavior.

intensity, and displacement and momentum thicknesses, were established for selected downstream locations; a comparison is also made with measured turbulent boundary layer characteristics.

Mean Velocity Profile Characteristics. Figure 8 shows a series of three spanwise velocity distributions (spanning the three central tabs) for $Y = 0.4h_{tab}$ at three different streamwise positions. A rather good symmetry is demonstrated for each profile, indicating that the tabs produce symmetric, repeatable behavior. For the $X = 2h_{tab}$ case, the minima in velocity occur in line with the center of each of the three tab wakes, and are flanked by corresponding maxima, indicating a strong cross-stream gradient. These minima are the mansifestation of the upward motion of low-speed fluid (from the surface) on the symmetry plane of the tab wake.

Figure 8 also illustrates a rapid equilibration and smoothing of the velocity profile with increased streamwise distance from

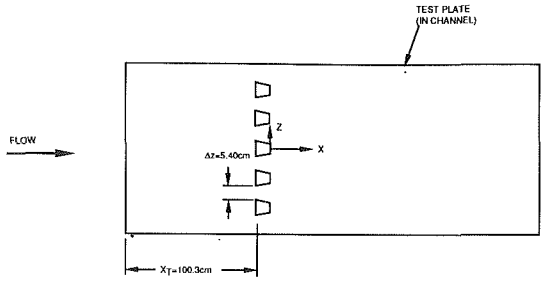

Fig. 7 Plan-view of array of tabs used for hot-film anemometry studies

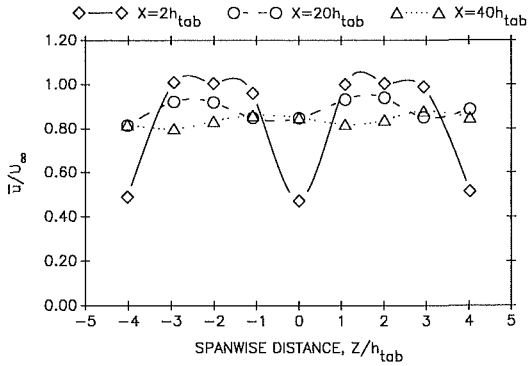

Fig. 8 Spanwise velocity profiles for three tabs at $Y = 0.4h_{tab}$

the tab. By $X = 20h_{tab}$, the spanwise profile still displays a regular spanwise variation, but of much smaller amplitude. This suggests that the initial flow structures stimulate a rapid spanwise dispersion of momentum via initially intense mixing, yielding a more uniform profile. By $X = 40h_{tab}$, the spanwise velocity profile approaches near uniformity, suggesting that the flow structures have essentially mixed out and dissipated, and that cross-stream equilibrium has been basically achieved.

Figure 9(*a*) shows velocity and turbulence intensity profiles measured at four streamwise locations along the tab centerline ($Z = 0$). In each figure the abscissa gives the vertical distance from the surface in terms of a local Reynolds number:

$$\mathrm{Re}_y = U_\infty y/\nu$$

For the $X = 2h_{tab}$ case, the velocity profiles reveal two distinct regions of velocity minimum and maximum. At $\mathrm{Re}_y \approx 3500$ a relative minimum is apparent, which corresponds to the general location of the observed heads of the tab-generated hairpin vortices. Due to rapid dispersion of vorticity by vortex interaction and viscous diffusion, the strong deficit in the velocity profile moves away from the surface and eventually flattens, with the profile asymptoting toward a turbulent-like boundary layer profile.

Figure 10 compares the velocity profiles taken at $X = 40h_{tab}$, both on the tab centerline and between two tabs ($Z = -2h_{tab}$), with a low Reynolds number turbulent boundary layer profile generated on the channel floor.[6] Note that $\mathrm{Re}_\theta = 866$ at the tab centerline position ($Z = 0$), $\mathrm{Re}_\theta = 505$ between tabs ($Z = 2h_{tab}$), and $\mathrm{Re}_\theta = 859$ for the turbulent boundary layer generated on the channel floor. Note also that all the velocity profiles shown in Fig. 10 demonstrate logarithmic behavior and match closely at higher values of Re_y, suggesting that the flow structures generated by the tabs produce turbulent-like velocity profiles within a relatively short distance (40 tab heights). Apparently, the combined action of the hairpin and

[6]By tripping the flow with a 0.64 cm diameter rod at the exit of the converging section; measured 3.33m from the trip rod.

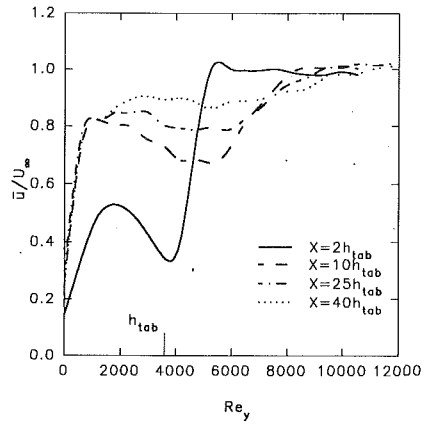

Fig. 9(*a*)

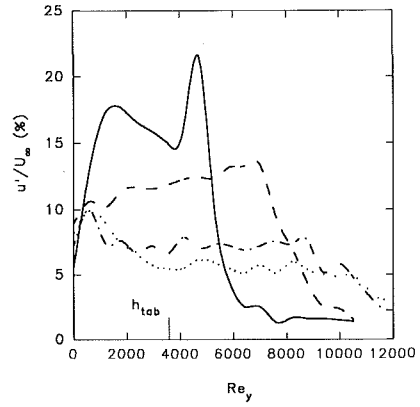

Fig. 9(*b*)

Fig. 9 Tab centerline (Z = 0) mean velocity (*a*) and turbulence intensity (*b*) profiles

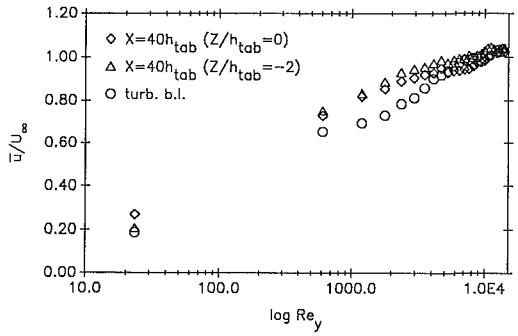

Fig. 10 Mean velocity profiles for Z/h_{tab} = 0 (tab centerline), Z/h_{tab} = − 2 (between two tabs), and a turbulent boundary layer

counter-rotating streamwise vortices generate a mixing process which leads to the rapid evolution of the initial flow structures into typical turbulent behavior; such a metamorphosis is also supported by the flow visualization results (e.g., Fig. 6).

Turbulence Intensity. Figure 9(*b*) displays turbulence intensity[7] at Z = 0 (tab centerline) for four streamwise locations. This figure indicates that at $X = 2h_{tab}$ the highest intensities occur near the location where the heads of the hairpin-like vortices were observed. Similar to what is observed for the mean velocity profiles, the outward migration and dissipation of the original flow structures is reflected by an outward shift and migration of the peak in turbulence intensity with increasing streamwise distance from the tab. As the wake structures move away from the wall, they entrain fluid and coalesce, therefore growing in extent. As the wake spreads, the flow becomes more uniformly mixed and the vorticity disperses. This is reflected by the initial outward dispersion of turbulence intensity, followed by a general decay in turbulence intensity with increased streamwise distances from the tab, except near the wall.

[7] u'/U_∞, where u' is the rms streamwise velocity fluctuation.

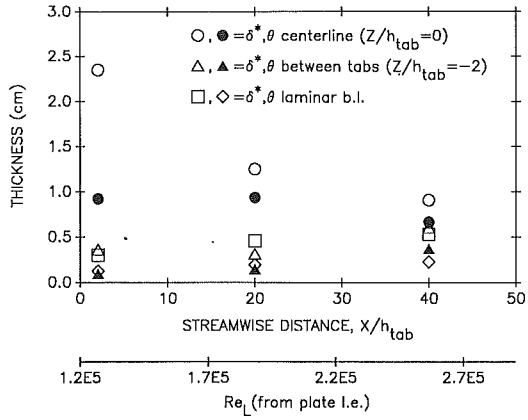

Fig. 11 Displacement thickness, δ^*, and momentum thickness, θ, for Z/h_{tab} = 0 and Z/h_{tab} = − 2

Boundary Layer Parameters. The integral properties of displacement thickness, δ^*, and momentum thickness, θ, were determined using a trapezoidal integration scheme, and are shown in Fig. 11 at both Z = 0 (tab centerline) and $-2h_{tab}$ (between two adjacent tabs).

As shown, the displacement thickness actually decreases in the streamwise direction along the tab centerline (Z = 0). This suggests that there is a transfer of higher-velocity fluid into the flow with increased streamwise distance. Note that at $X = 2h_{tab}$ (just downstream of the separation zone behind the tab), the displacement thickness is large, and slowly *decreases* with streamwise distance, thus "recovering" the fullness of the velocity profile. In contrast, the data for $Z = 2h_{tab}$ (between the tabs) shows a gradual *increase* in δ^* in the streamwise direction, suggesting a loss of higher velocity fluid, probably to the tab wake. This lateral exchange of fluid is further emphasized by the behavior of the momentum thickness, θ, which is directly proportional to the momentum deficit of the boundary layer. As shown in Fig. 11, the momentum thickness on the tab centerline changes very little between $X = 2h_{tab}$ and $X = 20h_{tab}$, and then decreases modestly to $X = 40h_{tab}$. Evidently, the momentum flux deficit along the tab centerline initially remains almost constant, and then decreases slightly with a recovery of higher momentum fluid. This constant momentum thickness is characteristic of a wake flow; the subsequent decrease is the result of higher-momentum fluid from the lateral high-speed regions feeding into the wake-like zone to re-energize it. Between the tabs, the initial momentum deficit is markedly small due to a strong acceleration of the upstream flow through the tab gaps, and due to a downflow of high momentum fluid induced by the streamwise vortices generated by the tab. By $X = 40h_{tab}$ the values of δ^* and θ at the two different spanwise locations have converged significantly, indicating that the flow is approaching spanwise equilibrium, due to spanwise mixing induced by the local flow structure.

Figure 12 shows the boundary layer shape factor, $H = \delta^*/\theta$, for both Z = 0 and $-2h_{tab}$. On the centerline (Z = 0) at $X = 2h_{tab}$, $H \approx 2.4$ which is typical for either a turbulent boundary layer near separation or a laminar boundary layer (Schlichting, 1979). Clearly, this H value indicates that the profile closely approixmates a turbulent boundary layer which is near or has just undergone reattachment. H then decreases to $\approx$ 1.3 at $X = 40h_{tab}$, which is typical for a low Reynolds

number turbulent boundary layer in a zero pressure gradient. For the data taken between tabs, $H \approx 2.4$ for $X = 2h_{tab}$ and decreases to 1.4 for $X = 40h_{tab}$. The value at $X = 2h_{tab}$ is typical for a zero pressure gradient laminar boundary layer, which is how the visualization results indicate the flow initially behaves after passing between the tabs. The value of H at $X = 40h_{tab}$ is very near the corresponding value for $Z = 0$, which again indicates that the flow is approaching uniformity, with H values consistent with those of a low Reynolds number turbulent boundary layer.

Velocity and Turbulent Intensity Contours. Figures 13 and 14 show mean velocity and turbulence intensity contours in the y–z plane, obtained for a single tab at streamwise distances of $X = 2h_{tab}$ and $X = 15h_{tab}$, respectively. Because of symmetry, only one half of the tab wake was measured. As shown in Fig. 13(*a*), the outer contour line indicates the approximate edge of the boundary layer, δ_{95} (where $u/U_\infty = 0.95$). The difference between each successive contour is 10 percent of the free-stream velocity, U_∞. Note that the streamwise velocity decreases sharply as the center of the streamwise vortex core is approached, decreasing to approximately 35 percent of U_∞. Also, note the sharp incursion of the contours near the bottom of the vortex. This indicates that the streamwise vortex, of clockwise rotation, causes a strong induction of outer-region, higher-speed fluid toward the surface and inwards toward the symmetry plane. This induction of high-speed fluid acts, in a sense, as an artificial sweep of high-speed fluid to replace the low-speed fluid ejected away from the surface along the symmetry plane (see Fig. 5), and illustrates the significant function that the tab-generated streamwise vortices play in promoting fluid and momentum exchange, and consequently local mixing.

Figure 13(*b*) shows the corresponding distribution of turbulence intensity in the tab wake. It is evident that the intensity is greatest in the region of the vortex core, where the local velocity is lowest. This plot shows information not discernible from the tab centerline turbulence intensity results of Fig. 9, which suggested that maximum intensity values were found near the heads of the hairpin-like vortices. Here, the maximum values occur near the center of the streamwise vortices, and are of greater intensity than near the hairpin heads. This is an important point since it indicates that the concentrated vorticity in the streamwise vortex core contributes significantly to the overall mixing process. Westphal et al. (1985), show results that suggest that turbulence levels are lower than average in the downwash region of a longitudinal vortex and higher in the upwash region. This is consistent with Fig. 13(*b*), which indicates that turbulence intensities near the of symmetry ($Z = 0$) are approximately 35 percent, whereas in the downwash region ($Z/h_{tab} \approx 1.3$) comparable intensities are roughly 5 to 10 percent, except very near the wall.

Figure 14 illustrates how flow in the tab wake is mediated by the mixing and dispersion of the initial flow structures. By $X = 15h_{tab}$, the strong defect in the initial velocity contours has been sharply reduced, and the turbulence intensities have decreased by almost a factor of 4, except very near the surface. Note also the absence of a velocity defect in the region of the initial streamwise vortex, suggesting that this initially strong vortex has been significantly dispersed.

Spectral Analysis. Figure 15 shows power spectra results obtained on the wake symmetry plane at four increasing downstream positions. Measurements were taken at $Y = 1.7h_{tab}$ for all four streamwise positions, which is the vertical location at $X = 2h_{tab}$ where the periodic shedding of the heads of the

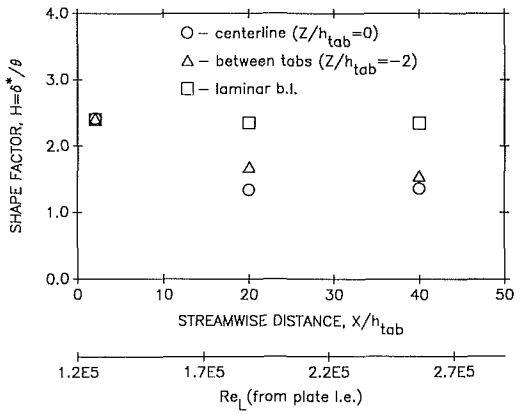

Fig. 12 **Boundary layer shape factor, H, for $Z/h_{tab} = 0$ and $Z/h_{tab} = -2$**

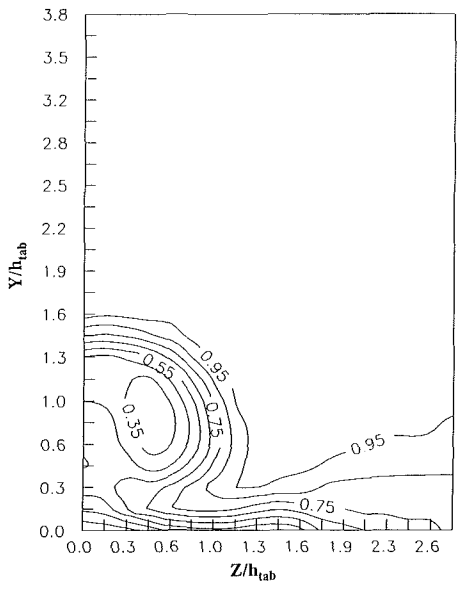

Fig. 13(*a*)

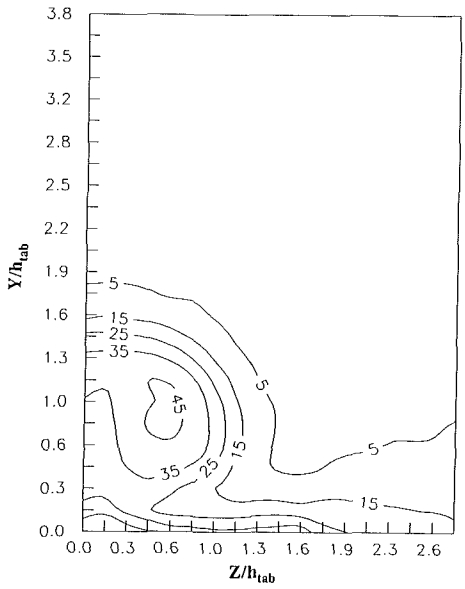

Fig. 13(*b*)

Fig. 13 **Contour map for single tab at $X = 2h_{tab}$. (*a*) Velocity, u/U_∞, (*b*) turbulence intensity, u'/U_∞ (percent)**

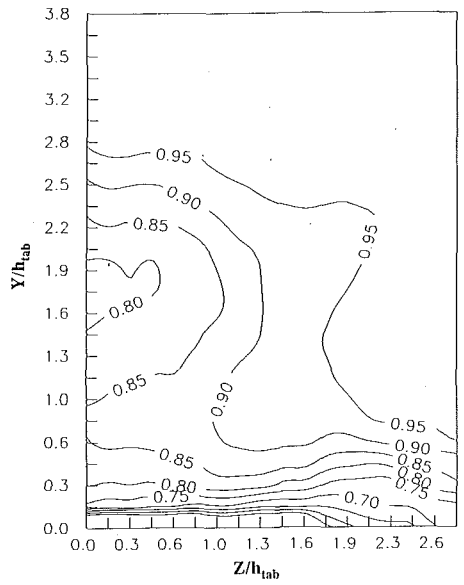

Fig. 14(*a*)

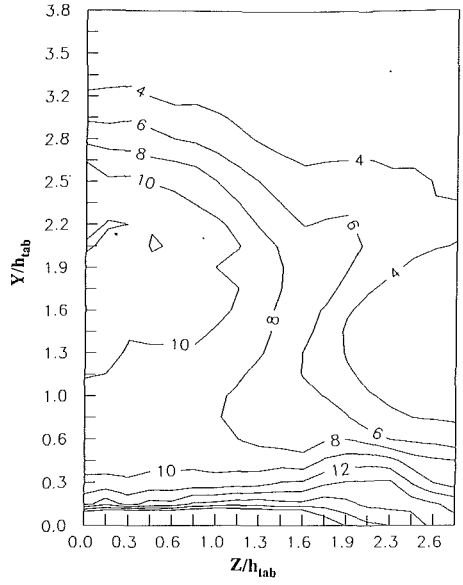

Fig. 14(*b*)

Fig. 14 Contour map for single tab at $X = 15h_{tab}$. (*a*) Velocity, u/U_∞, (*b*) turbulence intensity, u'/U_∞ (percent)

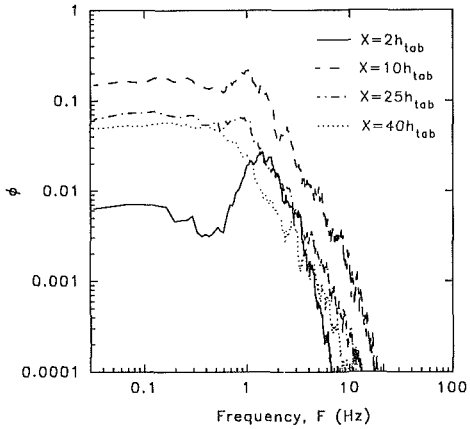

Fig. 15 Power spectra on tab centerline ($Z = 0$) at $Y = 1.7h_{tab}$. $X =$, $Re_{x_T} =$:—, ($2h_{tab}$, 1.2×10^5); ---, ($10h_{tab}$, 1.6×10^5); -·-·-, ($25h_{tab}$, 2.1×10^5); ....., ($40h_{tab}$, $2,6 \times 10^5$)

hairpin-like vortices is most strongly reflected in the velocity signal. At $X = 2h_{tab}$, a dominant periodicity of approximately 1.5 Hz is clearly present, reflecting the shedding frequency of the hairpin vortices. By $X = 10h_{tab}$, the dominant frequency component is less pronounced and has decreased to $\approx$ 1 Hz, with energy spreading to frequency components both lower and higher than the initial hairpin shedding frequency. A clear shift in the dominant peak in the spectra to lower frequencies is noted with increasing distance from the mixing tab; this is further evidence of the coalescence of the initial hairpin vortices into larger, less frequent flow structures (c.f. Figs. 6(*a*) and 6(*b*)). By $X = 25h_{tab}$ and $40h_{tab}$, the power spectra become more reflective of turbulent spectra, as a rapid dispersion of the initial flow structure continues. This mixing is the result of complicated processes of dispersion, amalgamation, and coalescence of the hairpin-like structures with increasing streamwise distance, as was illustrated in Fig. 6.

4 Summary and Conclusions

A passive mixing tab device was examined to better understand the process of momentum exchange and mixing in the tab wake. Detailed visualization studies of the tab mixing wake indicate that:

1) A pair of tip-type, counter-rotating streamwise vortices are generated by the tabs, creating a strong surface interaction which results in a common up-flow of low-speed fluid on the symmetry plane;
2) Distinct hairpin-like vortices are clearly shed from the tip of the tab; these structures form from the initial shear layer generated at the tab boundaries, with the legs of the structures enveloping the outer-edge of the tab wake; and
3) The hairpin vortices coalesce very rapidly with one another into larger amalgamations of vorticity, which are perceived as rapid boundary layer growth.

Velocity measurements indicate that:

1) Velocity profiles, both on the tab symmetry plane and between tabs, rapidly develop logarithmic law-of-the-wall type behavior, closely mimicking the behavior of a typical turbulent boundary layer;
2) The vortex core region of the streamwise counter-rotating vortices generates the highest initial turbulence intensity; the heads of the hairpin-like vortices yield the highest turbulence intensities on the symmetry plane;
3) In the near-wake of the mixing tab, the local displacement and momentum thickness are strongly spanwise variant, but rapidly recover to spanwise uniformity with streamwise distance; the shape factor, H, converges rapidly with streamwise distance to a value commensurate with a conventional turbulent boundary layer;
4) The spectral content of the mixing wake evolves rapidly from a strongly periodic flow to a conventional stochastic flow, characteristic of a turbulent boundary layer.

The passive mixing tab examined in this study is a highly-effective mixing device which facilitates mixing by the initial generation of organized flow structures. These flow structures comprise a symbiotic amalgam of hairpin-like vortices and counter-rotating streamwise tip vortices, both considered basic flow structures of turbulent boundary layers. The present results suggest that emulation of such initial turbulent structures can be employed to successfully enhance mixing in a systematic manner by capitalizing on the intrinsic behavior of organized vortex dynamics.

Acknowledgments

We would like to acknowledge the assistance and suggestions of Dr. A. H. Haidari, Dr. B. K. Taylor, and Dr. C. L. Magness in the performance of this research. The first author would also like to thank AT&T Bell Laboratories for the support of his graduate study, under which this research was completed.

References

Acarlar, M. S., and Smith, C. R., 1987a, "A Study of Hairpin Vortices in a Laminar Boundary Layer. Part 1. Hairpin Vortices Generated by a Hemisphere Protuberance," *Journal of Fluid Mechanics*, Vol. 175, pp. 1–42.

Acarlar, M. S., and Smith, C. R., 1987b, "A Study of Hairpin Vortices in a Laminar Boundary Layer. Part 2. Hairpin Vortices Generated by Fluid Injection," *Journal of Fluid Mechanics*, Vol. 175, pp. 43–85.

Ersoy, S., and Walker, J. D. A., 1985, "Viscous Flow Induced by Counter-Rotating Vortices," *Physics of Fluids*, Vol. 28, No. 9, p. 2687.

Fasano, J. B., 1991, "Kenics HEV Mixer Sets a New Standard for Turbulent Mixing Efficiency," *Proceedings of Mixing XIII*, Banff, Alberta.

Gretta, W. J., 1990, "An Experimental Study of the Fluid Mixing Effects and Flow Structure Due to a Surface Mounted Passive Vortex Generating Device," M. S. thesis, Lehigh University, Bethlehem, PA.

Head, M. R., and Bandyopadhyay, P., 1982, "New Aspects of Turbulent Boundary-Layer Structure," *Journal of Fluid Mechanics*, Vol. 107, p. 297.

Kline, S. J., and McClintock, F. A., 1953, "Describing Uncertainties in Single-Sample Experiments," *Mechanical Engineering*, Jan., pp. 3–8.

Lin, J. C., and Howard, F. G., 1989, "Turbulent Flow Separation Control Through Passive Techniques," AIAA paper No. AIAA -89-0976.

Lin, J. C., Selby, G. V., and Howard, F. G., 1991, "Exploratory Study of Vortex-Generating Devices For Turbulent Flow Separation Control," AIAA paper No. AIAA-91-0042.

Pauley, W. R., and Eaton, J. K., 1982, "The Fluid Dynamics and Heat Transfer Effects of Streamwise Vortices Embedded in a Turbulent Boundary Layer," Report MD-51 Department of Mechanical Engineering, Stanford University.

Perider, V. J., Smith, F. T., and Walker, J. D. A., 1991, "Vortex-Induced Boundary-Layer Separation. Part II: Unsteady Interacting Boundary-Layer Theory," *Journal of Fluid Mechanics*, Vol. 232, p. 133.

Perry, A. E., and Chong, M. S., 1982, "On the Mechanism of Wall Turbulence," *Journal of Fluid Mechanics*, Vol. 119, p. 173.

Robinson, S. K., 1991, "Coherent Motions in the Turbulent Boundary Layer," *Annual Review of Fluid Mechanics*, Vol. 23, pp. 601–639.

Schlichting, H., 1979, *Boundary Layer Theory*, 7th ed., McGraw-Hill, New York.

Schraub, F. A., Kline, S. J., Henry, J., Runstadler, P. W., and Littell, A., 1965, "Use of Hydrogen Bubbles for Quantitative Determination of Time-Dependent Velocity Fields in Low-Speed Water Flows," ASME *Journal of Basic Engineering*, Vol. 87, p. 429.

Smith, C. R., Fitzgerald, J. P., and Greco, J. J., 1991, "Cylinder End-wall Vortex Dynamics," *Physics of Fluids A*, Vol. 3, No. 9, p. 2031.

Smith, C. R., Greco, J. J., and Hopper, P. B., 1989, "Low-Loss Conditioning Using Concepts of Passive Vortex Generation," *Proceedings of ASME Forum on Industrial Applications of Fluid Mechanics*, T. Morrow, ed., ASME Press, pp. 57–62.

Smith, C. R., and Lu, L. J., 1989, "The Use of a Template-Matching Technique to Identify Hairpin Vortex Flow Structures in Turbulent Boundary Layers," *Proceedings of Zaric International Symposium on Wall Turbulence*, S. J., Kline, ed., Hemisphere.

Smith, C. R., and Schwartz, S. P., 1983, "Observations of Streamwise Vortices in the Near-Wall Region of a Turbulent Boundary Layer," *Physics of Fluids*, Vol. 26, No. 3, p. 641.

Smith, C. R., Walker, J. D. A., Haidari, A. H., and Sobrun, U., 1991, "On the Dynamics of Near-Wall Turbulence," *Philosophical Transactions of the Royal Society*, London Series A, Vol. 336, pp. 131–175.

Stevens, A. V., and Collins, G. A., 1955, "Turbulent Boundary Layer Control by Ramps or Wedges," Report ACA-55, Australian Aeronautical Research Commission.

Theodorsen, T., 1952, "Mechanism of Turbulence" *Proceedings of 2nd Mid-Western Conference on Fluid Mechanics*, Bulletin No. 149, Ohio State University, Columbus, Ohio.

Westphal, R. V., Eaton, J. K., and Pauley, W. R., 1985, "Interaction Between a Vortex and a Turbulent Boundary Layer in a Streamwise Pressure Gradient," *5th International Symposium on Turbulent Shear Flows*, Cornell University.

Film-Thickness, Pressure-Gradient, and Turbulent Velocity Profiles in Annular Dispersed Flows

A. N. Skouloudis

J. Würtz

Process Engineering Division,
JRC, Ispra,
Commission of the European Communities,
21020 Ispra (VA), Italy

A regional model has been described for dispersed turbulent two-phase flow which accounts for the transverse variation of velocity. The two-phase turbulence parameters are introduced in direct analogy to well-known single-phase flow parameters which are then correlated to experimental data. The advantages of this approach are its simplicity and the absence of arbitrary parameters which need calibration at different experimental ranges. Its generality has been tested by comparisons at high and low operating pressures with air-water and steam-water mixtures. Comparisons between calculated and measured values have been carried out for the film thickness and the pressure gradient at different experimental setups.

1 Introduction

It is generally desirable, at each particular position along a flow channel, to know the fraction of the total area occupied by the vapor phase (void-fraction), and for the same phase, the ratio of the mass-flow rate to the total (mass-dryness fraction). From their definitions these quantities are interrelated and they are also related to the average velocities of each phase. Usually, the local mass-dryness fraction can be calculated from the local thermodynamic conditions when the two phases are assumed in thermal equilibrium. Thus, only one additional relationship is required which can be based either on a phenomenological model or on an empirically derived correlation.

Empirically derived correlations have the disadvantage of doubtful validity when extrapolations are made. On the other hand, the phenomena associated with annular flows are complex and difficult to describe analytically. The presence of a disturbed interface between the two phases causes entrainment which has a direct influence on turbulence.

So far, many phenomenological models have approached the problem mainly by applying single-phase turbulence relationships which were of the same type as those established in pipe flows. The triangular relationship by Hewitt and Hall-Taylor (1970), is a typical approach of this kind in which the pressure gradient, the film thickness and the film flow are interrelated. By knowing any of the two quantities the third can be easily calculated. Also, by using a suitable relationship for the eddy diffusivity the velocity profile in the liquid film is calculated.

Levy and Healzer (1981), proposed a new model which uses the single-phase mixing length theory at a wavy liquid-gas interface. In this model the flow cross section is subdivided into three regions: a liquid film, a gas core of constant density, and a transition wavy layer between them. In the wavy region the density was assumed to vary exponentially in the transverse direction. The velocity distributions were taken to be discontinuous between the three regions and an empirical correlation was necessary for the velocity in the wavy region. Liquid entrainment ratio was taken into account by varying the exponent of the density profile in the transition layer. However, measured film thicknesses are generally over-predicted probably due to the assumption that the core region does not contain liquid droplets.

Abolfadl and Wallis (1986), also worked with the pressure gradient, film flow rate, gas flow rate, and the void fraction. Assuming a viscous liquid-film region, a turbulent film flow region and a gas core region, they have applied the shear stress profile in establishing a different relationship for a two-phase mixing length. This function was again based on experimental observations.

Recently, Jensen (1987) applied the triangular approach and several representative velocity profiles with the objective to develop an empirical correlation for the two-phase velocity profile in the core region. In his approach the film flow rate was best fitted to experimental observations by means of a non-linear multiplier. Even with this multiplier there were some problems at large mass-dryness fractions and high mass flow rates.

The basic idea behind the present velocity profile model is that it approaches the problem from the opposite direction. It assumes two turbulent velocity profiles which then are combined by ensuring continuity at the interface between two distinct flow regions. Experimental data are used in establishing the shape of the assumed turbulent velocity profiles. By knowing these velocity profiles the pressure gradient and thickness of the liquid film can be calculated.

2 Description of the Model

In the velocity profile model, the circular flow area is imagined to be divided into two regions, as indicated in Fig. 1.

Contributed by the Fluids Engineering Division for publication in the JOURNAL OF FLUIDS ENGINEERING. Manuscript received by the Fluids Engineering Division February 20, 1990; revised manuscript received December 11, 1992. Associate Technical Editor: E. E. Michaelides.

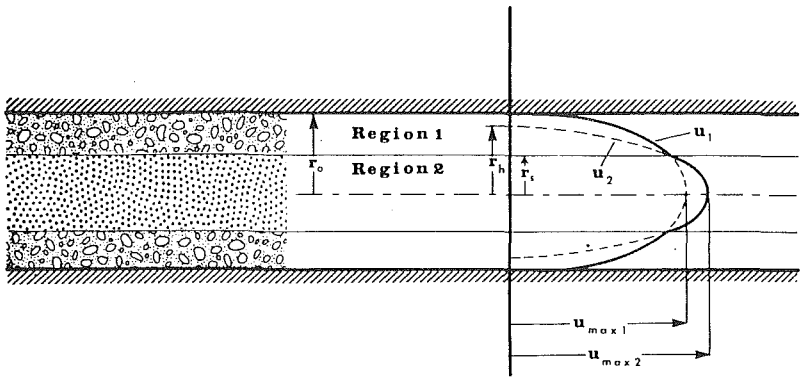

Fig. 1 The velocity profiles assumed

Each region is assumed to be occupied mainly by one phase (liquid or vapor), with the other phase uniformly mixed with it; the mixing is assumed sufficiently intimate to allow for the use of a single value for the velocity at each point. Normally the region next to the wall is assumed to be occupied predominantly by the liquid phase.

We make the usual assumption of local thermodynamic equilibrium of the phases, so that the mass-dryness fraction, x, can be used to relate the mass-flow rates of vapor and liquid, $\dot{m}_G$ and $\dot{m}_L$, by

$$x = \dot{m}_G/(\dot{m}_G + \dot{m}_L) \tag{1}$$

with a similar expression for each flow region:

$$x_1 \equiv \dot{m}_{G1}/(\dot{m}_{G1} + \dot{m}_{L1}) \tag{2}$$

$$x_2 \equiv \dot{m}_{G2}/(\dot{m}_{G2} + \dot{m}_{L2}) \tag{3}$$

Within each region the flow area is divided into sub-areas for liquid and vapor phases so that $A_{G1} + A_{L1} = A_1$. By aid of this expression and from the assumption of a homogeneous mixture in each region, the mean density of the mixture is:

$$\frac{1}{\bar{\rho}_1} = \frac{x_1}{\rho_G} + \frac{1-x_1}{\rho_L}. \tag{4}$$

and a similar expression is used for the core region. These expressions are derived directly from the definition of the local mass-dryness fractions together with the assumption that the ratio of the average gas and liquid velocities is 1 in each of the two flow regions shown in Fig. 1. This assumption was validated by Jensen (1987) who worked with the same range of experimental data as we use here, for which he has reported slip ratios between 1 and 1.03.

Several expressions are proposed by Hewitt and Hall-Taylor (1970), for the average viscosity of gas-liquid mixtures. For reasons of simplicity throughout the present work, the average viscosity in region 1 is assumed to be:

$$\frac{1}{\bar{\mu}_1} = \frac{x_1}{\mu_G} + \frac{1+x_1}{\mu_L}. \tag{5}$$

with a similar relationship used for the viscosity in region 2. This expression for the average viscosity is chosen due to its similarity to the average density derived by Eq. (4), and because for the core region, this expression also gives viscosities close to the gas viscosities used by other authors.

Although the mass-dryness fractions x_1 and x_2 are convenient ratios in the equations described above, they are difficult to measure. Thus, for taking into account the mass exchange between the two regions, it is useful to introduce the entrainment ratios e_1 and e_2; e_1 is the fraction of liquid entrained from the film (region 1) to the core region and e_2 is the fraction of vapor entrained from the core (region 2) into the film region, i.e.,

$$e_1 \equiv \frac{\dot{m}_{L2}}{\dot{m}_L} = \frac{(1-x_2)\dot{m}_2}{(1-x)(\dot{m}_1 + \dot{m}_2)} \tag{6}$$

$$e_2 \equiv \frac{\dot{m}_{G1}}{\dot{m}_G} = \frac{x_1 \dot{m}_1}{x(\dot{m}_1 + \dot{m}_2)}. \tag{7}$$

2.1 The Void Fraction And Mass-Dryness Fraction. Using the entrainment ratios just defined, it is possible to relate the void fraction to the mass-dryness fraction for each region, as well as for the whole flow. For region 1, using Eqs. (1), (6), and (7) together with the assumption that the average liquid and vapor velocities in each region are equal, it follows that:

$$\frac{A_{G1}}{A_{L1}} = \frac{\alpha_1}{1-\alpha_1} = \left(\frac{\rho_L}{\rho_G}\right)\left(\frac{e_2}{1-e_1}\right)\left(\frac{x}{1-x}\right), \tag{8}$$

and similarly for region 2,

Nomenclature

A = flow area [m^2]
c = numerical factor for the shear stress [—]
d = tube diameter [m]
e = entrainment ratio [—]
g = gravitational acceleration [m/s^2]
G = total mass flux [kg/m^2 s]
l = mixing length [m]
L = length from inlet to the end of test section [m]
m = region-1 power law exponent
$\dot{m}$ = mass flow rate [kg/s]
n = region-2 power law exponent
p = pressure [Pa]
r = distance from the axis [m]
r_o = pipe radius [m]
s = distance along the axis [m]
u = local velocity [m/s]
v^* = friction velocity
x = mass-dryness fraction [—]
α = area-dryness fraction [—]
θ = inclination to horizontal [deg]
λ = power law exponent for single phase flow [—]
μ = dynamic viscosity [kg/m s]
ρ = density [kg/m^3]
τ = shear stress [N/m^2]

Subscripts

G = gas phase
h = hypothetical quantity
L = liquid phase
max = maximum quantity
s = separation
w = wall
T = total
1 = quantity for region 1
2 = quantity for region 2

$$\frac{A_{G2}}{A_{L2}}=\frac{\alpha_2}{1-\alpha_2}=\left(\frac{\rho_L}{\rho_G}\right)\left(\frac{1-e_2}{e_1}\right)\left(\frac{x}{1-x}\right). \tag{9}$$

The void fractions for each region are defined from:

$$\alpha_1 \equiv A_{G1}/(A_{G1}+A_{L1}) \tag{10}$$

$$\alpha_2 \equiv A_{G2}/(A_{G2}+A_{L2}) \tag{11}$$

The $\alpha-x$ relationship for the whole flow involves the velocity distribution; for this, the defining equations are power law relationships for turbulent flow, i.e.,

$$\frac{u_1}{u_{\max,1}}=\left(1-\frac{r}{r_o}\right)^{1/m} \quad \text{for} \quad r_s \le r \le r_o \tag{12}$$

$$\frac{u_2}{u_{\max,2}}=\left(1-\frac{r}{r_h}\right)^{1/n} \quad \text{for} \quad 0 \le r \le r_s \tag{13}$$

In these equations r_0 is the radius of the pipe, r_s the radius of the interface between regions 1 and 2, and r_h is a hypothetical dimension used to specify the profile for the central region 2. The latter being the dimension of a hypothetical pipe will be correlated to the other two diameters r_o and r_s by ensuring continuity of the flow as described next.

The two parts of the velocity profile are matched by ensuring continuity of velocity at the interface, r_s, from which the ratio of the maximum velocities is:

$$\frac{u_{\max,2}}{u_{\max,1}}=\frac{\left(1-\frac{r_s}{r_o}\right)^{1/m}}{\left(1-\frac{r_s}{r_h}\right)^{1/n}}. \tag{14}$$

An additional closure relationship is obtained when a continuous shear stress distribution is taken at the interface. This shear stress is assumed to follow the Prandtl's mixing-length hypothesis (Schlichting, 1955) for fully developed flows from which,

$$\tau=\rho\, l^2 \left|\frac{du}{dr}\right|\frac{du}{dr}, \tag{15}$$

where l is the Prandtl mixing length. A similar mixing-length hypothesis is used by Levy and Healzer (1981), where l is—as in single-phase flow—assumed to be exclusively a function of the distance from the walls. This was also considered to be valid in the works of Abolfad and Wallis (1986). Thus, equal mixing lengths are taken at the interface between the two regions. From the application of Eq. (15) at the interface r_s and by the use of Eqs. (12), (13), and (14), the following geometric relationship is derived:

$$\left(\frac{r_h}{r_s}\right)=1+\frac{m}{n}\sqrt{\frac{\bar{\rho}_2}{\bar{\rho}_1}}\left(\frac{r_o}{r_s}-1\right). \tag{16}$$

The velocity distributions from Eqs. (12) and (13) can be also used for calculating the ratio of the mass-flow rates in the two regions, namely, the central core region against the region next to the wall:

$$\frac{\dot{m}_2}{\dot{m}_1}=\left(\frac{\bar{\rho}_2}{\bar{\rho}_1}\right)\left(\frac{u_{\max,2}}{u_{\max,1}}\right)\frac{\int_0^{r_s}(1-r/r_h)^{1/n}\, r\, dr}{\int_{rs}^{r_o}(1-r/r_o)^{1/m}\, r\, dr} \tag{17}$$

By inserting Eqs.(14) and (16) in Eq. (17) it is obtained:

$$\frac{\dot{m}_2}{\dot{m}_2}=\left(\frac{\bar{\rho}_2}{\bar{\rho}_1}\right)^{3/2}\left(\frac{2m+1}{2n+1}\right)\left(\frac{1+1/m}{1+1/n}\right)\left[\frac{r_h\left(\frac{r_h}{r_h-r_s}\right)^{1+1/n}-r_h-\left(\frac{n+1}{n}\right)r_s}{\left(\frac{m+1}{m}\right)r_s+r_o}\right] \tag{18}$$

From the definitions of the entrainment ratios (Eqs. (6) and (7)), the ratio of the total (liquid and vapor) mass-flow rates in each region is expressed as,

$$\frac{\dot{m}_2}{\dot{m}_1}=\frac{(1-e_2)x+e_1(1-x)}{(1-e_1)(1-x)+e_2 x} \tag{19}$$

For obtaining the desired relationship between the overall void fraction α and the mass-dryness fraction x, α should be expressed in terms of the geometric parameters of the velocity profile. For the total void fraction, the left-hand side of Eqs. (8) and (9) are used from where:

$$\frac{\alpha}{1-\alpha}=\left[\frac{\alpha_1+\alpha_2\left(\frac{r_s^2}{r_o^2-r_s^2}\right)}{(1-\alpha_1)+(1-\alpha_2)\left(\frac{r_s^2}{r_o^2-r_s^2}\right)}\right]. \tag{20}$$

From Eqs.(8) and (9) the void fractions α_1 and α_2 are expressed as function of the entrainment ratios e_1 and e_2 also, the hypothetical pipe radius r_h is related to r_s via Eq. (16). Hence, Eqs. (18) to (20) constitute an implicit relationship between α and x; there is a unique solution for any value of α and x from zero to unity. The solution is found numerically by a standard mathematical routine which locates the zero of a function within a given interval after suitable values have been assigned to the entrainment ratios e_1 and e_2. These values can be also used in describing the character of the flow; thus, by setting the entrainment ratios to zero the two regions of the flow are assumed to be occupied only by the liquid or vapor phase. Similarly, if one of the entrainment ratios is set to unity all of the corresponding phase is assumed to be entrained into the other region as a homogeneous mixture of bubbles or droplets.

2.2 Pressure Gradient. The axial pressure gradient is obtained from the force-momentum equation. For steady, adiabatic flow in a pipe, inclined relative to the horizontal plane,

$$-\frac{dp}{ds}=\frac{4\tau_w}{d}+[\alpha\rho_G+(1-\alpha)\rho_L]g\sin\theta \tag{21}$$

where τ_w is the wall shear stress and the acceleration terms are neglected. For thin films a linear profile for the shear stress is assumed from which:

$$\tau_w=\tau_h\frac{r_o}{r_h} \tag{22}$$

where τ_h is the wall shear stress for the flow in a pipe with the radius r_h, and for a fluid of density $\bar{\rho}_1$ and viscosity $\bar{\mu}_2$. This is calculated from Schlichting (1955), as

$$\tau_h=4\,\bar{\rho}_2\bar{u}_{2T}^2\left[2\,c_2\frac{\bar{u}_{2T}}{u_{\max,2}}\right]^{-2n/(n+1)}\left[\frac{\bar{\rho}_2\,\bar{u}_{2T}\,2r_h}{\bar{\mu}_2}\right]^{-2/(n+1)} \tag{23}$$

In Eq. (23), $\bar{u}_{2T}$ is the mean value of u_2 integrated over the whole flow area with radius r_h. The numerical factor c_2 (c for single-phase flow) is usually defined from a dimensionless expression for the power law velocity profile i.e.,

$$\frac{u}{v^*}=c\left(\frac{\rho(r_o-r)v^*}{\mu}\right)^{1/\lambda} \quad \text{where } v^*=\sqrt{\frac{\tau_w}{\rho}} \tag{24}$$

c is usually related to the power law exponent λ.

Table 1 Single phase turbulence parameters

Re	$\lambda = m$	c
$4.0 \cdot 10^3$	6.0	7.81
$2.3 \cdot 10^4$	6.6	8.37
$1.1 \cdot 10^5$	7.0	8.74
$1.1 \cdot 10^6$	8.0	10.41
$2.0 \cdot 10^6$	10.0	11.53

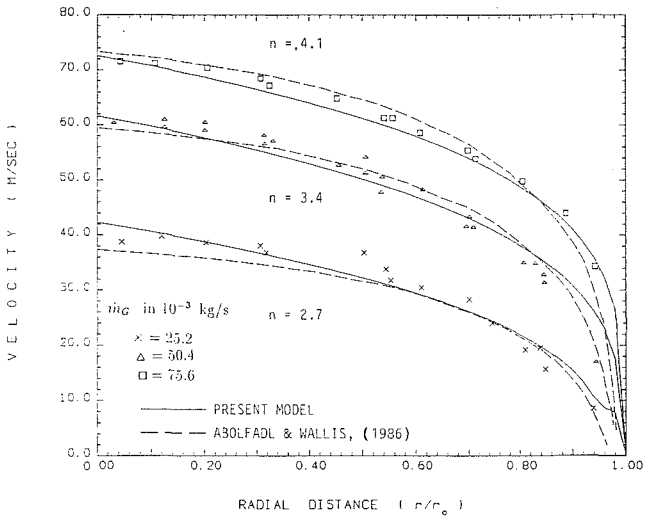

Fig. 2 Local velocity profiles of Gill et al. (1964), at $\dot{m}_L$ = 0.063 kg/s for air-water mixtures

3 Turbulence Related Parameters

The parameters introduced by the present model are the power law exponents m and n for the velocity profiles and the numerical factor c_2 used in the evaluation of the wall shear stress. For single-phase flow these parameters are related to the Reynolds number. For flow in smooth pipes, the power law exponent varies according to Schlichting (1955), as shown in Table 1. In all calculations carried out here, the values of Table 1 for the exponent m in the film region has been used. These values were based on the Reynolds number for region 1 where the average velocity was calculated by assuming that the film velocity profile was extended over the whole cross-section of the pipe.

For the power law exponent n in the core region the roughness of the interface between the two regions is taken into account by choosing values suitable for pipe flow with a rough wall. Schlichting (1955), suggests that near a rough wall, the velocity gradient is less steep than in smooth pipes and that a power law exponent less than 6 seems to be more representative. In Fig. 2 are shown three representative velocity profiles from Gill et al. (1964), for air-water flows at low pressures under adiabatic conditions.

The solid lines in Fig. 2 correspond to the profiles calculated with n in the interval between 2.7 and 4.1. The measured liquid entrainment ratios have been used in the calculations and zero vapor entrainment in the film region was assumed. For comparative reasons are also shown the profiles calculated by the model of Abolfadl and Wallis (1986). It is seen that the applied low values of n adequately describe the measured velocity profiles.

For establishing a relationship between the power law exponent for the core region and the interfacial roughness, the velocity profile has been calculated iteratively for different values of n. The standard deviation between the experimental and the calculated velocity was checked, and for each experimental case was found the value of n where the deviation became smallest.

All the velocity profile data available to us have been used

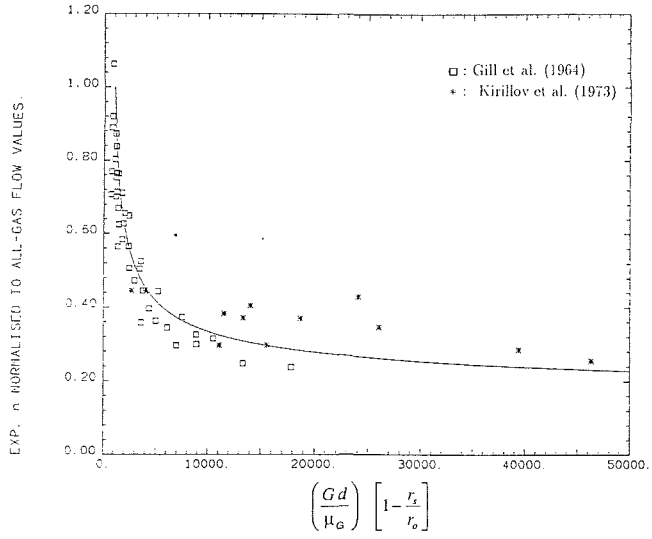

Fig. 3 Proposed correlation for the exponent n normalized against a single-phase exponent for gas flow with the same total mass flow rate

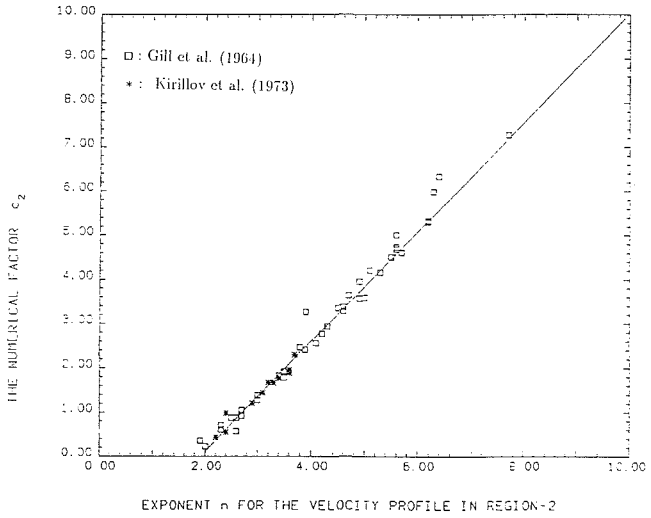

Fig. 4 Proposed correlation for the c_2 factor used in the shear stress calculations

in this analysis; these being the data by Gill et al. (1964) for vertical air-water flows at low operating pressure and the data of Kirillov et al. (1973) for vertical steam-water flows at 6.86 MPa. The optimized exponents are plotted in Fig. 3 as a function of the equivalent all-gas Reynolds number times the measured relative film thickness. The Reynolds number corresponds to all-gas flow, in the same tube, under the same operating conditions and with the same total mass-flow rate as that of the two-phase mixture. The power law exponent in Fig. 3 has been normalized by the exponents for single-phase flow, λ, obtained from Table 1 by applying the same equivalent all-gas Reynolds number. The experimental data seem to fit well the following expression

$$\frac{\lambda}{n} = 2 \log_{10}\left[\left(\frac{Gd}{\mu_G}\right)\left(1-\frac{r_s}{r_o}\right)\right] - 5; \quad \text{for } \left(\frac{Gd}{\mu_G}\right)\left(1-\frac{r_s}{r_o}\right) \geq 10^3 \quad (25)$$

which is the solid line drawn in Fig. 3.

In a similar way the numerical factor c_2, in Eq. (23) has been evaluated from measured pressure gradients using the same

Table 2 Summary of the operating conditions

Reference	Mixture	p MPa	d mm	L/d	G kg/m^2 s
Gill et al., 1964	Air-water	0.28	31.8	167	80–240
Kirilov et al., 1973	Steam-water	6.86	17.0	275	500–1000
Whalley et al., 1974	Air-water	0.28	31.8	167	80–800
J. Würtz, 1978	Steam-water	7.0	20.0	450	500–2000

set of experiments as in Fig. 3. These values are plotted in Fig. 4 against the corresponding power law exponent n. The solid line corresponds to the following relationship

$$c_2 = 1.24\ (n - 1.9); \quad \text{for } n \geq 2. \tag{26}$$

By comparison with Table 1 it is seen that the values for c_2 are lower than for smooth walls, indicating a larger shear stress caused by the rough interface and the entrained liquid.

4 Comparisons With Experiment

Aim of the experimental comparisons carried out, is to use the turbulence relationships proposed in Figs. 3 and 4 for predicting measured parameters related to annular dispersed flows. Comparisons have been made for air-water and steam-water mixtures as indicated in Table 2, where the operating conditions for the experiments are summarized. These conditions cover a wide range of operating pressures and total mass fluxes. These tests were performed in vertical tubes.

For the calculations with the velocity profile model, the entrainment ratios defined in Eqs. (6) and (7) must be known. Several models are available in literature from which the liquid entrainment ratio can be estimated. However, the scope of present work is not to compare entrainment models, so measured values of liquid entrainment have been used where possible. For the calculations referring to Kirillov et al. (1973), the liquid entrainment ratio e_1, has been calculated according to the correlation proposed by Ishii and Mishima (1982). For the onset of liquid entrainment Ishii and Grolmes (1975), have proposed a criterion based on a force balance at the crest of roll waves; entrainment is taken in to account when the vapor volumetric flux exceeds a critical value.

To the authors' knowledge, no correlation is available for estimating vapor entrainment in the liquid film. However, vapor entrainment phenomena have been mentioned by Hewitt and Dukler (1984). For demonstration purposes only, examples are given where the vapor entrainment ratio is taken to be a small portion of the total vapor mass-flow rate.

4.1 Film Thicknesses. Film thicknesses calculated by the velocity profile model are shown in Fig. 5 for the conditions corresponding to the experiments of Whalley et al. (1974). This figure illustrates the influence of vapor entrainment on the calculated film thicknesses and examines its importance especially for high mass-dryness fractions. Three different curves are given corresponding to vapor entrainment ratios of 0, 0.5 percent, and 1 percent. From this figures it is seen that for mass-dryness fractions below 40 percent the calculated film thicknesses are closer to the values measured when we assume 1 percent vapor entrainment ratio whereas, for higher mass-dryness fractions the experimental film thicknesses are reasonably well reproduced with a vapor entrainment ratio of 0.5 percent.

Calculations for the film thickness have been carried out for the experimental conditions stated in Table 2. The calculated results are plotted in Fig. 6 against measured values. No vapor entrainment is allowed in these calculations and there is a clear tendency for under-prediction. Similar results are shown in Fig. 7 but with 0.5 percent of the vapor entrained in the liquid film. The calculated film thicknesses are in this case more or less equally scattered along the line indicating agreement between predicted and measured values.

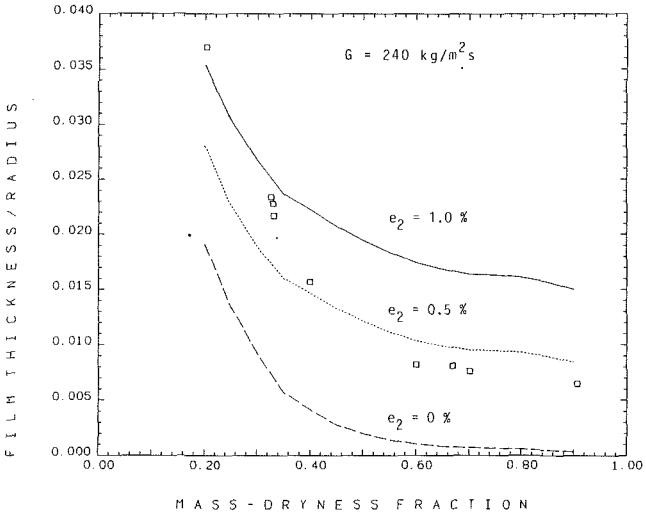

Fig. 5 Typical film thickness data from Whalley et al. (1974), for air-water mixtures at 0.28 MPa

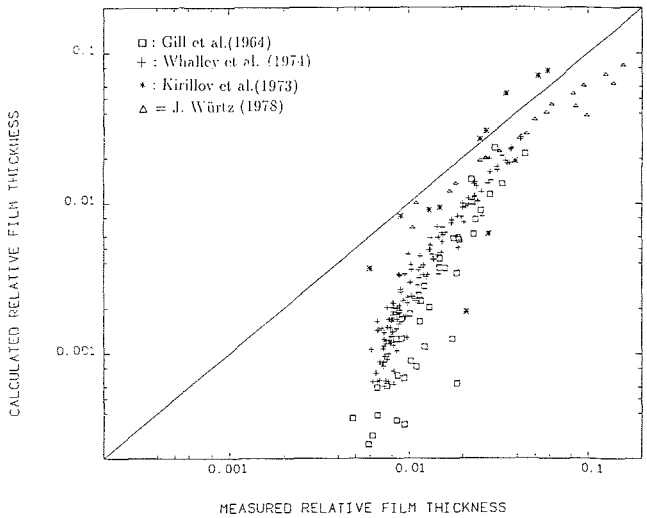

Fig. 6 Comparisons between measured and calculated film thicknesses without vapor entrainment at the film region

4.2 Pressure Gradients. The pressure gradients reported by J. Würtz (1978) for steam-water mixtures are shown in Fig. 8 as function of the mass-dryness fraction. The solid curves in the figure represent the calculations by the velocity profile model with no vapor entrainment at three different mass fluxes. The dashed lines refer to calculations with 0.5 percent of the vapor entrained in the liquid film. The calculations show that the vapor entrainment has larger influence at higher mass flow rates and high mass-dryness fractions.

Pressure gradients have been also calculated for the sources quoted in Table 2. For these, the measured values of film thickness have been used for calculating the value of the power law exponent n from the correlation proposed in Fig. 3. Figure 9 shows the predicted pressure gradients against measured ones for the case with no gas entrainment. Good agreement is obtained for the whole range of data examined.

5 Conclusions

The use of a compound power-law velocity profile is a fairly natural extension of the familiar single-phase power law profile in pipes. Such an extension received qualitatively support when

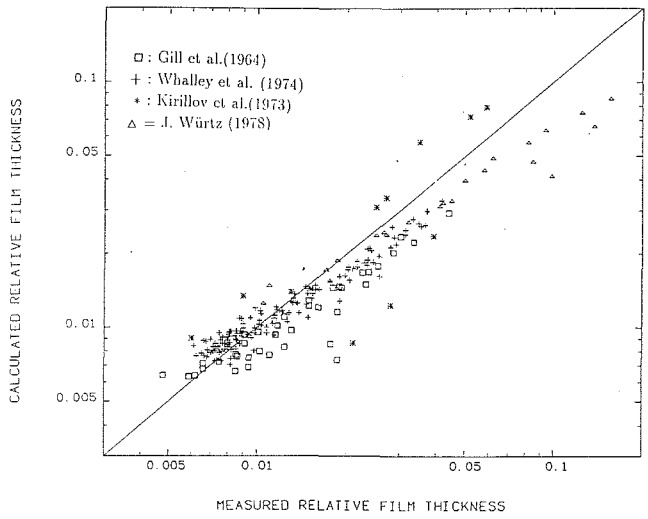

Fig. 7 Comparisons between measured and calculated film thicknesses with vapor entrainment e_2 = 0.5 percent

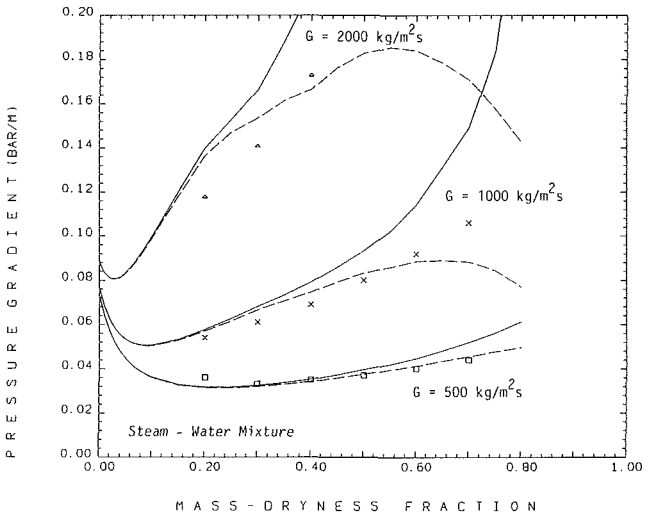

Fig. 8 Total pressure gradients from Würtz (1978) for steam-water. The solid line is without vapor entrainment and the dashed line with e_2 = 0.5 percent

measured and calculated radial velocity distributions are compared, as in Fig. 2.

The advantage of the velocity profile model described here is that for each characteristic phase it introduces distinct turbulence parameters in analogy to single-phase flows. These parameters are, the power law exponent used in describing the radial variation of velocity, and the numerical factor c_2 used for the calculation of the wall shear stress. These parameters are related to the turbulent flow conditions for the two different two-phase mixtures and suitable correlations for these parameters are proposed (Figs. 3 and 4). The variation of the parameters for the core region is different from what is known from single-phase flows. However, this is expected due to the different phenomenology of annular and dispersed flows.

Comparisons with measured film thicknesses and pressure gradients are carried out for operating pressures of 0.28 and 7.0 MPa for air-water and steam-water mixtures at different experimental facilities. For most calculations, experimental values of liquid entrainment ratios have been used. Due to the

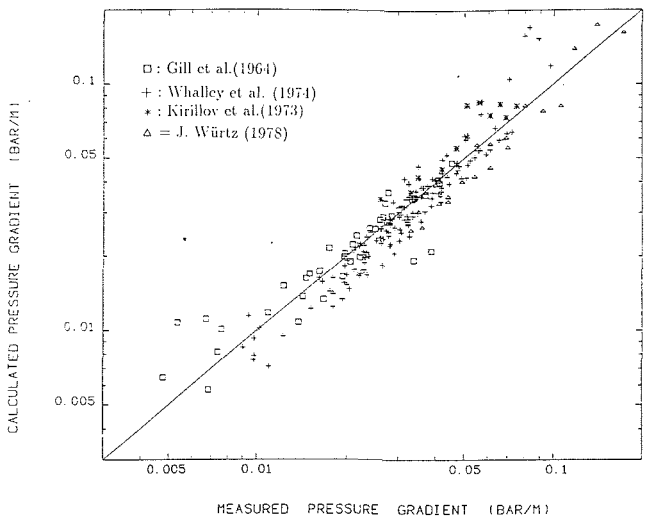

Fig. 9 Comparisons between experimental and calculated pressure gradients using measured film thicknesses

absence of information of vapor entrainment in the film region, only the sensitivity of the calculations has been examined by arbitrary varying this entrainment ratio.

In general, the comparison presented here demonstrate that the idea of double velocity profiles which take into account the transverse velocity variation, can be safely used for predictions. These predictions require only the knowledge of a single flow parameter, provided that the liquid and vapor entrainment relationships to the mass-dryness fraction are known.

References

Abolfadl, M., and Wallis, G. B., 1986, "An Improved Mixing-Length Model for Annular Two-Phase Flow with Liquid Entrainment," *Nuclear Science and Engineering*, Vol. 95, pp. 233–241.

Gill, L. E., Hewitt, G. F., and Lacey, P. M. C., 1964, "Sampling Probe Studies of the Gas Core in Annular Two-Phase Flow, Part 2. Studies of the Effect of Gas Phase Flow Rates on Phase and Velocity Distribution," *Chemical Engineering Science*, Vol. 19, pp. 665–682.

Hewitt, G. F., and Dukler, A. E., 1985, "Summary of the International Symposium on Two-Phase Annular and Dispersed Flows; Pisa, 24–29 June 1984," *PhysicoChemical Hydrodynamics*, Vol. 6, pp. 267–273.

Hewitt, G. F., and Hall-Taylor, N. S., 1970, *Annular Two-Phase Flow*, Pergamon Press, Oxford, pp. 76–97.

Ishii, M., and Grolmes, M. A., 1975, "Inception Criteria for Droplet Entrainment in Two-Phase Concurrent Flow," *American Institute of Chemical Engineers Journal*, Vol. 21, p. 308.

Ishii, M., and Mishima, K., 1982, "Liquid Transfer and Entrainment Correlation for Droplet-Annular Flow," *Proceedings of the 7th International Heat Transfer Conference*, Vol. 5, pp. 307–312.

Jensen, M. K., 1987, "The Liquid Film and the Core Region Velocity Profiles in Annular Two-Phase Flow," *International Journal of Multiphase Flow*, Vol. 13, pp. 615–628.

Kirillov, N. M., Komarov, N. M., and Subbotin, V. I., 1973, "Measurement of Certain Vapor-Liquid Flow Characteristics in a Circular Tube at a Pressure of 6.9 MPa," No. 241, *Preprint of the Inst. for Physics and Power Engineering*, Obninsk.

Levy, S., and Healzer, J. M., 1981, "Application of Mixing Length Theory to Wavy Turbulent Liquid-Gas Interface," ASME *Journal of Heat Transfer*, Vol. 103, pp. 492–500.

Schlichting, H., 1955, *Boundary Layer Theory*, 7th Ed., McGraw-Hill, New York, Chapters XX, XXI.

Whalley, P. B., Hewitt, G. F., and Hutchinson, P., 1974, "Experimental Wave and Entrainment Measurements in Vertical Annular Two-Phase Flow," *Proceedings of the Symposium on Multiphase Flow Systems*, Institute of Chemical Engineers, Vol. 1, pp. 1–24.

Würtz, J., 1978, "An Experimental and Theoretical Investigation of Annular Steam-water flow in Tubes and Annuli at 30 to 90 bar," Report 372, *Risø National Laboratory*.

Comparison of Numerical and Experimental Results for a Turbulent Flow Field With a Longitudinal Vortex Pair

J. X. Zhu
Research Engineer.

M. Fiebig
Professor.
Mem. ASME

N. K. Mitra
Professor.
Mem. ASME

Institut für Thermo- und Fluiddynamik,
Ruhr-Universität Bochum,
4630 Bochum 1, Germany

A numerical simulation of a three-dimensional turbulent flow with longitudinal vortices embedded in the boundary layer on a channel wall is presented. The flow is described by the unsteady incompressible Reynolds averaged Navier–Stokes equations and the standard k–ϵ turbulence model. A finite difference scheme based on the SOLA-algorithm is developed for the numerical solution of the governing equations. Comparison with the experimental data of Pauley and Eaton (1988 a, b) shows that the numerical computations predict the general characteristics of the flow correctly. Agreement to within 13 percent is obtained for the worst location in mean velocity fields. The average deviation of predicted mean streamwise velocity from the experimental data is 3.6 percent.

Introduction

Turbulent channel flows occur frequently in many heating and cooling devices. For example, in gas liquid or gas-gas heat exchangers, where extended surfaces in the form of fin plates are used extensively to reduce the thermal resistance on the gas side, the flow between two fin plates is turbulent in many applications. In order to enhance the heat transfer on the fin plates, longitudinal vortices can be introduced into the channel flows (Edwards et al., 1974; Fiebig et al., 1986). Longitudinal vortices promote mixing of the fluid between the near wall and the core region of the channel. This disturbs the boundary layer growth on the fin plates and thus enables high rates of heat transfer between the stream and the plates.

The authors' group is engaged in numerical investigations of turbulent flows and temperature fields in channels with built-in longitudinal vortex generators. To this end, a computer code for laminar flow investigation has been expanded to include the computation of the turbulent flow.

The purpose of the present work is:

1) to validate the modified computer code for calculating three-dimensional turbulent flows in a channel with longitudinal vortices and
2) to evaluate the k–ϵ turbulence model in order to determine its adequacy for calculating such flows.

To fulfill this purpose a well documented experiment of Pauley and Eaton (1988a,b) is simulated with the modified code.

Contributed by the Fluids Engineering Division for publication in the JOURNAL OF FLUIDS ENGINEERING. Manuscript received by the Fluids Engineering Division April 6, 1992; revised manuscript received December 4, 1992. Associate Technical Editor: T. T. Huang.

Description of the Computational Domain

Experimental data sets for three-dimensional turbulent flows containing longitudinal vortex pairs have been presented by Pauley and Eaton (1988a,b). Figure 1 shows a schematic of their experimental facility. This facility had a 200 cm long test section and was operated at a nominal freestream velocity of U_e = 16 m/s. The test section was a constant area duct. The longitudinal vortex pairs were generated by a pair of half delta-wing vortex generators mounted on the bottom wall. The half delta-wings had a height of 2 cm and a length of 5 cm. They were located 53 cm downstream of the inlet. The spacing between the two generators and their angles of attack were varied in the experimental study. The case with generator spacing of 4 cm and an 18 degree angle of attack, which was referred to as the base case in Pauley and Eaton (1988a), is chosen for the present simulation.

Measurements were presented by Pauley and Eaton (1988 a, b) at four cross sections: x = 66, 97, 142, 188 cm (see Fig. 1). The section x = 97 cm is selected as inlet of the computational domain, since there are no experimental data available for turbulence variables at the axial station x = 66 cm. The computational domain ends at the exit of the channel (x = 200 cm). An enlarged cross sectional view of the channel is shown in Fig. 2.

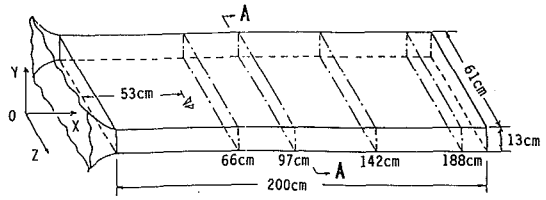

Fig. 1 Schematic of experimental facility of Pauley and Eaton (1988)

The y-z plan of the computational domain is specified by the dotted lines in Fig. 2. This is the region from -12 to 12 cm in z(span)-direction and from 0 (bottom wall) to 6.5 cm (half depth of the channel) in y(vertical)-direction.

The computational domain is restricted to such a dimensions, because at the cross section $x = 97$ cm, the data of Pauley and Eaton are available only for this area. The flow simulation is performed only for a symmetric half of the domain, i.e., in z-direction from 0 to 12 cm because of the symmetry about the central plane of the duct (plane I).

Governing Equations

The Reynolds averaged Navier–Stokes equations in conjunction with the eddy viscosity concept are used to describe the incompressible flow in the computational domain. These equations are written in a Cartesian tensor form as

Continuity

$$\frac{\partial U_i}{\partial x_i} = 0 \tag{1}$$

Momentum

$$\rho \frac{DU_j}{Dt} = -\frac{\partial p}{\partial x_j} + \frac{\partial}{\partial x_i}\left[(\mu + \mu_t)\left(\frac{\partial U_i}{\partial x_j} + \frac{\partial U_i}{\partial x_i}\right) - \frac{2}{3}\rho k \delta_{ij}\right] \tag{2}$$

where the turbulent viscosity μ_t is given by:

$$\mu_t = c_\mu \rho\, k^2/\epsilon \tag{3}$$

The turbulence kinetic energy k and its dissipation rate ϵ are computed from the standard k-ϵ model of Launder and Spalding (1974):

$$\rho \frac{Dk}{Dt} = \frac{\partial}{\partial x_i}\left(\frac{\mu_t}{\sigma_k}\frac{\partial k}{\partial x_i}\right) + G - \rho\,\epsilon \tag{4}$$

$$\rho \frac{D\epsilon}{Dt} = \frac{\partial}{\partial x_i}\left(\frac{\mu_t}{\sigma_\epsilon}\frac{\partial \epsilon}{\partial x_i}\right) + C_1 \frac{\epsilon}{k} G - C_2 \rho \frac{\epsilon^2}{k} \tag{5}$$

G denotes the production rate of k which is given by:

$$G = \mu_t \left(\frac{\partial U_i}{\partial x_j} + \frac{\partial U_j}{\partial x_i}\right)\frac{\partial U_i}{\partial x_j} \tag{6}$$

The standard constants are employed:

$$c_\mu = 0.09,\ C_1 = 1.44,\ C_2 = 1.92,\ \sigma_k = 1.0,\ \sigma_\epsilon = 1.3$$

Boundary Conditions

The measured data of Pauley and Eaton (1988a) for three velocity components, k as well as ϵ at the cross section $x = 97$ cm are utilized as inlet profiles of these variables for the computational domain.

The boundary conditions for the outlet and the other four boundary planes of the domain shown in Fig. 2 are treated as follows:

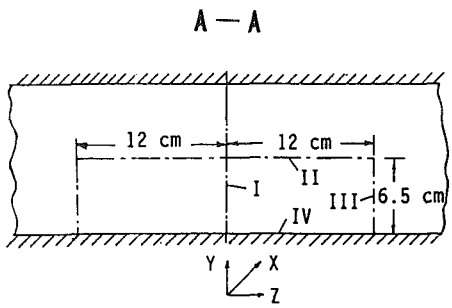

Fig. 2 Cross section of the computational domain

outlet: $\dfrac{\partial f}{\partial x} = 0;\quad f = \{U, V, W, k, \epsilon\}$

plane I, III: $W = 0;\quad \dfrac{\partial f}{\partial z} = 0,\quad f = \{U, V, k, \epsilon\}$

plane II: $V = 0;\quad \dfrac{\partial f}{\partial y} = 0,\quad f = \{U, W, k, \epsilon\}$

plane IV: $V = 0;$ wall functions for U, W, k, and ϵ.

The wall functions given in Launder and Spalding (1974) are used to bridge the near wall region:

$$\tau_w = \frac{\rho\, U_p\, c_\mu^{1/4}\, k_p^{1/2}\, \kappa}{\ln (E\, y^+)} \tag{7}$$

where

$$y^+ = \frac{\rho\, y_p\, c_\mu^{1/4}\, k_p^{1/2}}{\mu} \tag{8}$$

and $\kappa \simeq 0.42$, $E = 9.0$.

The subscript p refers to the grid point adjacent to the wall. The production rate of k and the averaged dissipation rates over a near wall cell for the k-equation as well as the value of ϵ at point p are computed, respectively, from

$$G_p = \tau_w \frac{U_p}{y_p} \tag{9}$$

$$\bar{\epsilon} = \frac{1}{y_p}\int_0^{y_p} \epsilon\, dy = \frac{c_\mu^{3/4} k_p^{3/2}}{\kappa y_p} \ln (Ey^+) \tag{10}$$

$$\epsilon_p = c_\mu^{3/4}\frac{k_p^{3/2}}{\kappa y_p} \tag{11}$$

Numerical Details

A numerical procedure, based on the SOLA algorithm (Hirt et al., 1975), was modified by the authors' group for the investigation of the velocity and temperature fields in three dimensional laminar channel flows with longitudinal vortex

Nomenclature

c_1, c_2, c_μ = constants in k-ϵ model
E = constant in the law of the wall ($=9.0$)
f = dependent variables
G = production of turbulence kinetic energy
H = channel height
k = turbulence kinetic energy
p = static pressure
Re = Reynolds number $\left(\dfrac{\rho U_e H}{2\mu}\right)$
t = time
U = streamwise mean velocity
U_e = freestream velocity
U_i = mean velocity
V = mean velocity in vertical direction
W = spanwise mean velocity
x = streamwise coordinate
x_i = Cartesian coordinates
y = vertical coordinate
y^+ = wall coordinate
Z = spanwise coordinate
ϵ = dissipation rate of turbulence energy
κ = von Karman constant
μ = molecular viscosity
μ_t = turbulent viscosity
ρ = density
σ_k = turbulent Prandtl number for diffusion of k
σ_ϵ = turbulent Prandtl number for diffusion of ϵ
τ_w = wall shear stress
Ω_x = streamwise vorticity

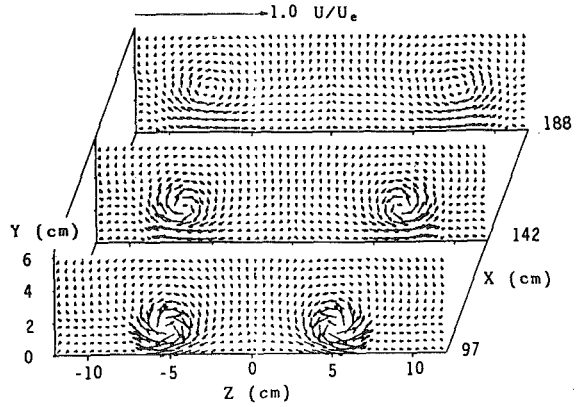

Fig. 3(a)

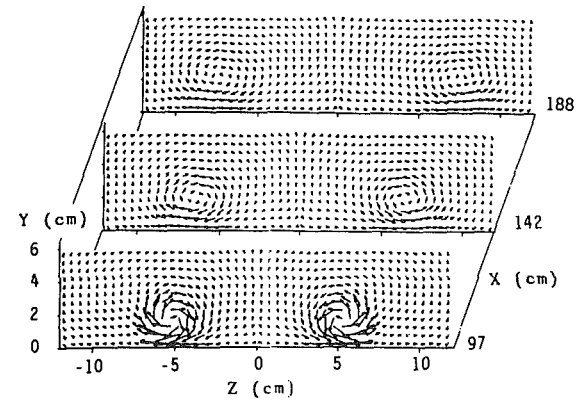

Fig. 3(b)

Fig. 3 Vector plots of secondary flow at different cross sections demonstrating transport and extent of the vortices.
(a) Experimental data of Pauley and Eaton; (b) computed results

generators (Fiebig et al., 1989). In the present work, this procedure has been extended to solve turbulent problems.

The SOLA algorithm solves the time dependent Navier–Stokes equations directly for the primitive variables by advancing the solution explicitly in time. The modification used here retains the solution route of the SOLA algorithm; an explicit time step for the momentum equations is followed by an implicit, iterative pressure and velocity upgrading. Since the flow field is uncoupled from the temperature field, they are determined in the following four steps:

1) A new velocity field is determined for the new time step from the momentum equations with use of velocity, turbulence variables (k and ϵ) and pressure at the old time;
2) The updated velocity field is corrected to obtain the pressure field at the new time step by an iterative procedure with aid of continuity equation until a divergence free velocity field is reached within a prescribed tolerance;
3) The fields of turbulence variables are updated using their old time values and velocity field at the new time step;

SOLA is a time-marching method which can compute both unsteady and steady flows. The solution of the steady Navier–Stokes equations are obtained when the time gradients of the dependent variables become negligibly small. Then the computation is declared to converge to the steady solution. In this work as the convergence criterion for steady flow the maximum time gradient of dependent variables $\max\{\Delta f/\Delta t\}$ in the whole computational domain has been considered. Here Δf denotes the iteration difference of the dependent variables between two consecutive time levels and Δt denotes the advancing time step, respectively. For a converged (i.e., steady) solution the $\max\{\Delta f/\Delta t\}$ is chosen to be less than 10^{-3}.

In order to determine the time step Δt numerical stability conditions for advective and diffusive flows have been considered and the time steps Δt have been calculated from the allowable Courant number and the diffusion number in the whole domain, see Hirt et al. (1975). The lowest value of thus obtained Δt multiplied by a safety factor (0.5) has been used for the explicit time-marching of the momentum equations. The chosen nondimensional Δt generally lies between 10^{-2} and 10^{-3}. If as convergence criterion Δt is used instead of $(\Delta f/\Delta t)$ this Δf in present calculations will lie between 10^{-5} and 10^{-6}. Since only steady flow results are obtained, the influence of Δt on the computations is of no importance.

The numerical mesh for the computational domain comprised of $70 \times 15 \times 26$ grid nodes in the x, y, and z directions. The CPU run time for the present simulation on a SUN 4/260 workstation is 1627 min. This corresponds to 0.0011 CPU sec for 1 grid point/iteration on this computer.

A great difficulty in turbulent flow computation is to assess and to attribute errors arising from the turbulence models and from the numerical approximation of the governing equations. Seldom the error in a numerical solution can be accurately evaluated. For assessing the accuracy of turbulence models, grid refinement is usually employed to reduce numerical error. However, it is always very costly. The grid-independency of the numerical simulation could not be studied in this work because of the limited computer capacity. However, computations in a similar geometry for laminar flows with grids of $13 \times 13 \times 13$, $26 \times 26 \times 26$ and $52 \times 52 \times 52$ have been carried out and grid independent average Nusselt number and apparent friction factor on the fin have been obtained by Richardson extrapolation. Results show that these grid independent qualities differ from the corresponding coarse grid value by less than 15 percent and from the fine grid value by less than 3 percent, see Güntermann (1992).

Results and Discussion

The flow is simulated for a Reynolds number of $Re_{H/2} = 67000$, based on half height of the channel. The experimental data of Pauley and Eaton (1988) and the numerical prediction are compared in Fig. 3 to Fig. 7.

Pauley et al. determined that the uncertainty in their mean velocity measurements was within 5 percent (1988 a, p. 60).

The postprocessing of both the experimental data and the computational results are performed with a program developed by the authors' group. Vector plots of the secondary flow and streamwise velocity and vorticity contours are shown in Fig. 3, Fig. 4, and Fig. 5, respectively, where the experimental data are presented in (*a*) and the computed results in (*b*).

The secondary velocity vectors in Fig. 3 provide a view of the vortex transport in the flow and the secondary flow strength and its decay in the different regions of the cross sections. A qualitative good agreement can be confirmed by comparing the experimental data and the numerical results in Fig. 3. The strength of the secondary flow in the vortex core, however, is under predicted.

In Fig. 4 (*a*) isolines of the streamwise velocity illustrate the strong interaction between the vortices and the boundary layer. The boundary layer is thinned in the downwash region where the secondary flow is directed towards the wall and thickened in the upwash region where the secondary flow is directed away from the wall. The vortices diverge as they move downstream, producing an ever widening region of boundary layer thinning between them. As indicated in Fig. 4 (*b*), all these essential

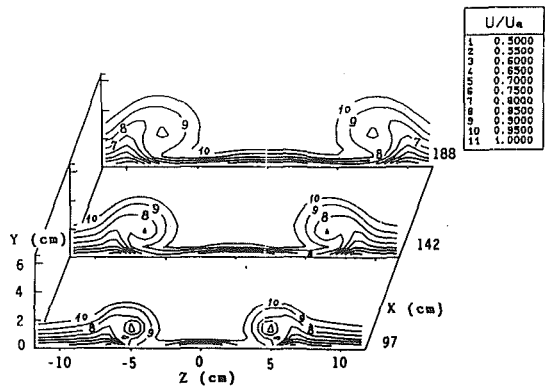

Fig. 4(*a*)

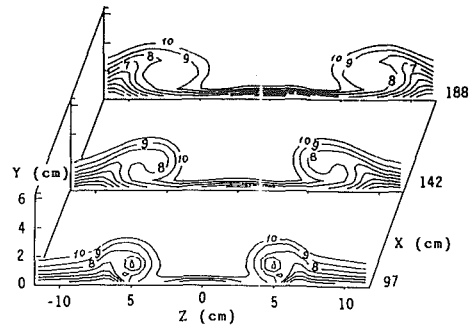

Fig. 4(*b*)

Fig. 4 Contours of streamwise velocity at different cross sections showing the interaction between the vortices and the boundary layer. (*a*) Experimental data of Pauley and Eaton; (*b*) computed results

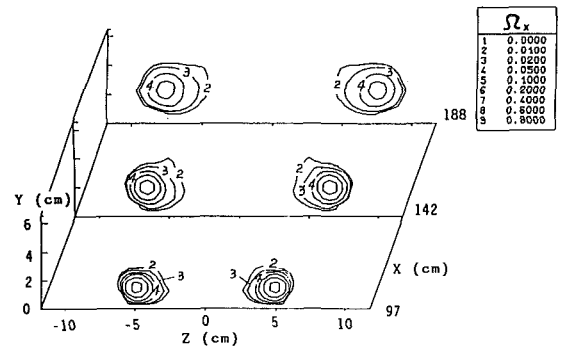

Fig. 5(*a*)

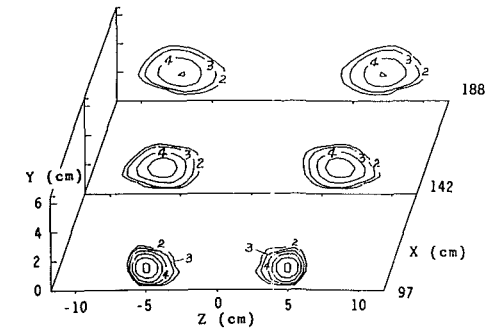

Fig. 5(*b*)

Fig. 5 Contours of streamwise vorticity at different cross sections showing positions of the vortex core and the decay of the peak vorticity. (*a*) Experimental data of Pauley and Eaton; (*b*) computed results

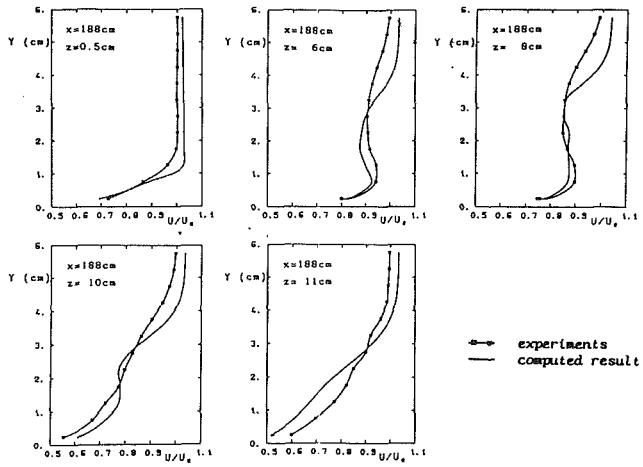

Fig. 6 Streamwise velocity profiles at axial station $x = 142$ cm.
experimental data of Pauley and Eaton
computed results

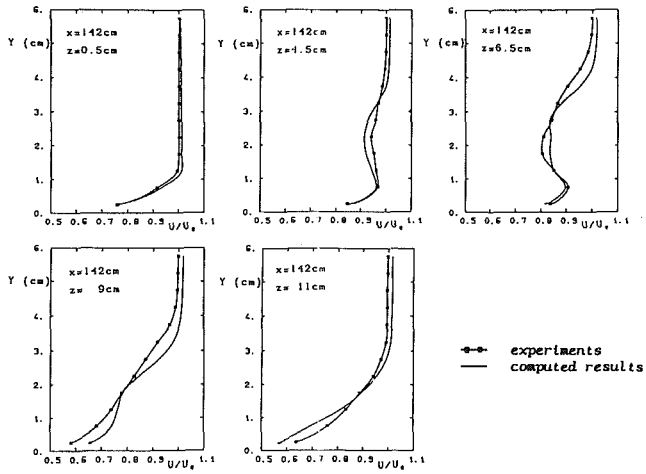

Fig. 7 Streamwise velocity profiles at axial station $x = 188$ cm.
experimental data of Pauley and Eaton
computed results

phenomena of the flow field are also captured by the simulation.

The structure and strength of the longitudinal vortices are demonstrated by the contours of streamwise vorticity Ω_x in Fig. 5. The streamwise vorticity is defined as

$$\Omega_x = \frac{\partial W}{\partial y} - \frac{\partial V}{\partial z} \tag{12}$$

A comparison between (*a*) and (*b*) of Fig. 5 reveals that the decay of the peak vorticity in the center of the vortex is faster in the computation than in the experiments. On the other hand, Fig. 5 shows that the positions of the vortex core at the two downstream cross sections $x = 142$ cm and $x = 188$ cm are well predicted.

The flattening of the vortex shape at the two downstream sections is more prominent in the numerical simulation than in the experiments. This is supposed to be a consequence of the used zero normal convection condition at the boundary plane II.

Figures 6 and 7 compare the computed and experimental profiles of normalized streamwise velocity at five spanwise locations. In Fig. 6 the five spanwise locations at $z = 0.5$, 4.5, 6.5, 9.0, and 11 cm represent the central region, downwash region, region of vortex core, upwash region, and outer vortex

region of the cross section at $x = 142$ cm, while in Fig. 7 the spanwise locations at $z = 0.5$, 6, 8, 10, and 11 cm stand for these five regions of the cross section at $x = 188$ cm.

In the central region ($z = 0.5$ cm) of the cross section at $x = 142$ cm, where the boundary layer is thinned significantly by the lateral divergence of the vortices (see Fig. 4), the velocity profile shows a usual two-dimensional distribution and is well predicted by the computation. In the vortex core ($z = 6.5$ cm) the boundary layer is strongly distorted and the streamwise velocity deficit is not correctly reproduced by the simulation (4 percent deviation). Below the vortex core (at $y = 0.25$ cm, 0.75 cm, 1.25 cm) a good agreement is observed. At the spanwise location $z = 9$ cm (upwash region) a large deviation (12.9 percent) is found in the vicinity of the wall. Similar behavior is observed at the axial station $x = 188$ cm (Fig. 7). The largest deviation (13 percent) of computed streamwise velocity from the experimental data of Pauley and Eaton (1988 a) appears at the position $x = 188$ cm, $y = 0.25$ cm, $z = 11$ cm.

Concluding Remarks

Although k-ϵ model is questionable for highly vortical flows, the comparison between measurements of Pauley and Eaton (1988a,b) and present computed results for the mean velocity field shows that the interaction of the longitudinal vortices with the boundary layer within a turbulent channel flow is captured qualitatively correctly by the numerical simulation. Agreement with the measured data to within 13 percent is achieved at the worst location. The root mean square deviation between predicted mean streamwise velocity and measured data is 3.6 percent. In general, the prediction is very good where the boundary layer is not severely distorted by the vortices. In regions where there is significant secondary flow the simulation does not accurately reproduce the velocity distribution.

Acknowledgment

J. X. Zhu is glad to acknowledge the scholarship of German Aerospace Research Establishment (Deutsche Forschungsanstalt für Luft- und Raumfahrt). Thanks go also to Prof. John K. Eaton for providing their data tape for the comparison of the results.

References

Edwards, F. J., and Alker, C. J. R., 1974, "The Improvement of Forced Convection Surface Heat Transfer Using Surface Protrusions in the Form of (A) Cubes and (B) Vortex Generators," *Proceedings of the 5th International Heat Transfer Conference*, Vol. 2, pp. 244–248.

Fiebig, M., Kallweit, P., and Mitra, N. K., 1986, "Wing Type Vortex Generators for Heat Transfer Enchancement," *Proceeding of the 8th International Heat Transfer Conference*, Vol. 6, pp. 2909–2914.

Fiebig, M., Brockmeier, U., Mitra, N. K., and Güntermann, Th., 1989, "Structure of Velocity and Temperature Fields in Laminar Channel Flows with Longitudinal Vortex Generators," *Numerical Heat Transfer*, Part A, Vol. 15, pp. 281–302.

Güntermann, Th., 1992, Dreidimensionale stationäre und selbsterregt schwingende Strömungs- und Temperaturfelder in Hochleistungsübertragern mit Wirbelerzeugern, Dissertation, Institut für Thermo- und Fluiddy-namik, Ruhr-Universität Bochum, Germany, p. 138.

Hirt, C. W., Nichols, B. D., and Romero, N. C., 1975, "SOLA—A Numerical Solution Algorithm for Transient Fluid Flows," Los Alamos Scientific Laboratory Rept. LA-5652, Los Alamos, NM.

Launder, B. E., and Spalding, D. B., 1974, "The Numerical Computation of Turbulent Flows," *Computational Methods for Applied Mechanics and Engineering*, Vol. 3, pp. 269–289.

Pauley, W. R., and Eaton, J. K., 1988 a, "The Fluid Dynamics and Heat Transfer Effects of Streamwise Vortices Embedded in a Turbulent Boundary Layer," Rept. MD-51, Thermosciences Division, Department of Mechanical Engineering, Stanford University.

Pauley, W. R., and Eaton, J. K., 1988 b, "Experimental Study of the Development of Longitudinal Vortex Pairs Embedded in a Turbulent Boundary Layer," *AIAA Journal*, Vol. 26, No. 7, pp. 816–823.

Hydraulic Forces Acting on a Circular Cylinder With Surface Source of Minute Air Bubbles and Its Cavitation Characteristics

A. Ihara
Associate Professor.

Hideo Watanabe
Research Associate.

Hiroyuki Hashimoto
Professor.

Institute of Fluid Science,
Tohoku University,
Sendai, Japan

Experiments are performed by using two circular cylinders made of porous filter material, that is, bronze sintered compact, with a different filter size, respectively, in a water tunnel. The effects of minute air bubbles injected from the surface of the circular cylinder into its boundary layer on its hydraulic force characteristics are investigated over the Reynolds number $(1.2 \sim 4.2) \times 10^5$*, changing the airflow rate of bubble injection. The pressure distributions on the porous cylinders are also measured. Their cavitation characteristics are studied, too. Compared with a smooth-surface cylinder, the critical Reynolds numbers of the porous cylinders decrease owing to the increase in the surface roughness caused by the bronze particles which compose the sintered compact. The effects of the bubble injection on the hydraulic force characteristics are different according to the size of the bronze particles. Though a little difference is recognized, the hydraulic force characteristics show a similar tendency in both cases of bubble injection and cavitation occurrence.*

Introduction

The effect of air bubbles introduced into a free stream of water past a circular cylinder on the hydraulic forces has been studied by Yokosawa et al. (1986) and Watanabe et al. (1990). A large reduction in the drag coefficient and a change of the pressure distribution were detected in the low critical flow range, even if a very small quantity of air bubbles were introduced (Watanabe et al., 1990). This could be attributed to earlier transition in the boundary layer. Such a remarkable effect cannot be found in the supercritical flow range, because the form drag occupies the most part of the total drag. It is very difficult for bubbles to approach the immediate vicinity of the model surface when the bubbles are introduced into the main stream. Instead, we can expect the greater influence on the hydraulic force acting on a test body if the bubbles are injected under the boundary layer. As the authors are aware, nobody has reported the hydraulic characteristics or phenomena when the air bubbles are injected from the model surface. The purpose of this research is to investigate the hydraulic characteristics acting on the test body with surface injection of air bubbles and to compare the results with those obtained in cavitating conditions, because the phenomena caused by air injection has been found to be similar to those caused by cavitation (Silberman and Song, 1961).

Circular cylinders are selected as a test model because we can easily get the suitable materials to make the test model. They are made of porous filter material, that is, bronze sintered compact, each with a different filter size. Experiments are conducted over the Reynolds number $1.2 \times 10^5 \sim 4.2 \times 10^5$.

Experimental Equipment

Water Tunnel. The water tunnel, which is described in detail by Murai and Ihara (1986), is of closed-return type and has a square test section have a height of 305mm and a width of 100mm as shown in Fig. 1. This water tunnel has a large reservoir (4m in diameter and 6m in height) to remove air bubbles contained in working water and thus the air bubbles injected from the surface of a test cylinder scarcely return to the test section. The velocity profile at the mid-height of the test section has been found to be uniform within the range of ± 0.3 percent outside the boundary layers on both side walls when measured via Pitot traverse method. The thickness of the boundary layer is about 5mm on each side wall. The turbulence intensity in the direction of the free stream is about 0.1 percent at 10.0m/s. The force coefficient and the local pressure coefficient are calculated in terms of an average velocity over the full span of the test section and the velocity outside the boundary layers, respectively. The temperature of the water ranges from 295 K to 302 K.

Test Circular Cylinders and Force Balance. Three circular cylinders are prepared. Each has a diameter d = 30mm and a length l = 100mm. Their aspect ratio and blockage ratio are about 3.3 and 0.1, respectively. The first is a smooth-surface cylinder, made of brass, with a surface average height of 0.2μm

Contributed by the Fluids Engineering Division for publication in the JOURNAL OF FLUIDS ENGINEERING. Manuscript received by the Fluids Engineering Division July 23, 1991; revised manuscript received January 9, 1993. Associate Technical Editor: A. Prosperetti.

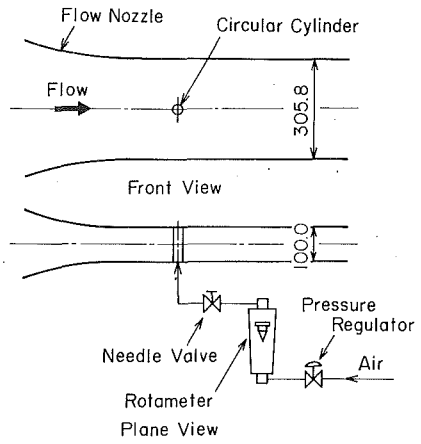

Fig. 1 Schematic diagram of the test section and control system of airflow rate

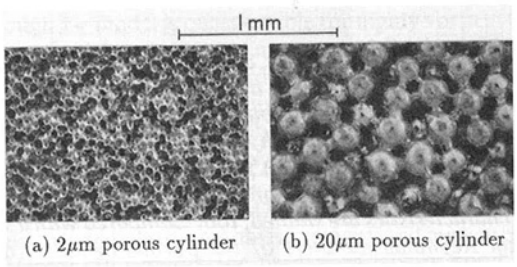

Fig. 2 Surface construction of the sintered bronze compact. (*a*) 2μm porous cylinder; (*b*) 20μm porous cylinder

after polished. The other two circular cylinders are of bronze sintered compact, available as a filter material. They have wall thickness of 2mm and nominal filter size of 2μm and 20μm, respectively. Hereafter, they will be called 2μm porous cylinder and 20μm porous cylinder, respectively.

The surface construction of the bronze sintered compact is shown in Fig. 2. From the measurements with a microscope, the mean diameter of the bronze particles which compose each cylinder is estimated to be $(50 \pm 3)\mu$m and $(200 \pm 20)\mu$m, respectively. The porosity of the bronze sintered compact is about 35 percent for both cylinders. Its permeability is about 5 darcys

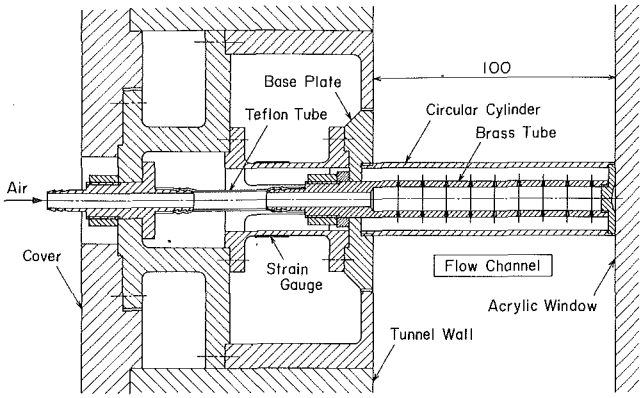

Fig. 3(*a*) For the measurement of force

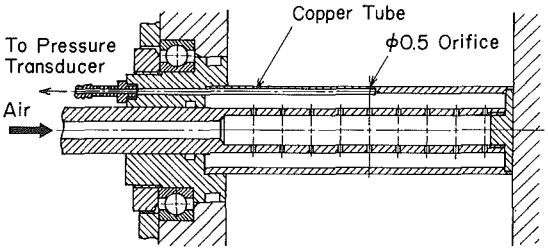

Fig. 3(*b*) For the measurement of surface pressure distribution

Fig. 3 Detail drawing of a porous cylinder

(0.5×10^{-7}cm^2) for the 2μm porous cylinder and about 20 darcys (2.0×10^{-7}cm^2) for the 20μm porous cylinder.

Two models are prepared for each cylinder; one for the force measurement (Fig. 3(*a*)) and the other for the measurement of surface pressure distribution (Fig. 3(*b*)). As shown in Fig. 3, a brass tube is inserted into the porous cylinder to reinforce it, serving to introduce compressed air as well. The compressed air is sent out into the boundary layer through pores in the porous wall in the form of minute air bubbles. The airflow rate is measured with a rotameter as shown in Fig. 1.

The force acting on the test cylinder is measured with a cantilever force balance of strain-gauge type, as shown in Fig. 3(*a*). The balance fitted with the test cylinder has a resonant frequency of about 340Hz for the 2μm porous cylinder, 360Hz

Nomenclature

A = frontal area of a circular cylinder normal to the direction of an undisturbed flow = ld (m^2)
C_D = drag coefficient = $2D/(\rho U_\infty{}^2 A) = C_{D\text{mean}} + C_D'$
C_L = lift coefficient = $2L/(\rho U_\infty{}^2 A) = C_{L\text{mean}} + C_L'$
C_p = pressure coefficient = $2(p - p_\infty)/(\rho U_\infty{}^2)$
C_Q = volumetric airflow ratio = Q_∞/AU_∞
D, L = drag, lift (N)
d = diameter of a circular cylinder (m)
f = peak frequency of fluctuating lift (Hz)
k_s = Nikuradse's sand-grain roughness (m)
l = length of a circular cylinder (m)
p = static pressure on the model surface at θ (N/m^2)
p_v = vapor pressure of water (N/m^2)
p_∞ = undisturbed pressure (N/m^2)
Q_∞ = volumetric airflow rate at p_∞ and T_∞ (m^3/s)
Re = Reynolds number = $U_\infty d/\nu$
St = reduced peak frequency of fluctuating lift = fd/U_∞
T_∞ = undisturbed temperature of water (K)
U_∞ = undisturbed flow velocity (m/s)

Greek symbols

ν = kinematic viscosity of water (m^2/s)
ρ = density of water (kg/m^3)
θ = azimuthal angle measured from the forward stagnation point (deg.)
σ = cavitation number = $2(p_\infty - p_v)/(\rho U_\infty^2)$

Subscripts

mean = mean value
min = minimum value
i = inception of cavitation
RMS = root-mean-square value of a fluctuating component

Others

$'$(prime) = fluctuating component

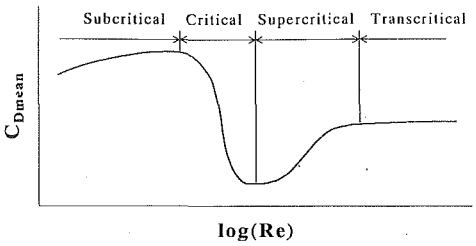

Fig. 4 Definition of flow range around a circular cylinder

for the 20μm porous cylinder and 400Hz for the smooth-surface cylinder in free space.

The cylinder for the measurement of the pressure distribution has an orifice of 0.5mm in diameter on its surface located at the center of its span, as shown in Fig. 3(*b*). It can be turned freely around its longitudinal axis. The orifice is made in the porous wall of the cylinder. Owing to the permeability of the porous material, the effective diameter of the orifice has a possibility to be different from the geometric one. The detected pressure could contain the effects of the pressure surrounding the orifice. We regard, however, that the detected pressure should primarily show the mean pressure at the orifice. The pressure is led to a differential pressure transducer of strain-gauge type through a fine copper tube (1.5mm outside diameter, 0.7mm inside diameter) buried in the wall of the cylinder.

The permeability of the porous material will also affect the hydraulic characteristics of the cylinder owing to a flow of water through the porous wall. A brief description on this problem is given in Appendix A. Correction for the effect of the interference of the tunnel walls is not performed. Further test descriptions such as tunnel velocity, tunnel pressure measurements, and data analysis are given by Murai and Ihara (1986), Ihara (1986), and Watanabe et al. (1990). The experimental uncertainties quoted in the figure captions have been obtained by the method of ANSI/ASME standards (ANSI/ASME PTC 19.1, 1985).

Results and Discussions

In the following, the flow range around the circular cylinders will be divided into four parts, as shown in Fig. 4, based on the curve representing the drag coefficient as a function of Reynolds number. This depends on the definition of Roshko (1961).

Fully Wetted Characteristics of Hydraulic Forces. In order to make a comparison, the mean drag coefficients C_{Dmean} and the reduced peak frequencies St of the fluctuating lift against the Reynolds number Re in fully wetted conditions are measured and shown in Fig. 5.

Critical Reynolds numbers of the porous cylinders decrease owing to the effect of the increased surface roughness caused by the bronze particles. For the 2μm porous cylinder, it is noted that the critical flow range lies over $Re \simeq 1.2 \sim 1.6 \times 10^5$ and the supercritical flow range over $Re \simeq 1.6 \sim 4.2 \times 10^5$.

Achenbach (1971) investigated the influence of surface roughness on the cross flow around a circular cylinder. His results, uncorrected for blockage effects, for the roughness parameters of $k_s/d = 900 \times 10^{-5}$, 450×10^{-5} and 110×10^{-5} are also shown as solid bold curves in Fig. 5(*a*). In our case, the mean diameter of the bronze particles which compose the 2μm porous cylinder is about 50μm, which results to a roughness parameter $k_s/d \simeq 170 \times 10^{-5}$ if the equivalent roughness to the sand-grain is assumed to be the diameter of the bronze particle. Compared with Achenbach's result of $k_s/d = 110 \times 10^{-5}$, this estimation of k_s/d is considered reasonable as shown in Fig. 5(*a*).

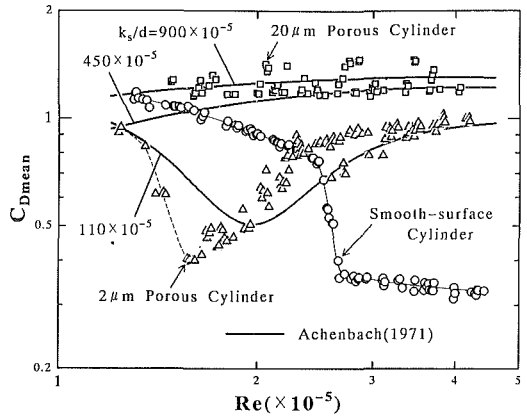

Fig. 5(*a*) C_{Dmean}

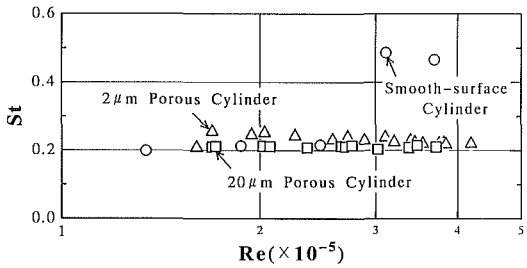

Fig. 5(*b*) St of fluctuating lift

Fig. 5 C_{Dmean} and St of fluctuating lift of test circular cylinders (Uncertainty in Re = $\pm 0.04 \times 10^5$, in C_{Dmean} = ± 0.05, in St = ± 0.01)

The mean drag coefficients C_{Dmean} of the 20μm porous cylinder ($C_{Dmean} \approx 1.2 \sim 1.4$) are larger than those of other test cylinders and scarcely change with Re. This indicates that the flow past the 20μm porous cylinder is in the transcritical flow range over the entire range of these measurements. It can be seen from Fig. 5(*a*) that the roughness parameter k_s/d of the 20μm porous cylinder lies between 450×10^{-5} and 900×10^{-5} from the comparison with the Achenbach's measurements. The result is reasonable, too, because the bronze particle of the 20μm porous cylinder has a diameter of about 200μm, which corresponds to $k_s/d \simeq 670 \times 10^{-5}$. From these, it can be concluded that the estimation of the surface roughness in terms of the grain size is appropriate.

A reduced peak frequency, St, obtained from the auto-power spectra of C_L' is plotted in Fig. 5(*b*). For the smooth-surface cylinder, St is about 0.2 in the subcritical flow range and 0.5 in the supercritical flow range. These values are almost coincident with those obtained by Schewe (1983) in a wind tunnel. The reduced peak frequency St of the 2μm porous cylinder at $Re \simeq 2.0 \times 10^5$ is about 0.25, which is larger than the value of the smooth-surface cylinder. It decreases with an increase in Re and asymptotically reaches the value of the smooth-surface cylinder in the subcritical flow range. On the other hand, St of the 20μm porous cylinder remains constant and almost agrees with the value measured by Schewe (1983) for the smooth-surface cylinder in the transcritical flow range. The peak in the auto-power spectra of C_L' is very distinct.

Root-mean-square (RMS) values of C_L' and C_D', denoted by $C_{L_{RMS}}'$ and $C_{D_{RMS}}'$ respectively, increase with an increase in the nominal filter size, that is, surface roughness.

Effects of Air Injection on Hydraulic Forces and Pressure Distributions. Figures 6 and 7 show the hydraulic force characteristics for the porous cylinders versus the non-dimensional airflow rate C_Q at $Re \simeq 2.0 \times 10^5$ and 3.4×10^5. Typical bubble flow visualization around the 2μm porous cylinder are shown

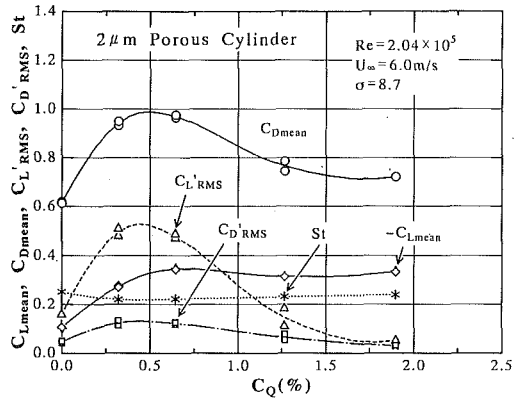

Fig. 6(*a*) Re ≃ 2.04 × 10^5

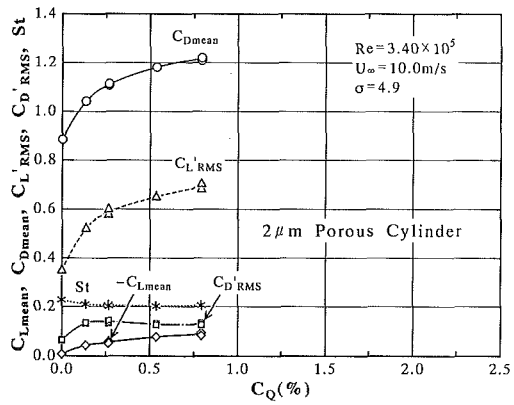

Fig. 6(*b*) Re ≃ 3.40 × 10^5

Fig. 6 Hydraulic force characteristics of the 2μm porous cylinder with air injection (Uncertainty in C_Q = ±0.1, in C_{Lmean}, C_{Dmean} = ±0.05, in St = ±0.01)

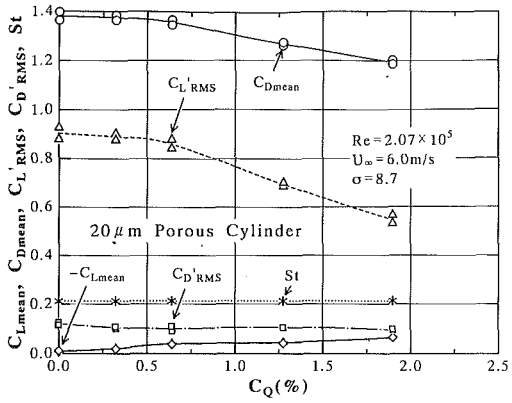

Fig. 7(*a*) Re ≃ 2.07 × 10^5

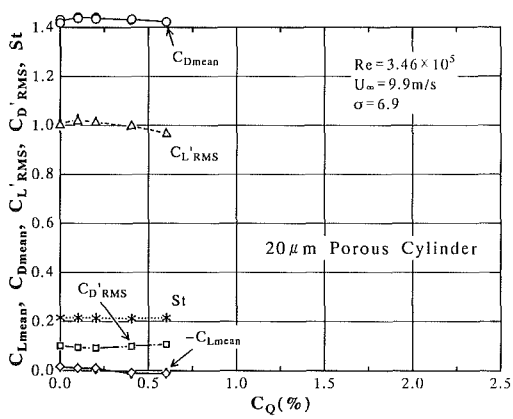

Fig. 7(*b*) Re ≃ 3.46 × 10^5

Fig. 7 Hydraulic force characteristics of the 20μm porous cylinder with air injection (Uncertainty in C_Q = ±0.1, in C_{Lmean}, C_{Dmean} = ±0.05, in St = ±0.01)

in Fig. 8. The corresponding pressure distributions are shown in Figs. 9 and 10.

2μm Porous Cylinder. At $\mathrm{Re} \simeq 2.04 \times 10^5$ (Fig. 6(*a*)), where the fully wetted flow is regarded to be in the middle of the supercritical flow range according to the experimental curve in Fig. 5(*a*), $C_{D\mathrm{mean}}$, $C'_{L_{\mathrm{RMS}}}$, and $C'_{D_{\mathrm{RMS}}}$ increase with airflow rate until they reach their maxima at $C_Q \simeq 0.6$ percent and then decrease gradually. On the other hand, St scarcely varies with airflow rate. As shown in Fig. 8, air bubbles are much distributed in the upper part of the wake by buoyancy on the bubbles because of the low flow velocity ($U_\infty \simeq 6.0$m/s). The wetted area on the lower surface of the cylinder is larger than that on the upper surface, and a relatively large downward lift, such as $C_{L\mathrm{mean}} \simeq -0.3$, is detected. The air bubbles are observed to flow out in the neighborhood of the minimum pressure regions.

The pressure distributions around this Reynolds number are shown in Fig. 9(*a*). Each curve corresponds to C_Q = 0.0 percent, $C_Q \simeq 0.6$ percent at which $C_{D\mathrm{mean}}$ is maximum, and $C_Q \simeq 1.3$ percent at which $C_{D\mathrm{mean}}$ is in decrease. At C_Q = 0.0 percent, the separation bubble usually found on a smooth-surface cylinder in the supercritical flow range cannot be found. The flow separates at almost 105° from the forward stagnation point.

In the case of air injection, the pressure distribution on the upper surface is different with that on the lower surface, because of the asymmetry of the flow field due to the buoyancy effect described above. The difference becomes remarkable with an increase in C_Q.

In Fig. 9(*a*) it is indicated that the base pressure at $C_Q \simeq 0.6$ percent is much lower than that at other airflow rate. This fact explains why $C_{D\mathrm{mean}}$ takes a maximum at such an airflow rate.

At $\mathrm{Re} \simeq 3.4 \times 10^5$ (Figs. 6(*b*) and 9(*b*)) where the flow state at the fully-wetted condition is regarded to be in the upper supercritical flow range, $C_{D\mathrm{mean}}$ and $C'_{L_{\mathrm{RMS}}}$ are on the increase even if C_Q reaches its maximum. The reduced peak frequency St is almost constant for all airflow rates. The asymmetry in the flow between the upper and lower surfaces is improved slightly and the downward lift decreases. When air bubbles are injected, the average base pressure decreases less than that at the fully-wetted condition. The mean drag coefficient $C_{D\mathrm{mean}}$ increases as well as at $\mathrm{Re} \simeq 2.04 \times 10^5$. This explains why $C_{D\mathrm{mean}}$ at the fully wetted condition takes a lower value than those at the air injection.

20μm Porous Cylinder. In Fig. 7 are represented the force characteristics of the 20μm porous cylinder with air injection. At the fully wetted condition, both flow states will be transcritical as recognized from Fig. 5(*a*). In contrast with the 2μm porous cylinder, $C_{D\mathrm{mean}}$ and $C'_{L_{\mathrm{RMS}}}$ decrease monotonously with an increase in C_Q. The root-mean-square value of the fluctuating-drag coefficient $C'_{D_{\mathrm{RMS}}}$ and the reduced peak frequency St are almost independent on C_Q. The absolute value of $C_{L\mathrm{mean}}$ is small. The pressure distributions at $\mathrm{Re} \simeq 1.86 \times 10^5$ and 3.12×10^5 are shown in Fig. 10. The minimum pressure and the base pressure slightly decrease with an increase in Re. Achenbach (1971) has reported the pressure distribution of the circular cylinders with various surface roughness at various Reynolds numbers. Our pressure distributions measured with

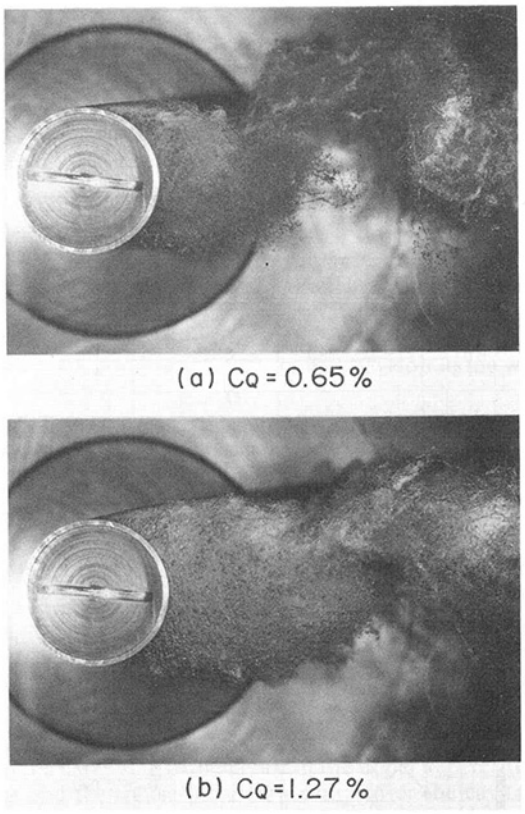

Fig. 8 Instantaneous photographs of the flow around the 2μm porous cylinder with air injection at Re $\simeq 2.04 \times 10^5$, $U_\infty \simeq 6.0$m/s, $\sigma \simeq 8.7$

the porous cylinders at the fully-wetted condition indicate the same tendency with his results for the effects of both the Reynolds number and surface roughness. In the case of air injection, the rise in the base pressure can be found at both Reynolds numbers, and gets higher as the airflow rate is progressively increased. This produces the change of C_{Dmean} as shown in Fig. 7.

In conclusion, in the transcritical flow range, in contrast with the supercritical flow range, the air injection induces the increase in the base pressure of the test cylinder, so that C_{Dmean} decreases.

Cavitation Characteristics of the Test Cylinders. The flow field around the test cylinder visualized by injected air bubbles and its hydraulic force characteristics are found to be quite similar to those observed by Ihara (1986) when cavitation occurs on a smooth-surface cylinder. This provided the motivation here to conduct cavitation tests in order to investigate the similarity between air injection and cavitation.

Surface irregularities can affect the fully-wetted boundary layer, and in turn the inception and development of cavitation. The effects of surface irregularities on cavitation characteristics of various test bodies have been studied by many investigators, e.g., Borden (1966), Holl (1960), Benson (1966), Numachi et al. (1965a and 1965b), Numachi (1967) and so on. As far as the present authors know, however, nobody has reported on the performance of a cavitating circular cylinder with large surface roughness.

The experiments are conducted in the range of the cavitation number σ from the fully-wetted condition to the one where the mean cavity length is almost the same with the length of the bubble filled region behind the test cylinder at the maximum C_Q. The Reynolds number Re selected for the test is $(3.43 \sim 3.66) \times 10^5$, and it corresponds to the supercritical flow range for the smooth-surface cylinder, upper supercritical one

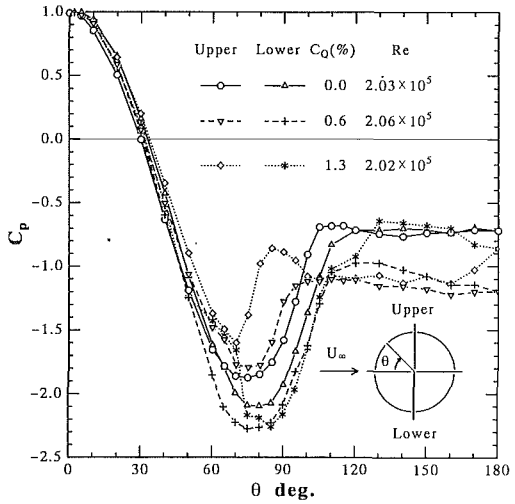

Fig. 9(*a*) Re $\simeq 2.04 \times 10^5$

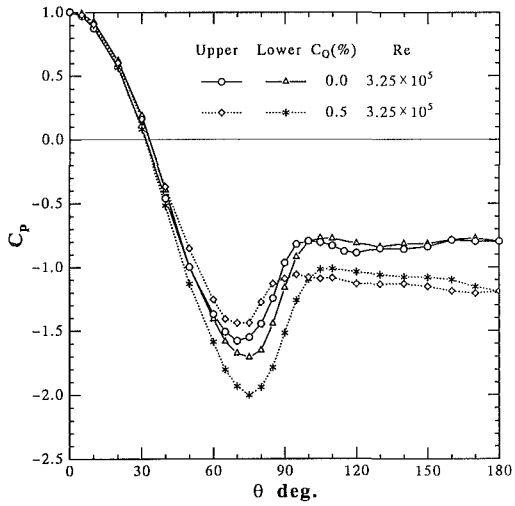

Fig. 9(*b*) Re $\simeq 3.25 \times 10^5$

Fig. 9 Pressure distribution around the 2μm porous cylinder (Uncertainty in $C_p = \pm 0.05$, in $\theta = \pm 0.5$ deg)

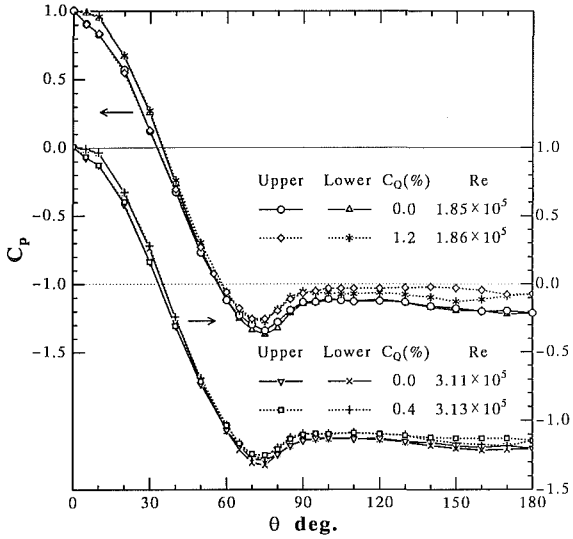

Fig. 10 Pressure distribution around the 20μm porous cylinder at Re $\simeq 1.86 \times 10^5$ and Re $\simeq 3.12 \times 10^5$ (Uncertainty in $C_p = \pm 0.05$, in $\theta = \pm 0.5$ deg)

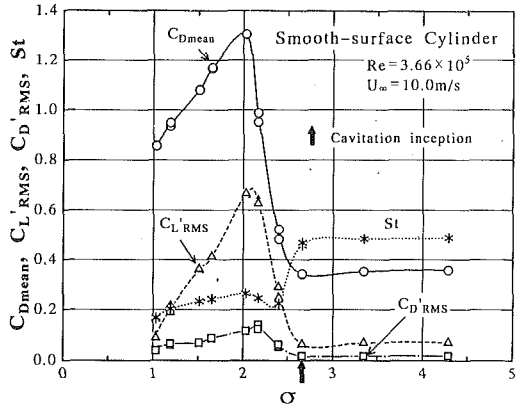

Fig. 11 Hydraulic force characteristics of the smooth-surface cylinder in cavitation at Re≃3.66 × 10^5 (Uncertainty in σ = ±0.05, in C_{Lmean}, C_{Dmean} = ±0.05, in St = ±0.01)

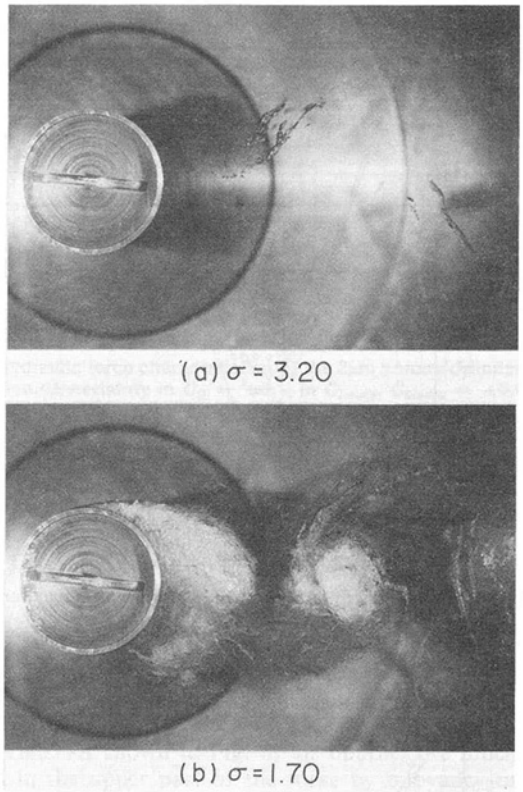

Fig. 12 Cavitation appearance on the 2μm porous cylinder at Re≃3.43 × 10^5, U_∞≃9.9m/s

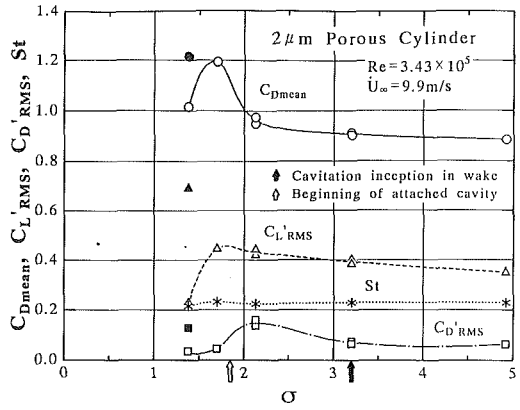

Fig. 13 Hydraulic force characteristics of the 2μm porous cylinder in cavitation at Re≃3.43 × 10^5. Full marks indicate C_{Dmean}, C'_{LRMS} and $C'_{D_{RMS}}$ in the case of air injection when the length of the air filled region is same with the cavity length at σ = 1.38. (Uncertainty in σ = ±0.05, in C_{Lmean}, C_{Dmean} = ±0.05, in St = ±0.01)

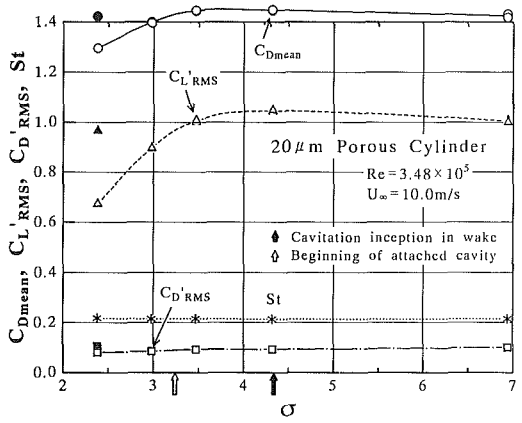

Fig. 14 Hydraulic force characteristics of the 20μm porous cylinder in cavitation at Re≃3.48 × 10^5. Full marks indicate C_{Dmean}, $C'_{L_{RMS}}$ $C'_{D_{RMS}}$ in the case of air injection when the length of the air filled region is same with the cavity length at σ = 2.38 (Uncertainty in σ = ±0.05, in C_{Lmean}, C_{Dmean} = ±0.05, in St = ±0.01)

for the 2μm porous cylinder and transcritical for the 20μ porous cylinder at the fully-wetted condition.

Smooth-Surface Cylinder. The cavitation characteristics are shown in Fig. 11. Cavitation inception is indicated by the appearance of a line, very fine and white, on each upper and lower surface of the circular cylinder along the spanwise direction at a cavitation number σ≃2.7. The location of this line is at an azimuthal angle of almost 100° from the forward stagnation point. When we consider the results reported by Ihara and Murai (1986), this inception point should be the reattachment point of the separated boundary layer. As σ decreases the cavitation continues to develop. The variation of the force characteristics and the cavity appearance with σ coincide well with that reported by Ihara (1986).

2μm Porous Cylinder. Unlike the case of the smooth-surface cylinder, cavitation appears first not on the cylinder surface but in its wake, as shown in Fig. 12(*a*). With a decrease in σ it develops further, and the cavitating zone in the wake begins to alternately attach to and separate from the rear surface of the cylinder. As σ decreases further, the cavity steadily attached to the cylinder (Fig. 12(*b*)). The cavitation characteristics are shown in Fig. 13.

The incipient cavitation number σ_i is about 3.2 which is much larger than $|C_{p_{min}}| = 1.7$ or 1.6. The mean drag coefficient C_{Dmean} does not increase soon after inception, but does so after the attached cavity is formed behind the cylinder. Compared with the smooth-surface cylinder, the variations of C_{Dmean} and $C'_{L_{RMS}}$ with σ has the same tendency but are relatively moderate. $C'_{D_{RMS}}$ reaches its maximum when the cavity begins to alternate between attaching to and separating from the cylinder.

20μm Porous Cylinder. The cavitation characteristics at Re≃3.48×10^5 are shown in Fig. 14. Cavitation incepts in the wake as well as the 2μm porous cylinder. The incipient cavitation number σ_i is about 4.3, which is much higher than that of the 2μm porous cylinder and $|C_{p_{min}}| \simeq 1.3$. This result means that the shearing stress in the wake behind the 20μm porous cylinder is higher than that behind the 2μm porous cylinder. The mean drag coefficient C_{Dmean} and the root-mean-square value of the fluctuating-lift coefficient $C'_{L_{RMS}}$ gradually de-

crease as σ decreases. The reduced peak frequency St and the root-mean-square value of the fluctuating-drag coefficient $C'_{D_{RMS}}$ are almost constant for σ. The reason of the decrease in $C_{D\text{mean}}$ with a decrease in σ is probably the same with that in the case of air injection.

Comparison With Air Injection and the Effect of Surface Roughness. For the 2μm porous cylinder $C_{D\text{mean}}$ and $C'_{L_{RMS}}$ begin to increase rapidly soon after the air injection starts but they do not begin to increase after the cavitation inception. This difference is probably caused by the difference in the distribution of the air bubbles and cavitation bubbles. In the case of air injection, the air bubbles are distributed over the model surface but cavitation bubbles develop in the wake, far behind the model surface.

As shown in Fig. 13, $C'_{L_{RMS}}$ and $C'_{D_{RMS}}$ indicate larger values in air injection than in cavitation when the length of the air filled region is almost the same with the cavity length. The reduced peak frequencies St indicate almost the same value in both cases and are independent on C_Q and σ.

In the case of the 20μm porous cylinder, both an increase of C_Q and a decrease of σ cause $C_{D\text{mean}}$ and $C'_{L_{RMS}}$ to decrease monotonously after the attached cavity is formed. However, as shown in Fig. 14, $C_{D\text{mean}}$ and $C'_{L_{RMS}}$ indicate larger values in air injection than in cavitation when the length of the air filled region is almost the same with the cavity length.

As stated above, the variations of the hydraulic force with C_Q and σ show similar behavior in the upper supercritical flow range and the transcritical flow range after the cavitation attached to the model surface. Both the air bubbles and cavitation bubbles are supplied at the location of the minimum static pressure on the model surface. Therefore, similar flow fields are formed around the test model in both cases.

The effects of the surface roughness on cavitation of the circular cylinder in the range Re = $1.2\times10^5 \sim 4.2\times10^5$ are very complicated. At a fixed Reynolds number within this range, the surface roughness changes the static pressure distribution on the surface of the test cylinder at the fully wetted condition. Similarly, the appearance of cavitation and its characteristics depend heavily on the surface roughness. For example, at a fixed subcritical flow range, surface roughness can induce a pressure distribution reminiscent of transcritical or upper supercritical flow range over a smooth-surface cylinder. As a result, the hydraulic force characteristics in cavitating conditions are disparate as shown in Figs. 11, 13, and 14 even if the Reynolds numbers are almost same. We therefore conclude that the surface roughness considerably influences the cavitation appearance and the hydraulic forces in cavitating conditions.

Conclusions

The effects of surface source of minute air bubbles on the hydraulic forces acting on a circular cylinder are studied by using porous cylinders over the Reynolds numbers range $1.2\times10^5 \sim 4.2\times10^5$. The pressure distributions around the porous cylinders are presented. Cavitation characteristics of the same models are also studied. The main results obtained from these measurements can be summarized as follows:

1. In the supercritical flow range,
   (*a*) The surface roughness eliminates the separation bubble on the circular cylinder and cavitation incepts in the wake.
   (*b*) The mean drag coefficient $C_{D\text{mean}}$ and the root-mean-square values of the fluctuating-force coefficients, $C'_{L_{RMS}}$ and $C'_{D_{RMS}}$, are increased by the injected air bubbles until they reach their maximum and then are decreased gradually with an increase in airflow rate.
   (*c*) Such a change is caused mainly by the change of the base pressure of the test cylinder.
   (*d*) Natural cavitation causes similar hydraulic force characteristics as stated in conclusion 1(*a*) after attached cavitation is formed behind the circular cylinder.
2. In the transcritical flow range, $C_{D\text{mean}}$ and $C'_{L_{RMS}}$ decrease gradually with both an increase in airflow rate and a decrease in cavitation number after the attached cavitation is formed behind the circular cylinder.
3. The surface roughness changes the pressure distribution considerably around the test model within the range of the Reynolds number from 1.2×10^5 to 4.2×10^5. As a result, it influences the cavitation appearance and the force characteristics in cavitating condition.

Acknowledgment

The authors would very much like to express their thanks to Mr. Y. Yamabe and other staff of the factory of the Institute for their help in manufacturing the experimental equipment, and would also like to thank Mr. K. Asano for his help in processing the photographs.

References

Achenbach, E., 1971, "Influence of Surface Roughness on the Cross-Flow Around a Circular Cylinder," *Journal of Fluid Mechanics*, Vol. 46, pp. 321–335.

ANSI/ASME PTC 19.1, 1985, "Measurement Uncertainty."

Benson, B. W., 1966, "Cavitation Inception on Three Dimensional Roughness Elements," DTMB Report, No. 2104.

Borden, A., 1966, "Prediction of Cavitation Inception Speeds on Rough Hydrodynamic Bodies," *Proceedings of 6th Symposium on Naval Hydrodynamics*, Washington, D.C., Paper 8.

Holl, J. W., 1960, "The Inception of Cavitation on Isolated Surface Irregularities," ASME *Journal of Basic Engineering*, Vol. 82, pp. 169–183.

Ihara, A., 1986, "Effects of Yaw Angle to Unsteady Hydraulic Forces Acting on a Cavitating Circular Cylinder," *Proceedings of International Symposium on Cavitation*, Sendai, Japan, Vol. 1, pp. 145–150.

Ihara, A., and Murai, H., 1986, "Cavitation Inception on a Circular Cylinder at Critical and Supercritical Flow Range," ASME JOURNAL OF FLUIDS ENGINEERING, Vol. 108, pp. 421–427.

Murai, H., and Ihara, A., 1986, "Effects of Free Stream Velocity on Cavitation Performance of Hydrofoils in Accelerating Cascade," *Proceedings of International Symposium on Cavitation*, Sendai, Japan, Vol. 1, pp. 115–120.

Numachi, F., Oba, R., and Chida, I., 1965a, "Effects of Surface Roughness on Cavitation Performance of Hydrofoils, Report 1," ASME *Journal of Basic Engineering*, Vol. 87, pp. 495–503.

Numachi, F., Oba, R., and Chida, I., 1965b, "Effect of Surface Roughness on Cavitation Performance of Hydrofoils: Report 2," ASME *Symposium on Cavitation in Fluid Machinery*, G. M. Wood et al., ed., pp. 16–31.

Numachi, F., 1967, "Effect of Surface Roughness on Cavitation Performance of Hydrofoils: Report 3," ASME *Journal of Basic Engineering*, Vol. 89, pp. 201–209.

Roshko, A., 1961, "Experiments on the Flow Past a Circular Cylinder at Very High Reynolds Number," *Journal of Fluid Mechanics*, Vol. 10, pp. 345–356.

Schewe, G., 1983, "On the Force Fluctuations Acting on a Circular Cylinder in Crossflow from Subcritical up to Transcritical Reynolds Numbers," *Journal of Fluid Mechanics*, Vol. 133, pp. 265–285.

Silberman, E., and Song, C. S., 1961, "Instability of Ventilated Cavities," *Journal of Ship Research*, Vol. 5, No. 1, pp. 13–32.

Watanabe, H., Ihara, A., and Onuma, S., 1990, "Effects of a Few Small Air Bubbles on the Performance of Circular Cylinder at Critical Flow Range in Water," ASME JOURNAL OF FLUIDS ENGINEERING, Vol. 112, pp. 67–73.

Yokosawa, M. et al., 1986, "Studies on Two-Phase Cross Flow. Part II: Transition Reynolds Number and Drag Coefficient," *International Journal of Multiphase Flow*, Vol. 12, No. 2, pp. 169–184.

APPENDIX A

On the Effect of a Flow of Water Through the Porous Wall on the Hydraulic Characteristics of the Circular Cylinder

Our experimental technique of using the circular cylinders with a porous wall allows for water flow into and out of the cylinder due to the non-uniform pressure distribution. This

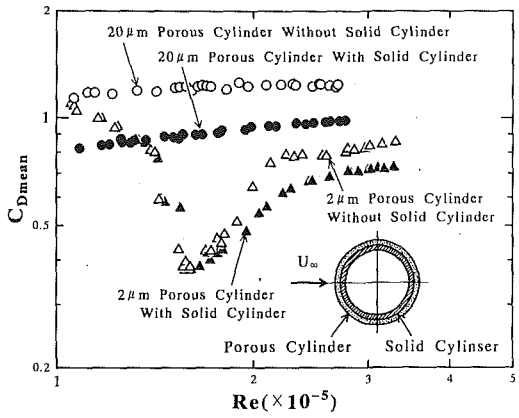

Fig. 15 Effect of a flow of water through the porous wall on C_{Dmean} of the test cylinders (Uncertainty in Re = $\pm 0.04 \times 10^5$, in C_{Dmean} = ± 0.05)

must have some effects on the hydraulic characteristics of the cylinder. Therefore, in order to investigate the effects of a flow of water through porous wall, we inserted another circular cylinder with a solid wall into the porous cylinder, as shown in Fig. 15, to prevent such a flow and measured the hydraulic forces. The mean drag coefficients C_{Dmean} are shown in Fig. 15 together with those obtained without the solid cylinder. They show clearly the influence of the water flow through the porous wall. It was also found by the pressure measurement that C_p at minimum pressure decreased and the separation point moved backward.

It was, however, technically difficult to inject air bubbles at a state in which the solid cylinder was left inserted. Hence, our measurements with the air-bubble injection necessarily contained the influence of the flow through the porous wall. Therefore, it is the reason to use the data of the porous cylinder not equipped with the solid cylinder in the fully wetted condition as a standard.

Vortex Shedding and Lock-On in a Perturbed Flow

Mary S. Hall
Science Applications International Corporation,
McLean, VA 22102

Owen M. Griffin
Naval Research Laboratory,
Washington, DC 20375-5351
Fellow ASME.

Vortex shedding resonance or lock-on is observed when a bluff body is placed in an incident mean flow with a superimposed periodic component. Direct numerical simulations of this flow at a Reynolds number of 200 are compared here with experiments that have been conducted by several investigators. The bounds of the lock-on or resonance flow regimes for the computations and experiments are in good agreement. The computed and measured vortex street wavelengths also are in good agreement with experiments at Reynolds numbers from 100 to 2000. Comparison of these computations with experiments shows that both natural, or unforced, and forced vortex street wakes are nondispersive in their wave-like behavior. Recent active control experiments with rotational oscillations of a circular cylinder find this same nondispersive behavior over a three-fold range of frequencies at Reynolds numbers up to 15,000. The vortex shedding and lock-on resulting from the introduction of a periodic inflow component upon the mean flow exhibit a particularly strong resonance between the imposed perturbations and the vortices.

Introduction

Vortex streets are formed in the wakes of circular cylinders and other bluff, or unstreamlined, bodies over a wide range of Reynolds numbers from approximately 50 to 10^6 and even higher. The physics of vortex street formation has been the focal point for many past experimental studies, e.g., Roshko (1954, 1955), Gerrard (1966), Bearman (1965, 1967), Griffin and Ramberg (1974) and, more recently, Ongoren and Rockwell (1988a, b), and Williamson and Roshko (1988), because of the importance of the near-wake flow to the eventual evolution of the overall middle and far-wake vortex patterns. Modern high-speed computers and direct numerical simulation techniques have allowed the vortex formation and modification processes to be studied numerically at high resolution (Karniadakis and Triantafyllou, 1989, 1992; Grinstein et al., 1991).

When a bluff cylinder is excited into resonant oscillations by an incident flow, the cylinder and its shed vortices have the same frequency near one of the characteristic frequencies of the body (Koopmann, 1967; Sarpkaya, 1979; Bearman, 1984; Griffin and Hall, 1991). This coincidence or resonance of the shedding and vibration frequencies is commonly termed lock-on, and such a state emerges when the body is oscillated externally in various orientations relative to the incident flow over the appropriate range of imposed frequencies and amplitudes (Koopmann, 1967; Griffin and Ramberg, 1974, 1976; Ongoren and Rockwell, 1988a,b; Nuzzi et al., 1992). Two recent experimental studies (Tokomaru and Dimotakis, 1991; Filler et al., 1991) have shown that rotational oscillations of a circular cylinder cause lock-on and result in marked changes in the geometry of the near-wake flow.

Vortex resonance or lock-on is observed experimentally when the incident mean flow has a sufficiently large periodic component superimposed upon it (Barbi et al., 1986; Armstrong et al., 1986, 1987). The cylinder remains stationary in the flow, but the vortex lock-on or resonance produced by the inflow perturbation modifies the character of the near-wake flow. This is equivalent to the in-line oscillations when the acoustic wavelength is long compared to the cylinder diameter.

The introduction of an appropriate sound field also can cause lock-on to occur (Blevins, 1985). And control of the vortex formation and shedding by periodic mass injection into the cylinder's boundary layer prior to separation has been demonstrated by Williams et al. (1992). All of these external disturbances are potential means for active control of the bluff body near-wake flow (Oertel, 1990; Rockwell, 1990).

Vortex lock-on and resonance phenomena have numerous practical engineering applications in addition to their importance in a fundamental physical sense. Applications abound in offshore exploration and drilling, Naval and marine hydrodynamics, and underwater acoustics. Other areas of engineering practice where these phenomena play important roles are civil and wind engineering, nuclear and conventional power generation, and electric power transmission.

The main topic of this paper is a particular case of vortex shedding resonance and lock-on in the near-wakes of bluff bodies. Vortex shedding in an incident flow with a periodic component superimposed on the basic mean flow is computed here to high resolution using the spectral element method. This is an interesting bluff body flow which has not been studied either computationally or experimentally in detail up to this time.

Flow Perturbation and In-Line Oscillation Experiments

The experiments of Armstrong et al. (1986, 1987) and of

Contributed by the Fluids Engineering Division for publication in the JOURNAL OF FLUIDS ENGINEERING. Manuscript received by the Fluids Engineering Division January 17, 1992; revised manuscript received November 4, 1992. Associate Technical Editor: F. T. Dodge.

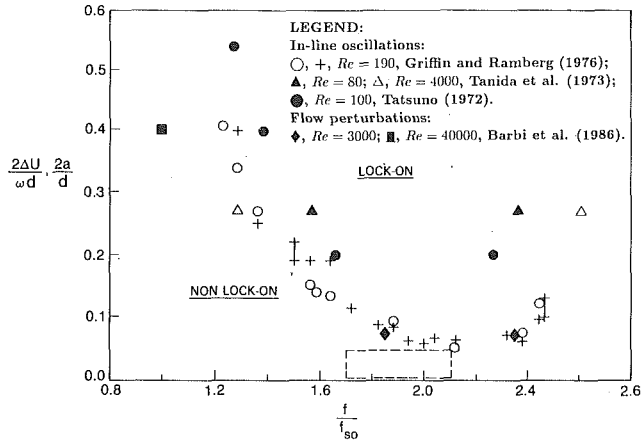

Fig. 1 Limits of the lock-on regime as a function of amplitude and frequency for in-line oscillations and inflow perturbations; from Griffin and Hall (1991)

Barbi et al. (1986) were conducted to examine vortex lock-on for a cylinder in a stream consisting of a steady uniform flow with a superimposed periodic component. The results of both studies show some very basic similarities with the earlier experiments of Griffin and Ramberg (1976), which are conducted to examine vortex shedding lock-on for a cylinder oscillating in-line with an incident flow. More recent experiments with in-line oscillations have been conducted by Ongoren and Rockwell (1988a,b).

The vortex lock-on measurements by Barbi et al. are compared with those of Griffin and Ramberg in Fig. 1. The vertical axis represents two different measures of the perturbation amplitude. For the experiments of Griffin and Ramberg the peak-to-peak amplitude of cylinder displacement is given by $2a/d$. And for the experiments of Barbi et al. the normalized "peak-to-peak" incident velocity perturbation is given by $2\Delta U/\omega d$. The horizontal axis is the ratio of the vibration frequency f and the Strouhal frequency f_{so} of a stationary cylinder. The two types of external disturbance are essentially identical for the case shown. Also shown are the cylinder vibration results of Tanida et al. (1973) and of Tatsuno (1972), reproduced from the paper by Griffin and Ramberg. The dashed lines enclose the results of Armstrong et al. (1986, 1987). Vortex lock-on and cross-flow oscillations usually occur near the Strouhal shedding frequency f_{so}. For in-line oscillations and flow perturbations the lock-on is caused by frequencies near twice the Strouhal frequency, $2f_{so}$, since the forcing fluctuations in the drag force are in the flow direction. However, in many cases the actual lock-on frequency is near the Strouhal frequency, or half the oscillation or perturbation frequency.

There is generally good agreement between the bounds of the lock-on regime for the two different types of external disturbance or flow control, though there is some scatter at the highest amplitudes. This is most likely due to Reynolds number effects, as noted by Barbi et al. The latter experiments were conducted at Re between 3000 and 40,000, whereas the results of Tanida et al., Tatsuno, and of Griffin and Ramberg were conducted at Re between 80 and 4000. The overall agreement is good.

The base pressure coefficient C_{pb} is influenced by the flow perturbations in much the same manner as in the case of cylinder oscillations. For the stationary cylinder the base pressure coefficient is near $C_{pb} = -1.44$; this value, though somewhat low for a circular cylinder, is in reasonable agreement with the results of West and Apelt (1982) for a comparable wind tunnel blockage ratio of nine percent. At the largest flow perturbation, the base pressure was decreased to $C_{pb} = -1.85$ at the point of maximum resonance, a reduced velocity of $U/f_{so}d = 2.5$ (or half the Strouhal value). The measured vortex formation region length l_f was reduced by this level of perturbation to $0.9d$ from $1.2d$, the value measured for the unperturbed flow (Armstrong et al., 1987). The mean drag coefficient C_D increased from 1.28 to 1.52 for the perturbed flow as compared to the unperturbed flow.

The Numerical Method

Recent advances in computational fluid dynamics permit new approaches to examining the effects of inflow perturbations and cylinder oscillations on the bluff body near-wake. One of these methods, which we employ herein, consists of superimposing an oscillatory component on the inflow boundary condition for a domain such as the spectral element grid (see Fig. 4). The computational results presented in this and the following section were obtained by means of direct numerical simulation of two-dimensional flow past a circular cylinder at sub-critical Reynolds numbers. The equations solved are the incompressible Navier–Stokes equation

$$\partial_t \mathbf{v} + (\mathbf{v} \cdot \nabla)\mathbf{v} = -\nabla p/\rho + \nu \nabla^2 \mathbf{v}$$

together with the continuity equation

$$\nabla \cdot \mathbf{v} = 0$$

A no-slip boundary condition is imposed on the surface of the cylinder, a Neumann boundary condition is used at the outflow, and periodic boundary conditions are imposed in the longitudinal or downstream direction at the cross-stream boundaries of the domain. At the inflow, a uniform stream with a superimposed time-periodic small amplitude perturbation is used in most of the cases presented in the section on computational results. In the first case discussed, that of natural or unforced vortex shedding, the inflow consists solely of a uniform stream.

The computer code employed here is a variation of the spectral element formulation used by Karniadakis and Triantafyllou (1989, 1992). Modifications of the code performed at NRL have not altered the basic spectral-element methodology, which is described in some detail in the above-mentioned references. However, numerous variations have been made in the computational grid and in the computed flow quantities over the grid in order to examine the details of the flow history and development, the velocity spectra, and the flow geometry of the near-wake of the cylinder. Briefly, a time-splitting algorithm is employed in the usual way, with the nonlinear term being solved first using a third-order explicit Adams-Bashforth scheme with a Courant stability condition. Incompressibility is enforced when the pressure term is solved in the second step, and boundary conditions are imposed in the third step, when the new velocity is found by implicit solution of the viscous term. In the second and third steps, intermediate values obtained from the previous steps are used as the "old" values. Although it is not possible to say formally what the resulting overall order of the splitting scheme is, the lowest order step is the third, implicit backward Euler step, which is order $O(\Delta t)$.

The spatial resolution of the computed flow can be affected in two ways: by choice of the size and number of elements and by choice of the order of Lagrangian interpolating polynomials used within the elements. In the present work, the fifty-six element grid was essentially the same as that shown in Karniadakis and Triantafyllou (1989), and can be seen in Fig. 4. Within each two-dimensional element sixth-order interpolating polynomials were used in both the streamwise and cross-stream directions, for a total of 7×7 or 49 Gauss-Lobatto collocation points within each element. This resulted in very fine resolution in that portion of the domain surrounding the cylinder, and a more coarse resolution in the far wake. Clustering of the collocation points near the element boundaries resulted in smooth solutions across these boundaries.

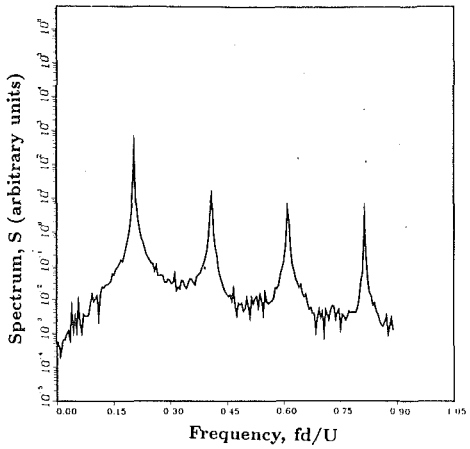

Fig. 2 (*a*) The spectrum corresponding to the *x*-component of the velocity U_x at the history point located at $(x,y) = (2,2)$. This is the natural shedding case (no perturbation) at Re = 200.

As with all spectral methods, a weighted residual technique is used to generate the discrete equations, and the system of discrete equations then is solved using a conjugate-gradient algorithm. A benchmark case demonstrates the ability of the code to accurately predict the important flow parameters involved in the simulation of vortex shedding from bluff bodies, using the shedding frequency and the vortex street wavelength as diagnostics. For this we chose natural or unforced shedding at Reynolds number Re = 100 based on cylinder diameter, since this case was also studied by Karniadakis and Triantafyllou (1989) and extensive results are available in their paper. Our predicted natural shedding frequency of St = 0.176 differs from the value of 0.179 predicted by Karniadakis and Triantafyllou (1989) by only 1.67 percent, which is insignificant owing to the fact that the St = 0.179 value overestimates recent experimentally determined values, e.g., Williamson (1989), by approximately eight percent.

No asymmetry is needed in the initial or boundary conditions in order to initiate the asymmetric vortex shedding in this simulation of natural shedding, as well as all of the Reynolds number Re = 200 simulations discussed in the next section. Rather, asymmetries due to computer truncation are sufficient to cause the vortex shedding to develop naturally as it does in any laboratory flow due to the presence of infinitesimal ambient disturbances. The asymmetry is not due to any numerical instability, but rather to the highly unstable nature of the symmetric flow that is realized briefly early-on in the computations. We refer to this early symmetric solution as the quasi-steady state of the flow.

Computation of the Flow

The first case for which we present numerical results is natural or unforced vortex shedding at a Reynolds number of 200. For this condition the inflow boundary condition at the left of the domain is a uniform flow, and the near-wake and vortex shedding patterns develop without forcing. We include this case for comparison with the perturbed flow results.

The spectrum corresponding to the *x*-component of the velocity U_x at a point $(x,y) = (2,2)$ is shown in Fig. 2, where the units are scaled by the cylinder diameter. The highest peak in the spectrum is located at the natural shedding frequency f_{so} corresponding to St = 0.195, and other peaks can be seen at higher harmonics of this shedding frequency. Approximately 2000 time intervals were used to produce this spectrum and all of the computed spectra discussed in this paper. Each time interval represents ten time steps in the calculation, and 2000 time intervals correspond to approximately thirty shedding cycles.

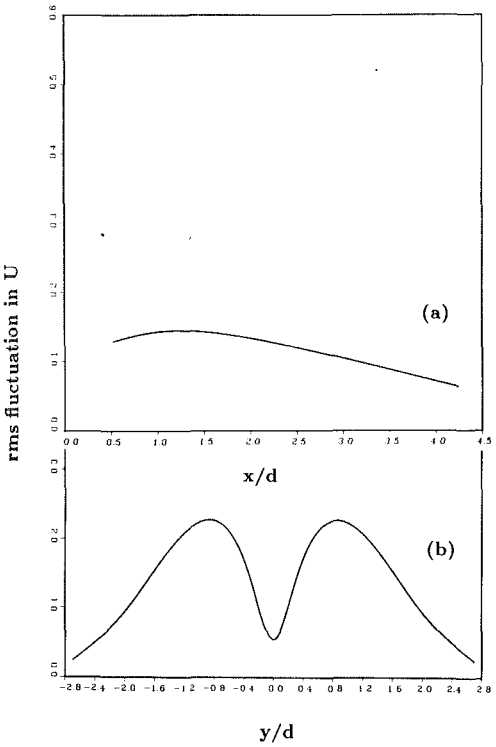

Fig. 3 (*a*) The rms fluctuation in the *x*-component of the velocity U_x along the wake centerline and (*b*) the rms fluctuation across the wake at *x* = 5 diameters downstream

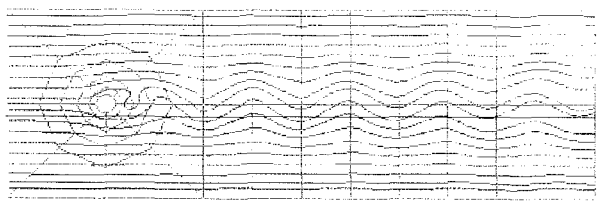

Natural shedding; Re = 200

Fig. 4 Instantaneous streamlines for natural shedding at Re = 200. The spectral element grid employed in the computations is shown superimposed on the spectrum.

The cylinder base-region flow in the vortex formation region is important to the development of the near-wake flow (Bearman, 1965; Gerrard, 1966), and to the ensuing physical evolution of the wake. One measure of the downstream extent of the formation region is the maximum in the fluctuating velocity which occurs just downstream of the cylinder on the wake centerline. The formation region length also can be measured in terms of the minimum of the local pressure coefficient C_p on the wake centerline (Roshko, 1954, 1955). The fluctuation u_{rms} of the *x*-component of velocity on the wake centerline is plotted in Fig. 3 as a function of distance downstream from the cylinder, as measured in multiplies of the cylinder diameter. The computed peak in u_{rms} is located at about 1.25 cylinder diameters downstream, which is comparable with measurements from laboratory experiments which have been reported in the literature (Bloor and Gerrard, 1966; Griffin, 1971).

A cross-wake distribution of the velocity fluctuation u_{rms} at $x = 5d$ is plotted in Fig. 3(*b*). The same quantity at $x = 3d$ is shown in Fig. 9(*a*) where it is superimposed on a perturbed flow case. The corresponding mean velocities are shown in Fig. 8. The deficit in the mean velocity is apparent as well as

the approach to the free stream condition as the distance from the centerline is increased. The peaks in the rms velocity at the two downstream locations also show the usual concentrated off-wake effects of the passing vortex pairs. The computed fluctuations in the wake are slightly less than comparable wind tunnel measurements near this Reynolds number (Griffin and Ramberg, 1974), probably owing to differences between the two-dimensional computations and the three-dimensional experiments.

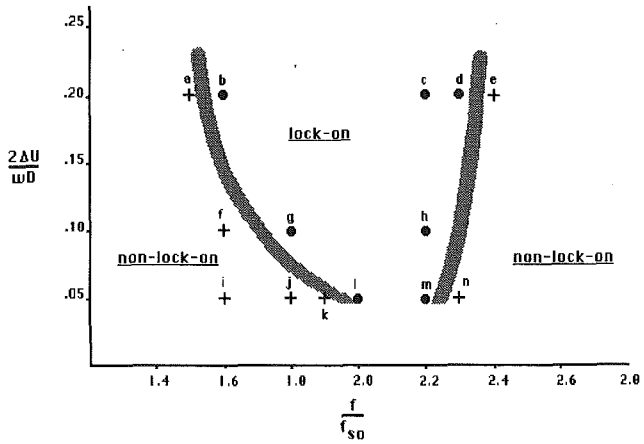

Fig. 5 Limits of the lock-on regime for perturbed flow at Re = 200. Each closed circle or cross represents a numerical simulation. Those simulations in which lock-on occurred are indicated by closed circles. The shaded region forms the approximate boundary between the lock-on and non-lock-on regimes.

The final result for the natural shedding case is the instantaneous streamline pattern shown in Fig. 4. Here the streamlines are spaced evenly across the computational domain at the inflow, and the spreading of the streamlines in the near wake gives some evidence of the deficit in the mean flow in the cross-wake direction, as was shown in Fig. 3(*b*). The wavelength of the vortex street for this unforced flow is $\lambda = 5d$, which is typical of the results shown in Fig. 12.

Next a perturbed boundary condition of the form

$$U_x = 1.0 + \Delta u \sin \omega t,$$

$$U_y = 0.$$

was enforced at the inflow, where U_x and U_y denote the x- and y-components of the velocity, respectively. Here $\Delta u = a\omega$, where $\omega = 2\pi f$, and the perturbation frequency $f = 2\alpha f_{so}$. The parameter a varied from 0.05 to 0.25, while α was varied to give values of the perturbation frequency ranging from $1.4f_{so}$ to $2.8f_{so}$ (Fig. 5). Each closed circle or cross in this figure represents a direct numerical simulation. Those that represent lock-on behavior are indicated by the closed circles.

The shaded regions in Fig. 5 indicate regions across which breakdown occurs, from a periodic, locked-on flow to a nonperiodic or quasi-periodic flow in which the primary frequency is the natural shedding frequency rather than the perturbation frequency. We have not attempted to define precisely the width of this region, but only to bracket it. As will be shown in the

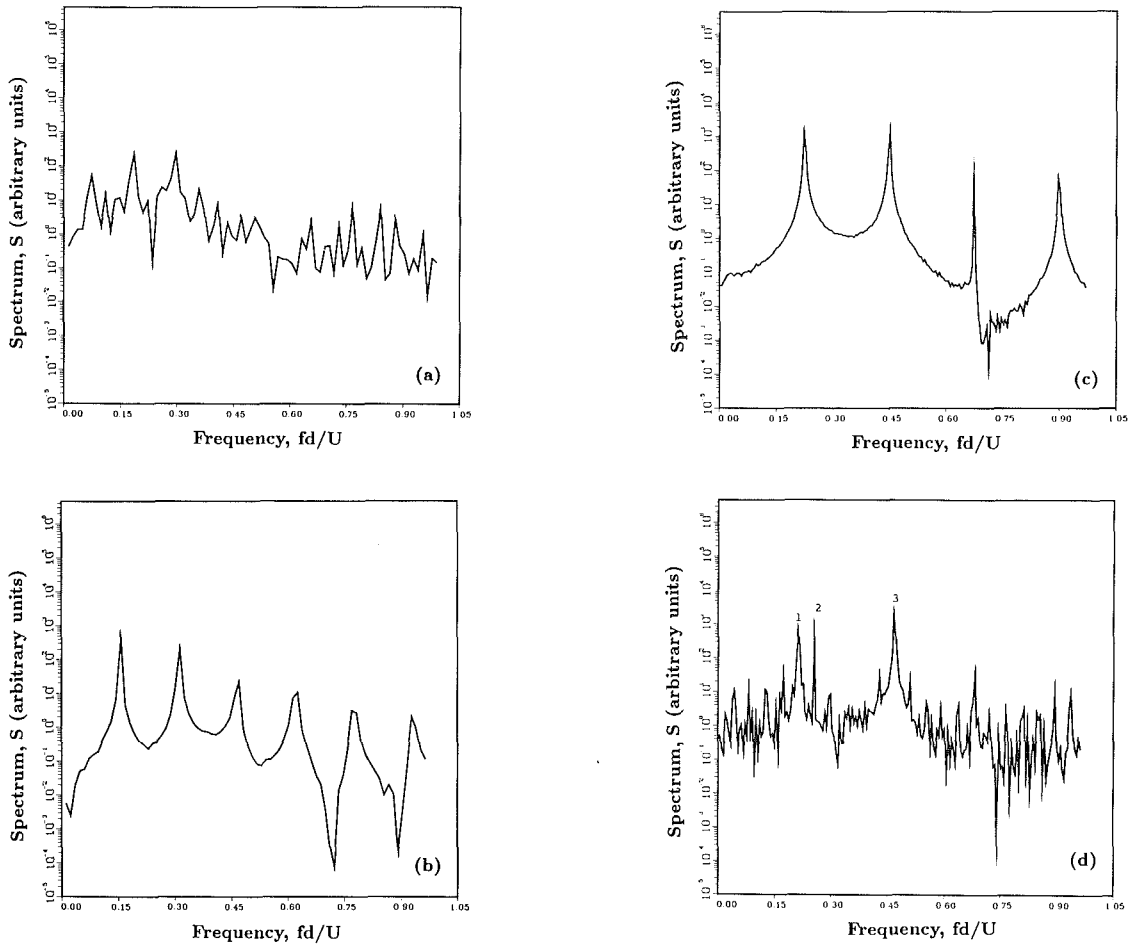

Fig. 6 The spectrum of the *x*-component of the velocity U_x at the history point located at $(x,y) = (2,2)$; (*a*) case *a* in Fig. 5, (*b*) case *b*, (c) case *d*, and (*d*) case *e*

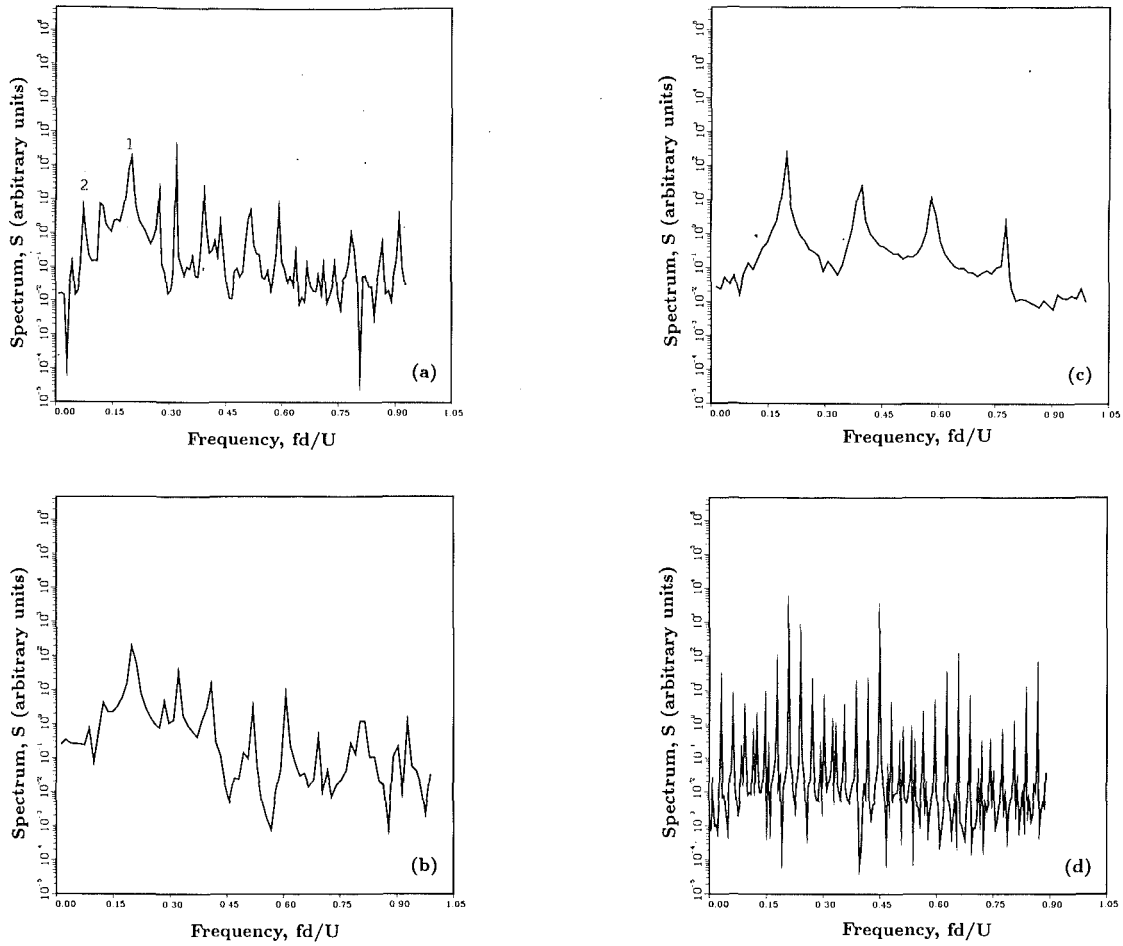

Fig. 7 The spectrum corresponding to U_x at $(x,y) = (2,2)$; (*a*) case *f* in Fig. 5, (*b*) case *i*, (*c*) case *l*, and (*d*) case *n*

following, in all of the cases lying outside of the lock-on region, the flow continues to be strongly influenced by the perturbation, as evidenced by the chaotic nature of the flow in contrast with the regular, periodic natural shedding case. However, we have chosen to define non-lock-on cases as those for which the highest peak in the spectrum occurs at the natural shedding frequency or at a frequency corresponding to neither the perturbation nor the natural shedding frequency.

We first examine cases *a*, *b*, *d*, and *e* in Fig. 5. For these four cases, the amplitude of the perturbation is held fixed while the frequency is increased from $1.5f_{so}$ (case *a*) to $2.4f_{so}$ (case *e*). A forcing frequency of $1.5f_{so}$ results in a nonperiodic velocity history with the spectrum in Fig. 6(*a*), which shows clearly the chaotic nature of the flow. The highest peak in the spectrum occurs just below the natural shedding frequency of $St = 0.195$. Increasing the forcing frequency from $1.5f_{so}$ to $1.6f_{so}$ results in case *b* in Fig. 5. The flow is periodic, with shedding frequency equal to $0.8\,f_{so}$, and thus lock-on has occurred. The flow pattern is more complex that that of the unperturbed case, and we see from the spectrum in Fig. 6(*b*) that there is now significantly more energy in the higher harmonics of the perturbation frequency than occurred in higher harmonics of f_{so}. The wavelength of the vortex pattern is $\lambda = 5.7d$, an increase of fourteen percent from the unforced value of $\lambda = 5d$.

Moving farther to the right in Fig. 5, we again increase the perturbation frequency to $2.3f_{so}$ for case *d*. Lock-on again takes place, this time at a frequency of $1.15f_{so}$. The spectrum corresponding to this case is shown in Fig. 6(*c*).

The results from case *e* demonstrate that we have crossed over the shaded region and are once again outside of the lock-on region. The dominant peak in the spectrum (Fig. 6(*d*)) occurs at neither the natural shedding frequency nor the perturbation frequency. The three highest peaks in the spectrum are labeled. Peak number 1 occurs just above the natural shedding frequency at approximately $St = 0.2$, peak number 2 occurs at half the perturbation frequency or $St = 0.23$, and peak number 3 occurs at the sum of these, or $St = 0.43$. Thus peak 3, the highest, is a higher harmonic of neither the natural shedding frequency nor the perturbation frequency, but of the average of the two. This case is indicative of a wider transitional region than we have shown in Fig. 5, in which the dominant frequency in the flow is neither the perturbation nor the natural frequency. Indeed, the presence of two nearby peaks in the spectrum suggests intermittency in the shedding frequency.

We next examine case *f* in Fig. 5, which lies just to the left of the lock-on region. Here the frequency of the perturbation is the same as in case *b*, but the amplitude has been decreased from 0.2 to 0.1 nondimensional units. Referring to the spectrum for case *b* in Fig. 6(*b*), we see the dramatic change brought about in the flow due to this change in amplitude. The peak in the spectrum for case *f*, labeled number 1 on Fig. 7(*a*), is at the natural shedding frequency of $St = 0.195$. The peak labeled number 2 occurs at half of the perturbation frequency, or approximately $St = 0.078$. When the amplitude of the perturbation is reduced further to 0.05 in case *i*, the spectrum in Fig. 7(*b*) shows that now the natural shedding frequency is clearly dominant, and thus this condition is farther outside the lock-on region than the previous result.

At this value of perturbation amplitude, we now examine the effects of increasing the perturbation frequency by pre-

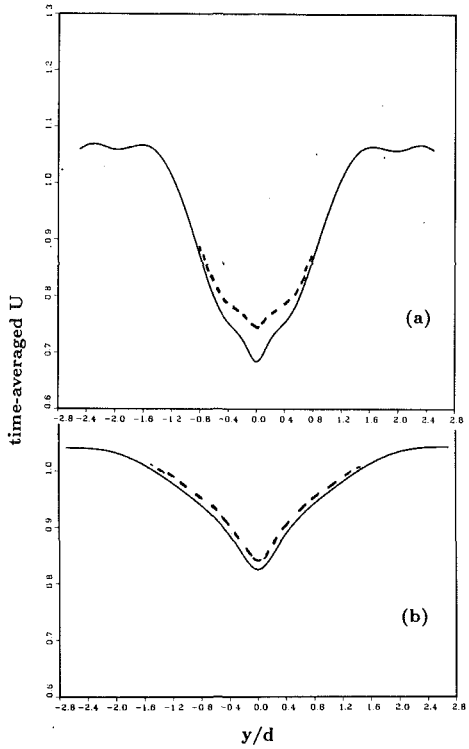

Fig. 8 The cross-stream distribution of mean velocity $U_x(y)$ at (*a*) $x = 3d$ and (*b*) $x = 5d$ downstream from the cylinder, case *g*. The results for the natural shedding case (dashed lines) are superimposed.

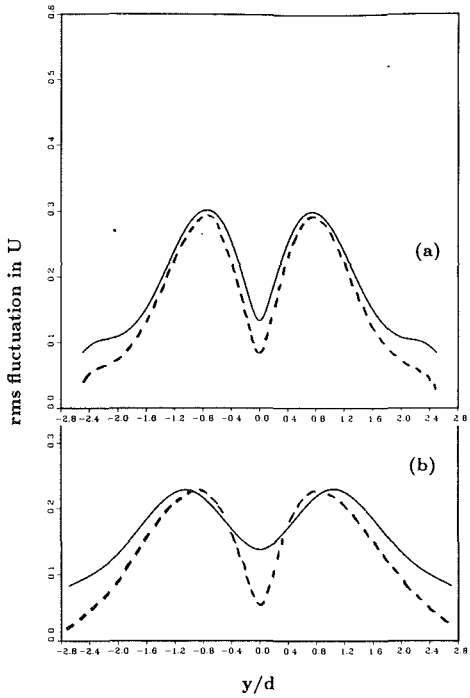

Fig. 9 The cross-stream distribution of rms velocity fluctuations corresponding to the mean velocities for case *g* in Fig. 8. The results for the natural shedding case (dashed lines) are superimposed.

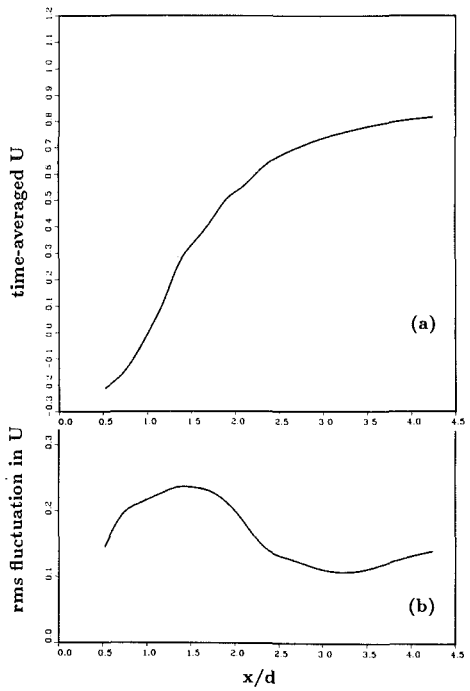

Fig. 10 The (*a*) mean flow and (*b*) rms fluctuation in the velocity along the wake centerline, for case *g*

senting results for cases *l* and *n*. A dramatic change occurs as the perturbation frequency is increased to $2.0f_{so}$ (case *l*). While the resulting flow resembles the natural shedding case, the frequency of the oscillation is lower than the natural shedding frequency obtained in the unforced case by approximately five percent (Fig. 7(*c*)), and higher harmonics correspond to multiples of this latter value. The reason for this discrepancy has not yet been determined conclusively; our original estimate of the natural shedding frequency at Reynolds number 200 was approximately five percent lower than that of Karniadakis and Triantafyllou (1989), while their estimate was judged to overestimate the experimentally determined value by approximately eight percent. Thus the present computed result is within an acceptable range.

A change again occurs as we increase the perturbation frequency to $2.3f_{so}$ for the final case *n*. The flow pattern again becomes complex as shown by the spectrum in Fig. 7(*d*), with the first dominant peak occurring at the natural shedding frequency of $St = 0.195$. A second peak of nearly equal height occurs at a frequency equal to approximately $St = 0.45$, or twice the perturbation frequency. Thus again we see the perturbation frequency having a greater effect on the higher harmonics of the flow.

For a more complete analysis of the near-wake flow in a lock-on condition, we further examine case *g*. As in the natural shedding case, we first measured the drop in the time-averaged *x*-component of the velocity across the wake at two different downstream locations. Time averaging again was done over approximately thirty shedding cycles. We see from Fig. 8(*a*), which shows computed velocities three diameters downstream from the cylinder, that the drop in mean velocity across the wake is approximately 35 percent. Comparing this with an approximately 30 percent drop in the natural shedding case (superimposed), indicates that the effect of the perturbation is to slightly decrease the mean flow along the centerline. However, the rms fluctuation corresponding to this mean flow is greater than that seen in the natural shedding case, with a proportionately greater fluctuation along the centerline. In the natural shedding case there was a nearly 70 percent drop in the rms fluctuation across the wake three diameters downstream from the cylinder. By comparison, the rms fluctuation in the perturbed flow exhibits an approximately 57 percent drop across the wake (Fig. 9(*a*)). Farther downstream at $x = 5d$ the time-averaged flows of the natural shedding perturbed cases are nearly identical (Fig. 8(*b*)). At this same downstream lo-

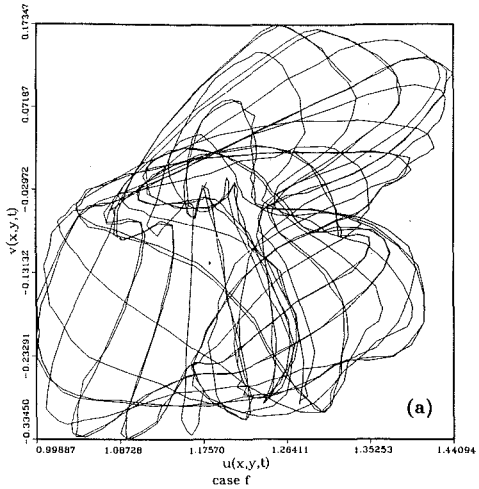

Fig. 11 Phase plane plots of U_x versus U_y for (*a*) case *f*, and (*b*) case *g*

cation, the maximum rms fluctuation of the perturbed flow has decayed approximately to that of the natural shedding case, but the fluctuation remains greater at the wake edges and along the wake centerline (Fig. 9(*b*)). The corresponding u_{rms} for the natural shedding case is shown in Fig. 3(*b*).

The mean flow and the rms fluctuation in the velocity along the centerline behind the cylinder are shown in Fig. 10. Comparing the rms fluctuation with the natural shedding case (Fig. 3(*a*)) we see that the peak of the fluctuation, which marks the end of the vortex formation region, has moved from its natural shedding position approximately one diameter downstream from the cylinder to a point approximately one and a half diameters downstream. This is an expansion of the vortex formation region with perturbation frequency when $f<2f_{so}$. Comparably, the downstream extent of the formation region is contracted when $f>2f_{so}$. Both of these modifications in the shedding are analogous to those observed when a circular cylinder undergoes both in-line and crossflow oscillations under lock-on conditions (Griffin and Ramberg, 1974, 1976; Ongoren and Rockwell, 1988a, b).

A zone of reversed mean flow is found adjacent to the cylinder as shown in Fig. 10, followed by a stagnation point ($\bar{U}=0$) and the transition to positive mean flow at approximately one diameter downstream. The extent of the reversed flow region is controlled by the perturbations in much the same way as the overall formation region.

The U_x versus U_y phase plane plots for cases *f* and *g* are shown in Fig. 11. The history point in both cases is once again located in the separated flow just outside the wake at $(x,y)=(2,2)$. These phase plane representations of the velocity demonstrate most graphically the periodic nature of the forced or lock-on state of the flow, as opposed to the chaotic state of the non-lock-on state.

Table 1 Longitudinal vortex spacing or wavelength in the near-wake of a circular cylinder vibrating in-line with an incident uniform flow; adapted from Griffin and Ramberg (1976)

Vibration frequency, f(Hz)	Frequency ratio, f/f_{so}	Vortex spacing, λ/d	Relative change, $\Delta\lambda/\lambda$	Vortex convection speed, $1/2\, f\lambda/U$
		Reynolds number = 190		
69.2	1.88	5.2	+0.07	0.94
73.6	2.00	4.9	0	0.93
75.6	2.06	4.7	−0.05	0.91
78.9	2.14	4.7	−0.04	0.96
80.4	2.18	4.4	−0.09	0.92
				Average = 0.93

Discussion of Results

The longitudinal vortex spacing or wavelength is a valuable physical diagnostic for the state of the spatial structure and development of the fully-developed vortex street. Measurements of the spacing for a variety of in-line and cross-flow oscillations, and also for the unforced wakes of stationary cylinders have been reported by Griffin and Ramberg (1976). These can be compared to the direct numerical simulations of Karniadakis and Triantafyllou (1989) and our recent NRL simulations that are discussed here. The wavelength of the pattern can be employed as a measure of the spatial state of the flow, as compared to phase plane diagrams of the streamwise and cross stream velocities, which can be employed in a comparable way to assess the temporal state of the near-wake.

One example given by Karniadakis and Triantafyllou (1989) is that of a wake forced by a localized spatially and temporally varying disturbance in the vortex formation region, with normalized amplitude and frequency, respectively, of $a=0.10$ and $f/f_{so}=0.75$. The center of the disturbance was located at $x=2$, $y=0$, measured in multiples of the cylinder diameter. This is a unique form of control disturbance which had not been investigated previously. For the unforced wake $\lambda=5d$, while for the forced wake $\lambda=7d$, an increase of forty percent in the wavelength.

Comparable measurements were made at Re = 190 by Griffin and Ramberg (1976) and the results are summarized in Table 1. The cylinder oscillations were in-line with the flow over a range of frequencies near twice the Strouhal frequency as in Fig. 1. The measured changes in the forced vortex spacing correspond directly with those achieved in the direct numerical simulations, since for $f<2f_{so}$ the wavelength increases while for $f>2f_{so}$ the wavelength decreases. Extrapolating the results in the table to the condition $f=1.6f_{so}$ in the present case and to $f=0.75f_{so}$ from Karniadakis and Triantafyllou using a least-squares fit given by Griffin and Ramberg, the vortex spacing is $\lambda=6.2d$. This compares reasonably well with both computations. The measured vortex spacing for the stationary cylinder at Re = 190 ($\lambda=4.9d$) is very nearly equal to the wavelength computed here at Re = 200, namely $\lambda=5d$.

The computed vortex street wavelengths are compared further with measurements for both forced and unforced conditions for Reynolds numbers from 100 to 2000 in Fig. 12. The computations agree well overall with the experiments, which show only a very slight dependence on Reynolds number in this range. The vertical scale is a normalized form of the vortices' convection speed, or the downstream translational speed of the vortex cores. The constant phase or convection

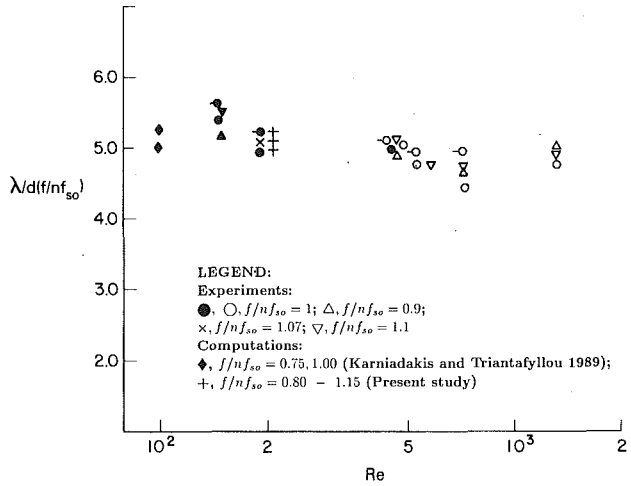

Fig. 12 Longitudinal vortex spacing $\lambda/d(f/nf_{so})$ as a function of Reynolds number Re. All of the measurements were made in the wakes of stationary and oscillating cylinders. The data points at Re = 190 and 200 correspond to in-line oscillations and inflow perturbations (composite of six) with $n=2$; all other data correspond to cross-flow oscillations (experiments) and near-wake perturbations (computations) with $n=1$.

speed is representative of a nondispersive physical system, as compared to the many dispersive, complex physical systems which occur in nature, e.g. surface water waves and mixing layers under certain conditions, where the phase speed depends on the wavelength or wavenumber and the frequency.

Several measurements of the pattern's convection speed also are given in the table. Though there is some scatter, the average value is $U_\phi = 0.93U$. Tokumaru and Dimotakis (1991) also found that the convection speed remained nearly constant at a similar value in a lock-on state produced by rotational oscillations at a Reynolds number of 15,000, even as both the imposed frequency of the oscillations varied over a three-fold range and the street wavelength underwent similarly marked changes. This gives some additional evidence that both forced and unforced or natural periodic vortex wakes have the same basic nondispersive character over a wide range of externally imposed disturbances.

These modifications of the near-wake flow are achieved by the imposition of relatively small inflow perturbations. Thus, seemingly small perturbations of the wake flow are capable of producing large changes in vortex strength and shed vorticity, base pressure and drag on a bluff circular cylinder or body of other cross-section. Modification and control of the basic formation or instability mechanisms of the wake can lead to substantial changes in the near-wake vortex pattern, and possibly even the middle- and far-wake flow as well as found by Cimbala et al. (1988), and by Browne et al. (1989).

Summary and Concluding Remarks

Several issues pertaining to bluff body near-wake flow control and modification have been investigated for a bluff body in a flow consisting of a basic mean flow with a superimposed periodic component. Direct numerical simulations of perturbed flow about a circular cylinder are in good agreement with experimental results, particularly in reproducing the vortex shedding resonance or lock-on regime boundaries at Re = 200. The lock-on regime defines the frequency range over which perturbations in the incident flow cause vortices to be shed at the forcing frequency rather than at the natural shedding frequency. At an amplitude of $2\Delta U/\omega d = 0.2$, perturbation frequencies in the range $1.6f_{so}$ to $2.3f_{so}$ result in lock-on, and the extent of this frequency range decreases with decreasing perturbation amplitude. The change in the lock-on boundary was more rapid at frequencies less than $2f_{so}$, which is in qualitative agreement with experiments from Fig. 1 and Koopmann (1967).

Computations of the near-wake flow show that in flow perturbations causing lock-on can control the location and extent of the vortex formation region and the level of velocity fluctuation both along and across the wake. Some typical results at $f<f_{so}$ show a shift downstream of the vortex formation region, as identified by the peak rms velocity fluctuation along the wake centerline, and an increased fluctuation level along the centerline that extends to at least five cylinder diameters downstream. These modifications to the near-wake flow are indicative of selectively increased vortex strength and shed vorticity in the near-wake as a result of the locking-on.

The computed values of the vortex wavelength λ in the perturbed flow are in good agreement with measurements in both unforced, or natural, and forced wakes for Reynolds numbers between 100 and 2000. The predominant vortex street frequency and wavelength adjust in such a way that a constant phase or convection speed of the pattern is achieved over a wide range of conditions which cause lock-on. Recent active control experiments with rotational oscillations of a circular cylinder at a Reynolds number of 15,000 show that the wake adjusts in the same way over a three-fold range of imposed frequencies. The essentially constant vortex phase or convection speed is indicative of the basic nondispersive physical character of forced and unforced, or natural, bluff body near-wakes.

Acknowledgments

This work was conducted as part of a research program in fluid dynamics and bluff body flows supported by the Naval Research Laboratory and the Office of Naval Research. We are grateful to Dr. George Karniadakis of Princeton University for numerous helpful discussions on both the spectral element method and the computations reported here.

References

Armstrong, B. J., Barnes, F. H., and Grant, I., 1986, "The effect of a Perturbation on the Flow Over a Cylinder," *Physics of Fluids*, Vol. 29, pp. 2095-2102.

Armstrong, B. J., Barnes, F. H., and Grant, I., 1987, "A Comparison of the Structure of the Wake Behind a Circular Cylinder in a Steady Flow With That in a Perturbed Flow," *Physics of Fluids*, Vol. 30, pp. 19-26.

Barbi, C., Favier, D. P., Maresca, C. A., and Telionis, D. P., 1986, "Vortex Shedding and Lock-on of a Circular Cylinder in Oscillatory Flow," *Journal of Fluid Mechanics*, Vol. 170, pp. 527-544.

Bearman, P. W., 1965, "Investigation of the Flow Behind a Two Dimensional Model with a Blunt Trailing Edge and Fitted with Splitter Plates," *Journal of Fluid Mechanics*, Vol. 21, pp. 241-255.

Bearman, P. W., 1967, "On Vortex Street Wakes," *Journal of Fluid Mechanics*, Vol. 28, pp. 625-641.

Bearman, P. W., 1984, "Vortex Shedding from Oscillating Bluff Bodies," *Annual Review of Fluid Mechanics*, Vol. 16, pp. 195-222.

Blevins, R. D., 1985, "The Effect of Sound on Vortex Shedding from Cylinders," *Journal of Fluid Mechanics*, Vol. 161, pp. 217-237.

Bloor, M. S., and Gerrard, J. H., 1966, "Measurements of Turbulent Vortices in a Cylinder Wake," *Proceedings of the Royal Society of London*, Series A, Vol. 294, pp. 319-342.

Browne, L. W. B., Antonia, R. A., and Shah, D. A., 1989, "On the Origin of the Organized Motion in the Turbulent Far-Wake of a Cylinder," *Experiments in Fluids*, Vol. 7, pp. 475-480.

Cimbala, J. M., Nagib, H. M., and Roshko, A., 1988, "Large Structure in the Far Wakes of Two-Dimensional Bluff Bodies," *Journal of Fluid Mechanics*, Vol. 190, pp. 265-298.

Filler, J. R., Marston, P. L., and Mih, W. C., 1991, "Response of the Shear Layers Separating from a Circular Cylinder to Small Amplitude Rotational Oscillations,' *Journal of Fluid Mechanics*, Vol. 231, pp. 461-489.

Gerrard, J. H., 1966, "The Mechanics of the Formation Region of Vortices Behind Bluff Bodies," *Journal of Fluid Mechanics*, Vol. 25, pp. 401-413.

Griffin, O. M., 1971, "The Unsteady Wake of an Oscillating Cylinder at Low Reynolds Number," ASME *Journal of Applied Mechanics*, Vol. 38, pp. 729-738.

Griffin, O. M., and Ramberg, S. E., 1974, "The Vortex Street Wakes of Vibrating Cylinders," *Journal of Fluid Mechanics*, Vol. 66, pp. 553-576.

Griffin, O. M., and Ramberg, S. E., 1976, "Vortex Shedding from a Cylinder

Vibrating in Line with an Incident Uniform Flow," *Journal of Fluid Mechanics*, Vol. 75, pp. 257–271.

Griffin, O. M., and Hall, M. S., 1991, "Vortex Shedding Lock-On and Flow Control in Bluff Body Wakes," ASME JOURNAL OF FLUID ENGINEERING, Vol. 113, pp. 526–537.

Grinstein, F. F., Boris, J. P., and Griffin, O. M., 1991, "A Numerical Study of Passive Pressure-Drag Control in a Plane Vortex Street Wake," *AIAA Journal*, Vol. 29, pp. 1436–1442.

Karniadakis, G. E., and Triantafyllou, G. S., 1989, "Frequency Selection and Asymptotic States in Laminar Wakes," *Journal of Fluid Mechanics*, Vol. 199, pp. 441–469.

Karniadakis, G. E., and Triantafyllou, G. S., 1992, "Three Dimensional Dynamics and Transition to Turbulence in the Wake of Bluff Objects," *Journal of Fluid Mechanics*, Vol. 238, pp. 1–30.

Koopmann, G. H., 1967, "The Vortex Wakes of Vibrating Cylinders at Low Reynolds Numbers," *Journal of Fluid Mechanics*, Vol. 28, pp. 501–512.

Nuzzi, F., Magness, C., and Rockwell, D., 1992, "Three-Dimensional Vortex Formation from an Oscillating, Non-Uniform Cylinder," *Journal of Fluid Mechanics*, Vol. 238, pp. 31–54.

Oertel, H., 1990, "Wakes Behind Blunt Bodies," *Annual Review of Fluid Mechanics*, Vol. 22, pp. 539–564.

Ongoren, A., and Rockwell, D., 1988a, "Flow Structure from an Oscillating Cylinder. Part I: Mechanisms of Phase Shift and Recovery in the Near Wake," *Journal of Fluid Mechanics*, Vol. 191, pp. 197–223.

Ongoren, A., and Rockwell, D., 1988b, "Flow Structure from an Oscillating Cylinder. Part II: Mode Competition in the Near Wake," *Journal of Fluid Mechanics*, Vol. 191, pp. 225–245.

Rockwell, D., 1990, "Active Control of Globally-Unstable Separated Flows," ASME *International Symposium on Nonsteady Fluid Dynamics* (*Proceedings*), FED-Vol. 92, pp. 379–394.

Roshko, A., 1954, "On the Drag and Shedding Frequency of Two-Dimensional Bluff Bodies," National Advisory Committee for Aeronautics, Washington, DC, Technical Note 3169.

Roshko, A., 1955, "On the Wake and Drag of Bluff Bodies," *Journal of the Aeronautical Sciences*, Vol. 22, pp. 124–132.

Sarpkaya, T., 1979, "Vortex Induced Oscillations: A Selective Review," ASME, *Journal of Applied Mechanics*, Vol. 46, pp. 241–258.

Stansby, P. K., 1976, "Base Pressure of Oscillating Circular Cylinders," *Proceedings of ASCE, Journal of Engineering Mechanics*, Vol. 104, pp. 591–600.

Tanida, Y., Okajima, A., and Watanabe, Y., 1973, "Stability of a Circular Cylinder Oscillating in Uniform Flow or in a Wake," *Journal of Fluid Mechanics*, Vol. 61, pp. 769–784.

Tatsuno, M., 1972, "Vortex Streets Behind a Circular Cylinder Oscillating in the Direction of Flow," *Bulletin of the Research Institute for Applied Mechanics of Kyushu University*, Vol. 36, pp. 25–37.

Tokumaru, P. T., and Dimotakis, P. E., 1971, "Rotary Oscillation Control of a Cylinder Wake," *Journal of Fluid Mechanics*, Vol. 224, pp. 77–90.

West, G. S., and Apelt, C. J., 1982, "The Effects of Tunnel Blockage and Aspect Ratio on the Mean Flow Past a Circular Cylinder with Reynolds Numbers Between 10^4 and 10^5," *Journal of Fluid Mechanics*, Vol. 114, pp. 361–377.

Williams, D. R., Mansy, H., and Amato, C., 1992, "The Response and Symmetry Properties of a Cylinder Wake Subjected to Localized Surface Excitation," *Journal of Fluid Mechanics*, Vol. 234, pp. 71–96.

Williamson, C. H. K., and Roshko, A., 1988, "Vortex Formation in the Wake of an Oscillating Cylinder," *Journal of Fluids and Structures*, Vol. 2, pp. 355–381.

Williamson, C. H. K., 1989, "Defining a Universal and Continuous Strouhal-Reynolds Number Relationship for a Laminar Vortex Shedding of a Circular Cylinder," *Physics of Fluids* , Vol. 31, pp. 2742–2744.

The Torsion Effect on Fully Developed Laminar Flow in Helical Square Ducts

Wen-Hwa Chen
Mem. ASME

Ray Jan

Department of Power Mechanical Engineering,
National Tsing Hua University,
Hsinchu, Taiwan 30043

The continuity equation and Navier-Stokes equations derived from a non-orthogonal helical coordinate system are solved by the Galerkin finite-element method in an attempt to study the torsion effect on the fully developed laminar flow in the helical square duct. Since high-order terms of curvature and torsion are considered, the approach is also applicable to the problems with finite curvature and torsion. The interaction effects of curvature, torsion, and the inclined angle of the cross section on the secondary flow, axial velocity, and friction factor in the helical square duct are presented. The results show that the torsion has more pronounced effect on the secondary flow rather than the axial flow. In addition, unlike the flow in the toroidal square duct, Dean's instability of the secondary flow, which occurs near the outer wall in the helical square duct, can be avoided due to the effects of torsion and/or inclined angle. In such cases, a decrease of the friction factor is observed. However, as the pressure gradient decreases to a small value, the friction factor for the toroidal square duct is also applicable to the helical square duct.

1 Introduction

The helical square duct has been used extensively in various industrial applications to enhance the rates of heat, mass and momentum transfer. The transition duct and the lobe mixer in a propulsion system are some of the examples. To improve the performance of these devices, an accurate and reliable analysis of the flow in the helical duct is necessary. This analysis can also be used as the basis for studying the flow in other devices, such as screw pumps, heat exchangers, and the passage between the blades of gas turbines or centrifugal compressors.

The shape of the helical square duct, as shown in Fig. 1, is determined by the dimensionless curvature κ and torsion τ. The torsion is defined as $\tau = ab/(b^2+c^2)$, where a is the width of the cross section of the helical duct, $2\pi b$ is the pitch of the helical duct, and c is the radius of the cylinder that the helical duct is wound around. The curvature induces a centrifugal force acting on the flow in the duct. The action of the centrifugal force in a toroidal duct has been studied by various numerical calculations by Joseph et al. (1975), Cheng et al. (1976), Ghia and Sokhey (1977), Ghia et al. (1987), and Chen and Jan (1990). The centrifugal force affects the flow from the inner wall near the center of the curvature to the outer wall of the duct and increases the friction loss. In addition, it also causes a secondary flow with a pair of counter-rotating vortices. For values of the Dean number above the critical, the secondary flow pattern will have an additional pair of vortices near the central outer region and such phenomenon is known as Dean's instability (Cheng et al., 1976). When the cross-section of the toroidal duct is inclined (Duh and Shih, 1989) however, this phenomenon is not observed.

Although the curvature effects from the centrifugal force in the toroidal duct are well understood, the number of studies that deal with the torsion effect on the flow in the helical square duct are limited. The flow in the helical pipe has been studied for circular (Manlapaz et al., 1980; Wang, 1981; Murata et al., 1981; Germano, 1982, 1989; Chen and Fan, 1986; Kao, 1987; Xie, 1990, Tuttle, 1990; Chen and Jan, 1992;) and elliptical cross sections (Germano, 1989). The findings of Wang

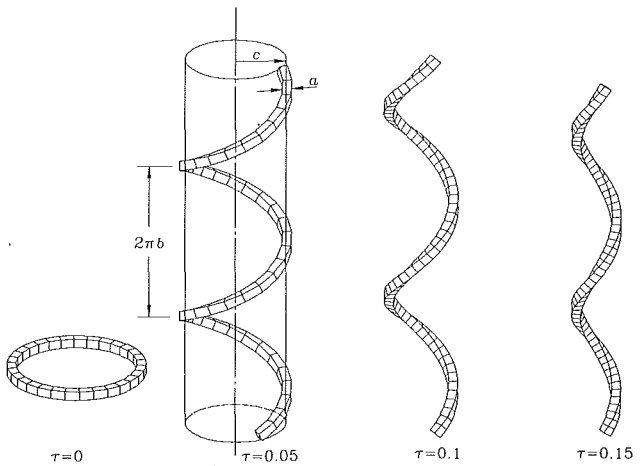

Fig. 1 The geometry of the helical square duct with $\kappa = 0.1$

Contributed by the Fluids Engineering Division for publication in the JOURNAL OF FLUIDS ENGINEERING. Manuscript received by the Fluids Engineering Division December 17, 1991; revised manuscript received March 3, 1993. Associate Technical Editor: J. Humphrey.

(1981) and Germano (1982) regarding the torsion effect on secondary flow in helical circular pipes have been inconsistent. Wang (1981) obtained the perturbation solution of the Navier-Stokes equations based on a nonorthogonal helical coordinate system and stated that the torsion effect on the secondary flow is important. However, introducing an orthogonal coordinate system rendered from a special transformation, Germano (1982) reported that the torsion effect is of second-order. Other perturbation solutions in the literature (Kao, 1987; Germano, 1989; Xie, 1990) reconfirmed the conclusion of Germano (1982). It is worthwhile to mention that those approaches are valid only for the cases with small curvature and torsion. Recently, this inconsistency has been settled qualitatively by Tuttle (1990) and Chen and Jan (1992), who by using a double series expansion method, found that different conclusions of the torsion effect on the secondary flow are attributed to the different coordinate system used by the individual observer. Nevertheless, for the helical pipe with elliptical cross section, a first-order torsion effect is observed (Germano, 1989). It is thus expected that torsion will play an important role on the secondary flow in the helical square duct.

Regarding frictional loss, it is known that the friction factor for the helical circular pipe can be replaced by that of the toroidal circular pipe, if the torsion is small (Manlapaz et al., 1980; Murata et al., 1981; Chen and Fan, 1986; Kao 1987). For the helical square duct, however, the torsion effect on friction loss has not been reported yet. The study of the friction factor for the helical square duct is necessary for the design of industrial devices.

The objective of this work is to study the torsion effect on the fully developed steady-state laminar flow in the helical square duct. The governing equations are derived by the nonorthogonal helical coordinate system as employed by Wang (1981) and Chen and Fan (1986). Since the high-order terms of curvature and torsion are taken into account, the solutions are not limited to small curvature and torsion. An accurate finite-element analysis model is formulated by the Galerkin method (Zienkiewicz and Taylor, 1989). The solutions are first verified by the flow in the toroidal square duct of which the torsion vanishes (Cheng et al., 1976; Ghia and Sokhey, 1977; Duh and Shih, 1989). The interaction effects of curvature, torsion, and inclined angle of the crossection on the secondary flow, axial velocity, and friction factor in the helical square duct are then drawn for representative cases.

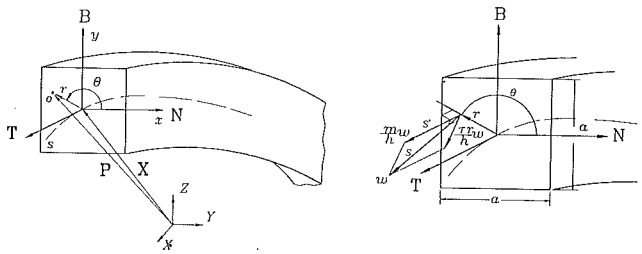

Fig. 2 The nonorthogonal and orthogonal helical coordinate systems (r, θ, s) and (r, θ, s')

2 Coordinate System and Governing Equations

To derive the governing equations directly, as shown in Fig. 2, the nonorthogonal helical coordinate system devised by Wang (1981) is adopted here. The transformation employed by Germano (1982) is therefore not necessary. The centerline of the helical square duct is described by the position vector $\mathbf{X}(s)$, where s represents the dimensionless arc length normalized by the equivalent hydraulic diameter of the helical duct De, which is defined as the width of the cross section of the helical square duct,

$$De = a.$$

Along the centerline, the unit tangent, normal and binormal vectors are mutually orthogonal and denoted as **T**, **N**, and **B**. The helical coordinate system (r, θ, s) is constructed with the coordinates (r, θ), defined by the plane of **N** and **B**, and the third coordinate s along the axial direction of the helical square duct. The radial distance r is measured from the centerline and the angle θ is measured from the normal **N** in counterclockwise sense. The quantities r and s are normalized by the equivalent hydraulic diameter De of the duct. The position vector **P** at an arbitrary point o is expressed as

Nomenclature

A = area of the cross section
a = width of the cross section of the helical square duct
$\mathbf{B}$ = binormal vector
$2\pi b$ = pitch of the helical duct
c = radius of the cylinder which the helical duct winds around
De = equivalent hydraulic diameter, a
$\{F\}$ = load vector due to the axial pressure gradient
f_1 = friction factor derived from the overall force balance, $-(\partial p/\partial s)/(2\mathrm{Re}\overline{w})$
f_2 = friction factor derived from the axial velocity gradient, $2(\partial w/\partial n)/(\mathrm{Re}\overline{w})$
f_s = friction factor of the straight square duct
g_{ij} = metric tensor
h = $(m^2+\tau^2r^2)^{1/2}$
K = Dean number, $\mathrm{Re}\,\kappa^{1/2}$
K_c = critical Dean number
$[K]$ = stiffness matrix
$\{M\}$, M_i = interpolation function
m = $1-\kappa r\cos\theta$
$[N]$, N_i = interpolation function
$\mathbf{N}$ = unit normal vector
n = inward unit normal
P = pressure
p = dimensionless pressure, $P\,\mathrm{De}^2/(\rho\nu^2)$
$\{Q\}$ = load vector due to the natural boundary conditions
$\{q\}$ = global nodal vector
$\mathbf{X}$ = the vector describes the centerline of a helical duct
Re = Reynolds number, $\overline{w}$
(r, θ, s) = nonorthogonal helical coordinates
(r, θ, s') = orthogonal helical coordinates
S^e = boundary area of element e
$\mathbf{T}$ = unit tangent vector
(U, V, W) = velocity components in r, θ, and s directions
(u, v, w) = dimensionless velocity components in r, θ, and s directions
(u', v', w') = dimensionless velocity components in r, θ, and s' directions
$\overline{w}$ = averaged axial velocity component
(x, y) = dimensionless rectangular coordinates in the (r, θ) plane
κ = dimensionless curvature
τ = dimensionless torsion
ν = kinematic viscosity
ρ = density
φ = inclined angle
χ = relaxation factor
Ω^e = area of element e

$$\mathbf{P} = \mathbf{X}(s) + r\cos\theta\mathbf{N}(s) + r\sin\theta\mathbf{B}(s). \quad (1)$$

Using Serret-Frenet formulas,

$$\mathbf{T} = \frac{d\mathbf{X}}{ds},\ \mathbf{N} = \frac{1}{\kappa}\frac{d\mathbf{T}}{ds},\ \mathbf{B} = \mathbf{T}\times\mathbf{N},\ \frac{d\mathbf{N}}{ds} = \tau\mathbf{B} - \kappa\mathbf{T}$$

and

$$\frac{d\mathbf{B}}{ds} = -\tau\mathbf{N},$$

we have

$$d\mathbf{P}\cdot d\mathbf{P} = dr^2 + (rd\theta)^2 + ((1-\kappa r\cos\theta)^2 + \tau^2 r^2)ds^2 + 2\tau r^2 d\theta ds,$$

where the dimensionless quantities, κ and τ, normalized by the equivalent hydraulic diameter De denote the curvature and torsion of the centerline of the duct, respectively. Thus, the metric tensor $[g_{ij}]$ is

$$[g_{ij}] = \begin{bmatrix} 1 & 0 & 0 \\ 0 & r^2 & \tau^2 r \\ 0 & \tau^2 r & h^2 \end{bmatrix}$$

where

$$h^2 = m^2 + \tau^2 r^2 \text{ and } m = 1 - \kappa r\cos\theta.$$

Although r and s coordinates and r and θ coordinates are mutually orthogonal, since g_{23} and g_{32} of the metric tensor are nonzero, the θ and s coordinates are nonorthogonal to each other except at the centerline of the duct where the direction of s coordinate coincides with the tangential vector $\mathbf{T}$.

For convenience, we introduced the following dimensionless velocity components u, v, and w and dimensionless pressure p as

$$u = \frac{De}{\nu}U,\ v = \frac{De}{\nu}V,\ w = \frac{De}{\nu}W$$

$$\text{and } p = \frac{P}{\rho}\left(\frac{De}{\nu}\right)^2,$$

where U, V, and W represent the physical velocity components in r, θ, and s directions, respectively. P is the pressure, ν is the kinematic viscosity and ρ is the density.

For steady-state, incompressible, fully developed laminar flow, $(\partial/\partial s)(u, v, w)$ vanishes, and (u, v, w) and p are independent of time. Furthermore, the axial pressure gradient $\partial p/\partial s$ is given for the study. Based on these, the governing equations can be written as follows (Chen and Fan, 1986):

Continuity Equation:

$$\frac{\partial u}{\partial r} + \frac{1}{r}\frac{\partial v}{\partial\theta} + \frac{u}{r} + \frac{\kappa}{m}(v\sin\theta - u\cos\theta) = 0 \quad (2)$$

Navier-Stokes Equations:

in r-direction:

$$u\frac{\partial u}{\partial r} + \frac{v}{r}\frac{\partial u}{\partial\theta} - \frac{v^2}{r} - \frac{2\tau}{h}vw - (\tau^2 r - \kappa m\cos\theta)\left(\frac{w}{h}\right)^2 = -\frac{\partial p}{\partial r} + \nabla^2 u - \frac{2}{r^2}\frac{\partial v}{\partial\theta} - \frac{2\tau}{hmr}\frac{\partial w}{\partial\theta} - \left(\frac{1}{r^2} + \left(\frac{\kappa\cos\theta}{m}\right)^2\right)u - \left(\frac{\kappa\sin\theta}{rm} - \frac{\kappa^2\cos\theta\sin\theta}{m^2}\right)v + \frac{2\kappa\tau\sin\theta}{h^3}w \quad (3)$$

in θ-direction:

$$u\frac{\partial v}{\partial r} + \frac{v}{r}\frac{\partial v}{\partial\theta} + \frac{vu}{r} - \frac{\kappa\sin\theta}{m}w^2 + \frac{2\tau}{hm}(u - v\kappa r\sin\theta)w = -\frac{h^2}{rm^2}\frac{\partial p}{\partial\theta} + \frac{\tau r}{m^2}\frac{\partial p}{\partial s} + \nabla^2 v + \left(\frac{2}{r^2} - \frac{2\kappa\tau^2 r\cos\theta}{m^3}\right)\frac{\partial u}{\partial\theta} + \frac{2\kappa\tau^2 r\sin\theta}{m^3}\frac{\partial v}{\partial\theta} + \frac{2\tau}{hm}\frac{\partial w}{\partial r} + \frac{h^2\kappa\sin\theta}{rm^4}u - \left(\frac{1}{r^2 m} - \frac{h^2\kappa\cos\theta}{rm^4} + \left(\frac{\kappa h}{m^2}\right)^2\right)v + \frac{2\tau}{h^3}\left(\kappa\cos\theta - \frac{\tau^2 r}{m}\right)w \quad (4)$$

in s-direction:

$$u\frac{\partial w}{\partial r} + \frac{v}{r}\frac{\partial w}{\partial\theta} + \frac{\kappa}{m}(v\sin\theta - u\cos\theta)w + \frac{\kappa\tau r\sin\theta}{hm}w^2 - \frac{r\tau^2}{h^2 m}(u - v\kappa r\sin\theta)\ w = +\frac{h}{m^2}\left(-\frac{\partial p}{\partial s} + \tau\frac{\partial p}{\partial\theta}\right) + \nabla^2 w + \frac{2\kappa\tau h}{m^3}\left(\frac{\partial u}{\partial\theta}\cos\theta - \frac{\partial v}{\partial\theta}\sin\theta\right) - \frac{2\tau^2 r}{mh^2}\frac{\partial w}{\partial r} + \frac{\kappa\tau h}{m^4}(v\kappa r - v\cos\theta - u\sin\theta) - \left(\frac{\kappa^2}{h^2} + \frac{\tau^2}{h^2}\left(1 - \frac{2}{m} + \frac{3}{h^2}\right)\right)w \quad (5)$$

where

$$\nabla^2 = \frac{\partial^2}{\partial r^2} + \left(\frac{1}{r} - \frac{\kappa\cos\theta}{m}\right)\frac{\partial}{\partial r} + \left(\frac{\kappa\sin\theta}{mr} - \frac{\kappa\tau^2 r\sin\theta}{m^3}\right)\frac{\partial}{\partial\theta} + \left(\frac{h}{rm}\right)^2\frac{\partial^2}{\partial\theta^2}.$$

The terms $(\kappa m\cos\theta)(w/h)^2$ in Eq. (3) and $(\kappa\sin\theta/m)w^2$ in Eq. (4) are nothing but the centrifugal force terms which produce the secondary flow in the helical square duct. The pressure gradient term $\tau r/m^2$ $(\partial p/\partial s)$ in Eq. (4) caused by the torsion can be observed clearly in the non-orthogonal helical coordinate system only. It swirls the flow and enhances the secondary flow described by this coordinate system. If these three components of momentum are expressed in an orthogonal coordinate system (r, θ, s') (Germano, 1982) as shown in Fig. 2, the pressure gradient term $\tau r/m^2$ $(\partial p/\partial s)$ in Eq. (4) will disappear. Thus, the major contribution of the torsion effect comes from the terms $(2\tau vw/h + r(\tau w/h)^2)$ in Eq. (3) and $2\tau uw/(hm)$ in Eq. (4).

As seen in Fig. 2, the x-axis and y-axis coincide with the unit normal $\mathbf{N}$ and binormal $\mathbf{B}$, respectively. Because both the x-axis and y-axis are nonorthogonal with respect to s coordinate, except at the center point, the governing equations derived based on (x, y) coordinates will be more complex than that based on (r, θ) coordinates. Although the governing equations are established by the nonorthogonal coordinates (r, θ, s) here, the finite-element numerical procedure developed can also be used to deal with the flow of the duct with other cross-sections.

To calculate the Reynolds number Re, owing to the nonorthogonality of the coordinate system, care should be taken to the axial velocity w which is not perpendicular to the r-θ plane where the flow passes through, except at the centerline of the helical square duct. As shown in Fig. 2, the axial velocity component which passes through this plane can be found as $w(m/h)$ and the average axial velocity through the r-θ plane is obtained as

$$\overline{w} = \frac{1}{A}\int_A \frac{m}{h}w dA, \quad (6)$$

where A is the area of the cross-section. Since the average axial velocity $\overline{w}$ provides a better description of the flow than the axial pressure gradient $\partial p/\partial s$ (Berger et al., 1983), the Reynolds number Re and the Dean number K are defined as

$$Re = \overline{w} \quad (7)$$

and

$$\mathrm{K} = \mathrm{Re}\,\kappa^{1/2}. \quad (8)$$

The friction factor

$$f_1 = \frac{1}{2Re\overline{w}}\left(-\frac{\partial p}{\partial s}\right), \quad (9)$$

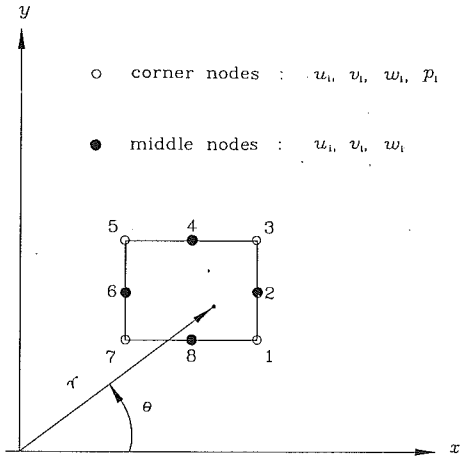

Fig. 3 Eight-node quadrilateral element

is obtained from the overall force balance for a differential axial length of the duct and the second friction factor

$$f_2=\frac{2}{Re\bar{w}}\left(\frac{\partial w}{\partial n}\right), \tag{10}$$

is obtained from the average axial velocity gradient along the duct wall, where n is the inward unit normal. Although f_1 and f_2 are defined in different ways, they denote the same quantity. Hence, for an exact flow solution, these two friction factors are identical. Thus, the calculations of f_1 and f_2 can provide a method to assess the accuracy of the numerical results (Cheng et al., 1976).

3 Numerical Techniques

Finite-Element Formulation. The Galerkin finite-element approach is adopted to solve the governing differential equations. The velocities and pressure are chosen and discretized as independent variables. The eight-node quadrilateral element as shown in Fig. 3 is used to divide the cross-section of the helical square duct. The velocities are interpolated by a quadratic polynomial and the pressure can be therefore interpolated by a linear function (Zienkiewicz and Taylor, 1989). As indicated in Fig. 3, the nodal velocities are assumed at all nodes and the pressure is chosen at corner nodes only. Thus, the velocities and pressure in an element can be expressed as

$$\begin{Bmatrix} u \\ v \\ w \end{Bmatrix} = [N] \begin{Bmatrix} u^e \\ v^e \\ w^e \end{Bmatrix}$$

and

$$p=\{M\}^T\{p^e\}, \tag{11}$$

where $\lfloor u^e, v^e, w^e \rfloor^T$ and $\{p^e\}$ denote the vectors of nodal velocities and pressure within element e, respectively. $[N]$ and $\{M\}$ are the interpolation functions which are well-documented in the literature (Zienkiewicz and Taylor, 1989). $\{\ \}^T$ and $\lfloor\ \rfloor^T$ represent the transpose of the column and row vectors.

Using the Galerkin weighted residual procedure, the global assemblies of the elemental contributions associated with the continuity equation and the Navier-Stokes equations are

$$\sum_{e=1}^{m}\int_{\Omega^e} M_i H(\ )d\Omega=0 \quad (i=1, 2, \ldots 4) \tag{12}$$

and

$$\sum_{e=1}^{m}\int_{\Omega^e} N_i L(\ )d\Omega=0 \quad (i=1,2, \ldots 8), \tag{13}$$

where Ω^e is the area of element e. $H(\ )$ and $L(\ )$ represent the continuity equation and the Navier-Stokes equations for the present steady-state, fully developed laminar flow, respectively. M_i and N_i are the appropriate interpolation functions. Using the Green's theorem (Sokolnikoff, 1964), the manipulation of the Laplace operator $\nabla^2(\ )$ in the Navier-Stokes equations can be further treated as

$$\sum_{e=1}^{m}\int_{\Omega^e} N_i\nabla^2(\ )d\Omega=-\sum_{e=1}^{m}\int_{\Omega^e}\left(\frac{\partial N_i}{\partial r}\frac{\partial(\ )}{\partial r}+\left(\frac{h}{r\,m}\right)^2\frac{\partial N_i}{\partial\theta}\frac{\partial(\ )}{\partial\theta}\right)d\Omega+\sum_{e=1}^{m}\int_{S^e} N_i\frac{\partial(\ )}{\partial n}\,dS. \tag{14}$$

S^e denotes the boundary area of element e.

Substituting Eqs. (11) and (14) into Eqs. (12) and (13), after necessary manipulations, the final simultaneous nonlinear algebraic equations can be obtained in a matrix form:

$$[K]\{q\}=\{Q\}+\{F\}, \tag{15}$$

where the global nodal vector $\{q\}=\Sigma_{e=1}^{m}\{q^e\}$, and $\{q^e\}^T=\lfloor u_1, u_2, \ldots, u_8, v_1, v_2, \ldots, v_8, w_1, w_2, \ldots, w_8, p_1, p_2, p_3, p_4\rfloor$. $[K]$ is the stiffness matrix. The column vectors $\{Q\}$ and $\{F\}$ denote the load vectors due to the natural boundary conditions and the axial pressure gradient, respectively. The details of matrices $[K]$, $\{Q\}$, and $\{F\}$ can be referred to Chen and Fan (1986). It is noted that the stiffness matrix $[K]$ is unsymmetrical and is a function of nodal variable vectors ($\{u\}$, $\{v\}$, $\{w\}$, and $\{p\}$) and the local vectors $\{Q\}$ and $\{F\}$ are kept constant in each iteration once the boundary conditions and axial pressure gradient are given.

Solution Algorithm. To solve the simultaneous nonlinear algebraic equations of Eq. (15), a successive approximation is used (Gartling, 1977). For clarity, Eq. (15) can be rewritten as

$$[K(\{q\}^i)]\{q\}^{i+1}=\{Q\}+\{F\} \quad (i=0, 1, 2\ldots), \tag{16}$$

where the superscript i and $i+1$ denote the stages of successive iterations. The iteration procedure used here is summarized as:

1. At $i=0$, assume an initial value for the nodal velocities and pressure, say, $\{q\}^0$.
2. Compute $[K]$, $\{Q\}$, and $\{F\}$.
3. Solve Eq. (16) and get the updated nodal vector $\{q\}^{i+1}$.
4. Check if the following convergence criterion is satisfied,

$$\frac{\max|\{q\}^{i+1}-\{q\}^i|}{\max|\{q\}^{i+1}|}<10^{-3}. \tag{17}$$

5. If it is satisfied, the numerical procedure is finished.
6. If Eq. (17) is not satisfied, introduce a relaxation factor χ to update $\{q\}^{i+1}$ as $\{q\}^{*(i+1)}$,

$$\{q\}^{*(i+1)}=\{q\}^i+\chi(\{q\}^{i+1}-\{q\}^i). \tag{18}$$

7. Take $\{q\}^{*(i+1)}$ as the new $\{q\}^i$ in Eq. (16) and repeat the iteration process from step 2 until the convergent test of step 4 is satisfied.

The initial value of each case is the convergence solution of the case with the closest Dean number K, curvature κ and torsion τ. The values of relaxation factor χ ranging from 1 to 0.1 are used as the Dean number increases.

The Mesh Arrangement and Boundary Conditions. There are 12×12 elements taken in the analysis. As shown in Fig. 4, according to the axial velocity gradient, the size of elements is designed unequally and more refined elements need to be taken near the boundary of the outer-wall region. The performance of this mesh has been examined from the accuracy of the computed friction factors, f_1 and f_2.

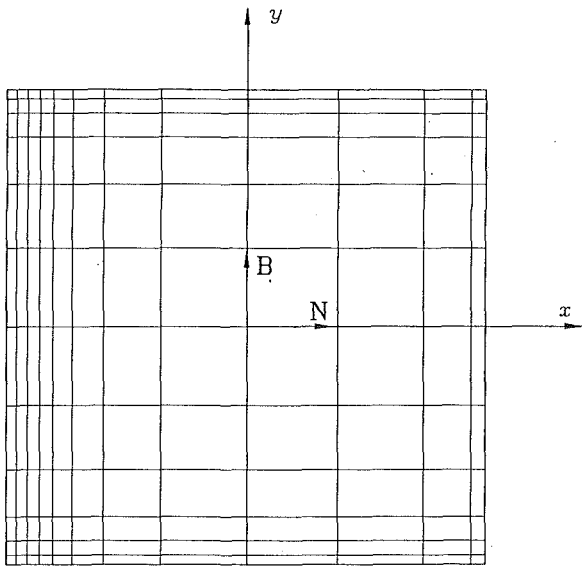

Fig. 4 Finite element mesh for the helical square duct

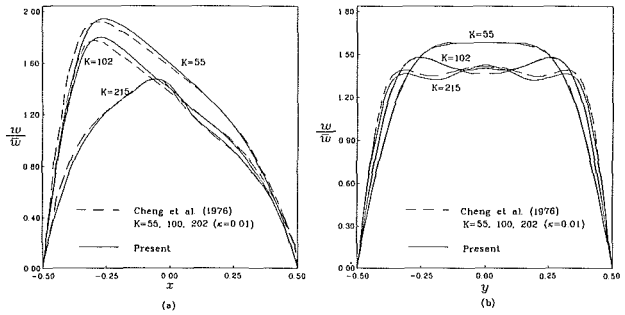

Fig. 5 Comparison of the axial velocity at (*a*) $y=0$ and (*b*) $x=0$

The non-slip boundary conditions used on the walls are

$$u=v=w=0. \tag{19}$$

When the torsion vanishes, the duct can be treated as a toroidal duct and the flow will be symmetric with respect to the x-axis. In such case, it is sufficient to solve the upper half of the cross-section with the following symmetric boundary conditions at the x-axis,

$$v=0, \text{ and } \frac{\partial u}{\partial y}=\frac{\partial w}{\partial y}=\frac{\partial p}{\partial y}=0. \tag{20}$$

4 Results and Discussion

Grid Dependence and Accuracy of the Solutions. The grid dependence has been checked with three different meshes, 12×12, 18×18, and 22×22, for the case of axial pressure gradient $\partial p/\partial s=-1.2\times10^5$, curvature $\kappa=0.1$ and torsion $\tau=0.15$. Compared with the results obtained by the finest mesh of 22×22 elements, the differences of the friction factor f_1 computed by the mesh of 12×12 elements and 18×18 elements are 2.5 and 1.2 percent, respectively. The corresponding patterns of the axial velocity and secondary flow are nearly the same. Since the computation time needed for 12×12 elements is several times less than those for 18×18 and 22×22 elements, the mesh of 12×12 elements is hence adopted in all computations.

The two friction factors f_1 and f_2 can also be used to estimate the accuracy of the results. As shown in Tables 1–3, the present computed results of some typical cases are given. The maximum difference between the friction factors f_1 and f_2, nor-

Table 1 Numerical results for the toroidal square duct

$\partial/p/\partial s$	κ	τ	K	f_1/f_s	f_2/f_s	$(f_1-f_2)/f_1\times100\%$
-2.0×10^4	0.01	0	57.7	1.22	1.21	0.8
-4.0×10^4	0.01	0	101.8	1.38	1.37	0.7
-4.5×10^4	0.01	0	112.0	1.41	1.42	−0.7
-5.0×10^4	0.01	0	122.1	1.44	1.42	1.4
-5.5×10^4	0.01	0	131.8	1.47	1.45	1.4
-5.6×10^4	0.01	0	130.1	1.51	1.52	−0.7
-5.9×10^4	0.01	0	133.9	1.55	1.53	1.3
-1.0×10^5	0.01	0	200.0	1.76	1.76	0
-1.1×10^5	0.01	0	214.8	1.80	1.79	0.5
-2.4×10^5	0.01	0	388.5	2.13	2.06	3.2
-3.8×10^5	0.01	0	551.9	2.42	2.33	3.7
-1.0×10^5	0.05	0	370.3	2.12	2.06	2.8
-1.0×10^5	0.15	0	553.9	2.46	2.34	4.9

Table 2 Numerical results for the helical square duct with $\partial P/\partial s=-1.2\times10^5$

κ	τ	K	f_1/f_s	f_2/f_s	$(f_1-f_2)/f_1\times100\%$
0.001	0	97.9	1.36	1.36	0
0.001	0.01	98.3	1.36	1.36	0
0.001	0.05	98.0	1.36	1.37	−0.7
0.001	0.1	122.7	1.09	1.08	0.9
0.001	0.15	129.0	1.03	1.04	−1.0
0.01	0	227.3	1.86	1.83	1.6
0.01	0.01	243.9	1.73	1.74	−0.6
0.01	0.05	242.0	1.74	1.75	−0.6
0.01	0.1	238.7	1.77	1.76	0.6
0.01	0.15	243.2	1.73	1.75	1.2
0.05	0	426.2	2.21	2.10	5.0
0.05	0.01	437.6	2.16	2.12	1.9
0.05	0.05	435.7	2.16	2.13	1.4
0.05	0.1	430.2	2.19	2.13	2.7
0.05	0.15	423.4	2.23	2.13	4.5
0.1	0	547.4	2.43	2.28	6.2
0.1	0.01	563.1	2.37	2.28	3.8
0.1	0.05	559.8	2.38	2.29	3.8
0.1	0.1	553.0	2.41	2.29	5.0
0.1	0.15	541.5	2.46	2.30	6.5

Table 3 Numerical results for the helical square duct with $\partial P/\partial s=-1.0\times10^4$

κ	τ	K	f_1/f_s	f_2/f_s	$(f_1-f_2)/f_1\times100\%$
0.001	0	11.1	1.00	1.00	0
0.001	0.05	11.1	1.00	1.00	0
0.001	0.1	11.1	1.00	1.00	0
0.001	0.15	11.1	1.00	1.00	0
0.01	0	32.7	1.08	1.07	0.9
0.01	0.05	32.8	1.07	1.07	0
0.01	0.1	33.0	1.06	1.06	0
0.01	0.15	33.4	1.05	1.05	0
0.05	0	63.1	1.25	1.23	1.6
0.05	0.05	63.2	1.24	1.23	0.8
0.05	0.05	63.2	1.24	1.23	0.8
0.05	0.15	63.2	1.24	1.23	0.8
0.1	0.05	83.4	1.33	1.31	1.5
0.1	0.1	83.3	1.33	1.31	1.5
0.1	0.15	83.1	1.33	1.31	1.5

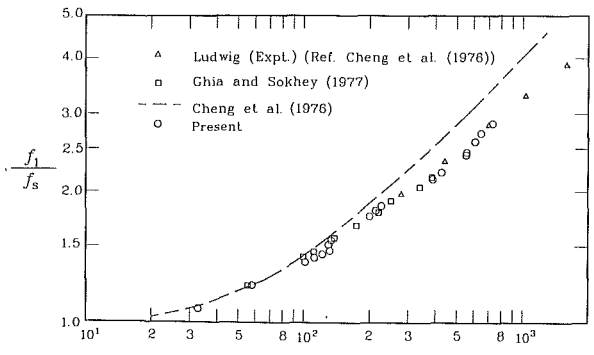

Fig. 6 The variation of normalized friction factor versus the Dean number K for the toroidal square duct

malized by the corresponding values for a straight duct f_s, is within 6.5 percent as the Dean number $K \leq 563.1$. Hence, the performance of the mesh displayed in Fig. 4 is the optimal one. For higher Dean numbers, the deviation is more obvious because the axial velocity gradient $\partial w/\partial n$ near the wall is steeper than that of the lower Dean numbers. To compensate for this, a more refined finite-element mesh near the wall is needed. Thus, the friction factor f_1, instead of f_2, should be used to calculate the frictional loss, especially at high Dean numbers.

Comparison With the Previous Studies for Toroidal Square Ducts. When the torsion vanishes, the helical square duct becomes a toroidal one. Results of the flow in such a duct are available in the literature. The computed profiles of the axial velocity along the x-axis and y-axis are shown in Fig. 5 and found in good agreement with the numerical data obtained by Cheng et al. (1976).

The variation of the friction factor ratio f_1/f_s versus the Dean number K for a wide range of $32.7 \leq K \leq 729.7$ is displayed in Fig. 6. For comparison purposes the experimental results of Ludwieg (Cheng, 1976) and the numerical study of Cheng et al. (1976) and Ghia and Sokhey (1977) are also shown.

Although the deviation of the present study from the correlated equation of Cheng et al. (1976) is observed at high Dean numbers, the trend that the friction factor is increasing with the Dean number is consistent with the findings of Lud-

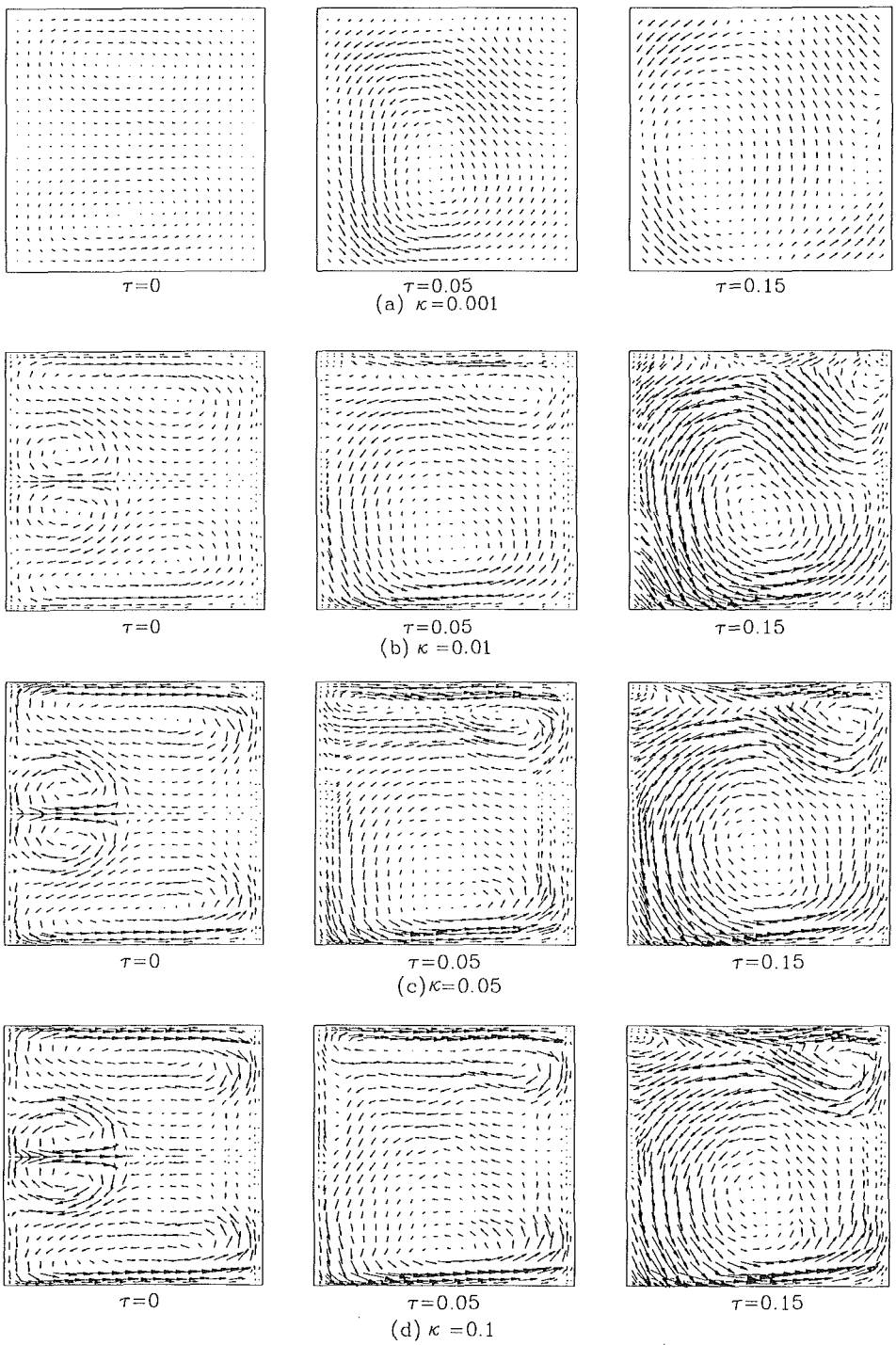

Fig. 7 The torsion effect on the secondary flow under various curvatures ($\partial p/\partial s = -1.2 \times 10^5$)

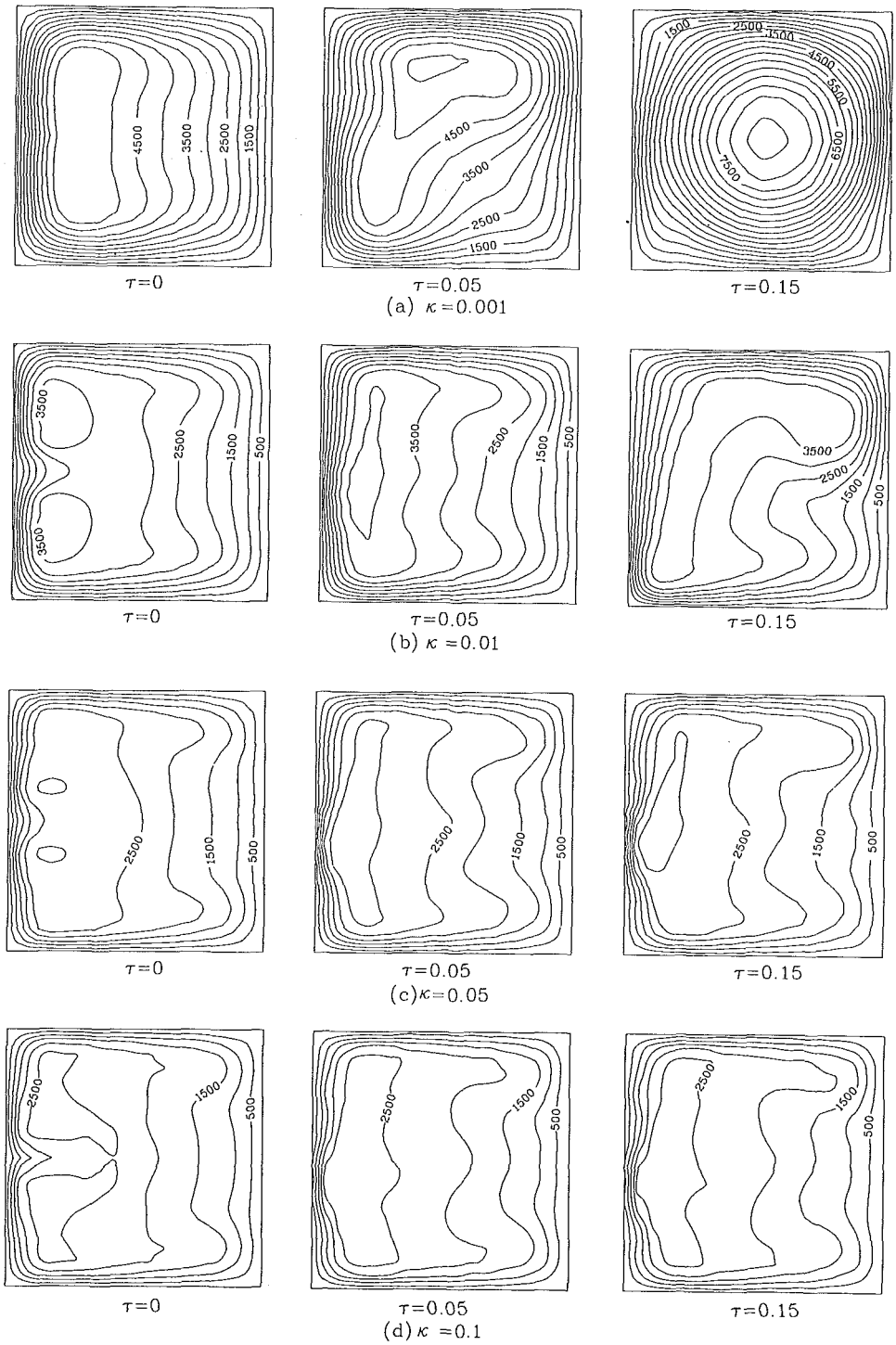

Fig. 8 The torsion effect on the axial velocity mw/h under various curvatures ($\partial p/\partial s = -1.2 \times 10^5$)

wieg (ref. (Cheng, 1976)) and Ghia and Sokhey (1977). The present study showed that Dean's instability occurs at Dean number $K \geq 133.9$ and persists even at $K = 729.7$. In the solutions of Cheng et al. (1976), however, Dean's instability disappears again at Dean number $K = 520$.

The Torsion Effect on the Secondary Flow. As seen in previous studies of the helical circular pipe, (Wang, 1981; Germano, 1982) the effects of torsion on secondary flow vary. This variation can be attributed to the different coordinate systems used. However, the physical effect of the torsion on the secondary flow can be viewed only in the orthogonal coordinate system. To realize the torsion effect on the secondary flow for the helical square duct, the velocities (u, v, w) defined in the nonorthogonal coordinate system (r, θ, s) should be transformed to the orthogonal coordinate system (r, θ, s'). As shown in Fig. 2, the axial velocity w can be divided into two components wm/h and $w\tau r/h$. By multiplying by a scale factor $(2\kappa)^{1/2}$, the component wm/h which is normal to the (r, θ) plane is the axial velocity w'. The component $w\tau r/h$ is the angular velocity component on the (r, θ) plane. The relations between the velocities (v, v, w) of the present study and (u', v', w') of Kao (1987) can be listed as:

$$u' = u,\ v' = v + w\frac{\tau r}{h} \text{ and } w' = w\frac{m}{h}(2\kappa)^{1/2}. \qquad (21)$$

The curvature and torsion effects on the secondary flow are displayed in Fig. 7. As torsion vanishes, only the centrifugal force acts. Hence, as shown in Fig. 7(*a*), the upper and lower vortices are symmetrical with respect to the *x*-axis and a pair of counter-rotating vortices are observed. As curvature increases, the strength of the secondary flow is enhanced and an additional pair of vortices is found (see Figs. 7(*b*), (*c*), and (*d*)). This phenomenon is noted as Dean's instability (Cheng et al., 1976) as the Dean number K exceeds its critical value K_c ($K_c = 133.9$ here). Besides, to satisfy the continuity equation, a pair of strong, parallel inward flows are also seen at the top and bottom walls.

When torsion increases, the pairs of vortices merge and the lower vortex grows larger and squeezes the upper one to a narrow region. This tendency is similar to that observed by Chen and Fan (1986) and Kao (1987) for the flow in the helical circular pipe. In the case of $\kappa = 0.001$ and $\tau = 0.15$ as seen in Fig. 7(*a*), the torsion effect is so dominant that the secondary flow pattern has only a rotating vortex and the upper vortex disappears completely. Although the upper vortex may grow larger as curvature increases, (see Figs. 7(*b*), (*c*) and (*d*) it is still smaller than the lower one even when the curvature increases to $\kappa = 0.1$. Furthermore, the sources and sinks of the secondary flow pattern which occurred at the boundaries of the duct wall are also noted by Germano (1989) for the helical elliptical duct.

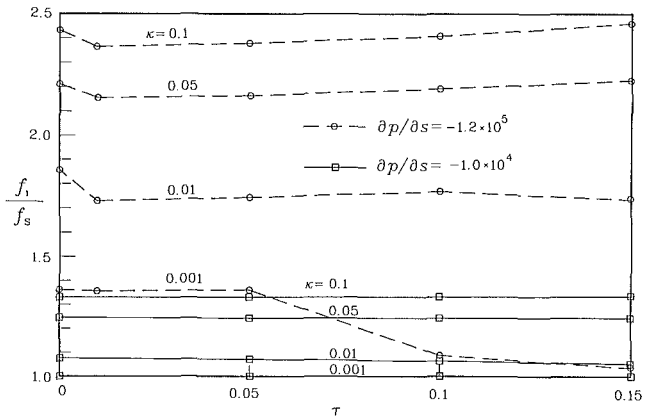

Fig. 9 The torsion effect on the friction factor ratio under various curvatures

The Torsion Effect on the Axial Velocity. The torsion effect on the axial velocity mw/h is displayed in Fig. 8. These are calculated under the same conditions mentioned in the previous section. For a toroidal duct, the centrifugal force throws the flow to the outer wall of the duct and the constant contours of axial velocity are symmetric with respect to the *x*-axis. As the curvature increases ($K > K_c$), (see Figs. 8(*b*), (*c*) and (*d*)) the phenomenon of Dean's instability reoccurs. Moreover, the axial velocity and the flow rate rate are reduced with curvature increases, as would be expected.

With the increase of the torsion, the flow is twisted about the center of the cross section and the peak of the axial velocity rotates clockwise to the upper wall. With the increase of curvature, the centrifugal force enhances and throws the flow to the outer wall.

When the flow is dominated by the torsion, as seen in the case of curvature $\kappa = 0.001$ and torsion $\tau = 0.15$ (see Fig. 8(*a*)), a uniform contour pattern which is almost symmetric with respect to the *x*- and *y*-axis is observed and the peak of axial velocity exists near the center of the duct. As the curvature increases to $\kappa = 0.01$, the torsion effect swirls the flow and makes the high speed region spread to both the upper and the outer wall (see Fig. 8(*b*)). Once the curvature increases further, the centrifugal force dominates the flow again.

The Torsion Effect on the Friction Factor. The torsion effect on the friction factor ratio under various curvatures is shown in Fig. 9. In the cases of the pressure gradient $\partial p/\partial s) = -1.2\times10^5$ and curvature $\kappa = 0.001$, an obvious decrease of friction factor ratio from torsion $\tau = 0.05$ to $\tau = 0.1$ is observed. This is due to the fact that a more uniform distribution of the axial velocity contour is obtained as the torsion is greater than 0.05 (see Fig. 8). In such cases, the flow is dominated by the torsion, the motion of the flow along the duct becomes more smooth and the friction factor ratio decreases. When the torsion is large enough ($\tau > 0.15$), the friction factor of the helical square duct approaches that of the straight square duct. Under the same pressure gradient, and as the curvature increases to $\kappa = 0.01$, 0.05 and 0.1, the Dean's instability occurs as the torsion vanishes and disappears as the torsion exists.

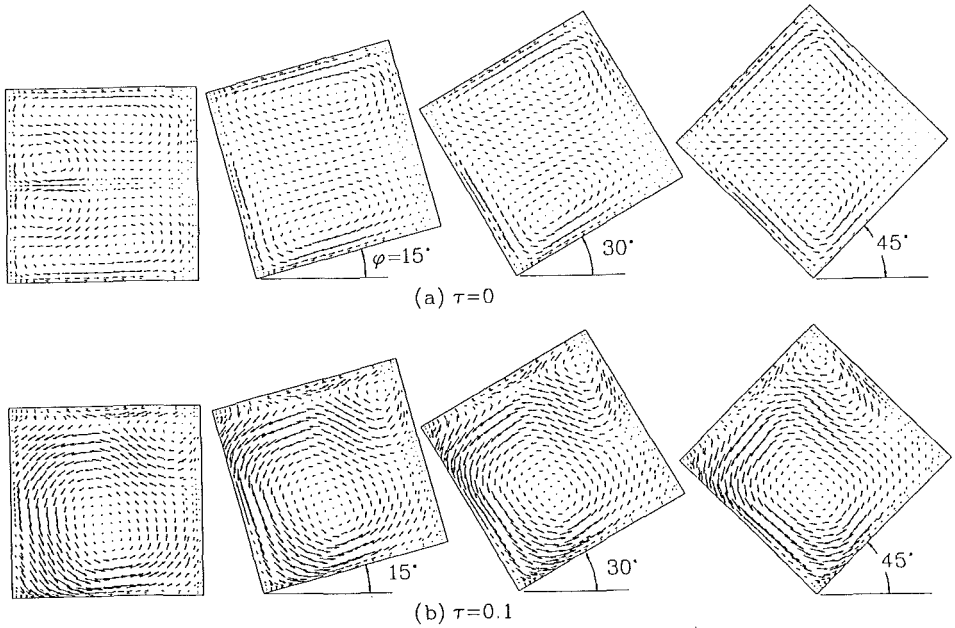

Fig. 10 The effect of inclined angle on the secondary flow ($\kappa = 0.01$ and $\partial p/\partial s = -1.0\times10^5$)

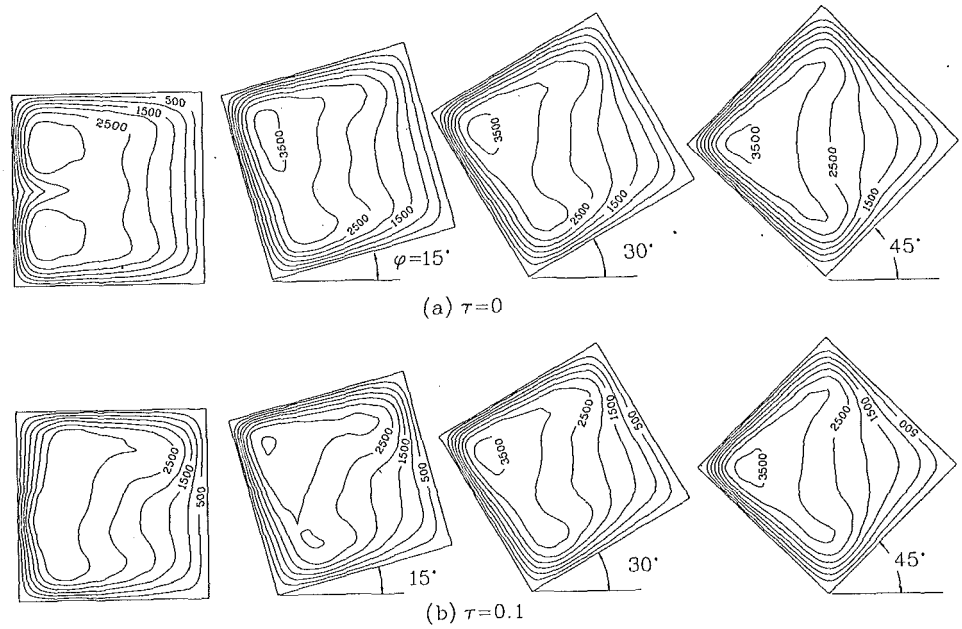

Fig. 11 The effect of inclined angle on the secondary flow ($\kappa = 0.01$ and $\partial p/\partial s = -1.0 \times 10^5$)

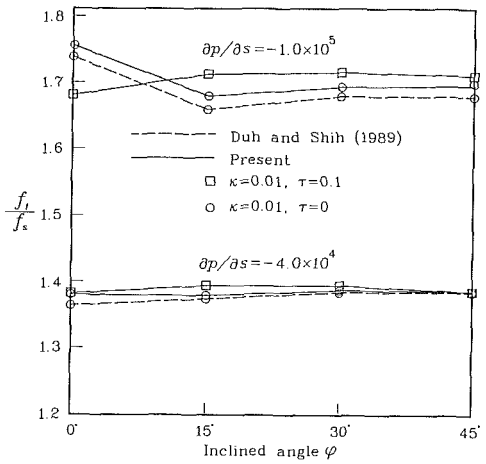

Fig. 12 The effect of inclined angle on the friction factor ratio

Hence, the friction factor ratio decreases at first and subsequently changes slightly as the torsion increases continuously.

In cases of a pressure gradient $\partial p/\partial s = -1.0 \times 10^4$, the torsion effect on the friction factor ratio is negligible. That is, if the pressure gradient is small enough, the friction factor ratio for the toroidal square duct can be used instead of that for the helical square duct for the same curvature.

The Effect of Inclined Angle. The centrifugal force is also influenced by the inclined angle of the cross section. Because the directions of the centrifugal force and the wall are not orthogonal, the flow in the inclined duct is different from that in the duct without inclining. The effects of the inclined angle of the square cross-section on the secondary flow and axial velocity are shown in Figs. 10 and 11, respectively. Inclined angles φ up to 45 deg were tested.

In Fig. 10(*a*), the secondary flow patterns of the toroidal square duct with various inclined angles are displayed. As reported by Duh and Shih (1989), the inclined angle does not permit the occurrence of the Dean's instability observed at $\varphi = 0$ deg. In addition, the inclined angle strengthens the secondary flow on the outer inclined boundaries. In the case of $\varphi = 45$ deg, since the effect of the centrifugal force is symmetric with respect to the x-axis, a symmetric secondary flow pattern is observed. Figure 10(*b*) shows the effect of the inclined angle for the helical square duct. As the inclined angle $\varphi = 0$, torsion induces a larger vortex that occupies most part of the cross section of the duct while a smaller one appears in the upper right corner of the duct. As the cross section inclines more, the smaller vortex grows larger and a stronger secondary flow on the outer inclined wall can be viewed. The rotation of the axial velocity contours and the translation of the maximum axial velocity region to the outermost corner are displayed in Fig. 11.

Figure 12 shows the variation of the friction factor ratio versus the inclined angle φ. As the torsion vanishes, the results are in excellent agreement with those of Duh and Shih (1989). The friction factor ratio for the cases of the axial pressure gradient $\partial p/\partial s = -4 \times 10^4$ does not exhibit any notable changes as the inclined angle changes. Hence, the friction factor for the toroidal square duct can be used for the helical square duct. However, for the cases with the axial pressure gradient $\partial p/\partial s = -1 \times 10^5$, the friction factor ratio has significant changes for inclined angles 0 deg $< \varphi <$ 15 deg. The friction factor ratio is the smallest at $\varphi = 0$ deg, if the Dean's instability does not occur. As the Dean's instability occurs, however, the friction factor ratio for the toroidal duct at $\varphi = 0$ is larger than that with nonvanishing inclined angles.

5 Concluding Remarks

Based on a nonorthogonal helical coordinate system, the characteristics of a fully developed laminar flow in the helical square duct have been studied using the Galerkin finite-element analysis procedure. The effects of finite curvature, finite torsion and the inclined angle of the cross section of the helical square duct on the secondary flow, axial velocity, and friction factor are presented. The solutions of the toroidal square duct are in agreement with previous studies (Cheng et al., 1976; Ghia and Sokhey, 1977; Duh and Shih, 1989). Several significant conclusions can be made:

1. Torsion has an important effect on the secondary flow. It enlarges the lower vortex and squeezes the upper one. As the torsion increases continuously, the lower vortex may occupy the entire cross-section of the duct and the upper one disappears.

2. The curvature effect throws the flow to the outer wall and makes the maximum axial velocity region occur near the

outer wall of the square duct. However, the torsion will rotate the axial velocity contour about the center of the cross section. As the flow in the helical square duct is dominated by the torsion, the maximum axial velocity will exist near the center of the duct and uniform distribution of the axial velocity is expected.

3. Dean's instability has the effect of increasing the friction factor. In addition, the friction factor of the toroidal square duct can be used for the helical square duct if the axial pressure gradient is small enough. If the curvature is small and the torsion large enough, that is, the flow is dominated by the torsion, the friction factor of the helical square duct approaches that of the straight duct even for a large axial pressure gradients.

4. The inclined angle of the helical square duct strengthens the secondary flow on the outer inclined boundaries. The curvature effect translates the maximum axial velocity region to the outermost corner in the inclined duct. Once the Dean's instability does not occur, the inclined angle does not have obvious effect on the friction factor.

5. The phenomenon of Dean's instability in the toroidal square duct occurs at Dean number $K = 133.9$ and persists of $K = 729.7$. For the helical or inclined square duct, however, this phenomenon is not observed.

Acknowledgment

The authors are grateful to the National Science Council of the Republic of China for the financial support through the grant NSC79-0401-E007-14.

References

Berger, S. A., Talbot, L., and Yao, L. S., 1983, "Flow in Curved Pipes," *Annual Review of Fluid Mechanics*, Vol. 15, pp. 461–512.

Chen, W. H., and Fan, C. F., 1986, "Finite Element Analysis of Incompressible Viscous Flow in a Helical Pipe," *Computational Mechanics*, Vol. 1, pp. 281–292.

Chen, W. H., and Jan, R., 1990 "Finite Element Analysis of Incompressible Viscous Flow in Curved Square Ducts," *The Chinese Journal of Mechanics*, Vol. 6, pp. 17–22.

Chen, W. H., and Jan, R., 1992, "The Characteristics of Laminar Flow in a Helical Circular Pipe," *Journal of Fluid Mechanics*, Vol. 244, pp. 241–256.

Cheng, K. C., Lin, R., and Ou, J. W., 1976, "Fully Developed Laminar Flow in Curved Rectangular Channels," ASME JOURNAL OF FLUIDS ENGINEERING, Vol. 98, pp. 41–48.

Duh, T. Y., and Shih, Y. D., 1989, "Fully Developed Flow in Curved Channels of Square Cross Sections Inclined," ASME JOURNAL OF FLUIDS ENGINEERING, Vol. 111, pp. 172–177.

Gartling, D. K., 1977, "A Finite Element Convergence Study for Accelerating Flow Problems," *International Journal for Numerical Methods in Engineering*, Vol. 11, pp. 1155–1174.

Germano, M., 1982, "On the Effect of Torsion of a Helical Pipe Flow," *Journal of Fluid Mechanics*, Vol. 125, pp. 1–8.

Germano, M., 1989, "The Dean Equations Extended to a Helical Pipe Flow," *Journal of Fluid Mechanics*, Vol. 203, pp. 289–305.

Ghia, K. N., and Sokhey, J. S., 1977, "Laminar Imcompressible Viscous Flow in Curved Ducts of Regular Cross-Section," ASME JOURNAL OF FLUIDS ENGINEERING, Vol. 99, pp. 640–648.

Ghi, K. N., Ghia, U., and Shin, C. T., 1987, "Study of Fully Developed Incompressible Flow in Curved Ducts, Using a Multi-Grid Technique," ASME JOURNAL OF FLUIDS ENGINEERING, Vol. 109, pp. 226–236.

Joseph, B., Smith, E. P., and Adler, R. J., 1975, "Numerical Treatment of Laminar Flow in Helically Coiled Tubes of Square Cross-Section," *AIChE Journal*, Vol. 21, pp. 965–973.

Kao, H. C., 1987, "Torsion Effect on Fully Developed Flow in a Helical Pipe," *Journal of Fluid Mechanics*, Vol. 184, pp. 335–356.

Manlapaz, R. L., and Churchill, S. W., 1980, "Fully Developed Laminar Flow in a Helically Coiled Tube of Finite Pitch," *Chemical Engineering Communication*, Vol. 7, pp. 57–78.

Murata, S., Miyake, Y., Inaba, T., and Ogawa, H., 1981, "Laminar Flow in a Helically Coiled Pipe," *Bulletin of the JSME*, Vol. 24, pp. 355–362.

Sokolnikoff, I. S., 1964, *Tensor Analysis*, Wiley, New York, NY.

Tuttle, E. R., 1990, "Laminar Flow in Twisted Pipes," *Journal of Fluid Mechanics*, Vol. 219, pp. 545–570.

Wang, C. Y., 1981, "On the Low-Reynolds-Number Flow in a Helical Pipe," *Journal of Fluid Mechanics*, Vol. 108, pp. 185–194.

Xie, D. E., 1990, "Torsion Effect on Secondary Flow in a Helical Pipe," *International Journal of Heat and Fluid Flow*, Vol. 11, pp. 114–119.

Zienkiewicz, O. C., and Taylor, R. L., 1989, *The Finite Element Method*, 4th ed., McGraw-Hill, New York, NY.

Probabilistic Simulation of Fragment Dynamics and Their Surface Impacts in the SSME Turbopump

A. Hamed

H. Moy

Department of Aerospace Engineering and Engineering Mechanics, University of Cincinnati, Cincinnati, OH 45221

Numerical simulations are used to model the dynamics of solid fragments in the high pressure fuel turbopump of the space shuttle main engine (SSME HPFTP). The simulations are conducted in a probabilistic structure in order to simulate the variance in the geometrical configuration, material properties and initial conditions of the solid fragments. The results of the particle dynamics simulations are presented in the form of the probability of surface impacts, and probability distributions of the impacting velocity and impingement angle.

Introduction

Solid fragments in the SSME HPFTP are a source of health monitoring concern because their impacts with surfaces can influence the life and performance of components and sensors. A summary of the results of a failure review of the SSME based on Unsatisfactory Condition Reports (UCRs) was presented by Teeter et al. (1987). According to this study, the high pressure fuel turbopump was the source of the largest number of UCRs, and cracking was the dominant type of failure. Besides cracking, other degradation mechanisms like cavitation, wear, rubbing, looseness, and misassembly can produce particle fragments in the engine environment. Sources of solid fragments include tanks, seals, blades, bearings and other components. A documentation of the particle ingestion history was carried out as part of Rocketdyne's Turbopump Instrumentation Final Assessment (Voyd, 1990) to characterize their sizes, shapes and sources.

Due to the fragments' higher inertia, their trajectories generally deviate from the flow streamlines and they tend to impact the solid surfaces. The amount of deviation depends on the fragment size, shape, material density and initial conditions. The paths taken by smaller, lighter fragments are dominated by the fluid forces. They tend to follow the flow streamlines more closely, and are less susceptible to surface impacts. The paths taken by larger, heavier fragments are dominated by their inertia. They deviate more from the streamlines, and impact the surfaces at higher impact angles. The particle dynamics modeling therefore requires an accurate representation of the interactions between the fragments and the fluid and between them and the solid surfaces. A knowledge of the impact locations, as well as the magnitude and direction of the impact velocity is critical to health monitoring, performance estimates and life predictions.

Contributed by the Fluids Engineering Division for publication in the JOURNAL OF FLUIDS ENGINEERING. Manuscript received by the Fluids Engineering Division July 24, 1991. Associate Technical Editor: S. Rohatgi.

In this investigation, numerical simulations are used to model the dynamics of solid fragments in the SSME HPFTP. Quasi three-dimensional calculations are used to determine the impeller flow field. A one-way interaction model is adapted regarding the interaction forces between the solid fragments and the flow. While a suspended particle trajectory is determined by the interaction forces, and its inertia, the effect of the interaction forces on the flow field is neglected. The numerical computations of the particle dynamics are performed in a probabilistic structure in order to simulate the variance in the solid fragments' shape, size, material density and initial conditions. The models for the interactions between the solid fragments and the impeller surfaces are based on empirical correlations of rebounding experimental data measured using LDV.

Particle Dynamics in the Flow Field

The equations governing the motion of solid fragments in the turbomachinery flow field are written in cylindrical polar coordinates relative to a frame of reference fixed with respect to the rotating blades.

$$\frac{d^2r_p}{dt^2} = F_r + \left(\frac{d\theta_p}{dt} + \omega\right)^2 \tag{1}$$

$$r_p \frac{d^2\theta_p}{dt^2} = F_\theta - \frac{2dr_p}{dt}\left(\frac{d\theta_p}{dt} + \omega\right) \tag{2}$$

$$\frac{d^2z_p}{dt^2} = F_z \tag{3}$$

where r, θ, z define the solid fragment location in cylindrical polar coordinates at time t. The centrifugal and Coriolis acceleration are represented by the last term on the right hand side of Eqs. (1) and (2), respectively. The first term on the

right-hand side of Eqs. (1) through (3) represents the force of interaction between the particles and flow per unit mass of solid fragments. Drag is the main force of interaction between the particles and the flow in a turbomachinery environment (Hamed et al., 1988). It is dependent on the size and shape of the material and on its velocity relative to the flow.

$$\overline{F}=\frac{\rho_f}{\rho_p}\frac{C_D}{Q/A}\left[\left(V_{r_f}-\frac{dr_p}{dt}\right)^2+\left(V_{\theta_f}-\frac{d\theta_p}{dt}\right)^2+\left(V_{z_f}-\frac{dz_p}{dt}\right)^2\right]^{1/2}(\overline{V}_f-\overline{V}_p) \quad (4)$$

where V_{r_f}, V_{θ_f}, V_{z_f} represent the relative flow velocities in the radial, circumferential and axial directions, respectively; ρ_f, ρ_p are the gas and solid particle material density, respectively, Q/A is the particle volume to surface area ratio, and C_D is the particle drag coefficient.

The particle trajectory computations were performed using a fourth order accurate Runge-Kutta scheme. The numerical integration of Eqs. (1)–(3) provides the location and velocity of the solid fragment in the flow field at successive time steps, starting from the initial conditions. When the particles impact any of the surfaces, the magnitude and direction of their rebounding velocity is required in order to continue the trajectory computations after these impacts. Empirical correlations of experimentally determined particle restitution ratios (Tabakoff, 1989) are used to determine the magnitude and direction of the rebounding velocity after the surface impact, which constitute the initial conditions for the remainder of the trajectory.

Fluid Forces. The various parameters affecting the drag coefficient and the empirical correlations for spherical particles were discussed by Hamed et al. (1988). Limited experimental data exists for the drag force on other particle geometries (Debler, 1990). Table 1 lists some of the drag coefficient correlations for some geometries that are pertinent to the present investigation, as probable candidates to approximate fragment configurations. The tabulated parameters include the ratio between the drag coefficient for a given configuration to that of a sphere. In the present investigation, the multiplication factors of Table 1 are used together with empirical correlations for spherical particles to represent the drag coefficient over the different ranges of the Reynolds number (Hamed et al., 1988). The latter is based on the fragment slip velocity relative to the flow. The characteristic time, τ, is the similarity parameter affecting the trajectories in the flow field. Identical trajectories would be expected for the same value of this parameter under different particulate flow conditions. Table 1 also lists the values of the ratio of the characteristic time for the indicated particle geometries to that of a sphere which can be seen to range between 1.3 and 2.5 for the indicated particle geometries.

The Flow Field. The high pressure fuel turbopump impeller is shown schematically in Fig. 1. The pump consists of three stages with gooseneck cross over ducts connecting each impeller exit to the following inducer. It is quite difficult to adapt most turbomachinery flow solutions to the particular HPFTP impeller configuration with three splitter blades in each main blade passage. The code developed by McFarland (1984) based on the panel method for turbomachinery flow analysis is well suited for multiple blade element geometries. It is applicable to inviscid flow and offers the advantage of resolving the flow at the blade leading and trailing edges to the desired accuracy. The code is based on the panel method, which is second order accurate in terms of the panel size. For a discussion of the numerical errors, the reader is referenced to McFarland (1982).

The solution was obtained on a number of S_1 (blade-to-blade) stream filaments using the multiplanel code of McFarland (1984). The blade input geometry at the shroud is shown in Fig. 2 with the panel control and end points. One can see the fine resolution at the leading and trailing edges. The flow computations were performed at 90 percent RPL (rated power level).

Table 1 Particle drag and similarity parameters

Particle Geometry	C_D (Range Re)	$\frac{C_{D_{shape}}}{C_{D_{sphere}}}$	τ/τ_{sphere}
●	0.40 (Re>3000)	1	1
◆	0.80 (10^4<Re<10^5)	2	1.89
■	1.05 (10^4<Re<10^5)	2.62	1.76
▮	1.16 (10^4<Re<10^5)	2.90	1.94
◖	0.42 (10^4<Re<10^5)	1.05	2.10
◀	0.5.(10^4<Re<10^6)	1.25	2.50

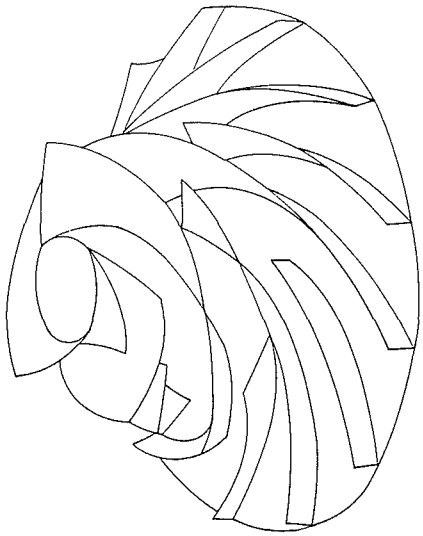

Fig. 1 SSME HPFTP impeller

Probabilistic Particle Dynamics Simulations

The problem of particle dynamics is probabilistic in nature because of the possible variance in the fragment's size, shape, material density, and initial conditions at the impeller inlet. The particle dynamics simulations are therefore performed in a probabilistic structure to model the influence of the variance in these parameters, on the particle surface impact characteristics. In the present study, the deterministic simulations of

Nomenclature

A = particle surface area
C_D = particle drag coefficient
F = drag force on the particle
M = meridional coordinate
r, z = radial and axial coordinates
t = time
V = relative flow velocity
ρ = density
θ = circumferential coordinate
τ = characteristic time for particles

Subscripts

f = fluid
p = particle
r, θ, z = components in cylindrical polar coordinate system

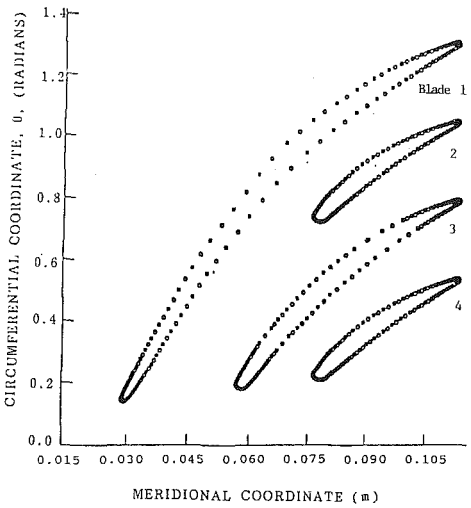

Fig. 2 Blade geometry at the shroud

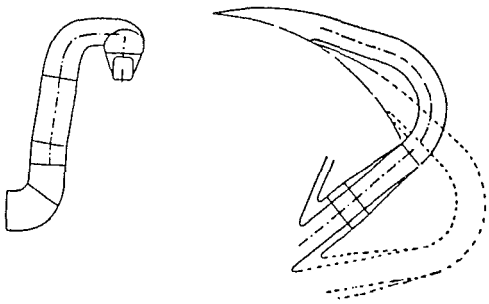

Fig. 3 Cross over duct

the particle trajectories were peformed a large number of times based on probabilistic distributions of the particle size, and initial conditions. The details of these distributions, and the basis on which they were determined for each case are given in the results and discussion.

Results and Discussion

The presented results of the probabilistic particle dynamics modeling demonstrate the effects of the variance in particle size and initial conditions. Probability distributions of particle impact locations, velocities and angles were obtained by simulating the trajectories for large samples consisting of one thousand particles. To demonstrate the effect of fragment size, results of trajectory computations are presented for two cases of solid fragments with characteristic lengths of 762 and 15 microns. In each case, an analysis of the particle trajectories in the cross over ducts preceding the impeller shown in Fig. 3, was used to obtain a probabilistic distribution of the location and velocity of the particle sample at the impeller inlet.

The first set of results are for seal fragments of 762 micron characteristic length and 8249.5 kg/m^3 material density. Figure 4 shows the computed distribution of the 762 micron particle velocity components normalized with respect to the average flow velocity at the impeller inlet as determined from the analysis of particle trajectories in the cross over ducts. Negative radial velocity components indicate particles traveling toward the hub as they enter the impeller.

Typical trajectory computations are presented in Fig. 5 for three of these particles. It is clear that the trajectories of these large fragments are dominated by their inertia, and that they deviate considerably from the flow streamlines and repeatedly impact the various blade passage surfaces. Impacts with the rotor blades impart large circumferential velocities to these

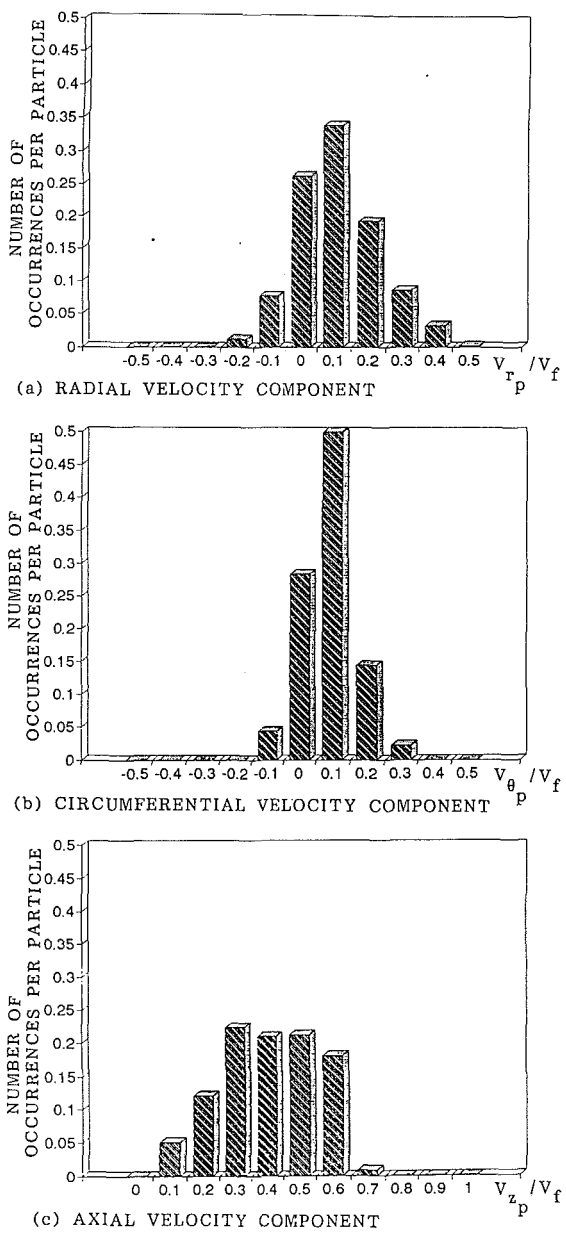

Fig. 4 Simulated variance in the 762 μm particle inlet velocity

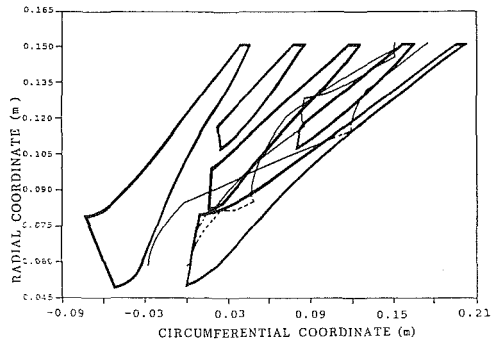

Fig. 5 Sample trajectories for the 762 μm particle

fragments which cause them to be centrifuged in the radial direction, further enhancing the deviation of their trajectories from the streamlines. The variance in the size of these larger particles does not influence the trajectories which are dominated by their inertia. Table 2 summarizes the results of blade

Table 2 Summary of impact probabilities for 762 micron particle (S = suction surface; P = pressure surface)

Impacted surface	Overall probability	Impact velocity (m/s) Mean	Mode	Probability of mode	Impact angle (deg) Mean	Mode	Probability of mode
HUB	0.113	238.81	91.44	0.017	12.20	15	0.028
SHROUD	0.661	268.56	274.32	0.242	16.27	10	0.290
BLADE 1(S)	0.235	135.12	91.44	0.059	19.81	10	0.068
BLADE 1(P)	0.396	247.96	367.76	0.068	8.26	5	0.200
BLADE 2(S)	0.064	333.03	*	*	33.53	*	*
BLADE 2(P)	0.089	362.11	396.24	0.038	1.09	1	0.043
BLADE 3(S)	0.043	262.60	*	*	13.71	*	*
BLADE 3(P)	0.220	315.00	335.28	0.080	4.44	2	0.045
BLADE 4(S)	0.012	338.73	*	*	17.23	*	*
BLADE 4(P)	0.043	375.18	*	*	1.62	*	*

* Impact velocity modes were not determined for surfaces with overall impact probabilities less than 0.08.

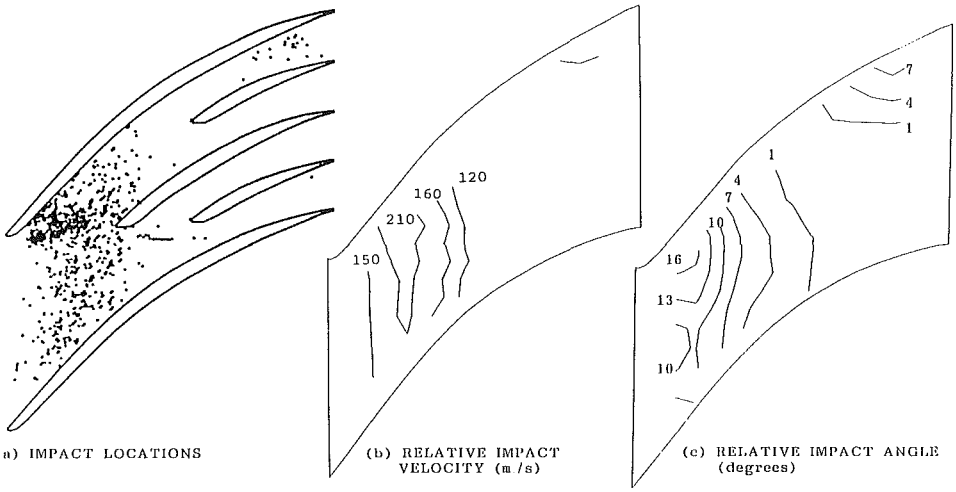

Fig. 6 Shroud impact data for the 762 μm particle

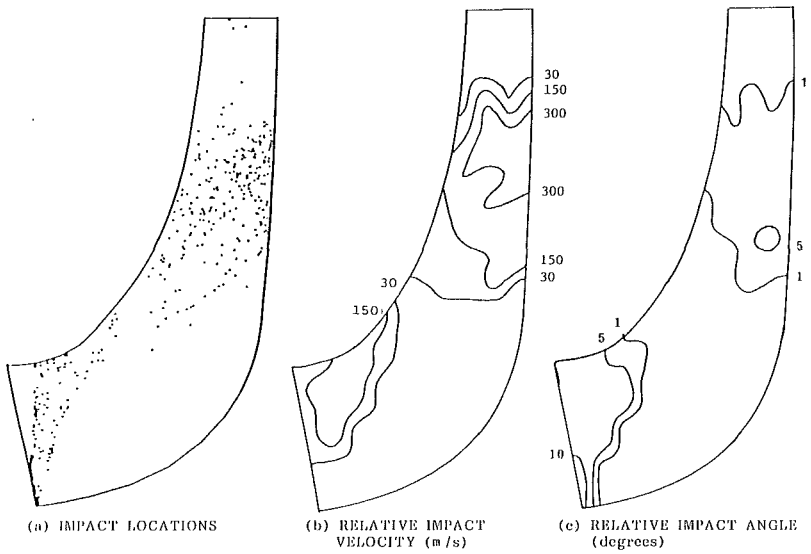

Fig. 7 Blade 1 pressure surface impact data for the 762 μm particle

surface impacts associated with one thousand simulated trajectories for these large fragments. According to the data presented in Table 2, the shroud has the highest overall impact probability of 0.661, followed by the main blade pressure surface with 0.396. The suction surfaces of the splitters are the least likely to be impacted, with the likelihood decreasing from the first to the second and then to the third.

Figures 6 and 7 present the associated impact locations and the mean values of the probable impact velocity and impingement angle. Figure 6 shows that the majority of impacts with

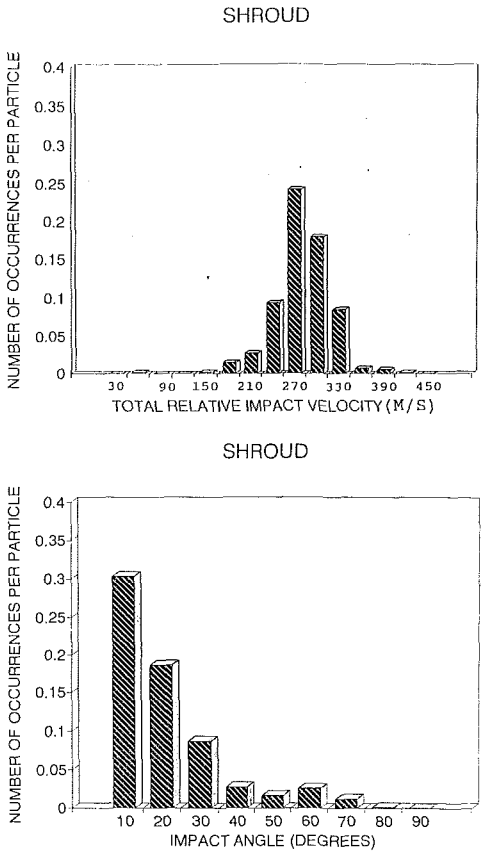

Fig. 8 Probabilistic distribution of 762 μm particle's impact conditions with the shroud

the shroud occur upstream of the leading edge of the second splitter. Figure 7 showing the probable impact locations with the main blade pressure surface indicates that these large fragments quickly centrifuge radially after their initial blade surface impacts starting at the lower third of the blade leading edge. The rest of the blade surface impact results, not presented here, indicate that the most probable impact locations on the splitter blades are near their leading edges.

The shroud surface impact data are presented in a different form in Fig. 8 to demonstrate the probabilistic nature of the simulated particle impacts. According to this figure, a high impact probability of 0.24 for the shroud is associated with the impact velocity of 270 m/s. An examination of the impact angle trends is important since brittle material type failure is associated with near normal impacts of 90 deg, while ductile material type cutting is associated with lower impact angles (Teeter et al., 1987). The probability of most hub or shroud impacts is in the 10 to 30 deg angle range. On the other hand, the impact data on the main blade pressure surface indicate a much lower probability of impact, with a maximum probability of occurrence of less than 0.07 for particle impact velocity of 360 m/s. Also small impact angles are associated with the main blade pressure surface, which mostly suffer glancing impacts at angles less than 15 deg.

The second set of results were obtained considering relatively smaller fragments of 15 micron diameter and 9130.5 kg/m^3 material density. These exist in the flow environment of the impeller due to the exfoliation of material from piping or tank structures. Figure 9 shows typical trajectory computations for six of these small particles. It is clear that these small particles follow more closely the streamlines, and are more affected by the aerodynamic drag. The variance in the size of these small particles can influence their trajectories, unlike the larger 762

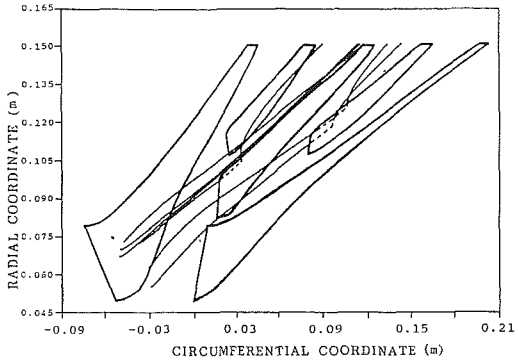

Fig. 9 Sample trajectories for the 15 μm particle

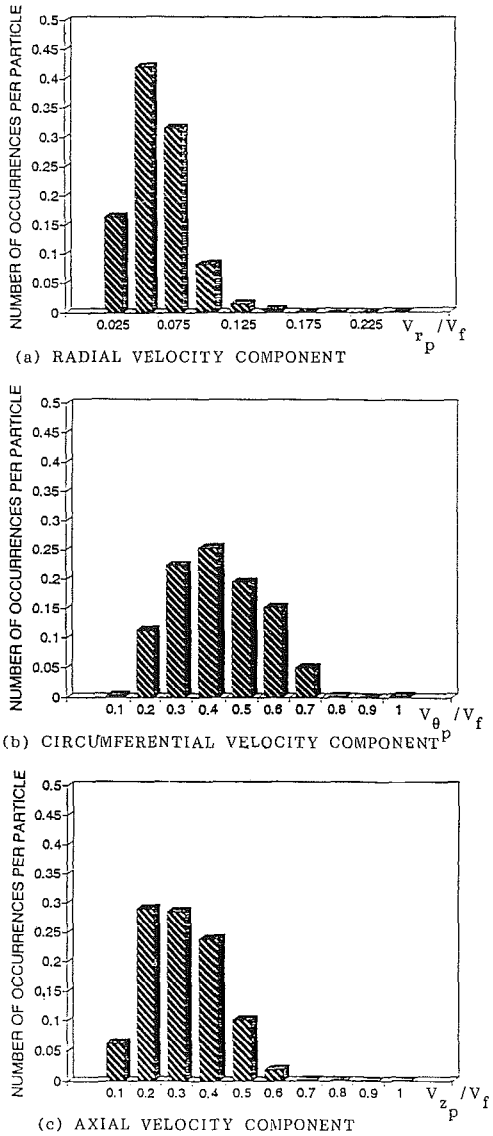

Fig. 10 Simulated variance in the 15 μm particle inlet velocity

micron particles whose dynamics are dominated by their inertia with little or no aerodynamic effects.

Uncertainty in particle size was modeled in the simulation of these smaller fragments' trajectories. The trajectory simulations were conducted for 1000 particles with a mean characteristic length of 15 microns and a standard deviation of 5 microns. Since these smaller particles follow the streamlines more closely in the cross over duct, their absolute velocities lag only a small percentage relative to the local flow velocity,

Table 3 Summary of impact probabilities for 15 micron particle (S = suction surface; P = pressure surface)

Impacted surface	Overall probability	Impact velocity (m/s)			Impact angle (deg)		
		Mean	Mode	Probability of mode	Mean	Mode	Probability of mode
HUB	0.115	27.88	*	*	18.56	*	*
SHROUD	0.258	126.56	152.40	0.089	7.21	5	0.136
BLADE 1(S)	0.158	90.04	121.92	0.059	4.35	2	0.080
BLADE 1(P)	0.032	91.48	*	*	9.25	*	*
BLADE 2(S)	0.012	199.15	*	*	6.95	*	*
BLADE 2(P)	0.096	175.78	182.88	0.043	25.19	10	0.038
BLADE 3(S)	0.001	155.00	*	*	27.47	*	*
BLADE 3(P)	0.117	118.59	152.40	0.043	14.33	10	0.073
BLADE 4(S)	0.007	200.05	*	*	10.35	*	*
BLADE 4(P)	0.028	180.60	*	*	10.48	*	*

* Impact velocity modes were not determined for surfaces with overall impact probabilities less than 0.08.

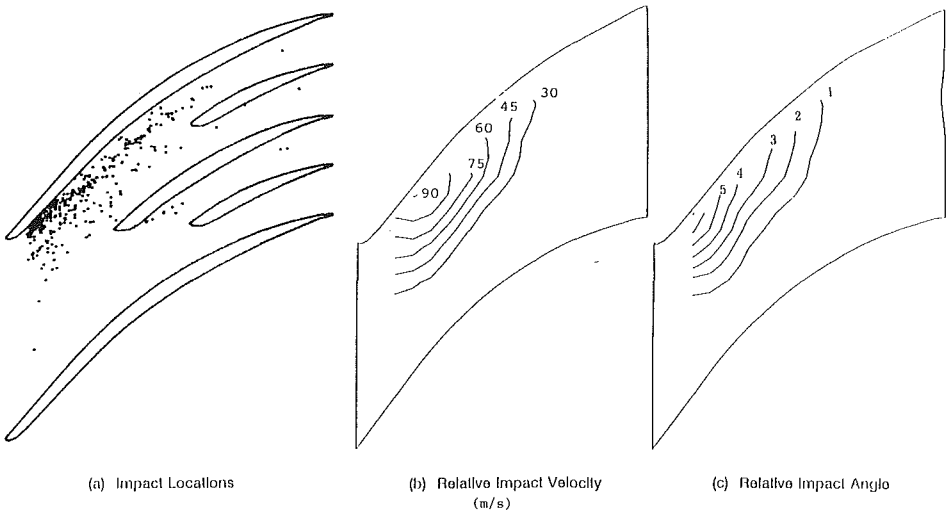

Fig. 11 Shroud impact data for the 15 μm particle

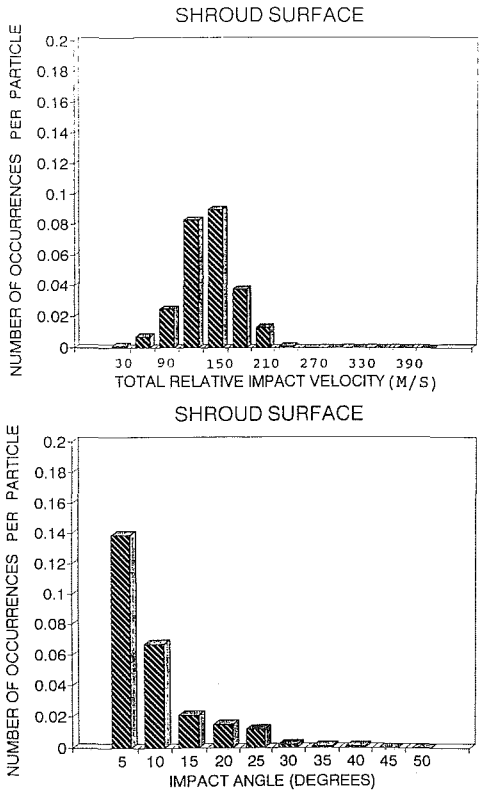

Fig. 12 Probabilistic distribution of the 15 μm particle's impact conditions with the shroud

and they are distributed in proportion to the fluid mass flux at the impeller inlet.

Figure 10 shows the simulated distribution of the particle inlet velocity components in the radial, circumferential, and axial directions based on the particle trajectory analysis in the cross over ducts of Fig. 4. Table 3 summarizes the results of blade passage surface impacts associated with one thousand small particle trajectories. According to the data presented in Table 3, the shroud has the highest overall impact probability of 0.258 followed by the main blade suction surface with 0.158. Comparing Tables 2 and 3, it is clear that the probability of a smaller particle impacting an impeller surface is considerably less than that of a larger fragment. In addition, the shroud's probability of being impacted by a 15 micron particle is less than half that by a 762 micron particle.

The shroud impact data obtained from one thousand simulated particle trajectories are presented in Figs. 11 and 12. According to Fig. 11, a 15 micron particle is most likely to impact the shroud near the main blade pressure surface upstream of the first splitter. The main blade and splitter surface impact velocities, not presented here, indicate that impacts by these smaller particles, if any, are most likely to occur near the leading edges with a very low probability of them having multiple impacts with the same surface. Comparing Figs. 8 and 12, one can conclude that the low impact velocities and impact angles are evidence of the greater influence of aerodynamic drag forces on these small particle trajectories.

Conclusions

This investigation was conducted to simulate the effects of variance in the size and associated initial conditions of the

ingested debris in the SSME HPFTP impeller on the blade, hub and shroud impacts. The results in the form of probability distribution functions for the impact locations, impact velocities and impingment angles, relative to the various impeller surfaces, were obtained from the simulations of the fragments' dynamics through the impeller flow passages in a probabilistic structure. The presented results are useful for life prediction and health monitoring purposes. They can be used to quantify the risk in terms of structural integrity and installed sensor reliability associated with the probability of impacts by ingested debris.

Acknowledgment

This research was sponsored by NASA Space Engineering Center for System Health Management Technology at the University of Cincinnati.

References

Debler, W. R., 1990, *Fluid Mechanics Fundamentals*, Prentice-Hall, Englewood Cliffs, NJ.

Hamed, A., 1990, "Simulation of the Aerodynamic Uncertainties in the SSME Turbopump," AIAA Paper 90-2294, July.

Hamed, A., Tabakoff, W., and Wenglarz, R., 1988, "Particulate Flows and Blade Erosion," Von Karman Lecture Series 1988-08, May.

McFarland, E. R., 1982, "Solution of Plane Cascade Flow Using Improved Surface Singularity Methods," ASME *Journal of Engineering for Power*, Vol. 104, No. 3, pp. 668–674, July.

McFarland, E. R., 1984, "A Rapid Blade-to-Blade Solution for Use in Turbomachinery Design," ASME *Journal of Engineering for Gas Turbines and Power*, Vol. 106, Apr., pp. 376–382.

Tabakoff, W., 1989, "Measurements of Particle Rebound Characteristics on Materials Used in Gas Turbines," AIAA Paper 89-1693, June.

Teeter, R. R., Tischer, A. E., Glover, R. C., and Kelley, B. A., 1987, "Diagnostic Needs of the Space Shuttle Main Engine," BCD-SSME-TR-87-1.

Voyd, M.B., 1990, NASA MSFC, Private Communication.

D. F. G. Durão

M. V. Heitor

A. L. N. Moreira

Instituto Superior Técnico,
Technical University of Lisbon,
Department of Mechanical Engineering,
1096 Lisboa, Codex,
Portugal

Flow Measurements in a Model Burner—Part 2

The isothermal swirling flow in the vicinity of a model oxy-fuel industrial burner is analyzed with laser-Doppler velocimetry together with laser-sheet visualization. The burner consists of a central axisymmetric swirling jet surrounded by sixteen circular jets, simulating the injection of oxygen in practical burners. The results extend those obtained for non-swirling flows, and presented in Part 1 of this paper, to the analysis of the dependence of the mixing efficiency of the burner assembly upon the swirl motion of the central jet and have the necessary detail to allow to assess the accuracy of calculation procedures of the flow in industrial burners. It is shown that swirl attenuates the three-dimensional structure typical of multijet flows in such a way that turbulence production and transport in the near burner zone are dominated by swirl-induced processes.

1 Introduction

Current designs of industrial burners usually incorporate swirl motion as a means to provide hot-gas recirculation to ensure flame stabilization (e.g., Gupta et al., 1984; Lawn, 1987). In addition, a double concentric geometry with a secondary air stream introduced through an annulus combine the advantage of good flame stability with that of increased flame length with a nearly uniform energy release, e.g., Wu and Fricker (1976). If the annulus is replaced by several axisymmetric jets, a multijet configuration is obtained, such as that typically used under oxy-fuel conditions (e.g., Bansal and McCombs, 1986) and preferred to coaxial axisymmetric geometries (e.g., Booker, 1982). However, the design of multijet burners has relied almost exclusively on empirical methods (e.g., Gibbs and Williams, 1983) and although a number of extensive studies on simple swirl burners have been undertaken (e.g., Mao et al., 1986; Tangirala et al., 1987; Hardalupas et al., 1990; Durão et al., 1990), a detailed study of multijet flow which could be used as a basis for the optimization of multijet swirl burners has not been published in the literature and is the main objective of this work.

This paper reports an experimental study of the flow pattern downstream of a model multijet burner head, typical of those found in glass furnaces operating with oxygen enrichment (e.g., Heitor and Moreira, 1992). The measurements follow those presented in Part 1 of this paper (i.e., Durão et al., 1991) for non swirling conditions, which have shown that multijet flows allow higher mixing rates than similar axisymmetric coaxial jets, such as those of Durão and Whitelaw (1976) and Ribeiro and Whitelaw (1980). The present results extend the analysis to the effect of swirling the primary air flow on the turbulent structure and mixing process in the vicintiy of the burner head, which is necessary to guide the optimization of operating conditions of existing burners and to allow to develop computer codes to provide a valuable tool for burner design. The effect of other parameters, such as the presence of combustion and the relative location of the primary and secondary flows, on the burner performance is discussed elsewhere. As a result, the present paper is limited to a very specific configuration, but representative of oxy-fuel burners where mixing of the fuel with the oxidant must be achieved close to the burner face to improve the safety of the installations. As a consequence, combustion efficiency is limited by the rates of mixing that can be achieved, which should be improved by imparting swirl to the primary air flow.

The paper is presented in five sections including this Introduction. Section 2 describes the experimental method and gives details of the flows analyzed. The experimental techniques used throughout the work are similar to those described in Part 1 of this paper and are presented in a condensed form. Sections 3 and 4 present and discuss the results, respectively, and the last section summarizes the main findings and conclusions of the work.

2 Experimental Method

This section provides information of the flows investigated and identifies the major differences relative to those analyzed in Part 1 of the paper. The instrumentation used to obtain the results is briefly described and the error sources associated with the present measurement are considered together with the assessments of accuracy. The arguments associated with these assessments are based on previous experiments and are provided in a condensed form. Details can be found in Moreira (1991).

2.1 Flow Configuration and Experimental Conditions. The experiments were conducted in the laboratory model of the oxy-fuel burner used in the processing glass furnace studied by Heitor and Moreira (1992) and described in Fig. 1. It includes a central axisymmetric jet with 17 mm in diameter, D_i surrounded by sixteen 6 mm circular jets of sec-

Contributed by the Fluids Engineering Division for publication in the JOURNAL OF FLUIDS ENGINEERING. Manuscript received by the Fluids Engineering Division June 2, 1991; revised manuscript received November 29, 1992. Associate Technical Editor: Ho, Chih-Ming.

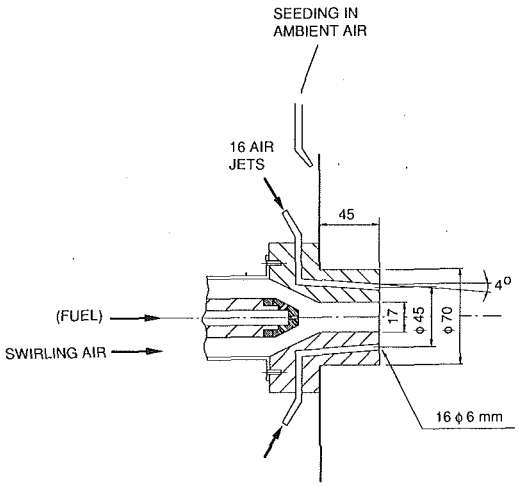

Fig. 1 Schematic diagram of burner assembly

Table 1 Flow Conditions

Run	Central jet (Primary air) Flow rate (l/s)	U_i (m/s)	Re ($\times 10^{-3}$)	Peripheral jets (Secondary air) Flow rate (l/s)	U_o (m/s)	Re ($\times 10^{-3}$)	U_i/U_o	S
S1	4.0	20	17.6	8.4	20	6.0	1.0	0.9
S2	4.0	20	17.6	16.8	40	12.0	0.5	0.9
S3	8.0	40	35.2	8.4	20	6.0	2.0	1.4

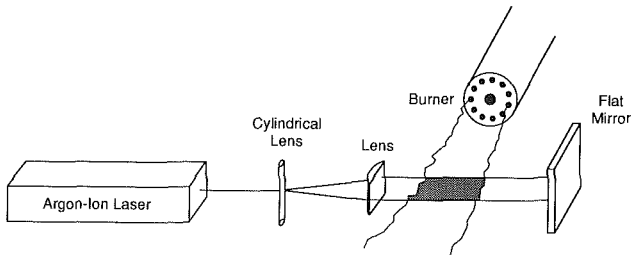

Fig. 2 Schematic lay-out of laser-sheet visualization technique

ondary air inclined at 4 deg toward the burner axis and with their center 45 mm away of the centerline. The central jet includes the fuel line and the primary air, which can encompass different swirl levels by combining an axial entry of air with a tangential stream provided by a swirl chamber with tangential slots. The fuel atomizer has the shape of the 30 deg truncated cone, but no flow was used through the fuel holes in the experiments reported here.

The air flow rates of the axial, tangential and outer streams were separately measured by calibrated standard orifice meters and integrated pitot-tube measurements have shown that the measured flow rates are accurate within 2 percent. The degree of swirl on the central jet is characterized by a non-dimensional swirl number defined as in Gupta et al. (1984) (see also the Nomenclature) and determined from velocity measurements at the exit plane of the burner.

The process of flame stabilization and, in particular, the extent to which the flame propagates and anchors at practical burner heads depends upon the distribution of local stoichiometry (e.g., Lawn, 1987), which is a function of the mixing which has taken place between the fuel and oxidant and is, therefore, influenced by the magnitude of the swirl number, S, and of the velocity ratio between the central and peripheral jets, U_i/U_o.

The isothermal flows analyzed in the present paper correspond to flow conditions within the limits of flame stabilization and were selected in order to provide significant changes from which the influence of swirl and velocity ratio could be inferred. Table 1 summarizes the test conditions considered, which include the anaysis of three different flows in the range $0.9 \leq S \leq 1.4$ for velocity ratios, U_i/U_o, between 0.5 and 2.0. The study is made on the basis of detailed mean and turbulent velocity measurements, which are to be compared with those reported for nonswirling flows in Part 1 of this paper (see Durão et al., 1991).

The origin of the axial, x, is taken at the exit plane of the burner head and the tangential velocity is taken positive in the anticlockwise direction when facing the burner. The symmetry of the flow was verified by measuring several complete radial profiles in the vertical and in the horizontal planes, which agree within the accuracy of the measuring equipment.

2.2 Measurement Technique and Accuracy. Flow visualization has been conducted by introducing atomized silicone-oil into the jets and illuminating the flow with a sheet of light obtained by spreading a laser beam (λ = 514.4 nm) with a cylindrical lens. A parallel light sheet of high and uniform intensity could be achieved with a collimating lens and a flat mirror, as shown in Fig. 2. A 35 mm camera was used to register the flow images in 400 ASA films at a rate varying from 8 and 60 Hz.

The mean and turbulent velocity characteristics of the flow were measured with a dual-beam laser-Doppler velocimeter based on an argon-ion laser light source at 514.5 nm (1W nominal). Sensitivity to the flow direction is provided by light-frequency shifting from acousto-optic modulation (double Bragg cells) with a resulting shift of the Doppler signal in the range 0 − 10MHz. The half-angle between the beams was

Nomenclature

D = diameter

G_x = axial flux of linear momentum

G_ϕ = axial flux of angular momentum

$$G_x = 2\pi \int_0^{D_i/2} \rho r \left[\overline{U}^2 - \frac{\overline{W}^2}{Z}\overline{u'^2} - \frac{(\overline{v'^2}+\overline{\omega'^2})}{2} \right] dr$$

$$G\phi = 2\pi \int_0^{D_i/2} \rho(\overline{U}\,\overline{W}r^2 + \overline{u'\omega'^2})dr$$

k = turbulent kinetic energy, $k = (\overline{u'^2} + \overline{v'^2} + \overline{w'^2})/2$

r = radial coordinate

R_{uv} = shear stress correlation coefficient, $R_{uv} = \overline{u'v'}/\left(\sqrt{\overline{u'^2}\cdot\overline{v'^2}}\right)$

R_{uw} = shear stress correlation coefficient, $R_{uw} = \overline{u'w'}/\left(\sqrt{\overline{u'^2}\cdot\overline{\omega'^2}}\right)$

S = swirl number, $S = 2G\phi/G_xD_i$, where:

U = axial velocity, $U = \overline{U} + u'$

U_{CL} = mean axial velocity along the centerline

U_i = mean velocity (flow rate/area) at the exit of the central jet

U_o = mean velocity (flow rate/area) at the exit of the outer jets

V = radial velocity, $V = \overline{V} + v'$

x = axial coordinate taken from the burner face

W = tangential velocity, $W = \overline{W} + w'$

4.92° and the calculated dimensions of the measuring volume at the e^{-2} intensity locations were 1.528 and 0.132 mm. The transfer function in the absence of frequency shift was 0.33 MHz/ms^{-1}.

The flows were seeded with powdered aluminum oxide (0.6 to 1 μm nominal diameter before agglomeration) dispersed in purpose-built cyclone generators (e.g., Glass and Kennedy, 1977). The light scattered by the particles was collected by a 200 mm focal length lens and focused into the pinhole aperture (0.300 mm) of a photomultiplier tube with a magnification of 0.74. The band-passed filtered Doppler signals were processed by a commercial frequency counter (TSI 1980B) interfaced with a 16-bit microcomputer.

The complete LDV system and the burner were mounted on two separate two-dimensional traversing units, allowing the positioning of the control volume within ±0.5 mm. The radial, V, and the tangential, W, velocity components were measured along the vertical and the horizontal planes of symmetry, respectively. The axial velocity component, U, was measured along the two planes of symmetry and the discrepancies have been found to be within the measurement accuracy. The distributions of the Reynolds shear stresses, $\overline{u'v'}$ and $\overline{u'w'}$, were obtained, respectively, along the vertical and the horizontal planes of symmetry, with the laser beams in the horizontal and vertical planes and at ±45°, as described by Durst et al. (1981).

Transit broadening (e.g., Zhang and Wu, 1987) and non-turbulent Doppler broadening errors (e.g., Kreid, 1974) mainly affect the variance of the velocity fluctuations and are estimated to be smaller than $2 \times 10^{-3}\ U_i^2$ and $7 \times 10^{-4}\ U_i^2$, respectively. The number of samples used to form the averages was always above 10000, which results in statistical (random) errors smaller than 1 and 4 percent for the mean and variance values, respectively, for a 95 percent confidence interval, e.g., Yanta and Smith (1978).

Systematic errors due to sampling bias were minimized by using data acquisition rates up to 5 KHz and, therefore, higher than the expected fundamental velocity fluctuation rate (e.g., Dimotakis, 1978). Following the analysis of Glass and Bilger (1978) for co-flowing streams, these errors are less than +9 and −10 percent for the mean and variance values, respectively. Bias errors due to unequal particle number density in the central and peripheral jets have been minimized by seeding separately each stream with similar particle concentrations, as discussed by Dibble et al. (1987). An overestimation of the resulting errors have been inferred from velocity measurements obtained by seeding only the outer or the inner stream, and found to be smaller than $0.2U_i$ and $4 \times 10^{-3}\ U_i^2$, respectively, for the mean and the variance values.

3 Results

The analysis of the flows considered in this paper makes use of flow visualization results, centerline velocity distributions and radial profiles of mean and turbulent velocity characteristics, which are presented in the three following sub-sections, respectively. The presentation is aimed at discussing the effect of swirl and of the velocity ratio U_i/U_o on the mean and turbulent flow patterns established in the vicinity of the burner head described. The ultimate objective is to provide a better understanding of the transport processes in the near burner region, as well as to discuss the related implications for the mathematical modelling of the flows considered.

3.1 Qualitative Analysis of the Near Burner Zone. Prior to the detailed measurements, visualization of the flow in the near burner zone was performed to guide the choice of the measurement locations and to provide a qualitative picture of the flow conditions analyzed in this paper. Figure 3(*a*) shows photographs obtained by illuminating the flow at three consecutive vertical planes parallel to the burner face (respectively, at x/D_i = 0.26; 1.0; 4.0) for typical swirling (run S1, S = 0.9) and nonswirling flows with the same velocity ratio, U_i/U_o = 1. The photographs were obtained with the technique described in Fig. 2 by introducing seeding particles only into the peripheral jets and allow to identify the three-dimensional structure of the annular mixing region. Close to the burner face, at x/D_i = 0.26,the effect of swirling the inner jet is negligible and the sixteen peripheral jets can be observed for the two flow conditions studied. Far downstream, at x/D_i = 1.0, the peripheral jets reach the centerline in the swirling flow, while the non-swirling flow exhibits a pattern typical of coaxial axisymmetric jets. This qualitative picture of the flow is maintained at least up to x/D_i = 4 and characterizes the increased rate of mixing induced by swirling the inner jet. The flow patterns can be further analyzed along the horizontal plane of symmetry, as shown in the photographs of Fig. 3(*b*). For the swirling flow the figure suggests the formation of a central recirculation zone, which gives rise to a nearly uniform concentration of seeding particles across the flow downstream of x/D_i = 0.85. The outer flow is dominated by the peripheral jets up to x/D_i = 1.0, but further downstream swirl increases the spreading rate of the flow due to a comparatively large entrainment of surrounding air, which is associated with a faster decay of the mean centerline velocity.

3.2 Centerline Distributions of Velocity Characteristics. Figure 4 presents centerline distributions of mean axial velocity and of axial and radial normal stresses for the runs S1, S2 and S3 of Table 1. The three flows include an initial region of reverse flow, which is associated with the sub-ambient static pressures induced by rotation and followed by regions of acceleration and near uniform velocity. The analysis of Durão et al. (1991) has already shown that in the absence of swirl the decay of the centerline velocity in the present configuration is faster than that of axisymmetric coaxial jets with the same velocity ratio (e.g., those of Durão and Whitelaw, 1976 and Ribeiro and Whitelaw, 1980), due to the comparatively high mixing rates typical of multijet configurations. The present results extend this conclusion to swirling flows: regardless of the swirl number, the decay of the centerline axial velocity (Figs. 4(*a*) and (*b*) is considerably increased by increasing the velocity ratio between the central and the peripheral jets, U_i/U_o. As a consequence, turbulent production in the vicinity of the centerline decreases due to the attenuation of the mean rate of strain at small radius. The results also show that the location of the downstream stagnation point is weakly dependent on the swirl number, S, and on the velocity ratio, U_i/U_o, but suggest that the location of the upstream stagnation point, which occurs upstream of the burner face for the three flows considered, depends upon the degree of swirl. We tentatively conclude that the length of the recirculation zone increases with the swirl number, while it decreases the maximum reverse (dimensionless) velocity.

The distributions of normal stresses, Figs. 4(*c*) and (*d*), exhibit two peaks with a maximum value lying in the vicinity of the burner exit and associated with the upstream stagnation point: the second peak of comparatively lower intensity is observed around the downstream stagnation point. The distributions are not significantly affected by the velocity ratio U_i/U_o and show large levels of turbulent anisotropy. In contrast with the nonswirling flows, the values of $\overline{v'^2}$ are higher than those of $\overline{u'^2}$ up to x/D_i = 5.0 with $\overline{u'^2}/\overline{v'^2} \leq 0.5$.

3.3 Detailed Velocity Characteristics of the Near Burner Zone. Figures 5 and 6 show radial distributions of the mean and turbulent velocity characteristics of run S1, measured along six consecutive axial locations between x/D_i = 0.26 and x/D_i = 9.00. The results are only presented for half of the measuring zone, but measurements obtained at x/D_i = 2.0 and 9.0 along

zone, but measurements obtained at $x/D_i = 2.0$ and 9.0 along a full diameter (see Moreira, 1991 for details) have confirmed the symmetry of the flow.

The analysis derived from the flow visualization and presented in Section 3.1 can be readily quantified by the mean axial velocity distributions. The peripheral jets maintain their individuality upstream of $x/D_i = 2.0$ where the flow is characterized by large gradients of mean velocity together with high values of the normal stresses. The turbulence levels rapidly decrease with the distance to the burner and while at $x/D_i = 0.26$ the maximum value of $\overline{u'^2}$ is about $130 m^2 s^{-2}$, it decreases to $31 m^2 s^{-2}$ at $x/D_i = 2.00$ and to $5.6 m^2 s^{-2}$ at $x/D_i = 4.0$. Consequently, the details of the flow development are considered in the following paragraphs in two main parts, namely upstream and downstream of $x/D_i = 2.0$.

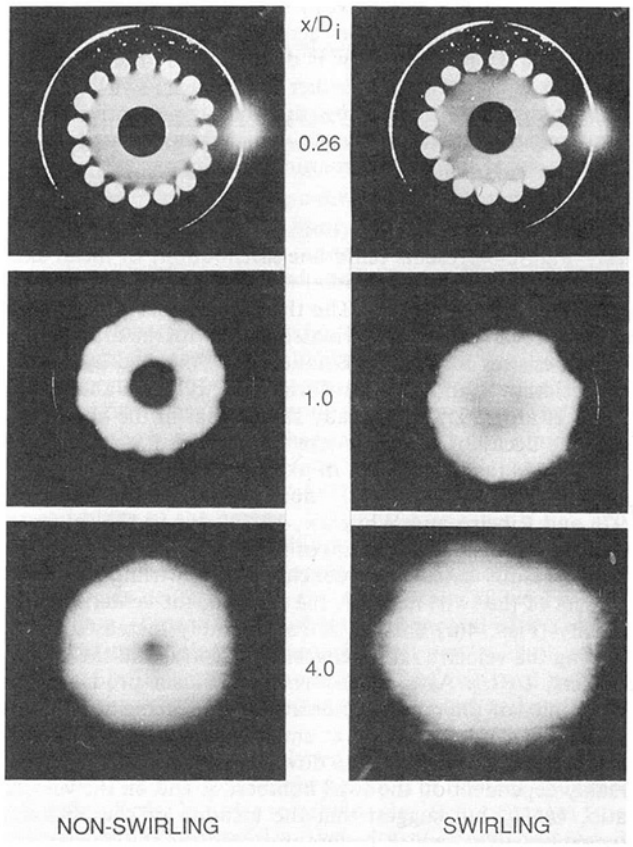

Fig. 3(*a*) Photographs obtained by illuminating the flows in three planes parallel to the burner face, namely at $x/D_i = 0.26$; 1.0 and 4.0

The initial profiles of the mean axial velocity clearly identify the central recirculation zone induced by swirl, which extends up to $x/D_i = 1.76$ with a maximum width at $x/D_i = 1.00$, where the mean reverse velocity reaches the maximum value of $\overline{U}/U_i = 0.5$. The profile at $x/D_i = 0.26$ also identifies the shear layer surrounding the recirculation zone and the peripheral jets, in a way that it quantifies the three-dimensional characteristics of the near-burner zone as discussed before. While the inner jet is characterized by a large outward radial velocity associated with swirl driven centrifugal forces, the outer jets move inwards due to their inclination and, as a consequence, the flow develops toward an axisymmetric type of swirling jet. The mean tangential velocity, $\overline{W}$, shows a distribution typical of solid body rotation (e.g., Gupta et al., 1984) in the vicinity of the central line, with an inflexion at the edge of the recirculation zone (i.e., at $r/D_i = 1.0$). The rapid expansion of the flow due to the imbalance in the conservation of momentum at the burner exit can be noted at $x/D_i = 0.26$, where the mean tangential velocity of the fluid between the peripheral and the central jet (i.e., at $0.6 < r/D_i < 1.0$) reaches 50 percent of $\overline{W}_{max}$. As a result, the shear forces developed at the inner shear layer of the peripheral jets induce a counter-rotating motion centered at $r/D_i = 1.1$, which is destroyed far downstream due to radial diffusion of angular momentum. Further downstream, at $x/D_i = 4.0$, the radial profile of $\overline{W}$ shows a distribution similar to that of a Rankine type of vortex.

Close to the burner exit (i.e., at $x/D_i = 0.26$) the normal stresses exhibit four peaks coincident with the largest gradients of mean velocity, in accordance with the generally accepted mechanism of production of turbulent kinetic energy by the interaction between turbulent motion and the mean rate of shear strain, e.g., Tenneskes and Lumley (1981). The turbulent field is anisotropic and exhibits peculiar features in that $\overline{v'^2}$ is larger than $\overline{u'^2}$ and $\overline{w'^2}$, except in the inner shear layer surrounding the central recirculation zone. Although these results must be constrasted with those obtained by Fujii et al. (1981) in swirled coaxial jets, they agree with those of Sislian and Cusworth (1986) in a single swirling jet in that maximum anisotropy occurs in regions of maximum shear. For example, it is noted that in the outer shear layer of the central jet where both $\partial\overline{U}/\partial r$ and $\partial\overline{V}/\partial r$ are negative, production of turbulent energy results in the preferential increase of $\overline{v'^2}$, due to the major contribution of the interaction between $\overline{v'^2}$ and $\partial\overline{V}/\partial r$ in the conservation of turbulent kinetic energy.

The results of Fig. 6(*d*) show that the shear stress $\overline{u'v'}$ is negative around the central recirculation zone, suggesting that faster moving elements of fluid ($u' > 0$) tend to move inward into the low-pressure recirculation region (i.e., $v' < 0$ and $u'v' < 0$), and is positive in the shear layer around the central

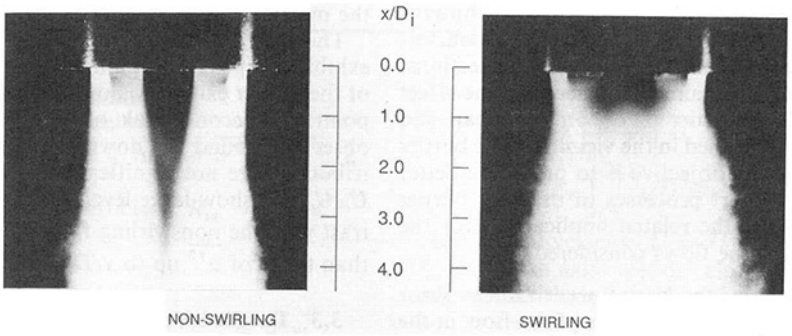

Fig. 3(*b*) Photographs obtained by illuminating the flows in the horizontal plane of symmetry

Fig. 3 Visualization of the nonswirling and swirling flows established in the vicinity of the burner heat obtained by seeding only the peripheral jets with silicone oil and by illuminating the flows with a sheet of laser light

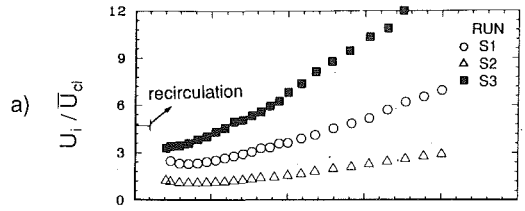

Fig. 4(*a*) Inverse of the mean axial velocity, $U_i/\overline{U}_{CL}$, in the wake flow downstream of the swirl-induced recirculation zone, for $4 \leq x/D_i \leq 40$

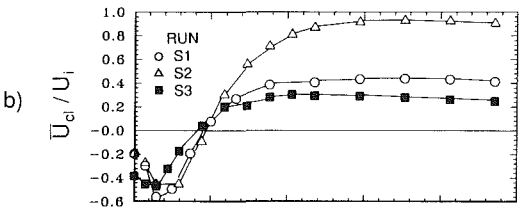

Fig. 4(*b*) Mean axial velocity, $\overline{U}_{CL}/U_i$, in the near burner zone upstream of $x/D_i = 10$

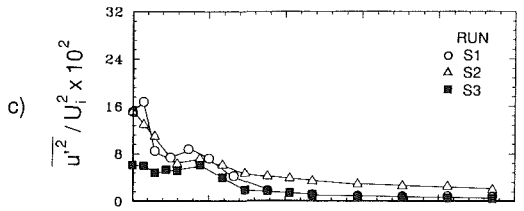

Fig. 4(*c*) Variance of axial velocity fluctuations, $\overline{u'^2}/U_i^2 \times 10^2$, in the near burner zone upstream of $x/D_i = 10$

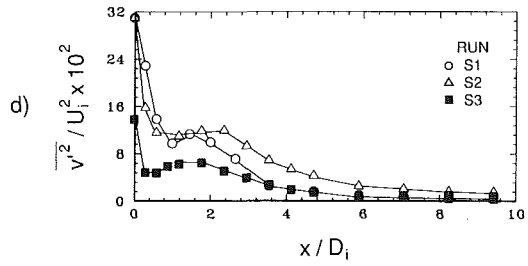

Fig. 4(*d*) Variance of radial velocity fluctuations, $\overline{v'^2}/U_i^2 \times 10^2$, in the near burner zone upstream of $x/D_i = 10$

Fig. 4 Mean and turbulent velocity distributions along the centerline; ○-Run S1; △-Run S2; ■-Run S3

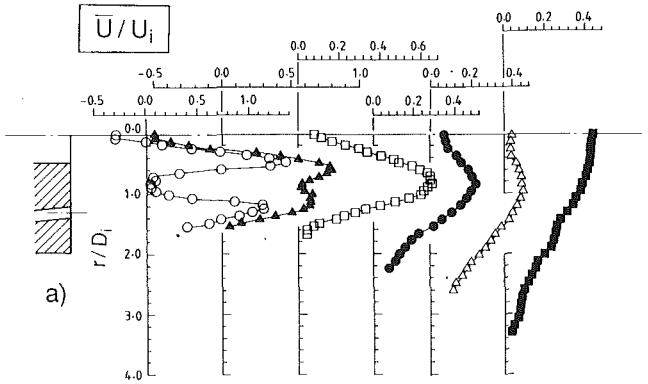

Fig. 5(*a*) Mean axial velocity, $\overline{U}/U_i$

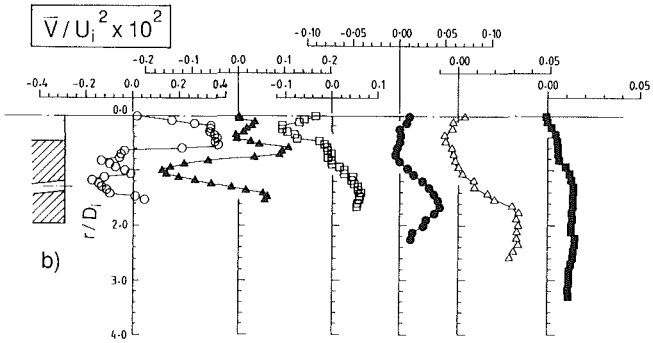

Fig. 5(*b*) Mean radial velocity, $\overline{V}/U_i$

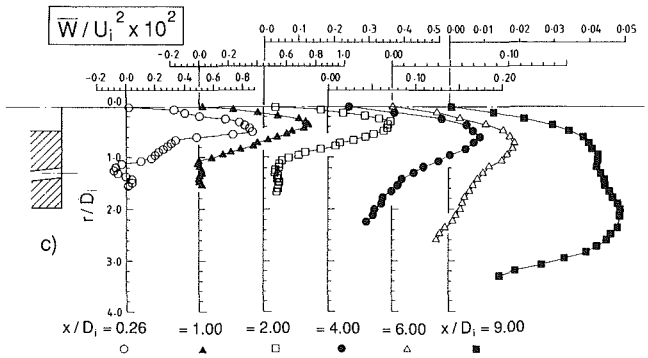

Fig. 5(*c*) Mean tangential velocity, $\overline{W}/U_i$

Fig. 5 Radial profiles of mean velocity characteristics for run S1.

jet because the outward movement of fluid particles into the low-pressure region between jets ($v' > 0$) corresponds to positive axial velocity fluctuations (i.e., $u' > 0$ and $u'v' > 0$). Similarly, the shear stress is again negative along the inner edge of the peripheral jets and positive along their outer edge, although with very small values comparatively to those measured in the inner flow region. The results also show that the sign of $u'v'$ is related to the sign of the shear strain, $\partial\overline{U}\partial r$, in accordance with a turbulent viscosity hypothesis, (e.g., Tenneskes and Lumley, 1981).

The shear stress $u'w'$ is smaller than $\overline{u'v'}$ as in other turbulent flows (e.g., Bradshaw, 1976), although at $x/D_i = 0.26$ the two quantities exhibit peak values of similar magnitude located in the shear layer around the central recirculation zone and along the edge of the central jet. As the flow develops downstream, the outer peak decays rapidly and the inner peak moves inward, in constrast to the behavior of $u'v'$.

Turning now to the analysis of the flow downstream of $x/D_i = 2.00$, the mean velocity distributions of Fig. 5 are similar to those typical of axisymmetric swirling jets with a Rankine vortex type of structure. The flow exhibits a central region of positive radial gradient of mean axial velocity and the shear stresses $u'v'$ and $u'w'$ still display two changes in sign with comparatively lower values for $\overline{u'w'}$.

Turbulence is nearly isotropic in the outer region (i.e., for $r/D_i > 0.7$) where $\partial\overline{U}/\partial r < 0$, but for smaller radius v'^2 is larger than u'^2. This behavior is again qualitatively similar to that observed downstream of free stagnation points in other turbulent recirculating flows, in which the normal strain $\partial\overline{U}/\partial x$ is positive and large and contributes as a sink of u'^2 in the balance of turbulent kinetic energy, while $\partial\overline{V}/\partial r$ is small but negative and contributes as a source of $\overline{v'^2}$. Accordingly to the step-wise energy transport mechanism (Bradshaw, 1976), energy transfer to u'^2 occurs through the interaction between pressure fluctuations and local velocity gradients, which redistributes turbulent energy among the other components of

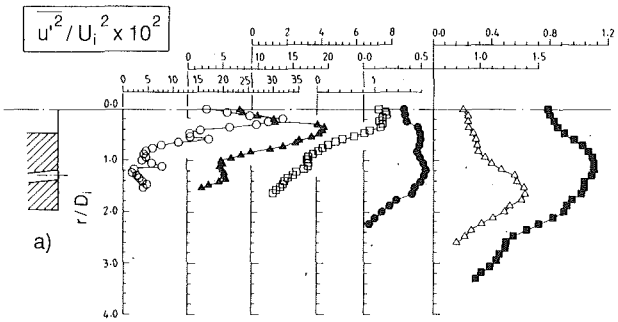

Fig. 6(*a*) Variance of axial velocity fluctuations, $\overline{u'^2}/U_i^2 \times 10^2$

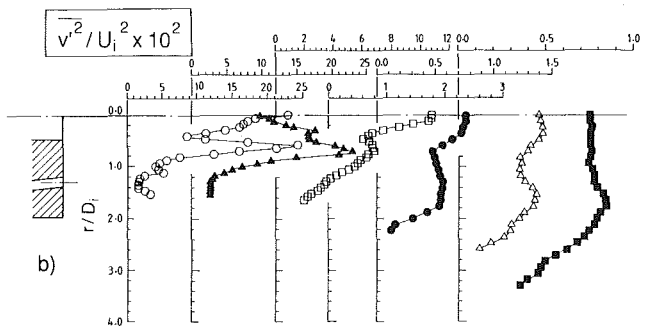

Fig. 6(*b*) Variance of radial velocity fluctuations, $\overline{v'^2}/U_i^2 \times 10^2$

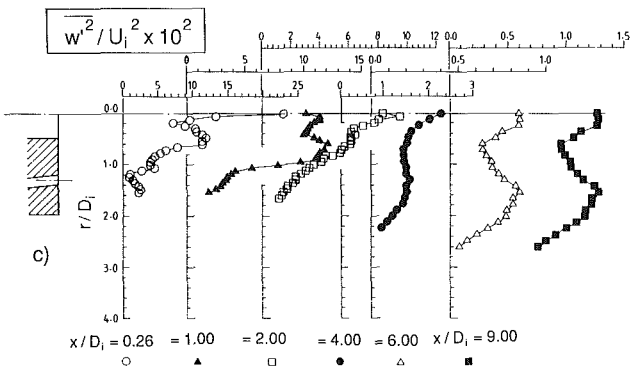

Fig. 6(*c*) Variance of tangential velocity fluctuations, $\overline{w'^2}U_i^2 \times 10^2$

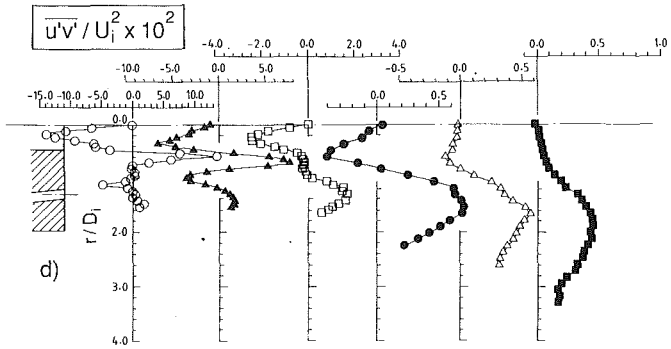

Fig. 6(*d*) Reynolds shear stress, $\overline{u'v'}/U_i^2 \times 10^2$

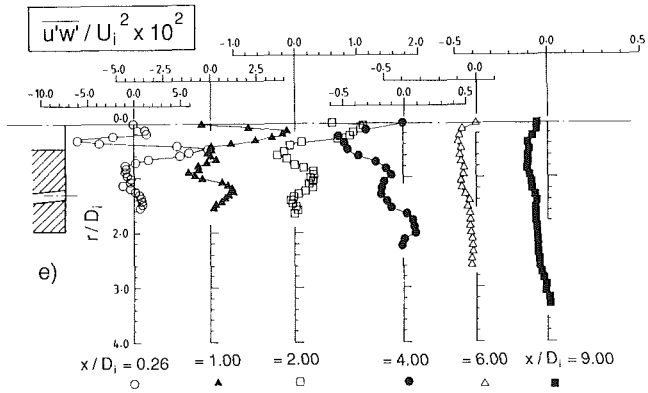

Fig. 6(*e*) Reynolds shear stress, $\overline{u'\omega'}/U_i^2 \times 10^2$

Fig. 6 Radial profiles of turbulent velocity characteristics for run S1

velocity fluctuations only after a balance is reached between the mean velocity and $\overline{v'^2}$. For the present flow, turbulence anisotropy persists up to $x/D_i = 9.00$ in contrast with the results of Sislian and Cusworth (1986) for a single swirling jet, because the effect of the peripheral jets is to increase the mean strain rates $\partial\bar{U}/\partial x$ and $\partial\bar{V}/\partial r$ relatively to that of a single jet.

Downstream of $x/D_i = 6.0$ the profiles of the mean axial velocity develop towards the fully developed state: the transfer of momentum toward the centerline decreases the positive radial gradients in the central region and the radial and tangential mean velocities become negligibly small. Consequently, the distributions of shear stresses show an increase in $\overline{u'v'}$ relative to $\overline{u'w'}$ with the maximum values appearing in the zone of maximum production of turbulent kinetic energy, which stems from the dominance of the axial velocity profiles.

4 Discussion

The detailed measurements presented in the previous section characterize the nature of the turbulent swirling flow established downstream of typical multi-jet burner assemblies and provide the necessary details to assess the extent to which computer codes may be used to extrapolate and interpolate the experimentally acquired information and used as a valuable tool for burner design. The aim of this section is to briefly discuss the results in terms of their contribution to optimize existing burner operating conditions and the development of turbulence modelling of complex flows with engineering interest.

The comparison between the results described before with those presented in Part 1 of this paper allows to confirm the importance of swirling the primary airflow in industrial burners of larger energy input, such as those operated under oxygen enriched conditions. The performance of the burners is influenced by the extent of the swirl-induced reverse flow zone, which influences the mixing which takes place between fuel and oxidant and, consequently, the distribution of local stoichiometry. This is important because it determines the extent to which the flame propagates and anchors at the burner head. Other factors which influence the performance of practical multi-jet burning systems include the degree of interaction of the outer jets with the central swirling flow, which is shown here to determine the spreading of the flames and to influence the extent of the reverse flow zones formed at the burner head between the primary and the secondary air flows. This aspect determines the formation of coke and the consequent blocking of the burners when heavy fuel oils are used. The results presented here are concerned with a specific configuration which limits the extent of the analysis of these factors, but provide a reliable set of data to evaluate calculation methods which can be used to extend the experimentally acquired information. This requires consideration of the details of the turbulence characteristics of the flow, which are discussed in the following paragraphs.

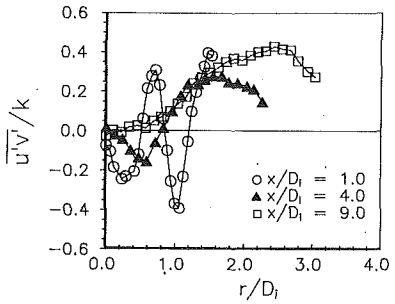

Fig. 7 Radial profiles of the ratio between the shear stress and the turbulent kinetic energy, $\overline{u'v'}/k$, for run S1

The analysis of the previous section shows that the near burner zone upstream of $x/D_i = 2.0$ is a region of large turbulent production. The results are qualitatively similar to those reported for comparatively simple axisymmetric swirling flows (e.g., Sislian and Cusworth, 1986; Durão et al., 1990) and suggest that the three-dimensional effects induced by the peripheral jets do not significantly affect the turbulent structure of the flow in contrast to the observations of Durão et al. (1991) for the correspondent nonswirling flows.

Structural parameters, such as the correlation coefficient of the shear stress, R_{uv}, and the ratio between shear stress and turbulent kinetic energy, have been calculated from the results and are discussed here to assess the extent to which the turbulence in the present flow is affected by *"unusual"* mechanisms. In the shear layer around the recirculation zone the maximum values of R_{uv} rapidly decrease from -0.7 at $x/D_i = 0.26$ to -0.3 at $x/D_i = 1.00$ in a way similar to other recirculating flows (e.g., Chandrsuda and Bradshaw, 1981, Heitor et al., 1987), although with comparatively larger peak values. Similar observations have been reported by Simpson et al. (1981a,b) along the edge of a recirculating boundary layer induced by an adverse pressure gradient and by Durão et al. (1990) along a swirl-driven recirculation zone, and have been attributed by Smiths et al. (1979) to the effect of extra-strain rates induced by steamline curvature. This mechanism is consistent with the sudden decrease of $\overline{u'v'}/k$ from -0.6 to -0.3 shown in Fig. 7, as reported by Gibson and Younis (1983) and Gibson et al. (1984) in a developing mixing layer with imposed curvature. In the outer shear layer the maximum values of R_{uv} and $\overline{u'v'}/k$ are, respectively equal to 0.5 and 0.3 and, therefore, similar to those reported by Harsha and Lee (1970) and Bradshaw et al. (1967) for *"well behaved"* turbulent shear flows. On the other hand, the distributions of R_{uw} and $\overline{u'w'}/k$ show values comparatively smaller and of the order of 0.25 and 0.4 respectively, in a way similar to that reported by Ramos and Somer (1985) and Durão et al. (1990) in other swirling flows.

An important feature of the present flows is the absence of large-scale high-energy oscillations,which distinguish them from those swirling flows containing energetic processing vortex cores or other low-frequency, high-energy oscillations, as reported by Beyler and Gouldin (1981) and Gouldin et al. (1985). Velocity histograms obtained for the three velocity components at several locations throughout the recirculation zone, not shown here for lack of space, exhibit unimodal distributions with a Gaussian like behavior except at the exit plane. There, near bimodal histograms were observed, although spectral analysis of time-resolved measurements has shown the absence of predominant frequencies in the spectrum of velocity fluctuation, at least in the range 0-200 Hz, and confirm the absence of any periodicity in the present flows.

The main implication of the present results to the evaluation of calculation methods to predict the flow in practical burners is that production of turbulent kinetic energy through the interaction of normal stresses with normal strains is important in swirling multi-jet flows and comparatively larger than that typical of simple jet flows. This is particularly important in the near burner zone, where calculations using a scalar effective-viscosity turbulence model will be inaccurate. Although the gradients of the normal stresses in streamline coordinates may not be large terms in the transport of mean momentum, the importance of the various production terms in generating turbulent kinetic energy implies that it is necessary to calculate the individual normal stresses adequately if the correct turbulent kinetic energy is to be obtained throughout the flow.

5 Conclusions

Flow visualization and detailed laser-Doppler measurements of mean and turbulent velocity characteristics are reported in the developing region of the nonreacting recirculating swirling flow in the vicinity of a model burner. The flow configuration used throughout this work consists in a central axisymmetric primary air jet, which can encompass different swirl levels and is surrounded by sixteen circular jets of secondary air. The flows analyzed correspond to conditions within the limits of flame stabilization which were selected in order to analyze the effect of swirling the primary air in the range $0.9 < S < 1.4$ and of the velocity ratio between the primary and the secondary air flows on the turbulence characteristics of the near burner zone.

The results show that the effect of swirling the primary air flow on the burner performance is important in that it promotes turbulent mixing and, therefore, the distribution of local stoichiometry in practical burning systems, although the size and strength of the swirl-induced recirculation zone is determined by the penetration of the secondary air flow. The peripheral jets limit the spreading of the swirling flow and should allow the occurrence of comparatively long flames of large energy input.

The development of the flow is determined by the processes of turbulent production in the near burner zone upstream of $x/D_i = 2.0$, where the interaction of normal strains and normal stresses are found to play an important role in the conservation of turbulent kinetic energy. The results show that the flow exhibits zones of large turbulence anisotropy, with $\overline{v'^2} > \overline{u'^2}$ around the centerline and $\overline{v'^2} < \overline{u'^2}$ in the outer entraining mixing layer, and identify large effects of flow recirculation and curvature on the turbulence structure parameters that determine the empirical constants in engineering models of turbulence. Far downstream of the burner head, the turbulent flow resembles that typical of axissymmetric swirling flows with convection of turbulent energy balanced by turbulent diffusion and dissipation.

Acknowledgments

The assistance of Messrs. Jorge Coelho and Carlos Carvalho in the preparation of the manuscript is appreciated. The experiments were made at the Centro de Termodinâmica Aplicada e Mecânica dos Fluidos da Universidade Técnica de Lisboa, CTAMFUTL-INIC and supported by the Commission of the European Communities.

References

Bansal, R. K., and McCombs, N. R., 1986, "Low Cost Pressure Swing Adsorption Oxygen Systems for Oxygen Enrichment of Glass Furnaces," *Proceedings of the XIV International Congress on Glass*, pp. 72–79.

Beyler, C. L. B., and Gouldin, F. C., 1981, "Flame Structure in a Swirl-Stabilized Combustor Inferred by Radiant Emission Measurements," *18th Symposium (International) on Combustion*, The Combustion Institute, pp. 1011–1019.

Booker, P. I., 1982, "Developments in the Use of Oxygen in Glass Furnace Combustion Systems," *Glass*, May, pp. 172–178.

Bradshaw, P., 1976, *Turbulence*, Spring-Verlag.

Bradshaw, P., Ferris, D. H., and Atwell, N. P., 1967, "Calculation of Boundary-layer Development Using the Turbulent Energy Equation," *Journal of Fluid Mechanics*, Vol. 28, pp. 593–616.

Chandrsuda, C., and Bradshaw, P., 1981, "Turbulence Structure of a Reattaching Mixing Layer," *Journal of Fluid Mechanics*, Vol. 110, pp. 171–194.

Dibble, R. W., Hartmann, V., and Schefer, R. W., 1987, "Conditional Sampling of Velocity and Scalars in Turbulent Flames Using Simultaneous LDV-Raman Scattering," *Experiments in Fluids*, Vol. 5, pp. 103–113.

Dimotakis, F., 1978, "Single Scattering Particle Laser-Doppler Measurements of Turbulence," AGARD CP13, Paper 10.7.

Durão, D. F. G., and Whitelaw, J. H., 1976, "Turbulent Mixing in the Developing Region of Coaxial Jets," ASME JOURNAL OF FLUIDS ENGINEERING, Vol. 95, pp. 467–473.

Durão, D. F. G., Heitor, M. V., and Moreira, A. L. N., 1990, "The Turbulent Characteristics of the Swirling Flow in Typical Burners," *Engineering Turbulence Modelling and Measurements*, W. Rodi and E. N. Ganic, eds., Elsevier Publisher, pp. 705–716.

Durão, D. F. G., Heitor, M. V., and Moreira, A. L. N., 1991, "Flow Measurements in a Model Burner-Part 1," ASME JOURNAL OF FLUIDS ENGINEERING, Vol. 113, pp. 668–674.

Durst, F. Melling, A., and Whitelaw, J. H., 1981, *Principles and Practice of Laser-Doppler Anemometry*, Academic Press.

Fujii, S., Eguchi, K., and Gomi, M., 1981, "Swirling Jets With and Without Combustion," *AIAA Journal*, Vol. 19, pp. 1742–1747.

Gibbs, M. B. and Williams, A., 1983, "Fundamental Aspects on the Use of Oxygen in Combustion Process-A Review," *Journal of the Institute of Energy*, pp. 74–83.

Gibson, M. M., and Younis, B. A., 1983, "Turbulence Measurements in a Developing Mixing Layer with Mild Destabilizing Curvature," *Experiments in Fluids*, Vol. 1, pp. 23–30.

Gibson, M. M., Verriopoulos, C. A., and Vlachos, N. S., 1984, "Turbulence Boundary Layer on a Mildly Curved Convex Surface," *Experiments in Fluids*, Vol. 2, pp.17–24.

Glass, M., and Bilger, R. W., 1978, "Turbulent Jet Diffusion Flame in a Co-Flowing Stream-Some Velocity Measurements," *Combustion, Science and Technology*, Vol. 18, pp. 165–177.

Glass, M., and Kennedy, I. M., 1977, "An Improved Seeding Method for High Temperature Laser Doppler Velocimetry," *Combustion and Flame*, Vol. 29, pp. 333–335.

Gouldin, F. C., Depsky, J. S., and Lee, S. L., 1985, "Velocity Field Characteristics of a Swirling Flow Combustor," *AIAA Journal*, Vol. 23, No. 1, pp. 95–102.

Gupta, A. K., Lilley, D. G., and Syred, N., 1984, *Swirl Flows*, Abacus Press, Energy & Engineering Science Series.

Hardalupas, Y., Taylor, A. M. K. P., and Whitelaw, J. H., 1990, "Velocity and Size Characteristics of Liquid-Fuelled Flames Stabilized by a Swirl Burner," *Proceedings of the Royal Society, Series A, London*, Vol. 428, pp. 129–155.

Harsha, P. T., and Lee, S. C., 1970, "Correlation Between Turbulent Shear Stress and Turbulent Kinetic Energy," *AIAA Journal*, Vol. 8, (8), pp. 1508–1510.

Heitor, M. V., Taylor, A. M. K. P., and Whitelaw, J. H., 1987, "The Interaction of Turbulence and Pressure Gradients in Baffle-Stabilized Premixed Flames," *Journal of Fluid Mechanics*, Vol. 181, pp. 384–413.

Heitor, M. V., and Moreira, A. L. N., 1992, "Temperature and Major Species Characteristics of an Industrial Glass Furnace," Submitted for publication in *FUEL*.

Kreid, D. K. 1974, "Laser-Doppler Velocimeter Measurements in Nonuniform Flow: Error Estimates," *Applied Optics*, Vol. 13 (8), pp. 1872–1881.

Lawn, C. J. 1987, *Principles of Combustion Engineering for Boilers*, Academic Press.

Mao, C. P., Wang, G. and Chigier, N. A., 1986, "An Experimental Study of Air-Assist Atomizer Spray Flames," *21st Symposium (International) on Combustion*, The Combustion Institute, pp. 665–673.

Moreira, A. L. N., 1991, "Experimental Analysis of Combusting Systems" (in Portuguese), Ph.D. thesis, Technical University of Lisbon.

Ramos, J. I., and Somer, H. T., 1985, "Swirling Flow in a Research Combustor," *AIAA Journal*, Vol. 23 (2), pp. 241–248.

Ribeiro, M. M., and Whitelaw, J. H., 1980, "Coaxial Jets With and Without Swirl," *Journal of Fluid Mechanics*, Vol. 96, Part 4, pp. 769–795.

Simpson, R. L., Chew, Y. T., and Shivaprasad, B. G., 1981a, "The Structure of a Separating Turbulent Boundary-Layer. Part 1: Mean Flow and Reynolds Stresses," *Journal of Fluid Mechanics*, Vol. 113, pp. 23–51.

Simpson, R. L., Chew, Y. T., and Shivaprasad, B. G., 1981b, "The Structure of a Separating Turbulent Boundary-Layer. Part 2: Higher Order Turbulence Results," *Journal of Fluid Mechanics*, Vol. 113, pp. 53–73.

Sislian, J. P. and Cusworth, R. A., 1986, "Measurements of Mean Velocity and Turbulent Intensities in a Free Isothermal Swirling Jet," *AIAA Journal*, Vol. 24 (2), pp. 303–309.

Smiths, A. J., Young, S. T. B., and Bradshaw, P., 1979, "The Effects of Short Regions of High Surface Curvature on Turbulent Boundary Layers," *Journal of Fluid Mechanics*, Vol. 94, Part 2, pp. 209–242.

Tangirala, V., Chen, R. H., and Driscoll, J. F., 1987, "Effect of Heat Release and Swirl on the Recirculation within Swirl-Stabilized Flames," *Combustion, Science and Technology*, Vol. 51, pp. 75–95.

Tenneskes, H., and Lumley, J. L., 1981, *A First Course in Turbulence*, The MIT Press, Cambridge, MA.

Wu, H., and Fricker, N., 1976, "The Characteristics of Swirl-Stabilized Natural Gas Flames. Part 2: The Behaviour of Swirling Jet Flames in a Narrow Cylindrical Furnace," *Journal of Institute of Fuel*, Vol. 29, pp. 144–151.

Yanta, W. J., and Smith, R. A., 1978, "Measurements of Turbulence-Transport Properties with a Laser Doppler Velocimeter," 11th Aerospace Science Meeting, AIAA Paper No. 73–169.

Zhang, Z. and Wu, J., 1987, "On Principal Noise of Laser-Doppler Velocimeter," *Experiments in Fluids*, Vol. 5, pp. 193–196.

N. T. Obot[2]

M. W. Wambsganss

D. M. France[3]

J. A. Jendrzejczyk

Materials and Components Technology Division,
Argonne National Laboratory,
Argonne, IL 60439

Correlation of Adiabatic Two-Phase Pressure Drop Data Using the Frictional Law of Corresponding States[1]

A method, based on that developed for single-phase flow, is proposed for the correlation of two-phase frictional pressure drop data. It is validated using air-water data obtained on small horizontal passages of rectangular and circular cross-section for values of total mass flux G in the 50–2000 kg/m^{2}s range. The pressure drop for air-water mixtures can be predicted from the proposed correlations provided the critical quality (or superficial gas Reynolds number) and the critical pressure gradient for transition from bubble/plug-to-slug flow are known. A comparison of the proposed method with that of Lockhart and Martinelli is presented and discussed.

1 Introduction

Extensive studies of frictional pressure drop for gas-liquid flows have been made for nearly a half-century. Despite the widespread literature, two-phase pressure drop prediction methods generally have not incorporated fundamental physical phenomena and consequently the resulting correlations include inherent errors. Such correlations are usually validated and optimized over small parametric ranges, but they are not generally applicable without this validation.

In principle, there is no reason that two-phase pressure drop data should not be correlated in terms of friction factor and Reynolds number defined either using the gas or mixture properties. With the latter, which is analogous to the homogeneous two-phase models, the treatment is frustrated by the fundamental difficulty that the physical properties of two-phase mixtures (such as density and viscosity) cannot be determined reliably. For instance, the available predictive equations (Chisholm, 1983) gave large differences in values of mixture viscosity for a specific quality.

It has been common practice to analyze data for two-phase frictional pressure gradients using the concept of friction multipliers, first introduced by Martinelli and co-workers (Lockhart and Martinelli, 1949; Martinelli and Nelson, 1948). It is almost of general knowledge that the Lockhart-Martinelli curves can overpredict gas-liquid and immiscible liquid-liquid data by up to 100 and 200 percent, respectively (Hoogendoorn, 1959; Govier and Omer, 1962; Charles and Lilleleht, 1966; Damianides, 1987; to mention a few).

The difficulty in reconciling the Lockhart-Martinelli method with the various experimental data is the result of a number of factors, the first of which relates to the flow mechanisms. Lockhart and Martinelli postulated, based simply on their data trend, that "a tentative value of 1000" for gas or liquid Reynolds number (Re_G or Re_L) is the upper limit for the existence of laminar isothermal two-phase flow, while the "rough preliminary criteria" for the transition region were reported to be between 1000 and 2000 for Re_G or Re_L. To date, no refinements to these values have been made and little is known about what constitutes laminar or transitional two-phase flow. Also, whether these boundaries vary with duct geometry, total mass flux, or flow direction (i.e., horizontal, vertical or downflow), or the extent to which they may be affected by liquid properties (e.g., viscosity and surface tension), has rarely been acknowledged in the literature. It follows that the corrections that may be needed to account for these factors are unknown.

Another reason for the poor agreement between the Lockhart-Martinelli correlation and experiments is that the friction multiplier Φ_{FL}^2 (or any of the other forms) and the Martinelli parameter $\mathbf{X}$ depend, to a marked extent, on the duct geometry for a fixed total mass flux G and a specified quality range. This is particularly true for small values of $\mathbf{X}$ which correspond to superficial liquid and gas Reynolds numbers in laminar and turbulent flow, respectively. The single-phase gradients in the definitions of Φ_{FL}^2 and $\mathbf{X}$ are geometry dependent, implying that the origin of the effect of duct geometry is transition to turbulent flow. Note that the differences in single-phase friction factor data are intimately associated with this phenomenon (Obot, 1988), and that the single-phase gradients are usually evaluated from the friction factor relations.

Chisholm (1967, 1973) developed a Lockhart-Martinelli type

[1]Based in part on the AIChE paper presented at the National Heat Transfer Conference, Minneapolis, MN, July 28-31, 1991.

[2]Also, Fluid Mechanics, Heat and Mass Transfer Lab., Dept. of Chemical Engineering, Clarkson University, Potsdam, NY 13699-5705.

[3]Also, Dept. of Mechanical Engineering, University of Illinois at Chicago, Chicago, IL 60680.

Contributed by the Fluids Engineering Division for publication in the JOURNAL OF FLUIDS ENGINEERING. Manuscript received by the Fluids Engineering Division January 24, 1992; revised manuscript received September 18, 1992. Associate Technical Editor: M. W. Reeks.

correlation with a coefficient that is dependent on, among other things, the types of flow (laminar and/or turbulent flow) of the liquid and gas. Friedel (1979) developed an empirical correlation using some 25,000 data points. The terms in the correlation include the Froude and Weber numbers, gas and liquid viscosities, friction factors and specific volume as well as the quality. Wambsganss et al. (1990a, 1992) showed that the differences between the actual and the predicted pressure gradients with both correlations can be significant. They modified the Chisholm correlation to optimize predictions over a specific range of interest. However, this useful result does not represent a general approach for predicting pressure drop in an arbitrary two-phase or two-component flow.

The objective of this study was to test the single-phase critical friction method (Obot, 1988; referred to hereafter as the frictional law of corresponding states) with two-phase flow data. The results of these analyses are presented in this paper along with a comparison of the present method with that of Lockhart and Martinelli (1949).

2 Analysis

For single-phase friction, data for smooth circular and noncircular passages were reconciled by accounting for the inseparably connected effects of transition to turbulence and the length scale needed to reduce the data to nondimensional form using the following relation (Obot, 1988; Obot et al., 1990):

$$\mathrm{Re}_m = \psi_R \mathrm{Re}_a; \quad f_m = \psi_f f_a \tag{1}$$

where $\psi_R = \mathrm{Re}_{c,r}/\mathrm{Re}_{c,a}$, $\psi_f = f_{c,r}/f_{c,a}$; $\mathrm{Re}_{c,r}$ and $f_{c,r}$ are the reference values of the critical Reynolds number and friction factor at the onset of transition to turbulent flow, respectively. The Reynolds number, friction factor and the corresponding critical values for any geometric or flow condition of interest are denoted by Re_a, f_a, $\mathrm{Re}_{c,a}$, and $f_{c,a}$. Equation (1) is a mathematical statement of the *frictional law of corresponding states*. It accounts for the variability of the critical parameters at the onset of transition to turbulent flow, and provides a generalized reference state of a physical nature for problem analysis.

Although the concept of two-phase friction factors is not new (Bergelin and Gazely, 1949; Govier and Short, 1958; Beattie, 1975), data correlation in terms of friction factor has been frustrated by two factors; first, the gas or liquid friction factor varies markedly with the total mass flux G and duct geometry; and second, no generally valid approach has been proposed to account for these effects. Of the possible definitions, the most useful form when dealing with data for fixed G values is the two-phase friction factor f_G based on the gas phase properties and it is given by:

$$f_G = \frac{(\Delta P/L)_{TP}\rho_G D_h A^2}{2\dot{M}_G^2} \tag{2}$$

The simplest parameter that could possibly be used to correlate f_G data is the quality x or the superficial gas Reynolds number Re_G; the latter is given by:

$$\mathrm{Re}_G = \dot{M}_G D_h / A\mu_G \tag{3}$$

To calculate f_G using adiabatic air-water data, a constant value of 1.2 kg/m^3 was used for ρ_G, while $\mu_G = 1.85 \times 10^{-5}$ kg/ms was the basis for all calculations of Re_G. It is noted that, for a given G, the superficial liquid Reynolds number Re_L barely changes for low values of quality x, decreases only moderately with x for intermediate quality, but drops off sharply with increasing x for high quality. These considerations prompted the definition of the two-phase friction factors in terms of the mass flowrate of the gas phase.

For two-phase flows, it is well-known that the pressure gradient versus quality curve exhibits a maximum in the vicinity of the transition from bubble/plug to slug flow (Ozawa et al., 1979; Ide and Matsumura, 1990; Wambsganss et al., 1990a, 1991), followed by a minimum with increasing quality. The pressure gradient versus the average flow velocity curve for single-phase flow is also characterized by two critical values. An analogy can then be drawn between the single-phase transition and the change from two-phase bubble/plug-to-slug flow pattern, thus affording the definition of the critical parameters, in particular, the critical quality and critical pressure drop. With the critical parameters established, the two-phase or two-component flow analog of Eq. (1) are given by:

$$\mathrm{Re}_m = (\mathrm{Re}_{c,r}/\mathrm{Re}_{G,ac})\mathrm{Re}_{G,a} = \psi_{R,G}\mathrm{Re}_{G,a} \tag{4}$$

$$x_m = (x_{c,r}/x_{c,a})x_a = \psi_x x_a \tag{5}$$

$$f_m = (f_{c,r}/f_{G,ac})f_{G,a} = \psi_{f,G} f_{G,a} \tag{6}$$

where the subscript c, r refers to the critical parameters for the reference condition.

Nomenclature

A = cross-sectional flow area, m^2
D, D_h = tube diameter, hydraulic diameter, m
f = Fanning friction factor
f_G = two-phase friction factor, Eq. (2)
f_m = reduced friction factor, Eqs. (1) and (6)
G = total mass flux, kg/m^{2}s
L = distance between pressure taps, m
$\dot{M}_G$ = gas phase mass flowrate, kg/s
$(\Delta P/L)_G$ = pressure gradient for gas flowing alone, Pa/m
$(\Delta P/L)_L$ = pressure gradient for liquid flowing alone, Pa/m
$(\Delta P/L)_{L0}$ = pressure gradient for mixture flowing as liquid, Pa/m
$(\Delta P/L)_{TP}$ = two-phase pressure gradient, Pa/m
Re_G = gas phase Reynolds number, Eq. (3)
Re_{L0} = liquid Reynolds number at zero quality
Re_m = similarity parameter, Eqs. (1) and (4)
$\mathbf{X}$ = Martinelli parameter, $[(\Delta P/L)_L/(\Delta P/L)_G]^{1/2}$
$\mathbf{X_m}$ = reduced Martinelli parameter, Eq. (10)
x = quality
x_c = critical quality
x_m = reduced quality or similarity parameter, Eq. (5)
μ_G = gas viscosity, kg/ms
ρ_G = gas density, kg/m^3
Φ_{FL} = square root of friction multiplier Φ_{FL}^2, $[(\Delta P/L)_{TP}/(\Delta P/L)_L]^{1/2}$
$\Phi_{FL,m}$ = value of Φ_{FL} at reduced conditions, Eq. (9)
Φ_{L0}^2 = two-phase friction multiplier, $(\Delta P/L)_{TP}/(\Delta P/L)_{L0}$
ψ_f = ratio of single-phase critical friction factor, Eq. (1)
$\psi_{f,G}$ = ratio of critical friction factor, Eq. (6)
ψ_R = ratio of single-phase critical Reynolds number, Eq. (1)
$\psi_{R,G}$ = ratio of critical Reynolds number, Eq. (4)
ψ_x = ratio of critical quality, Eq. (5)

Subscripts

a = value for arbitrary condition
c, a = critical value for arbitrary condition
c, r = reference critical value
G, a = value for arbitrary condition
G, ac = critical value for arbitrary condition
G, c = critical value

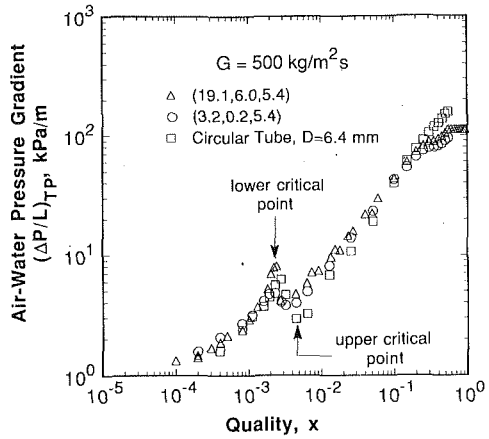

Fig. 1 Variation of air-water pressure gradient with quality (uncertainty in $(\Delta P/L)_{TP}$ = ±5 percent and in x = ±2 percent)

When the two-phase friction factor and Reynolds number are calculated using Eqs. (2) and (3), the two reference critical parameters ($Re_{c,r}$ and $f_{c,r}$) in Eqs. (4) and (6) can be the single-phase data or those for a particular G of the two-phase mixture. The choice of the reduced quality x_m as the similarity parameter instead of Re_m dictates the selection of the critical quality for a particular G as the reference value, but the reference critical friction factor can be taken as that for the particular G or the single-phase value. The denominator for each reference parameter is the two-phase critical value for any G value under consideration, while the remaining data for any such G are denoted by $Re_{G,a}$, x_a and $f_{G,a}$.

3 Experimental Data

The data used to calculate the results presented subsequently were obtained on the Argonne two-phase flow facility with small horizontal passages of rectangular and circular cross-section. The internal diameter of the circular tube was 6.4 mm. The three rectangular configurations are best characterized by (H, A_r, D_h) = (19.1, 6.0, 5.4), (3.2, 0.2, 5.4) and (9.5, 6.0, 2.7), where H is the channel height, A_r is the aspect ratio (H/W, W is the channel width) and D_h is the hydraulic diameter; the dimensions for H and D_h are in mm. The experiments were carried out at atmospheric pressure. The general description of the apparatus and the test procedures are detailed in (Wambsganss et al., 1990a,b, 1991) and will not be repeated here. Tests with the three rectangular arrangements covered a wide range of G values. The circular tube data were obtained only for G = 500 kg/m²s and these were intended to establish whether the general features of the profile for two-phase pressure gradient versus quality (or superficial velocity) were the same as those for the rectangular channels.

4 Results and Discussion

4.1 Two-Phase Flow Critical Parameters. It is emphasized at the outset that the total mass flux G was held fixed with increasing quality x beginning from x = 0, hence each test run was characterized by G and the liquid Reynolds number at zero quality Re_{L0}. The general trends for the critical parameters, illustrated herein using Re_{L0}, complement those given in terms of G in Obot et al. (1991a). Also, the flow regime maps for these narrow channels are not considered in this paper; the interested reader may wish to consult the detailed results in Wambsganss et al. (1991).

4.1.1 Pressure Gradient Versus Quality. Figure 1 shows typical variation of pressure gradient with quality for air-water mixture and G = 500 kg/m²s. This figure establishes that there are basically three regions; $(\Delta P/L)_{TP}$ initially increases with x, attains a maximum and a minimum at some values of x, and then increases with increasing x. It is noted that these general features are clearly in evidence for plots of pressure gradient versus the superficial gas velocity U_{GS} or mixture volumetric flowrate though, due to space limitations, such plots are not shown here. The characteristic features of Fig. 1 were also documented for capillary tubes by Ozawa et al. (1979).

The physical nature of the flow (laminar, transitional or turbulent) in each of the three regions of Fig. 1 is complicated by the fact that, unlike the single-phase counterpart, there are no well established criteria for laminar, transitional or turbulent two-phase flow. According to Ozawa et al. (1979), the intermediate zone of decreasing pressure gradients is the region over which there is a change from bubble/plug-to-slug flow. This is consistent with the results of the flow regime studies for each of the three rectangular geometries (Wambsganss and co-workers, 1991; 1990a,b).

Figure 1 shows that there are small differences between the three sets of data for a fixed G. This is a reflection of the moderate differences in the critical parameters. For instance, the lower critical (peak) values $((\Delta P/L)_{TP,c}, x_c)$ are (5.2, 0.0018), (4.8, 0.0024), and (6.3, 0.0028) for (19.1, 6.0, 5.4), (3.2, 0.2, 5.4) and the circular tube, respectively, with $(\Delta P/L)_{TP,c}$ in kPa/m. Expressed as the critical friction factor and the critical gas Reynolds number $(f_{G,c}, Re_{G,c})$, the values are (in the same order) (21.0, 264.7), (11.0, 350.4), and (12.5, 473.7).

The trends on Fig. 1 imply that, as with single-phase flow (Obot, 1988; Obot et al., 1990), two-phase flows having the same critical parameters, $f_{G,c}$ and $Re_{G,c}$, are dynamically similar to one another and will exhibit similar behavior at the same reduced conditions, either with respect to the flow regime or pressure gradient. This observation, which is central to the treatment of two-phase pressure gradients in this study, prompted a thorough analysis of the data to determine the effects of flow conditions and duct geometric details on the critical parameters.

4.1.2 Determination of Critical Points. Since a typical $(\Delta P/L)_{TP}$ versus x (or superficial gas velocity U_{GS}) profile is characterized by two critical points, the lower and the upper critical points which correspond to the locations of the maximum and minimum, respectively, it is sufficient to consider the lower values, insofar as the application of the corresponding states criterion is concerned. These values, denoted hereafter as $Re_{G,c}$, x_c and $f_{G,c}$, were determined from the pressure drop data for all channel configurations.

Also, for single-phase flow of air or water, it was established that the lower critical point, which corresponds to the onset of transition to turbulence, is exhibited by a sharp rise in the root-mean-square (rms) value of the wall pressure fluctuations (Obot et al., 1991b). Since the general shapes and behavior of the rms pressure profiles with increasing quality for the $0 < x \leq 0.05$ range do not differ materially from those for single-phase flow, the values of the critical quality were also deduced from the rms pressure data from which $Re_{G,c}$ values were calculated. The rms pressure data are given in the original publications from which the data in this paper were taken (Wambsganss et al., 1990a,b).

4.1.3 Trends for Critical Variables. Figures 2 and 3, respectively, are plots of x_c and $R_{G,c}$ versus Re_{L0}. The upper plot of each figure gives the appropriate values determined from the pressure gradient data for the three channel arrangements, while a comparison of the latter set with those deduced from the rms pressure data is given in each of the lower plots for the (19.1, 6.0, 5.4) configuration. The values determined from the two sets of pressure drop data reported by Ozawa et al. (1979) are also given in the upper plots of Figs. 2 and 3. In that study, Re_{L0} was held fixed with increasing superficial gas

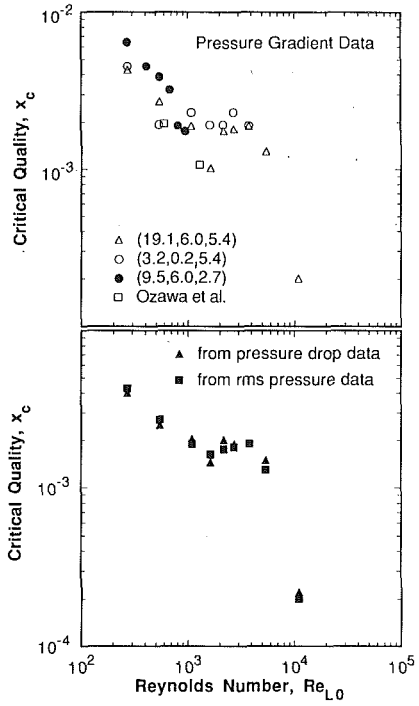

Fig. 2 Critical quality x_c versus liquid Reynolds number at zero quality Re_{L0} (uncertainty in x_c = ±4 percent and in Re_{L0} = ±2 percent)

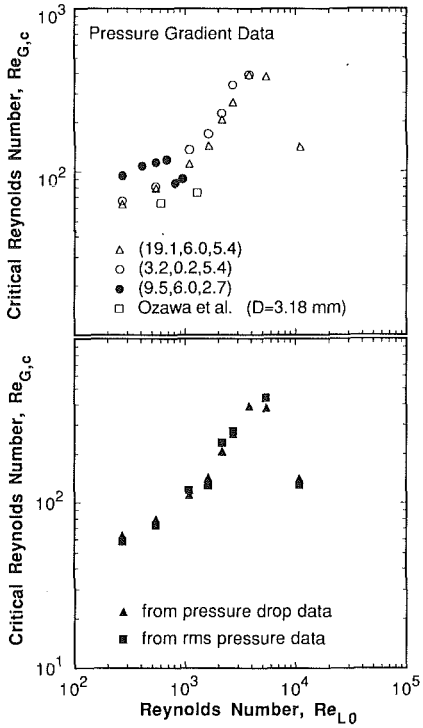

Fig. 3 Critical superficial gas Reynolds number $Re_{G,c}$ versus Re_{L0} (uncertainty in Re_G = ±4 percent)

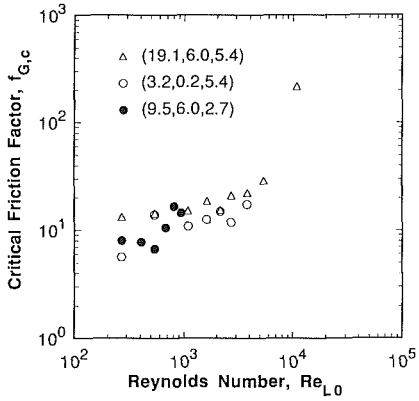

Fig. 4 Two-phase critical friction factor $f_{G,c}$ versus Re_{L0} (uncertainty in $f_{G,c}$ = ±7 percent)

velocity, hence the total mass flux varied with quality. Figure 2 shows that the critical quality decreases initially with Re_{L0}, is almost independent of Re_{L0} for $1000 < Re_{L0} < 4000$, but it drops off sharply when the liquid Reynolds number at zero quality corresponds to turbulent flow.

Figure 3 shows that $Re_{G,c}$ increases with Re_{L0} and passes through a maximum around the Re_{L0} value that corresponds to the onset of fully turbulent flow. It is noted that the lower and the upper values of the critical Reynolds number with air or water flowing alone were 2666 and 3770, respectively. Single-phase friction factors were obtained only with (19.1, 6.0, 5.4) and (9.5, 6.0, 2.7) channel geometries, and the differences between the two sets of critical Reynolds number values were no more than 25.

Whether $Re_{G,c}$ represents the critical Reynolds number below which the flow is laminar will be considered later. Suffice it to state here that these values of $Re_{G,c}$ are considerably lower than the value of 1000 suggested by Lockhart and Martinelli (1949). Also, the results suggest that, for laminar two-phase flow, the critical gas Reynolds number for transition to turbulent flow could very well be expected to depend on the mixture total mass flux and the geometric details of the flow channel.

From Figs. 2 and 3 it is evident that there are some differences between the three sets of data for the rectangular channel, notably at small values of Re_{L0} for which detectable effects of channel geometry on the flow pattern were observed (Wambsganss et al., 1990a,b). The closeness with which the values of x_c or $Re_{G,c}$ deduced from the rms pressure data using the single-phase criterion for transition to turbulence follow those determined from the pressure gradients appears to suggest that laminar two-phase flow may exist for Re_G (or x) $\leq Re_{G,c}$ (or x_c).

Finally, Fig. 4 shows the variation of the two-phase critical friction factor $f_{G,c}$ with Re_{L0}. For a given Re_{L0}, it is emphasized that each value of $f_{G,c}$ is associated with a value of x_c (Fig. 2) or $Re_{G,c}$ (Fig. 3). Figure 4 shows that $f_{G,c}$ increases with increasing Re_{L0}; the rise with liquid Reynolds number is very gradual for values of Re_{L0} in laminar flow. As with Figs. 2 and 3, there is some scatter of the experimental data for low Re_{L0}, a reflection of the differences in the mixture mass flowrate for equal Re_{L0} and channel geometry.

4.2 Two-Phase Friction Factors. Figure 5 is a typical plot of the two-phase friction factor f_G versus superficial gas Reynolds number Re_G for one of the three rectangular channel configurations and various values of G. The alternative representation as f_G versus x is given on Fig. 6; this is a consolidation of all data including those for the circular tube. For clarity, and due to the large amount of experimental data (a total of 720 data points) and parametric information, a uniform symbol is used for all data on Fig. 6. The data for each flow passage, delineated for each G tested, are given in Obot et al. (1991a).

Figure 5 shows that the logarithmic plot of f_G versus Re_G is represented by a series of nearly straight lines with a strong parametric dependence on G, and the slopes of these lines are almost insensitive to variations in mass flux for $Re_G < 10^4$. The alternative plot on Fig. 6 shows that, although the slopes of the lines are almost independent of the mass flux for $x <$

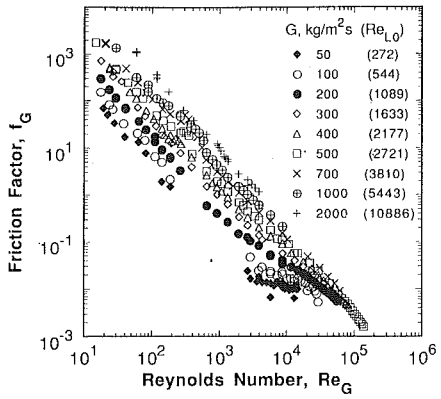

Fig. 5 Two-phase friction factor f_G versus superficial gas Reynolds number Re_G for the (19.1, 6.0, 5.4) channel (uncertainty in $f_G = \pm 7$ percent and in $Re_G = \pm 2$ percent)

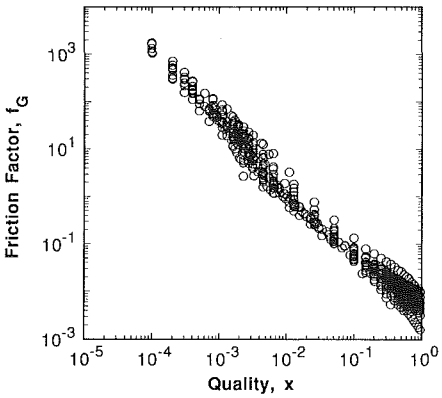

Fig. 6 Variation of two-phase friction factor f_G with quality x for $50 \leq G \leq 2000$ kg/m²s or $272 \leq Re_{L0} \leq 10886$

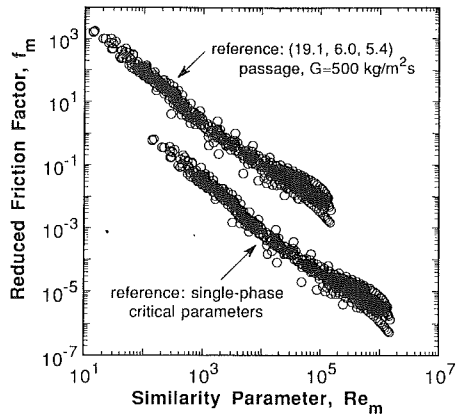

Fig. 7 Reduced friction factor f_m versus similarity parameter Re_m

0.3, the sensitivity of f_G to variations in G for a given x is less pronounced than that for a specified Re_G. This is a reflection of two factors: first, the critical quality is not a strong function of G or Re_{L0} (Fig. 2); and second, quality is a more appropriate parameter than Re_G for characterizing two-phase friction factor f_G because the liquid and gas flowrates are accounted for in its definition. Also, the well pronounced maximum and minimum, observed on the typical plot of Fig. 1, are exhibited by only a slight downward shift in plots of f_G versus Re_G or x (Obot et al., 1991a).

It is established from the present results that f_G varies roughly as the -1.35 and -1.33 power of Re_G and x for $10 < Re_G < 10^5$ and $10^{-4} < x \leq 0.6$ respectively. In other words, the two-phase pressure gradient $(\Delta P/L)_{TP}$ varies roughly as the 0.65 power of the superficial gas velocity U_{GS}. Thus, for a given mass velocity G, the decrease of f_G with Re_G is more pronounced, while $(\Delta P/L)_{TP}$ rises less rapidly with U_{GS}, than when the gas is flowing alone.

Beattie (1971) established three distinct regions for the pressure drop data based on plots of $(\Phi_{L0}^2 - 1)$ versus x (where Φ_{L0}^2 is a friction multiplier): a low quality region, a narrow intermediate zone, followed by a high quality region. Beattie showed that $(\Phi_{L0}^2 - 1)$ varied as the 7/6 power of x for both the low and high quality regions. This exponent was independent of mass flux at low and high qualities, but varied with mass flux in the intermediate zone. Although the pressure drop behavior at low and high qualities is confirmed by the present analysis, Figs. 5 and 6 show that, when the results are presented as f_G versus Re_G or x, the intermediate zone is virtually nonexistent.

Figure 6 shows that, even without the corrections to account for the differences in the critical values for two-phase friction factor and quality, the data for $x \leq 0.2$ can be represented by a mean curve with errors that are, for the most part, under ± 40 percent. In fact, the magnitudes of these deviations are even smaller than those obtained by Wambsganss et al. (1990a,b, 1992) with the Chisholm (1967, 1973) or Friedel correlation. The trend on Fig. 6 suggests that it is possible to treat adiabatic two-phase pressure drop data without the introduction of the usual dependence on the type of flow (laminar and/or turbulent flow of the liquid and gas). Strangely enough, although adiabatic two-phase flow pressure drop has been studied for nearly four decades, straightforward analysis of the type presented herein for variation with x and constant G has not been considered.

It is evident that the effect of G on Fig. 6 is more pronounced over the $x \leq 0.005$ region than for the $0.005 < x \leq 0.2$ range. This is not the result of uncertainties in the measurements. The speculation is that this is a two-phase analog of the single-phase situation where the effects of geometric/flow conditions on friction factor are more pronounced in laminar than turbulent flow. This is another indication that laminar two-phase flow may exist for $x < 0.005$.

Beyond a certain quality, typically in the range of values between 0.4 and 0.6 depending on G, the pressure gradient barely increases with increasing quality. This is reflected in the presence of inflection points followed by a further decrease of f_G with increasing Re_G (or x) for $G \leq 500$ kg/m²s. For $G = 700$, 1000, and 2000 kg/m²s, the upper limits to the range of quality covered in the experiments were 0.35, 0.013 and 0.007 respectively; hence, the profiles for these G values do not exhibit the above behavior.

4.3 Validation of the Proposed Method. As stated earlier, to apply the corresponding states relations, Eqs. (4)–(6), to two-phase flow data, there are two options. The single-phase critical values or the two-phase critical values for a particular G can be selected as the reference. Note that for air or water flowing alone, the values are 2666 and 0.0077 for $Re_{c,r}$ and $f_{c,r}$, respectively.

These two alternative representations of the same experimental data are illustrated in Figs. 7 and 8. In Fig. 7 the upper and the lower set of data are for the situations where the $G = 500$ kg/m²s two-phase critical data for the (19.1, 6.0, 5.4) configuration and the single-phase critical values were selected as the reference, respectively. For Fig. 8, the reference value for the abscissa ($x_c = 0.0018$) is that for the (19.1, 6.0, 5.4) channel and the two-phase critical friction factor ($f_{G,c} = 21.0$) for this channel is also used for the upper plot. The single-phase critical friction factor is the reference for the lower plot. Each profile on Figs. 7 and 8 was prepared using the 720 data points on Fig. 6. For reasons already stated in connection with Fig. 6, a uniform symbol is used for all data.

Figure 7 shows that, despite the marked variation of f_G with G (Fig. 5), the reduced data are closely approximated by single

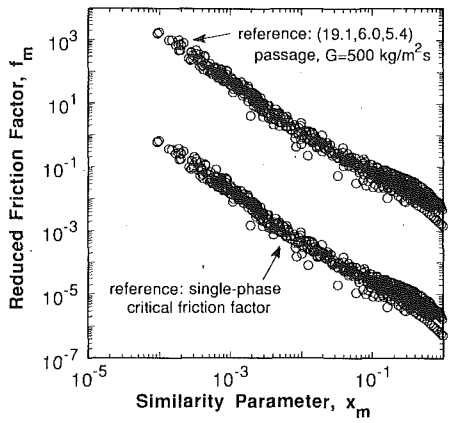

Fig. 8 Reduced friction factor f_m versus similarity parameter x_m

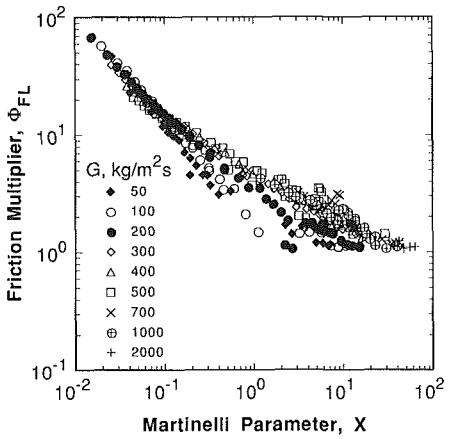

Fig. 9 Plot of Φ_{FL} versus Martinelli parameter X

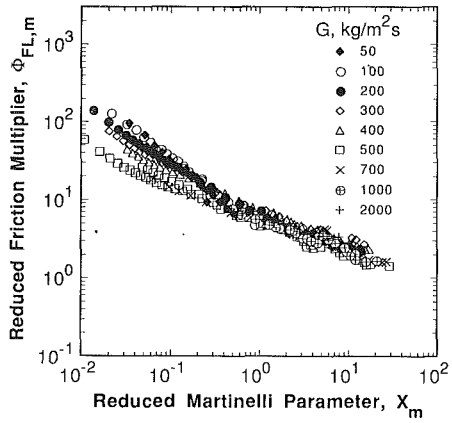

Fig. 10 Plot of $\Phi_{FL,m}$ versus X_m at the same reduced conditions

curves. With x_m as the similarity parameter (Fig. 8), the general behavior of these profiles is exactly the same as on Fig. 7 and there are little detectable differences between the two figures. This establishes Re_m or x_m as the similarity parameter for two-phase friction. Although the general trend is not modified by the choice of the reference critical values, the use of the single-phase data gives profiles that fall well below those obtained with a particular G data as the reference, a reflection of the differences in the calculated values of $\psi_{f,G}$ and $\psi_{R,G}$.

Empirical equations were fitted to each set of data on Figs. 7 and 8. For example, the predictive equation for the lower plot of Fig. 7 is given by:

$$f_m = \exp[A(\mathrm{Re}_m)] \tag{7}$$

where the best-fit expression for $A(Re_m)$ is:

$$A(\mathrm{Re}_m) = a_0 + a_1 \ln \mathrm{Re}_m + a_2(\ln \mathrm{Re}_m)^2 + a_3(\ln \mathrm{Re}_m)^3 \tag{8}$$

and $a_0 = 8.63$, $a_1 = -1.71$, $a_2 = -0.023$ and $a_3 = -0.003$. The validity range is $10^2 \le Re_m \le 10^6$ and the attendant reference critical values (single-phase) are $Re_{c,r} = 2666$ and $f_{c,r} = 0.0077$. The relations established for the other sets of data are given in Obot et al. (1991a). For each empirical correlation, the calculated values were within ±20 and ±30 percent of the experimental data for about 85 and 92 percent of the 720 data points, respectively.

In summary, to calculate two-phase pressure drop for comparable Re_{L0} or G range from Eqs. (7) and (8), the procedures are: 1) obtain estimates of the critical parameters ($Re_{G,ca}$ and $f_{G,ca}$) for the Re_{L0} values of interest from Figs. 3 and 4; 2) calculate Re_m values from $Re_m = (Re_{c,r}/Re_{G,ca})Re_{G,a}$ with $Re_{c,r} = 2666$; 3) compute f_m from Eqs. (7) and (8) and $f_{G,a}$ using $f_{G,a} = (f_{G,ca}/f_{c,r})f_m$ with $f_{c,r} = 0.0077$; and 4) calculate the two-phase pressure drop using values of $f_{G,a}$ from Eq. (2). Note that $Re_{G,a}$ and $f_{G,a}$ are the values for the conditions of interest. The validity range is $50 \le G \le 2000$ kg/m²s or $270 \le Re_{L0} \le 10{,}900$.

4.4 Lockhart-Martinelli Versus Present Method. Figure 9 is a plot of Φ_{FL} (the square root of the friction multiplier Φ^2_{FL}) versus the Martinelli parameter $\mathbf{X}$, prepared using the results on Fig. 5 and the $G = 500$ kg/m²s circular tube data. Due to graphical limitations, the same symbol is used for the rectangular and circular tube data for $G = 500$ kg/m²s. Because the results on Fig. 9 complement those given in Wambsganss et al. (1992), the general features are briefly noted here. The figure shows a family of curves for some range of $\mathbf{X}$ with G as the parameter. The curve for each G passes through a minimum and a maximum for some range of $\mathbf{X}$; the $\mathbf{X}$ locations correspond to the values of quality which afford similar features in the plots of pressure gradient versus quality (Fig. 1).

Given the existence of critical parameters for any G and the fact that the data on Fig. 9 are not generalized, one approach is to re-analyze the data by invoking the following corresponding states relations:

$$\Phi_{FL,m} = (\Phi_{FL,cr}/\Phi_{FL,ac})\Phi_{FL,a} \tag{9}$$

$$\mathbf{X_m} = (\mathbf{X_{c,r}}/\mathbf{X_{c,a}})\mathbf{X_a} \tag{10}$$

where $\Phi_{FL,cr}$ (= 3.5) and $\mathbf{X_{c,r}}$ (= 5.3) are the reference values based on the $G = 500$ kg/m²s data for the (19.1, 6.0, 5.4) rectangular passage. The subscripts a; c, a; FL, ac and FL, a refer to the data for the other G values including those for the circular tube.

Figure 10 shows that the collapse of the $50 \le G \le 2000$ kg/m²s data is good for $\mathbf{X_m} \ge 0.2$; the deviations about a regression curve are, for the most part, under ±20 percent, paralleling the behavior on Figs. 7 and 8. The $\mathbf{X_m} \ge 0.2$ range corresponds to about $\mathbf{X} \ge 0.15$ and $x \le 0.25$ on Figs. 9 and 6, respectively. The spread of the $50 \le G \le 500$ kg/m²s data for $\mathbf{X_m} < 0.2$ is primarily a reflection of the high quality pressure drop trend discussed already in the last paragraph of Section 4.2. The calculation of the gas phase pressure gradients for Re_G values up to 1.5×10^5 from the Blasius equation introduced errors in both $\mathbf{X}$ and $\mathbf{X_m}$, due to the dependence of friction factor for rectangular passages on the aspect ratio (Obot, 1988). Corrections to account for these small errors do not modify the general trend on Fig. 10.

Although the indication is that the Lockhart-Martinelli method can be used, along with the critical parameter corrections, to generalize two-phase pressure drop data over specific parametric ranges, the proposed two-phase friction factor concept is certainly preferred for several reasons, the first of which is simplicity. Also, the critical values for friction factor and Reynolds number are the only single-phase data that may be needed with the proposed method; but these are not required because the two-phase data can always be treated satisfactorily

using the critical parameters for a particular G as the reference for all calculations. From a practical viewpoint, the present method can be used for ducts of complex shapes even without the knowledge of the behavior for single-phase friction factor.

5 Concluding Remarks and Recommendations

To effect the present analysis, the argument was that an analogy can be drawn between single-phase transition to turbulence and the change from bubble/plug to slug flow. Several observations emerged from the results presented so far which tend to support the existence of laminar flow for the range of qualities below the critical point. These include the determination of the critical quality (or superficial gas velocity) using the single-phase method based on the rms pressure data (Figs. 2 and 3) and the greater sensitivity of f_G to G for the $x \leq 0.005$ region than for the $0.005 \leq x \leq 0.2$ range (Fig. 6). More importantly, the fact that the corresponding states method works for single-phase and two-phase flow is an indication that the flow behavior before and after the critical points are similar for both. The logical conclusion therefore is that there exists a well defined laminar two-phase flow zone for $x \leq x_c$ or $\mathrm{Re}_G \leq \mathrm{Re}_{G,c}$, at least when values of the liquid Reynolds number Re_{L0} are in the laminar flow range.

There are indications that the critical parameters are also in evidence for two-phase flow in vertical channels (Govier and Short, 1958; Oshinowo and Charles, 1974). These studies with tube diameters on the order 25.4 mm suggest that the critical parameters do exist for passages with hydraulic diameters that are greater than those considered herein. The implication is that, although the present analysis is made for horizontal passages having small hydraulic diameters, the method may be applicable to vertical flows as well as to larger diameter tubes. Also, the speculation is that the method should work for immiscible liquid-liquid flows because there are indications that these flows are also characterized by critical parameters (Charles and Lilleleht, 1966).

The difficulty in preparing similarity plots using previously published data is explained by the fact that measurements were made for the range of qualities that precluded determination of the critical values for quality and pressure drop. For the few studies that provided low quality data, see for example Ozawa et al. (1979), the analysis was complicated by the fact that the total mass flux was not held fixed with increasing quality. This procedure of acquiring two-phase pressure drop data for fixed G values was not followed in most previous studies.

Finally, the proposed method, like any other method, mandates extensive experimental verification before it can be used with confidence. The relevant low quality data for a range of G values and passage geometries are needed for the purpose of validation. Also, the speculation that the differences in fluid properties will manifest themselves through variations in the critical parameters needs to be verified. Further, in addition to straightforward studies of the prevailing flow patterns, the criteria for laminar, transitional and turbulent two-phase flow must be established because of their impact on compact heat exchanger design.

Acknowledgments

This research was funded by the U.S. Department of Energy, Office of Conservation and Renewable Energy, Division of Advanced Industrial Concepts, Mr. M. E. Gunn, Jr., Program Manager, and represents a U.S. contribution to Annex I of the International Energy Agency (IEA) Program on Research and Development in Heat Transfer and Heat Exchangers.

References

Beattie, D. R. H., 1975, "Friction Factors and Regime Transitions in High Pressure Steam-Water Flows," ASME Paper 75-WA/HT-4, ASME Winter Annual Meeting, Houston.

Beattie, D. R. H., 1971, "Two-Phase Pressure Losses-Flow Regime Effects and Associated Phenomena," Australian Atomic Energy Comm., AAEC/TM 589.

Bergelin, O. P., and Gazely, C., Jr., 1949, "Co-current Gas-Liquid Flow. 1-Flow in Horizontal Tubes," Heat Transfer and Fluid Mechanics Institute, Berkeley, California (published by ASME), pp. 5–18.

Charles, M. E., and Lilleleht, L. U., 1966, "Correlation of Pressure Gradients for Stratified Laminar-Turbulent Pipeline Flow of Two Immiscible Liquids," *Canadian Journal of Chemical Engineering*, Vol. 44, pp. 47–49.

Chisholm, D., 1983, *Two-Phase Flow in Pipelines and Heat Exchangers*, Longmans Inc., New York, pp. 94–96.

Chisholm, D., 1973, "Pressure Gradients due to Friction during the Flow of Evaporating Two-Phase Mixtures in Smooth Tubes and Channels," *International Journal of Heat and Mass Transfer*, Vol. 16, pp. 347–358.

Chisholm, D., 1967, "A Theoretical Basis for the Lockhart-Martinelli Correlation for Two-Phase Flow," *International Journal of Heat and Mass Transfer*, Vol. 10, pp. 1767–1778.

Damianides, C. A., 1987, "Horizontal Two-Phase Flow of Air-Water Mixtures in Small Diameter Tubes and Compact Heat Exchangers," Ph.D. dissertation, University of Illinois at Urbana-Champaign, Urbana, IL.

Friedel, M., 1979, "Improved Friction Pressure Drop Correlation for Horizontal and Vertical Two-Phase Pipe Flow," Paper 2, European Two-Phase Flow Group Meeting, Ispra, Italy.

Govier, G. W., and Omer, M. M., 1962, "The Horizontal Pipeline Flow of Air-Water Mixtures," *Canadian Journal of Chemical Engineering*, Vol. 40, pp. 93–104.

Govier, G. W., and Short, W. L., 1958, "The Upward Vertical Flow of Air-Water Mixtures. II. Effect of Tubing Diameter on Flow Pattern, Holdup and Pressure Drop," *Canadian Journal of Chemical Engineering*, Vol. 36, pp. 195–202.

Hoogendoorn, C. J., 1959, "Gas-Liquid Flow in Horizontal Pipes," *Chemical Engineering Science*, Vol. 9, pp. 205–217.

Ide, H., and Matsumura, H., 1990, "Frictional Pressure Drops of Two-Phase Gas-Liquid Flow in Rectangular Channels," *Experimental Thermal and Fluid Science*, Vol. 3, pp. 362–372.

Lockhart, R. W., and Martinelli, R. C., 1949, "Proposed Correlation of Data for Isothermal Two-Phase, Two-Component Flow in Pipes," *Chemical Engineering Progress*, Vol. 45, pp. 39–48.

Martinelli, R. C., and Nelson, D. B., 1948, "Prediction of Pressure Drop during Forced Circulation Boiling of Water," *Trans. ASME*, Vol. 70, pp. 695–702.

Obot, N. T., Wambsganss, M. W., France, D. M., and Jendrzejczyk, J. A., 1991a, "A Generalized Method for Correlation of Adiabatic Two-Phase Flow Frictional Pressure Drop Data," *AIChE Symposium Series, #283*, Vol. 87, pp. 289–298.

Obot, N. T., Jendrzejczyk, J. A., and Wambsganss, M. W., 1991b, "Direct Determination of the Onset of Transition to Turbulence in Flow Passages," ASME JOURNAL OF FLUIDS ENGINEERING, Vol. 113, pp. 602–607.

Obot, N. T., Esen, E. B., and Rabas, T. J., 1990, "The Role of Transition in Determining Friction and Heat Transfer in Smooth and Rough Passages," *International Journal of Heat and Mass Transfer*, Vol. 33, pp. 2133–2143.

Obot, N. T., 1988, "Determination of Incompressible Flow Friction in Smooth Circular and Noncircular Passages: A Generalized Approach Including Validation of the Nearly Century Old Hydraulic Diameter Concept," ASME JOURNAL OF FLUIDS ENGINEERING, Vol. 110, pp. 431–440.

Oshinowo, T., and Charles, M. E., 1974, "Vertical Two-Phase Flow: Part II. Holdup and Pressure Drop," *Canadian Journal of Chemical Engineering*, Vol. 52, pp. 438–448.

Ozawa, M., Akagawa, K., Sakaguchi, T., Tsukahara, T., and Fujii, T., 1979, "Oscillatory Flow Instabilities in Air-Water Two-Phase Flow System. (1st Report Pressure Drop Oscillation)," *Bulletin of the JSME*, Vol. 22, pp. 1763–1770.

Wambsganss, M. W., Jendrzejczyk, J. A., France, D. M., and Obot, N. T., 1992, "Frictional Pressure Gradients in Two-Phase Flow in a Small, Horizontal, Rectangular Channel," *Experimental Thermal and Fluid Science*, Vol. 5, No. 1, pp. 40–56.

Wambsganss, M. W., Jendrzejczyk, J. A., and France, D. M., 1991, "Two-Phase Flow Patterns and Transitions in a Small, Horizontal, Rectangular Channel," *International Journal of Multiphase Flow*, Vol. 17, pp. 327–342.

Wambsganss, M. W., Jendrzejczyk, J. A., France, D. M., and Obot, N. T., 1990a, "Two-Phase Flow Patterns and Frictional Pressure Gradients in a Small, Horizontal Rectangular Channel," Argonne National Laboratory Report ANL-90/19.

Wambsganss, M. W., Jendrzejczyk, J. A., France, D. M., and Obot, N. T., 1990b, "Two-Phase Flow Patterns and Frictional Pressure Gradients in a Small, Rectangular Channel: A Comparison between Two Horizontal Orientations," Argonne National Laboratory Report ANL-90/46.

Transient Interface Shape of a Two-Layer Liquid in an Abruptly Rotating Cylinder

Tae Gyu Lim

Sangmin Choi

Jae Min Hyun
Mem. ASME

Department of Mechanical Engineering,
Korea Advanced Institute of Science
and Technology,
Yusungku, Taejon 305-701, South Korea

A description is made of the transient shape of interface of a two-layer liquid in an abruptly rotating circular cylinder. The density of the lower layer is higher than that of the upper layer, but the viscosities may assume arbitrary values. The overall Ekman number is much smaller than unity, and the cylinder aspect ratio is 0(1). The classical Wedemeyer model, which deals with the spin-up from rest of a homogeneous fluid, is extended to tackle the two-layer liquid system. If the upper-layer fluid is of higher viscosity, the interface, at small and intermediate times, rises (sinks) in the center (periphery). After reaching a maximum height at the center, the interface tends to the parabolic shape characteristic of the final-state rigid-body rotation. If the lower-layer fluid is of higher viscosity, the interface, at small and intermediate times, sinks (rises) in the center (periphery). The deformation at the center reaches a minimum height, after which the interface approaches the final-state parabola. The gross adjustment process is accomplished over the spin-up time scale, $E_n^{-1/2}\Omega^{-1}$, where E_n and Ω denote the lower value of the Ekman numbers of the two layers and the angular velocity of the cylindrical container, respectively. These depictions are consistent with the physical explanations offered earlier. A turntable experiment is performed to portray the transient interface shape. The model predictions of the interface form are in satisfactory agreement with the laboratory measurements.

1 Introduction

The adjustment process of a viscous fluid in a rotating container has long been a centerpiece in rotating fluid dynamics research. The general term, spin-up, refers to the transient phase of fluid motions when the rotation rate of the container undergoes a change. The classical treatise of Greenspan and Howard (1963) was concerned with a homogeneous fluid in a closed cylindrical vessel when the rotation rate of the container was given a small step change from $\Omega_i \equiv \Omega - \Delta\Omega$ to $\Omega_f \equiv \Omega$, i.e., the Rossby number $\mathrm{Ro} \equiv \Delta\Omega/\Omega \ll 1$.

The linearized mathematical development of Greenspan and Howard is based on the assumption that the Ekman number $E \equiv \eta/\Omega H^2 \ll 1$. Here η is the kinematic viscosity of the fluid, H and R are the height and radius of the cylindrical container, and $H/R \sim 0(1)$ is assumed. This leads to the notion that direct effects of viscosity are confined to the boundary layers on the solid walls and the interior core can be considered to be essentially inviscid. The crucial mechanism is the Ekman layer pumping, which establishes the meridional circulation. In the bulk of interior core, the meridional circulation induces radially inward flows. This brings higher angular momentum radially inward from large radii. Consequently, the angular velocity at a given radial location in the interior increases with time. The transient process is substantially accomplished over the "spin-up timescale", $T_s \equiv \mathrm{E}^{-1/2}\Omega^{-1}$, which is an order of magnitude smaller than the diffusive time scale, $T_d \equiv \mathrm{E}^{-1}\Omega^{-1}$. The model of Greenspan and Howard sets the stage for modern research of spin-up dynamics. Subsequent works provided experimental verifications and further extensions of this basic model (see, e.g., Warn-Varnas et al., 1978; Fowlis and Martin, 1975).

When a homogeneous fluid is abruptly spun-up from the initial state of rest ($\Omega_i = 0$, $\Omega_f = \Omega$), the Rossby number Ro is unity, and the flows are strongly nonlinear. The prominent flow characteristics of this process were captured by an analytical model derived by Wedemeyer (1964). The vital role of the Ekman layer pumping remains to be qualitatively the same as for the linearized spin-up. The Wedemeyer model, with several physically insightful approximations, yields a simplified partial differential equation to describe the dominant azimuthal velocity. The interrelations between the azimuthal and meridional velocities are judiciously postulated. The major stages of adjustment of the global flow field are achieved over the spin-up timescale T_s. The Wedemeyer model has since been the focus of intensive validations, and the qualitative correctness of the model has been documented (e.g., Weidman, 1976; Watkins and Hussy, 1977; Kitchens, 1980a, 1980b; Hyun et al., 1983).

The aforementioned works are concerned with the case when

Contributed by the Fluids Engineering Division for publication in the JOURNAL OF FLUIDS ENGINEERING. Manuscript received by the Fluids Engineering Division March 30, 1992; revised manuscript received November 22, 1992. Associate Technical Editor: A. Prosperetti.

a homogeneous liquid of constant density completely fills the enclosed cylinder. An interesting question arises as to the process of spin-up from rest of a two-layer liquid system. Specifically, considerations are given to spin-up of two layers of immiscible liquids from the initial state of rest in a cylinder. The density of the liquid in the upper layer is lower than that in the lower layer. However, the kinematic viscosities of the two liquids may assume arbitrary values. The dynamics pertinent to this situation lead to an extension of the theory of spin-up from rest of a constant-density completely filled homogeneous fluid. In practical technological applications, the present problem is of direct relevance to centrifugal separation of biological and chemical substances (Berman et al., 1978). In particular, the positions of fluid intakes and discharges should be given careful considerations to obtain maximal efficiency in separative power.

The foregoing observation clearly points to a need to describe accurately the transient shape of the interface during spin-up from rest. A generalized mathematical formulation was developed by Pedlosky (1967), which was restricted to small rotational Froude numbers. Baker and Israeli (1981) addressed the problem of spin-up from rest of immiscible fluids. However, their analysis was limited to the cases of small internal rotational Froude numbers. Consequently, the interface in the above studies remained essentially horizontal. For larger variations in Froude numbers, Berman et al. (1978) examined both analytically and experimentally the behavior of the interface. However, their study was concerned with small deviations from the state of a pre-existing rigid-body rotation, which allowed linearized simplifications. These linearized solutions, therefore, are not directly applicable to the present problem of nonlinear process of spin-up from rest. Some of the qualitative descriptions of the interface, as well as the physical explanations of the linearized formulation, however, are equally valid for the present configuration. Of special interest is the case when the kinematic viscosity of the upper layer is larger than that of the lower layer. For this case, the upper layer attains the final solid-body rotation faster than the lower layer. Consequently, in the intermediate stages, the pressure in the upper layer, due to the centrifugal forces, is lower in the central axis and higher near the cylindrical sidewall. Accordingly, the originally flat interface tends to rise in the central region in the early phases of spin-up. As the bottom layer approaches the rigid-body rotation of the final state, the interface sinks down in the center in the later stages of spin-up, tending to the equilibrium parabola shape characteristic of a perfectly rigid-body rotation. This final-state interface shape is given as, $Z_f(r) = L/H + (R\Omega)^2(2r^2 - 1)/4gH$, in which L is the height of the originally flat interface, r the nondimensional radial coordinate scaled by R, and g the gravity. The rise of the interface in the central portion at early times after spin-up was pointed out and subsequently verified experimentally by Berman et al. (1978) for the afore-stated linearized problem of a pre-existing solid-body rotation. It will be demonstrated in the present study that this phenomenon is more pronounced in spin-up from rest.

The overall purpose of the present work is to portray the transient deformation of the initially flat interface. Laboratory turntable experiments of spin-up from rest are conducted, and the shape of the interface is depicted for two distinctively different configurations, i.e., whether the viscosity of the upper layer is higher or lower than that of the lower layer.

In parallel, the original Wedemeyer model for a homogeneous fluid has been modified to tackle the fluid configuration with a discrete density difference. Comparisons are made between the experimental data and the results based on the amended Wedemeyer model. These exercises indicate that, despite the inherent assumptions and approximations embedded in the Wedemeyer model, the two sets of results are mutually consistent.

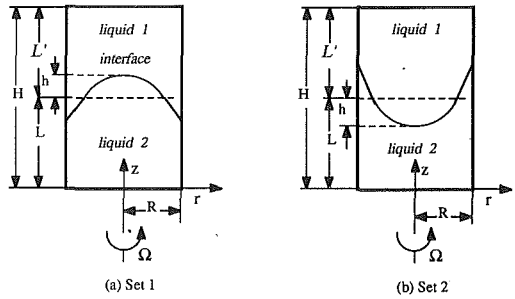

Fig. 1 Schematic diagram of the basic character of interface deformation at early times. (*a*) Set 1; (*b*) Set 2

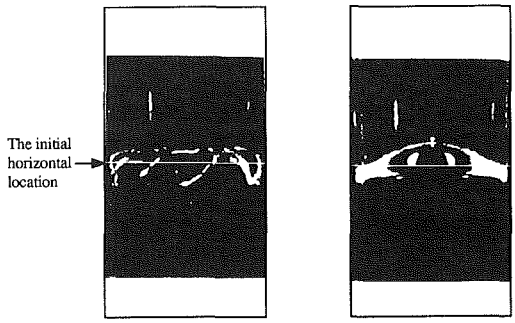

***Fig. 2(a)* A representative photograph showing the visualized interface shape. Conditions are for Set 1. Times are (*a*) 4 s, (*b*) 20 s.**

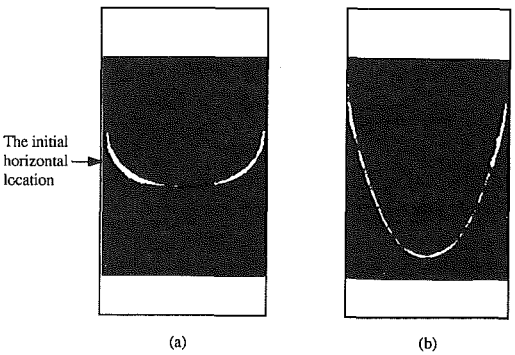

Fig. 2(*b*) The diametical cross section of the visualized interface shape. Conditions are for Set 2. Times are (*a*) 1.5 s, (*b*) 3.5 s

2 The Experiments

A series of controlled experiments was performed. The experimental apparatus consisted of a rotating turntable, a closed cylindrical vessel filled by two layers of immiscible liquids, a slit beam generator, and photographic image recording devices interfaced with a computer. These laboratory facilities have been developed over the years to carry out spin-up experiments of liquid systems. Much of the experimental procedures and measurement techniques was given in detail by the present authors (Choi et al., 1989, 1991) and they will not be repeated here. These experimental rigs were proven to be effective in the prior studies to determine the transient free surface shape during spin-up from rest of a homogeneous liquid.

In the present experiments, two representative sets of liquids were chosen for detailed analysis, i.e.,

Set 1: the upper layer is engine oil [$\rho_1 = 0.87$ g/cm^3, $\eta_1 = 0.3$ cm^2/s],
and the lower layer is water [$\rho_2 = 0.998$ g/cm^3, $\eta_2 = 0.01$ cm^2/s];

Set 2: the upper layer is corn oil [$\rho_1 = 0.922$ g/cm^3, $\eta_1 = 0.55$ cm^2/s], and the lower layer is glycerine [$\rho_2 = 1.235$ g/cm^3, $\eta_2 = 5.5$ cm^2/s].

Clearly, for the two sets, the density of the upper-layer liquid is smaller than that of the lower-layer. The results of Set 1 (2) are representative of the configuration in which the kinematic viscosity of the upper layer is larger (smaller) than that of the lower layer. For simplicity, we treat the case when the depth of the lower layer, L, is the same as that of the upper layer, i.e., $L = H/2$. The time-dependent shape of the interface in the early phases of spin-up can be characterized by the above two representative sets (see Fig. 1 and Fig. 2).

Two cylindrical tanks (one with radius (R) 60 mm and height (H) 224 mm for Set 1; another with R = 45 mm, H = 203 mm for Set 2) were fabricated with plexiglass and precision-machined. The angular velocity (Ω) of Set 1 (Set 2) was 6.4 rad/s (20.4 rad/s). These values of Ω were chosen in such a way that the deformed interface would not hit the bottom endwall disk for the case of Set 2. Also, for Set 1 these experimental parameters were found to generate reasonably smooth temporal variations of the interface. The physical properties of the liquids used in the experiments were determined from the manufacturer-supplied data, and they were reconfirmed by actual measurements. The variations of the properties due to the temperature changes were taken into account by undergoing several test measurements. In the actual implementation of the experiments, the images of the interface deformation were recorded typically at a 1/60 second interval.

3 The Analytical Model

The classical Wedemeyer (1964) model for the spin-up from rest of a completely-filled constant-density fluid is now extended to deal with the two-layer liquid system. The cylindrical frame (r, θ, z), with corresponding velocity components (u, v, w), are used for the analysis. The subscripts 1 and 2 denote the conditions in the upper and lower layers, respectively.

For flows of small Ekman numbers, the transient motion can conceptually be divided into an essentially inviscid interior core and the boundary layers on the solid walls. Within each layer, the fluid density is constant, and, therefore, the simplified version of the momentum equation for v, in nondimensional form, may be obtained for the interior core region,

$$\frac{\partial v_j}{\partial t}+u_j\left(\frac{\partial v_j}{\partial r}+\frac{v_j}{r}\right)=E_j\left(\frac{\partial^2 v_j}{\partial r^2}+\frac{\partial}{\partial r}\left(\frac{v_j}{r}\right)\right) \tag{1}$$

where $j = 1, 2$ to indicate the upper and lower layer. In (1), nondimensionalization has been made by using R, Ω^{-1}, and $R\Omega$ as reference values for length, time, and velocity, respectively.

In order to close the above system, the key step is to postulate a functional relationship between the radial and azimuthal velocity components, and this raises an issue of considerable complexity. In this connection, the approximations of Homicz and Gerber (1986), in dealing with the spin-up from rest of a liquid with a free surface, are useful. In this model, if the free surface intersects only the sidewall, the radial motion in the core is assumed to be made up of the contributions from the bottom Ekman layer, u_{BEL}, and the deformation of the free surface, u_{FS},

$$u=u_{BEL}+u_{FS} \tag{2}$$

Homicz and Gerber (1986), by incorporating several heuristic approximations, expressed u_{BEL} as functions of v and r. The relationship involving u_{FS} was essentially the same as that obtained by Goller and Ranov (1968). The basic reasoning is that, for the free surface motion, the fluid flux across the radial surface at a given radial location should be counterbalanced by the fluid volume change between the central axis and that radial location. Homicz and Gerber employed a slightly amended form of the classical results of Wedemeyer (Kitchens, 1980) to supply the functional relationship for u_{BEL}. These approaches admittedly lacked rigor. However, the goal of the analytical model development at this level was to depict, with reasonable accuracy, the global features of the transient free surface shape. The adequacy of this somewhat heavy reliance on phenomenological viewpoints was justified in this context. The qualitative validity of the results of the model due to Homicz and Gerber was elaborated by experimental observation of the free surface by Choi et al. (1989, 1991).

The approximation schemes of Homicz and Gerber are now similarly applied to the present problem of two-layer liquid system. It is postulated that, in the interior core,

$$u_1=u_{TEL}+u_{I1}$$

$$u_2=u_{BEL}+u_{I2} \tag{3}$$

where u_{TEL} and u_{BEL} denote the radial motions induced by the Ekman layer pumping at the top and bottom endwall disks, respectively. It is noted that radial motions are also generated by the deformation of the interface, which is akin to the situation involving the change of the free surface in the model of Homicz and Gerber. However, unlike the case of a free surface, the Ekman layer-like motions exist in the vicinities of the interface owing to the difference in azimuthal velocities between the two layers. In (3), u_{I1} (u_{I2}) refers to the overall contribution to the radial motion which is caused by the above two effects stemming from the interface deformation.

The equation depicting the interface contour $Z_I = Z_I(r, t)$ can be arrived at by taking into account the force balance, after neglecting the surface tension and viscous stresses (Goller and Ranov, 1969):

$$\frac{\partial Z_I}{\partial r}=F_2\frac{v_2^2}{r}-F_1\frac{v_1^2}{r} \tag{4}$$

in which the vertical coordinate has been normalized by the cylinder height H, and $F_j \equiv (\Omega R)^2/g_j H$ is the Froude number in each layer, and $g_j \equiv g(\rho_2 - \rho_1)/\rho_j$, $j = 1, 2$. Eq. (4) can be integrated to yield

$$Z_I(r,t)=Z_S+F_1\int_r^1\frac{v_1^2}{\zeta}\,d\zeta-F_2\int_r^1\frac{v_2^2}{\zeta}\,d\zeta \tag{5}$$

$$Z_S=\frac{L}{H}-F_1\int_0^1 v_1^2 r\,dr+F_2\int_0^1 v_2^2\,dr \tag{6}$$

where Z_S indicates the interface height at the sidewall.

In accordance with the Wedemeyer model, the interior radial flux induced by the Ekman layer pumping mechanism near the endwall disks is assumed to be distributed uniformly in z in the region between the endwall and the interface. Consequently, as expressed previously (Wedemeyer, 1964; Kitchens, 1980a; Homicz and Gerber, 1987)

$$u_{TEL}=-E_1^{1/2}k_1\frac{R}{H}\frac{r}{(1-Z_I)}f\left(\frac{v_1}{r}\right)$$

$$u_{BEL}=-E_2^{1/2}k_2\frac{R}{H}\frac{r}{Z_I}f\left(\frac{v_2}{r}\right) \tag{7}$$

In (7), the functional form f will be the same as those adopted by Homicz and Gerber:

$$f\left(\frac{v}{r}\right)=\left(\frac{v}{r}-1\right) \tag{8}$$

Furthermore, the empirically adjustable coefficients k_1 and k_2 in (7) are set to be a 1/2, which is consistent with the original Wedemeyer model.

The contributions to the radial motions due to the presence

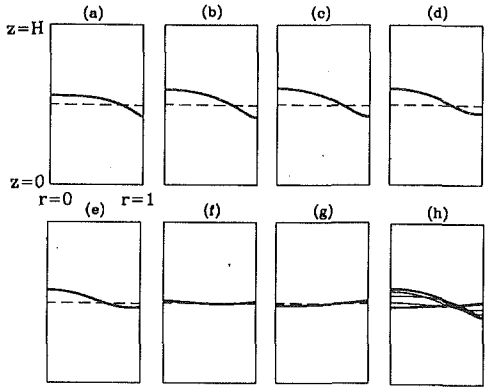

Fig. 3 Transient sequential plots of the interface. Conditions are for Set 1. Times are (*a*) t = 10.0, (*b*) t = 30.0, (*c*) t = 50.0, (*d*) t = 100.0, (*e*) t = 200.0, (*f*) t = 500.0, (*g*) t = 2000.0, (*h*) the interface deformations are overlapped.

of interface are now analyzed. As was conceived by Homicz and Gerber, the radial flow generated by the interface deformation can be equated to the rate of fluid volume change between the central axis and the radial location r. There is an additional element in the present problem involving the interface change. The Ekman layer-like viscous boundary layers exist on both sides of the interface owing to the interface shear. This effect can be modeled in a manner similar to the treatments involving the Ekman layer suction mechanism near solid boundaries (Greenspan, 1969). Combining the above considerations, we have (Berman et al., 1978; Baker and Israeli, 1981)

$$u_{I1}=\frac{(-1)}{r(1-Z_I)}\int_0^r \frac{\partial(1-Z_I)}{\partial t}\,\zeta\partial\zeta - \frac{1}{\beta+1}E_1^{1/2}\frac{R}{H}\frac{r}{1-Z_I}\left\{f\left(\frac{v_1}{r}\right)-f\left(\frac{v_2}{r}\right)\right\}$$

$$u_{I2}=\frac{(-1)}{rZ_I}\int_0^r \frac{\partial Z_I}{\partial t}\,\zeta\partial\zeta - \frac{\beta}{\beta+1}E_2^{1/2}\frac{R}{H}\frac{r}{Z_I}\left\{f\left(\frac{v_2}{r}\right)-f\left(\frac{v_1}{r}\right)\right\} \quad (9)$$

in which $\beta = (\rho_1/\rho_2)(\eta_1/\eta_2)^{1/2}$.

Substituting (3), (7), (8), (9) into (1) produces the desired differential equation having a single unknown in each layer. The initial and boundary conditions are $v_j(r, 0) = 0$, $v_j(0, t) = 0$, and $v_j(1, t) = 1$. The model of Homicz and Gerber (1986) for spin-up from rest of a liquid with a free surface is a special limiting example of the present formulation. It can readily be recovered by setting $\rho_1 = 0$ (for air in the upper layer) in the present formulation.

4 Results and Discussion

Numerical solutions to Eq. (1), together with (3), (7), (8), (9), are acquired by employing a Crank-Nicolson-type difference scheme. The second-order central differences were used for the spatial derivatives. The typical grid sizes were $\Delta r = 0.01$, $\Delta t = 1$, but they were varied appropriately to achieve the desired accuracy and reliability of the solutions.

The transient shape of the interface, as calculated, is now illuminated for the two representative configurations, i.e., Set 1 and Set 2.

Figure 3 displays the time-dependent contour of the interface for Set 1. It is clear that, at small times after the impulsive start of the spin-up, the interface rises in the central portion while it descends near the periphery. The physical mechanism responsible for the rise in the center was explained by Berman et al. (1978). The upper layer has higher viscosity, and, therefore, it attains a near-solid body rotation over a short span of

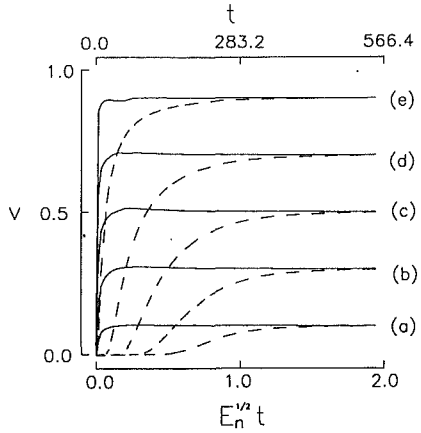

Fig. 4 Evolutions of azimuthal velocities. The radial positions are (*a*) r = 0.1, (*b*) r = 0.3, (*c*) r = 0.5, (*d*) r = 0.7, (*e*) r = 0.9. The velocity in the upper layer is shown by —, and in the lower layer by · · · ·. Conditions are for Set 1. $E_n = E_2$.

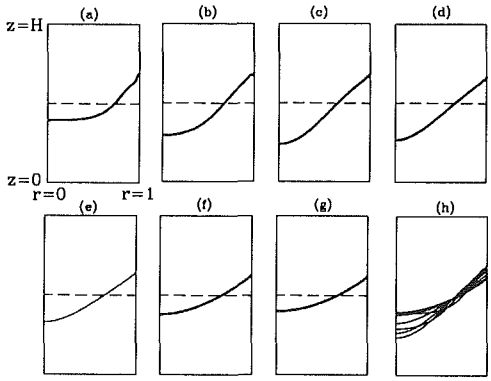

Fig. 5 Transient sequential plots of the interface. Conditions are for Set 2. Times are (*a*) t = 5.0, (*b*) t = 10.0, (*c*) t = 20.0, (*d*) t = 30.0, (*e*) t = 50.0, (*f*) t = 100.0, (*g*) t = 200.0, (*h*) the interface deformations are overlapped.

time. The lower layer needs a much longer adjustment time to reach the near-solid body rotation. The sequential plots of the azimuthal velocity profiles are also shown in Fig. 4. At small and moderate times, the almost rigid body rotation of the upper layer develops a strong radial pressure gradient and, consequently, the pressure in the center (periphery) becomes lower (higher). Because of this pressure distribution, the lower fluid rises (sinks) in the center (periphery). The interface deformation, as exhibited in Fig. 3, is consistent with this picture. As spin-up progresses further, the azimuthal velocity of the lower layer also approaches rigid-body rotation. The interface gradually sinks (rises) in the center (periphery); at large times, it attains the parabolic shape pertinent to the equilibrium state of a complete rigid-body rotation. It is notable in Fig. 4 that the global adjustment processes in both layers are substantially accomplished over the spin-up time scale, which is expressed (in dimensional form) by $E_2^{-1/2}\Omega^{-1}$. For Set 1, the viscosity of the lower layer (η_2) is smaller than that of the upper layer (η_1); consequently, the transient process throughout the entire cylinder is principally governed by the slowly-evolving flow in the lower layer. This spin-up time scale is consistent with the conventional spin-up time scale, which was originally obtained by Greenspan and Howard (1963).

The result of Set 2 is exhibited in Fig. 5, which depicts the transient interface shape. Also shown in Fig. 6 are the time-histories of the azimuthal velocities. The azimuthal velocity in the lower layer, with a higher viscosity, at a given radial location is higher than that in the upper layer. At small times,

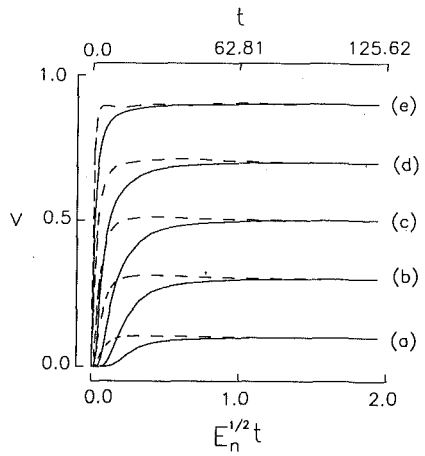

Fig. 6 Evolutions of azimuthal velocities. The radial positions are (*a*) $r = 0.1$, (*b*) $r = 0.3$, (*c*) $r = 0.5$, (*d*) $r = 0.7$, (*e*) $r = 0.9$. The velocity in the upper layer is shown by —, and in the lower layer by · · · ·. Conditions are for Set 2. $E_n = E_1$.

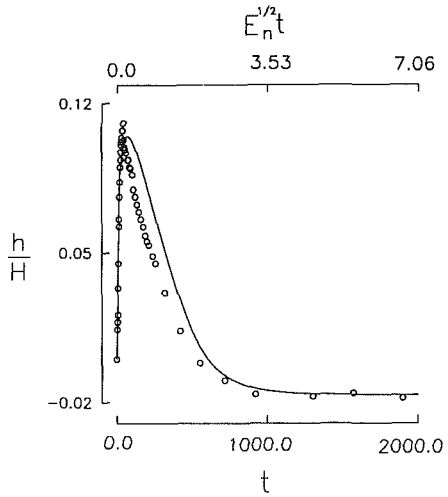

Fig. 7 Comparisons between the analytical model predictions (—) and the laboratory measurements (○) for Set 1. The ordinate shows the interface deformation at the cylinder center, *h*. $E_n = E_2$. [Maximum uncertainty in *h/H* is ± 0.025]

the low (high) pressure region is developed in the lower layer in the center (periphery). The interface sinks (rises) in the center (periphery) at small and intermediate times. At some moderate time instant, the interface level at the center reaches a minimum. This indicates that the difference in azimuthal velocities in two layers is very large. The interface afterwards gradually approaches the final-state equilibrium parabola as spin-up proceeds toward the rigid body rotation in the entire cylinder. As remarked previously, Fig. 6 clearly indicates that the overall adjustment of the fluid system is achieved over the spin-up time scale, $E_1^{-1/2}\Omega^{-1}$. For Set 2, the upper-layer fluid is of lower viscosity, and the gross features in the entire flow field are characterized by the time scale $E_1^{-1/2}\Omega^{-1}$.

The predicted shapes of the interface were compared with the parallel experimental measurements. Much in line with the procedures of Berman et al., comparisons are made by using the interface level at the center, *h*. This procedure is adopted since *h* is easy to monitor in the experiment; also, during the course of spin-up, the change in the interface shape is most pronounced at the center. As illustrated in Fig. 7 for Set 1, the steep rise of the interface at the center at small times is manifest. The slow adjustment to the final state value is also evident. For Set 2, as demonstrated in Fig. 8, the sinking of the interface at the center at small times is clearly discernible.

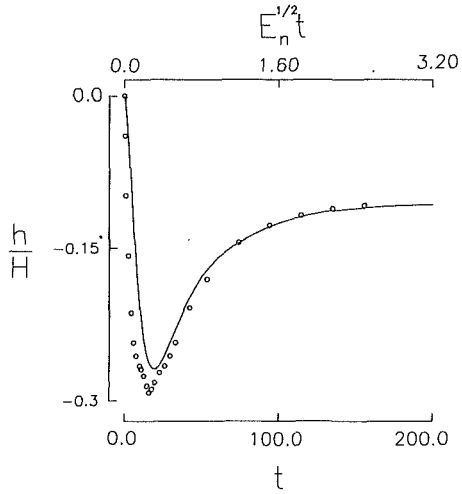

Fig. 8 Comparisons between the analytical model predictions (—) and the laboratory measurements (○) for Set 2. The ordinate shows the interface deformation at the cylinder center, *h*. $E_n = E_1$. (Maximum uncertainty in *h/H* is ±0.025)

The approach to the equilibrium value at large times is also captured well.

Comparisons shown in Figs. 7 and 8 indicate satisfactory agreement between the predictions of the present modified Wedemeyer model and the experiments. In these figures the axial position of the interface was observed first to rise (sink) to a maximum (minimum) height and then to decay (increase) to the level pertinent to the final-state rigid-body rotation.

5 Conclusion

An amended version of the original Wedemeyer model has been constructed to examine the spin-up from rest of a two-layer liquid. For two representative parameter sets, this extended Wedemeyer model has been solved numerically to depict the azimuthal velocity evolutions in the two layers.

If the upper-layer fluid is of higher viscosity, at small and intermediate times, the interface rises (sinks) in the center (periphery). After reaching a maximum height in the center, the interface approaches the parabolic shape characteristic of the final-state rigid-body rotation.

If the lower-layer fluid is of higher viscosity, at small and moderate times, the interface sinks (rises) in the center (periphery). The interface deformation at the center reaches a minimum height; afterwards, the interface tends to the final-state parabolic shape.

These qualitative patterns of the interface deformation are consistent with the physical explanations offered earlier by Berman et al. The parallel experimental measurements are corroborative of the time-dependent shape of the interface which is based on the numerical solution of this extended Wedemeyer model.

Acknowledgment

The authors are grateful to the referees who provided useful comments. These led to substantial improvements in the revised paper. Special appreciation is extended to the referee who returned a detailed, marked-up copy of the manuscript. This work was supported in part by research grants from the Korea Science and Engineering Foundation.

References

Baker, G. R., and Israeli, M., 1981, "Spinup from Rest of Immiscible Fluids," *Studies in Applied Mathematics*, Vol. 65, pp. 249–268.

Berman, A. S., Bradford, J., and Lundgren, T. S., 1987, "Two-Fluid Spin-Up in a Centrifuge," *Journal of Fluid Mechanics*, Vol. 84, Part 3, pp. 411–431.

Choi, S., Kim, J. W., and Hyun, J. M., 1989, "Transient Free Surface Shape in an Abruptly-Rotating, Partially-filled Cylinder," ASME JOURNAL OF FLUIDS ENGINEERING, Vol. 111, pp. 431–439.

Choi, S., Kim, J. W., and Hyun, J. M., 1991, "Experimental Investigation of the Flow with a Free Surface in an Impulsively Rotating Cylinder," ASME JOURNAL OF FLUIDS ENGINEERING, Vol. 113, pp. 245–249.

Fowlis, W. W., and Martin, P. J., 1975, "A Rotating Laser Doppler Velocimeter and Some New Results on the Spin-Up Experiment," *Geophysical Fluid Dynamics*, Vol. 7, pp. 67–78.

Goller, H., and Ranov, T., 1968, "Unsteady Rotating Flow in a Cylinder with a Free Surface," ASME *Journal of Basic Engineering*, Vol. 90, No. 4, pp. 445–454.

Greenspan, H. P., 1969, *The Theory of Rotating Fluids*, Cambridge University Press, New York, NY.

Greenspan, H. P., and Howard, L. N., 1963, "On a Time Dependent Motion of a Rotating Fluid," *Journal of Fluid Mechanics*, Vol. 17, Part 3, pp. 385–404.

Homicz, G. F., and Gerber, N., 1987, "Numerical Model for Fluid Spin-Up from Rest in a Partially Filled Cylinder," ASME JOURNAL OF FLUIDS ENGINEERING, Vol. 109, pp. 195–197.

Hyun, J. M., Leslie, F., Fowlis, W. W., and Warn-Varnas, A., 1983, "Numerical Solutions for Spin-Up from Rest in a Cylinder," *Journal of Fluid Mechanics*, Vol. 127, 1983, pp. 263–281.

Kitchens, C. W. Jr., 1980a, "Ekman Compatibility Conditions in Wedemeyer Spin-Up Model," *Physics of Fluids*, Vol. 23, pp. 1062–1064.

Kitchens, C. W. Jr., 1980b, "Navier-Stokes Equations for Spin-Up in a Filled Cylinder," *AIAA Journal*, Vol. 18, No. 8, pp. 929–934.

Pedlosky, J., 1967, "The Spin Up of a Stratified Fluid," *Journal of Fluid Mechanics*, Vol. 28, Part 3, pp. 463–479.

Warn-Varnas, A., Fowlis, W. W., Piacsek, S., and Lee, S. M., 1978, "Numerical Solutions and Laser-Doppler Measurements of Spin-Up," *Journal of Fluid Mechanics*, Vol. 85, pp. 609–639.

Watkins, W. B., and Hussey, R. G., 1977, "Spin-Up from Rest in a Cylinder," *Physics of Fluids*, Vol. 20, No. 10, pp. 1596–1604.

Wedemeyer, E. H., 1964, "The Unsteady Flow within a Spinning Cylinder," *Journal of Fluid Mechanics*, Vol. 20, Part 3, pp. 383–399.

Weidman, P. D., 1976, "On the Spin-Up and Spin-Down of a Rotating Fluid. Part I: Extending the Wedemeyer Model. Part II: Measurements and Stability," *Journal of Fluid Mechanics*, Vol. 77, Part 4, pp. 685–735.

Journal of Fluids Engineering

Technical Briefs

Unsteady Flow of a Power-Law Dusty Fluid With Suction

Ali J. Chamkha[1]

Equations governing flow of a particulate suspension exhibiting finite volume fraction in non-Newtonian power-law fluids are developed and applied to the problem of unsteady flow past an infinite porous flat plate with suction. Numerical results for small volume fraction for the displacement thicknesses for both phases and the skin-friction coefficient for the fluid phase are obtained using an implicit finite difference scheme and presented graphically to elucidate interesting features of the solutions.

Introduction

Much of the two-phase (particle-fluid) flow research treats the fluid phase as Newtonian in nature. This is because this type of fluids exhibits a linear relationship between the shear stress and the shear rate. However, many fluids of practical applications are non-Newtonian. Since particulate suspensions in non-Newtonian power-law fluids are encountered in wide variety of the process industry, it is of interest to understand their characteristics.

The problem of steady single-phase flow of a Newtonian fluid past a flat plate with uniform suction was solved exactly and reported some time ago by Schlichting (1955). Kapur (1963) obtained steady-state solutions for flow of pseudo-plastic and dilatant power-law fluids past a porous flat plate. Chamkha and Peddieson (1989) reported solutions for unsteady flow of a particulate suspension past an infinite flat plate with uniform fluid-phase suction. In their work, Chamkha and Peddieson (1989) considered only Newtonian fluids.

The aim of this paper is to extend the work of Chamkha and Peddieson (1989) to particulate suspensions in non-Newtonian power-law fluids. Both phases are modeled as interacting continua and the interphase forces between the two phases is modeled by Stokes linear drag theory. The continuum modeling approach of two-phase suspensions has been the subject of numerous papers (see, for instance, Hinze, 1963). The advantages of this approach lie in the simplification of the general transport equation of kinetic theory of flow by replacing phase change coordinates with space coordinates. This is done through the introduction of phenomenological relations and transport properties to account for viscous stresses, heat fluxes, and mass generations. In addition, this approach is applicable to fluids (such as liquids) whose microscopic details are unknown (see, Soo, 1990).

Governing Equations

Let the plate be situated along the x-axis at $y=0$ with the y-axis being normal to it. Let the flow be a uniform stream in the x-direction parallel to the plate. Far above the plate, assume that both phases are in equilibrium and moving with the free stream velocity V_∞. Further assume that fluid-phase suction with velocity V_s is imposed at the plate surface. In the development of the governing equations, it is also assumed that both phases are incompressible, the fluid-phase pressure gradient is negligible, and the volume fraction of suspended particles is finite and uniform.

To formulate the governing equations for the problem described above, the balance laws of mass and linear momentum for both the fluid and particulate phases along with constitutive equations for the stress tensors and the interphase force are used.

The balance laws of mass (for the fluid and particulate phases, respectively) can be written as

$$\partial_t \phi - \nabla \cdot ((1-\phi)\mathbf{V}) = 0,\ \partial_t \phi + \nabla \cdot (\phi \mathbf{V}_p) = 0 \qquad (1)$$

where ϕ is the particulate volume fraction, ∇ is the gradient operator, $\mathbf{V}$ is the fluid-phase velocity vector, and $\mathbf{V}_p$ is the particulate-phase velocity vector.

The balance laws of linear momentum (for the fluid and particulate phases, respectively) can be written as

$$\rho(1-\phi)(\partial_t \mathbf{V} + \mathbf{V} \cdot \nabla \mathbf{V}) = \nabla \cdot \underline{\underline{\sigma}} - \mathbf{f},\ \rho_p \phi(\partial_t \mathbf{V}_p + \mathbf{V}_p \cdot \nabla \mathbf{V}_p) = \nabla \cdot \underline{\underline{\sigma}}_p + \mathbf{f} \qquad (2)$$

where ρ is the fluid-phase density, $\underline{\underline{\sigma}}$ is the fluid-phase stress tensor, $\mathbf{f}$ is the interphase force per unit volume acting on the particle phase, ρ_p is the particle-phase density, and $\underline{\underline{\sigma}}_p$ is the particle-phase stress tensor.

Equations (1) and (2) are supplemented with the following constitutive equations

$$\underline{\underline{\sigma}} = (1-\phi)(-P\underline{\underline{I}} + 2\mu(\mathrm{II}, \phi)\underline{\underline{D}})$$

$$\underline{\underline{\sigma}}_p = \phi(-P_p\underline{\underline{I}} + 2\mu_p(\mathrm{II}_p, \phi)\underline{\underline{D}}_p)$$

$$\underline{\underline{D}} = \frac{1}{2}(\nabla \mathbf{V} + \nabla \mathbf{V}^T),\ \underline{\underline{D}}_p = \frac{1}{2}(\nabla \mathbf{V}_p + \nabla \mathbf{V}_p^T)$$

$$\mathrm{II} = \underline{\underline{D}} : \underline{\underline{D}},\ \mathrm{II}_p = \underline{\underline{D}}_p : \underline{\underline{D}}_p,\ \mathbf{f} = N\rho_p\phi(\mathbf{V} - \mathbf{V}_p) \qquad (3)$$

where P is the fluid-phase pressure, P_p is the particle-phase pressure, $\underline{\underline{I}}$ is the unit tensor, μ is the fluid-phase dynamic viscosity, μ_p is the particle-phase dynamic viscosity, $\underline{\underline{D}}$ is the fluid-phase rate of strain tensor, $\underline{\underline{D}}_p$ is the particle-phase rate of strain tensor, II is the second invariant of $\underline{\underline{D}}$, II_p is the second invariant of $\underline{\underline{D}}_p$, N is a momentum transfer coefficient,

[1]Staff Research Engineer, Fleetguard, Inc., Cookeville, TN 38502. Mem. ASME.

Contributed by the Fluids Engineering Division of The American Society of Mechanical Engineers. Manuscript received by the Fluids Engineering Division June 4, 1992; revised manuscript received December 2, 1992. Associate Technical Editor: M. W. Reeks.

and a superposed T denotes the transpose of a second-order tensor. In the present work ρ, ρ_p, and N will all be treated as constants.

For small particulate volume fraction ($\phi \ll 1$) $\mu = \mu(\text{II}) = (2\text{II})^{(n-1)/2}$ (n is a behavior coefficient), $\mu_p = 0$ (negligible particle-particle interaction), and $P_p = 0$ (see, for instance, Marble, 1970). The behavior coefficient n determines whether the fluid is Newtonian ($n = 1$) or non-Newtonian ($n \neq 1$).

It is convenient to nondimensionalize the governing differential equations given previously for small volume fraction by using

$$t = \nu\tau/V_\infty^2,\ y = \nu\eta/\mathbf{V}_\infty,\ \mathbf{V} = \mathbf{e}_x V_\infty F(\tau, \eta) - \mathbf{e}_y \mathbf{V}_s$$
$$\mathbf{V}_p = \mathbf{e}_x \mathbf{V}_\infty F_p(\tau, \eta) - \mathbf{e}_y \mathbf{V}_s,\ \nu = V_\infty^{2(1-1/n)}\ (c/\rho)^{1/n} \quad (4)$$

where c is a constant and $\mathbf{e}_x$ and $\mathbf{e}_y$ are unit vectors in the x and y directions, respectively.

Substituting Eqs. (4) into Eqs. (1) through (3) and rearranging yield

$$\partial_\tau F - \partial_\eta((\partial_\eta F)^n) - r_v\,\partial_\eta F + \kappa\alpha(F - F_p) = 0 \quad (5)$$

$$\partial_\tau F_p - r_v \partial_\eta F_p - \alpha(F - F_p) = 0 \quad (6)$$

where $r_v = V_s/V_\infty$, $\kappa = \rho_p\phi/\rho$, $\alpha = N\nu/V_\infty^2$ are the suction parameter, the particle loading, and the inverse Stokes number, respectively. Equations (5) and (6) represent the non-Newtonian power-law version of the dusty-gas model discussed by Marble (1970). It should be mentioned that ρ_p/ρ is very large and ϕ is very small such that $\rho_p\phi/\rho$ is finite. Therefore, κ could be equal to 1, 10, or even 100 and still apply to low particulate concentrations.

The initial and boundary conditions used to solve Eqs. (5) and (6) are

$$F(0,\eta) = 1.0,\ F_p(0, \eta) = 1.0,\ F(\tau, 0) = 0$$
$$\lim_{\eta\to\infty} F(\tau, \eta) = 1.0,\ \lim_{\eta-\infty} F_p(\tau, \eta) = 1.0 \quad (7)$$

The fluid-phase displacement thickness, the particle-phase displacement thickness, and the fluid-phase skin-friction coefficient are defined as follows:

$$\delta = \int_0^\infty (1-F)d\eta,\ \delta_p = \int_0^\infty (1-F_p)\,d\eta,\ C_f = (\partial_\eta F(\tau, 0))^n \quad (8)$$

Results

Closed-form solutions of Eqs. (5) and (6) are possible for dilute suspensions ($\kappa = 0$) and steady-state conditions. When $\kappa = 0$, the fluid-phase motion is independent of the presence of particles and Eq. (5) can be solved for F subject to Eqs. (7) to yield

$$F = 1 - (1 - (n-1)/n r_v^{1/n}\eta)^{n/n-1)} \quad (9)$$

The corresponding form of F_p obtained by solving Eq. (6) and using Eq. (9) is

$$F_p = 1 - \alpha/r_v\,\exp(\alpha/r_v\eta)\int_\eta^\infty \exp(-\alpha/r_v\eta)$$
$$\times(1-(n-1))/n r_v^{1/n}\eta)^{\,n/(n-1)}d\eta \quad (10)$$

Equation (10) can be carried out for specific values of n. In general, it can be solved numerically for any value of n. For a dilatant fluid ($n > 1$) it can be shown from Eq. (9) that the fluid-phase tangential velocity F approaches the free stream value after a finite height above the plate. This is given by

$$\eta_0 = n/((n-1)\,r_v^{1/n}) \quad (11)$$

Thus,

$$F = 1 - (1 - \eta/\eta_0)^{n(n-1)};\ \eta \le \eta_0$$
$$F = 1 \qquad ;\ \eta > \eta_0 \quad (12)$$

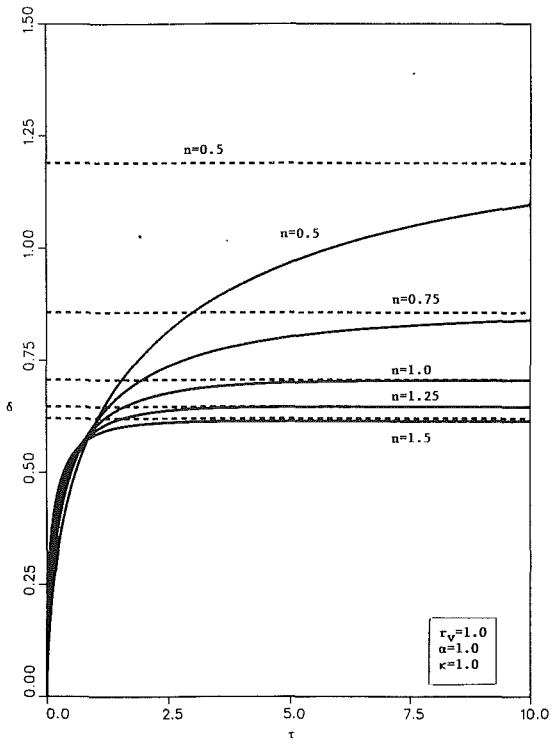

Fig. 1 Fluid-phase displacement thickness profiles

$$F_p = 1 - \alpha/r_v\,\exp(\alpha/r_v\eta)\int_\eta^{\eta_0} \exp(-\alpha/r_v\eta)(1-\eta/\eta_0)^{n/(n-1)}d\eta$$
$$;\eta \le \eta_0$$
$$F_p = 1 \qquad ;\eta > \eta_0 \quad (13)$$

The integral appearing in Eq. (13) can be carried out further for some values of $n > 1$ such that $k = n/(n-1)$ is an integer. This can be shown to give

$$F_p = 1 - \sum_{r=1}^{\infty}((-1)^r k!(1-\eta/\eta_0)^{k-r})/(k-r)!(\alpha/r_v\eta_0)^r);\eta \le \eta_0 \quad (14)$$

The initial-value problem consisting of Eqs. (5) through (7) is solved numerically using an extension of the implicit finite difference method described by Blottner (1970) to two-phase flow. The main components of the numerical method is the application of variables step sizes in the η and τ directions, and the iteration procedure. Since the largest changes in the dependent variables are expected to occur in the region close to the plate's surface, a small step size in η is used there to accurately approximate the derivatives numerically. On the other hand, far from the plate small changes in the dependent variables are expected. Therefore, a larger step size in η is used there. The initial step size close to the wall $\Delta\eta_1$ used was equal to 0.001. A constant small step size in τ is used (specifically $\Delta\tau = 0.001$) throughout the numerical computations. A representative set of graphical results will be presented and discussed below to illustrate the effects of the behavior coefficient n and the particle loading κ on the solutions.

Figures 1 and 2 show the development of the displacement thicknesses for both the fluid and particulate phase, respectively with time for various behavior coefficient values. The dotted lines in these and subsequent figures correspond to the steady-state solutions reached at large values of τ. It can be seen from these figures that particulate suspensions in dilatant fluids ($n > 1$) approach steady-state conditions faster and have lower displacement thicknesses than those of pseudo-plastic

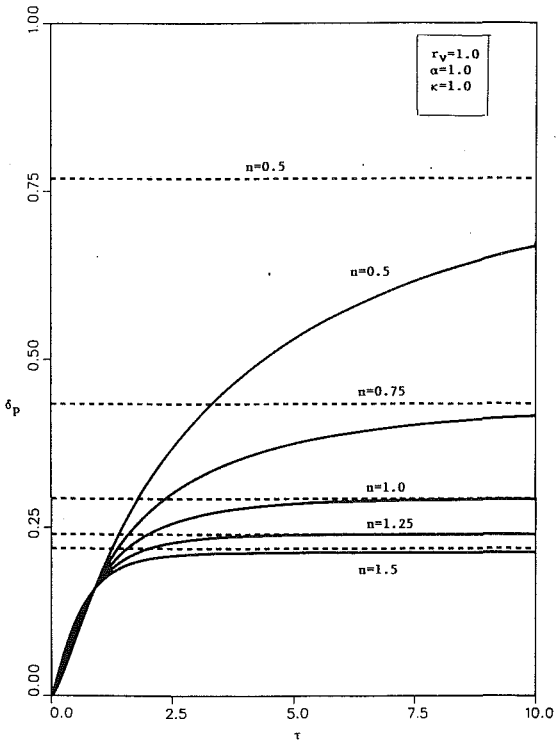

Fig. 2 Particle-phase displacement thickness profiles

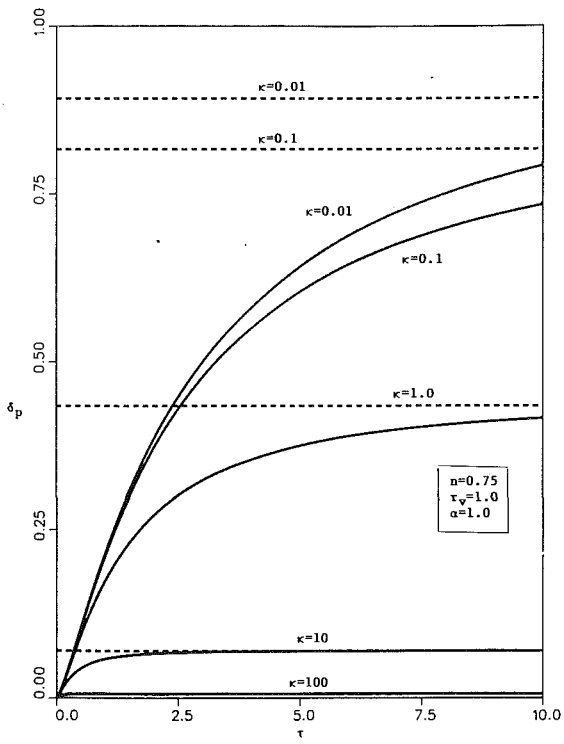

Fig. 4 Particle-phase displacement thickness profiles

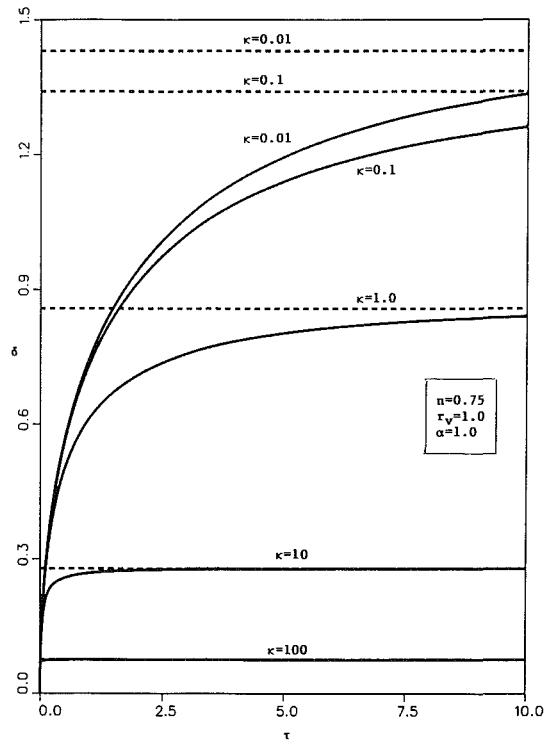

Fig. 3 Fluid-phase displacement thickness profiles

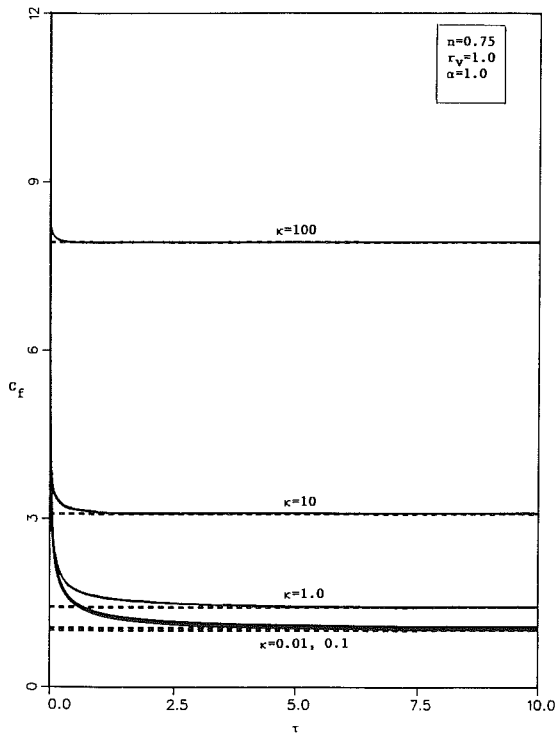

Fig. 5 Fluid-phase skin friction profiles

particulate suspensions. It should be mentioned that while increases in n have a significant effect on δ and δ_p, they appear to have little effect on C_f (figure not shown for brevity).

Figures 3 through 5 illustrate the behavior of δ, δ_p, and C_f versus time for $n=0.75$ and various values of κ, respectively. Increases in the particle loading κ have the tendency to confine viscous effects to an increasingly small region close to the plate surface. This, in turn, causes the slope of the fluid-phase velocity profile at the wall to increase. This is reflected in the decreases in both δ and δ_p and the increases in C_f as κ increases. In Fig. 5 C_f is very large for $\tau << 1$. This is associated with the singularity at $\tau=0$ and is not shown due to the scale of the figure. It should be mentioned that the exact solutions for the dilute limit presented earlier were used as a check on the

numerical method and were found to be in excellent agreement with the numerical results.

Conclusions

The transient behavior of a power-law dusty fluid flow past an infinite porous flat plate is solved numerically using an implicit finite-difference scheme. Closed-form solutions for the velocity profiles associated with the dilute steady-state limit are reported. A representative set of graphical results (chosen from many) is presented and discussed. It is hoped that the present work be used as means for understanding more complex problems involving non-Newtonian power-law particulate suspensions.

References

Blottner, F. G., 1970, "Finite Difference Methods of Solutions of the Boundary-Layer Equations," *AIAA Journal*, Vol. 8, pp. 193–205.

Chamkha, A. J., and Peddieson, J., 1989, "Unsteady Dusty-Gas Flow with Suction," presented at the 27th Annual meeting of the Society of Engineering Science.

Hinze, J. O., 1963, "Momentum and Mechanical-Energy Balance Equations for a Flowing Homogeneous Suspension with Slip Between the Two Phases," *Applied Scientific Research*, Vol. A11, pp. 33–46.

Kapur, J. N., 1963, "Flows of Power-Law Fluids Past a Flat Plate with Uniform Suction and Between Two Parallel Plates with Uniform Suction and Injection," *Journal of Physics Society*, Japan, Vol. 18, pp. 578–582.

Marble, F. E., 1970, "Dynamics of Dusty Gases," *Annual Review of Fluid Mechanics*, Vol. 2, pp. 397–446.

Schlichting, H., 1955, *Boundary Layer Theory*, Pergamon Press, pp. 230–232.

Soo, S. L., 1990, *Multiphase Fluid Dynamics*, Science Press, pp. 303–355.